

**IMPLEMENTING METABOLOMICS TOOLS IN THE
SEARCH OF ANTIOXIDANT AND ANTICANCER
AGENTS FOR BREAST CANCER FROM EUROPEAN
AND JORDANIAN CHAMOMILE AND ITS
ASSOCIATED ENDOPHYTES**

BY

DANA ADNAN MOH'D ATOUM

B.Sc., M.Sc.

Strathclyde Institute of Pharmacy

and Biomedical Sciences (SIPBS), Glasgow, UK

A thesis submitted to The University of Strathclyde in fulfilment of the
requirements for the degree of Doctor of Philosophy

May 2022

Declaration

This thesis is the result of the author's original research. It composed by the author and has not been previously submitted for examination which has led to award of the degree.

The copyright of the thesis belongs to the author under the terms of the United Kingdom Copyright Acts as qualified by the University of Strathclyde regulation 3.50. Due acknowledgment must always be made of the use of any material contained in or derived from this thesis.

Signed:

Date:

Acknowledgements

First and foremost, I would like to express my gratitude Allah for giving me the strength to accomplish this study and blessing me throughout my whole life. I would not be who I am without his blessings, care, and direction.

I would like to express my deepest gratitude to my supervisor, Dr RuAngelie Edrada-Ebel, for allowing me to be one of her students and for her extensive knowledge, patience, and encouragement. I owe her much for my skills as a researcher. Her encouragement, counsel, assistance, and direction were priceless. She is the best supervisor I could ever have! I would also want to thank my second supervisor, Mrs Louise Young, for her assistance with tissue culture and cytotoxicity tests. I would like also to pay my regards to Dr Rothwelle Tate for his help in PCR and ITS gene sequencing, Mr Craig Irving and Dr John Parkinson for allowing me to use their NMR facility in the Chemistry

Moreover, I am extremely grateful for the Hashemite University (HU) for generously funding my Ph.D.

I thank my fellow labmates in the Natural Products Metabolomics Group: Dr Ignacio, Dr Saif, Katarina, Kirsty and Elizabeth for their friendship and help. I wouldn't have enjoyed my last three years if you weren't there!

A very special gratitude goes out to my friends in Glasgow: Dr Rana, Suzan, Haya, Fatema, Rana T and Wasan for their precious loves and supports at any time.

And last but not least, I dedicate my heartfelt thanks to my beloved husband, Mustafa, who supports me all the time. I am also very blessed to have Dina and Ayla (my precious daughters) in my life. I would like to express my full gratitude and love for my amazing parents for their contributions throughout my whole life. Without them, my life achievements would be much harder to attain. God bless them and keep them healthy for the rest of their lives. In addition, I'd like to express my gratitude to my father-in-law Dr Haider (may his soul rest in peace), my mother-in-law Dina, my brothers Yazan, Mohammad, Ezzeddine, and my in-laws Areen, Mohammad, and Makram for their endless love, support, and prayers.

Publications and Poster Presentations

Murshid SSA, **Atoum D**, Abou-Hussein DR, Abdallah HM, Hareeri RH, Almukadi H, Edrada-Ebel R. (2022) Genus *Salsola*: Chemistry, Biological Activities and Future Prospective-A Review. *Plants (Basel)*. Mar 8;11(6):714. doi: 10.3390/plants11060714. PMID: 35336596; PMCID: PMC8953912.

Atoum D., Young L., Edrada-Ebel R., and Fernandez-Pastor I. “Use of multivariable data analysis in unravelling the metabolic differences between two varieties of Chamomile (*Matricaria chamomilla*)”. Poster presentation

5th Scottish Metabolomics Network Symposium. Nov 2019. Glasgow, UK.

16th Annual Conference of the Metabolomics Society. 27th -29th Oct 2020 Online

II Bio.Natural-Bioactive Natural Products Research. 18th-19th Nov 2021 Online

Table of Contents

Declaration	2
Acknowledgements	3
Publications and Poster Presentations	4
Table of Contents	5
List of Tables.....	16
List of Figures	19
Abbreviations	32
Abstract	35
1. Introduction.....	37
1.1. Drug discovery	37
1.2. Introduction to natural products	38
1.3. Natural products from plants in drug discovery	40
1.4. The role of endophytes in the production of secondary metabolites.....	42
1.5. Plant-endophyte interactions	44
1.6. Plant-endophyte interactions uses and benefits.....	45
1.7. Obstacles to work with plant-associated endophytes	46
1.8. <i>Matricaria chamomilla</i> , <i>Chamaemelum nobile</i> . Asteraceae	47
1.8.1. Botany	47
1.8.2. Chemical Composition.....	47
1.8.3. Medicinal uses and application	49
1.9. Metabolomics approach	50
1.9.1. Introduction to metabolomics	50
1.9.2. Tools of spectral analysis.....	54
1.9.3. MS analysis.....	55
1.9.4. NMR spectroscopy	56
1.9.5. Chemometrics and multivariate analysis	57
1.9.6. Applications of metabolomics in natural products research.....	61
1.10. Hypothesis and aims of the study	62
2. Materials and methods	66
2.1. Jordanian and European chamomile plant extraction.....	66
2.1.1. Materials and equipment.....	66

Table 2. 1: Materials and equipment used in the experiments	66
Materials and equipment	66
purpose	66
Origin place	66
Magnetic mixer	66
multi-purpose mixing or solubilisation either during plant extraction or sample preparation	66
Stuart, Stone, UK	66
Vortex Genie 2.....	66
Scientific Industries Inc, London, UK	66
HPLC-grade acetonitrile (ACN).....	66
plant extraction, plant partitioning, LC-HRMS and MPLC	66
Sigma-Aldrich, Poznań, Poland.....	66
Formic acid	66
HPLC-grade dichloromethane (DCM),	66
n-Hexane,	66
Acetone,	66
MeOH	67
(HPLC) grade EtOAc.....	67
Analytical-grade acetone	67
VWR, Fontenay-sous-Bois Cede, France	67
Rotary evaporator R-110	67
sample concentrated and dried under vacuum	67
Büchi, Flawil, Switzerland.....	67
Heating Block SBH130D/3 and sample concentrator SBHCONC/1	67
Concentrated extracts were reconstituted in EtOAc and dried under nitrogen... 67	
Stuart, Stone, UK	67
Ultra-wave sonicator.....	67
enhance solubilisation.....	67
Scientific Laboratory Supplies, Nottingham, UK.....	67
Direct-Q® water purification system.....	67
ultrapure water for solvent and media preparation	67
Merck Millipore, Massachusetts, USA	67
Accela HPLC coupled to an Exactive mass spectrometer	67

to run extracts fractions and samples	67
Thermo Scientific, Germany.....	67
Xcalibur 2.2	67
Mass data processing	67
Thermo Scientific, Heidelberg, Germany.....	67
ProteoWizard	67
data splitting to separate the data between the negative and positive ionisation files.....	67
USA	67
MZmine 2.53	68
mass data processing.....	68
http://mzmine.github.io/	68
An in-house excel sheet called Macro which coupled with Dictionary of Natural Products (DNP version 2021) database	68
Plant data base	68
CRC Press, Boca Raton, USA (Pluskal <i>et al.</i> , 2010).....	68
Deteriorated dimethyl sulfoxide (DMSO- d_6)	68
dissolve NMR samples	68
Sigma-Aldrich, Poznań, Poland.....	68
Deuterium water (D ₂ O).....	68
NMR tubes.....	68
tubes for the samples to run on NMR instrument.....	68
Norell, New York, USA	68
400 MHz Jeol-LA400 FT-NMR spectrometer system equipped with a 40TH5AT/FG prob	68
measuring NMR samples.....	68
Bruker, Rheinstetten, Germany	68
An AVANCE-III 600 instrument with a 14.1 T Bruker UltraShield magnet from the Department of Pure and Applied Chemistry.....	68
It has a 24 position autosampler, 3 channel console, is DQD and Waveform-equipped and can use either a BBO-z-ATMA-[³¹ P-183W/ ¹ H] probe or a TBI-z-[¹ H, ¹³ C, ³¹ P-1 ⁵ N] probe.....	68
MestReNova 14.2 developed Mestrelab Research	69
processing NMR spectra.....	69
Santiago de Compostela, Spain	69

TLC plates.....	69
TLC silica gel 60 F254 plates	69
Merck, Darmstadt, Germany	69
Human Caucasian Breast Carcinoma (ZR-75)	69
tested cell line	69
ATCC, US.....	69
Normal human foreskin fibroblast (HS-27) cell lines	69
RPMI 1640.....	69
media for the tested cells	69
invitrogen, USA	69
Foetal bovine serum (FBS),.....	69
media components	69
Glutamine and penicillin/streptomycin solution.....	69
Invitrogen, UK.....	69
Trytox X-100	69
negative control.....	69
Sigma, US	69
TrypLE Express	69
cell detachment	69
GIBCO, UK	69
AlamarBlue BUF012B	69
measuring cytotoxicity for pure compounds and selected fractions and extracts	69
Bio-Rad, UK	69
DMSO assay grade	69
bioassay samples solubilisation	69
Fisher Scientific, US	69
Ninety six-well plates	69
bioassay.....	69
TRP, Switzerland and Greiner bio-one, Austria.....	69
Falcon tubes	70
For centrifuge purpose	70
Corning, Mexico	70
Napco 5410 incubator.....	70

was humidified, kept at 37°C in the presence of 5% CO ₂	70
Napco, US	70
SterilGard biological safety cabinet.....	70
Sterile cabinet for biological work.....	70
The Baker Company, US	70
The IEC Medispin centrifuge	70
centrifuging samples	70
Thermo Scientific, Germany.....	70
Bright-Line hemocytometer.....	70
cell counting.....	70
Reichert, US.....	70
Water bath.....	70
sample heating for dissolving purpose.....	70
Clifton, UK	70
Microscope.....	70
observing cells	70
Olympus Optical, Japan.....	70
Wallac Victor 2.....	70
measuring fluorescence.....	70
PerkinElmer, UK	70
Microsoft Excel 2016.....	70
bar charts.....	70
Microsoft.....	70
Prism 6.0	70
plotting dilution curves	70
GraphPad Software, US	70
Hidex Sense Multilabel Plate Reader	70
plate reader.....	70
Thermo Scientific, Germany.....	70
2,2-diphenyl-1-picrylhydrazyl (DPPH)	70
antioxidant assay	70
Sigma-Aldrich, Poznań, Poland.....	70
Ascorbic acid	70
positive control in DPPH assay	70

Quercetin.....	70
2.1.2. Plant collection	71
2.1.3. Plant extraction	71
2.1.4. Solvent partitioning.....	71
2.1.5. Preparation of the samples for analysis and biological assay	72
2.1.6. Medium pressure liquid chromatography (MPLC)	77
2.1.7. Thin layer chromatography (TLC).....	77
2.1.8. Sample Preparation	78
2.2. Isolation and identification of endophytes from Jordanian chamomile	79
2.2.1. Materials and equipment	79
Table 2. 6: Materials and equipment used in the experiments.....	80
Materials and equipment	80
purpose	80
Origin place	80
Malt extract powder	80
inoculation of the endophytic fungi	80
Oxoid, Manchester, UK	80
Nutrient agar	80
Chloramphenicol.....	80
initial inoculation	80
Acros Organics, Geel, Belgium	80
HPLC grade isopropanol	80
mixed with 30% water for sterilisation.....	80
Sigma-Aldrich, Pozna, Poland.....	80
Sagrotan® spray	80
disinfectant.....	80
Sagrotan, Heidelberg	80
pH meter	80
measuring pH.....	80
Jenway, Staffordshire, UK.....	80
NaOH.....	80
adjusting pH of media.....	80
Sigma-Aldrich Pozna, Poland.....	80
incubator	80

inoculating medium was incubated at 27°C	80
Vindon Scientific, Oldham Lancashire, UK.....	80
MA media	80
initially grow the fungi	80
Thermo Scientific, Massachusetts, USA	80
Internal transcribed spacer (ITS) regions between the 16s and 23s rRNA genes of endophytes.....	80
identify fungi.....	80
electrophoresis gel plates comprising UltraPure™ TBE buffer 10X	80
ITS gene sequencing	80
Life technologies, Cramlington, UK.....	80
ethidium bromide 10mg/mL	80
Sigma-Aldrich, Continental, USA	80
Agarose-Molecular Grade.....	81
Camarillo, Bionline, US.....	81
Water-Molecular Biology reagent, REExtract-N-Amp™ PCR ReadyMix™, Extraction and Dilution solution.....	81
Sigma-Aldrich, St. Louis, USA.	81
primers ITS1 and ITS4	81
ITS1-(5'-TCC-GTA-GGT-GAA-CCT-GCG-G-3')	81
ITS4-(5'-TCC-TCC-GCT-TAT-TGA-TAT-GC-3') were.....	81
Integrated DNA Technologies, Coralville, Iowa, USA	81
the HyperLadder II and sample loading buffer.....	81
Bionline, Camarillo, USA.....	81
The Primus 96 Thermal Cycler.....	81
for DNA extraction and amplification	81
Ebersberg, Germany	81
the Perkin Elmer DNA Thermal Cycler 480 Manual	81
MWG AG Biotech	81
Electrophoresis plates	81
Bioscience Services, London, UK	81
voltage source	81
used for the amplified DNA on the electrophoresis gel plate.....	81
Kodak BioMax MBP300 from New Jersey, USA	81

INGENIUS gel.....	81
gel imaging for the plates.....	81
Syngene, Cambridge, UK.....	81
Illustra™ GFX PCR DNA and Gel Band Purification kit.....	81
extract the DNA after PCR of the DNA samples from electrophoresis gel	81
Cytiva, Massachusetts, US	81
DRI-BLOCK® DB-2A.....	82
solubilisation of agarose gel containing DNA was performed using a dry block	82
Techne, Chelmsford, UK.....	82
5415 D Centrifuge	82
centrifugation of the samples after each DNA extraction step	82
Eppendorf, Hamburg, Germany.....	82
Nanodrop 2000c Spectrophotometer	82
measuring DNA concentration of each sample	82
Thermo Scientific, Massachusetts, USA	82
FinshTV 1.4.0 software	82
analysing PCR results	82
Geospiza.....	82
Basic Local Alignment Search Tool (BLAST).....	82
available online from the National Centre for Biotechnology (NCBI)	82
Maryland, USA.....	82
2.2.2. Collection of plant samples.....	82
2.2.3. Preparation of malt extract agar media and fungal inoculation from Jordanian chamomile.	82
2.2.4. Fungal extracts for screening	83
2.2.5. Preparation of fungal inoculum for media optimisation.....	86
2.2.6. Chemical analysis: Extraction, chromatographic separation and structure elucidation.....	89
2.3. The metabolomics approach used in this study.....	93
2.3.1. Data Analysis Using MZmine 2.53 (Macintyre <i>et al.</i> , 2014).....	94
2.3.2. Chemometrics and multivariate analysis	96
3. Jordanian and European chamomile comparison for unravelling the anticancer and antioxidant differences	97
3.1. Literature Background.....	97

3.2.	Crude extracts and extract yield of the Jordanian and European chamomile	100
3.3.	Multivariate analysis of the crude extract of <i>M. chamomilla</i> varieties	102
3.3.1.	The biological activity of <i>M. chamomilla</i> crude extracts.....	103
3.3.2.	Multivariate analysis of NMR spectral data.....	107
3.3.3.	NMR spectroscopy of <i>M. chamomilla</i> fractions	111
3.3.4.	Multivariate analysis of LC-HRMS data	115
3.4.	Fractionation of the Extracts	120
3.4.1.	LC-HRMS analysis of <i>M. chamomilla</i> fractions	122
3.4.2.	Biological assay results of the bioactive fractions	128
3.5.	Structural elucidation of biologically active fractions.....	142
3.5.1.	Structure elucidation of F8-ChJ from Jordanian chamomile	143
3.5.2.	Structure elucidation of F2-ChE from the European chamomile.....	150
3.5.3.	Structure elucidation of F8-ChE from European chamomile.	156
3.5.4.	Structure elucidation of F11-ChE from European chamomile.	160
3.5.5.	Structure elucidation of F12-ChE from European chamomile.	167
3.6.	Summary	175
4.	Isolation and Screening of Fungal Endophytes from Jordanian chamomile. ...	176
4.1.	Literature background on fungal endophytes derived from chamomile. ..	176
4.2.	Isolation of endophytic fungi.	179
4.3.	Fungal extraction	180
4.4.	Bioassay screening of fungal extracts	182
4.4.1.	AlamarBlue® assay	182
4.4.2.	DPPH assay	184
4.5.	NMR analysis of fungal extracts	184
4.6.	LC-MS analysis of fungal extracts	195
4.7.	ITS gene sequencing	208
4.8.	Summary of the preliminary screening results	209
5.	Optimising the production of bioactive fungal extracts.....	210
5.1.	Optimising the production of anticancer bioactive metabolites in <i>A. ustus</i>	210
5.1.1.	Extract yields on different media.....	211
5.1.2.	Biological assay	212
5.1.3.	NMR spectroscopy for <i>A. ustus</i> extracts.....	213
5.1.4.	Multivariate analysis of NMR data.....	217

5.1.5. Multivariate analysis of LC-HRMS data	222
5.2. Optimising the production of anticancer bioactive metabolites in <i>A. solani</i> .	237
5.2.1. Extract yields on different media	239
5.2.2. Biological assay	241
5.2.3. NMR spectroscopy for <i>A. solani</i> extracts	242
5.2.4. Multivariate analysis of NMR spectral data	247
5.2.5. Multivariate analysis of LC-HRMS data	254
5.3. Summary	261
5.3.1. <i>A. ustus</i> optimisation	261
5.3.2. <i>A. solani</i> optimisation	262
6. <i>A. ustus</i> scale up and isolation of anticancer compounds	263
6.1. Literature background on the endophytic fungi <i>A. ustus</i>	263
6.2. Fractionation of the extract and multivariate analysis	267
6.3. Biological assay results of fractions	270
6.4. NMR spectroscopy of <i>A. ustus</i> fractions	271
6.5. LC-HRMS analysis of <i>A. ustus</i> fractions	280
6.6. HRMS analysis of <i>A. ustus</i> subfractions	289
6.6. Pure compounds isolation	297
6.6.1. Linoleic acid derivatives	301
6.6.2. Ophiobolins	315
6.6.3. Drimane sesquiterpene derivatives	327
6.6.4. Terretonin	357
6.7. Biological assay results of the pure compounds	367
6.8. Summary	370
7. General Discussion	371
7.1. Anticancer and antioxidant compounds from two varieties of chamomile ..	371
7.1.1. Metabolomic-guided isolation of target anticancer active metabolites ..	372
7.1.2. Proposed biosynthetic pathways of the isolated phenolic compounds ...	375
7.1.3. Role of isolated phenolics and flavonoids compound from chamomile	
varieties as anticancer and antioxidant activity	378
7.2. Anticancer compounds from the fungal endophyte of Jordanian chamomile.	
.....	381
7.2.1. LC and direct infusion mass spectroscopic-based metabolomic profiling of	
terpenoids	383

7.2.2. Proposed biosynthetic pathways of the isolated fungal compounds.....	387
7.2.3. Related bioactivities of isolated compounds and their known derivatives	393
7.3. Relationship between Jordanian chamomile and its endophyte	397
8. Conclusion and Future Work.....	400
8.1 Metabolomic profiling of potential anticancer and antioxidant metabolites from European and Jordanian chamomile for targeted isolation work	400
8.2. Metabolomic profiling of potential anticancer metabolites from <i>M.</i> <i>chamomilla</i> associated endophyte	401
8.3. Future work	403
9. References.....	405
10. Appendix	427

List of Tables

Table 1.1: Some of the analysis used in multivariate approaches (Wiklund, 2008). 58

Table 2. 1: Materials and equipment used in the experiments 66

Table 2.2: Required sample concentration for screening. 72

Table 2.3: Elution gradient used for LC-HRMS. 73

Table 2.4: Seeding densities (cell/cm²) for the used cell lines..... 77

Table 2.5: The constituents of anisaldehyde/sulfuric acid spray reagent..... 78

Table 2. 6: Materials and equipment used in the experiments 80

Table 2.7: PCR cycles. 85

Table 2.8: Elution gradient for the fractionation of *A. ustus* extracts 90

Table 2.9: Mobile phase % used in sub-fractionation of *A. ustus* fraction 11 and 12.
..... 91

Table 3.1: Yields of liquid-liquid partitioning extracts obtained from chamomile varieties 100

Table 3.2: EC₅₀ values of antioxidant activity assay of liquid-liquid partitioning extracts obtained from both varieties of *M. chamomilla* in mg/mL. Ascorbic acid and quercetin were used as the positive controls. 107

Table 3.3: Dereplication of the outliers with $p < 0.05$ determined from the OPLS-DA loadings plot (Figure 3.10B) of the bioactive metabolite from both varieties of *M. chamomilla* EtOAc extracts. Structures of putatively dereplicated compounds are shown in Figure 3.11..... 118

Table 3.4: Mobile phase used for the Büchi Sepacore® fractionation of the EtOAc extracts of both *M. chamomilla* varieties. 120

Table 3.5: Weights of fractions obtained from the Büchi Sepacore® fractionation of the EtOAc extracts of both varieties of *M. chamomilla* 121

Table 3.6: EC₅₀ for the bioactive fractions that possess antioxidant activity. n= number of samples 130

Table 3.7: IC₅₀ values in µM for the bioactive European chamomile fractions against the tested cell lines. If *SI* greater than 10 or the IC₅₀ of the tested normal cell was not obtainable, then the compound considered selective (Vontron-Sénécheau *et al.*, 2003). 133

Table 3.8: Dereplication of target bioactive metabolites against breast cancer (ZR-75) and antioxidant activity as predicted by OPLS-DA loadings S-plots. Metabolites were arranged according to their ascending p-values. Highlighted rows represent compounds that were isolated from both chamomile varieties. 136

Table 3.9: Fragments ions of a dicaffeoylquinic acid isomer at R_t 8.47 min as shown in Figure 3.30 144

Table 3.10. ¹ H and ¹³ C NMR data of F8-ChJ in CD ₃ OD.....	149
Table 3.11: ¹ H and ¹³ C NMR data of F2-ChE in comparison to chrysosplenetin (Alwahsh <i>et al.</i> , 2015).....	155
Table 3.12: ¹ H NMR data of F8-ChE and synthesised apigenin measured at 400 MHz.	159
Table 3.13: ¹ H NMR data(δ_H in ppm, mult, <i>J</i> in Hz) of F11-ChE in comparison to cynarin, a 1,3-dicaffeoylquinic acid analogue along with spectral data of 1,5-dicaffeoylquinic acid reported in the literature.	166
Table 3.14: ¹ H NMR data (δ_H in ppm, mult, <i>J</i> in Hz) of F12-ChE in comparison to that of 1,3- <i>O</i> -dicaffeoylquinic acid (F11-ChE) and 3,5- <i>O</i> -dicaffeoylquinic acid (F8-ChJ) measured at 400 MHz in DMSO- <i>d</i> ₆	172
Table 3.15: ¹ H NMR data (δ_H in ppm, mult, <i>J</i> in Hz) of F12-ChE in comparison to that of 4'→1- <i>O</i> -feruloyl- β -D-glucose and 1- <i>O</i> - feruloyl- β -D- glucose as reported in the literature.	174
Table 4.1: Isolated endophytes from <i>M. chamomilla</i> (Hatamzadeh <i>et al.</i> , 2020).	177
Table 4.2: Morphological feature of the isolated endophytes from Jordanian chamomile.	180
Table 4.3: Fungal extract yields in triplicates.	181
Table 4.4: Top 5 VIP (Variable Importance in Projection) dereplicated metabolites that define the discriminating features of anticancer bioactive extracts. The compounds are arranged according to their increasing <i>p</i> -values.	202
Table 4.5: Discriminating feature of fungal extracts obtained from different plant parts with <i>p</i> -values < 0.05. Compound structures are shown in Figure 4.16.	203
Table 4.6: The obtained bioactive endophytes and their identity.	208
Table 5.1: Yields obtained from <i>A. ustus</i> extracts grown in four different media and extracted after various incubation periods. All cultures were incubated at 27°C.	211
Table 5.2: Dereplication of discriminating metabolites of <i>A. ustus</i> for the different media. Structures are shown in Figure 5.12.	227
Table 5.3: Dereplicated metabolites that define the discriminating features of anticancer bioactive potato dextrose media extracts. The compounds are arranged according to their <i>p</i> -values. Structures are shown in Figure 5.14.	233
Table 5.4: Secondary metabolites previously isolated from <i>A. solani</i>	238
Table 5.5: Extract yields afforded by <i>A. solani</i> grown on five different media and collected at various incubation periods. All cultures were incubated at 27°C.	240
Table 5.6: Dereplication of discriminating metabolites of <i>A. solani</i> for different media. Structures of compound hits are shown in Figure 5.31.	258
Table 6.1: Reported sources, biological activity, and isolated compounds for <i>A. ustus</i>	264
Table 6.2: Weights of extracts after pooling similar fractions.	269

Table 6.3: Dereplication of target bioactive metabolites against breast cancer (ZR-75) as predicted by OPLS-DA loadings S-plots. Structures of compounds are shown in Figure 6.17. For multiple compound hits, hits were filtered according to a fungal genus prioritising the genus <i>Aspergillus</i>	285
Table 6.4: Dereplication of target bioactive metabolites against breast cancer (ZR-75) as predicted by OPLS-DA loadings S-plots of the LCMS data by direct infusion. The highlighted rows correspond to isolated compounds from <i>A. ustus</i>	294
Table 6.5: Weight of subfractions 1 to 12 of fraction 11 obtained by Reveleris FC using 0% to 20% of EtOAc in combination of n-Hexane.	299
Table 6.6: NMR spectral data for compound F11-12 in DMSO- <i>d</i> ₆ measured at 500 MHz.	308
Table 6.7: NMR spectral data for compound F11-11 in DMSO- <i>d</i> ₆ measured at 500 MHz.	314
Table 6.8: Weights of subfractions 13 to 18 from the bioactive fraction F11.....	315
Table 6.9: NMR spectral data for compound F11-17 in DMSO- <i>d</i> ₆ measured at 500 MHz..	325
Table 6.10: NMR data of F11-17 compared to that of ophiobolin K from the literature (Singh <i>et al.</i> , 1991).	326
Table 6.11: Weight of subfractions 19 to 32 from fraction 11 obtained by Reveleris FC using 50% to 100% of EtOAc in combination with n-Hexane. TLC chromatograms are shown in Figure 6.46.	327
Table 6.12: NMR data of F11-23 compared to the literature data (Hayes <i>et al.</i> , 1996).	338
Table 6.13: NMR spectral data for compound F11-23 in DMSO- <i>d</i> ₆ measured at 500 MHz.	339
Table 6.14: NMR spectral data for compound F11-29-8 DMSO- <i>d</i> ₆ measured at 500 MHz..	347
Table 6.15: NMR spectral data for compound F12-11-2 in DMSO- <i>d</i> ₆ at 500 MHz.	355
Table 6.16: NMR spectral data of compound F12-11-2 compared to that of literature (Liu <i>et al.</i> , 2009).....	356
Table 6.17: NMR data of F11-29-6 in DMSO- <i>d</i> ₆ measured at 500 MHz.....	365
Table 6.18: NMR data of F11-29-6 compared to that to literature(Lopez-Gresa <i>et al.</i> , 2009).	366
Table 6.19: IC ₅₀ concentrations (µM) for the bioactive isolated compound against respective cell lines. If <i>SI</i> greater than 10 or the IC ₅₀ of the tested normal cell was not obtainable, then the compound considered selective.	369
Table 7.1: Compounds isolated from the Jordanian and European chamomile varieties.	371
Table 7.2: Compounds isolated from the <i>A. ustus</i> extracts	381

List of Figures

Figure 1.1: Examples of compounds isolated from plant, fungi, and marine invertebrates	40
Figure 1.2: FDA-approved medications derived from plant natural products	42
Figure 1.3: Secondary metabolites isolated from German and Roman chamomile. (Bömke and Tudzynski, 2009, Isaac, 1979, Schilcher, 1987, Barton <i>et al.</i> , 1999, Reichling <i>et al.</i> , 1979).....	49
Figure 1.4: Schematic diagram for metabolomics approach A) metabolomic targeted approach B) metabolomic untargeted approach. Figure adapted from (Patti <i>et al.</i> , 2012).	52
Figure 1.5: The omics cascade. The metabolome is the most representative of the phenotype. Adapted from (Haukaas <i>et al.</i> , 2017)	54
Figure 1.6: Score plots for PCA and OPLS-DA approaches.	59
Figure 1.7: PCA scores and the loadings plots.	60
Figure 2.1: Workflow of applying metabolomics in the search for anticancer agents from the <i>A. ustus</i> endophyte.....	93
Figure 3.1: Secondary metabolites isolated from <i>M. chamomilla</i> (Shankar <i>et al.</i> , 2017, Sadraei <i>et al.</i> , 2017, Hostetler <i>et al.</i> , 2017).....	99
Figure 3.2: Workflow for <i>M. chamomilla</i> varieties for both Jordanian and European chamomile.....	101
Figure 3.3: Stacked ¹ H NMR spectra of Jordanian (ChJ) and European (ChE) chamomile extract in DMSO- <i>d</i> ₆ measured at 500 MHz. Highlighted spectra represent the bioactive fractions.	103
Figure 3.4: AlamarBlue® assay of 30 µg/mL crude fractions obtained by liquid-liquid partitioning of total crude extracts of A) Jordanian and B) European chamomile on breast cancer cell line ZR-75.....	104
Figure 3.5: Microscopic photo of breast cells after 48 hr incubation. A) Breast cancer cells without treatment. B) Breast cancer cells with Triton X. C) Breast cancer cells with EtOAc extract from European chamomile at a concentration of 30 µg/mL. Magnification power was 10X (objective lens) and the background was shown in green.....	105
Figure 3.6: DPPH assay for antioxidant activity of liquid-liquid partitioning extracts obtained from A) European and B) Jordanian chamomile in mg/mL. Ascorbic acid and quercetin were used as the positive controls.	106
Figure 3.7: (A) PCA scores and (B) loadings plots of the NMR spectral data of <i>M. chamomilla</i> . The R ² and Q ² values were 0.98 and 0.90, respectively. Encircled	

features on the loadings plot indicate the discriminating chemical shifts for the biologically active extracts.....	109
Figure 3.8: (A) OPLS-DA scores and (B) loadings of the NMR spectral data of <i>M. chamomilla</i> pre-classified according to their bioactivities in AlamarBlue® and DPPH assay results. The R ² and Q ² values were 0.98 and 0.80, respectively. Encircled features on the loadings plot indicate the discriminating chemical shifts for the biologically active extracts.....	110
Figure 3.9: Stacked ¹ H NMR spectra of Jordanian chamomile (ChJ) fractions in DMSO- <i>d</i> ₆ measured at 500 MHz. Boxed spectra represent the bioactive fractions.	111
Figure 3.10: Stacked ¹ H NMR spectra of European chamomile (ChE) fractions in DMSO- <i>d</i> ₆ measured at 500 MHz. Boxed spectra represent the bioactive fractions.	112
Figure 3.11: (A) PCA scores plot and (B) OPLS-DA loadings S-plot of the NMR spectral data of Jordanian and European fractions.....	114
Figure 3.12: Permutation test (100 permutations) of OPLS-DA model for Jordanian and European fractions of their antioxidant using DPPH® assay and anticancer activity against breast cancer cell line ZR-75.	115
Figure 3.13: (A) OPLS-DA scores and (B) loadings plot for the mass spectral data (ion peaks at <i>m/z</i>) of the crude extracts obtained by liquid-liquid partitioning. Encircled features in red indicate the discriminating features for the active EtOAc extracts, which were listed below in Table 3.3. The R ² and Q ² values were 1.00 and 0.96, respectively.	117
Figure 3.14: Structures of the discriminating bioactive metabolites, listed in Table 3.3, from EtOAc extract of both varieties of <i>M. chamomilla</i>	119
Figure 3.15: (A) PCA scores and (B) loading plots of the LC-HRMS data of <i>M. chamomilla</i> fractions for both varieties. Encircled in orange are the discriminatory features for the corresponding outlying variable fractions.	124
Figure 3.16: DMod X results to validate true outliers of the model. Variables above the red line are the true outliers that included Fractions ChE 6, 8, 9, 11, and 12	125
Figure 3.17: (A) OPLS-DA scores and (B) OPLS-DA loadings plots of the <i>m/z</i> ion peaks grouped between Jordanian and European chamomile fractions. R ² and Q ² scores were 0.976 and 0.88, respectively.....	127
Figure 3.18 : DPPH assay of the bioactive fractionated samples.	130
Figure 3.19: AlamarBlue® assay of fractions from both <i>M. chamomilla</i> varieties. Effect of 30 mg/mL A) Jordanian and B) European chamomile fractions on breast cancer cells.....	131
Figure 3.20: Standard curves to determine the IC ₅₀ values for the bioactive fractions A) F2 and B) F8 from the European chamomile tested against the breast cell line ZR-75.....	132
Figure 3.21: Effect of 30 µg/mL European chamomile active fractions against ZR-75 cancer cells and HS-27 normal cells.	132

Figure 3.22 : Standard curves to determine the IC ₅₀ values for the bioactive fractions A) F2 and B) F8 from the European chamomile tested against the normal cell line HS-27.	133
Figure 3.23: A) OPLS-DA scores plot and B) S-plot of the mass spectral data (MW) grouped between active and inactive fractions. R ² and Q ² values are equal to 1.0 and 0.41, respectively. The discriminatory features were labelled with their ion peaks at <i>m/z</i>	135
Figure 3.24: Total Ion Chromatogram (TIC) of the active fractions. The labelled ion peaks represent the isolated discriminating features highlighted in Table 3.8.	139
Figure 3.25: Structures of the discriminating bioactive metabolites against breast cancer (ZR-75) and antioxidant activity as listed in Table 3.8. Structures in black boxes were the isolated compounds in this study.	140
Figure 3.26: Schematic diagram summarising the isolation and elucidation of the bioactive compounds produced by the two <i>M. chamomilla</i> varieties.	142
Figure 3.27: Chemical structure of F8-ChJ	143
Figure 3.28. Extracted ion chromatogram and mass spectrum of F8-ChJ from the Jordanian chamomile showing source fragmentation at <i>m/z</i> 515.1182 [M-H] ⁻ eluting at 8.47 min.....	143
Figure 3.29: Fragment scheme of a dicaffeoylquinic acid isomer.....	144
Figure 3.30: ¹ H NMR spectrum of F8-ChJ in CD ₃ OD measured at 400 MHz.....	145
Figure 3.31: (¹ H- ¹ H) COSY correlation spectrum of F8-ChJ in CD ₃ OD measured at 400 MHz.	147
Figure 3.32: HMBC spectrum of F8-ChJ in CD ₃ OD measured at 400 MHz.....	148
Figure 3.33: chemical structure of F2-ChE.....	150
Figure 3.34A. Extracted ion chromatogram of F2-ChE for the ion peak at <i>m/z</i> 375.1080 [M+H] ⁺ at a RT of 15.5 min.....	150
Figure 3.35: ¹ H NMR spectrum of F2-ChE in DMSO- <i>d</i> ₆ measured at 400 MHz...	152
Figure 3.36: HMBC spectrum of F2-ChE in DMSO- <i>d</i> ₆ measured at 500 MHz.	154
Figure 3. 37: Chemical structure of F8-ChE	156
Figure 3.38A. Extracted ion chromatogram of F8-ChE for the ion peak at <i>m/z</i> 269.0450 [M-H] ⁻ eluting at RT of 12.5min	156
Figure 3.39: ¹ H NMR spectrum of F8-ChE in DMSO- <i>d</i> ₆ measured at 400 MHz...	158
Figure 3.40: Chemical structure of F11-ChE	160
Figure 3.41A. Extracted ion chromatogram of F11-ChE for the ion peak at <i>m/z</i> 517.1338 [M+H] ⁺ with a RT of 8.1 min.	160
Figure 3.42: ¹ H NMR spectrum of F11-ChE in DMSO- <i>d</i> ₆ measured at 400 MHz.	163
Figure 3. 43: Isopropylidene derivatisation of 1,3- <i>O</i> -dicaffeoylquinic acid.....	164
Figure 3.44: COSY NMR spectrum of the quinic acid moiety in F11-ChE measured in DMSO- <i>d</i> ₆ at 400 MHz.	165
Figure 3.45: Chemical structure of F12-ChE	167
Figure 3.46A: Extracted ion chromatogram of F12-ChE for the ion peak at <i>m/z</i> 355.1030 [M-H] eluting at a Rt of 7.23 min.	167

Figure 3.47: ^1H NMR spectrum of F12-ChE in DMSO- d_6 measured at 400 MHz.	169
Figure 3.48: COSY NMR spectrum F12-ChE measured in DMSO- d_6 at 400 MHz. Blue line represents the propenoic acid moiety, yellow line is the ABX system of the 1,3,4-trisubstituted phenyl system of the ferulic acid unit, and the green line traces the coupling protons for the glucose unit.	173
Figure 4.1: Schematic diagram for the screening of crude fungal extracts.	178
Figure 4.2: Alamarblue® assay against the breast cancer cell line ZR-75 for 30 $\mu\text{g/mL}$ extracts of fungal endophytes obtained from A) flower, B) roots, and C) stem. The red line indicates the bioactivity threshold, which must be below 40% of cell viability.	183
Figure 4.3: Dilution curves to determine the IC_{50} values of active fungal extracts against the breast cancer cell line ZR-75.	184
Figure 4.4: Stacked ^1H NMR spectra of the fungal extracts obtained from endophytes isolated from the flower part of the chamomile plant.	186
Figure 4.5: Stacked ^1H NMR spectra of the fungal extracts obtained from endophytes isolated from the root part of the chamomile plant. Spectrum from 1 to 3 represent the bioactive fungal extracts.	186
Figure 4.6: Stacked ^1H NMR spectra of the fungal extracts obtained from endophytes isolated from the stem part of the chamomile plant. Boxed spectra represent the bioactive extract.	187
Figure 4.7: A) PCA scores and B) loadings plots of the NMR spectral data of fungi extracts. The R^2 and Q^2 values were 0.98 and 0.26, respectively. Orange encircled variables on the PCA scores plot are the biologically active extracts against the breast cancer cell line ZR-75.	188
Figure 4.8: A) OPLS-DA scores and B) loadings plots of the NMR spectral data of fungal extracts grouped according to the plant parts the endophytes were obtained. The discriminatory chemical shifts in ppm from the respective extracts of the endophytes obtained from the flower were encircled green, those from the roots were encircled in blue and stem encircled in red.	190
Figure 4.9: A) OPLS-DA scores and B) loadings plots of the NMR spectral data of endophytic fungal extracts against their bioactivity on the breast cancer cell line ZR-75. R^2 and Q^2 values were 0.98 and 0.74, respectively. The difference between group $R^2X_0[1]$ is equal to 16.5% and the difference within groups $R^2X[2]$ is 9.2%. Encircled features on the loadings S-plot indicate the discriminating chemical shifts for the biologically active fractions against breast cancer cells line ZR-75.	192
Figure 4.10: Heatmap analysis of the NMR spectral data of endophytic extracts generated by MetaboAnalyst®. The boxed extracts are the biologically active extracts against the breast cancer cell line ZR-75 along with the discriminating chemical shifts unique to these anticancer fractions.	194

Figure 4.11: (A) PCA scores and (B) loading plots of the LC-HRMS fungal endophytes. Encircled features represent the discriminating ion peaks for the outliers R1-1, R1-2, and R1-3. $R^2 = 0.67$ and $Q^2 = 0.37$.	197
Figure 4.12: DMod X bar-plot to examine the occurrence of true outliers. fungal endophyte extract above the red line are the true outliers, which includes R1-1, R1-2, R1-3, and R2-3.	198
Figure 4.13: (A) OPLS-DA scores and (B) loading plots of LC-HRMS fungal endophytes. The highlighted box indicated the metabolites from R1-2. $R^2 = 0.86$ and $Q^2 = 0.76$. Discriminating features of the fungal endophyte extracts obtained from the different plant part are listed in Table 4.5.	199
Figure 4.14 : (A) OPLS-DA scores, B) loadings, and C) S- plots of LC-HRMS fungal endophyte grouped according to their bioactivity against breast cancer cell line ZR-75. The highlighted box indicated the metabolites from R1-2. $R^2 = 0.99$ and $Q^2 = 0.76$.	201
Figure 4.15: VIP analysis generated by MetaboAnalyst® for the LC-HRMS data fungal extracts of endophytes from various plant parts of Jordanian chamomile, The extracts were grouped according to their bioactivity against breast cancer cell line ZR-75. The boxed metabolites were the discriminating features hypothesised to be responsible for the anticancer activity of the extracts.	206
Figure 4.16: Structures of the discriminating metabolites of fungal extracts obtained from different plant as predicted by OPLS-DA loadings plots as listed in Table 4.5.	207
Figure 5.1: Histogram of extract weights of <i>A. ustus</i> obtained from four different media and incubated at 7, 15, and 30 days.	212
Figure 5.2: AlamarBlue® cell viability assay results of 30µg/mL of <i>A. ustus</i> extracts. The red line indicates the bioactivity threshold.	213
Figure 5.3: The ^1H NMR (500 MHz) data obtained from <i>A. ustus</i> extracts after incubation in solid-rice medium incubated for 7, 15, 30 days, measured in DMSO- d_6	214
Figure 5.4: The ^1H NMR (500 MHz) data obtained from <i>A. ustus</i> extracts after incubation in solid-oat medium incubated for 7, 15, 30 days, measured in DMSO- d_6	215
Figure 5.5: The ^1H NMR (500 MHz) data obtained from <i>A. ustus</i> extracts after incubation in potato-dextrose medium incubated for 7, 15, 30 days, measured in DMSO- d_6	216
Figure 5.6: The ^1H NMR (500 MHz) data obtained from <i>A. ustus</i> extracts after incubation in Wickersham medium incubated for 7, 15, 30 days, measured in DMSO- d_6	217

Figure 5.7: (A) PCA scores and (B) loading plots of ¹ H NMR spectral data of <i>A. ustus</i> extracts obtained from four different media incubated at 30 days. R ² = 0.994 and Q ² = 0.966.	219
Figure 5.8: (A) OPLS-DA scores and (B) loadings plots of ¹ H NMR spectral data of <i>A. ustus</i> extracts obtained after incubation on different media classified according to their AlamarBlue® results against breast cancer cell line ZR-75. R ² and Q ² values were 0.999 and 0.998, respectively. The difference between group R ² X _o [1] is equal to 55.7 % and the difference within groups R ² X[2] is 26.1%. Encircled features on the loadings plot indicate the discriminating chemical shifts for the biologically active extracts against breast cancer cells line ZR-75.....	221
Figure 5.9: (A) PCA scores (B) loading plots of LC-HRMS data of <i>A. ustus</i> extracts from four media incubated at 7, 15, and 30 days. R ² X= 0.811 and Q ² X = 0.534. Encircled features represent the discriminating ion peaks for the outlying extracts obtained from Wickersham media incubated for 7 and 30 days.....	224
Figure 5.10: Discriminating metabolites from fungal extracts obtained after 7 and 30 days of incubation in Wickersham media.	225
Figure 5.11: (A) OPLS-DA scores and (B) loading plots of LC-HRMS of <i>A. ustus</i> extract obtain from different media. The encircled box indicated the discriminating feature for each media extracts. R ² = 0.86 and Q ² = 0.76. The difference between group R ² X _o [1] is equal to 17.5% and the difference within groups R ² X[2] is 10.5%.	226
Figure 5.12: Structures of the discriminating metabolites from <i>A. ustus</i> extract obtained from different media and listed in Table 5.2	229
Figure 5.13: (A) OPLS-DA scores (B) OPLS-DA loadings S-plot of LC-HRMS data of <i>A. ustus</i> of different media extracts classified according to their bioactivity against breast cancer cells (ZR-75) (C) Expansion of the OPLS-DA loadings plot indicating the discriminating features for the active <i>A. ustus</i> extracts obtained from potato-dextrose media at 30 th day, which are labelled with their <i>m/z</i> values and were listed below in Table 5.3. R ² = 0.94 and Q ² = 0.51. The difference between group R ² X _o [1] is equal to 15.2% and the difference within groups R ² X[2] is 2.0%.	232
Figure 5.14: Structures of the discriminating bioactive metabolites from <i>A. ustus</i> extract obtained from potato dextrose media have been listed in Table 5.3.....	235
Figure 5.15: Total Ion Chromatogram (TIC) of the bioactive <i>A. ustus</i> extracts obtained from potato-dextrose media. The ion peaks that represent the discriminating features listed in Table 5.3 have been labelled.	236
Figure 5.16: Secondary metabolites previously isolated from <i>A. solani</i>	239
Figure 5.17: Histogram of extract weights of <i>A. solani</i> obtained from five different media and incubated at 7, 15, and 30 days.....	240
Figure 5.18: AlamarBlue® cell viability assay results of 30µg/mL of <i>A. solani</i> extracts. The red line indicates the bioactivity threshold.	241

Figure 5.19: The ¹ H NMR (measured in DMSO-d ₆ , 500 MHz) data obtained from <i>A. solani</i> extracts after inoculation on solid-rice medium incubated for 7, 15, 30 days.	242
Figure 5.20: The ¹ H NMR (measured in DMSO-d ₆ , 500 MHz) data obtained from <i>A. solani</i> extracts after inoculation on solid-oat medium incubated for 7, 15, 30 days.	243
Figure 5.21: The ¹ H NMR (measured in DMSO-d ₆ , 500 MHz) data obtained from <i>A. solani</i> extracts after inoculation on potato-dextrose medium incubated for 7, 15, 30 days.	244
Figure 5.22: The ¹ H NMR (500 MHz) data obtained from <i>A. solani</i> extracts after inoculation on Wickersham medium incubated for 7, 15, 30 days, measured in DMSO-d ₆	245
Figure 5.23: The ¹ H NMR (500 MHz) data obtained from <i>A. solani</i> extracts after inoculation on malt extract broth medium incubated for 7, 15, 30 days, measured in DMSO-d ₆	246
Figure 5.24: The stacked ¹ H NMR (measured in DMSO-d ₆ , 500 MHz) data obtained from <i>A. solani</i> extracts from the screening step in comparison to the five different media used during the media optimisation step incubated for 30 days.....	247
Figure 5.25: (A) PCA scores (B) loading plots of ¹ H NMR spectral of <i>A. solani</i> extracts from four media incubated at 15 and 30 days. R ² = 0.99 and Q ² = 0.95 after 7 components.	249
Figure 5.26: (A) OPLS-DA scores B) loadings plots of ¹ H NMR spectral of <i>A. solani</i> extracts obtained from different media. R ² and Q ² values were 0.99 and 0.79, respectively. The difference between group R ² X _o [1] is equal to 29.6% and the difference within groups R ² X[2] is 5.6%. Encircled features on the loadings plot indicate the discriminating chemical shifts	251
Figure 5.27: (A) PCA scores (B) loading plots of ¹ H NMR spectral of <i>A. solani</i> extracts from malt medium incubated at 15 and 30 days and MA medium. R ² = 1.0 and Q ² = 1.0 after 3 components.....	253
Figure 5.28: (A) PCA scores (B) loading plots of LC-HRMS of <i>A. solani</i> extracts from four media incubated at 15, 30 days. R ² X= 0.67 and Q ² X = 0.38. Encircled features represent the discriminating ion peaks for the extracts obtained from different media.	255
Figure 5.29: Discriminating metabolite from extracts of <i>A. solani</i> inoculated on oat media and incubated for 30 days.....	256
Figure 5.30: A) OPLS-DA scores and B) loading plots of LC-HRMS of <i>A. solani</i> extract obtain from different media. The encircled box indicated the discriminating feature for each media extracts. R ² = 0.80 and Q ² = 0.52. The difference between group R ² X _o [1] is equal to 18.0% and the difference within groups R ² X[2] is 4.7%.	257
Figure 5.31: Structures of the discriminating bioactive metabolites from <i>A. solani</i> extract obtained from potato dextrose media have been listed in Table 5.6.	260

Figure 6.1: Secondary metabolites previously isolated from <i>A. ustus</i> obtained from the marine algae <i>Codium fragile</i> (Liu <i>et al.</i> , 2013).....	266
Figure 6.2: Secondary metabolites isolated from <i>A. ustus</i> obtained from the sponge <i>Suberites domuncula</i> (Liu <i>et al.</i> , 2009).....	267
Figure 6.3: Collected fractions by FC.....	268
Figure 6.4: Summary TLC plate for the pooled fractions using a solvent system 97:03 % of DCM:MeOH after spraying with anisaldehyde-sulphuric acid reagent	268
Figure 6.5: Biological activity for Büchi fractions of <i>A. ustus</i> at 30 µg/mL against breast cancer cell line ZR-75. The red line indicates the bioactivity threshold, which must be below 20% of cell viability.....	270
Figure 6.6: IC ₅₀ for the bioactive fractions from <i>A. ustus</i>	271
Figure 6.7: Stacked ¹ H NMR spectra of the bioactive MPLC fractions with IC ₅₀ < 5.5 µg/mL. The highlighted blue box suggested the present of di or sesquiterpenes group.	272
Figure 6.8: Stacked ¹ H NMR spectra of the bioactive MPLC fractions with IC ₅₀ between 5.5-15 µg/mL.....	272
Figure 6.9: (A) PCA scores and (B) loadings plots of the NMR spectral data of the fractions. The R ² and Q ² values were 0.91 and -0.04, respectively.	274
Figure 6.10: OPLS-DA scores (A) and loadings (B) plots of the NMR spectral data of the MPLC fractions grouped according to their bioactivity against breast cancer cell line ZR-75. R ² and Q ² values were 0.93 and 0.80, respectively. The difference between group R ² X _o [1] is equal to 10.3% and the difference within groups R ² X[2] is 1.5%. Encircled features on the loadings plot indicate the discriminating chemical shifts for the biologically active fractions.....	276
Figure 6.11: Permutation test (100 permutations) for <i>A. ustus</i> fractions for the OPLS-DA model of their activity against breast cancer cell line ZR-75.....	277
Figure 6.12: Heatmap analysis of the NMR spectral data of the <i>A. ustus</i> fractions generated by MetaboAnalyst®. The boxed fractions are those biologically active against the breast cancer cell line ZR-75 along with the discriminating chemical shifts unique to the anticancer fractions.....	278
Figure 6.13: VIP scores of <i>A. ustus</i> fractions from MetaboAnalyst®. The highlighted yellow boxes show the discriminating chemical shift of the metabolites found in the bioactive fractions against the breast cancer cell line ZR-75.	279
Figure 6.14: PCA scores (A) and loadings (B) plots of the LC-HRMS data of <i>A. ustus</i> fractions. Encircled features represent the discriminating ion peaks for the outlier F16. The R ² and Q ² values were 0.71 and 0.35, respectively.....	282
Figure 6.15: (A) OPLS-DA scores, (B) loadings, and (C) S-plots of the LC-HRMS data of <i>A. ustus</i> fractions.	283
Figure 6.16: Total Ion Chromatogram (TIC) of the active fraction. The ion peaks that represent the discriminating features listed in Table 6.3 have been labelled....	284

Figure 6.17: Structures of the discriminating bioactive metabolites against breast cancer (ZR-75) as predicted by OPLS-DA loadings S-plots as listed in Table 6.3.	287
Figure 6.18: Heatmap analysis of the mass spectral data of the <i>A. ustus</i> fractions generated by MetaboAnalyst®. The boxed fractions are those biologically active against the breast cancer cell line ZR-75 along with the discriminating ion peaks unique to the anticancer fractions.	288
Figure 6.19: (A) PCA scores and (B) loadings plot of the LC-HRMS data of <i>A. ustus</i> purified subfractions. The discriminating features from each subfraction were encircled in the figure, F11-29-6 and F11-23 encircled in red, F11-17 encircled in blue, F12-11-2 and F12-6-5 encircled in orange and F11-11 and F11-12 encircled in green.	290
Figure 6.20: (A) OPLS-DA scores, (B) loadings and (C) S-plots of the LC-HRMS data of <i>A. ustus</i> subfractions of the active fraction F11.	293
Figure 6.21: Structures of the discriminating of target bioactive metabolites against breast cancer (ZR-75) as predicted by OPLS-DA loadings S-plots as listed in Table 6.4. compounds in the black box correspond to isolated compounds from <i>A. ustus</i> .	296
Figure 6.22: Total Ion Chromatogram (TIC) of fraction 11.	297
Figure 6.23: Schematic diagram for isolating the pure compounds from <i>A. ustus</i> extract.	298
Figure 6.24: Stacked ¹ H NMR spectra of subfractions from the fraction 11. The highlighted subfractions were subjected for further analysis.	300
Figure 6.25: Summary TLC plates for the fractionation of F11 using solvent system 75:25% of n-Hexane and EtOAc. TLC for subfractions 11 and 12 were shown in the black box.	301
Figure 6.26A: Chemical structure of compound F11-12	302
Figure 6.27: ¹ H NMR spectrum of compound F11-12 in DMSO- <i>d</i> ₆ measured at 500 MHz.	303
Figure 6.28: (¹ H- ¹ H) COSY correlation NMR spectrum of compound F11-12 in DMSO- <i>d</i> ₆ measured at 500 MHz.	305
Figure 6.29: HSQC NMR spectrum of compound F11-12 in DMSO- <i>d</i> ₆ measured at 500. Red correlations are CHs and CH ₃ s while blue are CH ₂ s.	306
Figure 6.30: HMBC NMR spectrum and observed ¹ H to ¹³ C correlations of compound F11-12 in DMSO- <i>d</i> ₆ measured at 500 MHz.	307
Figure 6.31: Chemical structure of compound F11-11	309
Figure 6.32: Mass spectral data of F11-11 on the ion peak at <i>m/z</i> 617.513 [M+H] ⁺ .	309
Figure 6.33: ¹ H NMR spectrum of compound F11-11 in DMSO- <i>d</i> ₆ measured at 500 MHz.	310
Figure 6.34: (¹ H- ¹ H) COSY correlation of the NMR spectrum of compound F11-11 in DMSO- <i>d</i> ₆ measured at 500 MHz.	311

Figure 6.35: HSQC NMR spectrum of compound F11-11 in DMSO- <i>d</i> ₆ measured at 500 MHz. Red correlations are CHs and CH ₃ s while blue are CH ₂ s group.....	312
Figure 6.36: HMBC NMR spectrum of compound F11-11 in DMSO- <i>d</i> ₆ measured at 500 MHz.	313
Figure 6.37: Stacked ¹ H NMR for subfractions 13 to 18. Fractions concentration was at 5mg/600μl in DMSO- <i>d</i> ₆ measured at 500MHz. The highlighted subfraction was subjected to further structural elucidation work.	316
Figure 6.38: TLC for subfractions 13 to 18 obtained from Reveleris FC using solvent system 70:30% of n-Hexane and EtOAc.	317
Figure 6.39: Chemical structure of compound F11-17	318
Figure 6.40. Mass spectral data of F11-17 on the ion peak at <i>m/z</i> 407.256 [M+Na] ⁺	318
Figure 6.41: ¹ H NMR spectrum of compound F11-17 in DMSO- <i>d</i> ₆ measured at 500 MHz.	319
Figure 6.42: HSQC NMR spectrum of compound F11-17 in DMSO- <i>d</i> ₆ measured at 500 MHz. Red cross peaks are CHs and CH ₃ s while blue are CH ₂ s.	321
Figure 6.43: HMBC NMR spectrum of compound F11-17 in DMSO- <i>d</i> ₆ measured at 500 MHz.	322
Figure 6.44: (¹ H- ¹ H) COSY correlation NMR spectrum of compound F11-17 in DMSO- <i>d</i> ₆ measured at 500 MHz.	323
Figure 6.45: ROESY NMR spectrum and the essential correlation of F11-17 in DMSO- <i>d</i> ₆ measured at 600 MHz.	324
Figure 6.46: TLC for subfractions 20 to 32 from fraction 19 using solvent system 70:30% n-Hexane and EtOAc. Boxed in blue was SF 23, which was directly selected for 2D NMR structure elucidation work and SF 29 that was subjected to further preparative TLC purification steps.	328
Figure 6.47 : Chemical structure of compound F11-23	329
Figure 6.48. Mass spectral data of F11-23 for the ion peak at <i>m/z</i> 409.198 [M+Na] ⁺	329
Figure 6.49: ¹ H NMR spectrum of compound F11-23 in DMSO- <i>d</i> ₆ measured at 500 MHz.	330
Figure 6.50: ¹³ C JMOD NMR spectrum of compound F11-23 in DMSO- <i>d</i> ₆ measured at 500 MHz.....	331
Figure 6.51: HSQC NMR spectrum of compound F11-23 in DMSO- <i>d</i> ₆ measured at 500 MHz. Red cross peaks are CH and CH ₃ while blue are CH ₂	332
Figure 6.52: (¹ H- ¹ H) COSY correlation NMR spectrum of compound F11-23 in DMSO- <i>d</i> ₆ measured at 500 MHz.	333
Figure 6.53: HMBC NMR spectrum correlation of compound F11-17 in DMSO- <i>d</i> ₆ measured at 500 MHz.	335
Figure 6.54: Drimane sesquiterpene nucleus structure	335
Figure 6.55: ROESY spectrum and essential correlation of compound F11-23 in DMSO- <i>d</i> ₆ measured at 600 MHz.	337

Figure 6.56: Chemical structure of compound F11-29-8.....	340
Figure 6.57: Mass spectral data of F11-29-8 at the ion peak m/z 397.162 [M+Na] ⁺	340
Figure 6.58: ¹ H NMR spectrum of compound F11-29-8 in DMSO- <i>d</i> ₆ measured at 500 MHz.	341
Figure 6.59: ¹ H- ¹ H-COSY correlation NMR spectrum of compound F11-29-8 in DMSO- <i>d</i> ₆ measured at 500 MHz.	343
Figure 6.60: HMBC NMR spectrum and essential correlations to determine the structure of compound F11-29-8 in DMSO- <i>d</i> ₆ measured at 500 MHz.	344
Figure 6.61: HSQC NMR spectrum of compound F29-19-8 in DMSO- <i>d</i> ₆ measured at 500 MHz. Red correlations are CHs and CH ₃ s while blue are CH ₂ s.	345
Figure 6.62: ROESY spectrum and essential correlation of compound F11-29-8 in DMSO- <i>d</i> ₆ measured at 600 MHz.	346
Figure 6.63: Chemical structure of compound F12-11-2.....	348
Figure 6.64: Mass spectral data of F12-11-2 at the ion peak m/z 419.2085 [M-H] ⁻	348
Figure 6.65: ¹ H NMR spectrum of compound F12-11-2 in DMSO- <i>d</i> ₆ measured at 500 MHz.	349
Figure 6.66: (¹ H- ¹ H) COSY correlation NMR spectrum of compound F12-11-2 in DMSO- <i>d</i> ₆ measured at 500 MHz.	351
Figure 6.67: HMBC NMR spectrum of compound F12-11-2 in DMSO- <i>d</i> ₆ measured at 500 MHz.....	352
Figure 6.68: HSQC NMR spectrum of compound F12-11-2 in DMSO- <i>d</i> ₆ measured at 500 MHz. Red correlations are CH and CH ₃ while blue are CH ₂	353
Figure 6.69: ROESY spectrum and essential correlation of F12-11-2 in DMSO- <i>d</i> ₆ measured at 600 MHz.	354
Figure 6.70: PTLC methods for purification of SF29-6 from subfraction F11-29 using solvent system 50:50 % of n-Hexane and EtOAc.	357
Figure 6.71: Chemical structure of compound F11-29-6.....	358
Figure 6.72: Mass spectral data of F11-12 at the ion peak m/z 493.183 [M+Na] ⁺	358
Figure 6.73: ¹ H NMR spectrum of compound terretonin F in DMSO- <i>d</i> ₆ measured at 500 MHz.	359
Figure 6.74: HSQC NMR spectrum of compound terretonin F in DMSO- <i>d</i> ₆ measured at 500 MHz. Red cross peaks are CH and CH ₃ while blue are CH ₂	361
Figure 6.75: (¹ H- ¹ H) COSY correlation NMR spectrum of terretonin F in DMSO- <i>d</i> ₆ measured at 500 MHz.	362
Figure 6.76: HMBC NMR spectrum of compound terretonin F in DMSO- <i>d</i> ₆ measured at 500 MHz.	363
Figure 6.77: ROESY spectrum and their essential correlation of compound terretonin F in DMSO- <i>d</i> ₆ measured at 600 MHz.....	364
Figure 6.78: Effect of pure compounds isolated from <i>A. ustus</i> on ZR-75 and HS-27 cells at 30μg/mL. The red line indicates the bioactivity threshold.	368

Figure 7.1: Schematic diagram of proposed biosynthesis of the isolated compounds from chamomile varieties. Enzyme abbreviations: CHS, chalcone synthase; CHI, chalcone isomerase; FNS, flavone synthase; F3H, flavanone 3-hydroxylase; F3'H, flavonoid 3'-hydroxylase; F6H, flavanone 6-hydroxylase; FLS, flavonol synthase; 7-OMT, 3-methylquercetin 7-O-methyltransferase; F6-OMT-, F6-O-methyltransferase; ROMT-9, rice O-methyltransferase-9; 4CL, 4-hydroxycinnamoyl-CoA ligase; HCT, hydroxycinnamoyl-CoA shikimate/quinic acid hydroxycinnamoyl transferase; HQT, hydroxycinnamoyl CoA quinate hydroxycinnamoyl transferase; C3'H, p-coumaroyl ester 3'-hydroxylase (Alcazar Magana <i>et al.</i> , 2021, Han <i>et al.</i> , 2016, Do <i>et al.</i> , 2007, Berim and Gang, 2013, Kim, 2006).....	377
Figure 7.2: The proposed biosynthetic pathway of linoleic acid derivatives. (Gajewski <i>et al.</i> , 2017, Akpınar-Bayazit, 2014). Enzyme abbreviations; MGAT: monoacylglycerol acyltransferase.....	388
Figure 7.3: The proposed biosynthetic pathway of terpenoids derivatives (Dairi <i>et al.</i> , 2011). Abbreviation; isopentenyl pyrophosphate (IPP), dimethylallyl pyrophosphate (DMAPP), farnesyl diphosphate (FPP).	390
Figure 7.4: The proposed biosynthetic pathway of terpenoids derivatives (Yan <i>et al.</i> , 2022, Wenyu <i>et al.</i> , 2022, Huang <i>et al.</i> , 2021, Matsuda and Abe, 2016). The isolated compounds from <i>A. ustus</i> are in the black box. Abbreviation; isopentenyl pyrophosphate (IPP), dimethylallyl pyrophosphate (DMAPP), farnesyl diphosphate (FPP), terpene cyclase B (DrtB), cytochrome P450 (DrtD), FAD-binding oxidoreductase (DrtC), polyketide synthase (DrtA), dehydrogenase (DrtF), the acyltransferase (DrtE), 3,5-dimethylorsellinic acid (DMOA), cytochrome P450 (Trt6), OblAAu, OblBAu and OblCAu are oxidases.....	392
Figure 7.5: The chemical structures of bioactive congeners that are structurally related to the isolated compounds.	393

Abbreviations

¹³ C NMR	Carbon NMR
¹ H NMR	Proton NMR
4CL	4-hydroxycinnamoyl-CoA ligase
7-OMT	3-methylquercetin 7-o-methyltransferase
A549	human caucasian lung carcinoma
ACA	acyl-CoA
AChE	acetylcholinesterase
ACN	Acetonitrile
ax	axial
BLAST	basic local alignment search tool
bp	base pair
br	broad
CE	capillary electrophoresis
C3'H	p-coumaroyl ester 3'-hydroxylase
CHI	chalcone isomerase
COLO 20	human colon cancer cell line
COSY	correlation spectroscopy
CYP	cytochrome
d	doublet
D ₂ O	deuterium water
DBE	double bond equivalents
DCM	dichloromethane
DCQA	dicafeoyl quinic acid
DH	dehydrogenation with a dehydratase
DMAPP	dimethylallyl pyrophosphate
DMOA	3,5-dimethylorsellinic acid
DMSO	dimethyl sulfoxide
DNA	deoxyribonucleic acid
DNP	dictionary of natural products
DPPH	2,2-diphenyl-1-picrylhydrazyl
DrtA	polyketide synthase
DrtB	terpene cyclase B
DrtC	FAD-binding oxidoreductase
DrtD, Trt6	cytochrome P450
DrtE	acyltransferase
DrtF	dehydrogenase
ELSD	evaporative light scattering detector
eq	equatorial
ER	enoyl reductase
ER	oestrogen receptor
EtOAc	EtOAc
F3'H	flavonoid 3'-hydroxylase
F3H	flavanone 3-hydroxylase

F6H	flavanone 6-hydroxylase
F6-OMT	F6-O-methyltransferase
FA	fatty acid
FBS	foetal bovine serum
FC	flash chromatography
FDA	The US Food and Drug Administration
FES	F-fluoroestradiol
FLS	flavonol synthase
FNS	flavone synthase
FPP	farnesyl diphosphate
GC-MS	gas chromatography-mass spectroscopy
HCA	hierarchical cluster analysis
HCT	hydroxycinnamoyl-CoA shikimate/quinic acid hydroxycinnamoyl transferase;
HeLa	human cervix adenocarcinoma
HepG2	lung cancer
HFF	human foreskin fibroblasts
HIF	pronounced hormone-inducing factor
hiPSC	human induced pluripotent stem cells
HS-27	human foreskin fibroblast cells
HL-60	human leukemia
HMBC	heteronuclear multiple-bond correlation
HMDB	human metabolome database
HMQC	heteronuclear multiple-quantum correlation
HPLC	high performance liquid chromatography
HQT	hydroxycinnamoyl CoA quinate hydroxycinnamoyl transferase
HSQC	heteronuclear single quantum correlation
IPP	isopentenyl pyrophosphate
IPP	isopentenyl pyrophosphate
ITS	internal transcribed spacer
JMod	J-modulated spin
K-562	leukemia cancer
KR	ketoacyl reductase
L5178Y	mouse lymphoma
LC-HRMS	liquid chromatography-high resolution mass spectroscopy
LCNMR	liquid chromatography nuclear magnetic resonance
m	multiplet
MA	malt-agar
MCF-7	breast cancer
MeOH	MeOH
MGAT	monoacylglycerol acyltransferase
min	minute
MPLC	medium pressure liquid chromatography

MWt	MWt
NMR	nuclear magnetic resonance
<i>m/z</i>	mass to charge ratio
MS	mass spectrometry
NOESY	nuclear overhauser effect spectroscopy
O2PLS	modified orthogonal projections to latent structures
OPLS-DA	orthogonal partial least squares discriminant analysis
PC	principal component
PC12	rat pheochromocytoma cell
PC-3	metastatic prostate cells
PCA	principal component analysis
PCR	polymerase chain reaction
PLS-DA	partial least squares, or projections to latent structures-discriminant analysis
PR	progesterone receptor
prep-HPLC	preparative high-performance liquid chromatography
PTLC	preparative thin layer chromatography
q	quartet
quint	quintet
ROESY	rotating-frame noe spectroscopy
ROMT-9	rice o-methyltransferase-9
ROS	reactive oxygen species
rRNA	ribosomal ribonucleic acid
s	singlet
SIMCA	soft independent modelling by class analogy
SKOV3	ovarian cancer cells
t	triplet
TLC	thin layer chromatography
UK	United Kingdom
US	United States
UV	ultraviolet
VIP	variable importance in projection
ZR-75	human caucasian breast carcinoma

Abstract

Matricaria chamomilla belongs to the Asteraceae family that has been used for treatment of several diseases. The metabolomic profile of this genus indicates the occurrence of bioactive flavonoids and terpenes. Two endemic varieties of Jordanian and European chamomile were compared to investigate differences in their biologically active compounds. Additionally, the metabolomic profile of their associated endophytes including *Aspergillus ustus* and *Alternaria solani* was also studied. Both fungi are well-known for their capability to produce a wide range of chemical metabolites that have biological activity. There is a clear and urgent need for novel drugs with enhanced effectiveness for the treatment of breast cancer because it is the second most common cancer in females. The toxicity of modern chemotherapy and the resistance of cancer cells to anticancer drugs leads us to search for novel therapies and preventative strategies for this insidious illness. A metabolomics-guided approach was applied by using NMR and LC-HRMS as profiling tools. The spectral data was processed using Xcalibur, MZmine 2.53, an in-house MS-Excel macro, and the Dictionary Natural Products for dereplication studies. Biological activities were tested using both AlamarBlue® and DPPH® assay to test their anticancer and antioxidant activities, respectively. The European chamomile semi-polar extract had antioxidant and anticancer activity against breast cancer cells ZR-75, while the Jordanian semi-polar extract only exhibited antioxidant activity. After fractionation, both varieties were found to contain dicaffeoyl quinic acid isomers that exhibited antioxidant activity. Glucoferulic acid isolated from European chamomile displayed antioxidant activity. However, the Jordanian variant exhibited the most potent antioxidant activity (Table 3.6). European chamomile produced more metabolites, which included chrysosplenetin and apigenin that had selective anticancer activity (Table 3.7) against ZR-75 cells and were nontoxic against HS-27 cells

On the other hand, preliminary bioassay screening of the endophytic fungal crude extract that was obtained from Jordanian *M. chamomilla* showed 80% growth inhibition of ZR-75. The bioactive endophytes, *A. ustus* and *A. solani*, were taxonomically identified using internal transcribed spacer gene sequencing. The fungi were incubated on different media at 7-, 15-, and 30-day incubation periods. *A. ustus*

was chosen for scale-up and isolation work because its extracts provided the most potent activity (figures) against the breast cancer cells, but no antioxidant activity was observed. *A. ustus* was scaled-up on potato-dextrose medium. However, *Alternaria solani* was discontinued for further work due to loss of bioactivity during media optimisation. After fractionation, seven compounds were isolated using 1D, 2D NMR data and direct fusion mass spectroscopy including three drimane-sesquiterpenes derivatives: 9 α -hydroxy-6 α [(2*E*,4*E*,6*E*)-octa-2,4,6-trienoyloxy]-5 α -drim-7-en-11,12-olide, ustusolate E and *E,E*-6-(6',7'-dihydroxy-2',4'-octadienoyl)-strobilactone A, terretonin F, and ophiobolin K. Additionally, two linoleic-acid derivatives including 1',2-diolinolein and 3'-hydroxy-2'-(palmitoyloxy)-propyl (9*Z*,12*Z*)-octadeca-9,12-dienoate. All the drimane sesquiterpenes derivatives were found to be active against breast cancer cells (ZR-75) with an IC₅₀ less than 6 μ M and found moderately toxic on HS-27 cells and selective on ZR-75 cells (figures). Additionally, 3'-hydroxy-2'-(palmitoyloxy)-propyl (9*Z*,12*Z*)-octadeca-9,12-dienoate and terretonin F were found to be active against ZR-75 cells with IC₅₀ of 2.47 μ M and 4.66 μ M, respectively. Both were considered not toxic on HS-27 and selective on ZR-75 cells. None of the isolated compounds from *A. ustus* exhibited antioxidant activities.

And so what is your conclusion

1. Introduction

1.1. Drug discovery

Historically, drug research depends primarily on natural products as the major source of medicines, which has had a significant impact on drug discovery and development (Alamgir, 2017). The pathway to drug discovery divides into three branches. The first approach is rational drug design, in which a medication is customised to its proposed target (Mandal *et al.*, 2009). The second method is combinatorial chemistry, in which a large number of compounds are produced *in silico* to establish a combinatorial library, which is then evaluated against the proposed target to select the most potent and active compounds (Gallop *et al.*, 1994, Liu *et al.*, 2017). The third approach in drug development is phenotypic screening of natural products. Phenotypic screening permits the assessment of the activity of natural products at the cellular, tissue, or whole-organism level without previous knowledge of the molecular mechanism of action of such natural products (Alvin *et al.*, 2014).

The process of developing a new drug starting from target identification to final product presentation and approval for public prescription by a governmental/local state authority (e.g. FDA—Food and Drug Administration, EMA—European Medicines Agency) takes 12–15 years, which costs companies millions of dollars (Mohs and Greig, 2017). Preclinical development includes specific activities such as studies of absorption, distribution, excretion, and metabolism, as well as screening for activity on cytochrome P450 (CYP) liver enzymes, assay metabolites for acute pharmacology, and *in vitro* toxicity (Pereira and Aires-de-Sousa, 2018). Then followed by clinical trials, which include Phase I, II, and III that comprises ethics review, *in vivo* metabolism assessment, pharmacokinetic studies, and as a final step, it entails

regulatory filings for new drug application (Hughes *et al.*, 2011, Pereira and Aires-de-Sousa, 2018).

1.2. Introduction to natural products

A natural product is any substance produced by living organisms, and there are three basic types (Hanson, 2003). The first category includes small MWt primary metabolites present in all biological systems. These include sugars, lipids, nucleic acids, and amino acids as examples. In metabolism and reproduction, primary metabolites are critical. The second category of metabolites has larger MWt than the primary metabolites such as lignin, proteins, and celluloses, which is significant in cellular structures. Secondary metabolites are the final category. Their function is determined by the organism's interaction with its environment and other species, whether through symbiosis or commensalism. Secondary metabolites are important compounds to study because they may serve as pollinator attractants or as a defence mechanism to protect organisms from predators and environmental stresses. Many secondary metabolites have biological effects of their own and may offer significant activity for medicinal applications (Hanson, 2003, Sarker and Nahar, 2012).

Natural products play an important role in the drug discovery. Plants have been used for the treatment of different illness and diseases for thousands of years. Mainly, secondary metabolites are responsible for the medicinal effect assumed in many plants (Dias *et al.*, 2012). Furthermore, natural product metabolites show a wide range of chemical structures and biological activities (Dias *et al.*, 2012). Most of the active ingredients of medicine have been extracted from natural products or derived from a natural compound, which is responsible to produce more than 80% of the drug substances (Harvey, 2008).

For decades, plants had been the main source for the extraction of natural products. However, with the emergence of new methodologies of isolation and purification, new biologically active natural products are being discovered from other kingdoms. As an example (Figure 1.1) , paclitaxel (Taxol®), widely used as a breast cancer drug, was isolated from the bark of *Taxus brevifolia* (a plant), penicillin was derived from a fungus *Penicillium notatum* discovered by Fleming in 1929 and plitidepsin was

isolated from the Mediterranean tunicate *Aplidium albicans* (a marine invertebrate), which is effective in treating various cancers (Cragg, 1998, Rinehart and Lithgow-Berelloni, 1991, Urdiales *et al.*, 1996, Abraham *et al.*, 1992). Different therapeutic indications have been described for various natural products that included anti-cancer, anti-inflammatory anti-diabetic, anti-fungal, antiviral and antimicrobial agents (Harvey, 2008).

Several types of plants have been investigated to study anti-cancer activity proving to be useful in the treatment and prophylaxis of cancer. Moreover, some of the active compounds from the plants seem to be safe and effective in different types of cancer (Khan *et al.*, 2019). For example, the active ingredients from *Phaleria macrocarpa* (also known as *Mahkota dewa*) and *Fagonia indica* (also known as *Dhamasa*) have historically been used for their anticancer properties (Shehab *et al.*, 2011, Faried *et al.*, 2007). In cancer cells, apoptosis may be induced by using metabolites that have been isolated from plant material. Gallic acid, which serves as the active component, was isolated from the fruit extract of *Phaleria macrocarpa* and has been shown to have a role in the activation of apoptosis in cell lines derived from lung cancer (LL-2), leukaemia (HL-60RG), and colon adenocarcinoma (Caco2) (Sohi *et al.*, 2003, Inoue *et al.*, 1994).

Natural products are still the most successful source of biologically-active lead compounds, even when compared with advanced strategies such as high-throughput screening of substances obtained through synthesis and combinatorial chemistry (Chagas-Paula *et al.*, 2015).

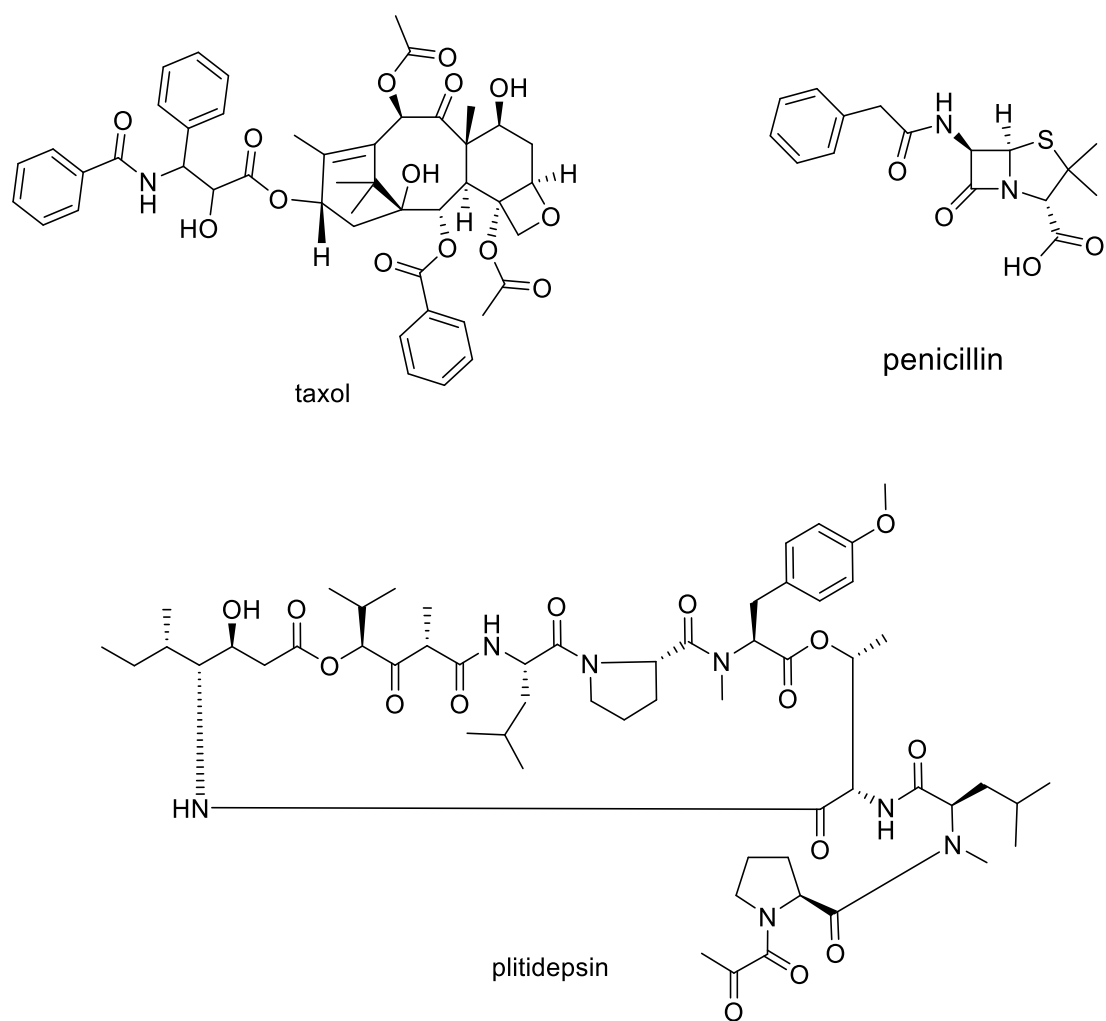


Figure 1.1: Examples of compounds isolated from plant, fungi, and marine invertebrates

1.3. Natural products from plants in drug discovery

Plants play an important part in drug discovery by producing a variety of bioactive compounds that are approved as medications by the Food and Drug Administration (FDA). Natural compounds have been effectively used as drug precursors in the development of more potent drugs, as well as pharmacological probes (Salim *et al.*, 2008). An example of a drug obtained from a plant is podophyllotoxin, which was found in the resin that was extracted from *Podophyllum peltatum* L. The synthetic derivative etoposide has been used to treat small-cell lung cancer and testicular cancer. Etoposide is a topoisomerase II inhibitor that binds tubulin and unravels

deoxyribonucleic acid (DNA), resulting in the breakage of DNA strands during the G2 phase of the cell cycle and cell death (Baldwin and Osheroff, 2005). Another drug is camptothecin, which is a quinoline alkaloid that was extracted from the bark and stem of *Camptotheca acuminata* Decne (Nyssaceae). In Traditional Chinese Medicine, the plant was used to treat cancer patients (Efferth *et al.*, 2007). Camptothecin is an inhibitor of topoisomerase I (Liu *et al.*, 2000). However, it was found that it had poor solubility and a high rate of adverse effects. Hence, two analogues, topotecan and irinotecan were synthesised, which were later developed and used in cancer treatment (Balunas and Kinghorn, 2005). Russian researchers extracted galantamine from *Galanthus woronowii* Losinsk and developed it against Alzheimer's disease. Galantamine has a dual mechanism of action. It works by inhibiting acetylcholinesterase (AChE) and modulating the nicotinic acetylcholine receptor, which slows down the neurological degeneration process (Aly *et al.*, 2011a). Another drug is artemether, which is used to treat acute malaria. It is a derivate of artemisinin, which is a sesquiterpene lactone derived from *Artemisia annua* L (Van Agtmael *et al.*, 1999). All the above compounds were shown in Figure 1.2.

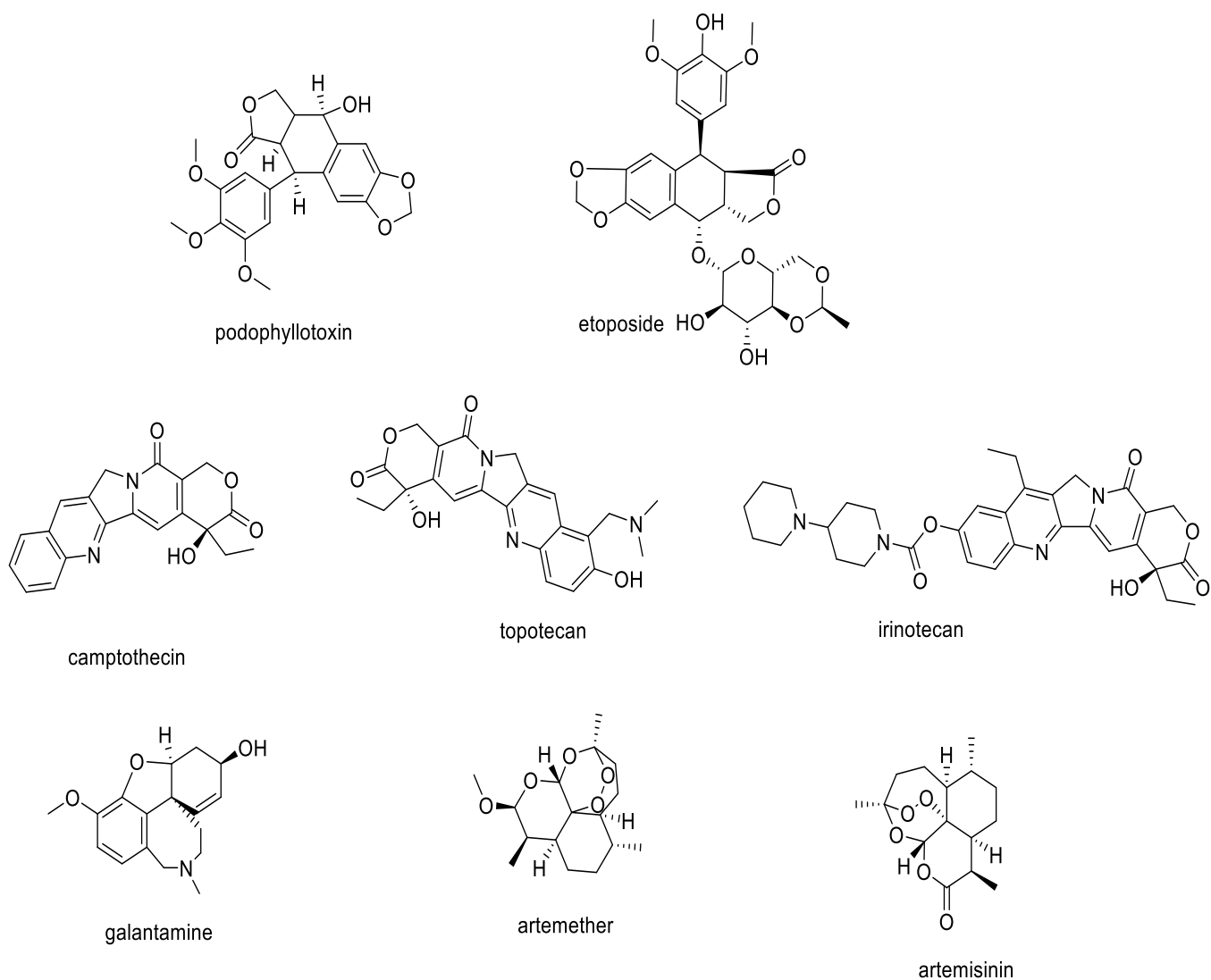


Figure 1.2: FDA-approved medications derived from plant natural products

1.4. The role of endophytes in the production of secondary metabolites

In 1866, Heinrich Anton, a German botanist and microbiologist, first introduced the word "endophyte" (Nisa *et al.*, 2015). Endophytes are microorganisms that colonise intercellular and intracellular sections of healthy plant tissues without causing obvious damage or activating defense responses (Yu *et al.*, 2010, Alvin *et al.*, 2014, Kusari *et al.*, 2014, Reinhold-Hurek and Hurek, 2011) These microorganisms are often fungi. However, they might also be bacterial such as actinomycetes (Nisa *et al.*, 2015, Bhimba *et al.*, 2012, Shah *et al.*, 2017). Plants serve as a source energy for a variety of endophytes that may be found in almost all plants, from herbs to trees and to algae (Strobel and Daisy, 2003, Samaga and Rai, 2016). Bioactive agents which have been

derived from fungal endophyte are responsible for different beneficial activities including anticancer, antiparasitic, anticancer agents, agrochemicals, antibiotics, immune suppressants and antioxidants (Strobel, 2003, Gunatilaka, 2006)

Basically, endophytic-plant symbiosis is not the sole symbiosis between plants and fungi. Mycorrhizal and endophytic fungi are the two subtypes of fungus-plant symbioses. The term "mycorrhiza" refers to a fungus that has a symbiotic interaction with plant roots, while "endophyte" refers to a fungus that lives within above-ground plant tissue and does not damage the plant. Mycorrhizal associations are more prevalent than endophytic associations and include the interaction between the plant, mutualistic fungus, and soil components. Mycorrhizal interactions are often non-pathogenic and the exchange of chemical signals between the root of the plant and the mycorrhizal fungus may stimulate the synthesis of specific metabolites by the plant (Yuan *et al.*, 2007). In contrast, endophytic interactions are more complex and often occur in the above-ground portions of plants. Nevertheless, roots may also contain endophytes (Yuan *et al.*, 2007). In the case of endophytic-plant associations, metabolites may be produced by the endophyte, by the plant because of endophytic eliciting factors that induce the production in the plant tissues, or by complex interactions between the endophyte and the plant that result in structural modifications or partial synthesis of the compound produced by one life form by the other (Ludwig-Muller, 2015, Wani *et al.*, 2015).

Endophyte-plant interactions have recently attracted researchers due to their potential to provide promising candidates and novel metabolites for drug development (Aly *et al.*, 2010, Strobel and Daisy, 2003). Endophytes associated with plants are becoming more popular as a source of biochemical variation. Moreover, endophytes' involvement in protecting plants from dangerous microorganisms and pathogens might be used to develop novel medicines and anti-infectives. Also, since the endophyte lives in a eukaryotic system, the produced substances may minimise cell toxicity (Strobel and Daisy, 2003, Chadha *et al.*, 2015). Endophytes' interaction with their environment may also allow them to develop unique secondary metabolites (Schulz *et al.*, 2002)

1.5. Plant-endophyte interactions

Endophytes do not cause any damage to their hosts, and their relationship with the plant is mutually beneficial (Grayer and Kokubun, 2001). Despite this, not all plant-microbe interactions are endophytic in nature. These interactions might be harmful, saprophytic (when an organism lives and feeds on decomposing organic matter to gain nutrition for growth), or helpful to the plant, depending on how they affect the plant's health. The interaction between plants and endophytes have been suggested to be more than 400 million years, as shown by the discovery of plant-associated microorganisms in fossilised stems and leaves of plants (Taylor and Taylor, 2000, Rodriguez and Redman, 2008). There is speculation that a horizontal genetic information transfer occurred between host plants and endophytes (Stierle *et al.*, 1993). This process include the movement of genetic information between organisms, which is responsible for the evolution of pathogens and contributes to the spread of antibiotic resistance genes among bacteria (with the exception of those that are passed down from parent to offspring) (Burmeister, 2015). So, it is possible that the same biosynthetic pathway has evolved in both the host plant and the endophyte, ensuing the synthesis of secondary metabolites that are comparable in both species (Alvin *et al.*, 2014, Bömke and Tudzynski, 2009).

Understanding the behaviour of microbes and their interactions in their natural and diverse environments and interactions between plants and endophytes is challenging. The identification of the plant by microbes is the initial stage in the process of plant-microbe interaction. Initiating a plant's reaction to microorganisms is the key for interaction to take place. This recognition might be accomplished by a physical contact involving adhesins, fimbriae, or flagella, or it could be accomplished through a chemical interaction involving the utilisation of signalling substances (Hardoim and Van Elsas, 2013, Lugtenberg *et al.*, 2002). Then, spore germination, endophyte penetration of the epidermis, and endophyte colonisation of plant tissues will occur. Good colonisation involves a strong defence by the microbe's cells, an effective intake of nutrients, and the weakening or eradication of other organisms seeking to colonise the same plant (Lugtenberg *et al.*, 2002, Nisa *et al.*, 2015, Sieber, 2007). Additionally, phase variation may play a role in evading the host's immune system. Finally, the

microorganism will initiate the creation of extracellular enzymes and secondary metabolites (Lugtenberg *et al.*, 2002). Endophytic fungi and bacteria lack chlorophyll, so they have lost the capacity to make photosynthesis. As a result, they spend all or a part of their life cycles colonising host organisms, particularly plants, for their carbon and energy sources without causing an obvious illness (Behie *et al.*, 2017, Grayer and Kokubun, 2001, Nisa *et al.*, 2015). On the other hand, plants also benefit from the secondary metabolites that the endophytes produce. It was hypothesised that secondary metabolites produced by a plant's colonised endophytes contribute to the plant's ability to respond to biotic and abiotic stress conditions (such as drought) (Giordano *et al.*, 2009).

As a result of this symbiotic interaction with its endophytes, a plant's biological defense against diseases is developed (Alvin *et al.*, 2014). The endophyte releases antibacterial, antifungal, antiviral, or insecticidal secondary metabolites, which would directly attack pathogens and lyse the affected cells, or by the induction of the plant's defence mechanism and promotion of its growth to compete for cell apoptosis, thereby enhancing the growth and competitiveness of the host plant in nature (Strobel, 2003, Berg and Hallmann, 2006, Nisa *et al.*, 2015, Alvin *et al.*, 2014). Furthermore, the secondary metabolites produced by endophytes might assist the host plant to adapt harsh environmental circumstances (Aly *et al.*, 2008). The synthesis of phytohormones by endophytes helps to stimulate the growth of plants (Owen and Hundley, 2004).

1.6. Plant-endophyte interactions uses and benefits

The secondary metabolites generated by endophytes and engaged in the host-endophyte interaction have considerable promise for drug development and have shown to be a promising source of medicinal natural products (Geris dos Santos *et al.*, 2003, Verma *et al.*, 2009, Nisa *et al.*, 2015). Furthermore, the endophytic secondary metabolites play an important role as antibiotics, anticancer agents, antioxidants, and anti-inflammatory agents that has incorporated their role in drug discovery (Chow and Ting, 2015, Sudha *et al.*, 2016, Zhang *et al.*, 2016).

Several studies have shown that the inoculation of *in vitro*-grown plants with endophytic fungus increases biomass and the generation of secondary metabolites in

plant suspension cells (Mucciarelli *et al.*, 2003, Sherameti *et al.*, 2005). Furthermore, coculture of various endophytes may promote the expression of silent gene clusters (under laboratory conditions, these clusters remain silent and inactivated) that may allow for the synthesis of novel and biologically active metabolites or for the stimulation of the production of known metabolites and the increase of their yield (Ola *et al.*, 2013).

In addition, some of the novel and biologically active secondary metabolites occurred as a minor component. So, this issue might be overcome by overexpressing of their biosynthetic gene clusters (clustered group of genes involved in the production of secondary metabolites) in cultivable organisms such as endophytes (Kalaitzis, 2013, Nah *et al.*, 2013, Stevens *et al.*, 2013).

1.7. Obstacles to work with plant-associated endophytes

On the other hand, plant-associated endophytes provide a few challenges that must be addressed to fully understand their function. First and foremost, it is critical that the fungal endophyte be appropriately identified. This may not always be a simple process since many fungi display various anamorphs (asexual reproductive cycle) and teleomorphs (sexual reproductive cycle) in plants and *in vitro* (Wiklund, 2008). Consequently, for fungal endophytes, traditional taxonomic identification is insufficient, which is based on the observable morphological characteristics. Meanwhile, sequencing of the internal transcribed spacer (ITS) region ribosomal ribonucleic acid (rRNA) is required to make an accurate identification (Gardes and Bruns, 1993, Horton and Bruns, 2001, Kusari *et al.*, 2014). ITS is a segment of non-functional RNA found between structural ribosomal RNAs (rRNA) of a common precursor transcript, which is particularly beneficial for clarifying relationships between congeneric taxa and closely related genera (Hao *et al.*, 2010). The ITS region has several advantages over other regions, including the fact that only a small amount of it is required for amplification because it contains well-conserved fungal specific priming sites that are directly adjacent to highly variable regions, which allows the use of the same primers to identify different genera and species, the availability of comparison sequences, and its correlation with morphologically defined species (Peay *et al.*, 2008). When it comes to bacterial endophytes, however, it is thought important

to do a 16S rRNA-based phylogenetic analysis (Hentschel *et al.*, 2001, Macintyre *et al.*, 2014).

It is also challenging to maintain the expression of biosynthetic genes, which are essential for the creation of new bioactive secondary metabolites under certain fermentation conditions. The production of secondary metabolites could be reduced during repeated sub-culturing, which is particularly true when monoculture methods are used. Since such conventional culture conditions do not stimulate the expression of specific endophyte cryptic gene clusters, the endophyte's synthesis of secondary metabolites will be less diversified than anticipated (Kusari and Spiteller, 2011, Kusari *et al.*, 2014, Scherlach and Hertweck, 2009).

1.8. *Matricaria chamomilla*, *Chamaemelum nobile*. Asteraceae

1.8.1. Botany

Chamomile is a flowering plant, which has been used in traditional folk medicine for centuries, and it is widely distributed around the globe (Singh *et al.*, 2011). It is commonly referred to as the star amongst medicinal plants (Schilcher, 1987). There are two varieties of chamomile: the German and Roman chamomile scientifically known as *M. chamomilla* and *Chamaemelum nobile*, respectively. Chamomile is a member Asteraceae or Compositae family, which is traditionally known for its healing applications (Srivastava and Gupta, 2015). Two endemic varieties of chamomile belonging to the same genera and growing in different environmental conditions were compared to find differences in their biological active compounds. These varieties include Jordanian and European chamomile that were identified as *M. chamomilla*.

Chamomile contains around 120 different secondary metabolites. The most important metabolites includes sesquiterpenes, flavonoids, coumarins, and polyacetylenes, those compounds families have proved to exhibit different biological activities (Pirzad *et al.*, 2006).

1.8.2. Chemical Composition

Chamomile contains 0.2-2% of volatile oil, the major components are essential oil and flavonoids, which have several biological activities. Apigenin and its glycosides are the most promising flavonoids (Schilcher, 1987). Some of the flavonoids identified in

M. chamomilla, such as apigenin, luteolin, and apiin, are also present in Roman chamomile, as are phenolic carboxylic acids (caffeic, ferulic), coumarins, and thiophene derivatives (Singh *et al.*, 2011). The main components of essential oil were chamazulene, *cis*- β -farnesene, eucalyptol, coumarin, galaxolide, and camphor (Bömke and Tudzynski, 2009). German chamomile flowers contain a higher concentration of terpenoids and chamazulene (a deep blue volatile principle) than Roman chamomile flowers, while the latter generates more ester-like compounds. (Srivastava *et al.*, 2010).

The major part for producing essential oil are flowers and flower heads. Sesquiterpene derivatives (75–90%) are dominant in chamomile flower oil, whereas monoterpenes are rare. Polyenes make up to 20% of the oil. The main components of the essential oil isolated from the flowers are (*E*)-farnesene, terpene alcohol (farnesol), chamazulene, α -bisabolol and bisabolol oxides A and bisabolol oxides B (Isaac, 1979, Schilcher, 1987, Barton *et al.*, 1999). The plant's leaves, stem and root also contain essential oils. Earlier studies showed the presence of (*Z*)-3-hexenol, (*E*)-farnesene, germacrene D, (*E*)-nerolidol, spathulenol, hexadec-11-yn-11,13-diene, and (*Z*)- and (*E*)-en-yn-dicycloethers in leaves and stem. While the root oil included linalool, nerol, geraniol (Reichling *et al.*, 1979). These oils had no chamazulene or bisabolol, however its oxides were the minor components (Singh *et al.*, 2011). Secondary metabolites isolated from German and Roman chamomile are shown on Figure 1.3.

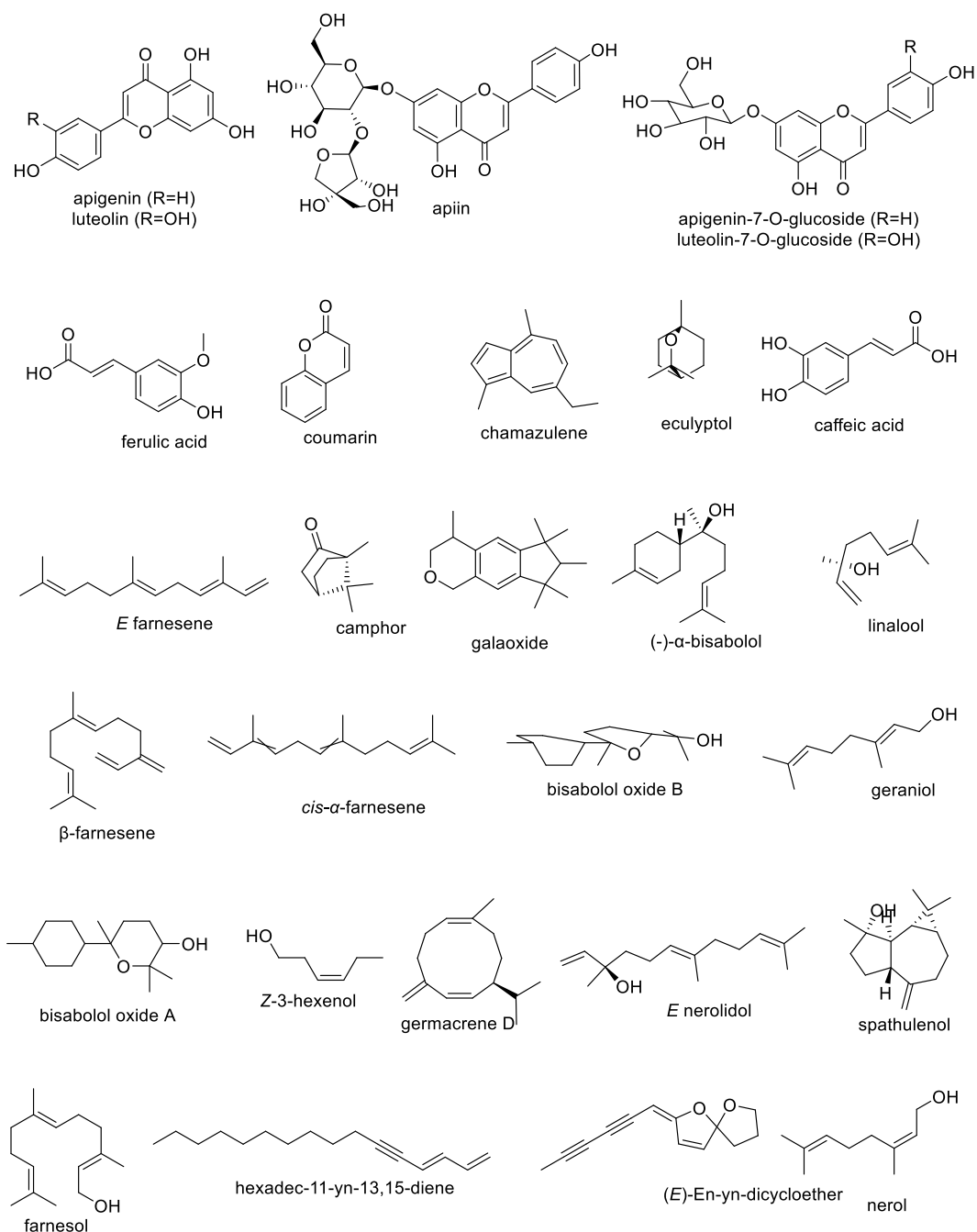


Figure 1.3: Secondary metabolites isolated from German and Roman chamomile. (Bömke and Tudzynski, 2009, Isaac, 1979, Schilcher, 1987, Barton *et al.*, 1999, Reichling *et al.*, 1979).

1.8.3. Medicinal uses and application

Historically, chamomile has been used for the treatment of several ailments including stomachics, carminatives, gingivitis, diuretic, anti-inflammatory, aromatic, acute

respiratory infection, common cold, irritable bowel syndrome, skin problems, dysmenorrhea, hemorrhoids, indigestion, insomnia, nausea, vaginitis, and for topical application (Tawfike *et al.*, 2013).

1.9. Metabolomics approach

1.9.1. Introduction to metabolomics

The term "metabolome" was first used in 1998, according to historical records (Oliver *et al.*, 1998). High Resolution Liquid Chromatography Mass Spectrometry (HR-LCMS), Gas Chromatography Mass Spectrometry (GCMS), and Liquid Chromatography Nuclear Magnetic Resonance (LCNMR) are hyphenated analytical techniques used in metabolomics research (Dunn *et al.*, 2005). These techniques are combined with available databases such as The Human Metabolome Database (HMDB), METLIN, the Golm metabolome databases in conjunction with cutting-edge chemometric tools such as MZmine, MZmatch, and MetaboLab. Data is statistically analysed using multivariate software such as SIMCA or a freeware like Metaboanalyst, which allows simple pattern recognition (Horai *et al.*, 2010, Hummel *et al.*, 2007, Wishart *et al.*, 2007, Smith *et al.*, 2005, Kind *et al.*, 2009). Integration of these approaches and methodologies has shown metabolomics to be an efficient and robust tool for drug discovery research.

Metabolomics is a discipline that focuses on identifying and fully analysing the changes in low-molecular-weight metabolites in biological systems. These metabolites are a diverse set of compounds that serve as building blocks for a variety of biological components or play critical roles in various cellular functions, including enzyme regulation and cell signalling. Metabolomics is extensively used to discover biomarkers for medical diagnostics and prognosis, to understand disease evolution processes, and to identify new therapeutic targets (Lin *et al.*, 2010, Johnson *et al.*, 2016).

Metabolomics is classified as either targeted or untargeted (Figure 1.4). Targeted metabolomics is aimed to investigate a pathway and analyse at length the impact of a target metabolite as a biomarker (Griffiths *et al.*, 2010, Patti *et al.*, 2012). An untargeted approach, on the other hand, examines as many metabolites as possible in a biological sample without prioritising any certain pathway, enzyme, or biomarker

(Patti *et al.*, 2012). Metabolomics has been adopted as an analytical platform in a wide range of research fields, including ecology (Lankadurai *et al.*, 2013), biomedical and systems biology (Weckwerth, 2003), toxicology (Ramirez *et al.*, 2013), nutrition and food science (Wishart, 2008), herbal products (Sun *et al.*, 2012), and most recently in natural products research (Tawfike *et al.*, 2013, Robinette *et al.*, 2012).

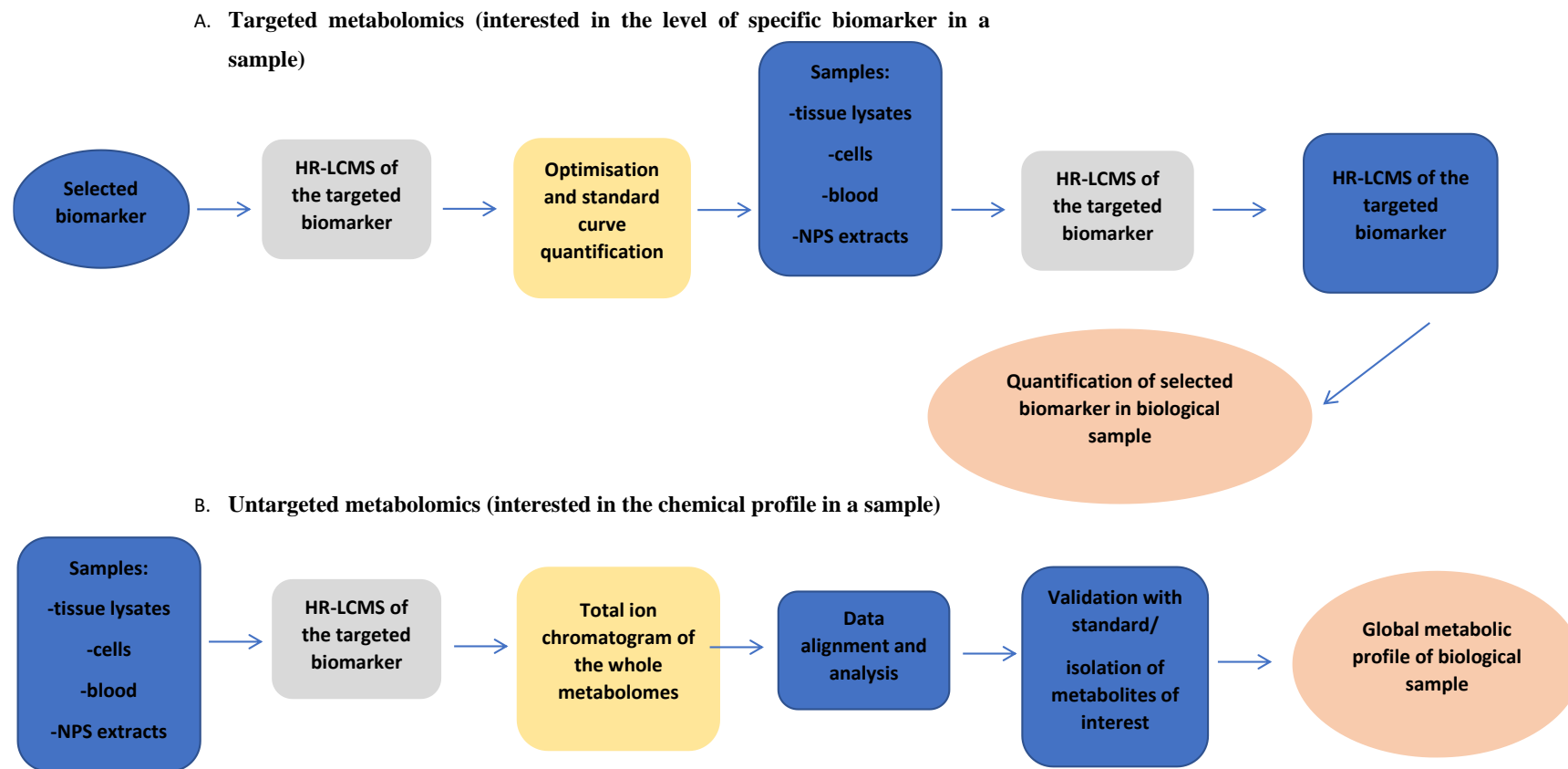


Figure 1.4: Schematic diagram for metabolomics approach A) metabolomic targeted approach B) metabolomic untargeted approach. Figured adapted from (Patti *et al.*, 2012).

The metabolome is a genomic end-product that defines the complete quantitative group of small MWt compounds (metabolites) present in a cell or organism that participate in metabolic processes (Dunn *et al.*, 2005). When compared to genes and proteins, whose function is subject to epigenetic regulation and 54 post-translational modifications, respectively, metabolites are small molecules that are chemically transformed during metabolism, providing functional information of cellular state and serving as direct signatures of a biochemical activity. As a result, they are easy to correlate with phenotypes (Patti *et al.*, 2012).

Metabolomics is one of the omics cascades, which includes genomics, proteomics, and transcriptomics that intends to qualitatively and quantitatively characterise the metabolome by using different analytical platforms and methodologies (shown in Figure 1.5 (McMurray *et al.*, 1989). In addition to the other omics techniques, metabolomics plays a crucial role in integrating genotype-phenotype data (Lopes *et al.*, 2017).

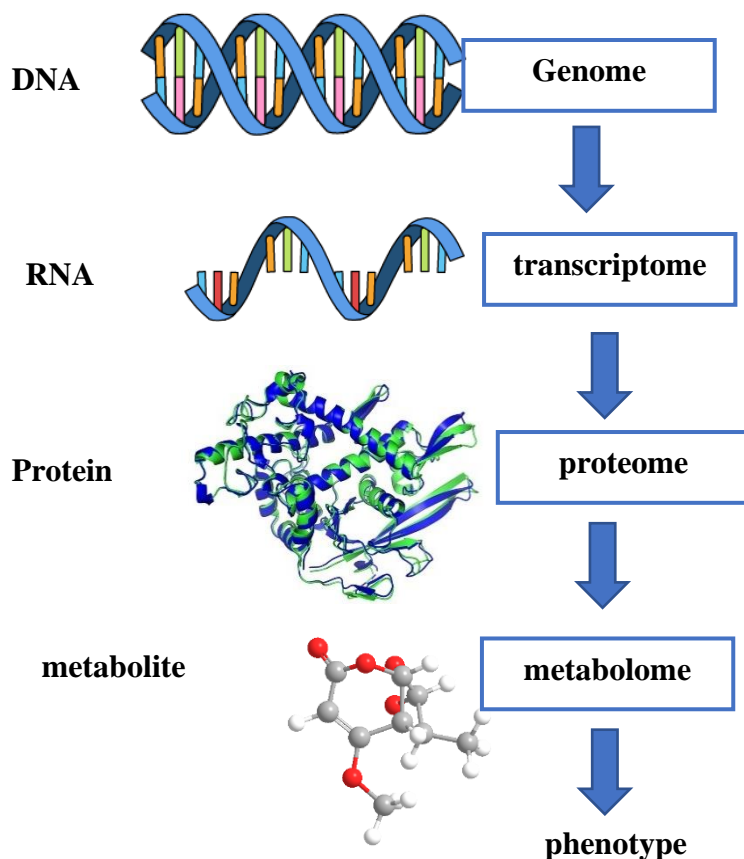


Figure 1.5: The omics cascade. The metabolome is the most representative of the phenotype. Adapted from (Haukaas *et al.*, 2017)

1.9.2. Tools of spectral analysis

It is difficult to identify and quantify metabolites in natural product extracts (Kjer *et al.*, 2010, Ebada *et al.*, 2008). This is because the secondary metabolites have various atomic arrangement, resulting in different chemical and physical characteristics. Identifying and measuring different chemical groups of natural products requires reliable, robust, selective, and high-resolution analytical tools. liquid chromatography-mass spectroscopy (LC-MS) and nuclear magnetic resonance (NMR) spectroscopy are complementary analytical methods that are used as metabolomics tools. MS is sensitive, but it may not be reproducible depending on the instrument type and ionisation capabilities of the metabolites. It is also advantageous

for elucidating unknowns by multiple MS fragmentation. Whereas, NMR data are more reproducible, but it may not be sensitive enough to identify metabolites at low quantities (Tawfike *et al.*, 2013). The most common metabolomics approaches are LCMS and NMR (Villas-Bôas *et al.*, 2005) and the obtained spectral dataset is further processed using different software such as MZmine, MetAlign, MestReNova, XCMS, MS-DIAL and MathDAMP (Katajamaa and Oresic, 2005, Lommen, 2009, Smith *et al.*, 2005, Baran *et al.*, 2006, Tsugawa *et al.*, 2015). Respective software can be coupled with online or commercially available libraries and databases like the Dictionary of Natural Products (DNP (Informa, 2021)), ChemSpider (Pence and Williams, 2010), MarinLit (Blunt *et al.*, 2012) or an in-house custom database to dereplicate secondary metabolites, which include separation and purification of novel secondary metabolites against natural products (Harvey *et al.*, 2015, Macintyre *et al.*, 2014). Then the processed data is further subjected to multivariate statistical analysis applying either unsupervised clustering such as partial component analysis (PCA) that aims to compress co-varying data from an X matrix into a smaller set of independent (orthogonal) latent variable or supervised clustering such as orthogonal partial least squares discriminant analysis (OPLS-DA) that provide information on the putative bioactive metabolite at the first fractionation step or detect putative biomarkers in a cellular process (Nejadgholi and Bolic, 2015, Robotti and Marengo, 2016, Morlock *et al.*, 2014). Many commercial or online databases are available for metabolomics research. For example: Dictionary of Natural Products has over 260 000 metabolites and the Dictionary of Marine Natural Products contains over 48 000 (Informa, 2021), ChemSpider (Pence and Williams, 2010), MarinLit (Blunt *et al.*, 2012), which has about 58 000 compound for marine natural products. AntiBase (Laatsch, 2011) is a database used for microbial metabolites and supported the dereplication strategy.

1.9.3. MS analysis

MS is used for identification and/or quantification of different classes of metabolites and characterised by their mass to charge ratio (m/z) (Becker *et al.*, 2012). A mass

spectrometer consists of a sample inlet, an ion source, a mass analyser, and a detector with functions that introduce the sample into the mass spectrometer, generating gas-phase ions through an ionisation technique, separating the ions according to their m/z value, and generating an electric current proportional to the abundances of the incident ions (Becker *et al.*, 2012). Metabolite identification and quantification are now possible with the development of capillary electrophoresis (CE), gas chromatography (GC), and high-performance liquid chromatography (HPLC). The use of MS in metabolomics has several important benefits. It is highly sensitive to detect and identify metabolites from a small volume of samples. Employing high resolution mass measurements afford ease in mass spectral data interpretation and molecular formula prediction (Lindon *et al.*, 2000). In contrast to NMR spectroscopy, however, MS is a destructive, meaning that the sample cannot be recovered once it has been analysed (Lindon *et al.*, 2000, Wishart *et al.*, 2009).

1.9.4. NMR spectroscopy

NMR spectroscopy is a method that is frequently applied in metabolomics research. This method has many advantages that include the following: it is specific while at the same time non-selective; it is non-destructive; it does not require separation or derivatisation; it is quick; and it provides highly reproducible and quantitative results (Wishart, 2016, Dunn *et al.*, 2005, Viant *et al.*, 2003). The NMR spectrum is unique to each compound and provides unique structural information about the parts of the sample being studied by combining the information on chemical shift (nature of chemical environment), signal multiplicities (neighbouring signals), homonuclear and heteronuclear coupling constants, integral of the signal (number of protons), spin-spin coupling (number and nature of neighbours and connectivity information (Dunn *et al.*, 2005, Dona *et al.*, 2016).

Although the one-dimensional proton ($1D-^1H$) NMR is the most common type of NMR experiment. There are currently other NMR techniques that can be performed that provide additional chemical and structural information, which include COSY

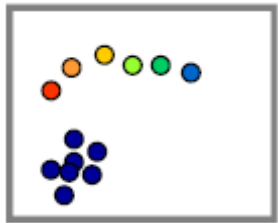

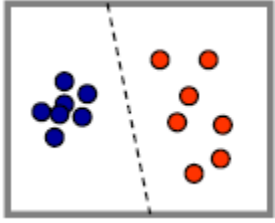
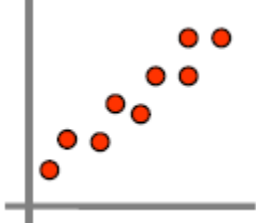
(homonuclear correlation spectroscopy), HSQC (heteronuclear single quantum coherence), HMBC (Heteronuclear Multiple Bond Correlation), and ROESY (Rotating-Frame NOE Spectroscopy) spectral data. The COSY spectrum indicates which H atoms are coupling with each other. While HSQC and HMBC indicate correlation between ^1H nmr spectrum on one axis and the ^{13}C nmr spectrum on the other by direct bond correlation and two to four bonds correlation, respectively. On the other hand, ROESY indicate proton to proton coupling in the space. These techniques are useful in situations where the ^1H NMR is unable to provide enough data to completely characterise the metabolite (Villas-Bôas *et al.*, 2005, Viant *et al.*, 2003).

1.9.5. Chemometrics and multivariate analysis

A multivariate statistical analysis of the processed data could be performed for data pattern visualisation. The analysis was done by using unsupervised clustering such as PCA, or hierarchical clustering (HCA), soft independent modelling by class analogy (SIMCA), or PLS, PLS-DA and OPLS-DA as well as modified orthogonal projections to latent structures (O2PLS) (Nejadgholi and Bolic, 2015, Robotti and Marengo, 2016, Morlock *et al.*, 2014, Wiklund, 2008).

PLS can be used to discriminate between two classes such as healthy versus diseased states to target biomarkers for diagnosis and treatment. It can also be used to discriminate between bioactive versus inactive natural products to pinpoint secondary metabolites responsible for specific bioactivity. This approach is an expansion of the supervised PLS regression method that incorporates a new component, the orthogonal signal correction filter (OSC), which allows systemic variation in X that is orthogonal to or uncorrelated to Y to be recognised OPLS-DA (Figure 1.6) give the information on the putative bioactive metabolite either at the first fractionation step or in a cellular process (Wold *et al.*, 1987). All the multivariate approaches are summarised in Table 1.1.

Table 1.1: Some of the analysis used in multivariate approaches (Wiklund, 2008).

PCA: Overview	SIMCA: Classification	PLS-DA and OPLS- DA: Discrimination	O2PLS: Regression
Trends	Pattern recognition	Discriminating between groups	Comparing blocks of omics data
Outliers	Diagnostics	Biomarker candidates	Metabolomic vs proteomic vs genomic
Quality control	Healthy/diseased	Comparing studies or instrumentation	Correlation spectroscopy
Biological diversity	Toxicity mechanisms		
Patient monitoring	Disease progression		
			

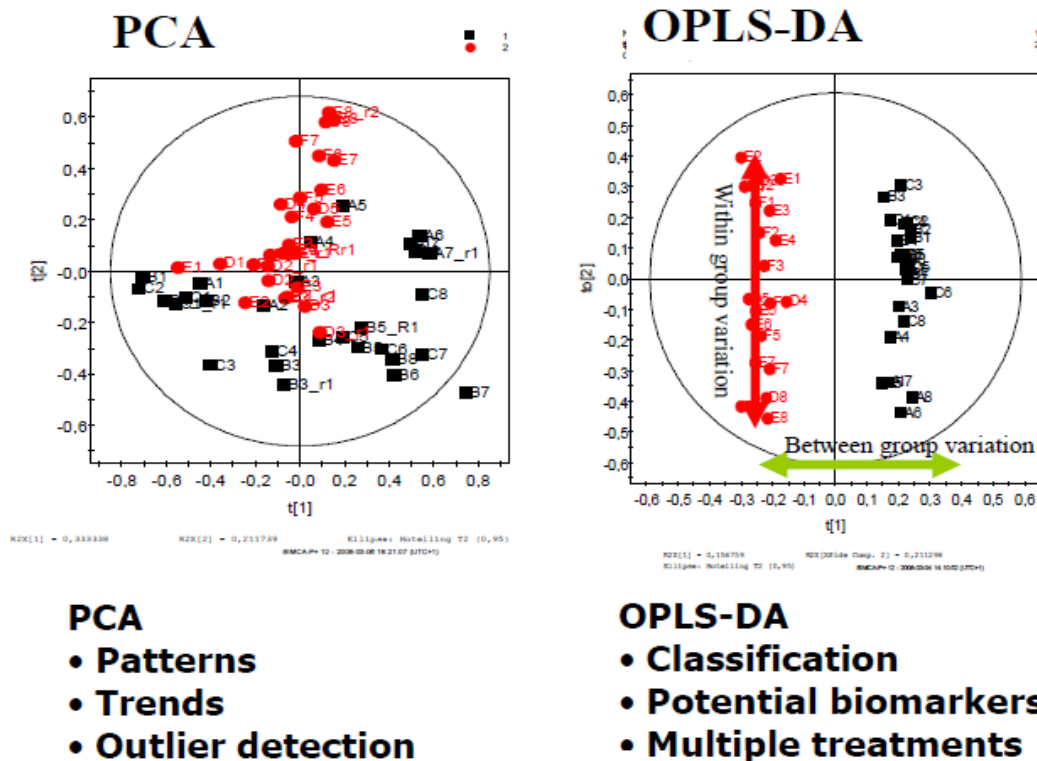


Figure 1.6: Score plots for PCA and OPLS-DA approaches.

Processed MS and NMR data results to a matrix of signal intensities, which can be employed for statistical analytical tools (Spicer *et al.*, 2017). Using PCA that is considered the first step in metabolomics data analysis and an exploratory and visualisation method (Figure 1.6). This analysis provides an overview of the variability of the dataset when the samples are grouped based on similarity or differences within the group of samples, allowing for more accurate interpretation of the results. This makes it possible to identify patterns, groups, and outliers (Wold *et al.*, 1987, Dona *et al.*, 2016).

PCA uses two types of plots, the scores plot and the loadings plot. The scores plot summaries the observations (each point represent individual sample). Whereas the loadings plot provides the information about the variable that have the greatest impact

on the positioning of the samples in the scores plot and are responsible for the clustering of samples, as shown in Figure 1.7 (Geladi, 2003).

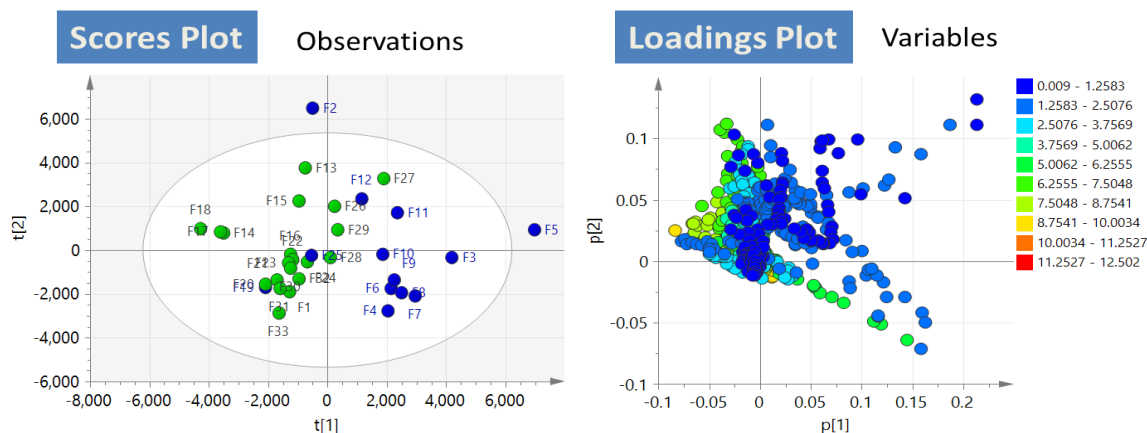


Figure 1.7: PCA scores and the loadings plots.

Supervised pattern recognition approach is used after PCA analysis to maximise separation between different groups of samples and to find metabolic signs that contribute to classification (Dona *et al.*, 2016). OPLS-DA is the most widely used supervised technique, it gives the same predictive power as PLS but a better interpretation of the important variables than PLS. This technique gives information on the factors that contribute to class separation (Bylesjö *et al.*, 2006).

The manual-based structural elucidation approach is a sophisticated, time-consuming, and difficult process. The information gained from 1D and 2D NMR data, as well as information from metabolite databases such as DNP and AntiMarin, is combined to accomplish reliable metabolite identification in this manner (Dona *et al.*, 2016). The majority of the metabolites detected by NMR spectroscopy and MS were identified using information accessible in a variety of databases; however, some of the metabolites were unknown, unidentified, or really unique, which made the elucidation process more challenging (Dona *et al.*, 2016).

1.9.6. Applications of metabolomics in natural products research

Metabolomics has made significant contributions in finding natural products for drug discovery. Metabolomics has brought several crucial applications, such as tracking novel compounds and active metabolites or optimising the production of secondary metabolites. It is possible to employ both PCA and OPLS-DA to guide the separation of compounds and the prioritisation of fractions for future work isolation, so saving time and resources while directing the effort toward the isolation of novel and bioactive compounds (Tawfike *et al.*, 2013, Harvey *et al.*, 2015, Covington *et al.*, 2017). This is based on the ability of metabolomics to compare and screen secondary metabolites, identifying outliers, differences, and biomarkers among experimental groups either they were of different sources or different fractions related to the same source. This will help in tracking the production of novel and bioactive target metabolites and/or biomarkers that become accessible at the earlier stages of the work (Tawfike *et al.*, 2013, Wu *et al.*, 2015). Later, this biomarker is separated, and its structural information provided by the NMR or LC-HRMS is used to compare it with the dereplication database (Wu *et al.*, 2015). 2D NMR and fragmentation patterns in MS/MS spectra in conjunction with molecular networking assessment might be utilised to identify the chemical if the core structure is known but the functional groups are unknown. Even if its nucleus is unique, a complete de novo NMR structural analysis is required (Tawfike *et al.*, 2013).

It is also possible to use metabolomics throughout the scaling-up process to optimise fermentation conditions and to identify and maintain the synthesis of interesting secondary metabolites (Tawfike *et al.*, 2013, Schulz *et al.*, 2002). As fermentation conditions are changed, a metabolomics approach can monitor metabolic production. This enables metabolomics to be used as a quality control tool (Tawfike *et al.*, 2013, Wu *et al.*, 2015, Toya and Shimizu, 2013). Metabolomics might potentially be utilised as a technique for phytomedicine quality control. Variations across species, adulteration, environmental changes, post-harvest treatment, and extraction may all

result in a distinct metabolite profile and have a considerable impact on the effectiveness of phytomedicines. All these modifications might be recognised using PCA (Yuliana *et al.*, 2011). Moreover, metabolomics can be utilised to correlate the chemical profile and bioactivity pattern of some phytomedicines in which the activity is the consequence of synergy between several individually inactive chemical constituents. The bulk of chemical constituents is monitored to ensure that biological activity is maintained (Yuliana *et al.*, 2011). Moreover, it is possible to mine metabolomics data to discover biosynthetic precursors that may be employed to promote the synthesis of a certain functional novel product (Harvey *et al.*, 2015).

1.10. Hypothesis and aims of the study

According to the World Health Organization, cancer is the second leading cause of death worldwide, accounting for 9.6 million deaths in 2018. Breast cancer in women is the second highest cancer incidence among different type of cancer (Bray *et al.*, 2018). Despite enormous attempts to develop effective chemotherapy drugs, toxicity and selectivity remain enormous issues. The toxicity of modern chemotherapy and the resistance of cancer cells to anticancer drugs leads us to search for novel therapies and preventative approaches for this insidious illness. Breast cancer was chosen as the primary focus of this research and antioxidant activity was added as a second target to study the ability of the isolated compounds to reduce free radicals in cancer.

First hypothesis: The metabolomics approach will enable the comparison of the chemical and biological diversity between Jordanian and European chamomile that could be correlated to their anticancer activity against breast cancer and antioxidant activity.

Second hypothesis: In the search for anticancer for breast cancer and antioxidant agents from Jordanian chamomile-associated endophytes, a metabolomics approach will pinpoint the biologically active compounds in the first fractionation step. Time for isolation work would be more efficient compared to the standard bioassay-guided

isolation method, in which all fractions should be tested for biological activity after each fractionation stage resulting to lower yields for the target active compounds. The compounds that have been identified and classified by multivariate analysis will be targeted for isolation, structural elucidation, and their bioactivity will be statistically pre-determined. Furthermore, dereplication at an early stage will aid in the isolation of novel molecules.

The aim of this study is to isolate anticancer and antioxidant compounds from European, Jordanian chamomile and its associated endophytes. The studied chamomile plant was *M. chamomilla*. *M. chamomilla* revealed several biological activities including antioxidant, antibacterial, antifungal, anti-parasitic, insecticidal, anti-diabetic, anti-cancer, and anti-inflammatory activities. These properties enable me to study anticancer and antioxidant activities of both Jordanian and European chamomile of same species. In addition to study anticancer against breast cancer, antioxidant activity was measured to help prevention of cancer as it decreases the free radical and decreases the incidence of cancer. Furthermore, metabolomics was implemented to find the variation of metabolic profile for both chamomile varieties growing in different environment condition. Further analysis was done on Jordanian *M. chamomilla* associated endophytes to find novel compounds with anticancer and antioxidant activities. The following objectives were carried out:

1. For European chamomile and Jordanian chamomile.
 - a. To solvent partition the crude extract to polar, semipolar and non-polar extracts.
 - b. To screen for anticancer activity against breast cancer cells and antioxidant activity using DPPH assay
 - c. To implement NMR and LC-HRMS to dereplicate target biologically active compounds.
 - d. To chromatographically fractionate the targeted active compounds.
 - e. To identify the isolated compounds by 1D NMR, 2DNMR and LC-HRMS.

- f. To assay the isolated targeted compounds for anticancer activity against breast cancer cell, cytotoxicity against normal cells and for antioxidant activity.
2. For Jordanian *M. chamomilla* associated endophytes
 - a. To isolate fungal endophytes from the studied plants and identify them using ITS gene sequencing.
 - b. To screen the fungal extracts for anticancer activity against breast cancer cell and antioxidant activity.
 - c. To optimise the media for scaling-up each of the endophytic fungus that would facilitate the best yield, the most chemically diverse extract, and the most potent biological activity.
 - d. To employ a metabolomics-bioassay guided approach to pinpoint the biologically active compounds during media optimisation work prior to scaling-up.
 - e. To chromatographically fractionate and isolate the targeted anticancer active compounds.
 - f. To elucidate the isolated and purified compounds using 1D NMR, 2DNMR and LC-HRMS.
 - g. To test the isolated compounds against anticancer activity on breast cancer cells and for cytotoxicity against normal cells.

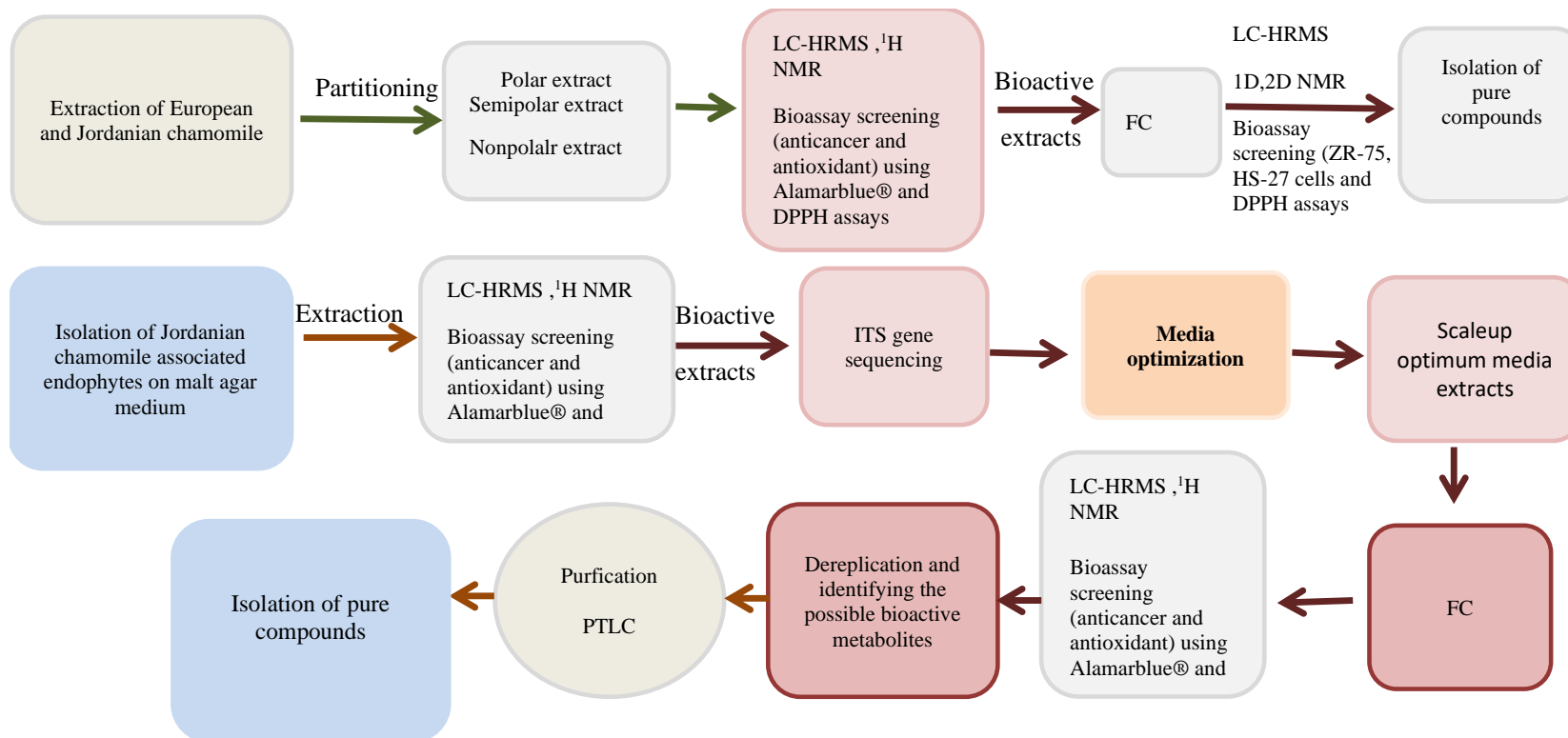


Figure 1.8: The workflow for isolating the bioactive metabolites from European, Jordanian chamomile and its associated endophytes

2. Materials and methods

2.1. Jordanian and European chamomile plant extraction

2.1.1. Materials and equipment

Table 2. 1: Materials and equipment used in the experiments

Materials and equipment	purpose	Origin place
Magnetic mixer	multi-purpose mixing or solubilisation either during plant extraction or sample preparation	Stuart, Stone, UK
Vortex Genie 2		Scientific Industries Inc, London, UK
HPLC-grade acetonitrile (ACN)	plant extraction, plant partitioning, LC-HRMS and MPLC	Sigma-Aldrich, Poznań, Poland
Formic acid		
HPLC-grade dichloromethane (DCM),		
n-Hexane,		
Acetone,		

MeOH		
(HPLC) grade EtOAc		
Analytical-grade acetone		VWR, Fontenay-sous-Bois Cede, France
Rotary evaporator R-110	sample concentrated and dried under vacuum	Büchi, Flawil, Switzerland
Heating Block SBH130D/3 and sample concentrator SBHCONC/1	Concentrated extracts were reconstituted in EtOAc and dried under nitrogen	Stuart, Stone, UK
Ultra-wave sonicator	enhance solubilisation	Scientific Laboratory Supplies, Nottingham, UK
Direct-Q® water purification system	ultrapure water for solvent and media preparation	Merck Millipore, Massachusetts, USA
Accela HPLC coupled to an Exactive mass spectrometer	to run extracts fractions and samples	Thermo Scientific, Germany
Xcalibur 2.2	Mass data processing	Thermo Scientific, Heidelberg, Germany
ProteoWizard	data splitting to separate the data between the negative and positive ionisation files.	USA

MZmine 2.53	mass data processing	http://mzmine.github.io/
An in-house excel sheet called Macro which coupled with Dictionary of Natural Products (DNP version 2021) database	Plant data base	CRC Press, Boca Raton, USA (Pluskal <i>et al.</i> , 2010)
Deteriorated dimethyl sulfoxide (DMSO- d_6)	dissolve NMR samples	Sigma-Aldrich, Poznań, Poland
Deuterium water (D ₂ O)		
NMR tubes	tubes for the samples to run on NMR instrument	Norell, New York, USA
400 MHz Jeol-LA400 FT-NMR spectrometer system equipped with a 40TH5AT/FG prob	measuring NMR samples	Bruker, Rheinstetten, Germany
An AVANCE-III 600 instrument with a 14.1 T Bruker UltraShield magnet from the Department of Pure and Applied Chemistry	It has a 24 position autosampler, 3 channel console, is DQD and Waveform-equipped and can use either a BBO-z-ATMA- ³¹ P-183W/ ¹ H] probe or a TBI-z- ¹ H, ¹³ C, ³¹ P- ¹⁵ N] probe.	

MestReNova 14.2 developed Mestrelab Research	processing NMR spectra	Santiago de Compostela, Spain
TLC plates	TLC silica gel 60 F254 plates	Merck, Darmstadt, Germany
Human Caucasian Breast Carcinoma (ZR- 75)	tested cell line	ATCC, US
Normal human foreskin fibroblast (HS-27) cell lines		
RPMI 1640	media for the tested cells	invitrogen, USA
Foetal bovine serum (FBS),	media components	
Glutamine and penicillin/streptomycin solution		Invitrogen, UK
Trytox X-100	negative control	Sigma, US
TrypLE Express	cell detachment	GIBCO, UK
AlamarBlue BUF012B	measuring cytotoxicity for pure compounds and selected fractions and extracts	Bio-Rad, UK
DMSO assay grade	bioassay samples solubilisation	Fisher Scientific, US
Ninety six-well plates	bioassay	TRP, Switzerland and Greiner bio-one, Austria

Falcon tubes	For centrifuge purpose	Corning, Mexico	
Napco 5410 incubator	was humidified, kept at 37°C in the presence of 5% CO ₂	Napco, US	
SterilGard biological safety cabinet	Sterile cabinet for biological work	The Baker Company, US	
The IEC Medispin centrifuge	centrifuging samples	Thermo Scientific, Germany	
Bright-Line hemocytometer	cell counting	Reichert, US	
Water bath	sample heating for dissolving purpose	Clifton, UK	
Microscope	observing cells	Olympus Optical, Japan	
Wallac Victor 2	measuring fluorescence	PerkinElmer, UK	
Microsoft Excel 2016	bar charts	Microsoft	
Prism 6.0	plotting dilution curves	GraphPad Software, US	
Hidex Sense Multilabel Plate Reader	plate reader	Thermo Scientific, Germany	
2,2-diphenyl-1-picrylhydrazyl (DPPH)	antioxidant assay	Sigma-Aldrich, Poznań, Poland	
Ascorbic acid	positive control in DPPH assay		
Quercetin			

2.1.2. Plant collection

Jordanian chamomile plants used in this study were collected from Bereen Amman in March 2019 by Mrs. Souhair Atoum, Jordan while the European chamomile dried flower parts were bought from Neals Yard Remedies in Glasgow. The taxonomic identities of both Jordanian and European samples were identified as *M. chamomilla*, which was confirmed by Keith Watson, botanist curator of Kelvingrove Museum in Glasgow.

2.1.3. Plant extraction

The extraction method was accomplished using two solvents to extract phytochemical compounds, 10 gms of each plant (flower part) were weighed, 150 mL of acetone was added and stirred for 3 hours using magnetic stirrer plate. The extraction was soaked overnight and was filtered the next day and collected in a rounded bottom flask. Extraction with acetone was performed twice as previously shown. Another solvent was used, 150 mL of MeOH (MeOH) was stirred for 3 hours using magnetic stirrer plate. The extraction was soaked overnight and was filtered the next day and collected in round-bottom flasks. Extraction with MeOH was done twice. The collected extraction of both solvents was collected in same round-bottom flasks and evaporated using rotary evaporator. Then, the extract was transferred into a small pre-weighed vials and was weighed for each plant.

2.1.4. Solvent partitioning

Two-phased partitioning was prepared to separate each extract into aqueous, semipolar and nonpolar. Starting with 90 mL of MeOH that was added to each plant extraction with 10 mL of distilled water and was sonicated for 5 minutes at 40 °C using ultra-wave sonicator. The extracts were transferred into separatory funnel and 100 mL of hexane was added. The funnel was closed and was shaken gently. After reaching equilibrium, two phase layers were formed. The two layers were separated and extraction with hexane was performed three times to collect nonpolar extract.

MeOH-water extract was evaporated, and 100 mL of water was added. Further extraction of the previous water extract was accomplished with 100 mL EtOAc 3 times using a separatory funnel. Producing two extracts aqueous and semipolar extract for each plant. The three extracts of each plant were evaporated, collected in small pre-weighed vials and weighed for further identification.

2.1.5. Preparation of the samples for analysis and biological assay

NMR, LC-HRMS, and bioassay samples were prepared as summarised in Table 2.2. The generated spectral data was processed then subjected to multivariate analysis using the software SIMCA.

Table 2.2: Required sample concentration for screening.

Screening test	Concentration	Solvent used
LC-HRMS	1 mg/mL	MeOH
NMR	5 mg/600 μ L	DMSO- d_6 , D ₂ O
DPPH assay	1 mg/mL	DMSO
AlamarBlue® assay	10 mg/mL	DMSO

2.1.5.1. NMR spectroscopy

The nonpolar and semipolar samples were dissolved in 600 μ l DMSO- d_6 and the aqueous samples were dissolved in 600 μ l D₂O. Then all the samples were transferred to NMR tubes at a concentration of 5 mg/mL. The ¹H NMR spectra was recorded. The data was then analysed using SIMCA 17.0 and MestReNova 14.2.

2.1.5.2. LC-HRMS spectroscopy

HPLC grade MeOH and ACN were used to dissolve the nonpolar and semipolar samples while distilled water was used for the aqueous samples at a concentration of

1 mg/mL. The ACE 5 C18 column was utilised in this experiment. The solvent system consisted of two components: ACN (solvent A) and water (solvent B), both of which contained 0.1% v/v of formic acid. The injection volume was 10 μ L, and the flow rate was 300 mL per minute. The standard gradient is shown in the following Table 2.3. HRMS analysis was carried out in both positive and negative modes in a mass range ranging from m/z 150 to 1500, with the positive mode being the most sensitive. The spray voltage was 4.5 kV at the time of the experiment. The temperature of the capillary was 320°C. Then the data was analysed using MZmine 2.53, Excel-MACRO, and SIMCA 17.0 software.

Table 2.3: Elution gradient used for LC-HRMS.

Time (minutes)	% A	% B
0	90	10
30	0	100
35	0	100
36	90	10
45	90	10

The LC-HRMS chromatograms and spectra were viewed in Thermo Xcalibur 2.2.

2.1.5.3. DPPH assay

Calibration assay for DPPH

DPPH molecule is 2,2-diphenyl-1-picrylhydrazyl, which is a stable free radical molecule to be used in an antioxidant activity. This mechanism is based on delocalisation of electron, which gives rise to deep violet, resulted by an absorption in ethanol solution at 520 nm.

Before performing the assay procedure on the plant extract, the calibration assay for DPPH should be prepared first. A positive control of ascorbic acid and quercetin were used and negative control of DMSO. A stock solution was prepared of 1mg/mL for

each ascorbic acid and quercetin by dissolving ascorbic acid in water and quercetin in absolute ethanol. Also, a stock solution of DMSO was dissolved in absolute ethanol 100% v/v. A dilution of each ascorbic acid, quercetin and DMSO was prepared in 2-fold serial dilution to have 8 points of concentration 1, 0.5, 0.25, 0.125, 0.0625, 0.03125, 0.007813 mg/mL for ascorbic acid (% w/v) and mL/mL for DMSO (% v/v). 0.1, 0.3, 0.6 mM concentrations of DPPH were dissolved in absolute ethanol. Three controls were prepared of 0.1, 0.3, 0.6 mM DPPH in absolute ethanol.

Each solution was placed in triplicate in 96-well plate, then each concentration of DPPH was placed over the tested solutions. The plate was shaken and stood for 30 minutes in a dark place. The absorbance was measured at 520 nm and the % antioxidant activity was calculated by the following equation:

$$\% \text{ Antioxidant activity} = \frac{\text{OD control} - \text{OD sample}}{\text{OD control}} \times 100\%$$

Plotted dose-response curve between and % of antioxidant activity vs Concentration was performed and linear regression analysis was done to calculate the effective concentration to scavenge DPPH free radical at 50% (EC₅₀).

Procedure for DPPH assay

For testing the antioxidant activity of both chamomile varieties of aqueous, semipolar and nonpolar extracts were used. Positive controls of ascorbic acid and quercetin were used while DMSO was used as blank. Stock solutions of 1mg/mL of semipolar and nonpolar plant extracts were prepared and dissolved in DMSO, while the aqueous extract was prepared in distilled water. Two-fold serial dilution was prepared to have 8 points of concentration (1, 0.5, 0.25, 0.125, 0.0625, 0.03125, 0.007813) in mg/mL for each plant extract in DMSO for semi polar and nonpolar plant extract, while distilled water for the aqueous extracts.

Each extract of the plant and the negative and positive control was placed in 96-well plate in triplicate. The antioxidant activity was tested by placing the 0.6mM DPPH solution. 0.6mM of DPPH in absolute ethanol was used as control.

The plate was shaken and stand for 30 minutes in dark place. The absorbance was measured at 520 nm and the % antioxidant activity was calculated by the following equation:

$$\% \text{ Antioxidant activity} = \frac{\text{OD control} - \text{OD sample}}{\text{OD control}} * 100\%$$

Plotted dose-response curve between % antioxidant activity and Log concentration was performed, and linear regression analysis was performed to calculate the effective concentration to scavenge DPPH free radical at 50% (EC₅₀).

2.1.5.4. Anticancer assays

Investigation for potential bioactive anticancer compounds was preliminary performed against breast cancer cells (ZR-75).

Sample preparation

The nonpolar and semipolar samples were dissolved in DMSO, and the aqueous samples were dissolved in distilled water and were kept at -20 °C.

Media preparation

RPMI 1640 medium was prepared for ZR-75 cells as the following protocol:

60 mL was taken out of the 500 mL medium bottle and discarded. The medium was supplemented with 5 mL of (5000 IU/μL – 5000 μg/μL) penicillin-streptomycin, 5 mL of 200mM L-glutamine (× 100). The pH was adjusted to 7.4 by the addition of NaOH. 50 mL of FBS were added.

Cell splitting and seeding

The cell lines were stored in liquid nitrogen and thawed in a 37°C using water bath. 5 mL of the prepared media were poured into a 25 cm² seeding flask. In the seeding

flask, the cell lines were poured. The medium was replaced the next day with new medium.

After the cell lines had grown and adhered to the flask's surface, they were split. The media was removed before the cell lines were washed twice with 5 mL of phosphate buffer saline. After adding 3 mL of TrypLE Express, the mixture was incubated for about 10 minutes at 37 °C.

To stop the TrypLE Express, the flask was gently tapped, and 7 mL of the medium was added. After transferring the cell lines to Falcone tube, they were centrifuged. The supernatant was then discarded, and the cells were resuspended in 5 mL of media after being tapped with a finger. Hemacytometer was used to determine the number of suspended cells.

For seeding the flask, the following formula was used to determine the volume of the suspension to be transferred to a new flask, containing 5 mL of the fresh medium:

$$v = \frac{\text{seeding density (cells/cm}^2\text{)} \times \text{area of the flask (cm}^2\text{)}}{\text{cell count} \times 10^4(\text{cells/ml})}$$

The flask was then incubated at 37 ° C and 5% CO₂ in a humidified incubator. For seeding 96-well plate, the volume of the suspension was determined in accordance with the following formula to prepare the required number of cell lines to be cultivated on the plate.

$$v = \frac{\text{seeding density (cells/cm}^2\text{)} \times 10}{\text{cell count} \times 10^4(\text{cells/ml})}$$

Table 2.4 illustrates the seeding density for the cell lines utilised in a flask and plate. On the 96-well plate, 75 µL of the cell culture was added. As a positive control, 2 µL of media was added to the cells after they were treated with 30 µg/mL of the plant extract. As a negative control, 4% of TrytonX was used.

AlamarBlue assay

The cultures were incubated for 48 hours at 37°C in a humid incubator containing 5% CO₂. AlamarBlue was used to test the viability of the cells. Alamar blue was added to the wells at a concentration of 10% of their volume, which were then incubated for 5 hours. Using a Wallac Victor 2 fluorometer, the fluorescence was measured. The Alamar Blue assay was performed three times with repeated measurements. Excel and graphpad prism were used to analyse the data.

Table 2.4: Seeding densities (cell/cm²) for the used cell lines

Cell line	Flask	96 well plates
ZR-75	8 x 10 ³	1 x 10 ⁵
HS-27	2 x 10 ⁴	1 x 10 ⁵

2.1.6. Medium pressure liquid chromatography (MPLC)

MPLC, also known as flash chromatography (FC), is a separation method that is similar to open column chromatography but uses pressure to elute the sample from the column more quickly. After testing on a TLC plate, the solvent system was selected. Normal phase columns were employed in both the Büchi and Reveleris® Flash Forward systems, and they were conditioned with the beginning solvent solution before loading dry samples that were combined with celite. If the Büchi system was used, fractions were collected manually in 100 mL Erlenmeyer flasks; if the Reveleris® Flash Forward system was utilised, fractions were collected automatically in test tubes. Following that, TLC analysis was performed on all fractions, and the related fractions were combined.

2.1.7. Thin layer chromatography (TLC)

TLC was employed to identify compounds based on their R_f value and colour under UV light or after reaction with various spraying reagents. It was used to determine the purity of a sample and to estimate the composition of a mixture of compounds. Additionally, it was used to assess the appropriateness of several solvent systems used

in column chromatography. To achieve adequate separation of compounds on the column, the mobile phases used in the MPLC/FC system were optimised using TLC plates. Mobile phase selection was based on the R_f value of the initial eluting component. The R_f value of the spots should be between 0.3 and 0.5 to prevent a fast rate of elution of the individual components in the sample, equilibration of the TLC chamber with the mobile phase was achieved by adding filter paper and allowing them to saturate. Under both short and long UV lamps, the elution spots were identified. Under short UV light, compounds that quenched fluorescence or phosphorescence might be seen as black patches. Under short UV wavelengths, conjugated double bond systems and aromatics might also be recognised as coloured dots. Additionally, TLC plates were coated with anisaldehyde/sulfuric acid reagent and heated to 200°C using a heat gun (Table 2.5). This spray reagent is used to determine the presence of a wide variety of natural products, including essential oil components, steroids, terpenes, sugars, phenolic compounds, and sapogenins (Wall, 2005).

Table 2.5: The constituents of anisaldehyde/sulfuric acid spray reagent.

Component	Volume (mL)
Anisaldehyde	0.5
MeOH	85
Glacial acetic acid	10
Concentrated sulfuric acid	5

2.1.8. Sample Preparation

NMR, LC-HRMS, and bioassay samples were prepared as summarised previously in Table 2.2. For structure elucidation, all compounds were submitted to Applied Chemistry department to use their 500MHz Bruker NMR instruments. This was done to perform ¹H, HMBC and COSY, all experiments were processed using MestReNova 14.2. For Proton Spectra, smoothing with Whittaker Smoother, baseline correction with Whittaker Smoother, apodisation with Gaussian 1.00 and manual phase

correction were carried out in MestReNovA. While COSY analysis, smoothing with Whittaker Smoother, reducing t1 noise and symmetrising as COSY-like were performed.

2.2. Isolation and identification of endophytes from Jordanian chamomile

2.2.1. Materials and equipment

Table 2. 6: Materials and equipment used in the experiments

Materials and equipment	purpose	Origin place
Malt extract powder	inoculation of the endophytic fungi	Oxoid, Manchester, UK
Nutrient agar		
Chloramphenicol	initial inoculation	Acros Organics, Geel, Belgium
HPLC grade isopropanol	mixed with 30% water for sterilisation	Sigma-Aldrich, Pozna, Poland
Sagrotan® spray	disinfectant	Sagrotan, Heidelberg
pH meter	measuring pH	Jenway, Staffordshire, UK
NaOH	adjusting pH of media	Sigma-Aldrich Pozna, Poland
incubator	inoculating medium was incubated at 27°C	Vindon Scientific, Oldham Lancashire, UK
MA media	initially grow the fungi	Thermo Scientific, Massachusetts, USA
Internal transcribed spacer (ITS) regions between the 16s and 23s rRNA genes of endophytes	identify fungi	
electrophoresis gel plates comprising UltraPure™ TBE buffer 10X	ITS gene sequencing	Life technologies, Cramlington, UK,
ethidium bromide 10mg/mL		Sigma-Aldrich, Continental, USA

Agarose-Molecular Grade		Camarillo, Bioline, US
Water-Molecular Biology reagent, REExtract-N-Amp™ PCR ReadyMix™, Extraction and Dilution solution		Sigma-Aldrich, St. Louis, USA.
primers ITS1 and ITS4	ITS1-(5'-TCC-GTA-GGT-GAA-CCT-GCG-G-3') ITS4-(5'-TCC-TCC-GCT-TAT-TGA-TAT-GC-3') were	Integrated DNA Technologies, Coralville, Iowa, USA
the HyperLadder II and sample loading buffer		Bioline, Camarillo, USA
The Primus 96 Thermal Cycler	for DNA extraction and amplification	Ebersberg, Germany
the Perkin Elmer DNA Thermal Cycler 480 Manual		MWG AG Biotech
Electrophoresis plates		Bioscience Services, London, UK
voltage source	used for the amplified DNA on the electrophoresis gel plate	Kodak BioMax MBP300 from New Jersey, USA
INGENIUS gel	gel imaging for the plates	Syngene, Cambridge, UK
Illustra™ GFX PCR DNA and Gel Band Purification kit	extract the DNA after PCR of the DNA samples from electrophoresis gel	Cytiva, Massachusetts, US

DRI-BLOCK® DB-2A	solubilisation of agarose gel containing DNA was performed using a dry block	Techne, Chelmsford, UK
5415 D Centrifuge	centrifugation of the samples after each DNA extraction step	Eppendorf, Hamburg, Germany
Nanodrop 2000c Spectrophotometer	measuring DNA concentration of each sample	Thermo Scientific, Massachusetts, USA
FinshTV 1.4.0 software	analysing PCR results	Geospiza
Basic Local Alignment Search Tool (BLAST)	available online from the National Centre for Biotechnology (NCBI)	Maryland, USA.

2.2.2. Collection of plant samples

The plant material was collected in March 2019, three days prior to isolation of the fungal endophytes, kept in a sterile plastic bag in the refrigerator at 2-8°C. Jordanian chamomile plants used in this study were collected from Bereen Amman, Jordan and were identified as *M. chamomilla*.

2.2.3. Preparation of malt extract agar media and fungal inoculation from Jordanian chamomile.

7.5 gm of each malt extract and agar extract and 0.1 gm chloramphenicol were weighed and were placed in a 500 mL bottle. All the components were solubilised with deionised water and added up to 500 mL. The pH was adjusted between 7.4-7.8 by the addition NaOH. The prepared medium was autoclaved and was poured in liquid status into petri dish under the laminar flow hood. The laminar was disinfected with Sagratan spray and 70 % of isopropanol.

2.2.3.1. Initial inoculation of endophytic fungi from plant parts

Under sterile conditions, the plant parts were cut into three parts: flower, stem and roots.

Each part was dipped in sterile autoclaved deionised water and then disinfected with 70% isopropanol using a sterile clamp. After sterilising the plant's parts with isopropanol to kill each epiphytic microorganism, each part was washed with deionised water and then it was dissected to expose the internal tissues to the MA media in the petri dish for inoculation. One petri dish was left empty as a control. All the samples were inoculated between 10- 21 days at 27°C in the incubator. Under the laminar flow hood, the fungal endophyte was cut from each petri dish and transferred in MA medium for better isolation of the pure endophyte.

2.2.3.2. Fungal culture purification step.

MA medium was prepared as described in 2.2.3 for the second endophytic inoculation without the addition of chloramphenicol. Re-plating of each endophyte was accomplished. All the plates were inoculated at 27 °C For 7-21 days. Chemical profiling, biological screening, voucher storage, and taxonomical identification were all accomplished from the inoculation of sufficient plates. The isolated endophytes have been coded according to their plant part.

2.2.4. Fungal extracts for screening.

2.2.4.1. Extraction of metabolites from the incubated endophytes

Each purified fungus was re-inoculated on nine MA plates as prepared in section 2.2.3. Every extract was prepared in triplicate. According to their growth rates, the triplicates were categorised into slow and fast-growing groups. The fast-growing fungi were incubated for 15 days, while the slow-growing endophytes were incubated for 21 days.

After incubation, each plate was cut into eight parts with all of its components, including the medium and fungus, and transferred to a 250 mL conical flask. Then,

200 mL of EtOAc was added and covered with foil to be soaked overnight under the fume hood. On the next day, each extract was homogenised using the homogeniser. The homogenised flasks have been subjected to extraction by using a Buchner funnel. While the mycelia were extracted twice with 100ml of EtOAc. The extract was filtered, and the filtrate was evaporated using the rotary evaporator. Then, the extract was dissolved with a small amount of EtOAc and transferred into small vials for weighing.

All the samples were dried and weighed for LC-HRMS, NMR and bioassay screening. The dried extracts were stored at 2-5C° until further use for chemical profiling with NMR and MS, as well as prior to the biological assays.

2.2.4.2. ITS gene extraction and amplification

A fungal layer was cut and transferred to a 0.5 mL Eppendorf tube from each endophyte's second incubation. Following this, 100 µL of extraction solution was added and vigorously mixed. The contents of Eppendorf tubes were incubated at 95°C in DNA Thermal Cycler 480 Manual for 10 minutes. Following that, each tube was filled with 100 µL of the dilution solution.

For the PCR and amplification of the gene, 4 µL of the gene product was added to a 25 µL combination of REExtract-N-Amp™ PCR ReadyMix™, 3 µL of the forward primer ITS1, 3 µL of the reverse primer ITS4, and 18 µL of water-molecular biology reagent. As described in Table 2.7, the prior combination was exposed to a PCR reaction using a Primus 96 Thermal Cycler. After the PCR was completed, 2 µL of sample loading buffer was loaded to each sample.

Table 2.7: PCR cycles.

Step	Temperature (°C)	Duration (min)	Cycles
Initial denaturation	95	3	1
Denaturation	95	1	-
Annealing	56	1	35
Extension	72	1	-
Final extension	72	10	1
Hold	4	-	-

Gel electrophoresis

Agarose gel was produced by dissolving 0.5 g agarose and 2 µL ethidium bromide in 50 mL of 1x TrisBorateEDTA (TBE) solution. After pouring the gel into a gel electrophoresis plate, it was allowed to harden. The plate was then filled with the diluted TBE 1x buffer. Six µL of HyperLadder II was placed into one of the plate's wells. Then, 15 µL of the blank and amplified genes were introduced three times into the other wells to get enough genes for sequencing. The gel was operated for 45 minutes at 60 volts. After the run was completed, the gel was inspected under UV light and the amplified gene bands were sliced and kept at 2–8°C in the refrigerator. By comparing the band size of each endophyte's gene to the HyperLadder II reference, the band size of each endophyte's gene was calculated.

Extracting, measuring the concentration and the sequencing of the obtained PCR product

To extract the amplified genes,

illustra™ GFX PCR DNA Purification Kit protocol was used. The agarose gel pieces containing the gene fragments were weighed for each sample. Following that, three times their volume of solubilisation solution was added to them. After that, the mixture was incubated for 10 minutes in DRI-BLOCK® with occasional mixing using a vortex mixer. After adding an equivalent amount of isopropanol to the solubilised gene-agarose mixture, it was homogenised using a vortex mixer. Then illustra™ Binding

Columns were prepared. Each of the binding columns was placed in a 2 mL collecting tube. After that, 500 μ L of the column preparation solution was added to each binding column and centrifuged for 1 minute. The preparation solution was drained into the collecting tube and discarded. The combination of solubilised gel solution and binding column was then loaded and centrifuged for 1 minute. The solution collected in the collecting tube was discarded after centrifugation. Then, the solubilised gel solution mixture was loaded into the binding column and centrifuged for 1 minute. After centrifugation, the solution collected in the collection tube was discarded. After that, 700 μ L of the wash solution was added to the binding column. This was followed by another minute of centrifugation. After finishing, the solution and collecting tubes were discarded. After placing the binding columns in fresh collecting tubes, 25 μ L of previously heated elution solution was added and centrifuged for 1 minute. Following that, the binding columns were discarded, and the genes were eluted and collected in the collection tubes using the elution solution. Finally, the concentration of the gene solution was determined and transmitted for sequencing using a Nanodrop spectrophotometer. The sequences obtained were read using the FinchTV programme and compared to hits in databases accessible through the BLAST (<http://blast.ncbi.nlm.nih.gov/Blast.cgi>).

2.2.4.3. Sample preparation of fungal crude extracts for screening.

Four screening assays were performed on the crude fungal extracts. NMR, LC-HRMS, anticancer assay, and antioxidant assay were performed. The samples were prepared as summarised previously in Table 2.2. SIMCA17.0 software was used to analyse the spectral data and perform multivariate analysis.

2.2.5. Preparation of fungal inoculum for media optimisation.

Fungal stock cultures were prepared by placing a small cut from the culture in cryogen-vials containing 30 % glycerol and 70 % malt extract broth. Fungal cultures were inoculated on fresh MA plates for media optimisation work and incubated for 15

days for *A. solani* and 21 days for *A. ustus* at 27°C. These fungi were active in the screening step, so they were continued for the media optimisation.

2.2.5.1. Preparation of Wickersham medium for liquid cultures

Each flask is composed of 3 g of yeast extract, 3 g of malt extract, 5 g of peptone and 10 g of glucose. Water was added up to 1000 mL. The pH was adjusted to 7.4 by the addition of NaOH. The media was then submitted to autoclaving.

2.2.5.2. Preparation of rice medium for solid cultures

Each flask is composed of 100 g of rice and 100 mL of water. Components were kept overnight before autoclaving.

2.2.5.3. Preparation of oat medium for solid cultures

Each flask is composed of 100 g of oat and 100 mL of water. Components were kept overnight before autoclaving.

2.2.5.4. Preparation of potato medium for liquid cultures

To prepare potato infusion, 200 g of unpeeled potatoes were sliced and boiled for 30 minutes in 1-liter distilled water. Filtration was performed using cheesecloth, potato slices were discarded. A 20 g of glucose was added to the potato infusion, then distilled water was added up to 1 litre-volume. The media was submitted to autoclaving.

2.2.5.5 Cultivation

For the media optimisation, the selected endophytes were grown in 500 mL flasks of Wickersham, potato media, rice, and oat media for three incubation periods, 7, 15 and 30 days. All incubations took place in the incubator at 27 °C.

2.2.5.6. Extraction of fungi grown in liquid medium

After the incubation was ended, EtOAc was added to each flask to extract the metabolites that were produced (500 mL for media optimisation flasks). After that, the EtOAc was homogenised with the flask's contents and kept overnight. The following day, it was filtered through a filter paper under vacuum using a Buchner funnel and collected in collection flasks. The homogenised mixture was then partitioned in a separatory funnel, so the EtOAc would be separated from the contents of the medium. The partitioning step was performed thrice with new portion of EtOAc added each time to extract the most amounts possible of metabolites. Then, the EtOAc will be evaporated by the rotary evaporator, the extract will be collected in a vial and weighed.

2.2.5.7. Extraction of fungi grown in solid medium

EtOAc was initially added to each flask to kill the endophyte and extract the secondary metabolites. The mycelia and the rest of the media was homogenised with 200 mL of EtOAc then filtered through cotton wool into collection flasks. This step was repeated seven times to maximise the extraction of the metabolites. The EtOAc filtrate was evaporated and concentrated using a rotary evaporator. The dried EtOAc extract was then weighed and reconstituted in 130 mL of 10 % aqueous MeOH and subjected to partitioning in a separatory funnel with an equal volume of hexane to separate the lipophilic fatty acids that will partition mainly in the non-polar solvent hexane from the other types of compounds. The partitioning was repeated seven times before evaporating the solvents and concentrating the extracts from the two solvent phases. The dried extracts were again weighed.

2.2.5.8. Sample Preparation

NMR, LC-HRMS, and bioassay samples were prepared to provide the spectral and biological data necessary to select the media for the scale-up work. The samples were

prepared as summarised above in Table 2.2. The generated spectral data was processed then subjected to multivariate analysis using the software SIMCA 17.0.

2.2.6. Chemical analysis: Extraction, chromatographic separation and structure elucidation

2.2.6.1. Scaled-up fermentation and extraction

Potato-dextrose extract liquid media was chosen to scale-up the crude extract yield from *A. ustus*. Twenty flasks of the fungal inoculum for scale-up cultures of *A. ustus* were prepared as described in section 2.2.7.4. Two-litre Erlenmeyer flasks were used for 1 L of culture and were incubated as stand cultures at 27°C for 30 days. Half-litre of EtOAc was added to each flask and again macerated for 24 h to stop *A. ustus* growth and other metabolic processes. After 24 h, the culture flasks were homogenised for 15 minutes. For extraction of potato-dextrose extract, the organic EtOAc phase layer was separated from the aqueous phase with a separatory funnel. Liquid-liquid extraction was performed exhaustively with EtOAc. The multiple batches of EtOAc extracts were pooled, concentrated under vacuum and transferred to a tared vial for storage until fractionation.

2.2.6.2. Fractionation of *A. ustus* extract obtained from potato-dextrose extract

Ten grams of the crude extract were reconstituted in 6 mL of EtOAc and added to 7.5 g of celite. The concentrated extract solution was added dropwise the celite to ensure homogenous mixing, and the mixture was dried overnight in fume hood. A prepacked column of silica with a dimension of 40x150mm was used as a stationary phase. DCM and MeOH were used as the main solvent of the mobile phase. To prevent solvation of silica from the pre-packed column, MeOH percentage should not exceed 80%. Because DCM might be abrasive on the piston pump seals, the column was equilibrated with 100% DCM for 10 minutes at a reduced flow rate of 50 mL/min. The chromatographic separation was achieved by stepwise gradient elution with increasing MeOH ratio from 1 to 20% in 160 minutes at a flow rate of 100 mL/min. Acetone and

MeOH were used to wash the column. Table 2.8 shows the elution gradient for the chosen mobile phase for fractionation.

Table 2.8: Elution gradient for the fractionation of *A. ustus* extracts

Mobile phase %				
Time (min)	DCM	MeOH	Acetone	Flow rate mL/min
0	100	0	0	50
10	100	0	0	50
40	99	1	0	100
70	95	5	0	100
130	90	10	0	100
160	80	20	0	100
180	0	30	70	100
200	0	30	70	100

2.2.6.3. Purification of fraction 11 and fraction 12 obtained from *A. ustus* grown in potato-dextrose media

Fraction 11 (700mg) and fraction 12 (700mg) were dissolved in 5ml EtOAc and mixed with 4g celite powder. The mixture was allowed to dry. The dried sample-celite combination was loaded into a 12g silica column for the Reveleris FC system using a loader. EtOAc and n-hexane were used as the mobile phase, the ratios of summarised in Table 2.9. The subfractions were determined by observing peaks using both ELSD and UV detectors. UV wavelengths of 254 and 280nm were employed. The column was washed with acetone and MeOH (70:30).

Table 2.9: Mobile phase % used in sub-fractionation of *A. ustus* fraction 11 and 12.

Time (min)	Mobile phase %				Flow rate mL/min
	% n-Hexane	EtOAc	MeOH	Acetone	
0	100	0	0	0	40
10	90	10	0	0	40
30	85	15	0	0	40
60	80	20	0	0	40
80	50	50	0	0	40
100	20	80	0	0	40
120	0	100	0	0	40
150	0	0	30	70	40

2.2.6.4. Purification of subfraction 29 from fraction 11 of A. ustus extract obtained from potato-dextrose media.

Preparative TLC was chosen for the sub fractionation of fraction 29 due to its low yield of 32mg. The fraction was dissolved in 600µl of EtOAc. A volume of 150µl was loaded as a band on every 20×20cm silica TLC using four TLC plates in total. n-Hexane and EtOAc (75:25) was used as the mobile phase. TLC plates were developed three times to ensure the maximum separation between bands.

2.2.6.5. Purification of subfraction 6, 7 and 11 from fraction 12 of A. ustus extract obtained from potato-dextrose media.

Preparative TLC was prepared for the subfractions 6 (30mg), 7 (28mg) and 11 (35mg) of fraction 12. The fraction was dissolved in 600µl of EtOAc. A volume of 150µl was loaded as a band on every 20×20cm silica TLC using four TLC plates in total. n-Hexane and EtOAc (75:25) was used as the mobile phase. TLC plates were developed three times to ensure the maximum separation between bands.

2.2.6.6. Direct infusion MS

Each sample was weighed and dissolved in MeOH to prepare a concentration of 1 mg/mL for direct infusion MS analysis. ACE 5 C18 column was used. Solvent system was made up of ACN (solvent A) and water (solvent B), both with 0.1 % formic acid. High resolution MS analysis was performed in both positive and negative modes in a mass range that varied from m/z 150 to 1500. The spray voltage was 4.5 kV. The capillary temperature was 320°C.

2.2.6.7. NMR spectroscopy

Samples were prepared as described in section 2.18 For structure elucidation, all compounds were submitted to applied chemistry department to use their 500MHz Bruker NMR instruments. This was done to perform ¹H, HMBC, HSQC, COSY, ROESY, and ¹³C JMOD).

2.3. The metabolomics approach used in this study

Metabolomics workflow was designed to isolate anticancer metabolites from the studied endophytes. It is illustrated in Figure 2.1

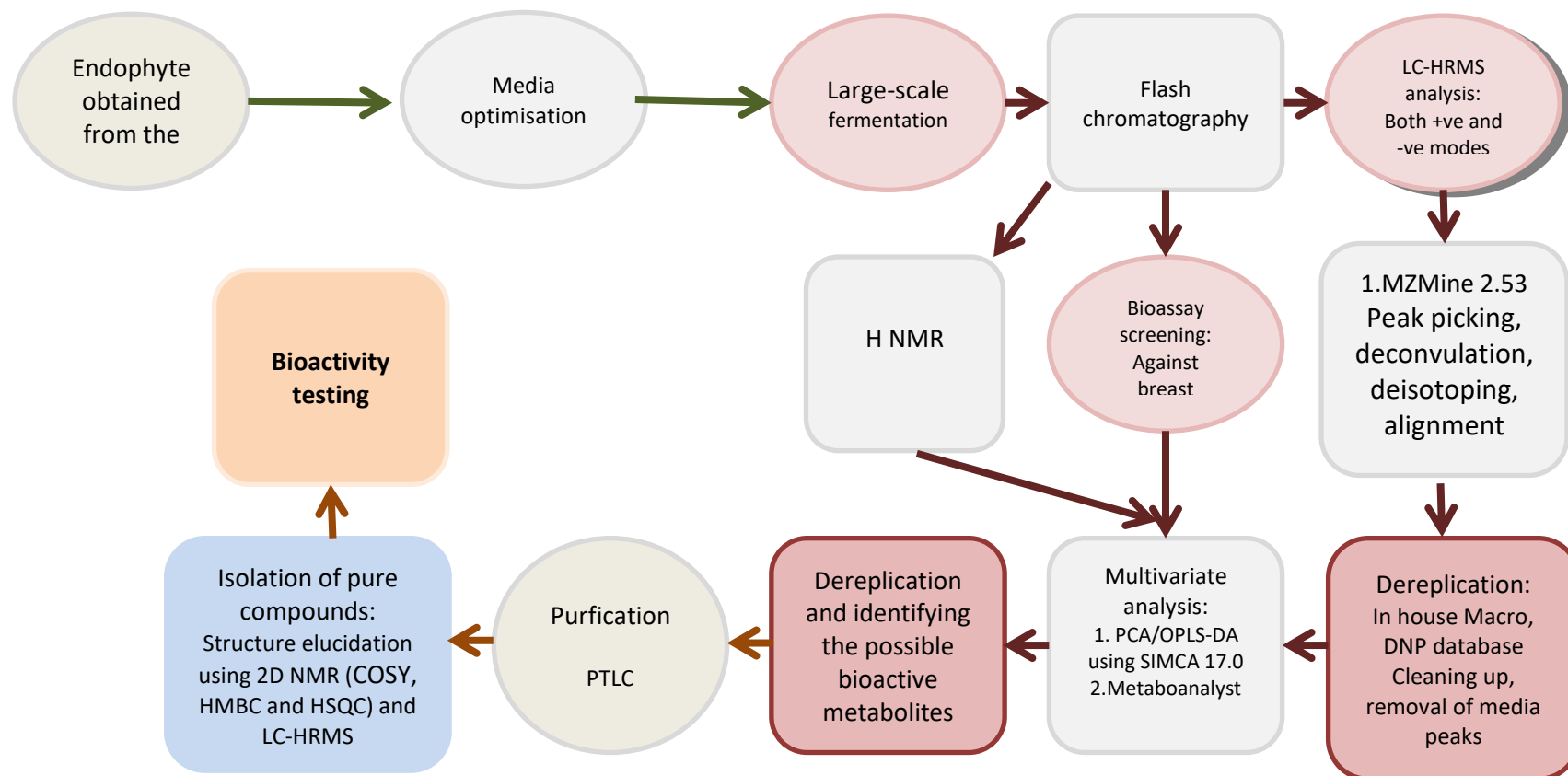


Figure 2.1: Workflow of applying metabolomics in the search for anticancer agents from the *A. ustus* endophyte.

2.3.1. Data Analysis Using MZmine 2.53 (Macintyre *et al.*, 2014)

The LC-HRMS chromatograms and spectra were viewed in Thermo Xcalibur 2.2. The raw LC-MS data were sliced into positive and negative ionisation modes using ProteoWizard's MassConvert file slicer. MZmine 2.53 was used to import and process the sliced MS data (Pluskal *et al.*, 2010). The chromatograms were first cropped to 0.0-45.0 minutes. For peak detection, a centroid mass detector with a noise level of 1.0E3 and an MS level of 1 was used. The chromatogram builder was set to a minimum time span of 0.2 min, minimum height of 1.0E4 and m/z tolerance of 0.001 m/z or 5.0 ppm. The algorithm used for chromatogram deconvolution was the local minimum search. The chromatographic threshold was set at 5%. The minimum retention time (RT) was 0.4 minutes, the minimum relative height was 5%, the minimum absolute height was 1.0E4, the minimum peak top/edge ratio was 2, and the peak duration range was 0.2-5.0 minutes. For isotopes, the isotopic peaks grouper was used with a m/z tolerance of 0.001 m/z or 5.0 ppm, a RT tolerance of 0.2 absolute minutes, a maximum charge of 2, and the most intense representative isotope utilised. RT normalisation was performed using the RT normaliser with m/z tolerance of 0.001 m/z or 5.0 ppm while the RT tolerance and the minimum standard intensity were set to 5% (relative) and 5.0E4 respectively. The peak lists were aligned uniformly using the join aligner (m/z tolerance 0.001 m/z or 5.0 ppm, weight for m/z : 20, RT tolerance 5.0 percent relative, weight for RT: 20). The aligned peak list was gap-filled using the peak finder function (tolerances for intensity: 30%, m/z : 0.001 m/z or 5.0 ppm, and RT: 0.5 min). The RT tolerance was set to 0.2 absolute (min), the m/z tolerance to 0.001 m/z or 5.0 ppm, and the maximum relative adduct peak height to 30%. The adducts Na, K, and NH₄ were used in the positive mode, formate in the negative mode, and ACN+H in both modes. Additionally, a sophisticated search was conducted utilising [M+H]⁺ for positive ionisation and [M-H]⁻ for negative ionisation. RT Tolerances was set to 0.2 absolute (min), m/z to 0.001 or 5.0 ppm, and the maximum complex peak height was set to 50%. After that, the data was exported as a CSV file for additional cleaning.

SIMCA 17.0 was used to analyse the data. The MZmine ID number was merged with the ionisation mode to provide a unique primary ID for the MS data, whereas the other variables such as retention time, m/z , and MWt were considered secondary IDs. The data sets were originally analysed using PCA, an unsupervised statistical analysis approach. Following that, a supervised statistical analysis approach utilising OPLS-DA was used to compare groups and distinguish metabolites based on a known variable used to classify the groups. Both approaches used Pareto scaling, and models were verified R^2 and Q^2 coefficients, as well as permutation tests in the case of the supervised method. The above-mentioned in-house EXCEL macro was then used to determine the top twenty features (ordered by peak intensity) and their related putative identities in each sample by producing unique CSV files for each extract. ChemBioFinder version 13 was used to find database hits (PerkinElmer Informatics, Cambridge, UK)

Both LC-HRMS and NMR spectroscopy are commonly used in metabolomics. LC-HRMS has the advantage of being more sensitive than the NMR, detecting compounds that are present as femtograms in the extracts. Moreover, it can identify compounds based on their exact mass and fragmentation pattern and the addition of other limiters such as retention time could enhance its identification. However, it is limited by the ionisation capability of the metabolites (Krug and Müller, 2014, Tawfike *et al.*, 2013, Griffiths *et al.*, 2010). On the other hand, NMR is better for structure elucidation. Nevertheless, it is not sensitive enough to detect minor metabolites that present in lower concentrations.

Dereplication is defined as the process of implementing spectroscopy in the identification of known metabolites in the early stages of isolation (Krug and Müller, 2014, Harvey *et al.*, 2015). This is achieved by using LC-HRMS, where hits with certain m/z values are compared to available databases like DNP. Along with multivariate analysis that pinpoints the active compounds, this allows prioritising fractions for further purification and helps saving time and money in the process of

isolating novel bioactive compounds. Combining data given by LC-HRMS or NMR to a multivariate data analysis tool allows scientists to compare and detect differential metabolites in biological samples.

2.3.2. Chemometrics and multivariate analysis

Multivariate data analysis is a chemometrics' tool that is applied to extract relevant information from measured data. Thus, visualising this data and enabling the prediction of its outcomes. The use of common instrumental analysers produces multivariate collinear data. Measured variables, which describe the system, provide similar information content. These collinear variables and thus, the structure of data, could be combined and described by fewer factors, called latent variables or principal components (Rajalahti and Kvalheim, 2011). Different approaches in multivariate analysis include PCA, SIMCA, PLS-DA, OPLS-DA to latent structures O2PLS (Wiklund, 2008).

3. Jordanian and European chamomile comparison for unravelling the anticancer and antioxidant differences

3.1. Literature Background

Many examples of endemic plant varieties with a wide variation in their secondary metabolite fingerprint have been described in the literature. For these reasons, two endemic varieties of chamomile were compared to find differences in their biological active compounds. Multivariate statistical analysis was employed to measure the depth of this variation.

Environmental conditions closely affect the biosynthesis of the primary and secondary metabolites in specimens of same plant (Sampaio *et al.*, 2016, Zanatta *et al.*, 2021). Physiological adaptations of plants are in many instances under the influence of the ecosystem that surround them (Petit *et al.*, 2001). Secondary metabolites play different roles in the plant interactions, such as competition, symbiosis, metal transport, differentiation, etc (Demain and Fang, 2000). Some volatile terpenes are involved in plant communication and defensive system (Rohloff and Bones, 2005, Ormeño *et al.*, 2008). Plant polyphenols has multiple functions as UV-screening pigments or counter oxidative stress agents (Di Ferdinando *et al.*, 2014).

Structural elucidation reports of chamomile flowers constituents have allowed to identify approximately 120 different secondary metabolites, including 28 types of terpenoids and 36 polyphenolic compounds (McKay and Blumberg, 2006). Most important constituents attributed to therapeutic properties have been correlated to their secondary metabolites such as phenolic acids and sesquiterpenes, flavonoids, coumarins, and polyacetylenes (Figure 3.1) (Shankar *et al.*, 2017, Sadraei *et al.*, 2017, Hostetler *et al.*, 2017). Known polyphenols of chamomile are the biologically active flavonoids, apigenin and its methylated, acetylated, and glycosylated derivatives have properties as therapeutic agents (Landis-Piwowar *et al.*, 2008, Salehi *et al.*, 2019, Moharram *et al.*, 2017).

This plant endemic study explores the variations in the biological active compounds between two varieties of the same species that have grown under different environmental conditions. It was aimed to employ HPLC-MS and NMR to targeted metabolomics fingerprint of both varieties of chamomile, identify patterns in the types of secondary metabolites present in both samples and find novel active compounds in the Jordanian variety.

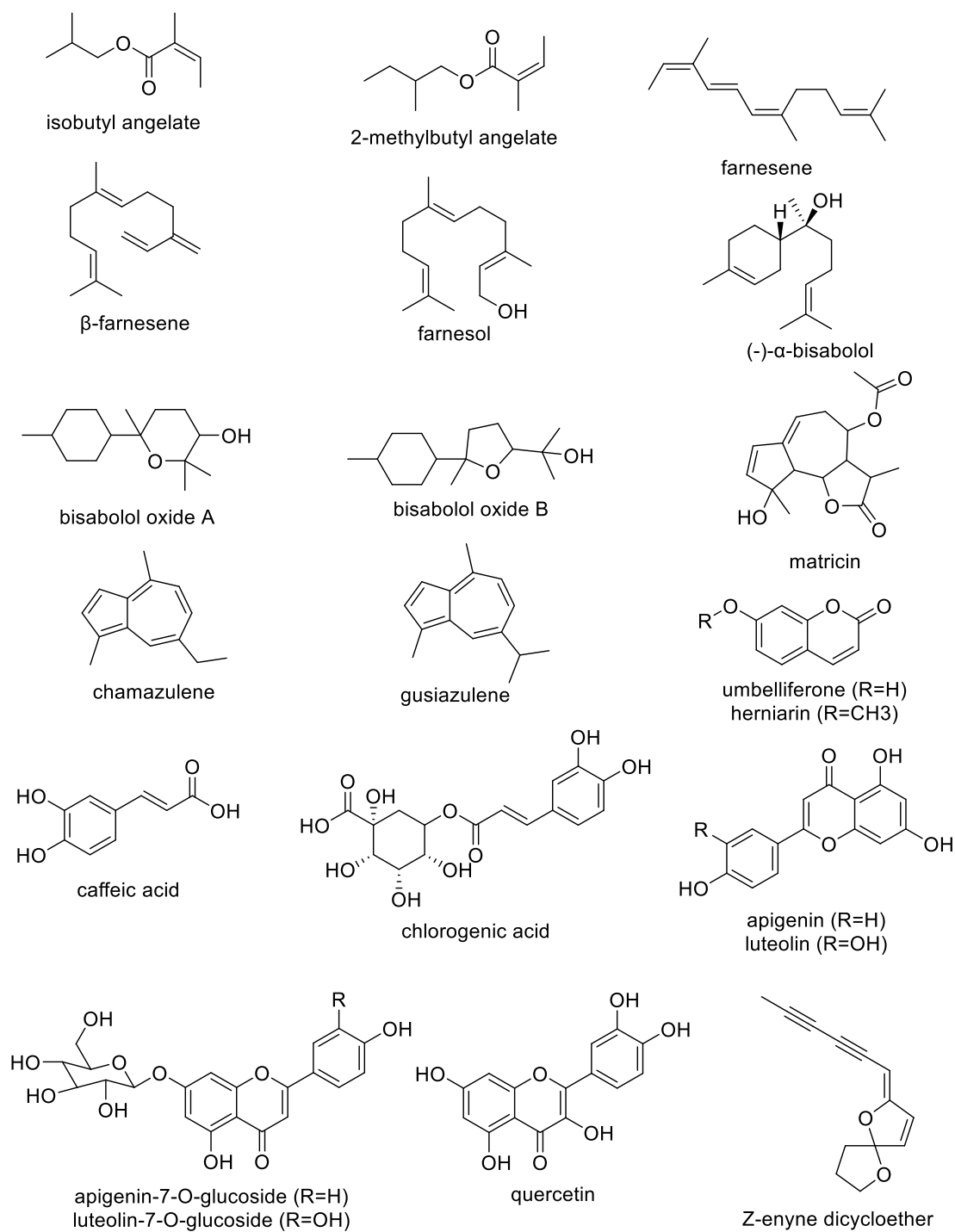


Figure 3.1: Secondary metabolites isolated from *M. chamomilla* (Shankar *et al.*, 2017, Sadraei *et al.*, 2017, Hostetler *et al.*, 2017).

3.2. Crude extracts and extract yield of the Jordanian and European chamomile

The same extraction procedure was employed for both Jordanian and European chamomile plant, flower parts were used in the extraction for both varieties. Liquid-liquid partitioning was performed on the dried total crude extracts to obtain the EtOAc, aqueous MeOH and n-Hexane extracts (Table 3.1). The obtained weight of the dried n-Hexane extract of the Jordanian chamomile was 0.19 g (1.9%), the weight of the dried aqueous MeOHic extract was 9.6 g (96%) and for EtOAc extract was 0.18 (0.18%). Meanwhile, the n-Hexane extract in the European chamomile was 0.3 g (0.3%), the aqueous MeOH was 9.9 g (99%) and was 0.34 g (0.34%) for the EtOAc extract as shown in Table 3.2. The extracts were further subjected to bioassay screening and further chromatographic isolation work (Figure 3.3)

Table 3.1: Yields of liquid-liquid partitioning extracts obtained from chamomile varieties

Chamomile varieties	crude (g)	n-Hexane (g)	10%aq MeOH (g)	EtOAc (g)
Jordanian chamomile	10	0.19	9.6	0.18
European chamomile	10	0.30	9.9	0.34

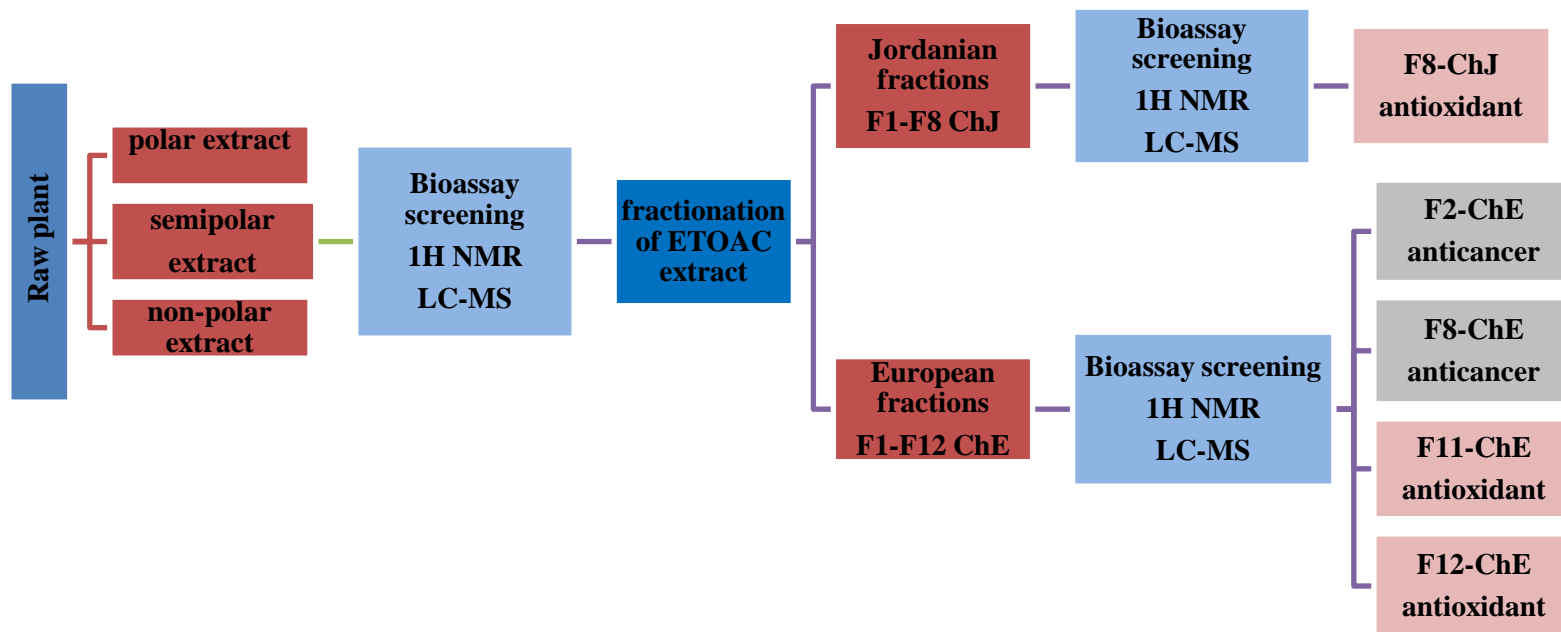


Figure 3.2: Workflow for *M. chamomilla* varieties for both Jordanian and European chamomile.

3.3. Multivariate analysis of the crude extract of *M. chamomilla* varieties

To investigate the chemical characteristics, all the extracts were subjected for ^1H NMR and HRESI-MS. The ^1H NMR spectra of the extract were stacked and presented in Figure 3.3. The bioactive extracts were highlighted with a black box for both varieties. The biological activity was performed by testing the antioxidant activity and testing anticancer activity against breast cancer ZR-75.

The extracts were examined by ^1H NMR spectroscopy to establish the class of the major compounds present in each (Figure 3.3). Analysis of the ^1H NMR spectral data revealed that the n-Hexane extracts for both varieties were rich with lipids, glycosylated and with other various aliphatic compounds. These were indicated by the presence of ^1H NMR signals resonating mainly at 0.80 to 5.0 ppm. However, the aqueous extracts contained more hydroxylated compounds evident by the occurrence of peaks between 3.0 and 5.0 ppm. On the other hand, the bioactive EtOAc extracts of both chamomile varieties mainly consisted of aromatic compounds that was accounted for protons found between 6.0 and 7.5 ppm.

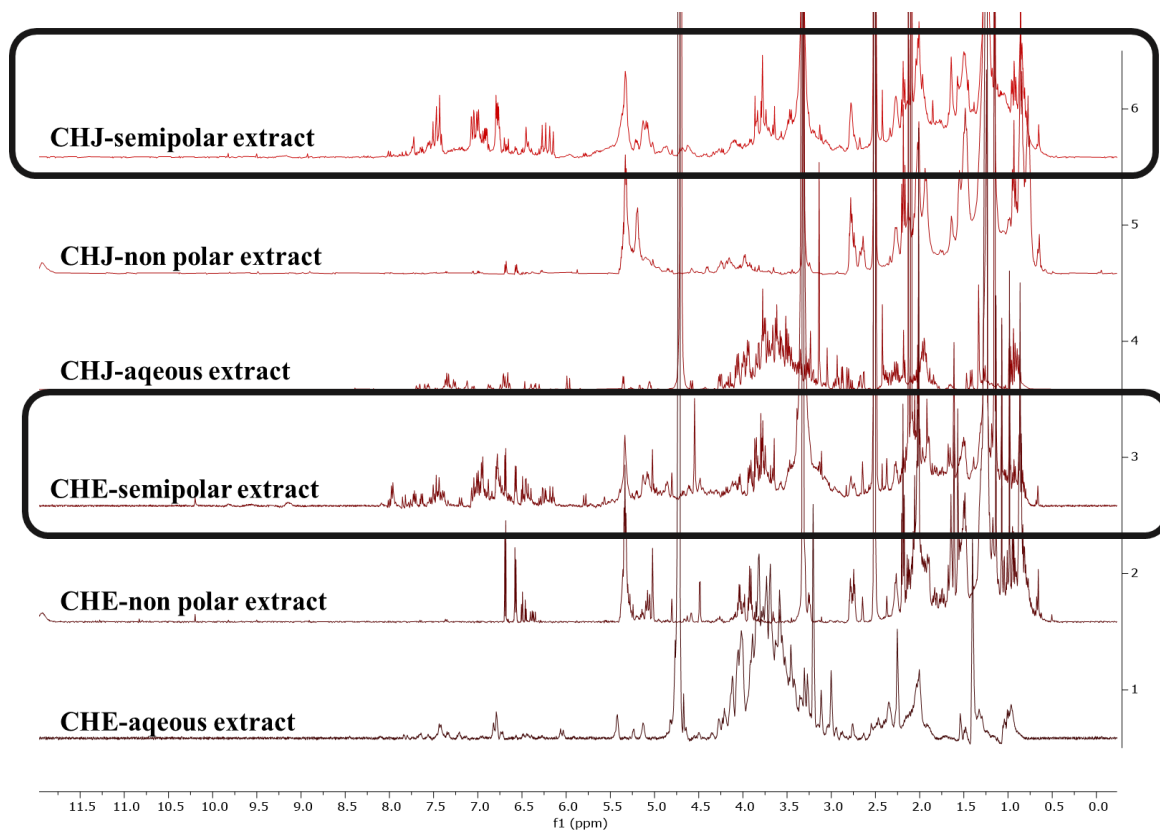


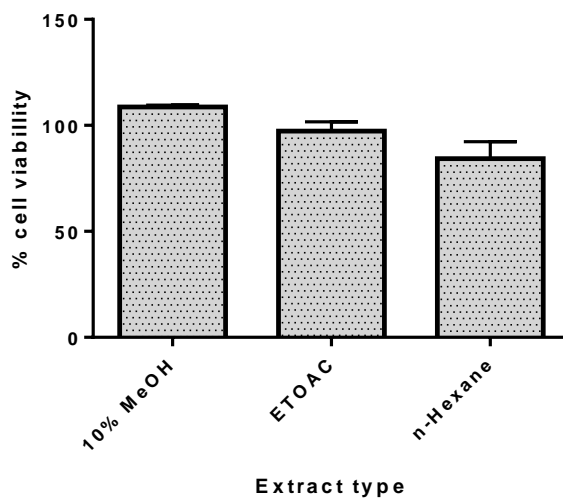
Figure 3.3: Stacked ^1H NMR spectra of Jordanian (ChJ) and European (ChE) chamomile extract in $\text{DMSO-}d_6$ measured at 500 MHz. Highlighted spectra represent the bioactive fractions.

3.3.1. The biological activity of *M. chamomilla* crude extracts

The obtained extracts were tested *in vitro* against breast (ZR-75) (Figures 3.4 and 3.5). AlamarBlue® was used to determine the viability of the cancer cells in the presence of the plant extracts. The European EtOAc extract exhibited activity against breast cancer ZR-75 cell line at 85% that is a cell viability of 15% (Figures 3.4 and 3.5). On the other hand, antioxidant activity was also observed in both European and Jordanian EtOAc extracts as shown in Figure 3.6 and Table 3.2. The antioxidant activity was measured using a DPPH assay. Ascorbic acid and quercetin were used as positive controls. EC_{50} values were determined for both bioactive extracts, which was equal to

0.16 mg/mL for the Jordanian and 0.2 mg/mL for the European chamomile EtOAc extract. The n-Hexane and aqueous MeOH extracts of both varieties were found inactive in the AlamarBlue® and DPPH assays.

A Effect of the Jordanian chamomile on Breast cancer cell (ZR-75) at 30 µg/ml



B Effect of the European chamomile on Breast cancer cell (ZR-75) at 30 µg/ml

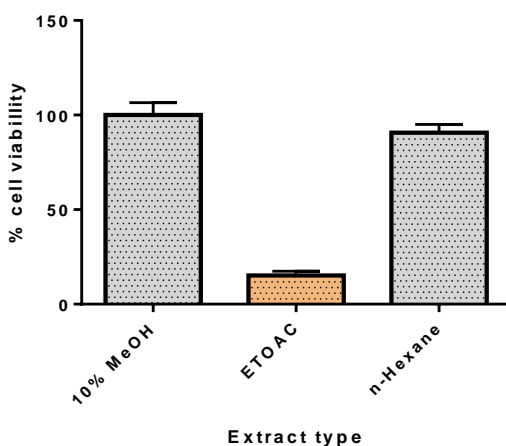
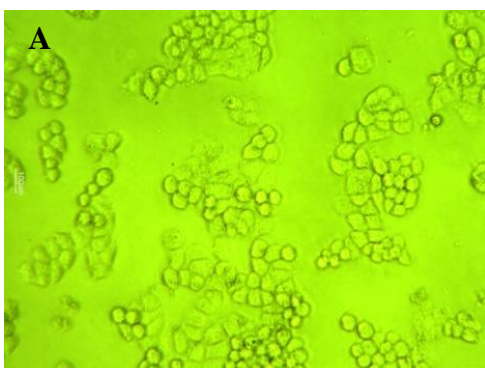
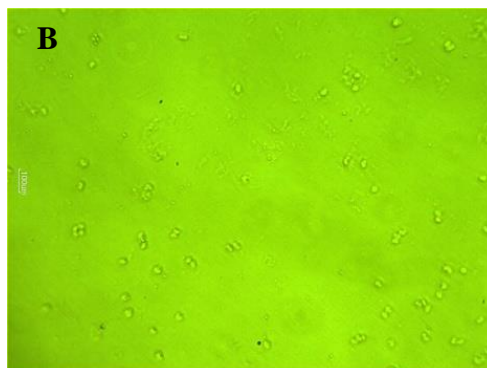


Figure 3.4: AlamarBlue® assay of 30 µg/mL crude fractions obtained by liquid-liquid partitioning of total crude extracts of **A**) Jordanian and **B**) European chamomile on breast cancer cell line ZR-75.

Untreated control



Negative control



EtOAc extract of ChE

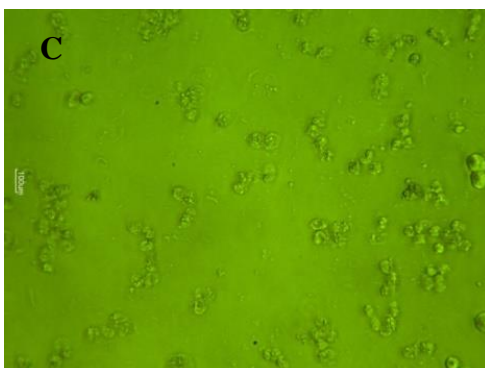


Figure 3.5: Microscopic photo of breast cells after 48 hr incubation. **A)** Breast cancer cells without treatment. **B)** Breast cancer cells with Triton X. **C)** Breast cancer cells with EtOAc extract from European chamomile at a concentration of 30 µg/mL. Magnification power was 10X (objective lens) and the background was shown in green.

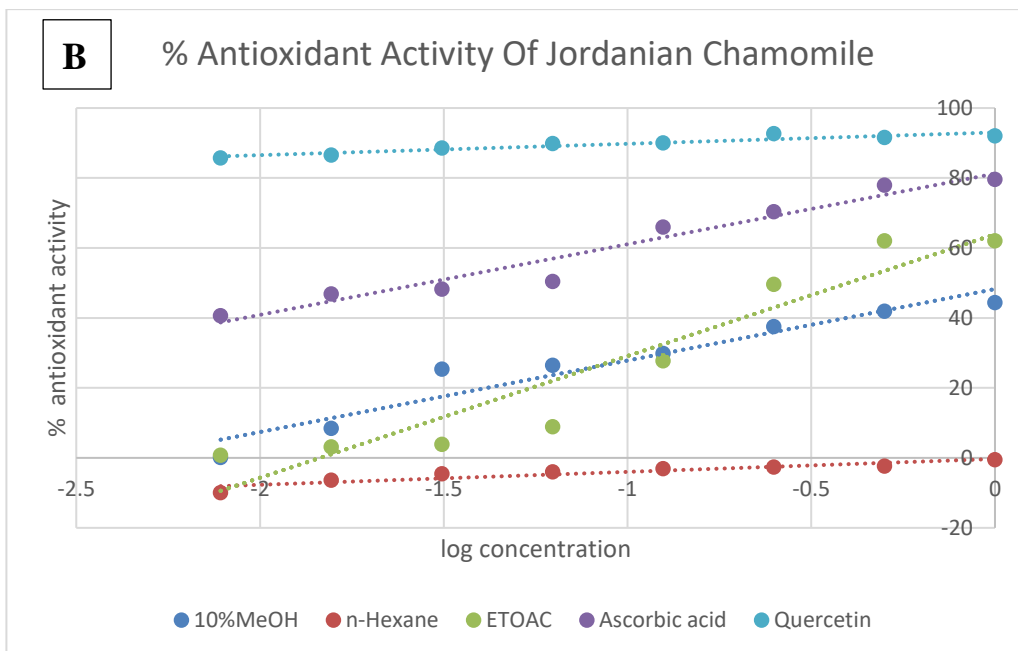
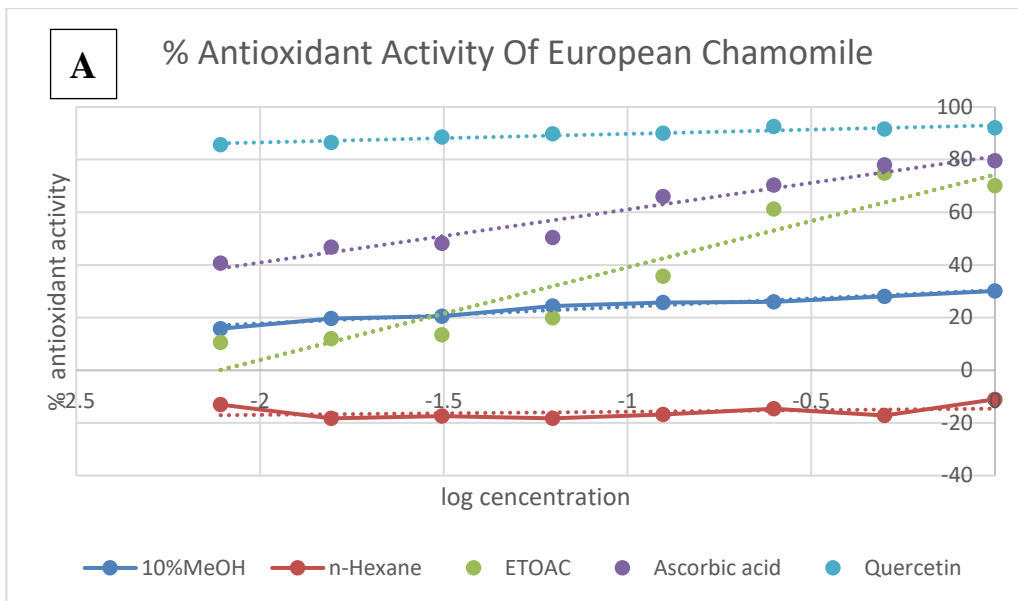


Figure 3.6: DPPH assay for antioxidant activity of liquid-liquid partitioning extracts obtained from **A)** European and **B)** Jordanian chamomile in mg/mL. Ascorbic acid and quercetin were used as the positive controls.

Table 3.2: EC₅₀ values of antioxidant activity assay of liquid-liquid partitioning extracts obtained from both varieties of *M. chamomilla* in mg/mL. Ascorbic acid and quercetin were used as the positive controls.

Type of extract	Jordanian chamomile (mg/mL)	European Chamomile (mg/mL)
n-Hexane	inactive	inactive
10% aq MeOH	>1	inactive
EtOAc	0.20	0.16
ascorbic acid	0.11	0.11
quercetin	0.03	0.03

3.3.2. Multivariate analysis of NMR spectral data

The AlamarBlue® and DPPH assay results were incorporated with the spectral dataset for multivariate analysis. The PCA scores scatter plot naturally grouped the bioactive EtOAc extracts in the upper left quadrant, while the n-Hexane extracts were positioned in the lower left quadrant. On the other hand, the aqueous MeOH extracts of both varieties were grouped together at the right quadrants of the plot, suggesting their similar chemical profiles (Figure 3.7A). The loadings plot of NMR data showed that these bioactive extracts contained glycosylated and aromatic metabolites as implied by the ¹H resonances at 3.00 to 4.00 and 6.00 to 7.00 ppm, respectively (encircled in blue), shown in Figure 3.7B. The R² was 0.98 and Q² was 0.90 after six components, which indicated a good, fitted model with good predictability.

For the OPLS-DA scores plot (Figure 3.8A), the extracts were pre-classified according to their bioactivity results in the AlamarBlue® and DPPH assays. The bioactive EtOAc extracts of Jordanian and European varieties were found dispersed in the lower and upper left quadrant, respectively. This could be explained by the different chemical profiles for the respective extracts. On the other hand, the inactive extracts were in the right quadrants of the scores plot. For the OPLS-DA loadings plot illustrated in Figure 3.8B, the EtOAc extracts for Jordanian chamomile revealed the presence of metabolites with chemical shifts resonating between 6.00 and 7.00 ppm, while a few

glycosylated resonances at 3.0 to 4.0 ppm (encircled in red) were also evident. Meanwhile, the NMR spectral data of European chamomile extracts exhibited a higher density of resonances between 2.0 and 4.0 ppm, indicating the presence of acylated and hydroxylated active metabolites (encircled in blue). On the other hand, the n-Hexane and aqueous extracts for both chamomile varieties were distributed in the right quadrants of the OPLS-DA scores plot. The corresponding loadings plot exhibited the presence of resonances between 0.00 and 5.00 ppm for the inactive extracts, suggesting the presence of lipids and glycosylated compounds. The R^2 was 0.98 and Q^2 was 0.80, indicating good fitness and predictability. The R^2 indicates fitness of the model and Q^2 indicates predictive ability of the model. The variation score between groups was 24.9% but just 8.9% within groups, indicating lesser diversity within the respective groupings but a more defined difference between the active and inactive extracts.

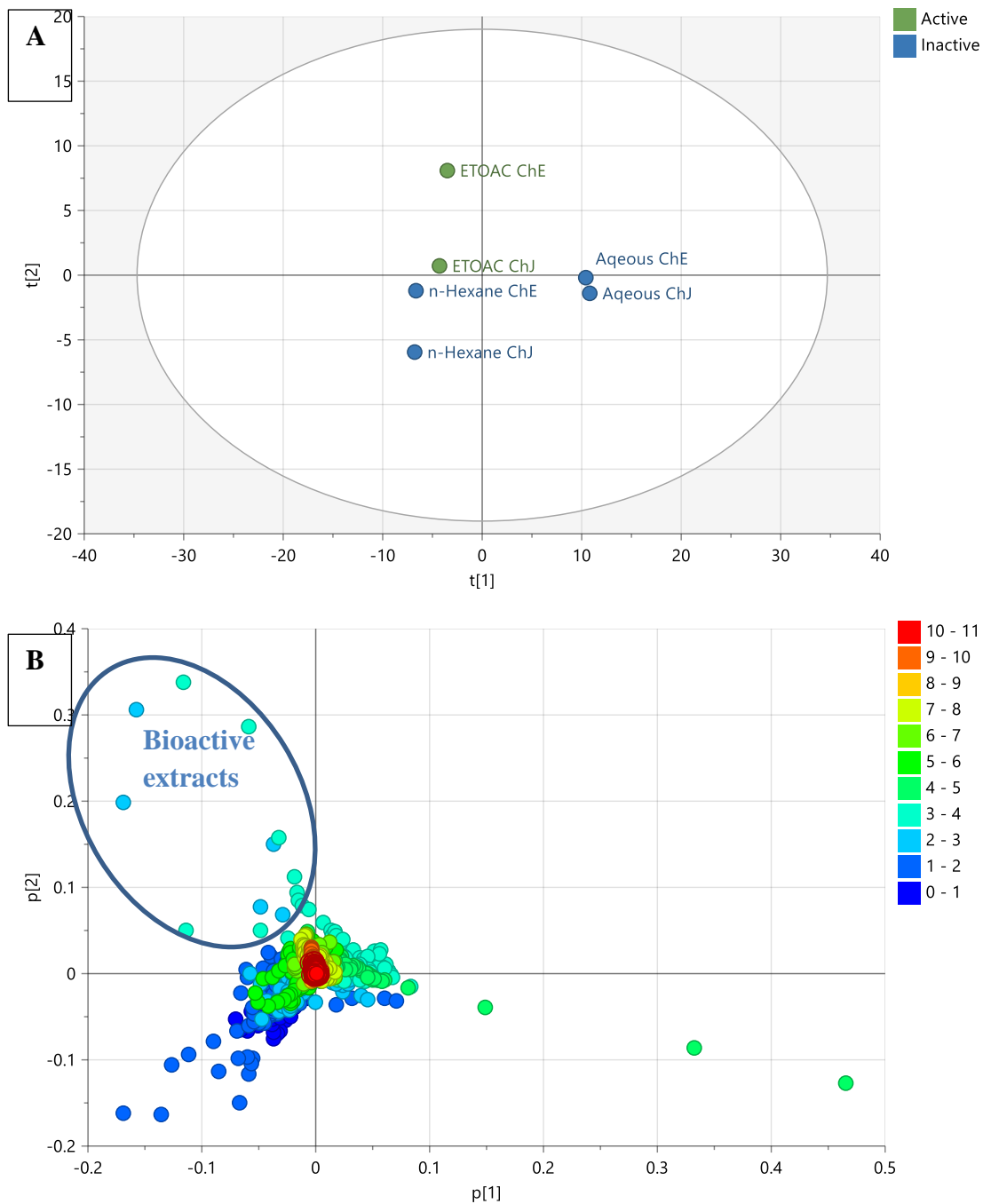


Figure 3.7: (A) PCA scores and (B) loadings plots of the NMR spectral data of *M. chamomilla*. The R^2 and Q^2 values were 0.98 and 0.90, respectively. Encircled features on the loadings plot indicate the discriminating chemical shifts for the biologically active extracts.

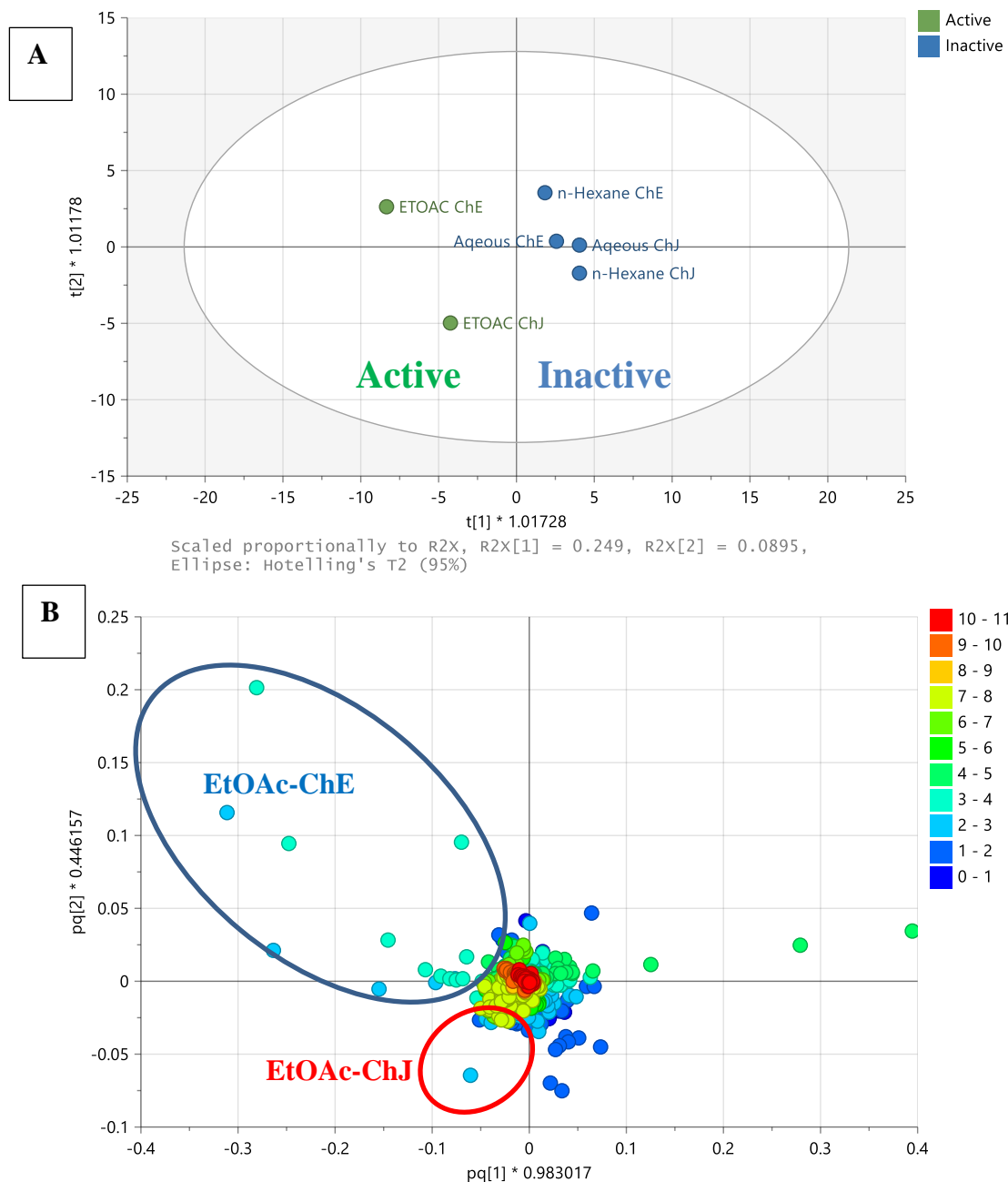


Figure 3.8: (A) OPLS-DA scores and (B) loadings of the NMR spectral data of *M. chamomilla* pre-classified according to their bioactivities in AlamarBlue® and DPPH assay results. The R^2 and Q^2 values were 0.98 and 0.80, respectively. Encircled features on the loadings plot indicate the discriminating chemical shifts for the biologically active extracts.

3.3.3. NMR spectroscopy of *M. chamomilla* fractions

The ^1H NMR spectra of the Jordanian and European chamomile fractions were stacked and presented in Figures 3.9 and 3.10, respectively. The bioactive fractions in the Jordanian plant have peaks between 6.0 and 9.0 ppm, which is characteristic of aromatic compounds such as phenylpropanoids. Furthermore, the European bioactive fractions showed the presence of aromatic compounds indicated by resonances between 6.5 and 8.0 ppm as well as for glycosylated compounds implied by peaks between 3.0 and 4.0 ppm.

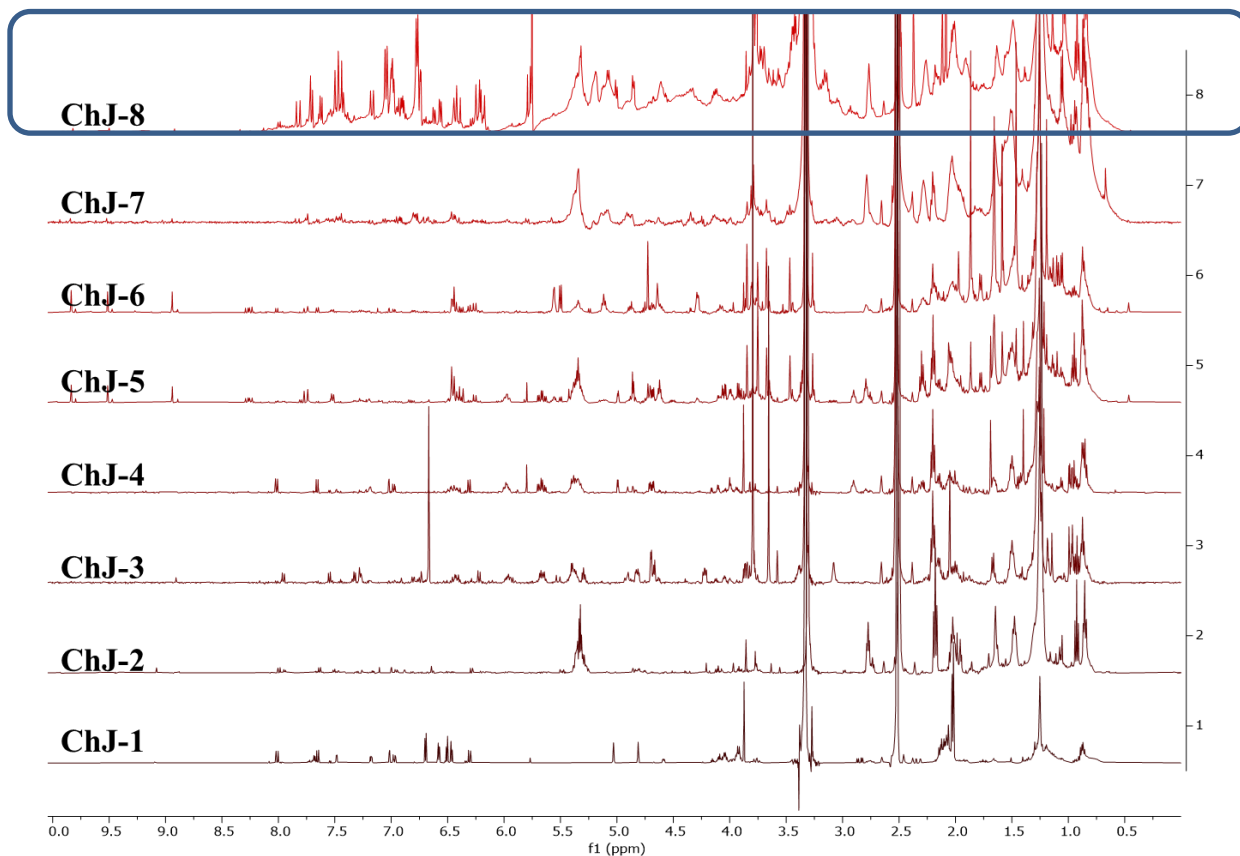


Figure 3.9: Stacked ^1H NMR spectra of Jordanian chamomile (ChJ) fractions in $\text{DMSO-}d_6$ measured at 500 MHz. Boxed spectra represent the bioactive fractions.

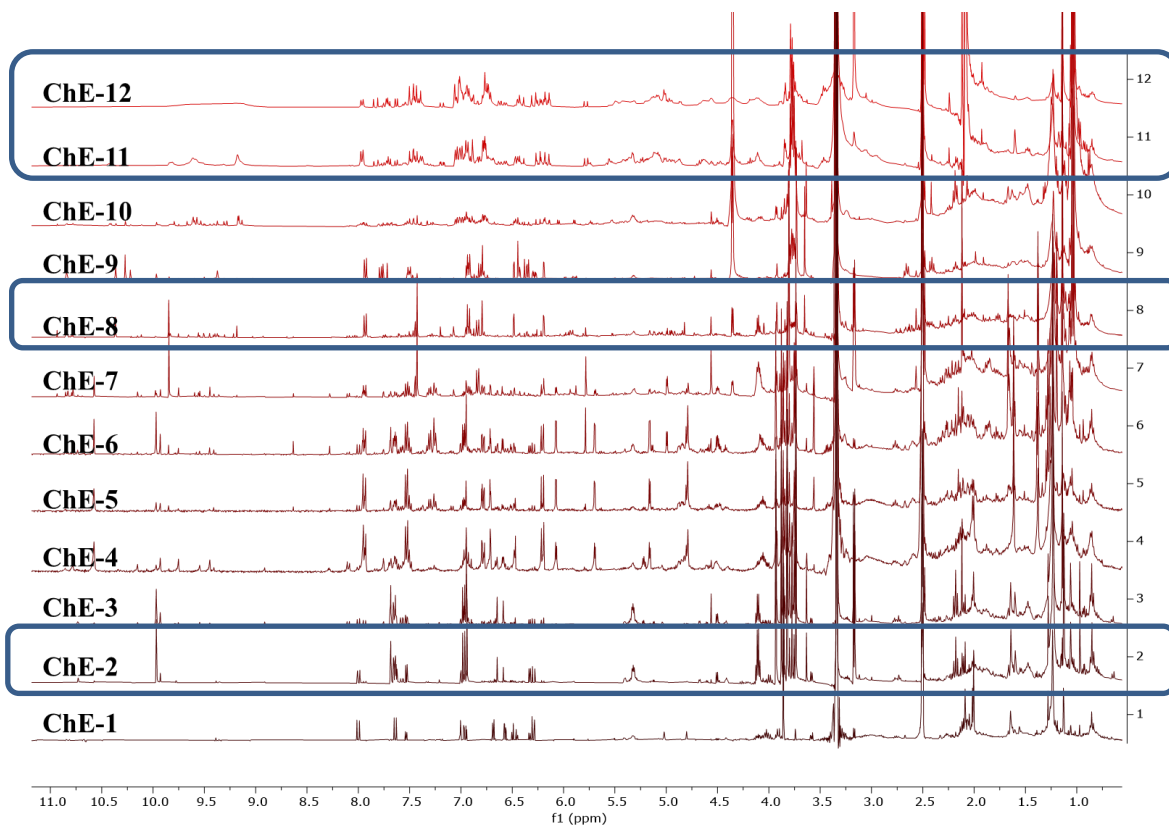


Figure 3.10: Stacked ¹H NMR spectra of European chamomile (ChE) fractions in DMSO-*d*₆ measured at 500 MHz. Boxed spectra represent the bioactive fractions.

The same extraction and fractionation methodologies were employed for both the active semi-polar extracts of the two chamomile varieties. The PCA scores plot of the NMR spectral data (Figure 3.11A) showed differences between the European and Jordanian varieties. The fractions obtained from the Jordanian herb were quite homogeneous and closely clustered that implied a strong similarity in their chemical profiles. Quite the opposite, the European fractions were more dispersed and diverse with the most polar fraction F12 emerging as an outlier. The ^1H NMR spectra of fractions 11 and 12 revealed significant differences from the earlier eluted non-polar fractions. Several signals from the aliphatic to the vinylic region were absent in the most polar fractions of the European chamomile. This was in accordance to the separation of the more polar fractions observed in the PCA scores plot of their NMR spectral data, as shown in Figure 3.11A). In the generated model, R^2 was 0.92 and Q^2 was 0.58, suggesting a model with good fitting but predictability was of medium strength, which was caused by the dispersion of the fractions from the European chamomile extract.

Comparative assessment of the NMR spectral data of the fractions was done by OPLS-DA. As illustrated by a S-plot (Figure 3.11B), the European chamomile afforded more of the glycosylated compounds unique to the variety, which was implied by the discriminating peaks found between 3 and 4 ppm. On the other hand, the discriminating features for the Jordanian variety were represented by higher density of resonances between 6 and 7 ppm, which complied for polyphenolic proton chemical shifts. Validation scores of the model gave a R^2 value of 0.97 and Q^2 of 0.95, whereas the R^2Y intercept was at 0.99 and the Q^2Y intercept was at -1.04. These numbers suggested both excellent fitting and prediction. The difference between R^2 and Q^2 values was 0.02, indicating that the model was not overfitted. The validity of the model was further confirmed by a permutation. The fact that Q^2Y was negative, -1.04, provided more evidence of its validity (Figure 3.12). Furthermore, the percentage variation $R^2X_o[1]$ between groups is 34.2% while within groups $R^2X[1]$ is 9%.

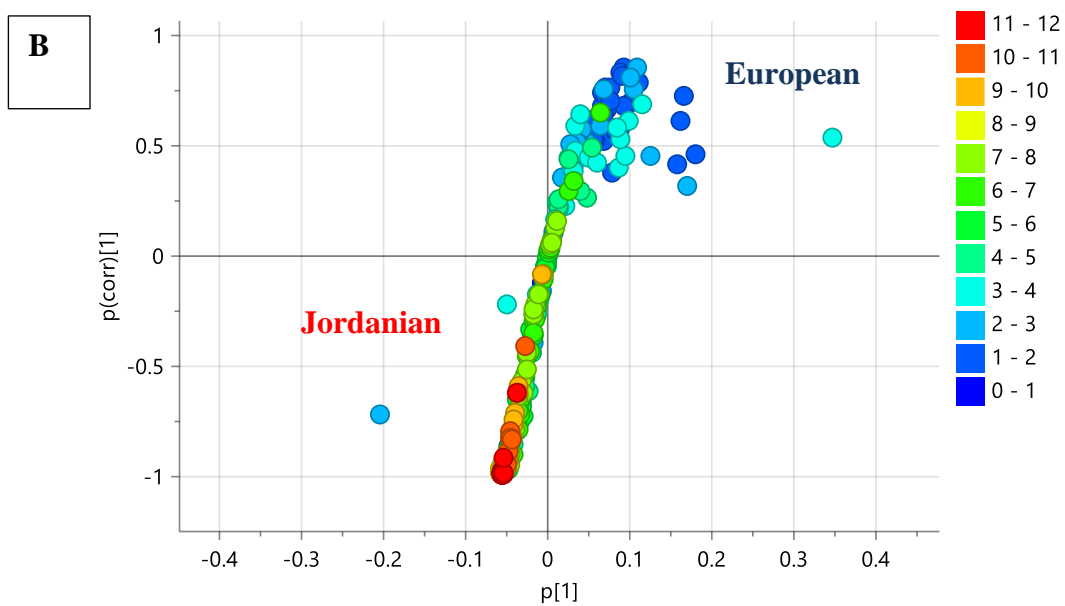
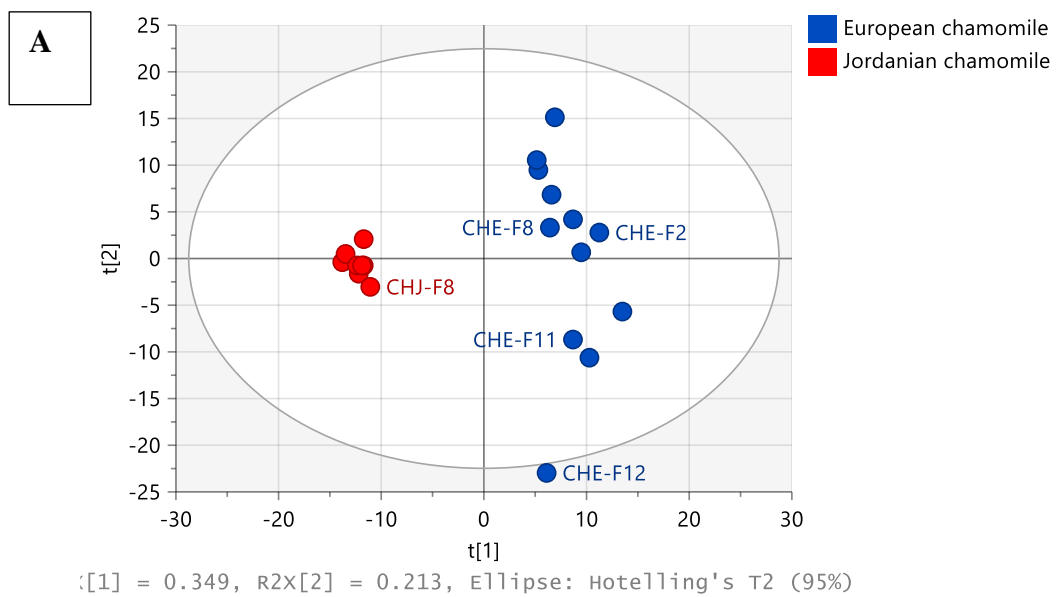


Figure 3.11: (A) PCA scores plot and (B) OPLS-DA loadings S-plot of the NMR spectral data of Jordanian and European fractions.

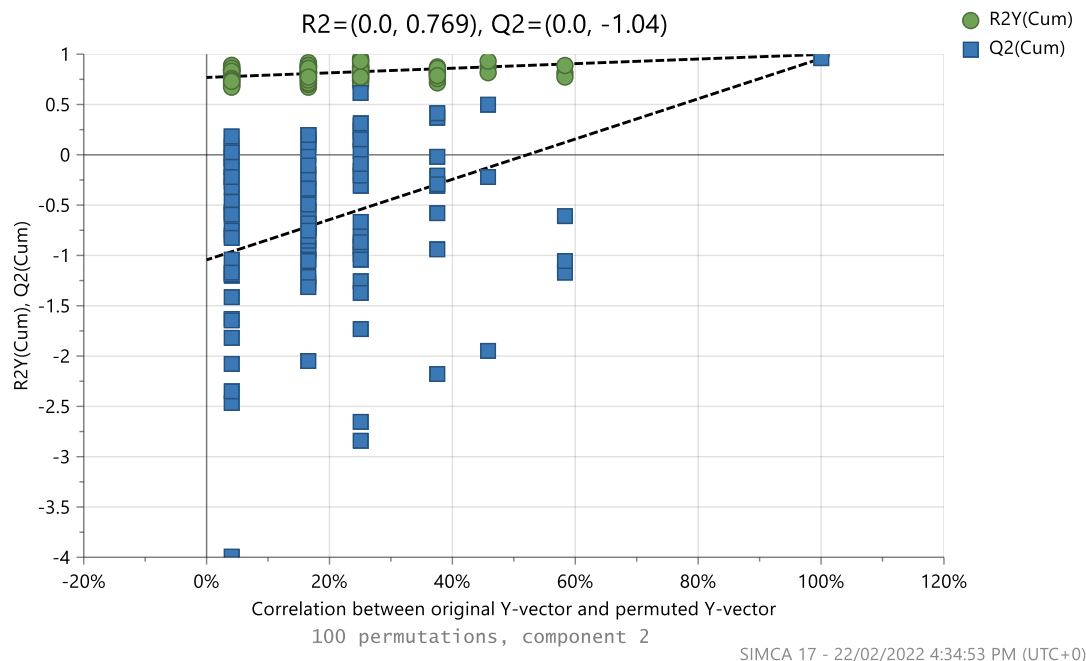


Figure 3.12: Permutation test (100 permutations) of OPLS-DA model for Jordanian and European fractions of their antioxidant using DPPH® assay and anticancer activity against breast cancer cell line ZR-75.

3.3.4. Multivariate analysis of LC-HRMS data

The results from the anticancer and antioxidant assays were incorporated with the LC-MS data for multivariate analysis. The extracts were grouped according to their bioactivity. The active extracts were allocated in the right quadrants of OPLS-DA scores plot, while the inactive extracts were in the left quadrants, as shown in Figure 3.13A. The biologically active EtOAc extracts from both Jordanian and European chamomile were dispersedly distributed in the lower and upper left quadrants, respectively, indicating different chemical profiles for the respective varieties. The inactive extracts included aqueous MeOH and n-Hexane extracts from both varieties. The OPLS-DA model gave validation scores of 1.00 and 0.96 for fitness (R^2) and predictability (Q^2), respectively, that afforded a difference of less than 0.3, which indicated a strong model without being overfitted. The variation $R^2X_o[1]$ between

groups was 25.9% while within groups $R^2X[1]$ was 41.2%. The large variation scores within the respective groups suggested quite a diverse chemical profile between each of the individual extracts in terms of their mass spectral data. From the OPLS-DA loadings plot (Figures 3.13B), the bioactive metabolites displayed a m/z value range between 270 and 600 Da, indicating a medium molecular mass, which supported the ^1H NMR data that could support evidence for the presence of phenylpropanoids and flavonoid compounds. The inactive extracts showed ion peaks for lower MWs compounds between 150 and 340 Da.

OPLS-DA loadings plot (Figures 3.13B) afforded the discriminating metabolites that were encircled in the red while those with p -values < 0.05 were listed in Table 3.3. From the dereplication results, discriminating metabolites with p -values < 0.05 were listed in Table 3.3 and their structures were shown on Figure 3.14. These included N_3285 and N_3284 with ion peaks found at m/z 353.0880 and 515.1196 Da, respectively, that were derivatives of caffeoyl quinic acid, which have been described for their antioxidant activity (Forino *et al.*, 2015). These metabolites were found in the Jordanian chamomile EtOAc extract. Furthermore, discriminating metabolites with MZmine ID P_7541, P_21550, N_3306, P_845 with m/z values of 449.1079, 465.1028, 465.1029, 463.0887, 495.1133 Da were dereplicated as flavonoid derivatives. Numerous flavonoids have been shown to have anticancer properties. However, the molecular mechanisms behind this effect have not been completely understood (Kopustinskiene *et al.*, 2020). The latter metabolites were found in the European chamomile EtOAc extract, which supported the evidence for its anticancer activity against breast cancer cells. A correlation between total phenolic content and antioxidant activity have been earlier reported (Al-Rimawi *et al.*, 2016), but not with total flavonoid content.

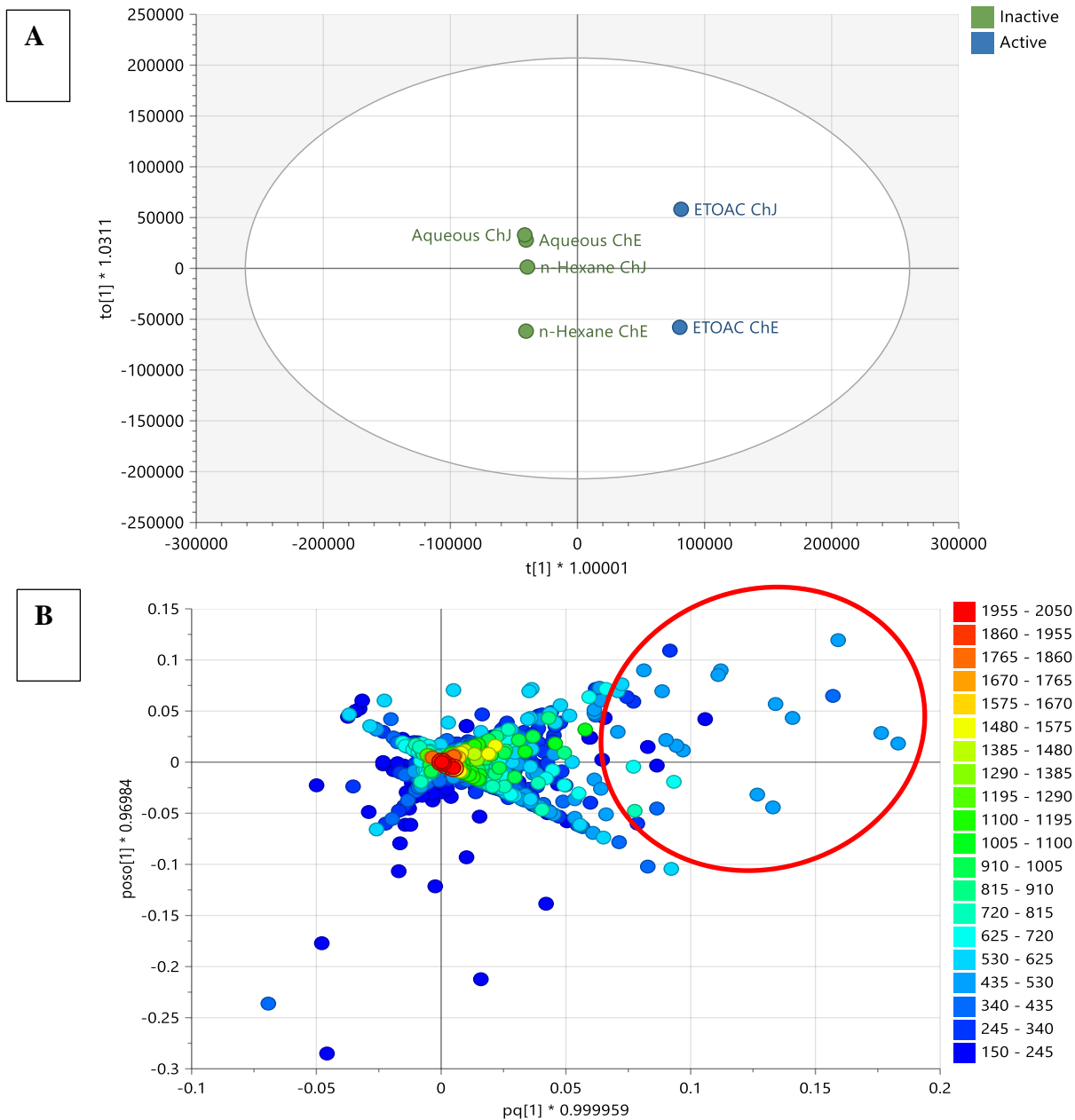


Figure 3.13: (A) OPLS-DA scores and (B) loadings plot for the mass spectral data (ion peaks at m/z) of the crude extracts obtained by liquid-liquid partitioning. Encircled features **in red** indicate the discriminating features for the active EtOAc extracts, which were listed below in Table 3.3. The R^2 and Q^2 values were 1.00 and 0.96, respectively.

Table 3.3: Dereplication of the outliers with $p < 0.05$ determined from the OPLS-DA loadings plot (Figure 3.13B) of the bioactive metabolite from both varieties of *M. chamomilla* EtOAc extracts. Structures of putatively dereplicated compounds are shown in Figure 3.14.

No.	Var ID	<i>p</i> -values	<i>m/z</i>	Rt (min)	MWt	Name	Molecular formula	Reported Source in the database
1	P_1931	3.60E-06	163.0389	7.84	162.0317	7-hydroxy-2 <i>H</i> -1-benzopyran-2-one	C ₉ H ₆ O ₃	<i>M. chamomilla</i>
2	N_3284	5.31E-05	515.1196	8.43	516.1269	3,5-di- <i>O</i> -caffeoylquinic acid; 7'' <i>Z</i> -isomer	C ₂₅ H ₂₄ O ₁₂	<i>Arnica montana</i>
3	P_1848	2.16E-04	517.1341	8.43	516.1269	3'',4''-di-acetylcosmosiin (apigenin glycoside)	C ₂₅ H ₂₄ O ₁₂	<i>M. chamomilla</i>
4	P_21550	2.51E-04	465.1029	7.55	464.0956	2',4',5,5',7 pentahydroxyflavone	C ₂₁ H ₂₀ O ₁₂	<i>Artemisia hispanica</i>
5	P_7541	2.51E-04	465.1028	7.55	464.0956	Quercetin-7-glycosides	C ₂₁ H ₂₀ O ₁₂	<i>Athamanta macrophylla</i>
6	N_3306	1.36E-03	463.0887	7.61	464.0960	3',4',5,5',7 pentahydroxy 3 methoxyflavone	C ₂₂ H ₂₂ O ₁₃	<i>Oenothera speciosa</i>
7	P_1044	2.83E-03	499.1235	8.46	498.1162	Elenoside	C ₂₅ H ₂₂ O ₁₁	<i>Justicia hyssopifolia</i>
8	N_3290	5.26E-03	493.0991	7.72	494.1064	3- <i>O</i> -methylgossypetin 7-glucoside	C ₂₂ H ₂₂ O ₁₃	<i>Artemisia fragrans</i>
9	N_3285	1.06E-02	353.0880	8.34	354.0952	5- <i>O</i> -caffeoylquinic acid; (<i>E</i>)-form	C ₁₆ H ₁₈ O ₉	<i>Cynara scolymus</i> , <i>Cydonia oblonga</i> , <i>Aster scabe</i>
10	P_845	1.50E-02	495.1133	7.76	494.1061	3,4',5,6,7 pentahydroxy 3'-methoxyflavone	C ₂₂ H ₂₂ O ₁₃	<i>Eupatorium tinifolium</i>
11	P_716	4.06E-02	787.3694	12.56	786.3622	<i>N</i> ¹ , <i>N</i> ⁵ , <i>N</i> ¹⁰ , <i>N</i> ¹⁴ -tetra-trans- <i>p</i> -coumaroylspermine.	C ₄₆ H ₅₀ N ₄ O ₈	<i>M. chamomilla</i>

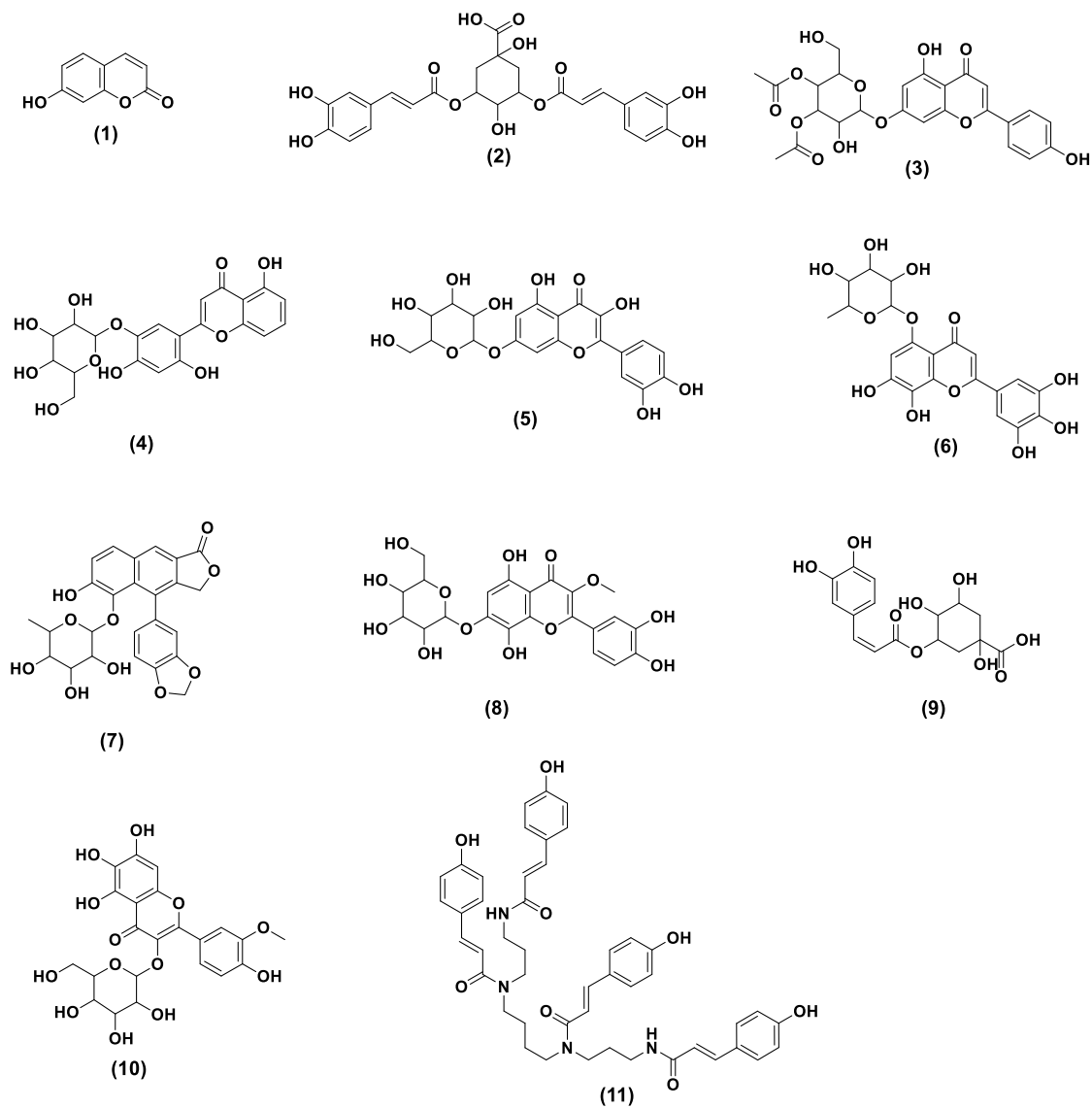


Figure 3.14: Structures of the discriminating bioactive metabolites, listed in Table 3.3, from EtOAc extract of both varieties of *M. chamomilla*.

3.4. Fractionation of the Extracts

Bioactive EtOAc extracts from both chamomile varieties were fractionated employing the same solvent gradient. A semi-automated FC was carried out using a two-pump Büchi Sepacore® system. A gram of the Jordanian and two grams of the European extracts were respectively loaded in silica and eluted over a Versa Flash Silica cartridge column 40x150mm. The chromatographic protocol was performed using a solvent system as presented in Table 3.4. At a flow rate of 100 mL/min, the fraction collection volume was set at 100 mL/flask. TLC was carried out to display the separation profiles of the fractions and similar fractions were pooled together. The pooled fractions were concentrated under vacuum by a rotary evaporator to give 12 major fractions from the European chamomile and 8 major fractions from the Jordanian variety (Table 3.5). The total percentage recovery of the European fractions was 40.1 %, whereas for the Jordanian fractions, it was 75.2%. The resulting fractions were analysed using ¹H NMR and HRESI-MS for metabolomic profiling studies and tested for antioxidant and anti-cancer activity.

Table 3.4: Mobile phase used for the Büchi Sepacore® fractionation of the EtOAc extracts of both *M. chamomilla* varieties.

Time (min)	% MeOH	%DCM	%Acetone
0	1	99	0
20	1	99	0
30	2	98	0
40	3	97	0
46	5	95	0
52	10	90	0
60	30	0	70

Table 3.5: Weights of fractions obtained from the Büchi Sepacore® fractionation of the EtOAc extracts of both varieties of *M. chamomilla*.

European chamomile fractions	Weight (mg)	Jordanian chamomile fractions	Weight (mg)
ChE-1	32.1	ChJ-1	31.6
ChE-2	33.1	ChJ-2	30.0
ChE-3	23.8	ChJ-3	26.7
ChE-4	6.2	ChJ-4	14.8
ChE-5	11.4	ChJ-5	38.2
ChE-6	11.7	ChJ-6	34.4
ChE-7	40.0	ChJ-7	277.4
ChE-8	8.2	ChJ-8	299.5
ChE-9	28.2		
ChE-10	194.0		
ChE-11	10.8		
ChE-12	2.0		
Total amount	401.5	Total amount	752.6
Recovery %	40.1%		75.2

3.4.1. LC-HRMS analysis of *M. chamomilla* fractions

HRMS was used to assist in the dereplication of the metabolites found in the fractions obtained by preparative chromatography. NMR experiments carried out on the fractions complemented the putative identification of known compounds. Furthermore, the distribution of metabolites in both varieties sorted by their MWt showed some significant differences between samples.

On the first approach, the PCA model (Figure 3.15) was based on the MWt distribution of the metabolites found in both chamomile varieties. The PCA scores plot (Figure 3.15A) of the LC-HRMS data of both varieties revealed that fractions obtained from the Jordanian herb were overlappingly clustered together indicating a strong similarity in metabolomic profiles between all these fractions. Like the indicative results obtained from the NMR spectral data, fractions from European variety were dispersed with the most polar fractions F10, F11, and F12 appeared as outliers (Figure 3.15A).

The European chamomile fractions may be classified into three groups: Fractions 1 to 9 (encircled in green), Fractions 10 and 11 (encircled in blue), and Fraction 12 (encircled in red). Fractions 1 to 9 overlapped with the Jordanian chamomile fractions, indicating similarity in their chemical profile.

Despite the high score of 0.961 for the goodness of fit (R^2), the model has a low predictability score (Q^2) of 0.356 after nine components. Polar fractions F10, F11, and F12 were presented as outliers (Figure 3.15A), indicating that there was a strong likelihood that they had a more distinct profile when compared to the other fractions in the sample. The loadings plot in Figure 3.15B demonstrated the discriminatory features for these outlying fractions. F10-ChE and F11-ChE were discriminated by metabolites with MWts of 354.094 (N_3484), 516.125(N_9100 and N_4575), 517.129 (N_11743) and 1032.25 (N_5222) Da. Whereas F12-ChE was discriminated by metabolites with MWts of 354.099 (N_2089), 516.134 (N_14912), 712.232 (N_14913) and (1032.27) N_14914 Da.

N_9100, N_4575 and N_3484 were putatively dereplicated in Table 3.8 as either a polyphenolic compound or flavonoid. These metabolites were also detected from the crude active EtoAc extracts as shown Table 3.3 and were coded P_1848, N_3284, and N_3285 in the positive and negative mode found at m/z 517.1341 $[M+H]^+$, 515.1196 $[M-H]^-$, and 353.0880 $[M-H]^-$, respectively. N_14914 was identified as a complex of 515.126 and 515.126 (N_9100 and N_4575) m/z . while the others did not give any hits and remain unidentified.

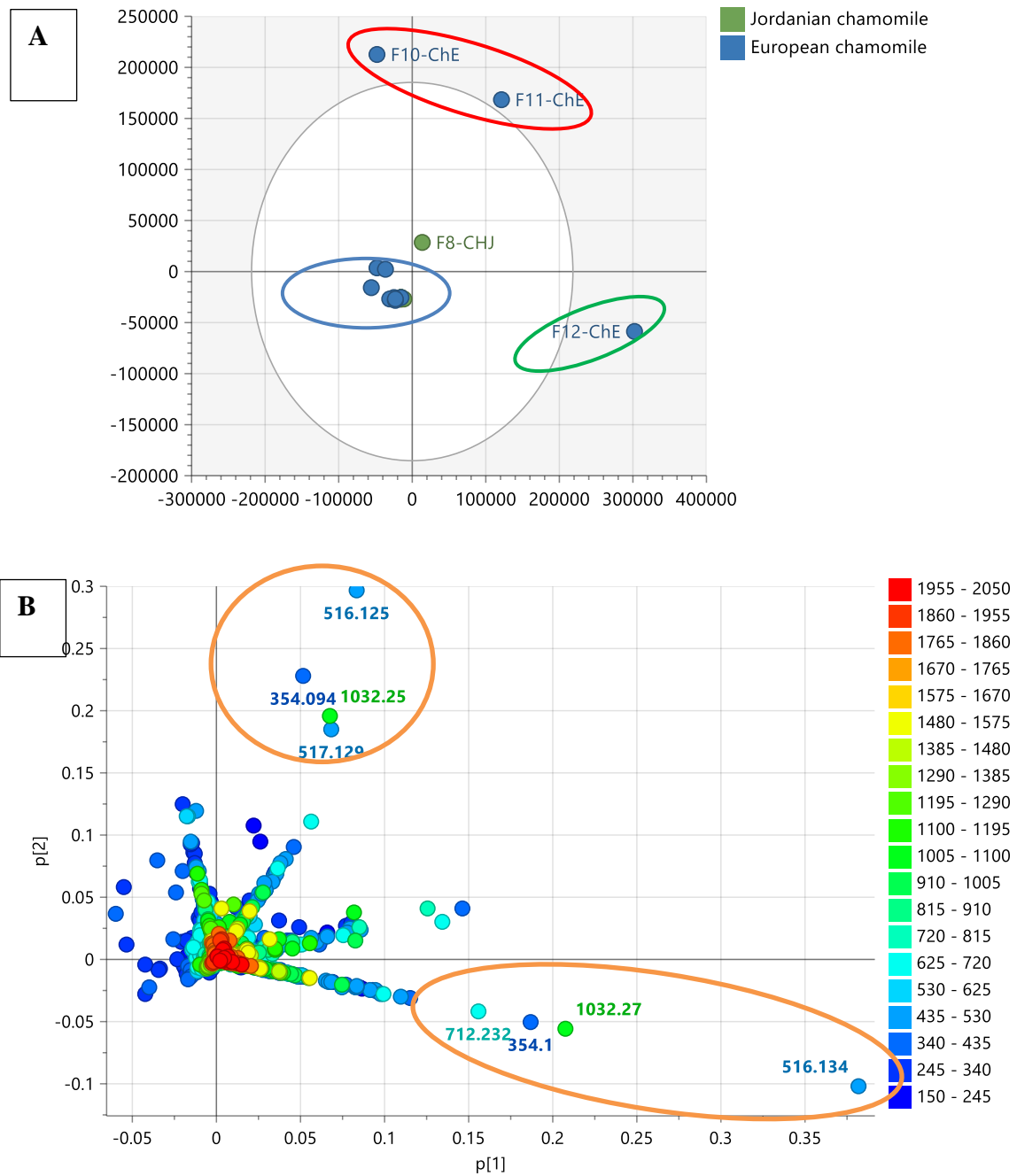


Figure 3.15: (A) PCA scores and (B) loading plots of the LC-HRMS data of *M. chamomilla* fractions for both varieties. Encircled in orange are the discriminatory features for the corresponding outlying variable fractions.

Furthermore, the fractions were evaluated to determine whether they were real outliers using DModX. Fractions 11 and 12 were identified as true outliers, indicating that a high possibility of having a more distinct profile when compared to the other fractions. As seen by the DModX plot, variables above the red line are true outliers, which also included Fractions 6, 8, and 9 (Figure 3.16). However, F10 was not classified as an outlier.

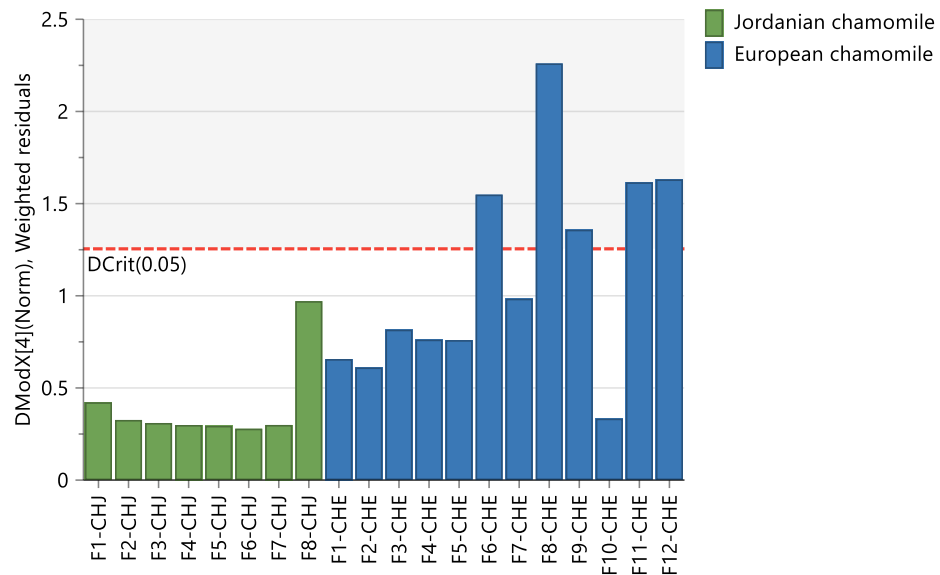


Figure 3.16: DMod X results to validate true outliers of the model. Variables above the red line are the true outliers that included Fractions ChE 6, 8, 9, 11, and 12

For a more accurate observation of the chemical variations between both varieties, an OPLS-DA showed further evidence for the difference between the metabolomic profiles of the two varieties. The presence of metabolites with wider range of MWs from 150 to 1600 Da was found in the European variant. Whereas, the Jordanian variant afforded a narrower MW range of metabolites between 600 and 800 Da (Figure 3.17A).

The loadings plot was generated from the OPLS-DA scores plot model (Figure 3.17B). The discriminating features for the European variety with ion peaks $[M-H]^-$ at m/z 373.093, 269.045, 515.127, 515.118 and 1031.260 Da were associated with the active fractions of the corresponding to F2-ChE, F8-ChE, F11-ChE and F12-ChE (355.103), respectively. Interestingly, ion peaks $[M-H]^-$ at m/z 515.127, and 515.118 Da were already pinpointed as the discriminating features for the active EtOAc extracts and 1031.260 is a complex of 515.127 Da. Determination of the active fractions is presented under Section 3.4.3. The generated model has an R^2 of 0.97 and a Q^2 of 0.88. These values suggested that the fitting and prediction were valid. Additionally, the difference between Q^2 and R^2 was 0.072, less than 0.3, suggesting that no overfitting occurred. The variation between two groups $R^2X_o[1]$ was 21.8%. While the variation within group $R^2X[1]$ was at 8.9%, which indicated that the fractions within the two classes were very similar in their chemical profile. While on the other hand, there is a defined difference between the Jordanian and European variants, since the variance score between groups is significantly bigger than the variance score within groups.

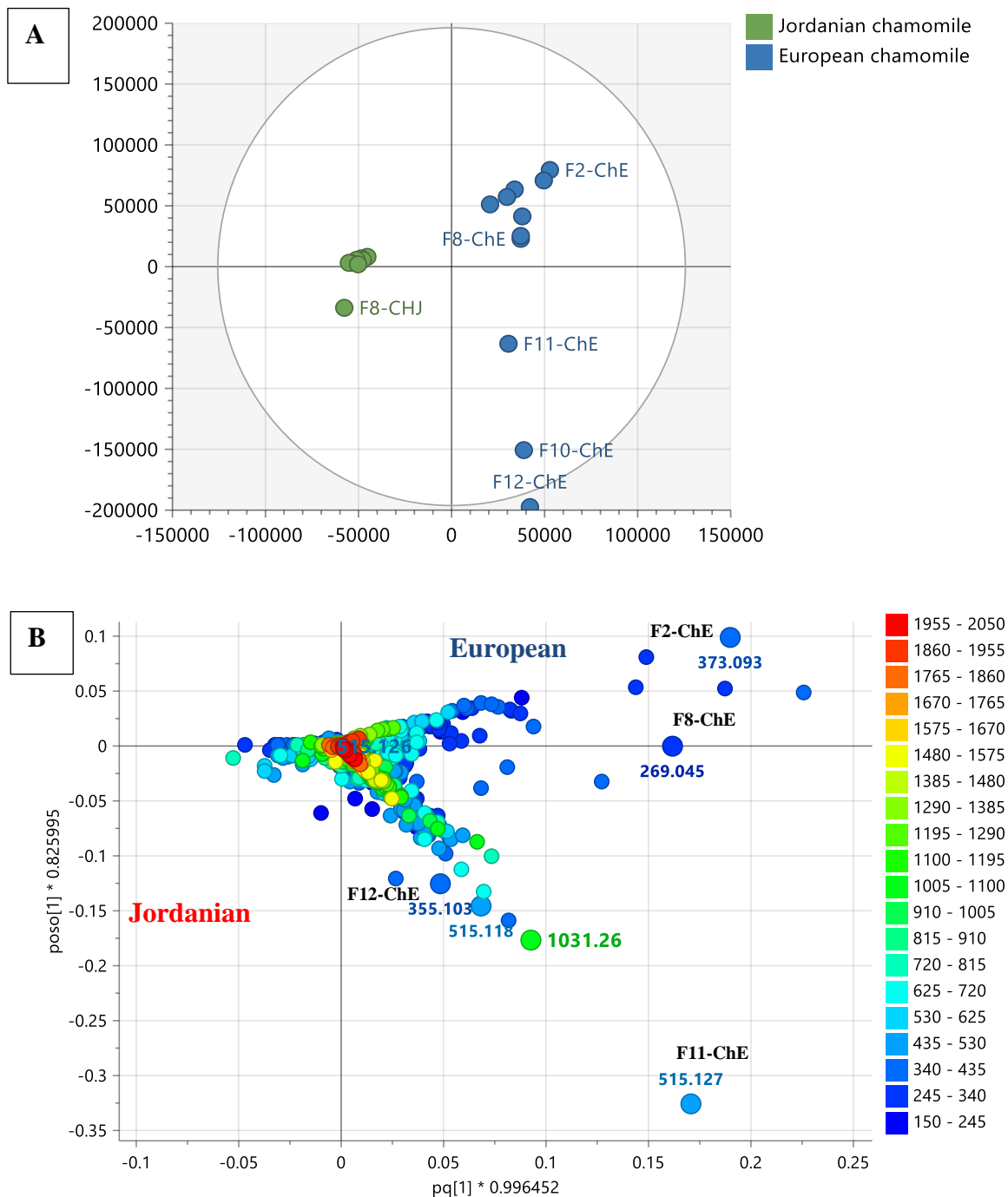


Figure 3.17: (A) OPLS-DA scores and (B) OPLS-DA loadings plots of the m/z ion peaks grouped between Jordanian and European chamomile fractions. R^2 and Q^2 scores were 0.976 and 0.88, respectively.

3.4.2. Biological assay results of the bioactive fractions

The resulting fractions were tested using DPPH assay for antioxidant activity. F11 and F12 from the European variety while only F8 from the Jordanian variety showed antioxidant activity (Figure 3.18), the EC_{50} values of each bioactive fraction were calculated, as shown in Table 3.6. Fraction 8 of the Jordanian variety was the most potent antioxidant among all the fractions, which afforded an EC_{50} value of 0.076 mg/mL. On the other hand, Fractions 11 and 12 showed an antioxidant activity with EC_{50} values of 0.311 and 0.165 mg/mL, respectively. Quercetin and ascorbic acid were used as positive controls that exhibited EC_{50} s of 0.146 and 0.034, respectively.

Moreover, fractions of both varieties were tested against both breast cancer (ZR-75). The cell viability was measured at sample concentration of 30 μ g/mL. Only fractions F2-ChE and F8-ChE of the European variety exhibited anticancer activity against the breast cancer cell line ZR-75. F2 and F8 showed 17% and 21% of cell viability, respectively (Figure 3.19).

Furthermore, using eight concentrations, the IC_{50} values against the breast cancer cell line ZR-75 were determined for the bioactive fractions F2-ChE and F8-ChE (Figure 3.20). F2-ChE exhibited an IC_{50} of 1.94 μ M, while F8-ChE showed an IC_{50} of 1.41 μ M. The isolated bioactive fractions were also assayed for their toxicity against human foreskin fibroblast cell line HS-27 and the results are shown in Figures 3.21 and 3.22. The IC_{50} value for F2-ChE against HS-27 was not obtainable while F8-ChE had an IC_{50} value of 3.18 μ M. The IC_{50} values of both samples were in the ppm range. The toxicity of the compounds was determined based on the IC_{50} of normal HS-27 cells, if the IC_{50} is more than 90 μ g/mL, the compound is considered as not cytotoxic. Generally, if the IC_{50} value falls between 2 and 89 μ g/mL, the compound is classified as moderately cytotoxic and if it is less than 2 μ g/mL, the compound is considered cytotoxic (Mazlan *et al.*, 2020b). The selectivity index (*SI*) was calculated by dividing IC_{50} of the test cancer cell over the IC_{50} of the normal tested cells. If the *SI* value was greater than 10 or if the IC_{50} value of a compound against the normal

HS-27 cell line could not determine from the dilution curve, then this suggested that the tested compounds were considered selective (Vonthron-Sénécheau *et al.*, 2003).

The selectivity index for F2-ChE and F8-ChE were not obtainable, which indicated both fractions were selective. Both compounds had an IC₅₀ on the normal HS-27 cells above 90 µg/mL, which suggested that were not toxic. F2-ChE and F8-ChE were found selective against the tested breast cancer cell line and was not toxic against the normal cell line HS-27 (Table 3.7).

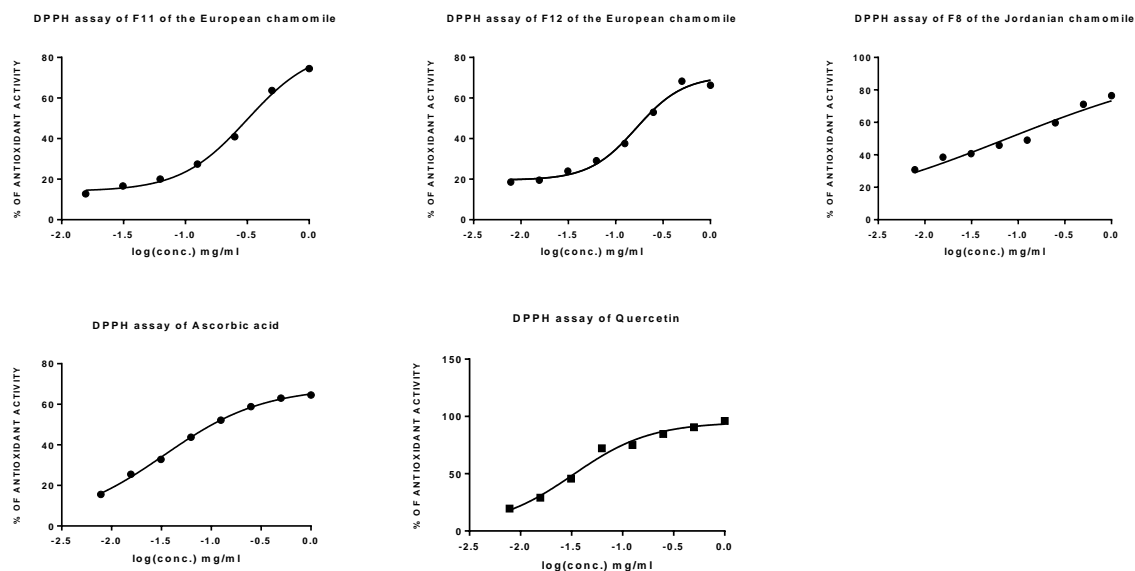


Figure 3.18 : DPPH assay of the bioactive fractionated samples.

Table 3.6: EC₅₀ for the bioactive fractions that possess antioxidant activity. n= number of samples

	Trend line equation	R ²	EC ₅₀ mg/mL	EC ₅₀ μM	n
F11 ChE	$y = 15.466\ln(x) + 68.738$	0.9156	0.311	603	3
F12 ChE	$y = 11.573\ln(x) + 67.599$	0.9249	0.165	463	3
F8 ChJ	$y = 9.3158\ln(x) + 74.126$	0.9605	0.076	147	3
ascorbic acid	$y = 10.592\ln(x) + 70.222$	0.9664	0.146	829	3
quercetin	$y = 16.534\ln(x) + 104.2$	0.9383	0.034	113	3

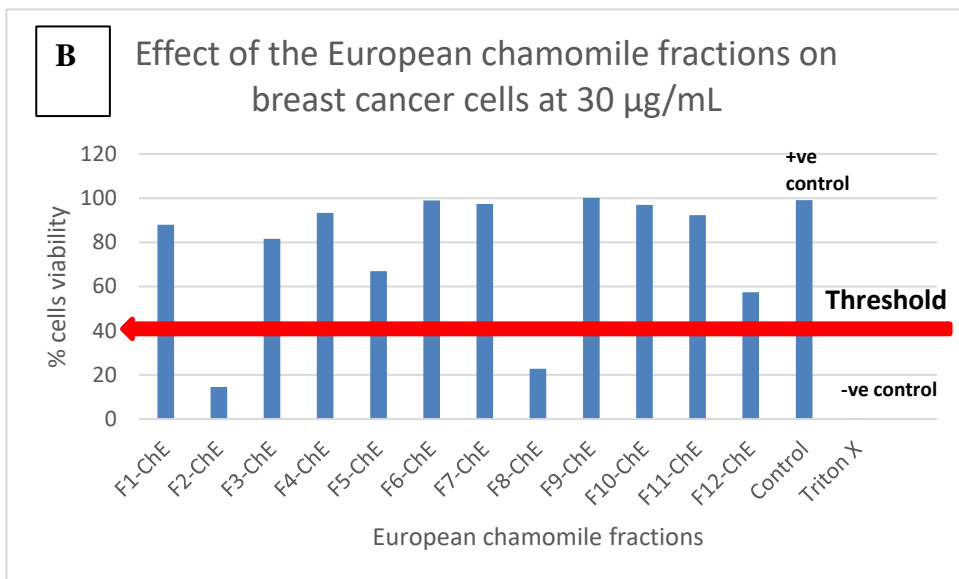
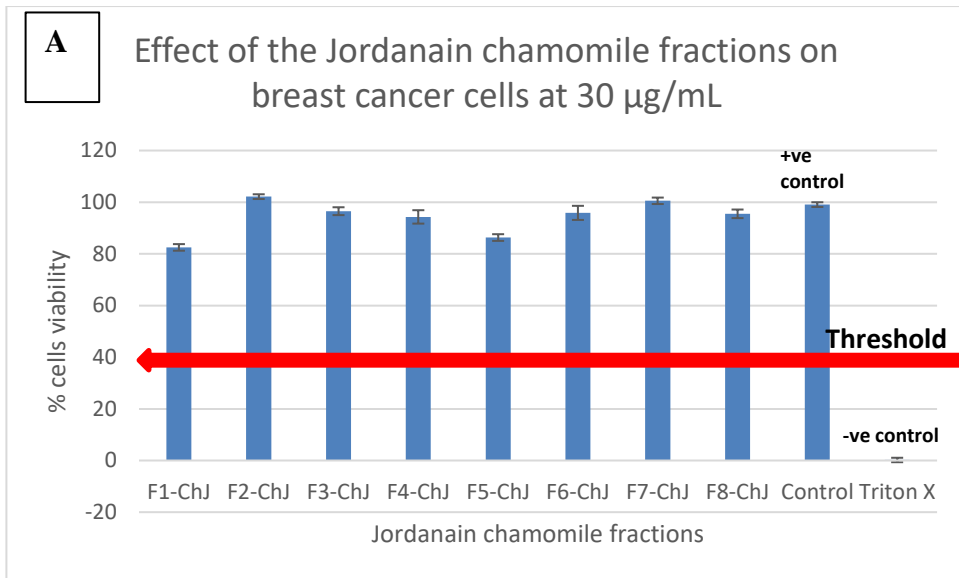


Figure 3.19: AlamarBlue® assay of fractions from both *M. chamomilla* varieties. Effect of 30 mg/mL **A**) Jordanian and **B**) European chamomile fractions on breast cancer cells.

A**B**

Standard Curve for F2 of the European chamomile on ZR95 (Breast cancer cells) **Standard Curve for F8 of the European chamomile on ZR95 (Breast cancer cells)**

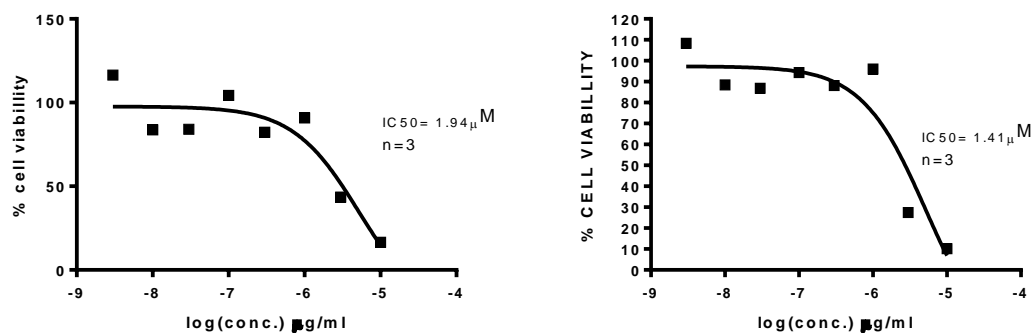


Figure 3.20: Standard curves to determine the IC_{50} values for the bioactive fractions **A)** F2 and **B)** F8 from the European chamomile tested against the breast cell line ZR-75.

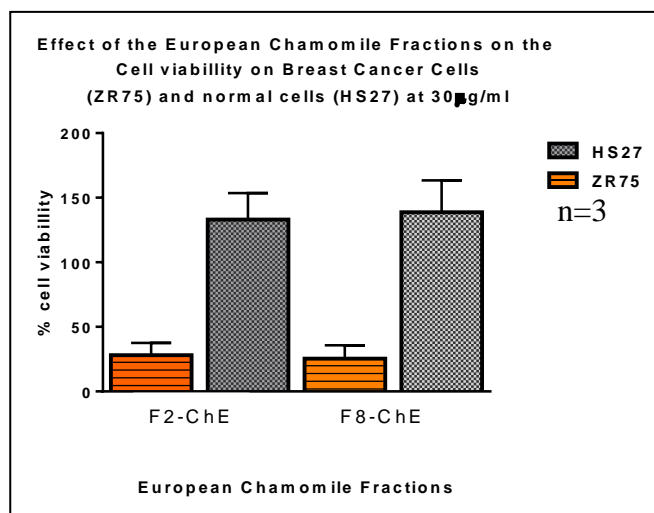
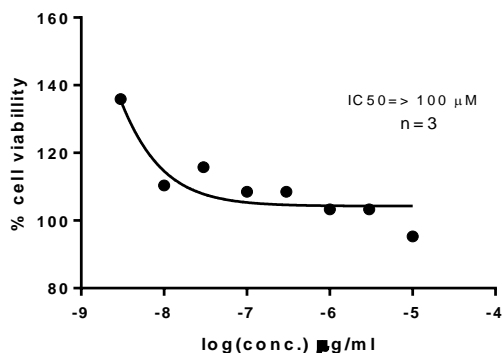


Figure 3.21: Effect of 30 $\mu\text{g/mL}$ European chamomile active fractions against ZR-75 cancer cells and HS-27 normal cells.

A Standard Curve for F 2 of the European chamomile on HS27 (Normal cells)



B Standard Curve for F 8 of the European chamomile on HS27 (Normal cells)

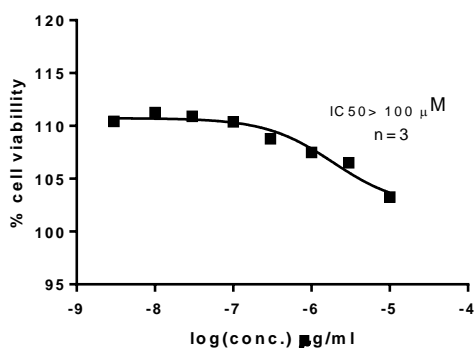


Figure 3.22 : Standard curves to determine the IC_{50} values for the bioactive fractions **A)** F2 and **B)** F8 from the European chamomile tested against the normal cell line HS-27.

Table 3.7: IC_{50} values in μM for the bioactive European chamomile fractions against the tested cell lines. If SI greater than 10 or the IC_{50} of the tested normal cell was not obtainable, then the compound considered selective (Vonthron-Sénécheau *et al.*, 2003).

Bioactive fraction	IC_{50} ZR-75(μM)	IC_{50} HS-27(μM)	IC_{50} HS-27($\mu g/mL$)	toxicity	SI
F2-ChE	1.94	> 100	>90	Not toxic	(selective)
F8-ChE	1.41	> 100	> 90	Not toxic	(selective)

Legend: SI =selectivity index. If IC_{50} of HS-27 > 90 $\mu g/mL$ =not toxic, 2-89 $\mu g/mL$ =moderate cytotoxicity and if less than 2= cytotoxic

To validate the hypothetical association of the discriminating features for the European variety with its active fractions, an OPLS-DA model was also generated between active and inactive fractions regardless of the chamomile variety. The comparison would pinpoint the bioactive metabolites responsible for the antioxidant activity and anticancer against breast cancer cell line ZR-75. The bioactive fractions of F8-ChJ, F2-ChE, F8-ChE, F11-ChE and F12-ChE were grouped together apart from the inactive fractions (Figure 3.23A). The results in Figure 3.23B showed that the isolated anticancer compounds, presented under Section 3.5, with MWts of 270.053, 356.11, 374.1, 516.125, and 516.134 Da were all found on the active quadrant of the S-plot. Dereplication data for these metabolites were highlighted in Table 3.8. The total ion chromatograms (TIC) shown on Figure 3.24 reveals the relative intensity of the isolated discriminating features for the anticancer fractions. Structures of the discriminating bioactive metabolites that were proposed to be active antioxidant and anticancer against breast cancer (ZR-75) were listed in Table 3.8 and presented in Figure 3.25.

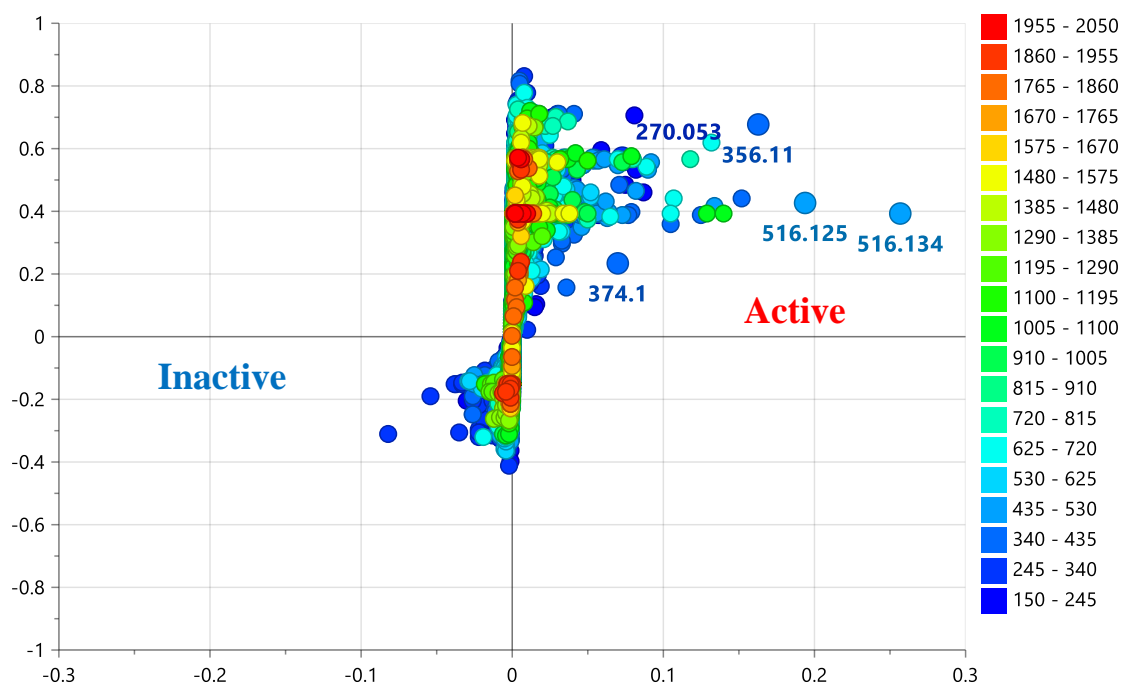
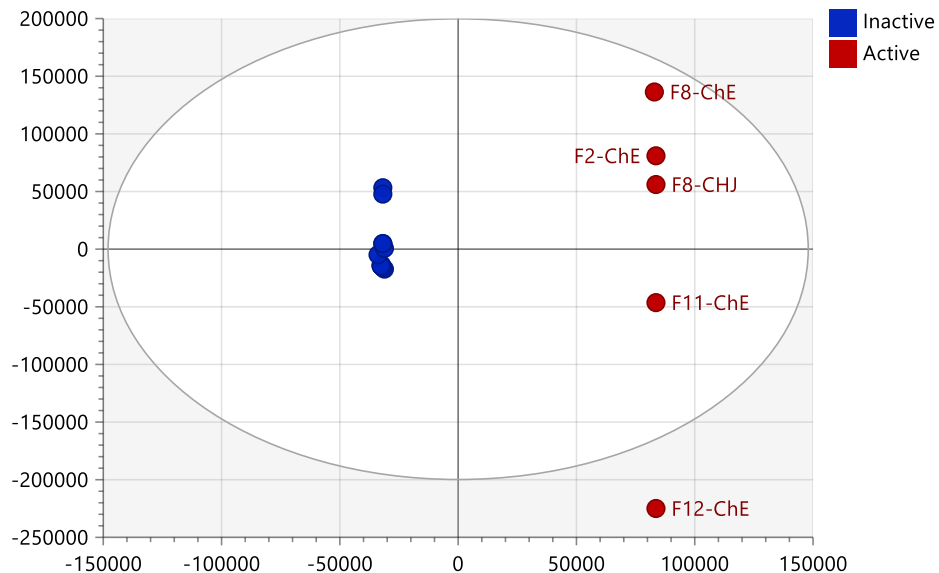


Figure 3.23: A) OPLS-DA scores plot and B) S-plot of the mass spectral data (MW) grouped between active and inactive fractions. R^2 and Q^2 values are equal to 1.0 and 0.41, respectively. The discriminatory features were labelled with their ion peaks at m/z .

Table 3.8: Dereplication of target bioactive metabolites against breast cancer (ZR-75) and antioxidant activity as predicted by OPLS-DA loadings S-plots. Metabolites were arranged according to their ascending p-values. Highlighted rows represent compounds that were isolated from both chamomile varieties.

Primary ID	p-value	m/z	Rt (min)	MWt	Compound name	molecular formula	Source
N_5225	0.0020	355.1031	5.54	356.1104	1- <i>O-p</i> -coumaroylglucose (1)	C ₁₆ H ₂₀ O ₉	<i>M. chamomilla</i> <i>Cimicifuga heracleifolia</i> <i>Cimicifuga dahurica</i> <i>Equisetum arvense</i>
					4'- <i>O</i> -β-D-allopyranoside (2)		
					4'- <i>O</i> -β-D-galactopyranosid (3)		
					<i>Z</i> -Glucoferulic acid (4)		
N_3180	0.0137	269.0452	12.55	270.0525	4',5,7-trihydroxyisoflavone (5)	C ₁₅ H ₁₀ O ₅	<i>Leguminosae subf.</i>
N_11757	0.0144	655.4065	13.55	656.4137	bractic acid (6)	C ₃₅ H ₆₀ O ₁₁	<i>Ajuga bracteosa</i>
N_2695	0.0145	785.3552	12.92	786.3625	spermine; <i>N</i> ¹ , <i>N</i> ⁵ , <i>N</i> ¹⁰ , <i>N</i> ¹⁴ -tetrakis(4-hydroxy- <i>E</i> -cinnamoyl) (7)	C ₄₆ H ₅₀ N ₄ O ₈	<i>M. chamomilla</i>
N_11748	0.0146	445.2447	13.37	446.2520	2-acetyl-3- <i>O</i> -(2-methylpropanoyl) β-D-glucose-4- <i>O</i> -(8-methylnonanoyl) (8)	C ₂₂ H ₃₈ O ₉	<i>Solanum aethiopicum</i>
N_9100	0.0146	515.1190	8.10	516.126	<i>O</i> -[3,4-dihydroxy- <i>E</i> -cinnamoyl-4-α-D-glucopyranoside] (9)	C ₂₅ H ₂₄ O ₁₂	<i>Erycibe obtusifolia</i> <i>M. chamomilla</i> <i>Arnica montana</i>
					3'',4''-di-acetyl cosmosiin*; (10)		
					3,5-di- <i>O</i> -caffeoylquinic acid; 7'' <i>Z</i> -isomer* (11)		

Primary ID	p-value	m/z	Rt (min)	MWt	Compound name	molecular formula	Source
N_11749	0.0165	971.4864	14.43	972.4937	calendasaponin B (12)	C ₄₈ H ₇₆ O ₂₀	<i>Calendula officinalis</i>
N_11744	0.0165	447.0921	7.68	448.0994	carthamone (13)	C ₂₁ H ₂₀ O ₁₁	<i>Carthamus tinctorius</i>
N_3234	0.0169	329.2329	12.89	330.2402	6,9,10-trihydroxy-7-octadecenoic acid (14)	C ₁₈ H ₃₄ O ₅	<i>Sparganium stoloniferum</i>
N_11753	0.0188	441.2497	14.53	442.2570	asebotoxin VI (15)	C ₂₃ H ₃₈ O ₈	<i>Pieris japonica</i>
N_5224	0.0202	655.1293	9.14	656.1366	Tinctoside (16)	C ₃₁ H ₂₈ O ₁₆	<i>Anthemis tinctoria</i>
N_11652	0.0236	493.0977	7.79	494.1049	3-O-β-D-glucopyranoside (17) O-β-D-Galactopyranoside (18)	C ₂₂ H ₂₂ O ₁₃	<i>Eupatorium tinifolium</i>
N_5231	0.0421	355.1026	7.23	356.1098	1-O-p-coumaroylglucose (19)	C ₁₆ H ₂₀ O ₉	<i>M. chamomilla</i> <i>Cimicifuga heracleifolia</i> <i>Cimicifuga dahurica</i> <i>Equisetum arvense</i>
					4'-O-β-D-allopyranoside (20)		
					4'-O-β-D-galactopyranosid (21)		
					Z-Glucoferulic acid (22)		
N_5236	0.0515	463.0874	7.56	464.0947	myricetin-7-rhamnoside (23)	C ₂₁ H ₂₀ O ₁₂	<i>Myrsine africana</i>
N_5226	0.0653	711.2130	7.23	712.2203	theaflavoside II (24)	C ₃₂ H ₄₀ O ₁₈	<i>Camellia sinensis</i>
N_3484	0.0670	353.0872	8.85	354.0944	E-5-O-caffeoylquinic acid (25)	C ₁₆ H ₁₈ O ₉	<i>Cynara scolymus</i> <i>Cydonia oblonga</i>
N_4575	0.0772	515.1182	8.47	516.1255	3,5-di-O-caffeoylquinic acid (26)	C ₂₅ H ₂₄ O ₁₂	<i>Cynara scolymus</i>
N_11743	0.0868	516.1220	8.29	517.1290	No hits	-	-
N_2900	0.1009	431.0976	8.61	432.1049	thalictiin (27)	C ₂₁ H ₂₀ O ₁₀	<i>Thalictrum thunbergia</i> <i>Chrysanthemum morifolium</i>

Primary ID	p-value	m/z	Rt (min)	MWt	Compound name	molecular formula	Source
N_5222	0.105102	1031.2400	8.35	1032.25	No hits	-	-
N_14912	0.1085	515.1265	8.09	516.1338	antibiotic a 503083f; methyl ester (28)	C ₁₉ H ₂₄ N ₄ O ₁₃	<i>Streptomyces sp. SANK 62799</i>
N_14913	0.1085	711.2250	7.23	712.2320	No hits	-	-
N_14914	0.1085	1031.2606	8.09	1032.2679	Complex of m/z 515.1265 and 515.1265	-	-
N_2089	0.1104	353.0930	8.48	354.0993	No hits	-	-
N_2649	0.1406	359.0772	13.57	360.0845	chrysosplenol D (29)	C ₁₈ H ₁₆ O ₈	<i>Cyanostegia microphylla</i> , <i>Chrysosplenium alternifolium</i> , <i>Chrysosplenium tetrandrum</i> ,
N_435	0.3460	373.0926	15.56	374.0999	4',5-dihydroxy-3,3',6,7-tetramethoxyflavone (30)	C ₁₉ H ₁₈ O ₈	<i>Chrysosplenium spp.</i>

*Structures are shown under Figure 3.11

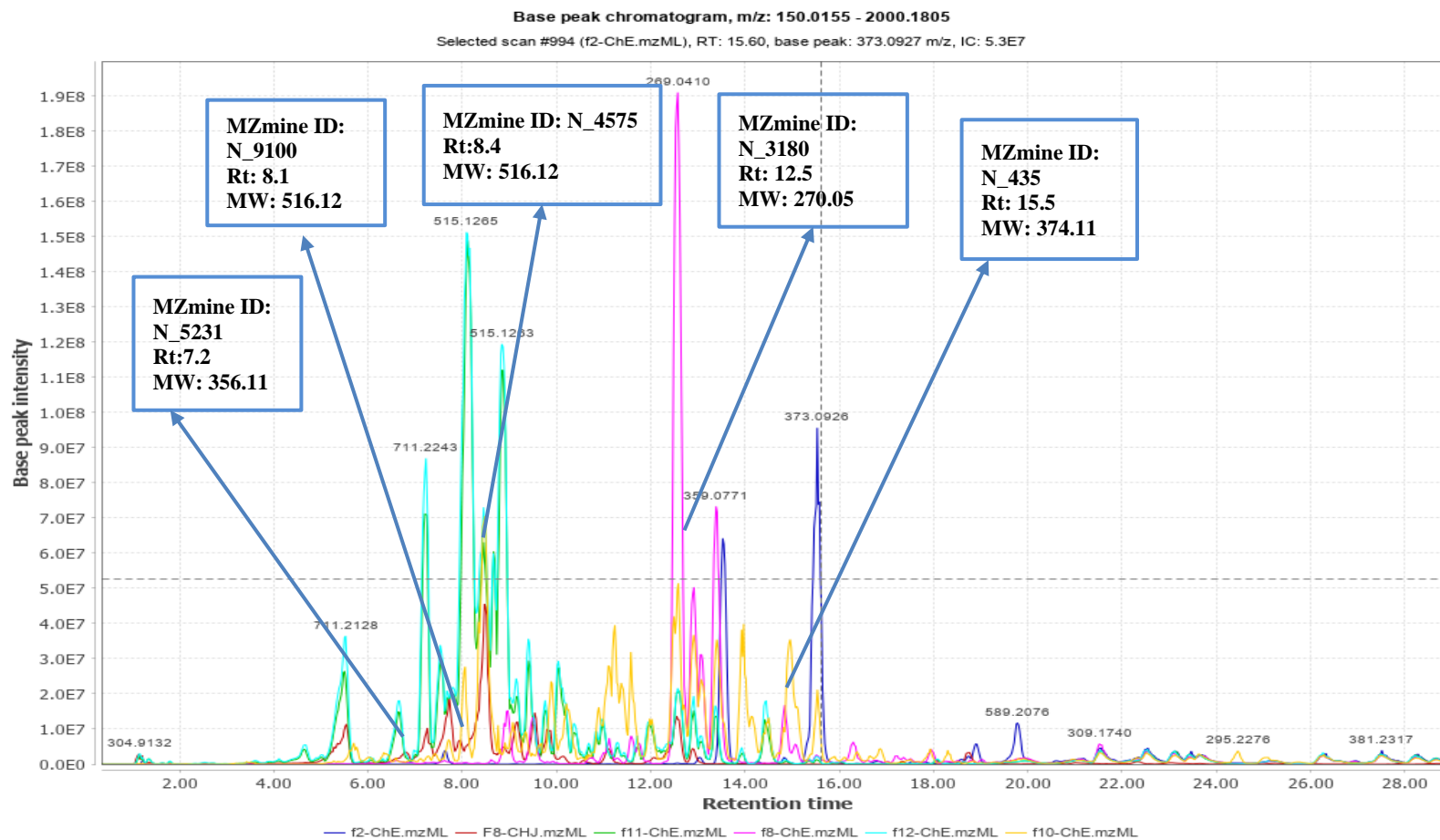


Figure 3.24: Total Ion Chromatogram (TIC) of the active fractions. The labelled ion peaks represent the isolated discriminating features highlighted in Table 3.8.

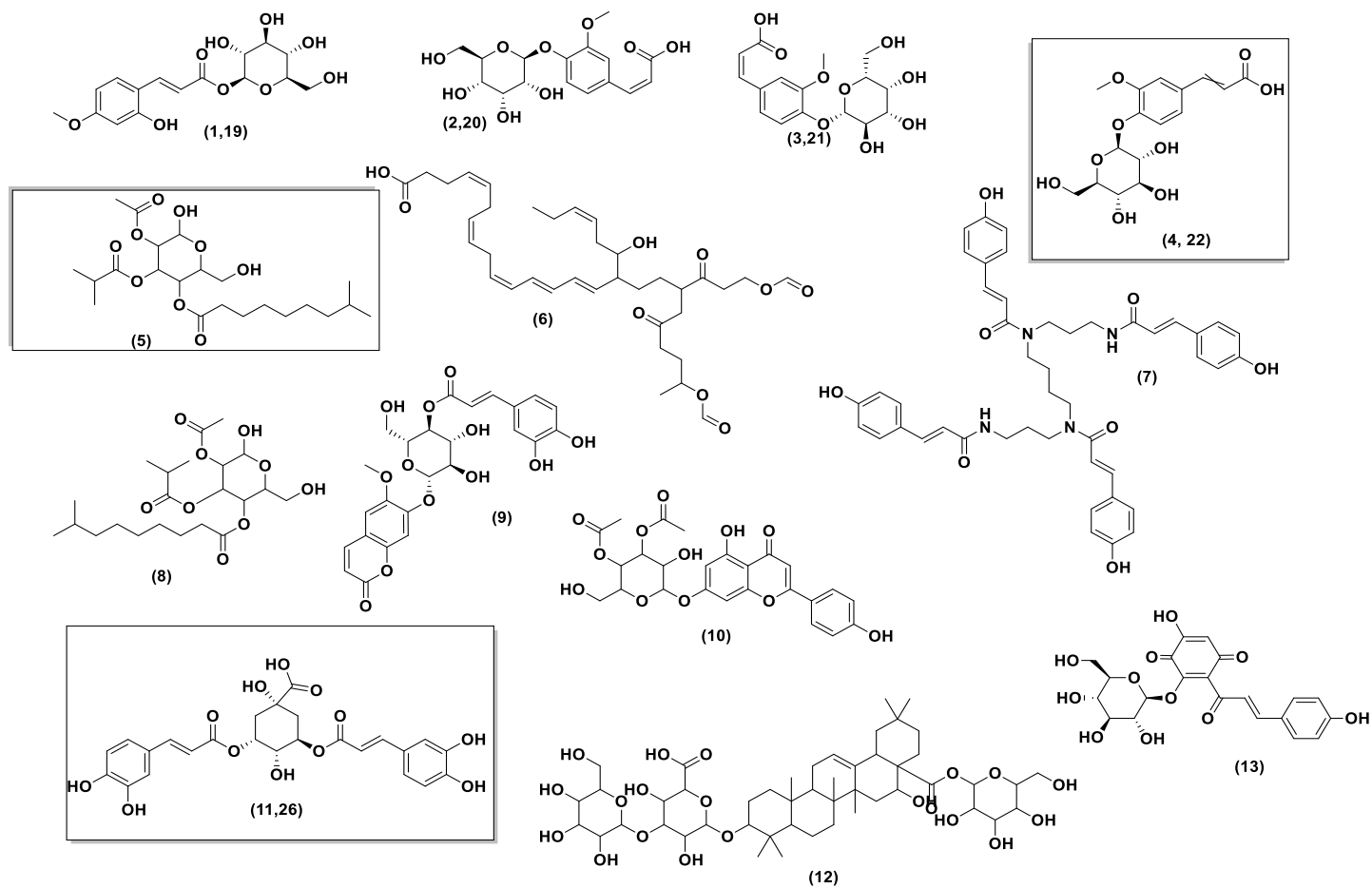


Figure 3.25: Structures of the discriminating bioactive metabolites against breast cancer (ZR-75) and antioxidant activity as listed in Table 3.8. Structures in black boxes were the isolated compounds in this study.

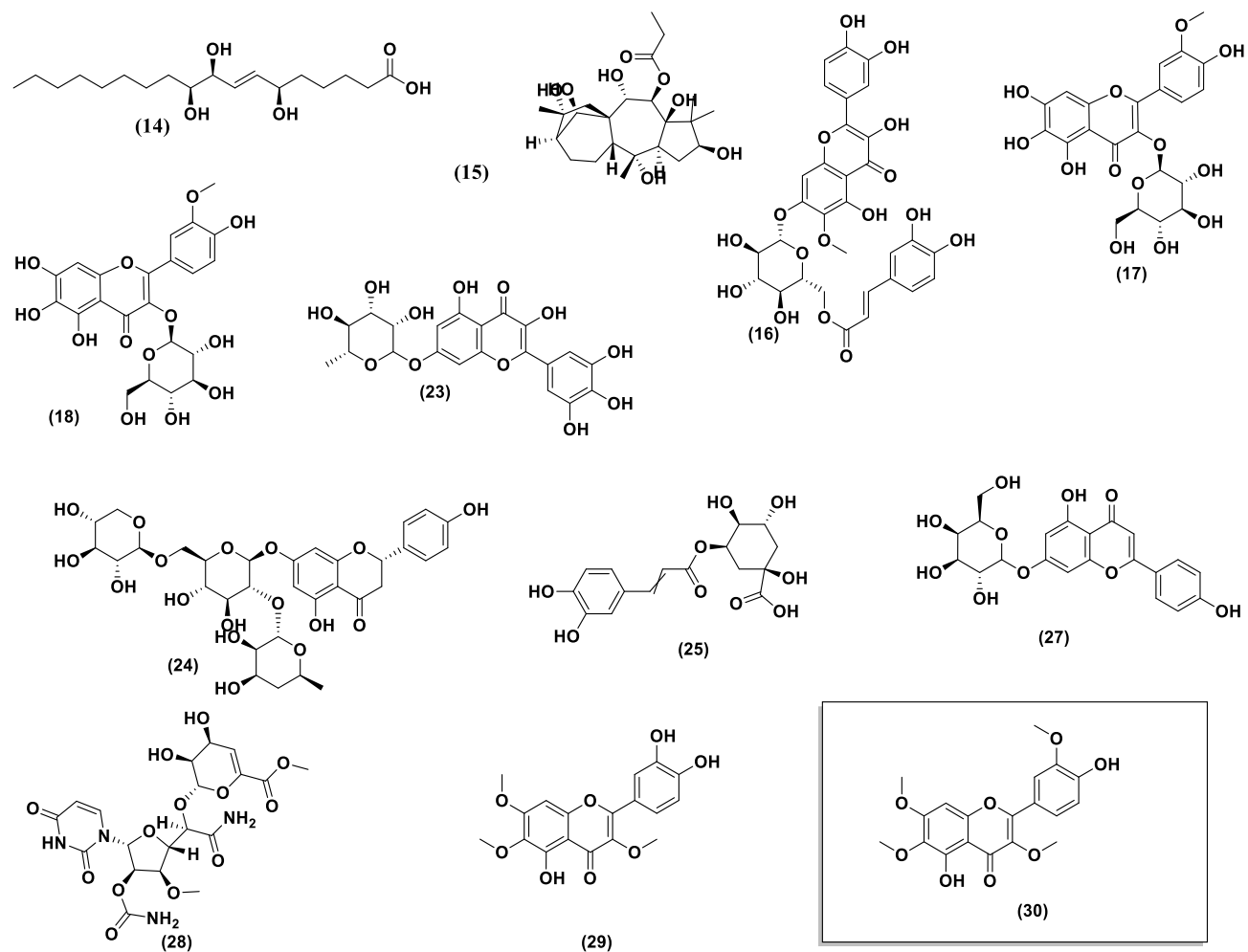


Figure 3.26 (continued): Structures of the discriminating bioactive metabolites against breast cancer (ZR-75) and antioxidant activity as listed in Table 3.8. Structures in black boxes were the isolated compounds in this study.

3.5. Structural elucidation of biologically active fractions

The bioactive compounds were submitted for ^1H NMR, 2D NMR and LC-HRMS. The dereplication study on the antioxidant and anticancer fractions of both varieties were performed by using the HPLC-MS data, which help to find major metabolites present in the active fractions that were unidentified using the DNP database. Dereplication can be performed by analysis of exact mass and fragmentation patterns, as well as using retention time, which can aid in identification of compounds. Structure elucidation of the bioactive compounds was accomplished on F8 of the Jordanian chamomile and F2, F8, F11, and F12 of the European chamomile (Figure 3.26).

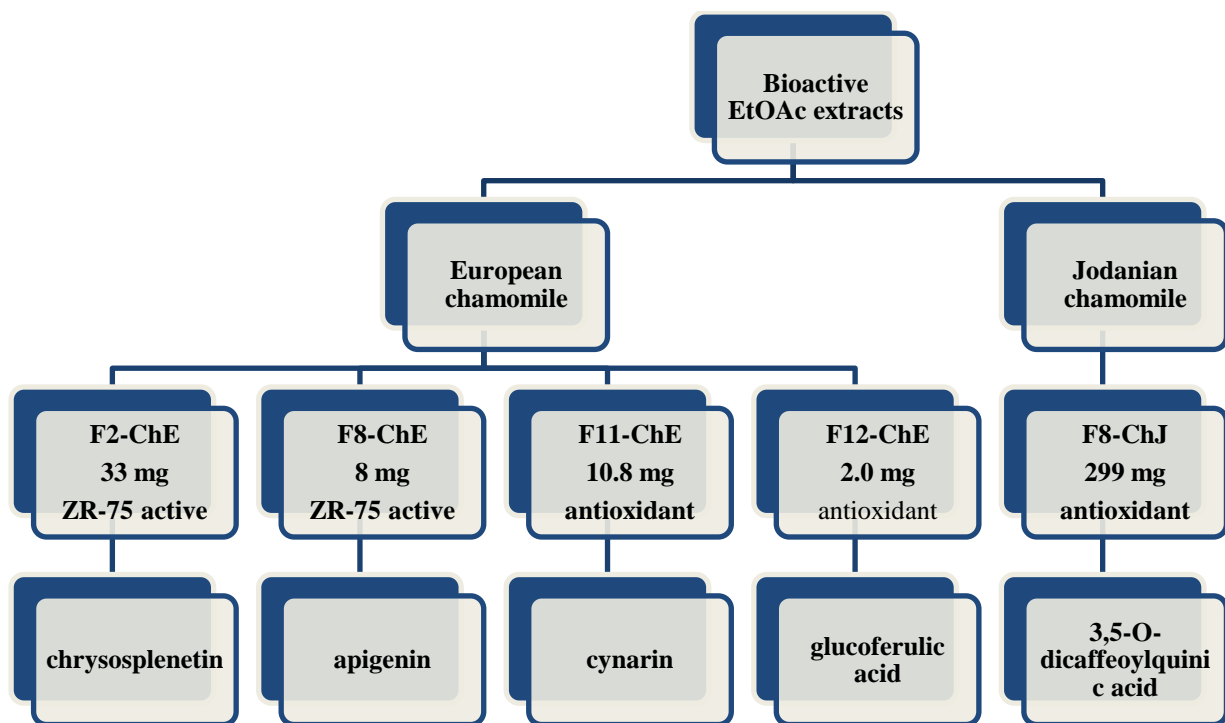
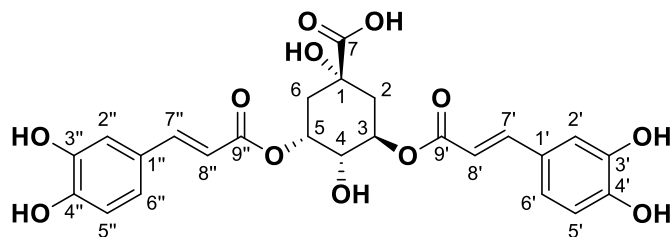


Figure 3.26: Schematic diagram summarising the isolation and elucidation of the bioactive compounds produced by the two *M. chamomilla* varieties.

3.5.1. Structure elucidation of F8-ChJ from Jordanian chamomile



Chemical Formula: $C_{25}H_{24}O_{12}$

Exact Mass: 516.1264

3,5-*O*-dicaffeoylquinic acid

Figure 3.27: Chemical structure of F8-ChJ

Formula	Calculated Mass	Target Mass	Double Bond Equivalence	Absolute Error (ppm)	Error (mDa)	Error (ppm)	Fitness
$C_{25}H_{23}O_{12}$	515.11895	515.11824	14.5	1.39	-0.72	-1.39	1.000

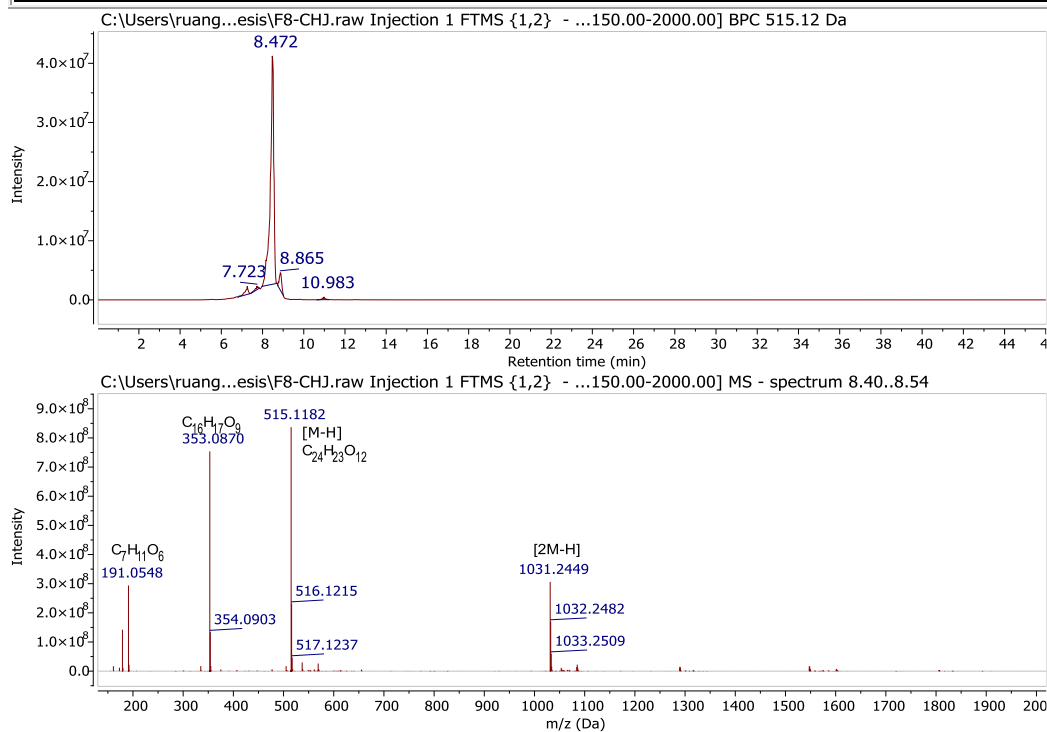


Figure 3.28. Extracted ion chromatogram and mass spectrum of F8-ChJ from the Jordanian chamomile showing source fragmentation at m/z 515.1182 $[M-H]^-$ eluting at 8.47 min.

The total ion chromatogram of the bioactive fraction F8-ChJ (Figure 3.28) presented a major compound with following ions peaks at m/z 179.0341 for $C_9H_7O_4$, 191.0552 for $C_7H_{11}O_6$, 353.0879 for $C_{16}H_{17}O_9$, 515.1187 for $C_{25}H_{23}O_{12}$ $[M-H]^-$, and 1031.2450 for $[2M-H]^-$ $C_{50}H_{47}O_{24}$ with a RT of 8.47 min and average intensity of $4.0E+7$ (Figure 3.29). The fragmentation pathway of the spectral data was comparable to those reported in the literature. The MS fragmentation of F8-ChJ is compatible to that of a dicaffeoylquinic acid isomer (Figure 3.29). These fragmentations were confirmed by exact mass measurement of the ions presented in Table 3.9.

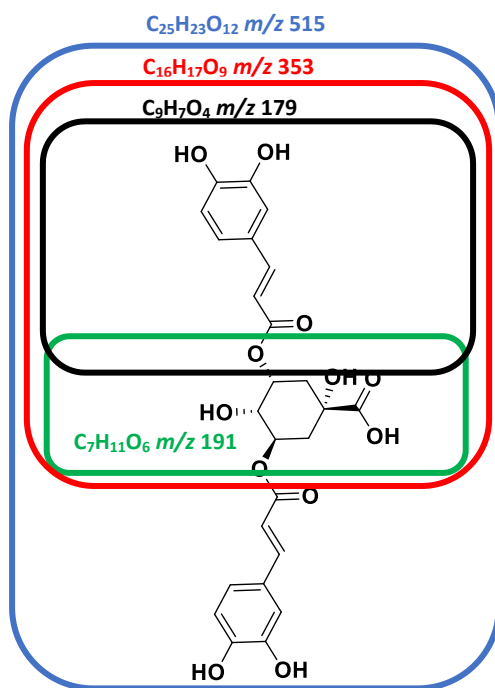


Figure 3.29: Fragment scheme of a dicaffeoylquinic acid isomer.

Table 3.9: Fragments ions of a dicaffeoylquinic acid isomer at R_t 8.47 min as shown in Figure 3.29

fragment moiety	molecular formula	m/z	Highlighted box
dicaffeoylquinic acid	$C_{25}H_{23}O_{12}$	515.1187	blue
3 or 5- <i>O</i> -caffeoyl quinic acid	$C_{16}H_{17}O_9$	353.0879	red
caffeic acid	$C_9H_7O_4$	179.0341	black
quinic acid	$C_7H_{11}O_6$	191.0552	green

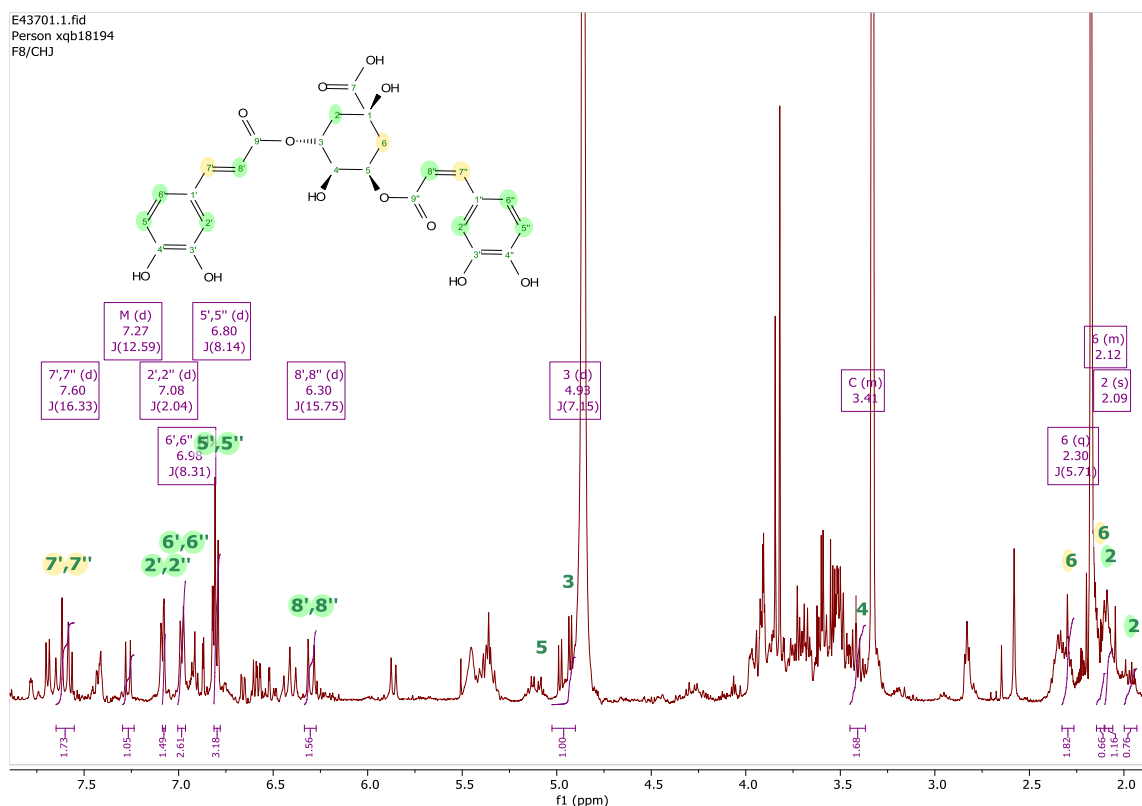


Figure 3.30: ^1H NMR spectrum of F8-ChJ in CD_3OD measured at 400 MHz.

F8-ChJ was isolated as a yellow amorphous powder with a yield of 299 mg. HREIMS analysis showed molecular ion peak at m/z 515.134 $[\text{M}-\text{H}]^-$, corresponding to the molecular formula $\text{C}_{25}\text{H}_{23}\text{O}_{12}$. The ^1H NMR spectrum in Figure 3.30 revealed the presence of three oxygenated methine protons at δ_{H} 5.36 (1H, t, $J=6.0$, H3), 5.86 (1H, d, $J=13.1$, H5), and 4.94 (1H, dd, $J = 13.0, 6.0$ Hz, H4), two methylenes at δ_{H} 2.30 (1H, q, $J = 5.7$ Hz, $\text{H}_{6\text{eq}}$), 2.12 (1H, m, $\text{H}_{6\text{ax}}$), 2.09 (1H, br s, $\text{H}_{2\text{eq}}$), 1.97 (1H, m, $\text{H}_{2\text{ax}}$). Furthermore, the ^1H NMR spectrum disclosed the presence of two pairs of aromatic ABX protons at δ_{H} 7.08 (1H, d, $J = 2.0$ Hz, H2' and H2''), 6.98 (1H, brd, $J = 8.3$ Hz, H6' and H6''), 6.80 (1H,

d, $J = 8.1$ Hz, H-5' and H-5''), and four trans-oriented olefinic protons at δ_{H} 7.63, (each 1H, d, $J = 16.5$ Hz, H7' and H-7'') and 6.30 (each 1H, d, $J = 16.5$ Hz, H-8', H-8''), which were attributed to a trans-caffeoyl moiety. The existence of two caffeoyl units was clear based on the integration of the proton peaks. The large coupling constant of 16.5 Hz between the olefinic protons of the caffeoyl moiety suggested a trans-configuration.

The ^1H - ^1H COSY spectrum showed coupling between the oxygenated methines H3, H4, and H5 with proton resonances at ca.2 ppm for H2 and H6, which suggested the presence of a quinic acid nucleus that is responsible for the isolated spin system highlighted in green lines and box (Figure 3.31). The coupling protons for the ABX (yellow line and box) and olefinic (blue line and box) systems were observed in the downfield region between 6.0 and 8.0 ppm.

The quaternary carbons were detected using HMBC correlation (Figure 3.32), there were three carbonyls (C9', C9'', and C7 at 167.2, 167.2, and 176.5 ppm, respectively); four hydroxylated aromatic carbons C3', C4', C3'', C4'' at 147.5, 146.5, 147.5 and 146.5 ppm, respectively; an alkyl-substituted aromatic carbon for C1' and C1'' at 121.6 ppm; and one oxygenated aliphatic quaternary carbon at 71.7 ppm for C1.

There were no clear HMBC correlations that supported the connectivity of two caffeoyl residues on the quinic acid group. The caffeoyl moiety had an ester linkage with a hydroxyl group of the quinic acid unit, which deshielded the corresponding methine proton significantly downfield. Alternately, if signals of the quinic acid ring protons H3, H4, and H5 were shifted upfield, then the caffeoyl group would be attached to the hydroxyl group at C1 of the quinic acid as earlier described in the literature (Horman *et al.*, 1984; Clifford, 1986; Slacanin *et al.*, 1991). The proton signals of H-3 (4.94 ppm) and H-5 (5.86) were significantly deshielded, implying that the attachment of C-1 of the caffeoyl moiety to the hydroxyl group of the quinic acid unit. Accordingly, full assignment of the spectral data of F8-ChJ was identified as 3,5-*O*-dicaffeoylquinic acid (Tolonen *et al.*, 2002). The ^1H and ^{13}C NMR assignments are presented in Table 3.10.

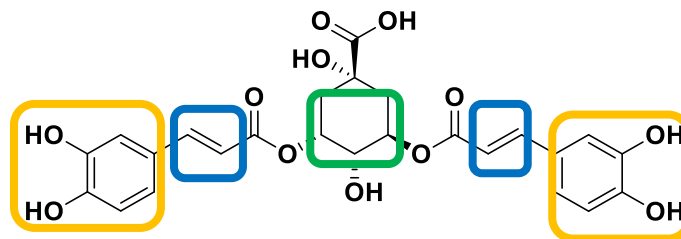
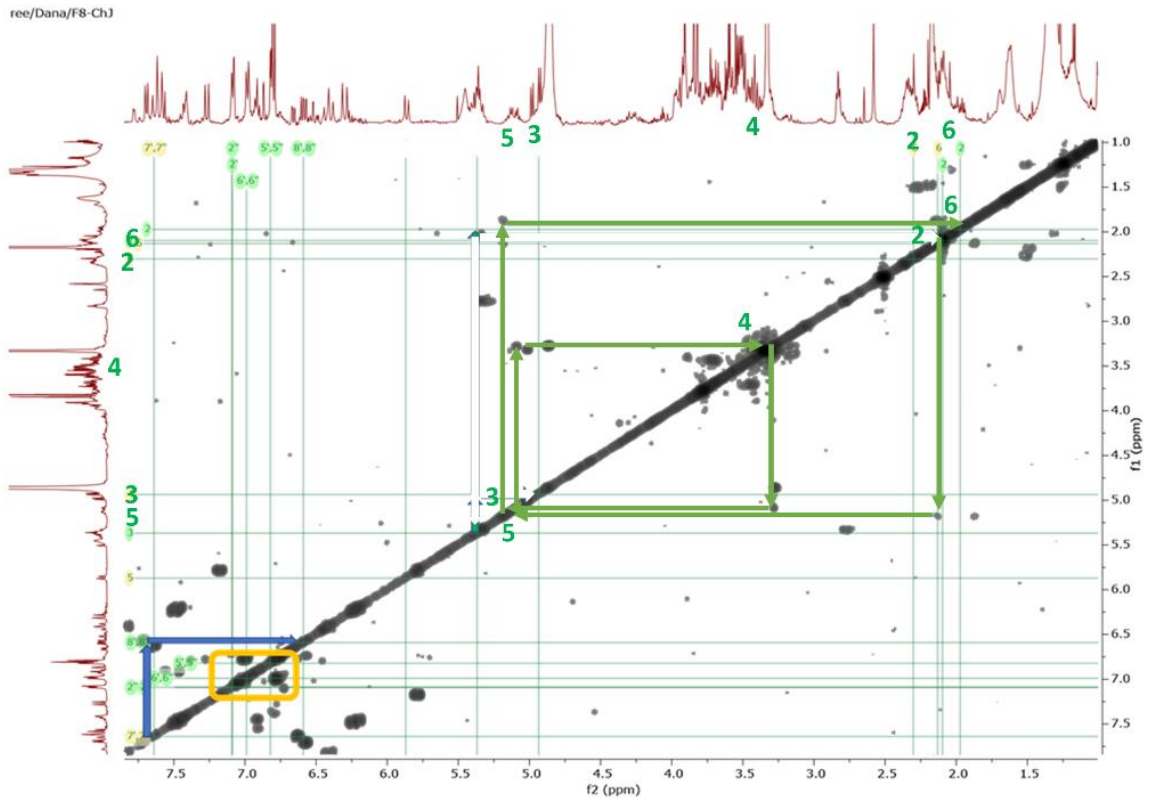


Figure 3.31: (^1H - ^1H) COSY correlation spectrum of F8-ChJ in CD_3OD measured at 400 MHz.

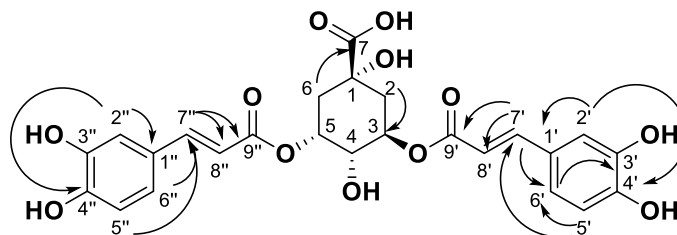
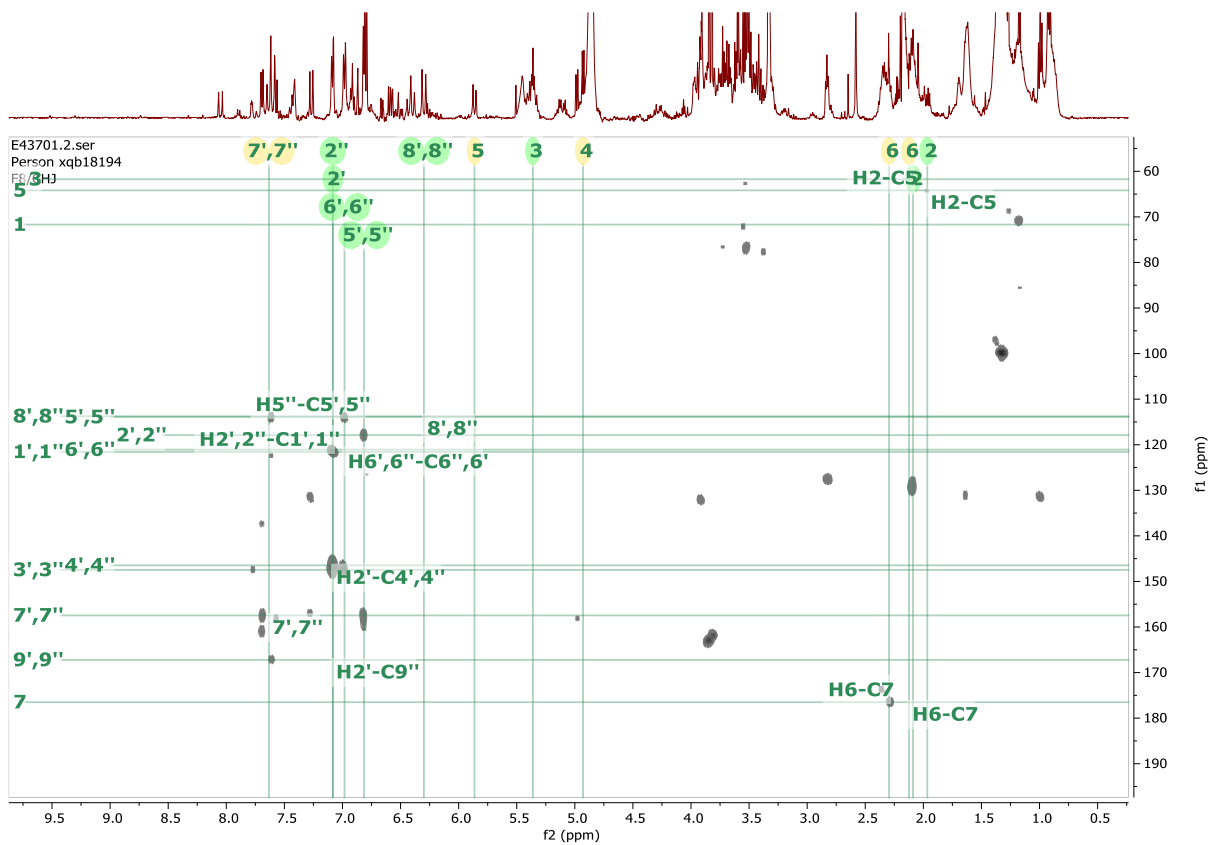
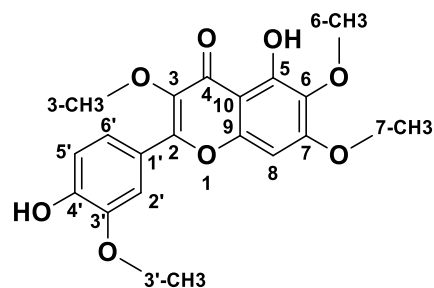


Figure 3.32: HMBC spectrum of F8-ChJ in CD₃OD measured at 400 MHz.

Table 3.10. ^1H and ^{13}C NMR data of F8-ChJ in CD_3OD .

Position	δ_{C}	δ_{H} (mult, J in Hz)	COSY	HMBC
1	71.7 qC			
2	38.0 CH_2	2.09, 1.97	3	
3	61.7 CH	5.36 t (6)	2, 4	
4	64.1 CH	4.94 dd (13.0, 6.0)	3, 5	
5	64.2 CH	5.86 d (13.1)	4, 6	
6	39.7 CH_2	2.30 q (5.7) 2.12 m	5	C7
7	176.5 qC			
1'	121.6 qC			
2'	117.9 CH	7.08 d (2.0)		C1', C4'
3'	147.5 qC			
4'	146.5 qC			
5'	113.9	6.80 d (8.1)	6'	C7'
6'	121.0 CH	6.98 brd, (8.3)	5'	C3', C5'
7'	157.4 CH	7.60 d, (16.3)	8'	C5', C6', C8', C9'
8'	113.7 CH	6.30 d, (15.7)	7'	
9'	167.2 qC			
1''	121.6 qC			
2''	117.9 CH	7.08 d (2.0)		C1'', C4''
3''	147.5 qC			
4''	146.5 qC			
5''	113.9 CH	6.80 d (8.1)	6''	C7''
6''	121.0 CH	6.98 brd, (8.3)	5''	C3'', C5''
7''	157.4 CH	7.60 d, (16.3)	8''	C5'', C6'', C8'', C9''
8''	113.7 CH	6.30 d, (15.7)	7''	
9''	167.2 qC			

3.5.2. Structure elucidation of F2-ChE from the European chamomile.



Chemical Formula: C₁₉H₁₈O₈

MWt: 374.1000

chrysosplenetin

Figure 3.33: chemical structure of F2-ChE

Formula	Calculated Mass	Target Mass	Double Bond Equivalence	Absolute Error (ppm)	Error (mDa)	Error (ppm)	Fitness
C ₁₉ H ₁₈ O ₈	375.10744	375.10803	11.0	1.56	0.58	1.56	1.000

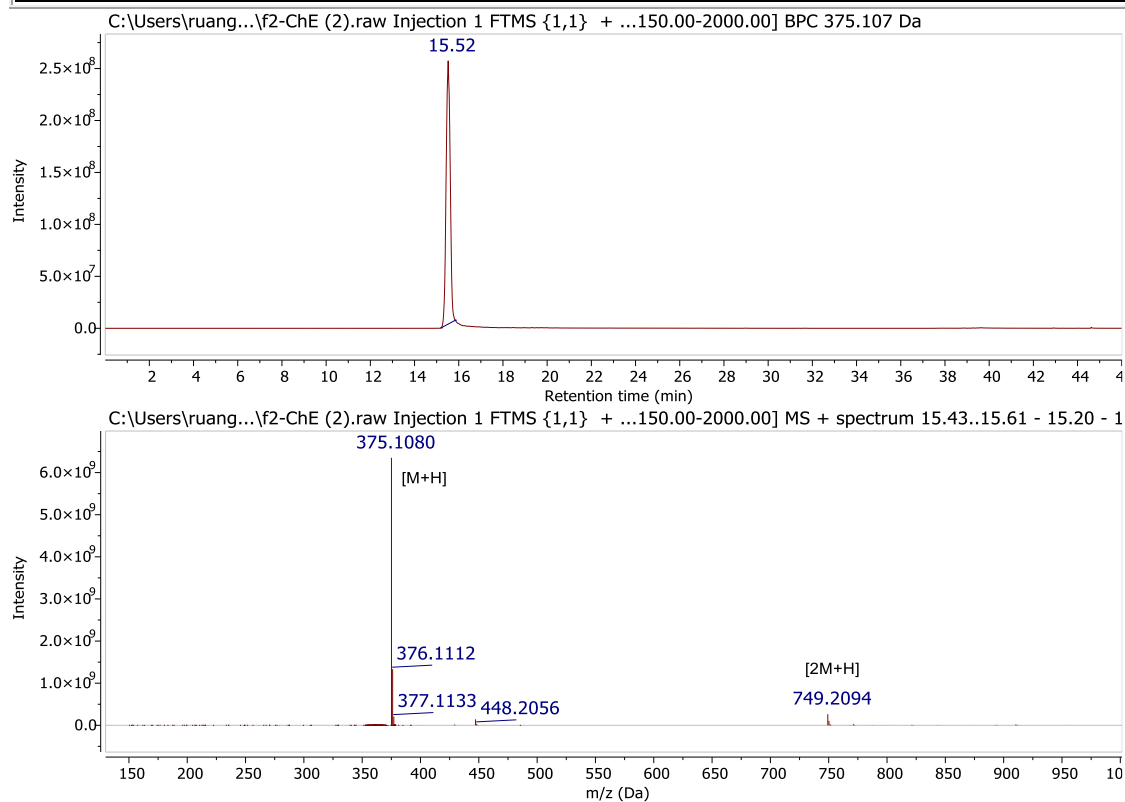


Figure 3.34A. Extracted ion chromatogram of F2-ChE for the ion peak at m/z 375.1080 $[M+H]^+$ at a RT of 15.5 min.

Formula	Calculated Mass	Target Mass	Double Bond Equivalence	Absolute Error (ppm)	Error (mDa)	Error (ppm)	Fitness
C ₁₉ H ₁₇ O ₈	373.09234	373.09271	11.5	0.98	0.36	0.98	1.000

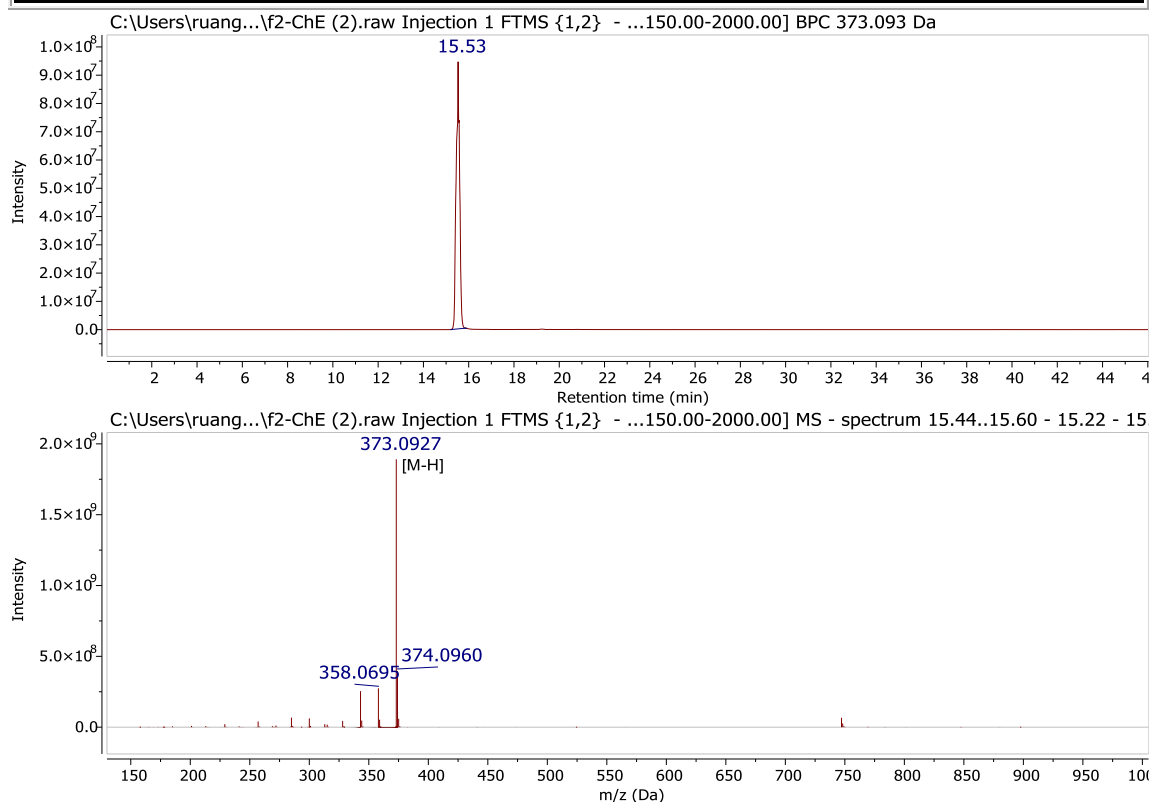


Figure 3.34B. Extracted ion chromatogram of F2-ChE for the ion peak at m/z 373.0927 $[M-H]^-$ at a RT of 15.5 min.

F2-ChE (33 mg) afforded a high yield with a TIC peak area of $3.64E+09$ (Figure 3.34). HRMS established a molecular formula of C₁₉H₁₉O₈ with an ion peak at m/z 375.1080 $[M+H]^+$ and 749.2094 $[2M+H]^+$ eluting at 15.5 min (Figure 3.34A). In the negative mode, the ion peak at m/z 373.0927 $[M-H]^-$ was observed for the molecular formula C₁₉H₁₇O₈ (Figure 3.34B).

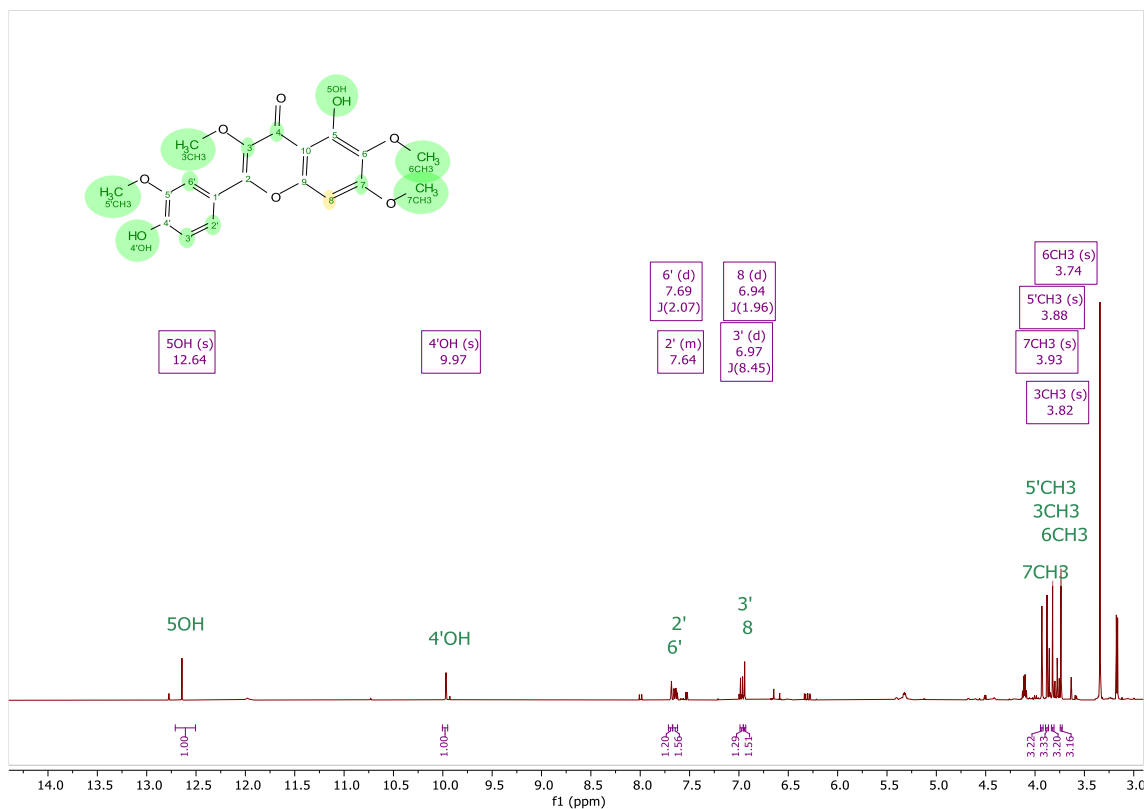


Figure 3.35: ^1H NMR spectrum of F2-ChE in $\text{DMSO}-d_6$ measured at 400 MHz.

The ^1H NMR spectrum of F2-ChE in Figure 3.35 showed the presence of four methoxy singlets at δ_{H} 3.98 (3H, s, H7), 3.88 (3H, s, H5'), 3.82 (3H, s, H3), and 3.74 (3H, s, H6), and four aromatic protons at δ_{H} 7.69 (1H, d, $J=2.07$ Hz, H6'), 7.64 (1H, dd, $J=2.07$ and 8.45 Hz, H2'), 6.97 (1H, d, $J=8.45$ Hz, H3'), 6.94 (1H, s, H8). The multiplicities and coupling constants of H2', H3', and H6' were typical of a tri-substituted aromatic ABX system. In addition, two hydroxyl signals at δ_{H} 12.64 (s, 5-OH) and 9.97 (s, 4'-OH) were observed.

The HMBC spectrum shown in Figure 3.36 helped assigned the ^{13}C resonances for F2-ChE, which included δ_{C} 159.3 (C-2), 137.9 (C-3), 178.6 (C-4), 152.2 (C-5), 131.9 (C-6), 162.7 (C-7), 155.6 (C-9), 105.9 (C-10), 121.0 (C-1'), 112.2 (C-3'), 150.6 (C-4'), 155.5 (C-

5'), and 121.1 (C-6'). HMBC correlations disclosed the presence of four aromatic methine carbons (through cross peaks with C3' and C6' at 112.3, and 121.1 ppm, respectively), and ten non-protonated carbons (four of them were aromatic (C2, C9, C10, and C1' at 159.3, 155.6, 105.9, and 121.0 ppm, respectively), two quaternary aromatic attached to a hydroxyl group (C4' and C5 at 150.6, and 152.2 ppm, respectively), four quaternary aromatic carbons attached to methoxy groups (C3, C6, C7, C3' at 137.9, 131.9, 162.7, and 155.5, respectively) and one carbonyl ketone at 178.6 ppm for C4.

HMBC correlations in Figure 3.36 established the connectivity of the substructures postulated from the ¹H NMR spectral data. Correlations from 5-OH to C5, C6 and C10 ascertained ring A of a flavonoid structure. Allocating ring C was achieved from correlations between H2'' to C3', C4' and C5' as well as H5' to C6'. Furthermore, the HMBC cross peak between H8 at 4.98 ppm with C5, C6, C7, and 10 was used to identify ring B. The structure of F2-ChE was identified as 4',5-dihydroxy-3,3',6,7-tetramethoxyflavone also known as chrysosplenetin. NMR spectral data of F2-ChE presented in Table 3.11 was compatible and identical to chrysosplenetin as described in the literature (Alwahsh *et al.*, 2015).

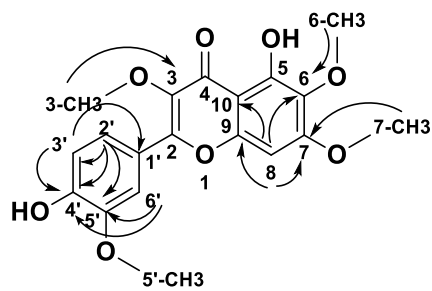
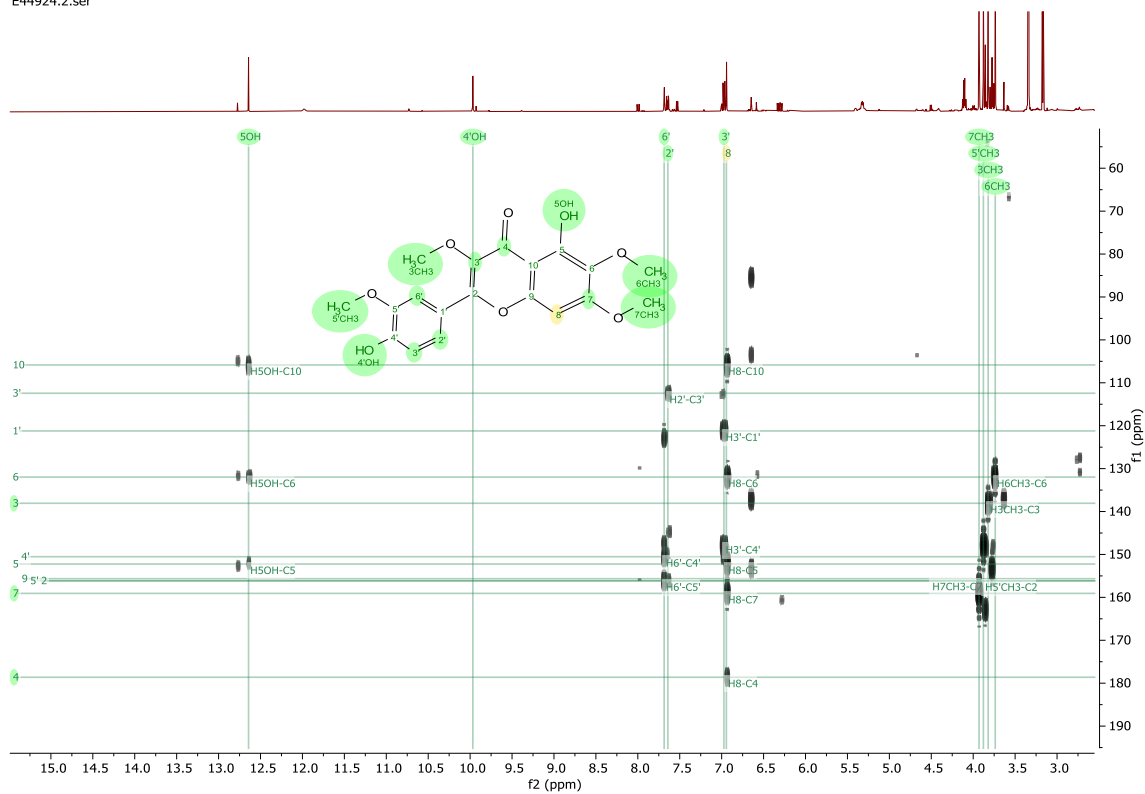
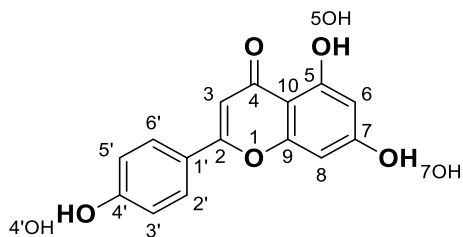


Figure 3.36: HMBC spectrum of F2-ChE in DMSO- d_6 measured at 500 MHz.

Table 3.11: ^1H and ^{13}C NMR data of F2-ChE in comparison to chryso splenetin (Alwahsh *et al.*, 2015)

Atom no.	^{13}C (mult) in MeOH- d_6^*	^{13}C lit. in CDCl_3	^1H lit. (mult) in DMSO- d_6 J in Hz		^1H (mult) in DMSO- d_6 J in Hz		HMBC
2	159.3 qC	156.10					
3	137.9 qC	138.73					
4	178.6 qC	178.95					
5	152.2 qC	152.79					
6	131.9 qC	132.34					
7	162.7 qC	158.86					
8	n.d.	90.45	6.94 s		6.94 s		C5, C6, C7, C9, C10
9	155.6 qC	152.38					
10	105.9 qC	106.61					
1'	121.0 qC	122.45					
2'	n.d.	110.99	7.65 dd	2.14, 8.33	7.64 dd	2.0, 8.5	C3', C4', C5'
3'	112.2 CH	114.72	6.97 d	8.39	6.97 d	8.5	C1', C4'
4'	150.6 qC	148.51					
5'	155.5 qC	146.51					
6'	121.1 CH	122.68	7.69 d	2.14	7.69 d	2.0	C4', C5'
5-OH	n.d.		12.64 s		12.64 s		C5, C6, C10
4'-OH	n.d.		9.97 s		9.97 s		
6-OCH ₃	n.d.	60.98	3.74 s		3.74 s		C6
3-OCH ₃	n.d.	60.25	3.82 s		3.82 s		C3
3'-OCH ₃	n.d.	56.22	3.88 s		3.88 s		C5'
7-OCH ₃	n.d.	56.44	3.93 s		3.98 s		C7
* ^{13}C assignment obtained from HMBC spectrum; n.d. (not detected)							

3.5.3. Structure elucidation of F8-ChE from European chamomile.



Chemical Formula: C₁₅H₁₀O₅

Exact Mass: 270.0525

apigenin

Figure 3.37: Chemical structure of F8-ChE

Formula	Calculated Mass	Target Mass	Double Bond Equivalence	Absolute Error (ppm)	Error (mDa)	Error (ppm)	Fitness
C ₁₅ H ₉ O ₅	269.04555	269.04744	11.5	7.04	1.89	7.04	1.000

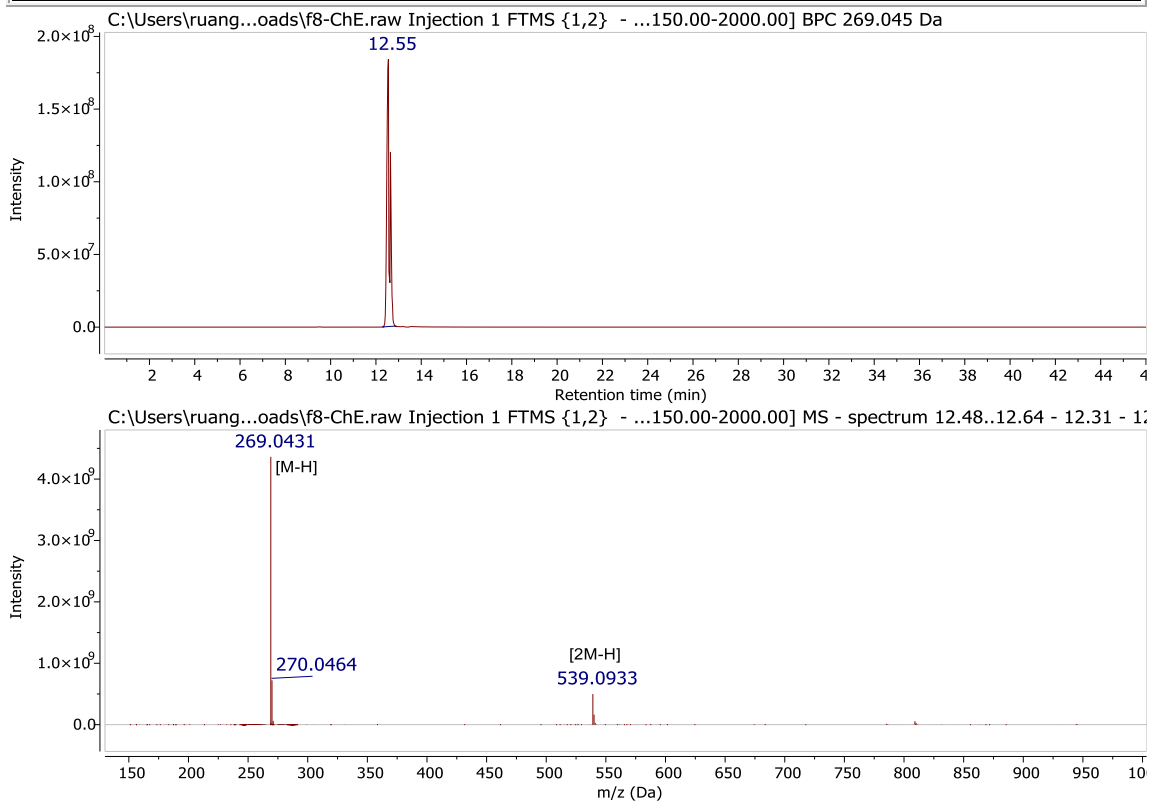


Figure 3.38A. Extracted ion chromatogram of F8-ChE for the ion peak at m/z 269.0450 $[M-H]^-$ eluting at RT of 12.5min .

Formula	Calculated Mass	Target Mass	Double Bond Equivalence	Absolute Error (ppm)	Error (mDa)	Error (ppm)	Fitness
C ₁₅ H ₁₀ O ₅	271.06010	271.06000	11.0	0.38	-0.10	-0.38	1.000

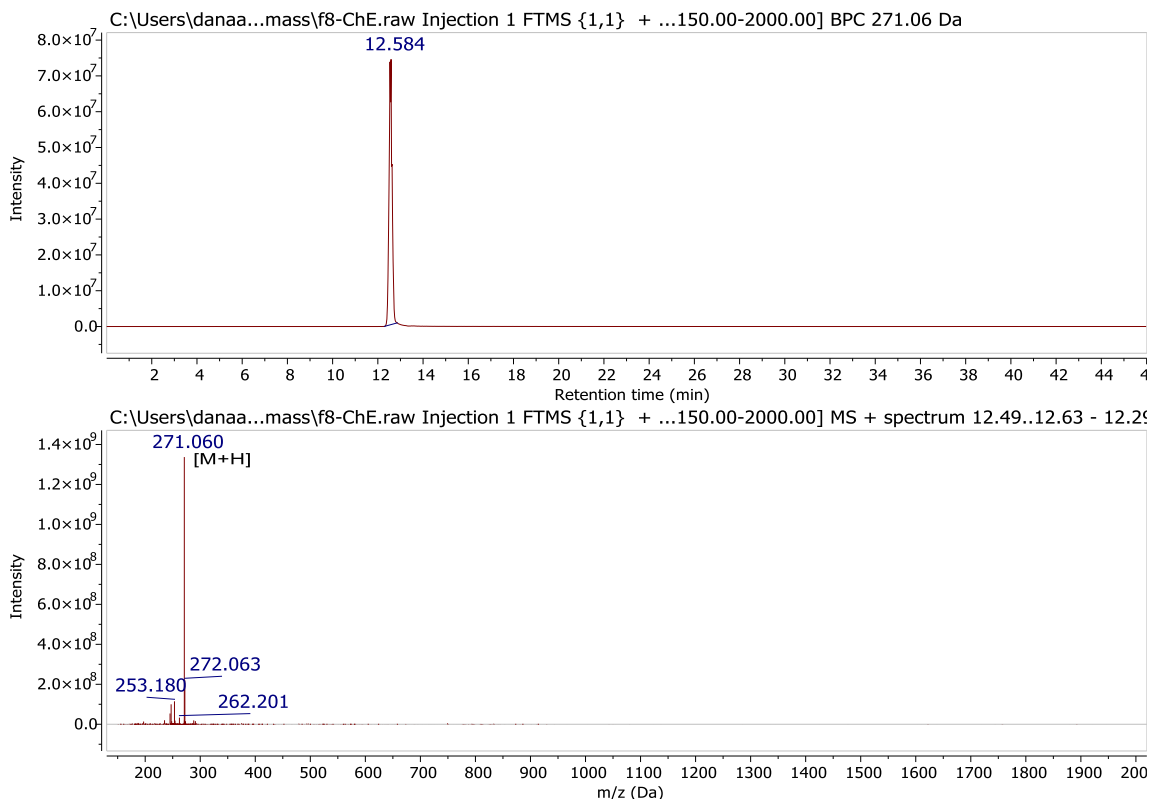


Figure 3.38B. Extracted ion chromatogram of F8-ChE for the ion peak at m/z 271.0600 [M+H]⁺ eluting at RT of 12.5 min .

F8-ChE (Figure 3.38) gave an ion peak at m/z 269.0474 for C₁₅H₉O₅ [M-H]⁻ and 539.1022 [2M-H]⁻ at a RT of 12.5 min and a peak area of 1.015E+09 (Figure 3.38A). In the positive mode, an ion peak was observed at m/z 271.0600 [M+H]⁺ (Figure 3.38B). F8-ChE gave a yield of 8 mg.

The ¹H NMR spectrum in Figure 3.39 revealed the presence of three hydroxyl singlets at δ_H 12.96 (5OH), 10.34 (4'OH) and 10.19 (7OH); seven aromatic protons at δ_H 7.93 (2H, dd, J = 9.4, 2.9 Hz, H2', H6'), 6.93 (2H, m, H3', H5'), 6.78 (1H, s, H-3), 6.48 (1H, d, J = 2.1 Hz, H8), and 6.19 (1H, d, J = 2.1 Hz, H6). The resonances at δ_H 7.93 and 6.93 that

integrated for 2H each with a coupling constant of 9.4 Hz for a doublet indicated an AA'BB' system. Dereplication of the mass spectral data of the bioactive fractions putatively identified the presence of 4',5,7-trihydroxyisoflavone or apigenin. Comparison of the extrapolated NMR resonances observed for F8-ChE to those of a synthesised apigenin (Victor *et al.*, 2017), both measured in DMSO-*d*₆ at 400 MHz, afforded similar spectral data (Table 3.12). The structure of F8-ChE was elucidated then elucidated as apigenin.

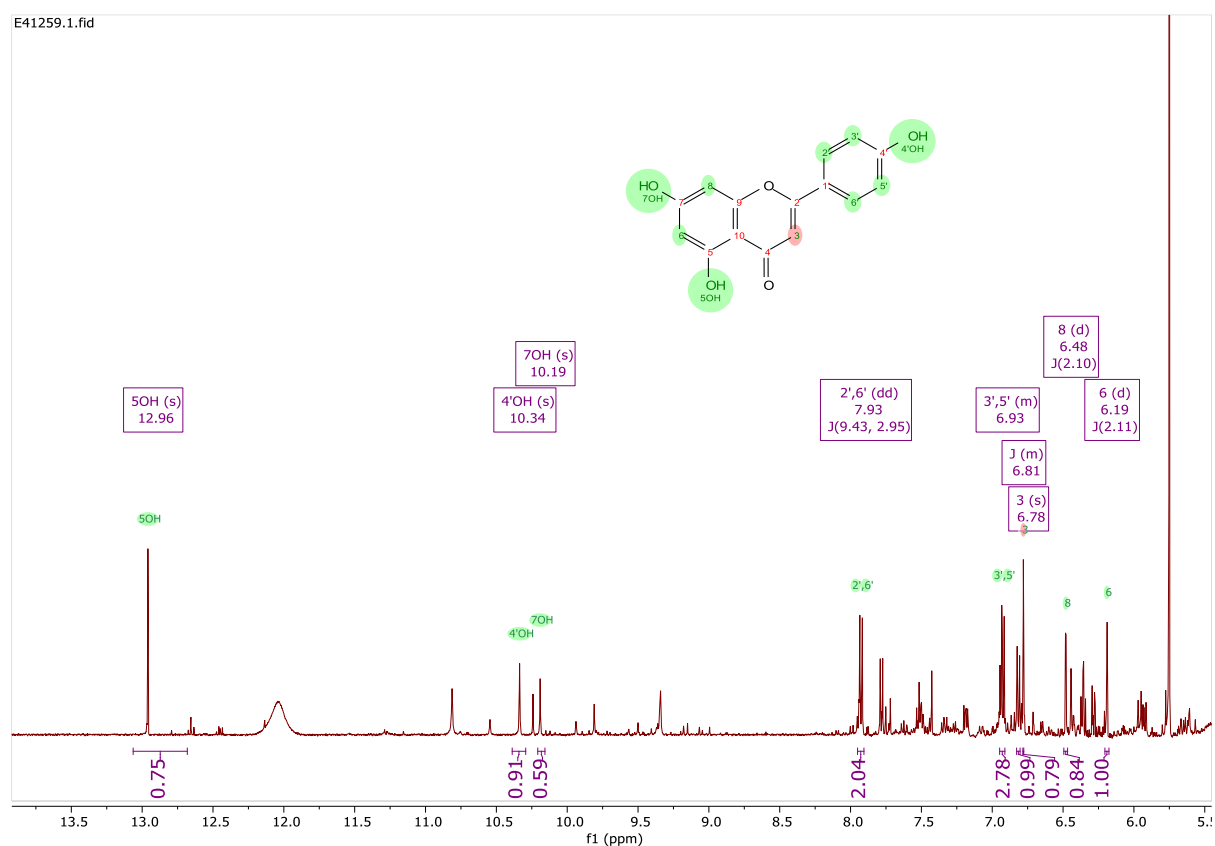
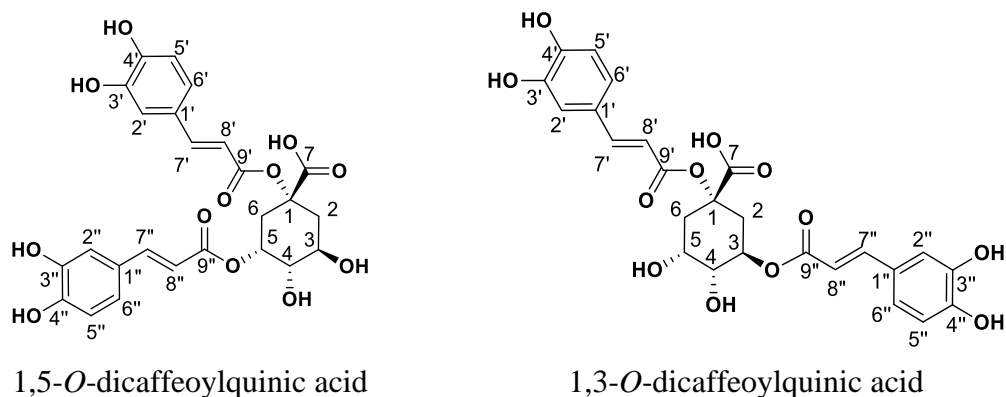


Figure 3.39: ¹H NMR spectrum of F8-ChE in DMSO-*d*₆ measured at 400 MHz.

Table 3.12: ^1H NMR data of F8-ChE and synthesised apigenin measured at 400 MHz.

Atom no.	^1H (mult) F8-ChE (DMSO- d_6)	^1H (mult) synthesised apigenin (DMSO- d_6)
3	6.78 s	6.75 s
6	6.19 d, $J = 2.1$ Hz	6.17 d, $J = 2.11$ Hz
8	6.48 d, $J = 2.1$ Hz	6.46 d, $J = 2.10$ Hz
2'	7.93 dd, $J = 9.4, 2.9$ Hz	7.91 d, $J = 9.43$ Hz
3'	6.93 m	6.94 m
5'	6.93 m	6.94 m
6'	7.93 dd, $J = 9.4, 2.9$ Hz	7.91 d, $J = 9.43$ Hz
5-OH	12.96 s	12.95 s
4'-OH	10.34 s	10.50 overlapping brs
7-OH	10.19 s	10.50 overlapping brs

3.5.4. Structure elucidation of F11-ChE from European chamomile.



Chemical Formula: C₂₅H₂₄O₁₂

MWt: 516.1261

1,3 dicaffeoyl quinic acid

Figure 3.40: Chemical structure of F11-ChE

Formula	Calculated Mass	Target Mass	Double Bond Equivalence	Absolute Error (ppm)	Error (mDa)	Error (ppm)
C ₂₅ H ₂₅ O ₁₂	517.13460	517.13383	13.5	1.50	-0.77	-1.50

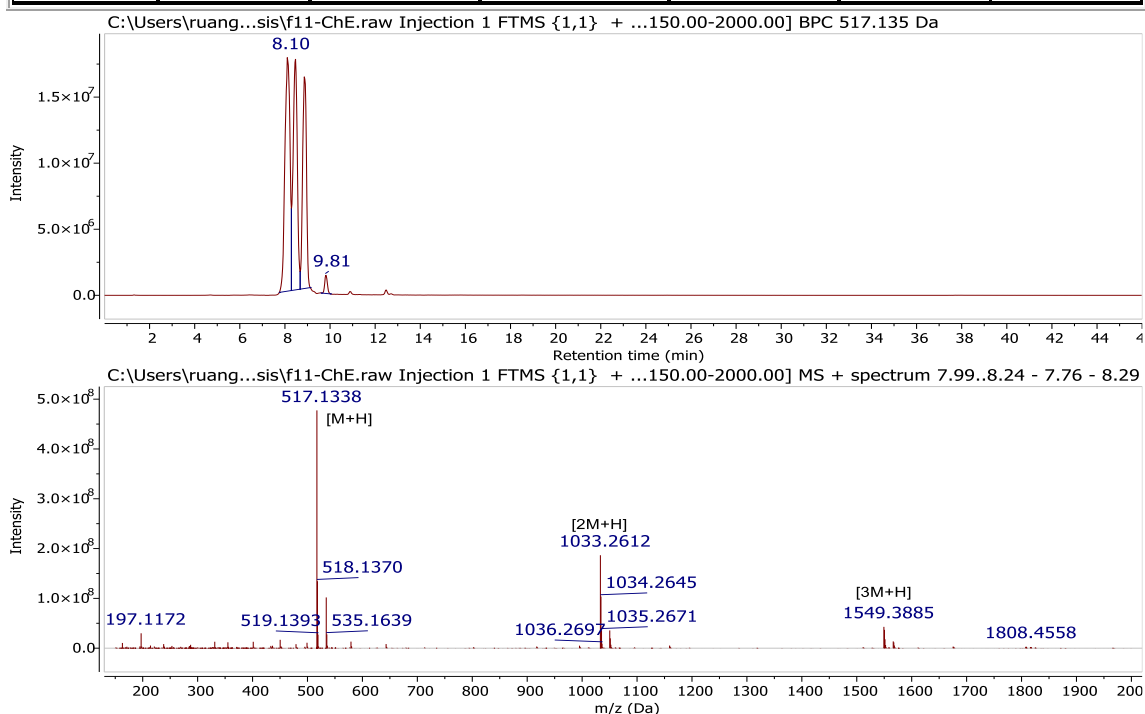


Figure 3.41A. Extracted ion chromatogram of F11-ChE for the ion peak at m/z 517.1338 [M+H]⁺ with a RT of 8.1 min.

Formula	Calculated Mass	Target Mass	Double Bond Equivalence	Absolute Error (ppm)	Error (mDa)	Error (ppm)
C ₂₅ H ₂₃ O ₁₂	515.11895	515.11753	14.5	2.76	-1.42	-2.76

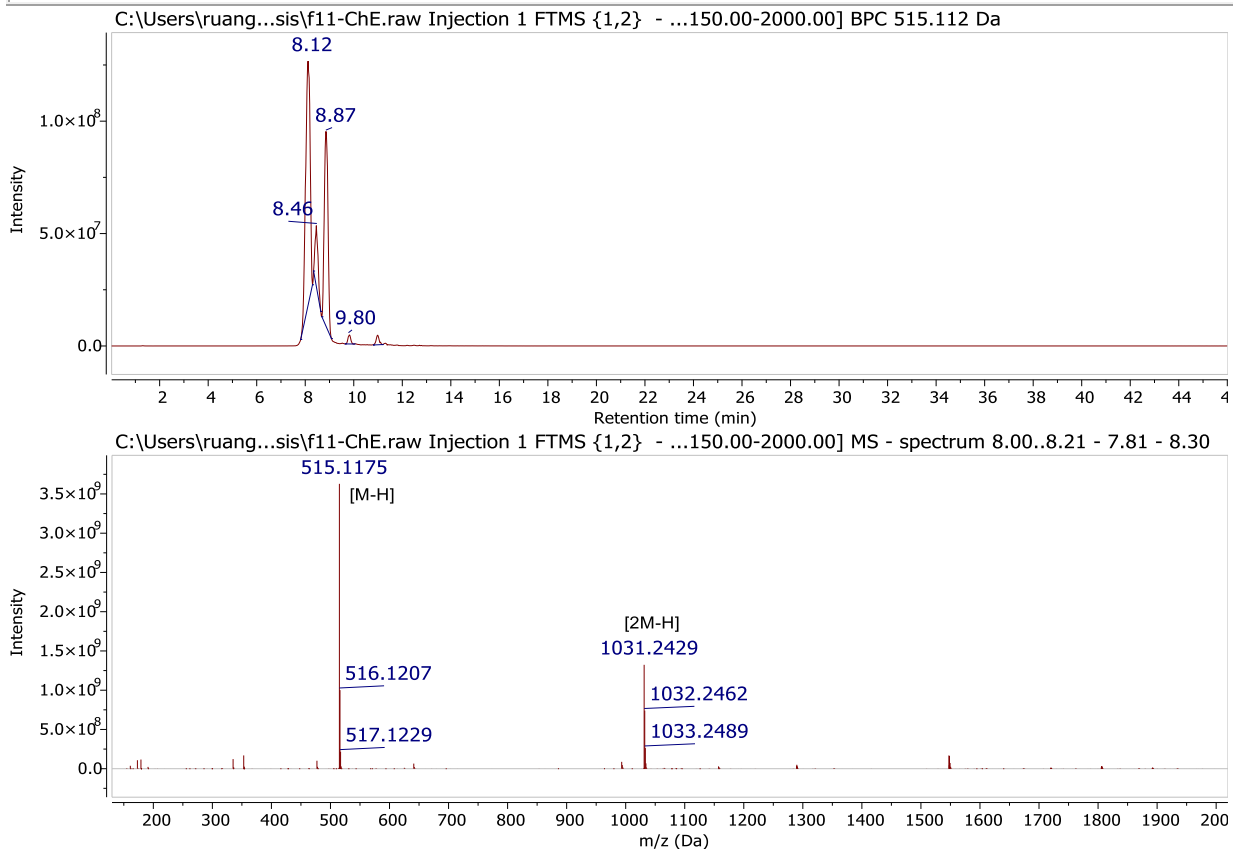


Figure 3.41B. Extracted ion chromatogram of F11-ChE for the ion peak at m/z 515.1117 [M-H]⁻ with a RT of 8.1 min.

F11-ChE was isolated as a yellow amorphous powder with a yield of 10.8 mg. Mass spectrometric results suggested a DBE of 14, which accounted for three rings, eight double bonds from the aromatic system, and three carbonyl groups as part of the structure. HREIMS established a chemical formula of $C_{25}H_{24}O_{12}$ for the ion peak at m/z 517.1338 $[M+H]^+$, in addition to ion peaks at m/z 1033.2612 $[2M+H]^+$ and 1549.3885 $[3M+H]^+$ (Figure 3.41A). In the negative mode, an ion peak was observed at m/z 515.1179 $[M-H]^-$ and 1031.2451 $[2M-H]^-$ at a RT of 8.1 min (Figure 3.41B).

1H NMR spectrum of F11-ChE (Figure 3.42) was comparable to that of F8-ChJ and are structural isomers having the same MWts and gave a difference of 0.3 seconds in their elution time. Although the spectral data of F11-ChE and F8-ChJ, they were still not identical. Both respective isomers were found to be the most abundant in each of the varieties. However, the spectral data of both metabolites were very different to that of any of di-acetyl cosmosiin analogues, which are acylated apigenin glycosides reported from *M. chamomilla*, (Olennikov and Kashchenko, 2016). Although apigenin was a major component in the European variety as implied by the TIC in Figure 3.24, the bioactivity of the extracts was led by the di-*O*-caffeoylquinic acid analogues found in fractions F11-ChE and F8-ChJ.

The 1H NMR spectral data of F11-ChE displayed the typical trans olefinic doublet pairs of a propenoic acid moiety or caffeoyl unit at approximately 6.5 and 7.5 ppm as well as the characteristic coupling pattern for 1,3,4-trisubstituted phenyl ABX system. However, in comparison to the 1H NMR spectrum of F8-ChJ, there was a more distinct separation of the trans olefinic 1H signals for the two caffeoyl units. Instead of observing twice the number of integrations for two overlapping protons like in F8-ChJ, resonances for the trans olefinic doublet pairs and meta doublets gave two sets of chemical shifts for each of the caffeoyl moieties as presented in Table 3.13. The chemical shift of the methine proton on C3 was deshielded downfield in F11-ChE, which indicated the esterification of the caffeoyl unit on 3-*OH* and loss of caffeoyl moiety on C2, C4, C5 because these

carbons were shielded upfield. The second caffeoyl unit was attached on the hydroxyl unit on C1 when compared to the literature (Table 3.13).

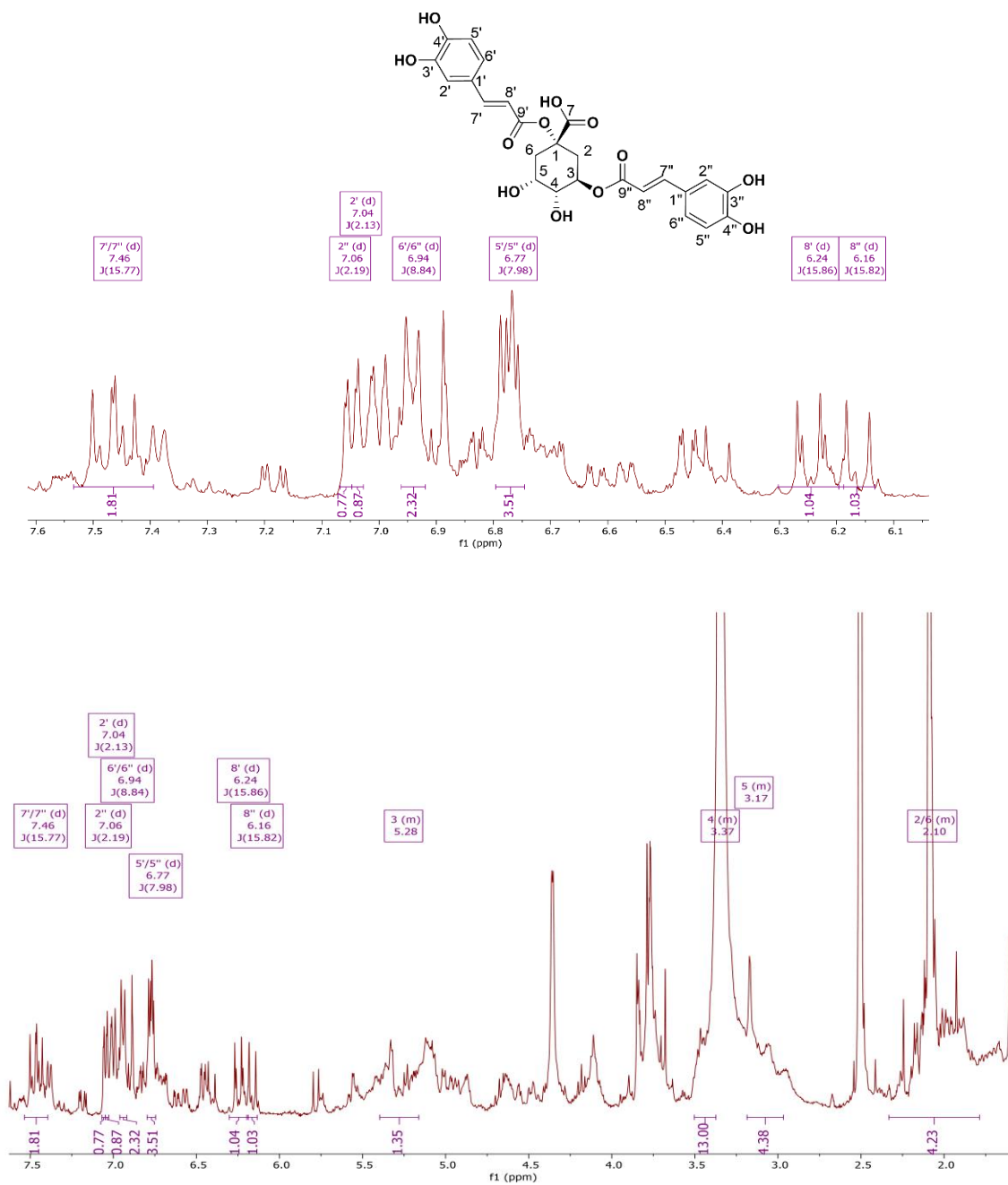


Figure 3.42: ¹H NMR spectrum of F11-ChE in DMSO-*d*₆ measured at 400 MHz.

The ^1H assignments for F11-ChE and esterification on C3 were also established by a COSY spectrum as shown in Figure 3.44. Commencing upfield at 1.94 and 2.14 ppm for H2A and H2B, a cross peak was observed downfield at 5.20 ppm for H3, which continued to 3.40 ppm for H4 then to 3.27 ppm for H5 and finally ended upfield at 1.69 and 1.84 ppm for H6A and H6B. By inspection and comparison of the spectral data of F11-ChE (Table 3.13) with those reported in the literature, the isolated compound was elucidated as 1,3-*O*-dicaffeoylquinic acid (Wan *et al.*, 2017, Tolonen *et al.*, 2002, Horman *et al.*, 1984, de Falco *et al.*, 2016). However, in the literature there has been a confusion between the nomenclatures of 1,5- and 1,3-*O*-dicaffeoylquinic acid. A classic example is cynarin, isolated from artichokes, was first reported as 1,3-di-*O*-caffeoyl-D-(-)-quinic acid (Horman *et al.*, 1984) but were being drawn as the 1,5 analogue on databases and monographs (e.g. Dictionary of Natural Products, PubMed). Confirmation of the structure for a 1,3 analogue would entail isopropylidene derivatisation of the free vicinal hydroxyl units in *cis* configuration to form an *O*-ketal ring (Carlotto *et al.*, 2015). The quinic acid moiety bears three vicinal hydroxyl groups where C4 and C5 are *cis*-oriented while C3 and C4 are *trans* to each other. Hence, a selective acetylation would only occur for 1,3-*O*-dicaffeoylquinic acid to form the 4,5-isopropylidene ketal ring (Figure 3.43).

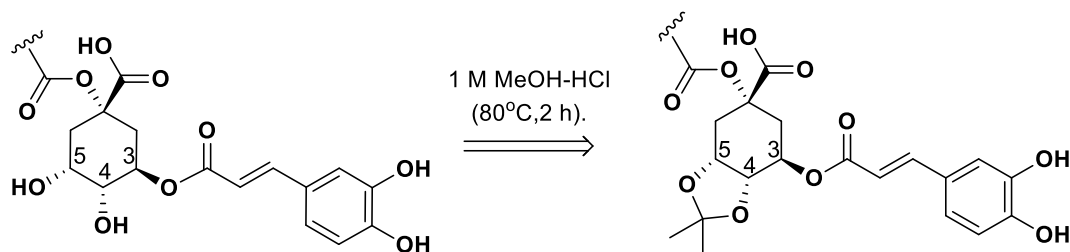


Figure 3. 43: Isopropylidene derivatisation of 1,3-*O*-dicaffeoylquinic acid

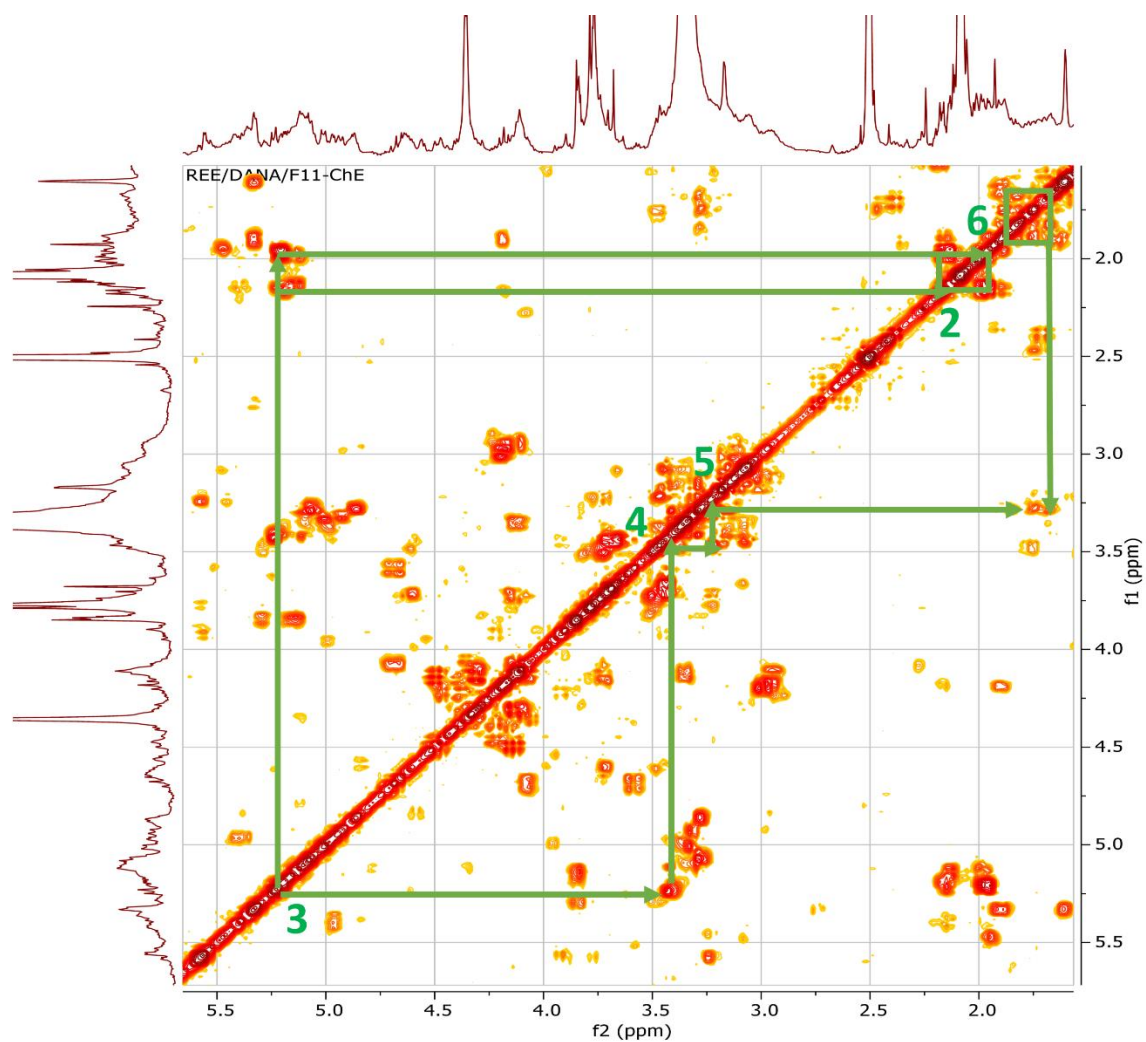


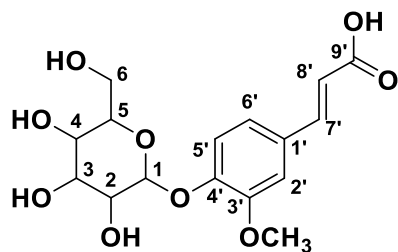
Figure 3.44: COSY NMR spectrum of the quinic acid moiety in F11-ChE measured in DMSO- d_6 at 400 MHz.

Table 3.13: ^1H NMR data (δ_{H} in ppm, mult, J in Hz) of F11-ChE in comparison to cynarin, a 1,3-dicaffeoylquinic acid analogue along with spectral data of 1,5-dicaffeoylquinic acid reported in the literature.

Atom no.	^1H (mult, J in Hz) F11-ChE (DMSO- d_6) 400 MHz	1,3-dicaffeoylquinic acid* (de Falco <i>et al.</i> , 2016) (D_2O) 400 MHz	1,5-dicaffeoylquinic acid (Wan <i>et al.</i> , 2017) (MeOD) 400 MHz	1,5-dicaffeoylquinic acid (Tolonen <i>et al.</i> , 2002) (D_2O) 500 MHz
2	1.94 m 2.14 m	2.29 axial (2.34 dd, $J = 3.5, 15.5$) § 2.88 equatorial (2.77 ddd, $J = 3.5, 3.0, 15.5$) §	2.43 m 2.54 dd, $J = 3.5, 10.2$	2.22 dd, $J = 3.5, 15.5$ 2.50 ddd, $J = 3.8, 2.8, 15.5$
3	5.20 m	5.36 equatorial (5.43 ddd, $J = 3.5, 3.5, 3.5$) §	4.28 brd, $J = 3.5$	4.27 ddd, $J = 3.5, 3.8, 3.5$
4	3.40 m	4.23 axial (4.67 dd, $J = 9.5, 3.5$) §	3.76 dd, $J = 3.0, 8.1$	3.86 dd, $J = 9.6, 3.5$
5	3.27 m	3.62 axial (4.23 ddd, $J = 9.5, 4.5, 10.5$) §	5.37 ddd, $J = 3.7, 8.1, 8.1$	5.29 ddd, $J = 9.6, 4.3, 10.8$
6	1.69 m 1.84 m	1.83 axial (1.88 dd, $J = 10.5, 13.5$) § 2.53 equatorial (2.50 ddd, $J = 4.5, 3.0, 13.5$) §	2.05 dd, $J = 11.1, 13.8$ 2.43 m	1.99 dd, $J = 10.8, 13.8$ 2.56 ddd, $J = 4.3, 2.8, 13.8$
2'	7.04 d, $J = 2.1$	6.81	7.04 brs	7.12 d, $J = 2.1$
5'	6.77 d, $J = 8.0$	6.88 d, $J = 8.0$ Hz	6.78 d, $J = 8.1$	6.88 d, $J = 8.2$
6'	6.94 br d, $J = 8.8$	6.58	6.96 d, $J = 8.1$	7.05 dd, $J = 8.2, 2.1$
7'	7.48 d, $J = 15.9$	7.58 d, $J = 16.0$ Hz	7.58 d, $J = 15.9$	7.59 d, $J = 16.1$
8'	6.25 d, $J = 15.9$	6.32 d, $J = 16.0$ Hz	6.27 d, $J = 15.9$	6.39 d, $J = 16.1$
2''	7.06 d, $J = 2.2$	6.81	7.04 brs	7.15 d, $J = 2.1$
5''	6.77, d, $J = 8.0$	6.88 d, $J = 8.0$ Hz	6.76 d, $J = 8.1$	6.86 d, $J = 8.2$
6''	6.94 br d, $J = 8.8$	6.58	6.94 d, $J = 8.1$	7.08 dd, $J = 8.2, 2.1$
7''	7.45 d, $J = 15.8$	7.58 d, $J = 16.0$	7.55 d, $J = 15.9$	7.58 d, $J = 16.2$
8''	6.16 d, $J = 15.8$	6.32 d, $J = 16.0$	6.24 d, $J = 15.9$	6.32 d, $J = 16.2$

*Identified as cynarin by the authors. § Spectral data set reported by Horman *et al.*, (1984) for quinic acid of cynarin in acetone- d_6 measured at 300MHz.

3.5.5. Structure elucidation of F12-ChE from European chamomile.



Chemical Formula: C₁₆H₂₀O₉

MWt: 356.1179

4'→1-*O*-feruloylglucose

glucoferulic acid (lavandoside)

Figure 3.45: Chemical structure of F12-ChE

Formula	Calculated Mass	Target Mass	Double Bond Equivalence	Absolute Error (ppm)	Error (mDa)	Error (ppm)
C ₁₆ H ₂₀ O ₉	357.11801	357.11799	7.0	0.07	-0.02	-0.07

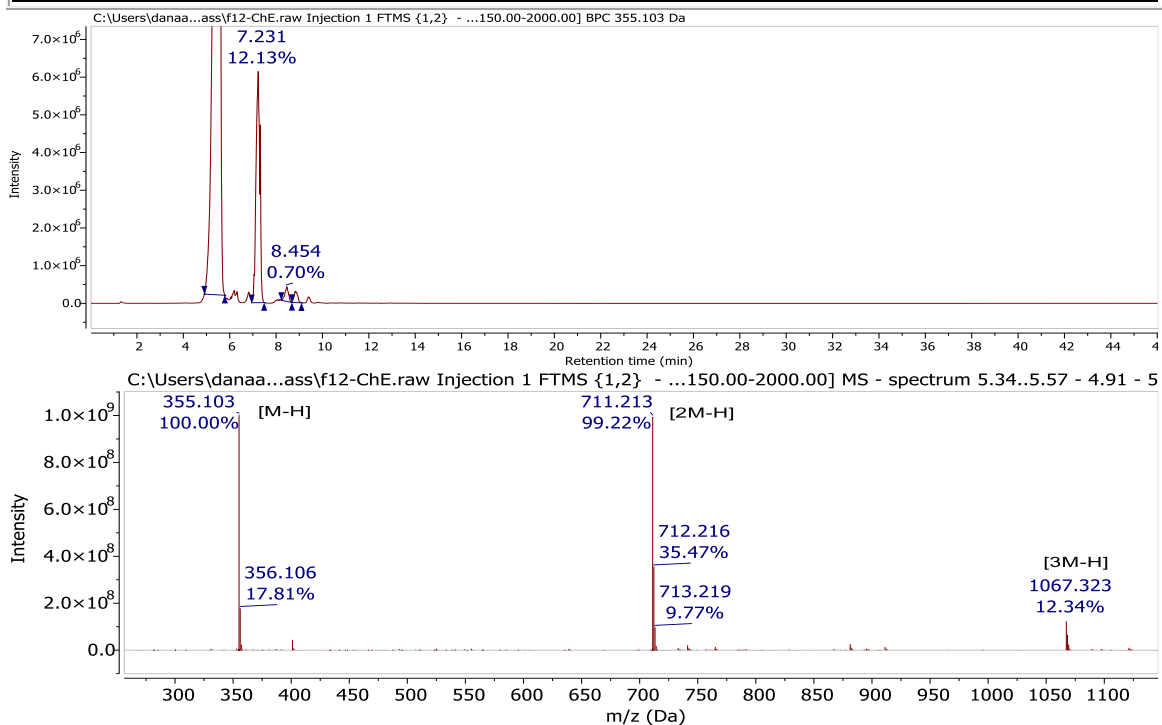


Figure 3.46A: Extracted ion chromatogram of F12-ChE for the ion peak at m/z 355.1030 [M-H] eluting at a Rt of 7.23 min.

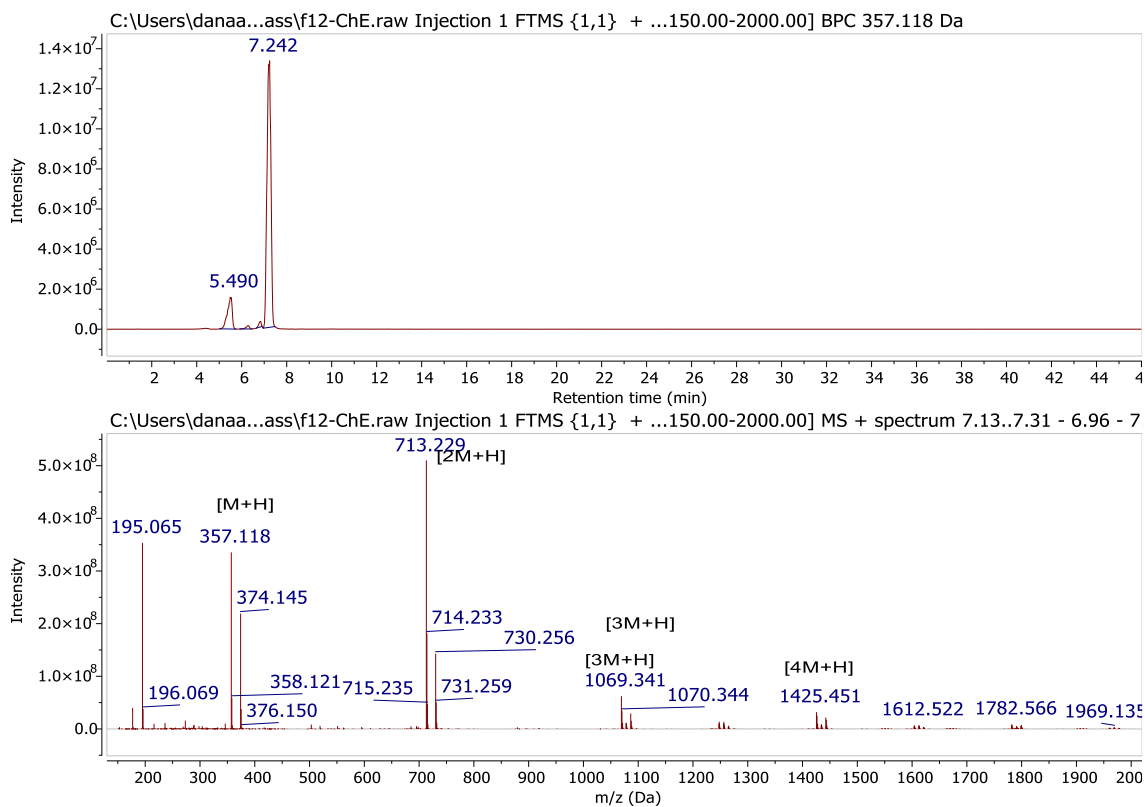


Figure 3.46 B: Extracted ion chromatogram of F12-ChE for the ion peak at m/z 357.1180[M+H] eluting at a Rt of 7.24 min.

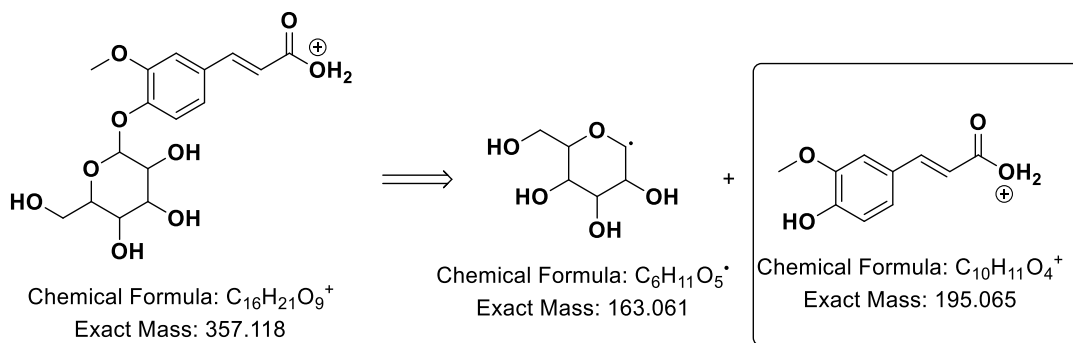


Figure 3.46C: Source fragmentation of the ion peak at m/z 357.1180 of F12-ChE.

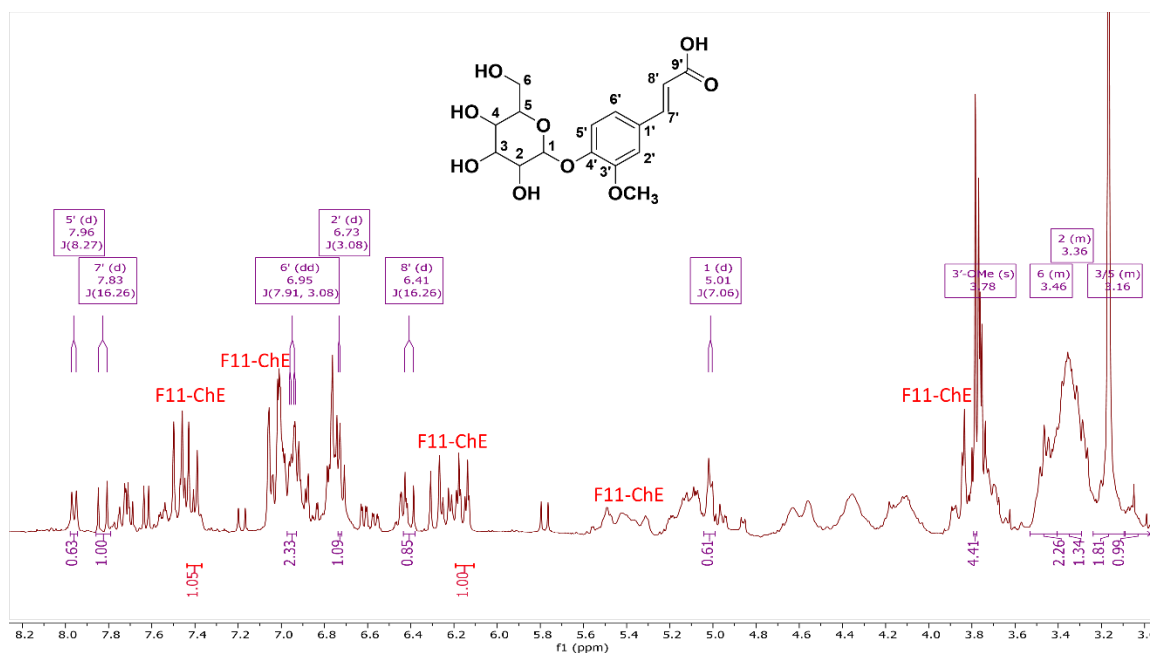


Figure 3.47: ¹H NMR spectrum of F12-ChE in DMSO-d₆ measured at 400 MHz.

F12-ChE was obtained as a white amorphous powder with a yield of 2.0 mg. High resolution mass spectrometric data gave a MW of 356.1179 Da and established a chemical formula of C₁₆H₂₀O₉ for the ion peak at m/z 355.1030 [M-H]⁻, in addition to ion peaks at m/z 711.2130 [2M-H]⁻ and 1067.3230 [3M-H]⁻ (Figure 3.46A). In the positive mode, an ion peak was observed at m/z 357.1180 [M+H]⁺ in addition to 713.2291 [2M+H]⁺, 1069.3402 [3M+H]⁺, and 1425.4507 [4M+H]⁺ (Figure 3.46 B). Source fragmentation of the ion peak at m/z 357.1180 yielded the peak at m/z 195.065 (Figure 3.46C) that corresponded to the aglycone structure upon the loss of a glucose unit.

The ¹H NMR spectrum of F12-ChE in Figure 3.47 was almost identical to that of F11-ChE as it is a mixture of the components found in the latter fraction at almost 1:1 ratio that was demonstrated by an almost equal integrals of the olefinic protons found in both structures. F12-ChE and F11-ChE share the component, 1,3-*O*-dicaffeoylquinic acid, that is the main metabolite from the latter fraction, which is the major impurity in F12-ChE and vice versa. Due to the very low yields of both fractions, it was not feasible to subject

them to further purification work. Both fractions, F11-ChE and F12-ChE, exhibited antioxidant activities with EC₅₀ values of 0.311 (603 μM) and 0.165 (463 μM) mg/mL, respectively. F12-ChE displayed a higher potency than F11-ChE, which could be due to the additional effectiveness of the component in F12-ChE or could also be a result of synergistic biological activity of the two components.

Furthermore, the ¹H NMR spectrum of F12-ChE disclosed a comparable pattern of resonating proton signals for a trans olefinic doublet pairs of a propenoic acid moiety at 7.83 and 6.41 ppm with a coupling constant of 16.3 Hz, like those found for the structures of 1,3-*O*-dicaffeoylquinic acid (F11-ChE) and 3,5-*O*-dicaffeoylquinic acid (F8-ChJ). The characteristic coupling pattern for 1,3,4-trisubstituted phenyl system was also observed in the ¹H NMR spectrum of F12-ChE. However, in comparison to the ¹H NMR spectra (Table 3.14) of the dicaffeoyl analogues elucidated in F8-ChJ and F11-ChE, the *ortho*-coupled doublet on C5' went downfield by 1 ppm at δ_H 7.96 (*J* = 8 Hz) and the *meta*-coupled doublet on C2' was shifted upfield by 0.3 ppm at δ_H 6.73 (*J* = 3 Hz), while the *ortho-meta* doublet of doublet on C6' remained unchanged at δ_H 6.95 (*J* = 3.1, 7.9 Hz). These changes in chemical shifts of the ABX system in the aromatic region implied a modification in substituents on the phenyl ring. The presence of a methoxy signal that was not apparent in the ¹H NMR spectrum of F8-ChJ for 3,5-*O*-dicaffeoylquinic acid, indicated a ferulic acid unit in F12-ChE with the methylation of the hydroxyl group in C3' observed at 3.78 ppm. Nevertheless, the largest ¹H shift change affected the proton doublet on C5', which postulated the possible glycosylation on C4'.

The ¹H assignments for the feruloyl moiety and the glucose unit were established by correlation NMR spectroscopy (COSY) as shown in Figure 3.48. On the aromatic region is the feruloyl unit, which is represented by the blue line for the propenoic acid moiety and the yellow line is the ABX system of the 1,3,4-trisubstituted phenyl system of the ferulic acid unit that commenced at 7.83 and 7.96 ppm, respectively. The green line did reveal the presence of a glucose unit that started at the anomeric ¹H doublet at 5.01 ppm with a coupling constant of 7.1 Hz, which suggested a β-D-glucose configuration (Pearson

and Spessard, 1975). The ^1H assignments for the glucose substituent followed through δ_{H} 3.35 (1H, m, H2), 3.19 (1H, m, H3), 3.01 (1H, m, H4), 3.12 (1H, m, H5), and concluded at 3.46 (2H, m, H6).

In Table 3.14, F12-ChE was also compared to 1-*O*-feruloyl- β -D-glucose (Takaya *et al.*, 2003), where the chemical shifts of the feruloyl units were more comparable to those of dicaffeoylquinic acid analogues found in F8-ChJ and F11-ChE. In 1-*O*-feruloyl- β -D-glucose, the glucose unit is attached to the propenoic acid unit like in the caffeoylquinic acid congeners. Further comparison to literature data (Table 3.15), the structure of F12-ChE was elucidated as 4' \rightarrow 1-*O*-feruloylglucose, also known as glucoferulic acid (Galland *et al.*, 2007) or lavandoside (Kurkin *et al.*, 2008).

Table 3.14: ^1H NMR data (δ_{H} in ppm, mult, J in Hz) of F12-ChE in comparison to that of 1,3-*O*-dicaffeoylquinic acid (F11-ChE) and 3,5-*O*-dicaffeoylquinic acid (F8-ChJ) measured at 400 MHz in DMSO- d_6 .

Atom no.	4'→1- <i>O</i> -feruloylglucose F12-ChE	1,3- <i>O</i> -dicaffeoylquinic acid F11-ChE	3,5- <i>O</i> -dicaffeoylquinic acid F8-ChJ
1	5.01 d, $J = 7.1$		
2	3.41 – 3.29 m	2.14 m 1.94 m	2.09 1.97
3	3.24 – 3.10 m	5.20 m	4.96 m
4	3.09 – 2.93 m	3.40 m	3.41 m
5	3.24 – 3.10 m	3.27 m	5.11 m
6	3.53 – 3.40 m	1.69 m 1.84 m	2.30 q, $J = 5.7$ 2.12 m
2'	6.73 d, $J = 3.1$	7.04 d, $J = 2.1$ 7.06 d, $J = 2.2$	7.08 d, $J = 2.0$ 7.08 d, $J = 2.0$
5'	7.96 d, $J = 8.3$	6.77 d, $J = 8.0$ 6.77, d, $J = 8.0$	6.80 d, $J = 8.1$ 6.80 d, $J = 8.1$
6'	6.95 dd, $J = 3.1, 7.9$	6.94 br d, $J = 8.8$ 6.94 br d, $J = 8.8$	6.98 brd, $J = 8.3$ 6.98 brd, $J = 8.3$
7'	7.83 d, $J = 16.3$	7.48 d, $J = 15.9$ 7.45 d, $J = 15.8$	7.60 d, $J = 16.3$ 7.60 d, $J = 16.3$
8'	6.41 d, $J = 16.3$	6.25 d, $J = 15.9$ 6.16 d, $J = 15.8$	6.30 d, $J = 15.7$ 6.30 d, $J = 15.7$
3'-OCH ₃	3.78 s		

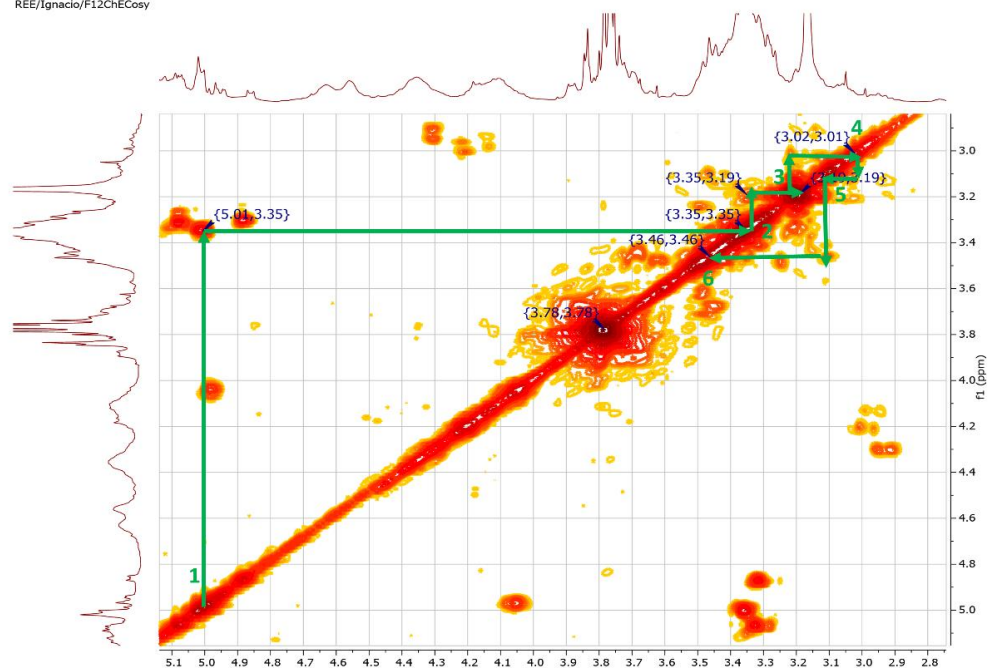
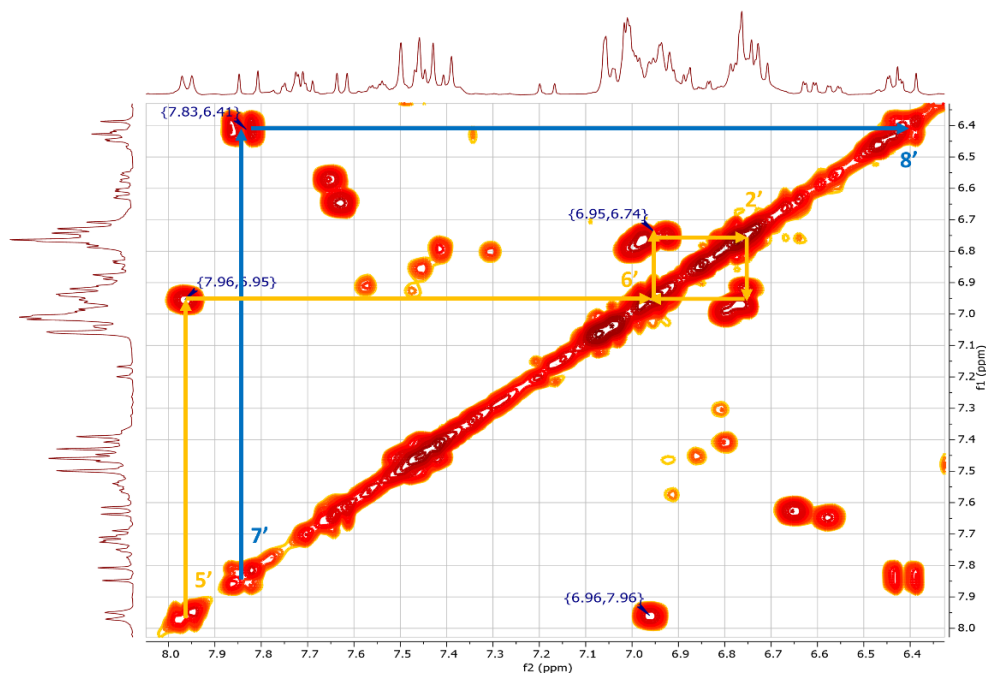


Figure 3.48: COSY NMR spectrum F12-ChE measured in DMSO- d_6 at 400 MHz. Blue line represents the propenoic acid moiety, yellow line is the ABX system of the 1,3,4-trisubstituted phenyl system of the ferulic acid unit, and the green line traces the coupling protons for the glucose unit.

Table 3.15: ^1H NMR data (δ_{H} in ppm, mult, J in Hz) of F12-ChE in comparison to that of 4'→1-*O*-feruloyl- β -D-glucose and 1-*O*-feruloyl- β -D-glucose as reported in the literature.

Atom no.	F12-ChE (DMSO- d_6) 400 MHz	4'→1- <i>O</i> -feruloyl- β -D-glucose (Kurkin <i>et al.</i> , 2008) (CH ₃ CN:C ₆ D ₆) 250 MHz	1- <i>O</i> -feruloyl- β -D-glucose (Takaya <i>et al.</i> , 2003) (MeOD) 400 MHz
1	5.01 d, $J = 7.1$	4.98 d, $J = 7.2$	5.56 d, $J = 7.8$
2	3.41 – 3.29 m	3.20 – 3.60 m	3.40 – 3.50 m
3	3.24 – 3.10 m	3.20 – 3.60 m	3.40 – 3.50 m
4	3.09 – 2.93 m	3.20 – 3.60 m	3.40 – 3.50 m
5	3.24 – 3.10 m	3.20 – 3.60 m	3.4-3.5
6	3.53 – 3.40 m	3.64 dd, $J = 12.0, 5.0$ 3.84 dd, $J = 12.1, 1.9$	3.86 dd, $J = 1.9, 12.2$
2'	6.73 d, $J = 3.1$	6.80 d, $J = 2.3$	7.20 d, $J = 1.9$
5'	7.96 d, $J = 8.3$	7.52 d, $J = 8.6$	6.81 d, $J = 8.3$
6'	6.95 dd, $J = 3.1, 7.9$	6.57 dd, $J = 2.3, 8.6$	7.09 dd, $J = 1.9, 8.3$
7'	7.83 d, $J = 16.3$	8.04 d, $J = 16.0$	7.61 d, $J = 15.9$
8'	6.41 d, $J = 16.3$	6.43 d, $J = 16.0$	6.39 d, $J = 15.9$
3'-OCH ₃	3.78 s	3.76 s	3.89 s

3.6. Summary

Two endemic species of chamomile, namely the Jordanian and European variants were compared to find the differences in their biological activity and chemical profiles. From both varieties, crude extracts were prepared using solvents of various polarities and tested for their biological activity to determine the exclusivity of the biologically active metabolites in certain extraction solvents.

All the extracts were assayed for their antioxidant activity using the DPPH® assay and anticancer activity against breast cancer cells ZR-75. The EtOAc fraction of the European variant exhibited anticancer activity against ZR-75 breast cancer cell line, which afforded a 16% of cell viability. Furthermore, both European and Jordanian EtOAc extracts exhibited antioxidant activity. The EC₅₀ values were 0.16 mg/mL for the Jordanian chamomile EtOAc extract and 0.2 mg/mL for the European chamomile EtOAc extract.

Both extracts were fractionated and tested again for their biological activity. Structure elucidation of the five bioactive compounds was performed using LC-HRMS coupled with dereplication database and NMR experiments, all of them were pinpointed by multivariate analysis to exhibit the putative bioactivity. The isolated target compounds were all known compounds. The results revealed that chrysosplenetin (F2-ChE) and apigenin (F8-ChE) compounds from European fractions had anticancer activity against ZR-75 cells with IC₅₀ values of 1.94 and 1.41 μM, respectively. Those compounds were also assayed for their toxicity against human foreskin fibroblast cells (HS-27) and both were not toxic and selective, as illustrated in Table 3.7. 1,3 dicaffeoyl quinic acid (F11-ChE) and glucoferulic acid (F12-ChE) from European chamomile displayed antioxidant activity with EC₅₀ values equal to 603 and 436 μM, respectively. On the other hand, 3,5-di-O-caffeoylquinic acid (F8-ChJ) in the Jordanian variant exhibited the most potent antioxidant activity with EC₅₀ value of 147 μM. The next step will be to extract the fungal endophytes from Jordanian *M. chamomilla* and search for the bioactive extracts that are able to produce anticancer and antioxidant compounds.

4. Isolation and Screening of Fungal Endophytes from Jordanian chamomile.

4.1. Literature background on fungal endophytes derived from chamomile.

"Endophytes" are microorganisms, most often fungus and bacteria, that spend their whole life cycle in the inter- and/or intracellular space of the tissues of host plants and do not cause disease in the host plant (Wilson, 1995). Each plant coexists with microbes that reside inside its tissues and produce its metabolites, which are found to be beneficial (Robinette *et al.*, 2012, Mani *et al.*, 2015). Endophyte-host interactions may be very intimate, to the point where microorganisms can even produce the same chemical compounds as the host (Alvin *et al.*, 2014). Endophytic fungi may be found in various types of plants, including trees, herbaceous plants, algae, and grasses (Nisa *et al.*, 2015). With the strong symbiotic interaction that occurs between endophytic fungi and their host plants, endophytes have developed a powerful ability to produce new bioactive chemicals, the creation of which is fed by carbohydrates found in their host plants (Aly *et al.*, 2011b).

In the literature, there has been only one study on fungal endophytes from *M. chamomilla*, as summarised in Table 4.1. Endophytes were obtained from the leaf, stem, and root segments of *M. chamomilla* collected from North-eastern of Iran. The isolated endophytic fungi were tested for their ability to produce L-asparaginase. L-asparaginase is a crucial anticancer enzyme that is used as first line of treatment in acute lymphoblastic leukaemia (Theantana *et al.*, 2009). Extracellular L-asparaginase was detected in three fungal isolates, which is consistent with the hypothesis that endophytes associated with medicinal plants have the potential to be medicinally useful (Hatamzadeh *et al.*, 2020).

In this current study, isolated endophytic fungi from the Jordanian *M. chamomilla* were screened for their ability to produce anticancer and antioxidant bioactive compounds. Schematic diagram for screening crude fungal extracts is shown in Figure 4.1. Due to the availability of fresh samples to commence the work on fungal endophytes in Spring 2019, it was only feasible to work with the Jordanian samples. Fresh European

chamomile was only available from the Botanical gardens for the summer season. Because of the limited logistic space of the laboratory, the work was planned for Spring of 2020, but the pandemic lockdown started so this part of the project was then cancelled.

Table 4.1: Isolated endophytes from *M. chamomilla* (Hatamzadeh *et al.*, 2020).

Host plant	Isolated endophytes	Plant part
<i>M. chamomilla</i>	<i>Phoma haematocycla</i>	stem
	<i>Paramyrothecium roridum</i>	root
	<i>Stemphylium amaranthi</i>	leaf
	<i>Xylariaceae sp.</i>	stem
	<i>Epicoccum nigrum</i>	stem
	<i>Didymella tanaceti</i>	stem

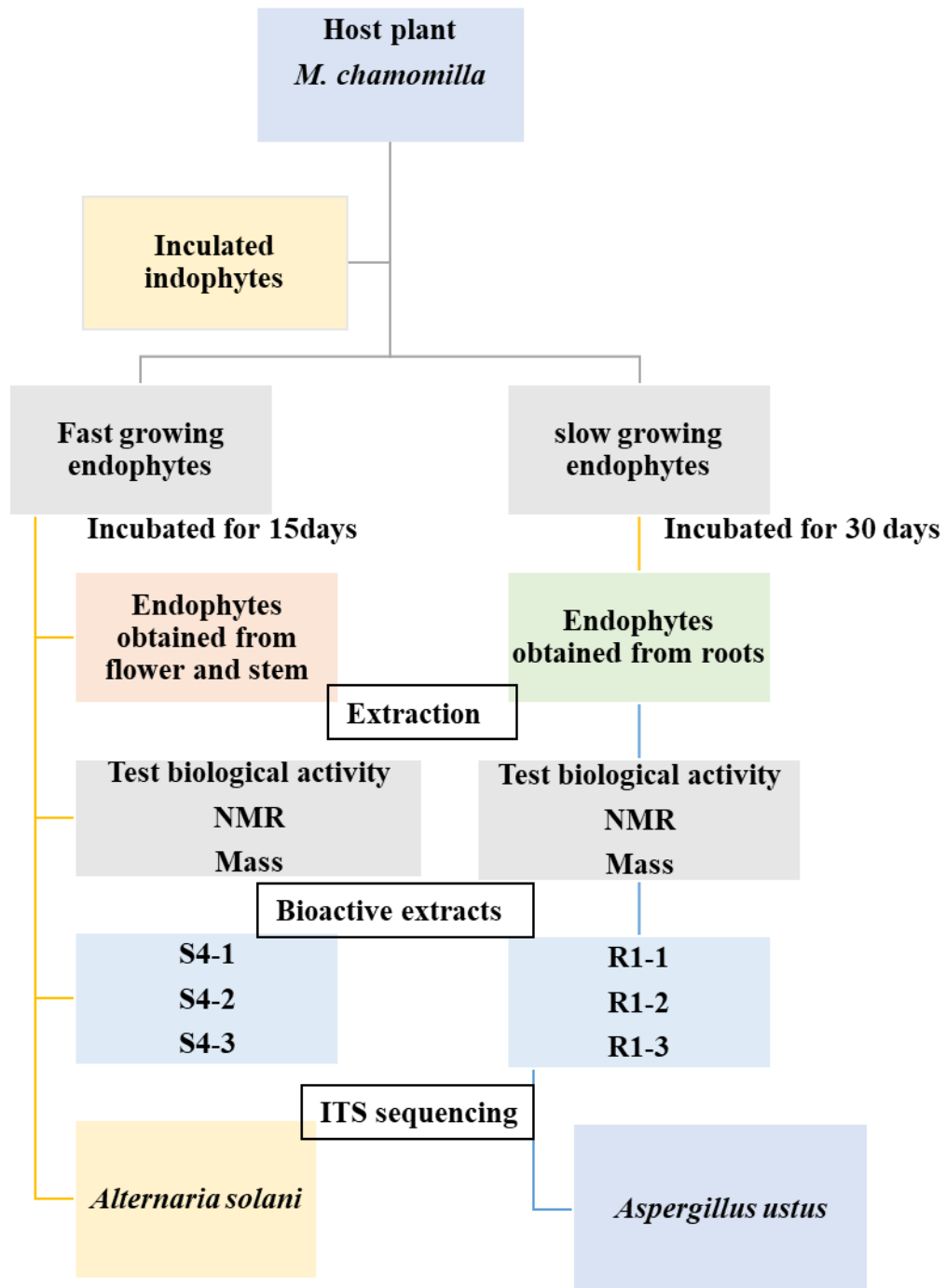


Figure 4.1: Schematic diagram for the screening of crude fungal extracts.

4.2. Isolation of endophytic fungi.

In this study, ten endophytic fungi were isolated from the interior tissues of Jordanian chamomile plants. These endophytic fungi were cultivated and utilised for further chemical analysis, as well as anticancer and antioxidant biological assays. The isolated and purified endophytes were incubated in MA medium. MA was chosen for the growth of endophytic fungal isolates because it provides primary metabolites (such as sugars and peptides), as well as the fact that it can serve as a source of carbon and nitrogen to produce secondary metabolites in the fungal isolates.

The chamomile parts were cleaned and surface-sterilised with 70% ethanol to kill any epiphytes that occurs on the plant then rinsed in sterile distilled water. Internal tissues of the stem, root, and flower were aseptically placed on MA medium. Chloramphenicol was incorporated into the media for the initial inoculation step to inhibit the development of endophytic bacteria and only to target the isolation of endophytic fungi. Three replicates of petri dishes were used for each plant part. The petri plates were incubated at 27 °C.

On further re-inoculation of the isolated purified fungi, chloramphenicol-free malt extract agar media were utilised. The presence chloramphenicol can lead to inaccurate findings in analysing the chemical profile and the biological activity of the extracts, that could suppress the detection of low yielding bioactive metabolites.

The isolated endophytic fungi were purified by repeated inoculation. Fungal samples in triplicates were coded according to plant part source and their morphological features as listed in Table 4.2.

Table 4.2: Morphological feature of the isolated endophytes from Jordanian chamomile.

Plant part	appearance of the endophyte	Endophyte code
flower	white centre, brown edges	F1-1, F1-2, F1-3
	white, fluffy	F2-1, F2-2, F2-3
	white with black spores	F3-1, F3-2, F3-3
		F4-1, F4-2, F4-3
stem	white centre, green edges	S2-1, S2-2, S2-3
	light green	S1-1, S1-2, S1-3
	white, water like	S3-1, S3-2, S3-3
	colourless, water like	S5-1, S5-2, S5-3
	white centre, yellow edges	S4-1, S4-2, S4-3
root	pink centre, white edges	R1-1, R1-2, R1-3
	yellow spot, fluffy white	R2-1, R2-2, R2-3

Legend: stem (S), root (R), and flower (F)

4.3. Fungal extraction

Due to the variations in growth rates across isolated fungal strains, ten fungi were classed as fast- or slow-growing fungi. The fast-growing fungal isolates were incubated for 15 days to minimise biomass overgrowth, which might result in the further consumption of secondary metabolites produced by the fungal strain that will eventually kill the fungus. Whereas the slow-growing fungi were cultured for 30 days to ensure that sufficient extract yields were available for biological testing and chemical profiling. To ensure proper metabolomics data analysis, a medium blank was also incubated for both incubation periods and compared to the fungal extracts.

At the end of the incubation period, each of the fungal culture replicate was transferred to a 250-mL conical flask and macerated overnight with EtOAc then homogenised the following day. The homogenised mixture was vacuum filtered and extracted again three times with equal volumes of EtOAc. The extracts were dried using a rotary evaporator and transferred in tared vials. Yields of each extract replicate were recorded and reported in Table 4.3.

Table 4.3: Fungal extract yields in triplicates.

Plant part	Endophyte code	Weight (mg)	Plant part	Endophyte code	Weight (mg)	
flower	F1/1	79.6	stem	S2/1	47.1	
	F1/2	66.9		S2/2	11.1	
	F1/3	51.2		S2/3	10.4	
	F2/1	51.3		S3/1	21.0	
	F2/2	71.4		S3/2	9.6	
	F2/3	19.0		S3/3	11.2	
	F3/1	108.2		S4/1	16.0	
	F3/2	75.2		S4/2	11.8	
	F3/3	63.3		S4/3	16.5	
	F4/1	71.3		root	R1/1	25.4
	F4/2	62.4			R1/2	28.6
	F4/3	83.1			R1/3	29.3
stem	S1/1	10.9	R2/1	17.1		
	S1/2	13.5	R2/2	33.6		
	S1/3	19.1	R2/3	42.8		
Legend: stem (S), root (R), and flower (F)						

4.4. Bioassay screening of fungal extracts

A preliminary screening of the fungal extracts was performed to test their anticancer and antioxidant activity. AlamarBlue® and DPPH® assay were used.

4.4.1. AlamarBlue® assay

All ten fungal extracts were tested against breast cancer cell line ZR-75 at a concentration of 30 µg/mL, only two endophytes possessed activity and afforded less than 40% viability of the tested cells. Fungal extracts of endophytes obtained from the flower part were found inactive against breast cancer cells, as depicted in Figure 3.2A. Meanwhile, fungal extracts, R1-2 and R1-3, afforded anticancer activity against the tested cell line, which afforded 80% cell growth inhibition (Figure 4.2B). R1-2 and R1-3 were two of the triplicates of an endophytic fungal strain obtained from the root part. Furthermore, replicate set, S4-1, S4-2, and S4-3, of a fungal isolate obtained from the stem was also found active at 81% growth inhibition of ZR-75 cells, as shown in Figure 4.2C

Using a dilution curve, IC₅₀ values of the bioactive fungal extracts against ZR-75 were determined as illustrated in Figure 4.3. Both fungal extracts obtained from the root and the stem afforded an IC₅₀ value of 1.3 µg/mL.

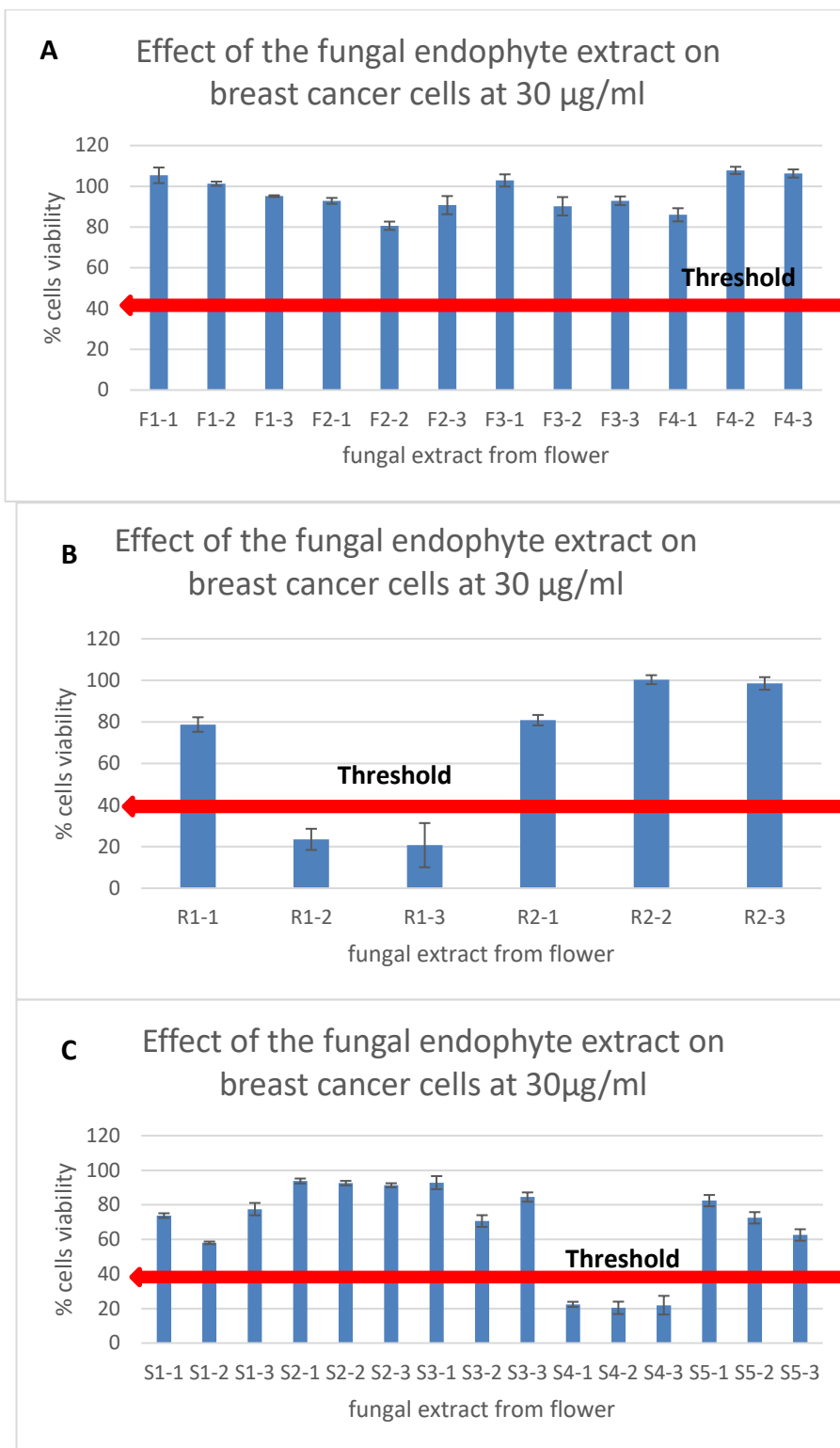


Figure 4.2 :Alamarblue® assay against the breast cancer cell line ZR-75 for 30 µg/mL extracts of fungal endophytes obtained from **A**) flower, **B**) roots, and **C**) stem. The red line indicates the bioactivity threshold, which must be below 40% of cell viability.

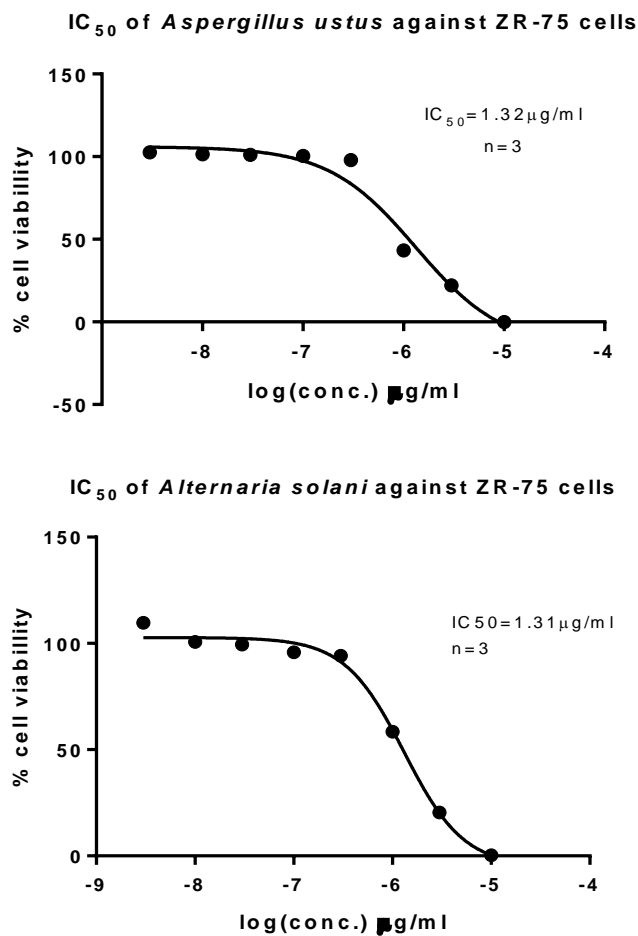


Figure 4.3: Dilution curves to determine the IC₅₀ values of active fungal extracts against the breast cancer cell line ZR-75.

4.4.2. DPPH assay

The antioxidant activity was tested using DPPH® assay. Ascorbic acid and quercetin were used as positive control. None of the fungal endophytes afforded any antioxidant activity.

4.5. NMR analysis of fungal extracts

¹H NMR spectral data were recorded for all fungal extracts to get an overview of the chemical composition and functional groups present in each sample. The stacked ¹H NMR spectrum for the fungal endophytes obtained from the flower revealed the

absence of interesting peaks at chemical shift between 5.00 to 8.00 ppm, as observed in Figure 4.4, which indicated the poor production of secondary metabolites. Furthermore, these extracts did not possess any activity on the tested biological assays. Hence, these fungal endophytes were excluded for further isolation work.

^1H NMR spectra of fungal extracts obtained from the root were stacked and shown in Figure 4.5. The ^1H NMR spectra revealed the presence of fatty acid signals, which was explained by the presence of high intensity peaks at the aliphatic region that resonated between 0.90 to 2.00 ppm. This suggested the presence of long chain methylene units (enclosed in blue box). Furthermore, α -protons of a carboxylic end resonated at δ_{H} 2.10 – 2.40 (enclosed green box) that could be related to esterified terpenes that could be present in the bioactive endophyte. These endophytes were producing secondary metabolites rich in hydroxylated compounds as highlighted in the red box at 4.00 to 5.00 ppm. In addition, olefinic protons in unsaturated fatty acids were found at δ_{H} 5.00 – 5.50 (enclosed in orange box). Aromatic and/or olefinic signals were observed between 5.90 to 7.25 ppm (enclosed in a black box). The bioactive extracts, R1-2 and R1-3 did have higher intensity peaks between 4.5 and 7.5 ppm. Despite the inactivity of extract R1-1, its ^1H NMR spectrum was identical to those of R1-2 and R1-3. The assay result discrepancy between the replicates could be accounted for possible pipetting errors in transferring the extracts to assay plates. Other errors could have occurred during the preparation of the stock solution and the dilution of the samples; if the stock solution and dilution of the samples are incorrectly made, it will have an impact on the subsequent experiments since they were used for many other experiments. Stock solutions were kept at $-20\text{ }^{\circ}\text{C}$.

The stacked ^1H NMR spectra for fungal extracts obtained from endophytes isolated from the stem part are shown in Figure 4.6. There was an obvious production of unique secondary metabolites due to higher intensity of resonances between the aliphatic and aromatic region that covered a wide range of resonances from 0.50 to 8.00 ppm, as enclosed by the blue box in Figure 4.6. Thus, despite their low yields, they were shown to be biologically active, indicating their potential to produce strong anticancer metabolites.

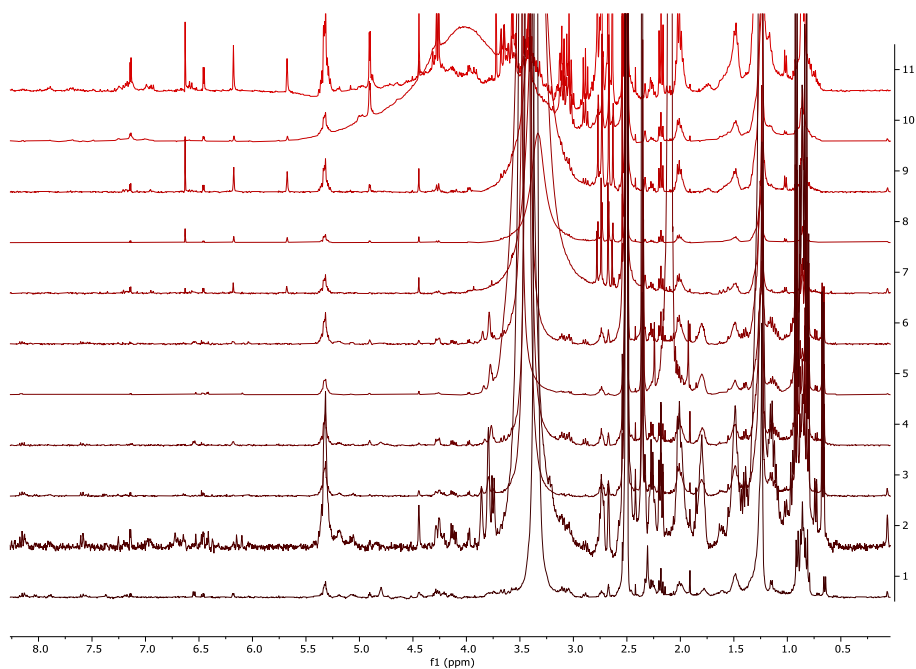


Figure 4.4: Stacked ¹H NMR spectra of the fungal extracts obtained from endophytes isolated from the flower part of the chamomile plant.

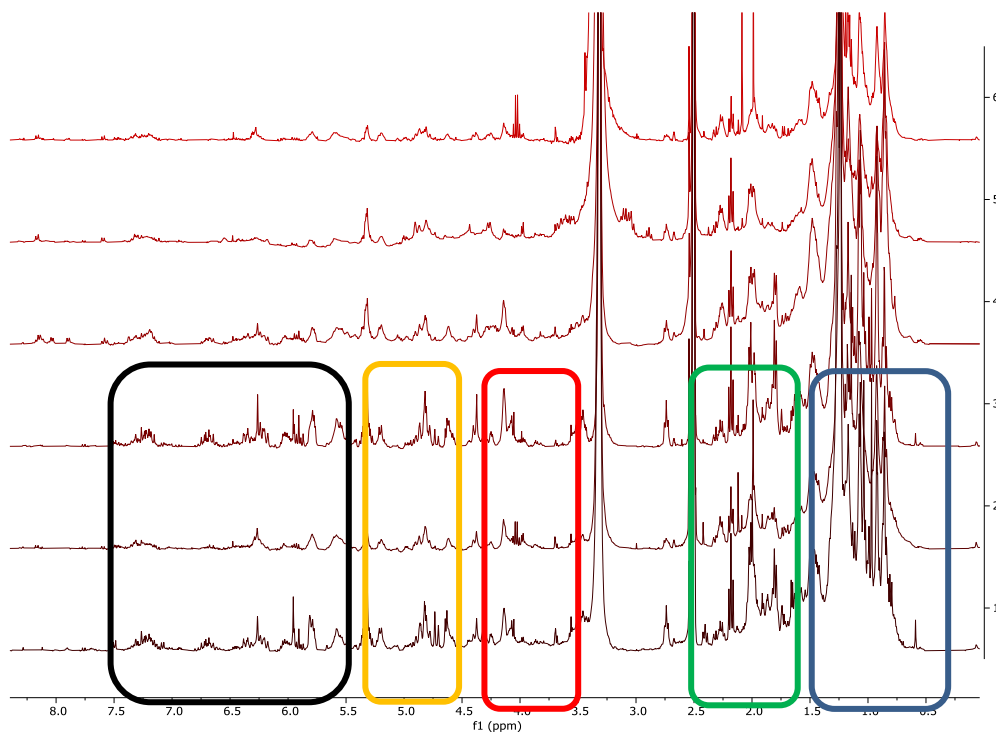


Figure 4.5: Stacked ¹H NMR spectra of the fungal extracts obtained from endophytes isolated from the root part of the chamomile plant. Spectrum from 1 to 3 represent the bioactive fungal extracts.

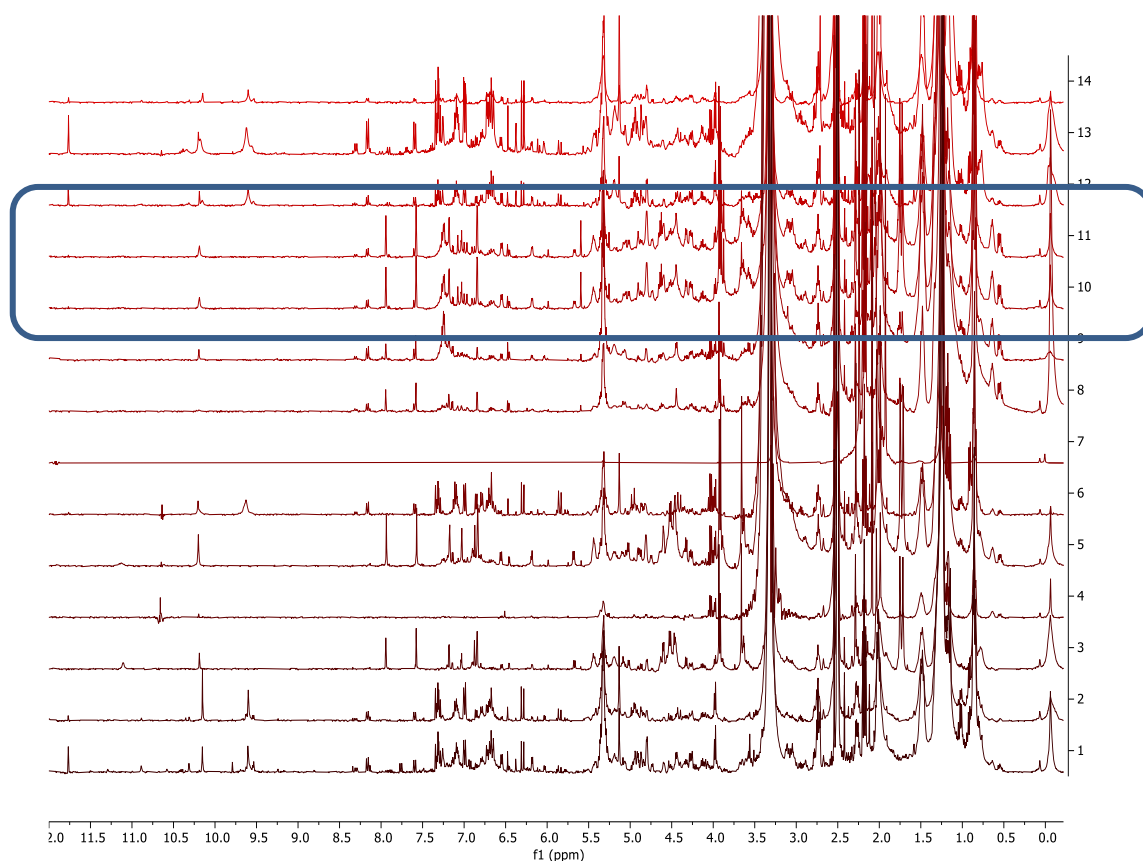


Figure 4.6: Stacked ¹H NMR spectra of the fungal extracts obtained from endophytes isolated from the stem part of the chamomile plant. Boxed spectra represent the bioactive extract.

The PCA-scores plot shows the similarity and differences between extracts. The PCA-loadings plot reveals the type of functional groups and chemical profile for each group of extracts. The extracts were categorised according to their isolated plant parts as shown in Figure 4.7A. Flower endophytic extracts were dispersed in the upper left quadrant of the PCA scores plot. The extracts from fungal endophytes obtained from the stem were dispersed between the left and right lower quadrants. Meanwhile, the anticancer fungal extracts from endophytes isolated from the root and stem were found overlapping in the lower left quadrant of the plot (encircled orange), which implied their similar features and chemical profiles. On the corresponding loadings plot in Figure 4.7B that consisted of upfield chemical shifts of 0 to 3 ppm (blue). The R^2 and Q^2 values were 0.98 and 0.26, respectively, which indicated a model of good fitness

but poor predictability. The almost random dispersal of the extracts of the endophytes from the flower and stem could have resulted to a poor predictability score.

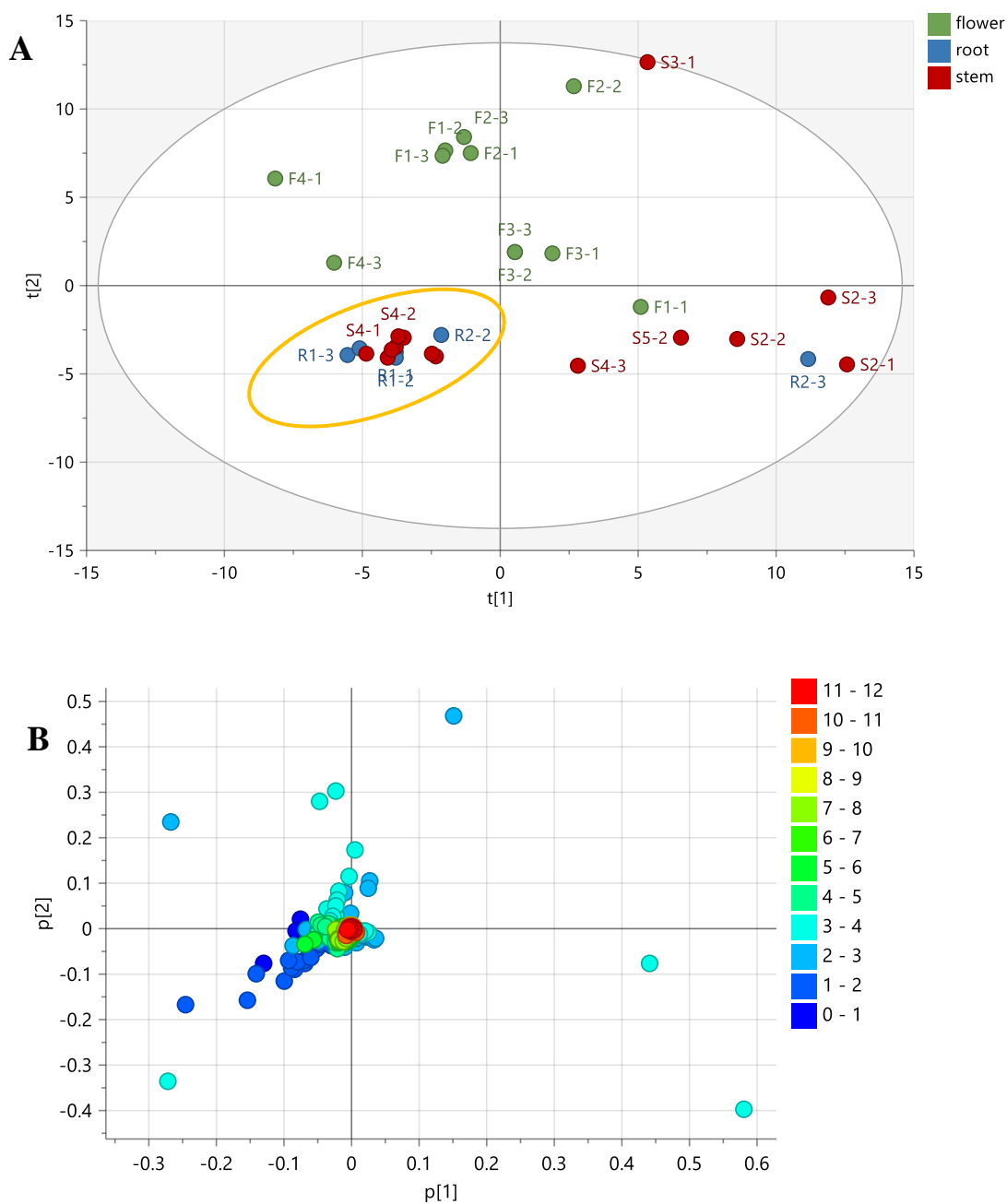


Figure 4.7: **A)** PCA scores and **B)** loadings plots of the NMR spectral data of fungi extracts. The R^2 and Q^2 values were 0.98 and 0.26, respectively. Orange encircled variables on the PCA scores plot are the biologically active extracts against the breast cancer cell line ZR-75.

Additionally, an OPLS-DA was performed to identify the distinguishing functional units for the fungal extracts grouped according from which plant part were the endophytes isolated. The fungal extracts obtained from the endophytes isolated from the flower part were distributed on the right quadrants of the OPLS-DA scores plot (Figure 4.8A), while extracts of endophytes from the stem were concentrated on the lower left quadrant. Whereas those obtained from the root part were dispersed on the upper left quadrant. The active fungal extracts R1-1, R1-2 and R1-3 from the roots were in the uppermost edge of the left quadrant (encircled red).

As presented by the corresponding OPLS-DA loadings plot in Figure 4.8B. Poor production of secondary metabolites was observed for the extracts of endophytes from the flower part. The group was mainly characterised by sugar types of metabolites that was indicated by their chemical shifts between 3.00 and 4.00 ppm (encircled green). This leads to quite an interesting query whether the floral endophytes play an important role in the saccharide build-up in the pollen.

Furthermore, those secondary metabolites detected from the extracts of endophytes from the stem showed the occurrence of a wider range of ^1H resonances from 3.00 to 10.00 ppm (encircled red) that would be compatible to structures of glycosylated phenolic compounds. For extracts of endophytes from the root part, a higher ratio of aliphatic signals resonating between 0.50 and 2.00 ppm were observed (encircled blue). In addition, resonances for olefinic and aromatics presented from 5.00 to 8.00 ppm were being shared between extracts of endophytes from both the stem and root parts. However, those endophytes from the stem parts seem to produce fewer secondary metabolites than those from the roots, which could also be due to their lower yields. Metabolites afforded by endophytes from the stem were highly glycosylated, which were indicated by ^1H signals from 3.00 to 4.00 ppm. The model gave a goodness of fit of 0.94 and good predictability of 0.66.

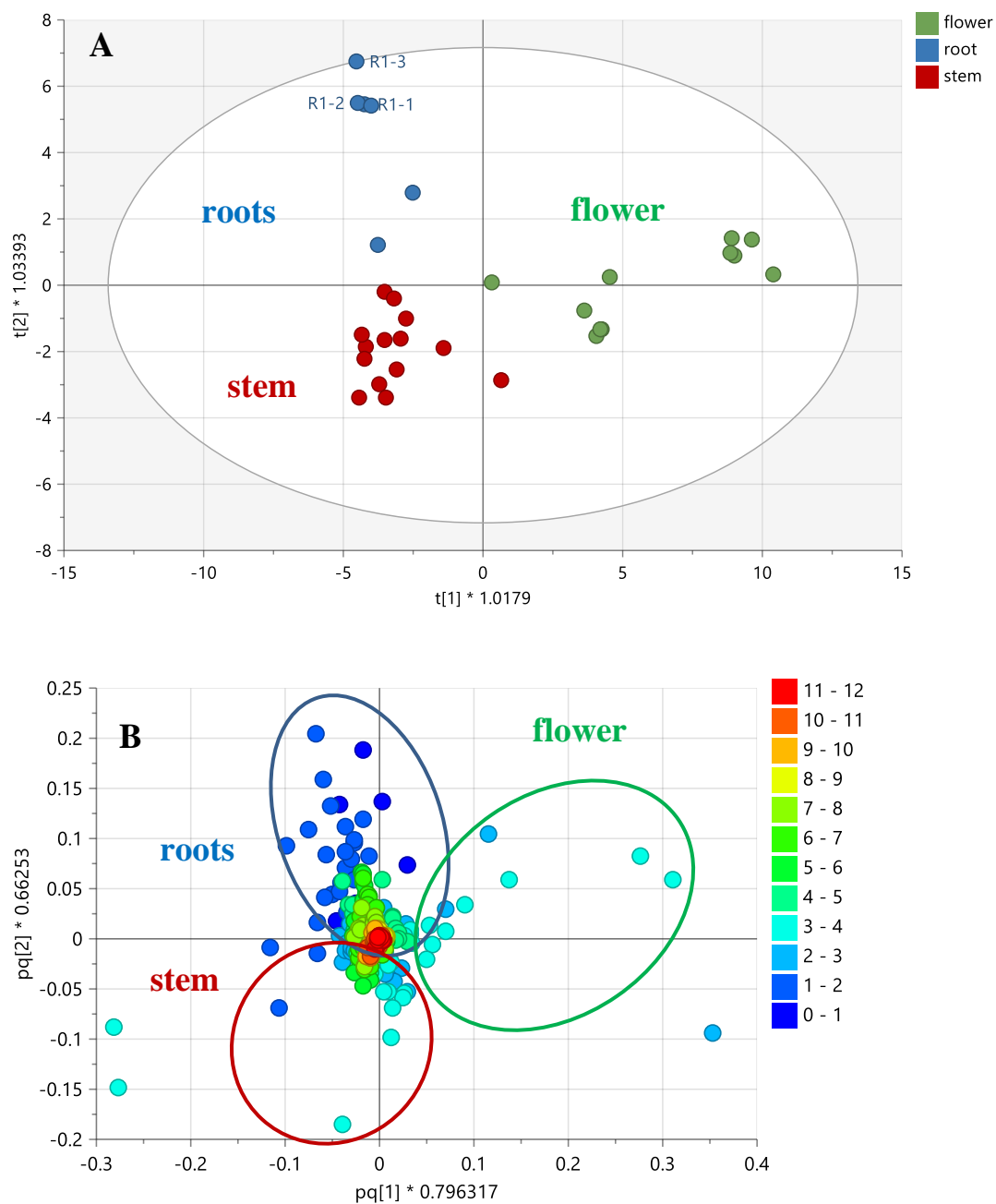


Figure 4.8: A) OPLS-DA scores and B) loadings plots of the NMR spectral data of fungal extracts grouped according to the plant parts the endophytes were obtained. The discriminatory chemical shifts in ppm from the respective extracts of the endophytes obtained from the flower were encircled green, those from the roots were encircled in blue and stem encircled in red.

Multivariate analysis was also accomplished by grouping the fractions according to their bioactivity on the breast cancer cell line ZR-75. Incorporating the results of AlamarBlue® assay on OPLS-DA, the active extracts were positioned on the right quadrants and inactive extracts on the left side of the OPLS-DA scores plot, as shown in Figure 4.9A. A S-plot was generated from OPLS-DA loadings plot, the discriminating chemical shifts from the bioactive extracts were encircled in orange, as illustrated in Figure 4.9B. plot. The loadings S-plot showed the occurrence of wider range of resonance between 1.00 and 8.00 ppm for the active extracts, which indicated a high possibility of unique chemical profile. This wide range of chemical shifts implied the occurrence of aromatic, olefinic, and aliphatic units. In comparison, the inactive fractions exhibited a higher ratio of glycosylated peaks, which resonated mainly at a narrower range between 3.00 to 4.00 ppm. R^2 and Q^2 values were 0.97 and 0.74, respectively, which indicated a model with excellent fitness and predictability that is better than the PCA model. However, $R^2X_o[1]$ gave a variation score of 16.5 percent between groups while only 9.2 percent within groups, indicating low diversity within group. The variation score across groups is bigger than the variation score within groups, which indicated an excellent separation between the active and inactive extracts.

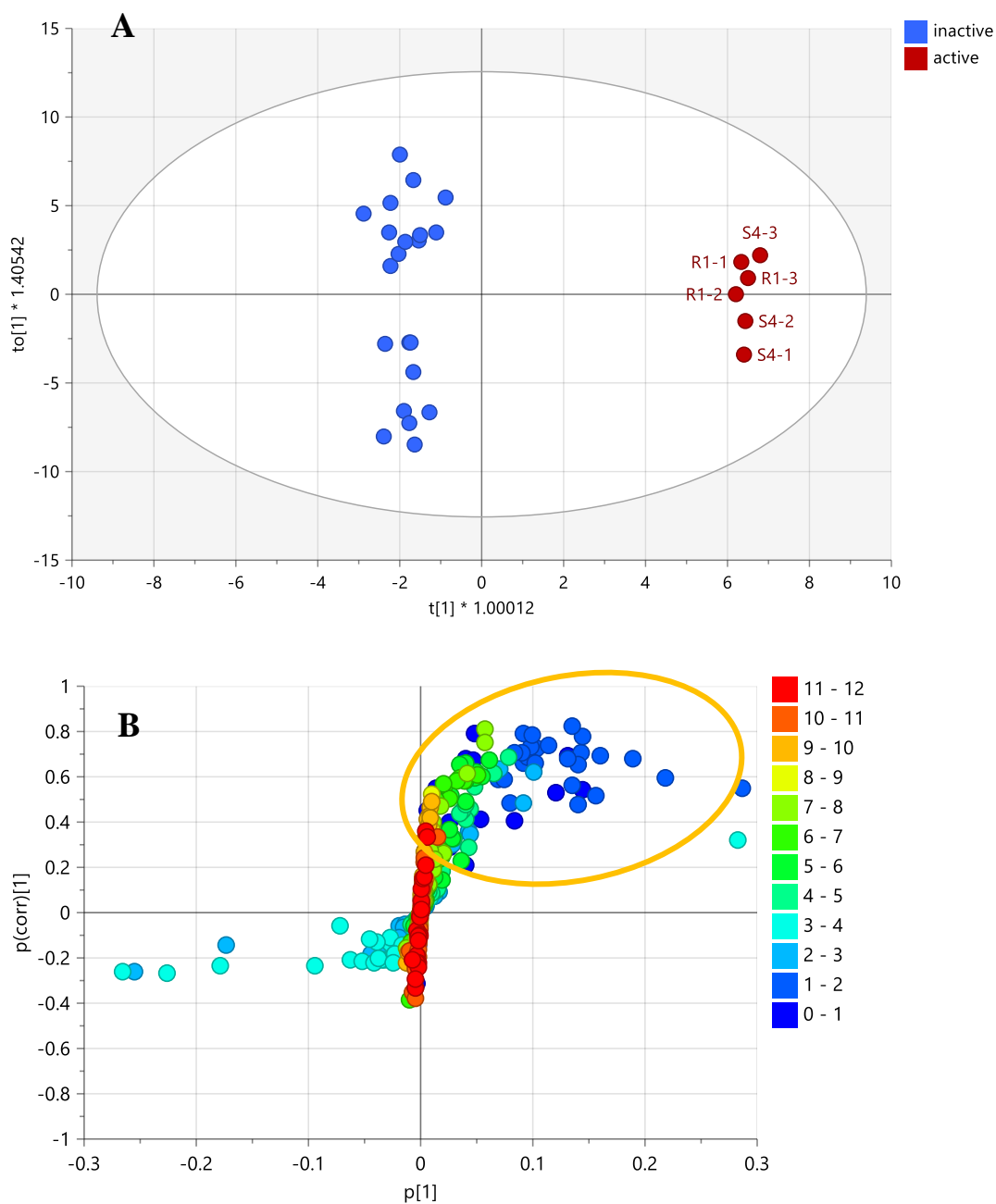


Figure 4.9: **A)** OPLS-DA scores and **B)** loadings plots of the NMR spectral data of endophytic fungal extracts against their bioactivity on the breast cancer cell line ZR-75. R^2 and Q^2 values were 0.98 and 0.74, respectively. The difference between group $R^2X_0[1]$ is equal to 16.5% and the difference within groups $R^2X[2]$ is 9.2%. Encircled features on the loadings S-plot indicate the discriminating chemical shifts for the biologically active fractions against breast cancer cells line ZR-75.

The ^1H NMR spectral data of the fungal extracts were also subjected to MetaboAnalyst®. The heatmap verified the existence of unique metabolites with chemical shifts ranging from 1.00 to 2.00 ppm in bioactive extracts from the roots and stem, indicating the presence of biologically active aliphatic compounds. However, high number of metabolites with chemical shifts ranging from 5.00 to 8.00 ppm was also detected in the bioactive extracts, signifying the exclusive occurrence of olefinic and aromatic compounds as well (Figure 4.10). The heatmap analysis produced results that were consistent with those obtained from the OPLS-DA loadings plot. Additionally, the heatmap revealed that the active fractions had a greater diversity of chemical changes at higher intensities.

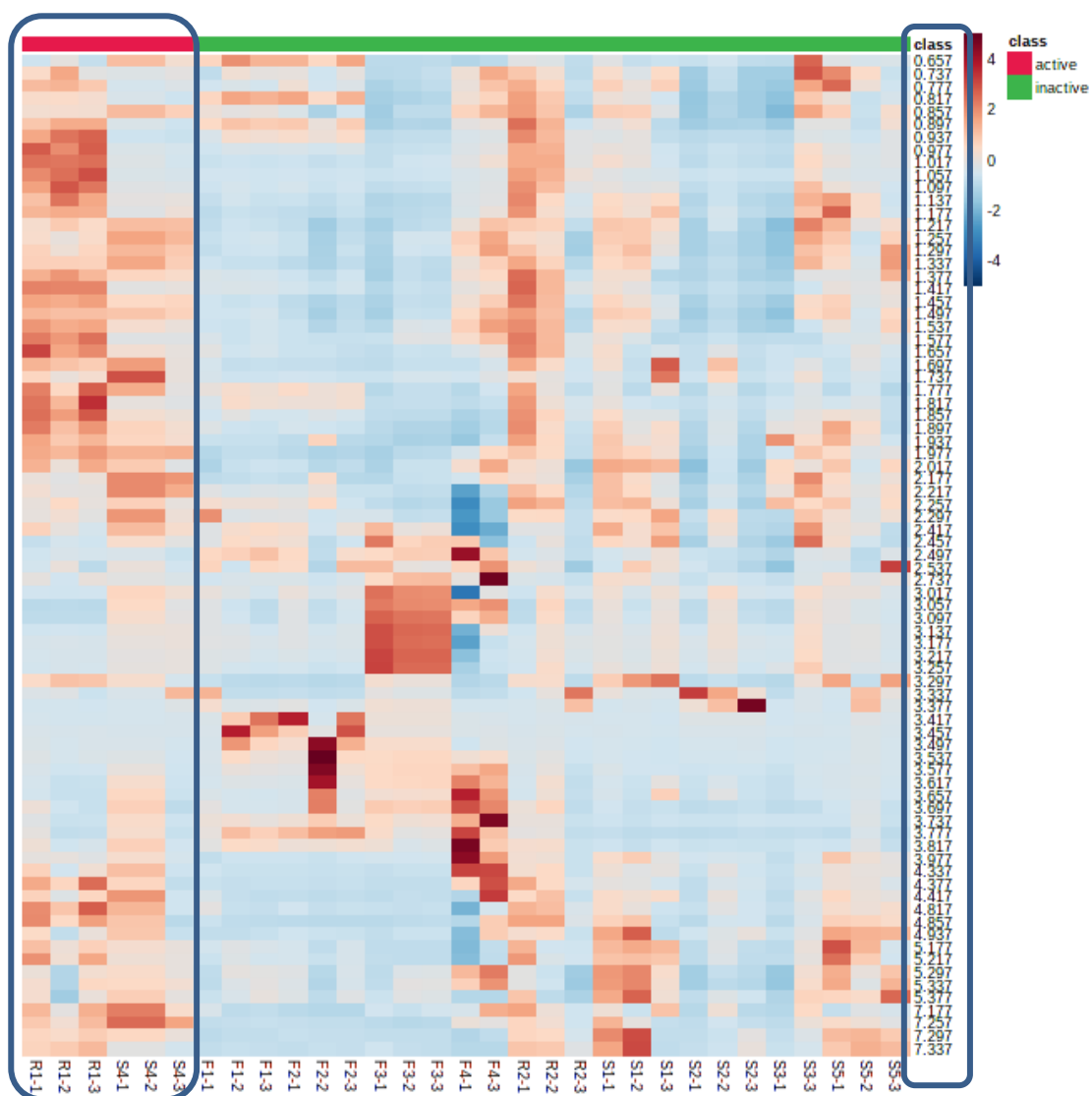


Figure 4.10: Heatmap analysis of the NMR spectral data of endophytic extracts generated by MetaboAnalyst®. The boxed extracts are the biologically active extracts against the breast cancer cell line ZR-75 along with the discriminating chemical shifts unique to these anticancer fractions.

4.6. LC-MS analysis of fungal extracts

The PCA scatter plots of the LC-HRMS data for the fungal extracts are shown in Figure 4.11. The fungal extracts of endophytes obtained from the root part, particularly R1-1, R1-2, and R1-3, were separated on the right quadrants of the scores plot signifying their unique chemical profiles. Those extracts of endophytes from the flower and stem parts were distributed on the upper and lower left quadrants, respectively. Some fungal extracts of endophytes obtained from the stem overlapped with those isolated from the flower parts that implied similarity in their chemical profiles. This may also possibly have been influenced by the low yield of the fungal extracts from stem endophytes that showed undepleted media components commonly found in extracts of endophytes isolated from the flower part.

The anticancer extracts, R1-2 and R1-3 with R1-1, all originating from the same endophytic fungus appeared to be the most segregated. R1-1 and R1-3 were exhibited as outliers. The extracts were examined using a DModX bar-plot to determine if they were true outliers. As shown in Figure 4.12, the true outliers were the variables that extended above the red line, which included R1-1, R1-2, R1-3, and R2-3. A unique set of discriminating metabolites was observed in the loadings plot on Figure 4.11B that indicated a higher density of chemical features with MWs between 240 and 1140 Da. Furthermore, the outlying active extracts obtained from the root endophytes were discriminated by the “end point” metabolites N_3, N_11, N_4049, and N_77 with ion peaks at m/z 325.185, 339.200, 389.610, and 956.594 Da, respectively. N_11 was putatively identified as 4-methylbenzenesulfonyl-1-dodecanol and was from an unknown source. whereas N_4049 was putatively identified as 6-*O*-(5-carboxy-2*E*,4*E*-pentadienoyl)11,12-epoxy-7-drimene-6 β ,9 α ,11 α -triol was obtained from *A. ustus* that was earlier isolated from the marine sponge *Suberites domuncula* collected from the Adriatic Sea (Liu *et al.*, 2009). while the others did not give any hits and remains unidentified. In parallel, four discriminating metabolites were detected for the stem endophytes that included MZmine IDs N_1, P_357, P_34 and N_60 found at m/z 283.0615, 181.0852, 211.1438 and 257.0460, respectively, and were dereplicated from the DNP database as 1-hydroxy-2,3-dimethoxyanthraquinone, 3-

propylgentisylquinone, 6-(1-methylethyl)-3-(2-methylpropyl)-2(1*H*)-pyrazinone, and the last discriminating metabolite gave no hits. On the other hand, four discriminating metabolites were obtained from the endophytes isolated from the flower parts, which entailed MZmine IDs N_2313, P_5465, N_93 and N_92 were found at *m/z* 196.0974, 198.1123, 417.1620 and 415.1862, respectively and were dereplicated from the DNP database as tenuazonic acid, isotenuazonic acid, bufogargarizanine C and the last discriminating metabolites afforded no hits. The list of discriminating metabolites is presented in Table 4.5 and the compound structures are shown in Figure 4.16. After five components, the R^2 and Q^2 values were 0.67 and 0.37, respectively, these values indicated good fitting and poor prediction of this model due to the Q^2 value of below 0.5 due to overlapping variables between extracts of endophytes obtained from the flower and stem parts. However, despite of poor predictability, it was possible to read out the unique features for the endophytes isolated from the respective plant parts indicating the exclusivity of these isolated endophytes.

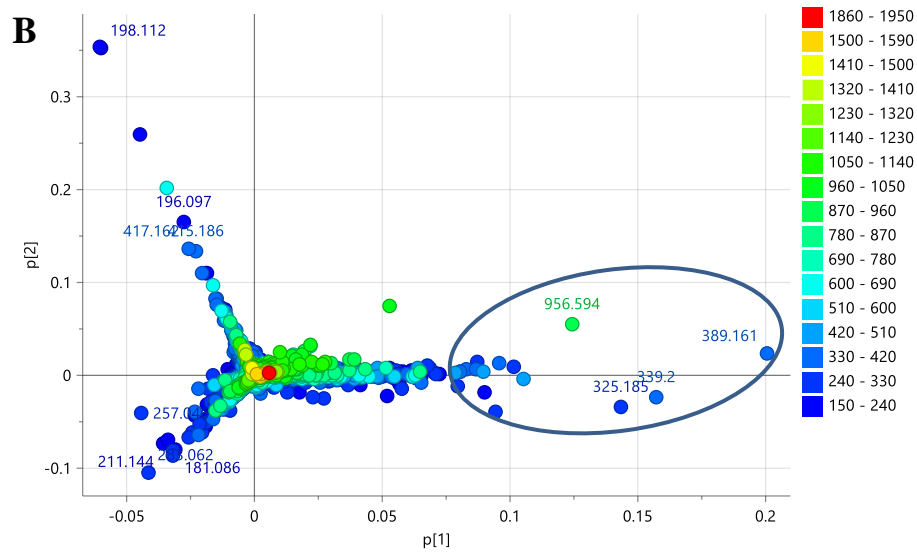
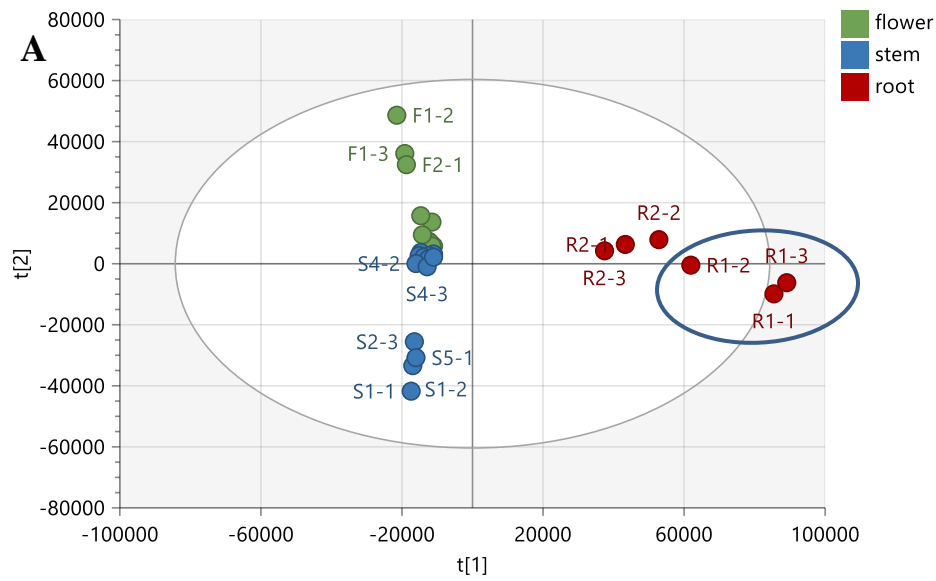


Figure 4.11: (A) PCA scores and (B) loading plots of the LC-HRMS fungal endophytes. Encircled features represent the discriminating ion peaks for the outliers R1-1, R1-2, and R1-3. $R^2 = 0.67$ and $Q^2 = 0.37$.

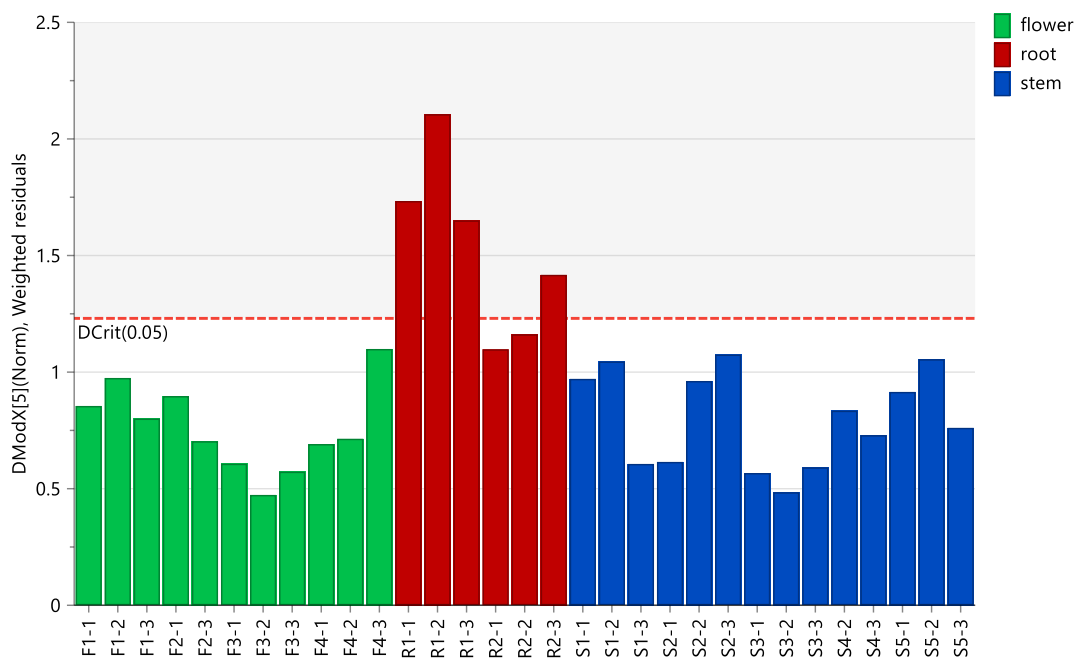


Figure 4.12: DMod X bar-plot to examine the occurrence of true outliers. fungal endophyte extract above the red line are the true outliers, which includes R1-1, R1-2, R1-3, and R2-3.

An OPLS-DA analysis was performed to provide a clearer illustration of the differences in metabolic profiles between endophytic fungi isolated from the different plant parts (Figure 4.13A). It afforded a fitness (R^2) and predictability (Q^2) scores of 0.86 and 0.76, respectively. This indicated good fitting and prediction of the generated model, which improved when compared to the PCA model above. The fungal extracts of endophytes obtained from the flower part were positioned in the upper right quadrant and contained mainly metabolites with MW ranging from 240 to 690 Da (encircled green), as shown in figure 4.13B. Whereas, the extracts of endophytic fungi from the stem were located in the lower right quadrant containing metabolites with a wider range of MWs from 150 to 123 Da (encircled red) but no metabolites with MWs between 510 and 690 Da. The fungal extracts of endophytes from the root were distributed on the left axis quadrants of the loadings plot (encircled blue). In terms of the distribution of the MW features between the three plants parts, the metabolites for the endophytes obtained from the stem and root parts shared almost a similar range of MWs.

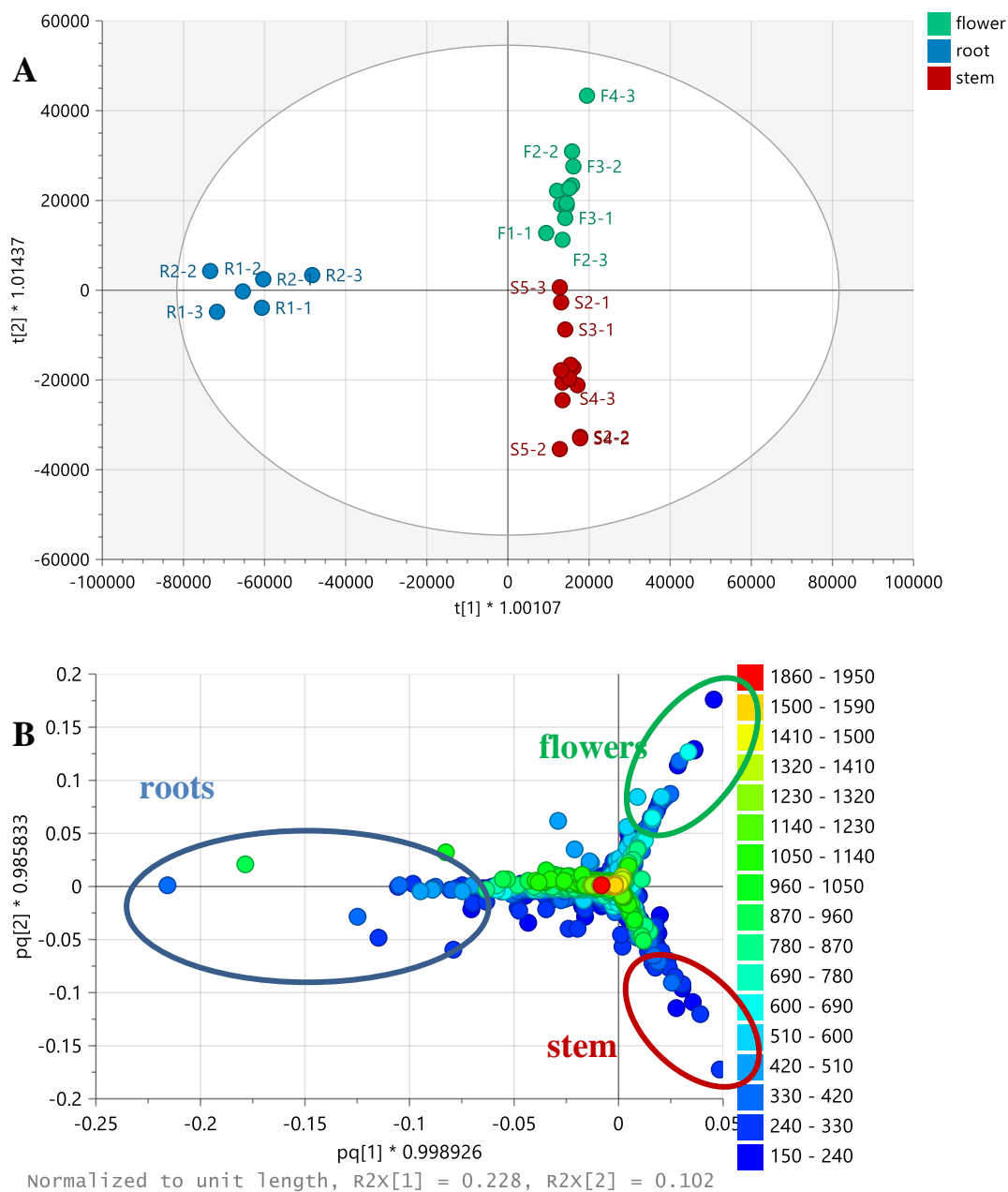


Figure 4.13: (A) OPLS-DA scores and (B) loading plots of LC-HRMS fungal endophytes. The highlighted box indicated the metabolites from R1-2. $R^2 = 0.86$ and $Q^2 = 0.76$. Discriminating features of the fungal endophyte extracts obtained from the different plant part are listed in Table 4.5.

The OPLS-DA of the active versus the inactive extracts was also generated as presented in Figure 4.14. It gave fitness and predictability scores of 0.99 and 0.76, respectively, indicating good fitting and prediction of the generated model. The variation score between groups was 11.2% while within groups, it was only 2.1%. The OPLS-DA scores plot in Figure 4.14A positioned the active extracts on the right quadrants, showing R1-2 as an outlier on the lower left quadrant. Meanwhile, the inactive extracts were dispersed on the left quadrants of the scores plot, as shown in Figure 3.13A. The outlying R1-2 extract was discriminated by metabolites encircled in orange with p -values < 0.05 (Figure 4.13B), which indicated a strong model with a confidence interval of more than 95%. Four metabolites with MZmine IDs N_5, N_4831, N_4049 and N_11 were found at m/z 311.169, 435.203, 389.161 and 339.200 were dereplicated from the DNP database as 4-methylbenzenesulfonyl-dihydrocitronellol, ergosecalinine, 6-*O*-(5-carboxy-2E,4E-pentadienoyl)11,12-epoxy-7-drimene-6 β ,9 α ,11 α -triol, and 4-methylbenzenesulfonyl-1-dodecanol, respectively. Two ion peaks of compounds at m/z 311.169 and 339.200 were from unknown sources. While m/z 389.161 was isolated from the fungus *A. ustus* and described to exhibit cytotoxic activity against tumour cell lines, including L5178Y, HeLa, and PC12 cells (Liu *et al.*, 2009). On the other hand, ion peak at m/z 435.203 was the first reported dioxomorpholine and isolated from the ergot fungus *Claviceps purpurea* (Abe *et al.*, 2014). Structures of the compounds are presented in Figure 4.16.

Furthermore, the discriminating features that were encircled in Figure 4.13B from flower, stem and root with p -values < 0.05 , were predicted and dereplicated as listed in Table 4.5. The detected discriminating metabolites for the outlying root extracts from the PCA model were the same as the predicted active metabolites in the OPLS-DA model.

On Table 4.4, as indicated by OPLS-DA, the top 5 VIP metabolites were predicted and dereplicated. These VIP metabolites were defined as the discriminating features for anticancer activity of the extracts. VIP scores were generated by MetaboAnalyst®, which were comparable with the results from VIP analysis by SIMCA® as highlighted in the black box in Figure 4.15. These discriminating metabolites would be targeted for isolation work

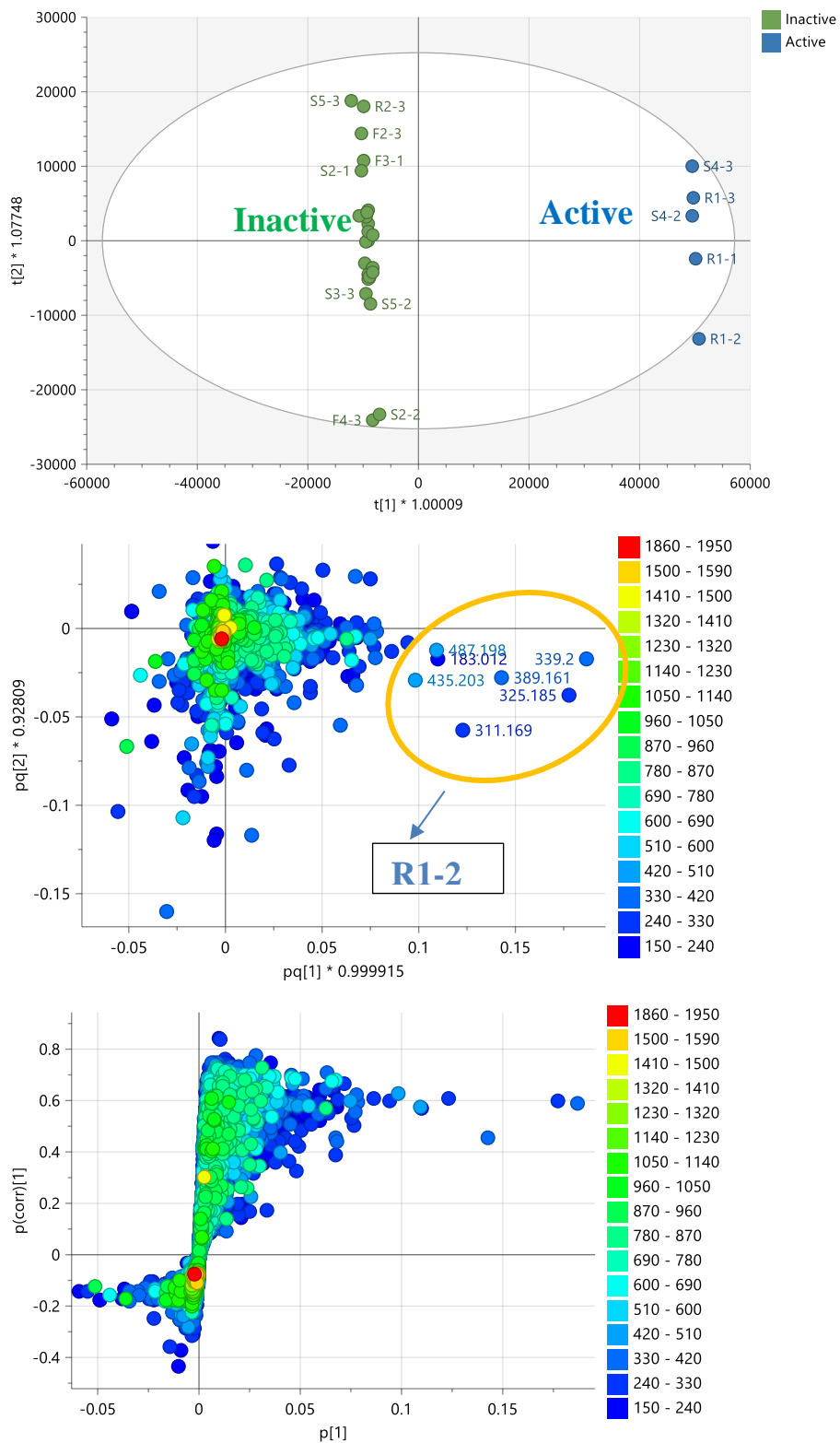


Figure 4.14 : A) OPLS-DA scores, B) loadings, and C) S- plots of LC-HRMS fungal endophyte grouped according to their bioactivity against breast cancer cell line ZR-75. The highlighted box indicated the metabolites from R1-2. $R^2 = 0.99$ and $Q^2 = 0.76$.

Table 4.4: Top 5 VIP (Variable Importance in Projection) dereplicated metabolites that define the discriminating features of anticancer bioactive extracts. The compounds are arranged according to their increasing *p*-values.

Primary ID	<i>p</i> -value	<i>m/z</i>	Rt	MW	Compound Hit	molecular formula (DBE)	Compound hits (sources)
N_4831	0.0001	435.2030	13.56	436.2110	ergosecalinine	C ₂₄ H ₂₈ N ₄ O ₄ (9)	<i>Claviceps purpurea</i>
N_5	0.0003	311.1690	21.68	312.1760	4-methylbenzenesulfonyl-dihydrocitronellol	C ₁₇ H ₂₈ O ₃ S (4)	1 hit, unrecorded source
N_11	0.0004	339.2000	25.65	340.2080	4-methylbenzenesulfonyl-1-dodecanol	C ₁₉ H ₃₂ O ₃ S (4)	1 hit, unrecorded source
N_4049	0.0090	389.1610	15.99	390.1690	6- <i>O</i> -(5-carboxy-2 <i>E</i> ,4 <i>E</i> -pentadienoyl)11,12-epoxy-7-drimene-6β,9α,11α-triol	C ₂₁ H ₂₆ O ₇ (9)	103 hits, <i>A. ustus</i>
N_90	0.4290	196.0970	11.89	197.1050	tenuazonic acid	C ₁₀ H ₁₅ NO ₃ (3)	20 hits, <i>Alternaria tenuis</i> , <i>Alternaria longipes</i> , <i>Alternaria linicola</i> , <i>Alternaria alternata</i> , <i>Alternaria tenuissima</i> , <i>Aspergillus sp. F1404</i> , <i>Aspergillus tamarii</i>

Legend: For multiple hits, chosen compounds listed in the table were filtered for fungal source only.

Table 4.5: Discriminating feature of fungal extracts obtained from different plant parts with p -values < 0.05. Compound structures are shown in Figure 4.16.

Var ID	p -value	m/z	Rt	mass	compound hit	molecular formula	reported source
Discriminating features of the fungal extracts obtained from the roots							
N_4101	2.4E-17	247.1342	16.13	248.1415	1-hydroxy-1,3,5,7(14)-bisabolatetraen-15-oic acid (1)	C ₁₅ H ₂₀ O ₃	<i>Aspergillus sp.</i>
N_4049 N_4826	1.1E-13	389.1613	15.99	390.1686	6- <i>O</i> -(5-carboxy-2 <i>E</i> ,4 <i>E</i> -pentadienoyl)11,12-epoxy-7-drimene-6 β ,9 α ,11 α -triol (2)	C ₂₁ H ₂₆ O ₇	<i>A. ustus</i>
N_4827	1.3E-08	391.1771	14.37	392.1844	krepene A (3)	C ₂₂ H ₃₂ O ₂ S ₂	<i>Cladiella krempfi</i>
P_2837	4.3E-08	253.1794	14.62	252.1721	deoxyuvidin B (4)	C ₁₅ H ₂₄ O ₃	<i>Alternaria brassicae</i> , <i>A. ustus</i>
N_4838	4.2E-06	393.1930	13.97	394.2003	10-deoxy alternaric acid (5)	C ₂₁ H ₃₀ O ₇	<i>A. solani</i>
N_4825	7.3E-06	363.1458	14.85	364.1531	fudecadione B (6)	C ₁₉ H ₂₄ O ₇	<i>Aspergillus sp.</i> , <i>Penicillium sp.</i> BCC 17468
N_4839	1.1E-04	263.1294	13.67	264.1367	ustusorane F (7)	C ₁₅ H ₂₀ O ₄	<i>A. ustus</i> 094102
N_4831	1.6E-04	435.2034	13.56	436.2107	ergosecalinine (8)	C ₂₄ H ₂₈ N ₄ O ₄	<i>Claviceps purpurea</i>
N_4085	1.1E-03	487.1982	17.26	488.2055	no hits	-	-
N_5	6.5E-03	311.1692	21.68	312.1765	4-methylbenzenesulfonyl-dihydrocitronellol No structure found	C ₁₇ H ₂₈ O ₃ S	-
N_77	1.7E-02	956.5944	20.07	957.6016	no hits	-	-
N_3	1.8E-02	325.1848	23.57	326.1920	no hits	-	-
N_11	2.3E-02	339.2003	25.65	340.2076	4-methylbenzenesulfonyl-1-dodecanol (9)	C ₁₉ H ₃₂ O ₃ S	-

Discriminating features of the fungal extracts obtained from the flower							
N_2313, N_90	2.1E-01	196.0974	11.90	197.1047	tenuazonic acid (10)	C ₁₀ H ₁₅ NO ₃	<i>Alternaria tenuis</i> <i>Aspergillus sp.</i>
P_237	5.1E-03	231.1224	7.90	230.1151	S-(6-hydroxyhexyl)itaconic acid (11)	C ₁₁ H ₁₈ O ₅	<i>A. niger</i> , <i>Penicillium sp.</i> J05B-3-F-1
N_93	6.9E-03	417.1620	10.25	418.1693	bufogargarizanine C (12)	C ₁₆ H ₂₆ N ₄ O ₉	Isol. from the skin of <i>Bufo</i> <i>bufo gargarizans</i>
N_91	1.9E-02	628.2568	11.81	629.2641	no hits	-	-
N_92	2.2E-02	415.1862	11.94	416.1935	no hits	-	-
P_5465, P_357	3.9E-02	198.1123	11.82	197.1050	isotenuazonic acid (13)	C ₁₀ H ₁₅ NO ₃	<i>Alternaria tenuis</i> <i>Aspergillus sp.</i>
P_17	4.8E-02	239.1388	11.80	238.1315	N-[(4-acetylamino)butyl-5-(hydroxymethyl)-1H-pyrrole-2-carboxaldehyde (14)	C ₁₂ H ₁₈ N ₂ O ₃	<i>Fusarium incarnatum</i> HKI00504
P_15	4.9E-02	199.1155	11.85	198.1083	no hits	-	-
P_1	5.0E-02	347.2210	17.62	346.2137	laricifolin B (15)	C ₂₁ H ₃₀ O ₄	<i>Hypericum olympicum</i>
Discriminating feature of the fungal extracts obtained from the stem							
P_460	3.7E-02	177.0544	8.57	176.0472	1,3,8-naphthalenetriol (16)	C ₁₀ H ₈ O ₃	<i>A. fumigatus</i> , <i>Alternaria</i> <i>sp.</i>
P_357	1.9E-02	181.0857	15.21	180.0785	3-propylgentisylquinone (17)	C ₁₀ H ₁₂ O ₃	<i>Paecilomyces berolinensis</i> <i>fungal isolate</i> CR1223-D
P_34	1.3E-05	211.1439	6.89	210.1366	6-(1-methylethyl)-3-(2-methylpropyl)-2(1H)-pyrazinone (18)	C ₁₁ H ₁₈ N ₂ O ₂	<i>A. oryzae</i>
P_359	5.3E-04	285.0753	19.47	284.0680	macrosporin (19)	C ₁₆ H ₁₂ O ₅	<i>A. solani</i>
N_7	9.1E-04	211.0397	19.50	212.0470	3-hydroxyxanthone (20)	C ₁₃ H ₈ O ₃	-

N_1	1.0E-03	283.0616	19.48	284.0689	1-hydroxy-2,3-dimethoxyanthraquinone (21)	C ₁₆ H ₁₂ O ₅	<i>Rubia tinctorum</i> <i>Morinda citrifolia</i>
N_4	1.1E-03	240.0431	19.47	241.0503	cotarnoline hydrochloride (22)	C ₁₁ H ₁₂ ClN O ₃	-
N_2	1.3E-03	268.0382	19.48	269.0455	no hits	-	-
P_360	2.8E-03	280.2631	16.89	279.2558	2,4-tetradecadienoic acid isobutylamide (23)	C ₁₈ H ₃₃ NO	<i>Chrysanthemum frutescens</i>
P_364	2.2E-02	263.1274	21.64	262.1201	<i>O</i> -prenylporriolide (24)	C ₁₅ H ₁₈ O ₄	<i>Alternaria porri</i>
P_358	2.2E-02	306.1694	16.18	305.1621	porritoxin (25)	C ₁₇ H ₂₃ NO ₄	<i>Alternaria porri</i> , <i>A. solani</i>
P_1503	2.7E-02	181.0858	18.73	180.0785	3-propylgentisylquinone (26)	C ₁₀ H ₁₂ O ₃	<i>Paecilomyces berolinensis</i> <i>fungus isolate CR1223-D</i>
N_2473	3.9E-02	286.1090	10.94	287.1163	pyrophen (27)	C ₁₆ H ₁₇ NO ₄	-
For multiple hits, chosen compounds listed in the table were filtered for a fungal source and members of the Asteraceae family only.							

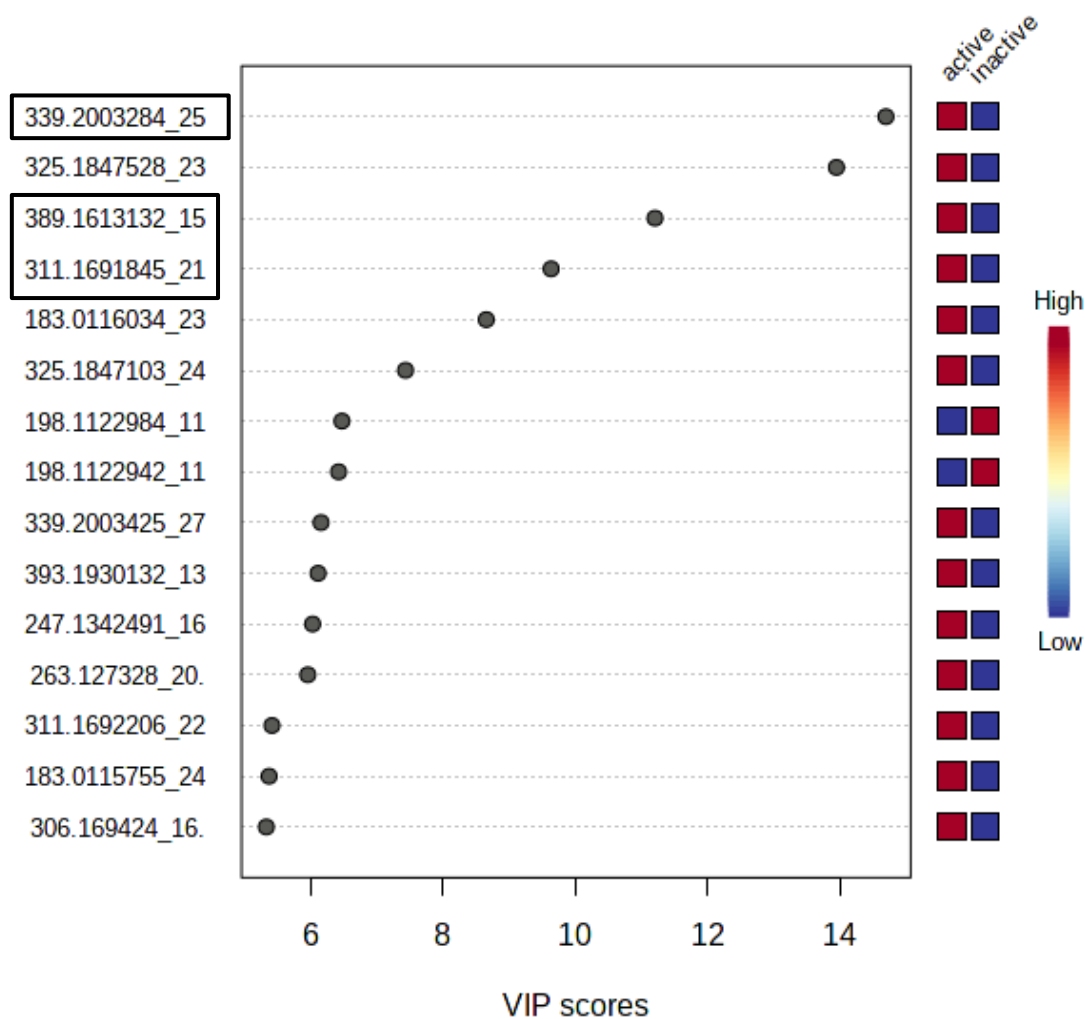


Figure 4.15: VIP analysis generated by MetaboAnalyst® for the LC-HRMS data fungal extracts of endophytes from various plant parts of Jordanian chamomile, The extracts were grouped according to their bioactivity against breast cancer cell line ZR-75. The boxed metabolites were the discriminating features hypothesised to be responsible for the anticancer activity of the extracts.

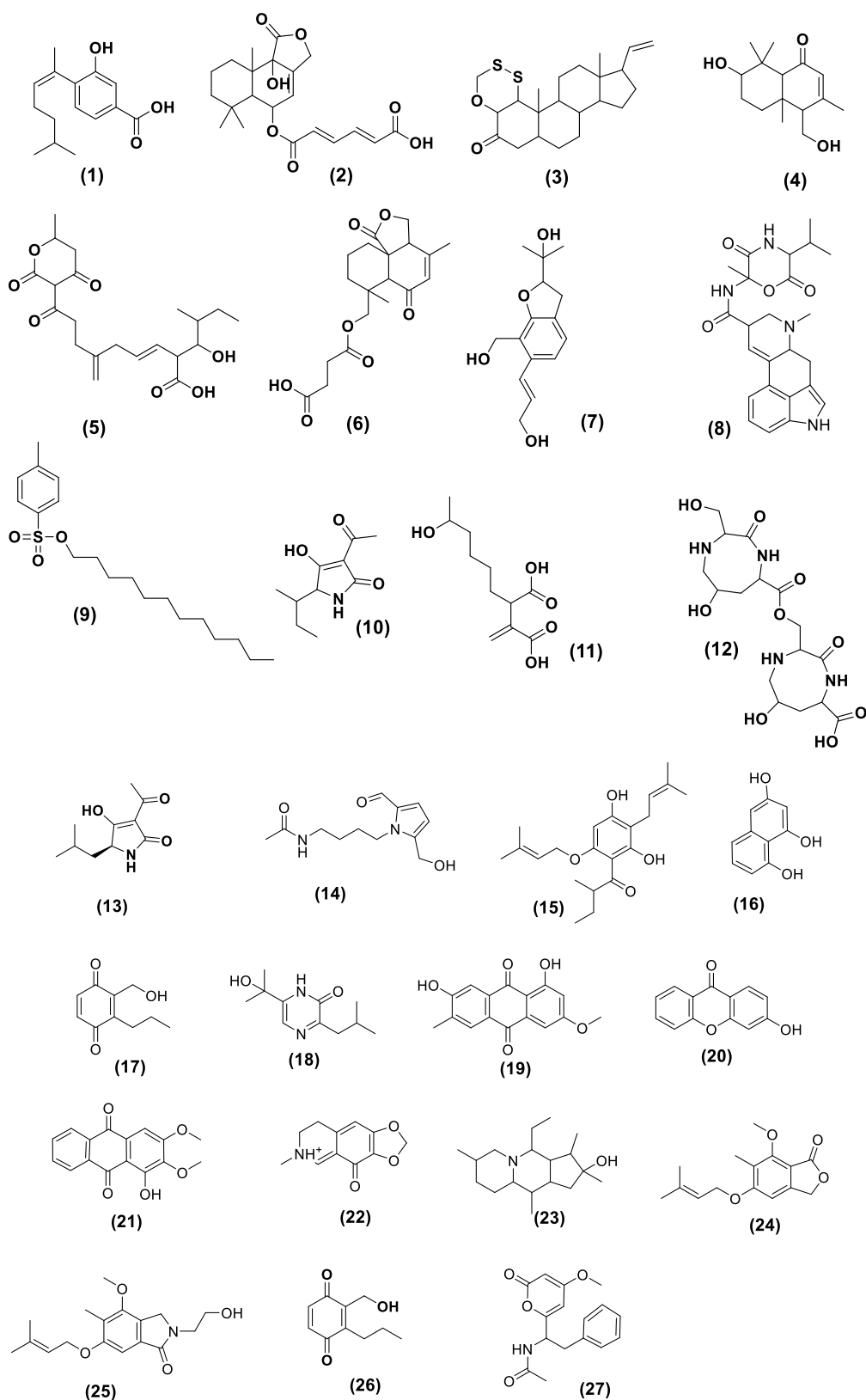


Figure 4.16: Structures of the discriminating metabolites of fungal extracts obtained from different plant as predicted by OPLS-DA loadings plots as listed in Table 4.5.

4.7. ITS gene sequencing

The bioactive isolated endophytic fungi were subjected to ITS gene sequencing, to identify the fungus strain responsible for the bioactivity. Upon visualising the gel, DNA bands were present in the electrophoresis plates under the UV. For quality control, the blank sample was placed in the plate and ran alongside the fungi samples. Any contamination in the plate should be detected by the blank sample.

Two endophytes were chosen for medium optimisation based on their chemical profile and biological activity, including *A. ustus* and *A. solani*, as shown in Table 4.6. Using the FinchTV program, the sequencing results from BLAST were processed and compared to NCBI-blast database. The ITS sequencing results were illustrated in Appendix 1 and 2.

Table 4.6: The obtained bioactive endophytes and their identity.

Plant source	Sample ID	Concentration ng/mL	Band size (bp)	Endophytic Fungus
flower	R1-2	10.1	1800-2000	<i>A. ustus</i>
	R1-3	9.2	1800-2000	
seed	S4-2	5.5	500-700	<i>A. solani</i>
	S4-3	6.1	500-700	

4.8. Summary of the preliminary screening results

Among the tested fungal isolates, only two endophytes (*A. ustus* and *A. solani*) were able to significantly reduce the cell viability of the breast cancer cells by more than 80 percent but none of the isolated endophytes exhibited antioxidant activity. There were a few factors that needed to be taken into consideration for future media optimisation and scale-up work. These factors included biological activity, high extract yield, and the uniqueness of chemical profiles of the individual extracts. According to the results of the multivariate analysis of their NMR and mass spectral datasets, both *A. ustus* and *A. solani* produced extracts with the most distinct chemical profiles. Furthermore, IC_{50} were calculated. In the anticancer bioassays, both endophytes were potent and had an IC_{50} s of approximately 1.3 $\mu\text{g/mL}$. Nevertheless, *A. solani* produced lower yields when compared to *A. ustus*.

Endophytes have higher sustainability compared to the plant because the microorganisms are not dependent on the season to grow them. Dormant cultures can be stored in the repository and taken anytime for the inoculation and scaleup. Since the production of the compounds are not also dependent whether the plant is stressed or not, the more is the application of endophytes as a source is of a greater advantage.

5. Optimising the production of bioactive fungal extracts

5.1. Optimising the production of anticancer bioactive metabolites in *A. ustus*

Aspergillus and other filamentous fungus are well-known for their capability to produce a wide range of chemical metabolites that have biological activity (Tawfike *et al.*, 2017). These compounds are classified chemically by their biosynthetic origin, which include Immunosuppressants, antibiotics, mycotoxins, and cholesterol-lowering (Keller *et al.*, 2005).

There are 26 identified *Aspergillus* species in the section Usti. Most of them are unable to live at 37°C and are hence not considered human pathogens such as *A. ustus*. (Jurjevic and Peterson, 2016). *A. ustus* are prolific generator of wide variety of natural products including metabolites of mixed polyketide and terpene biosynthesis such as the meroterpenoids, sesquiterpenes and sesterterpenes, which are produced in large quantities (Geris and Simpson, 2009, Ebel, 2010). Drimane sesquiterpenoid alcohols and lactones are widely recognised bioactive metabolites obtained from *A. ustus* (Liu *et al.*, 2009, Lu *et al.*, 2009).

Numerous research groups have investigated the chemical composition of *A. ustus*. This species produces mycotoxins that are meroterpenoid derivatives, isochromane derivatives, drimane sesquiterpene esters, and ophiobolins (Lu *et al.*, 2009). Many of them displayed an interesting biological activity, including suppression of plant growth and inhibition of endothelin-type B receptors (Li *et al.*, 2022, Shang *et al.*, 2022). The produced secondary metabolites of the isolated endophyte from Jordanian chamomile will be discussed in detail in chapter 6. In this chapter, a metabolomics-guided approach was used to optimise fermentation conditions for *A. ustus* and to detect the production of interesting secondary metabolites during the scaling-up process.

5.1.1. Extract yields on different media.

Solid media produced higher yields of extract than liquid media. As depicted in Table 5.1, the highest yield of *A. ustus* extract was gained from oat medium. Meanwhile, the lowest extract yield was obtained from Wickersham liquid medium, both of which were cultured for 30 days. The obtained yield of the extracts of *A. ustus* after 7, 15, and 30 days of incubation on four different media are listed in Table 5.1 and shown in the histogram shown below (Figure 5.1). *A. ustus* has achieved the peak of its log growth phase after 30 days of incubation in both oat and potato-dextrose media moving into the stationary as demonstrated in Figure 5.1. So, the optimum extract yields for potato-dextrose and oat media, were afforded on the 30th day. As result of incubation on Wickersham broth as well as in rice broth for 30th day, the extract yields started to decline, which indicated the completion of the stationary phase and beginning of the death phase. On 15th day of incubation, the extract yield from rice and Wickersham media has reached its optimum.

Table 5.1: Yields (in mg) obtained from *A. ustus* extracts grown in four different media and extracted after various incubation periods. All cultures were incubated at 27°C.

Type of medium	Incubation period		
	7 Days	15 Days	30 Days
Liquid media			
Potato-dextrose	37.9	72.4	228.6
Wickersham media	75.2	119.4	106.7
Solid media			
Rice media	188.1	220.5	169.5
Oat media	378.6	489.0	690.1

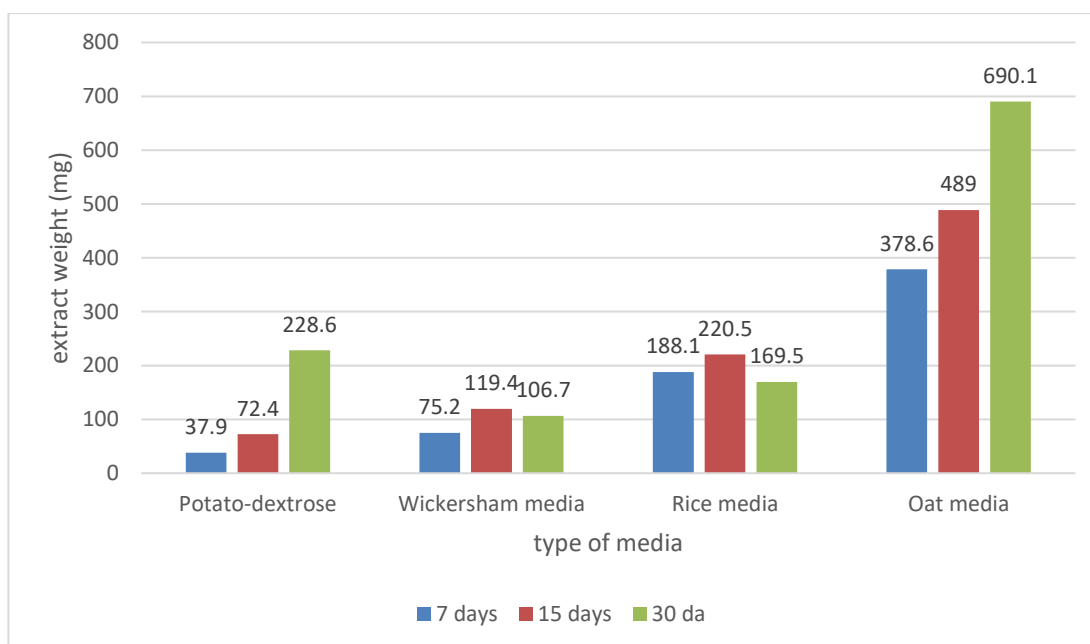


Figure 5.1: Histogram of extract weights of *A. ustus* obtained from four different media and incubated at 7, 15, and 30 days.

5.1.2. Biological assay

Before selecting the optimal medium for large-scale fermentation, the biological activity of *A. ustus* extracts obtained from various media were tested against ZR-75 cells. As depicted in Figure 5.2, only potato-dextrose medium afforded a strongly active fungal extract against breast cancer (ZR-75) cell line after 30 days of incubation, where cell viability was almost zero. However, the fungal extracts from the potato-dextrose medium incubated for 7 and 15 days were inactive, giving a percent cell viability of about 80%. The extract obtained after 30 days of incubation in potato-dextrose was most suitable for scaleup work. The rest of the other *A. ustus* extracts obtained from the other media were inactive against ZR-75 cells. Both ^1H NMR and LC-HRMS data were used to investigate the chemical composition of the afforded extracts.

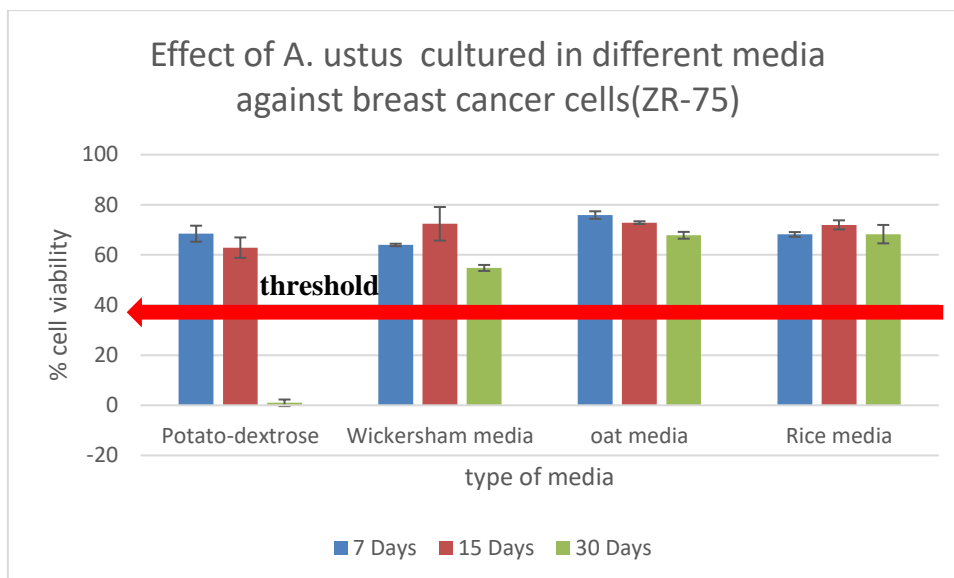


Figure 5.2: AlamarBlue® cell viability assay results of 30 μ g/mL of *A. ustus* extracts. The red line indicates the bioactivity threshold.

5.1.3. NMR spectroscopy for *A. ustus* extracts

5.1.3.1. Rice media

The proton NMR spectra of *A. ustus* extracts obtained from rice medium after 7, 15, and 30 days of incubation were comparable to those of the blank media. So, the production of secondary metabolites was very small, as shown in Figure 5.3. The NMR spectrum of the resulting extract afforded the presence of unsaturated fatty acids identical in the blank medium. This was indicated by methylene resonances for an aliphatic chain observed at 1.00 to 1.50 ppm along with α -proton signals at 2.00 to 2.40 ppm. Furthermore, the ^1H NMR spectrum revealed the presence olefinic proton resonating at 5.25 ppm. However, the endophyte started to generate a small amount of aromatic chemicals at 30 days of incubation. The secondary metabolites included aromatics compounds that are indicated by the blue box in Figure 5.3 (δ_{H} 6.00 – 7.00). These were substituted by electron withdrawing groups that shifted the protons of the benzene ring downfield to 7.25 ppm.

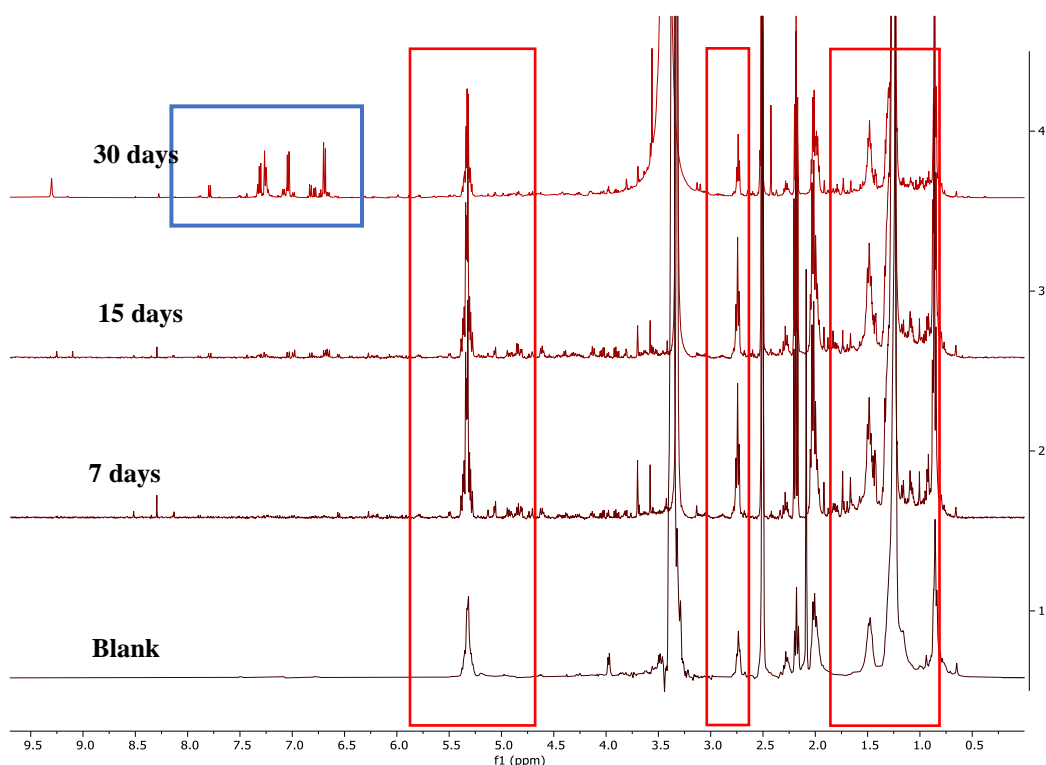


Figure 5.3: The ¹H NMR (500 MHz) data obtained from *A. ustus* extracts after incubation in solid-rice medium incubated for 7, 15, 30 days, measured in DMSO-d₆

5.1.3.2. Oat media

The ¹H NMR spectra obtained from oat blank medium and fungal extracts revealed no significant differences. Most of the solid oat medium peaks remained in the endophyte extract after 30 days of incubation, as shown by the red boxes in the Figure 5.4. This indicated that the fungus may not be consuming or processing media nutrients resulting in poor secondary metabolites production but there could be an increase production of primary metabolites as reflected by the high biomass produced in comparison to the other culture media employed.

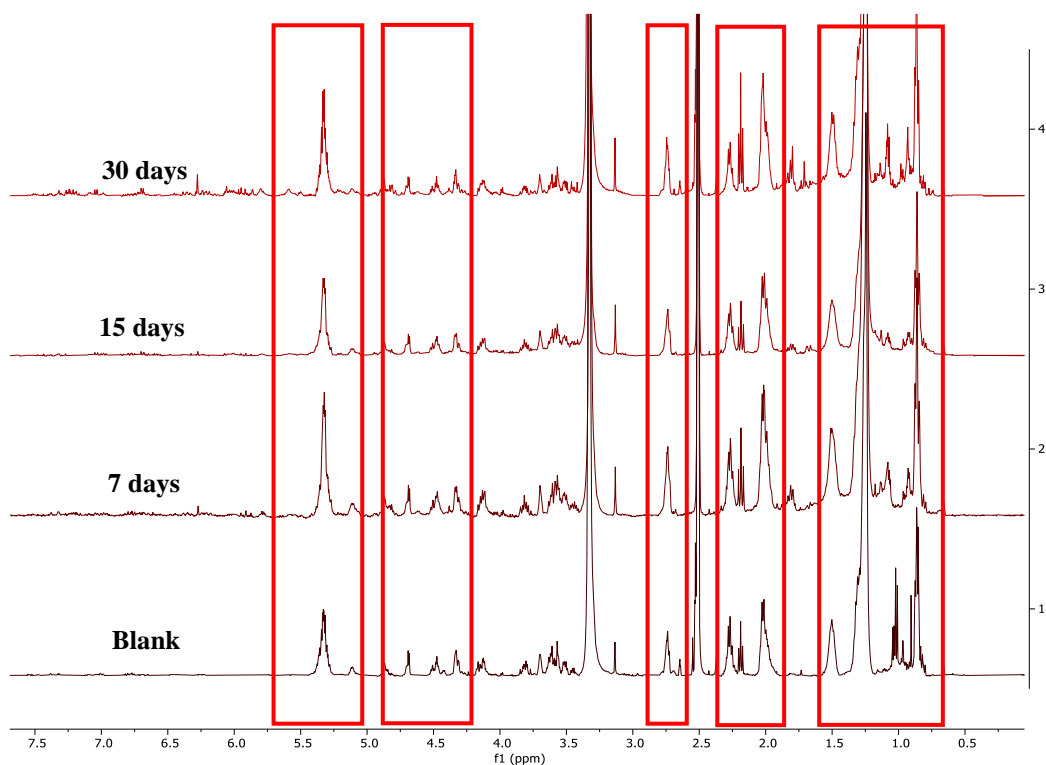


Figure 5.4: The ^1H NMR (500 MHz) data obtained from *A. ustus* extracts after incubation in solid-oat medium incubated for 7, 15, 30 days, measured in DMSO-d_6

5.1.3.3. Potato-dextrose media

As illustrated by the ^1H NMR spectra (Figure 5.5) for potato-dextrose medium extracts, the biosynthesis of the secondary metabolites was detected at 15 and 30 days. The secondary metabolites could be related to olefinic or aromatics compounds that are indicated by the blue box (δ_{H} 5.90–7.00) in Figure 5.5. High-intensity of signals could be noticed at 0.50 to 2.50 ppm (green box), representing aliphatic parts, which were comparable to blank's components (red box). Additionally, incubating the endophyte for 30 days, increased the concentration and diversity of secondary metabolites produced, as seen in the black box. This was implied by the presence of additional signals at 9.00 to 10.0 ppm in the ^1H spectra of the fungal extract obtained at 30 days of incubation. *A. ustus* extracts obtained from potato-dextrose medium afforded high yield of aliphatic and hydroxylated and compounds as indicated by resonances exhibited at 0.50 and 5.50 ppm, respectively, including various saturated and unsaturated fatty acids.

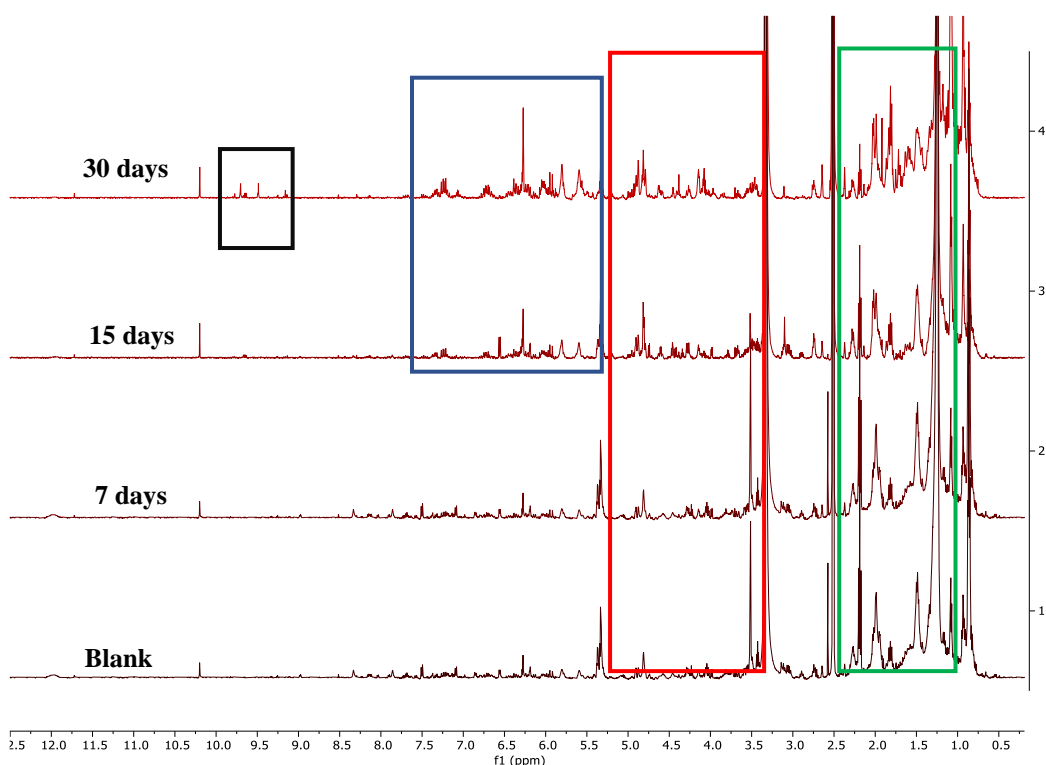


Figure 5.5: The ¹H NMR (500 MHz) data obtained from *A. ustus* extracts after incubation in potato-dextrose medium incubated for 7, 15, 30 days, measured in DMSO-d₆

5.1.3.4. Wickersham media

When the endophyte was incubated in liquid-Wickersham media, the number of compounds produced was very low. In the liquid-Wickersham culture extracts, most signals observed in the ¹H NMR spectra were derived from the medium components, as shown in Figure 5.6 (highlighted in blue boxes). As depicted in Figure 5.6, fatty acid signals were observed in the ¹H NMR spectrum. The huge intensity signals at 1.00 to 1.50 ppm is typical for methylene units of a long fatty acid chain. Furthermore, the olefinic protons present in unsaturated fatty acids were found at around 5.00 to 5.50 ppm. The proton signals at 2.10 to 2.40 ppm could be accounted for α-protons of a terminal carboxylic acid moiety.

After 30 days of incubation, the endophyte began to produce a small quantity of aromatic compounds. This was observed with the occurrence of proton signals at 6.00 to 6.50 ppm, as shown in Figure 5.6 (red box). However, the production of these

molecules were very low when compared to the fatty acids, as exhibited by their high intensity peaks.

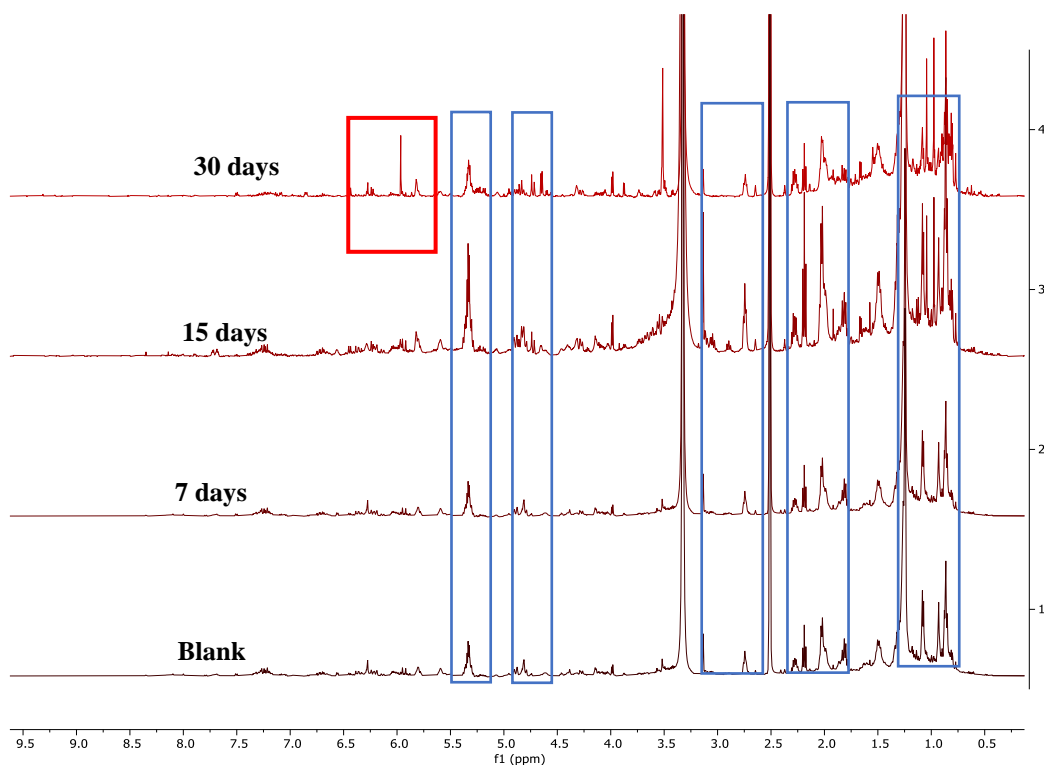


Figure 5.6: The ¹H NMR (500 MHz) data obtained from *A. ustus* extracts after incubation in Wickersham medium incubated for 7, 15, 30 days, measured in DMSO-d₆

5.1.4. Multivariate analysis of NMR data

PCA scores plot of the ¹H NMR spectral data of *A. ustus* extracts illustrated similarity and difference between various media incubated for 30 days, as shown in Figure 5.7. Extracts obtained from the four media at 7th and 15th day of incubation were excluded. *A. ustus* is a slow growing fungus that significant growth could be first observed on the 21st day of incubation. As a result, poor production of metabolites was observed at 7th and 15th day of incubation. As seen in Figure 5.7A, the extracts were categorised according to the different media at 30 days of incubation. The generated PCA-loadings plot (Figure 5.7B) depicted the type of functional groups present in each extract of *A. ustus* inoculated on various media. The ¹H NMR spectral data of potato-dextrose medium extracts were dispersed in the lower left quadrant (encircled blue) of the PCA loadings plot, which showed high intensity of peaks at the aliphatic region between

0.0 and 2.00 ppm with few peaks at the olefinic region between 5.00 and 7.00 ppm. The extracts obtained from the oat media were dispersed between the left and right upper quadrant were mainly characterised by sugar types of metabolites indicated by their chemical shifts between 3.00 and 5.00 ppm (encircled red). Sugars or carbohydrates could have been extracted from the undepleted oat media or are primary metabolites that have been further produced by the fungus resulting to an increase biomass yield. Meanwhile, the *A. ustus* extracts from Wickersham medium were found in the upper left quadrant of the plot containing few metabolites resonating mainly between 5.00 and 6.00 (encircled green). Poor production of secondary metabolites was observed for the Wickersham media extracts. This may be influenced by the poor yield of the fungal extracts from Wickersham medium. Whereas extracts obtained from rice media were located at the right side of the plot containing metabolites that showed more diversity in their chemical profile with a wider range of resonance between 0.00 and 8.00 ppm (encircled orange). R^2 and Q^2 values were 0.994 and 0.966 respectively, which indicated an excellent fitted model and predictability. The difference between R^2 and Q^2 values was less than 0.3, which suggested the model was not overfitted.

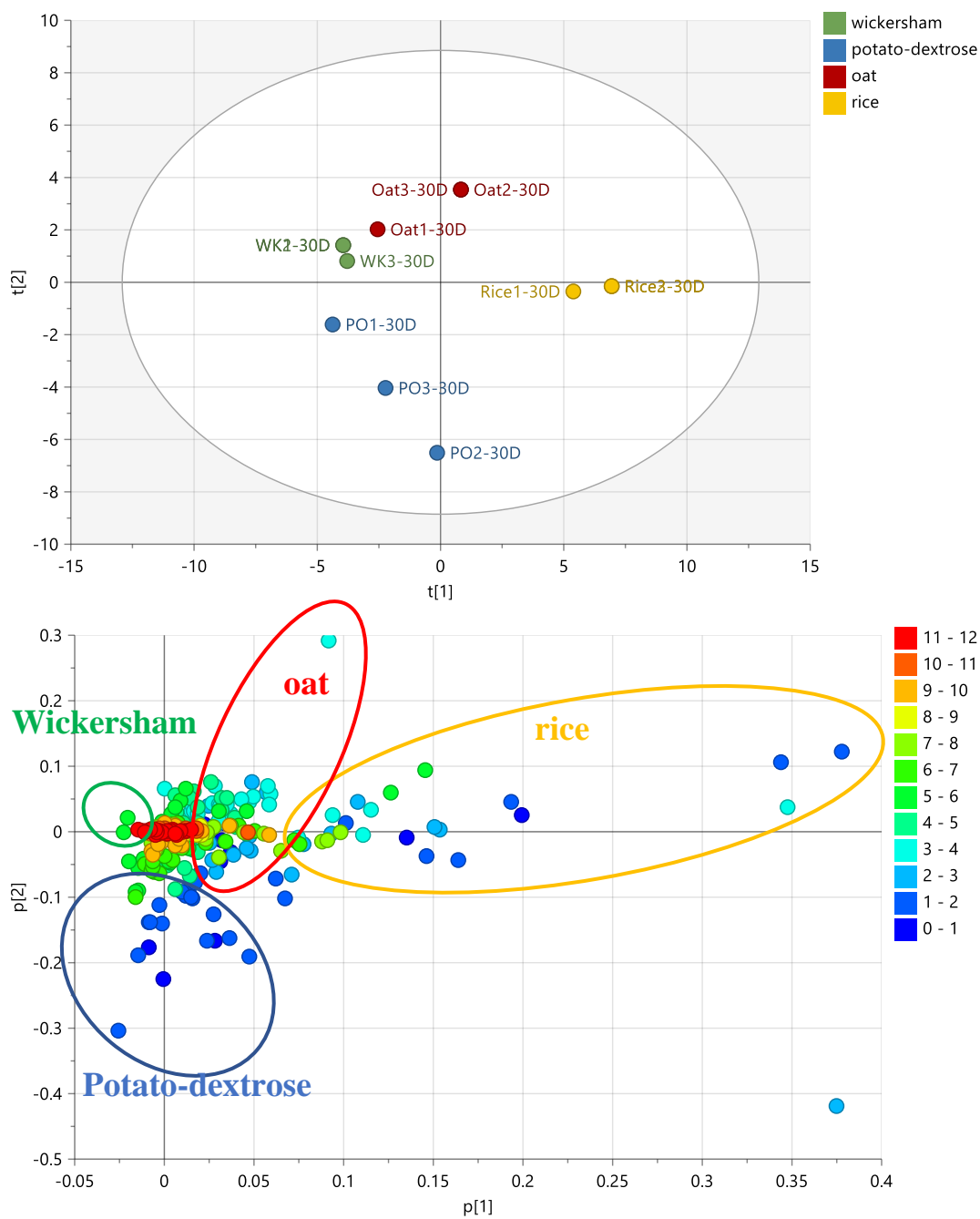


Figure 5.7: (A) PCA scores and (B) loading plots of ¹H NMR spectral data of *A. ustus* extracts obtained from four different media incubated at 30 days. $R^2 = 0.994$ and $Q^2 = 0.966$.

Additionally, OPLS-DA was performed by classifying the media extracts based on their bioactivity against the breast cancer cell line ZR-75. Incorporating the results of AlamarBlue® on OPLS-DA, the active extracts were positioned on the right and inactive extracts on the left side of the scores plot, as shown in Figure 5.8A. According to the OPLS-DA loadings plot, the upper right active quadrant entailing the potato-dextrose extract after incubation for 30 days were dominated with resonances between 0.00 and 2.00 ppm indicating the occurrence of aliphatic compounds. However, the occurrence of a wider range of resonances between 4.00 and 7.00 ppm indicating the presence of hydroxylated, olefinic and aromatic active compounds seem to be common to both active and inactive extracts. The discriminating chemical shifts from the bioactive media extracts were encircled in red, as illustrated in Figure 5.8B. whereas the inactive media extracts exhibited a wider range of resonance between 0.00 to 8.00 ppm. R^2 and Q^2 values were 0.999 and 0.998, respectively. This indicated a model with excellent fitness and predictability. However, $R^2X_o[1]$ gave a variation score of 55.7 % and the difference within groups $R^2X[2]$ of 16.1%. The variation score across groups is bigger than the variation score within groups, which indicated an excellent separation between the active and inactive extracts.

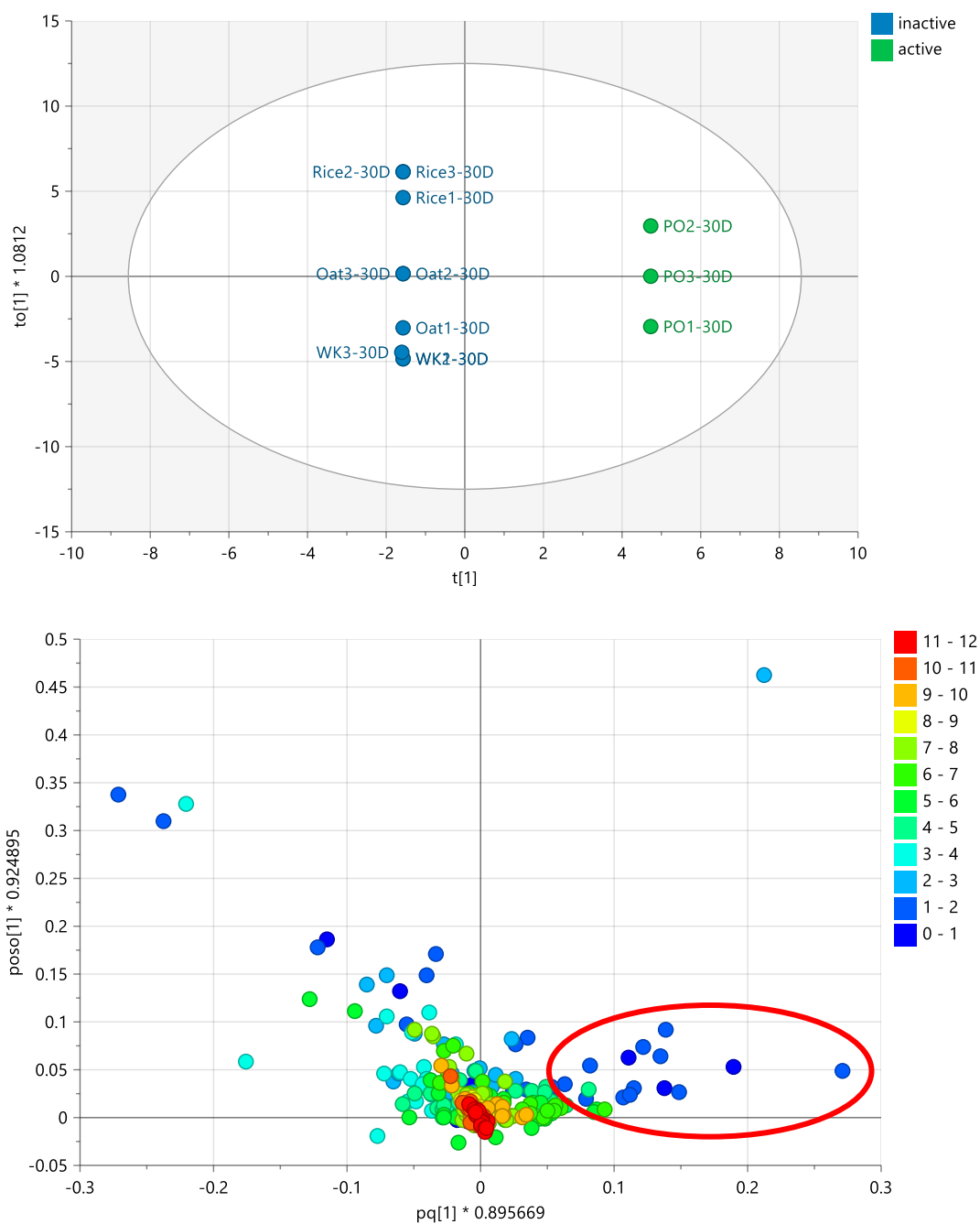


Figure 5.8: (A) OPLS-DA scores and (B) loadings plots of ^1H NMR spectral data of *A. ustus* extracts obtained after incubation on different media classified according to their AlamarBlue® results against breast cancer cell line ZR-75. R^2 and Q^2 values were 0.999 and 0.998, respectively. The difference between group $R^2X_0[1]$ is equal to 55.7 % and the difference within groups $R^2X[2]$ is 26.1%. Encircled features on the loadings plot indicate the discriminating chemical shifts for the biologically active extracts against breast cancer cells line ZR-75.

5.1.5. Multivariate analysis of LC-HRMS data

For multivariate analysis, a PCA scores plot was generated for the LC-MS data. The extracts were grouped according to the different media in which the fungus was inoculated for 7, 15 and 30 days. As of the observed variance between the incubation time of various growth media, extracts from 7 and 15 days of incubation were included in the study. The PCA scores plot (Figure 5.9 A) of the LC-HRMS data of *A. ustus* revealed that extracts obtained from potato-dextrose, rice and oat after 30 days of incubation were found in the right side of the plot, which implied a strong similarity in their metabolomic profiles (encircled in red). Meanwhile, Wickersham media extracts incubated for 7 and 30 days were outlying on the lower and upper left quadrants, respectively (encircled blue). While extracts obtained from Wickersham media at 15th day were dispersed in the lower left quadrant. This suggested that there was a strong likelihood that a more distinct profile was afforded with Wickersham medium between the three incubation periods when compared to the other media extracts. Furthermore, *A. ustus* extracts obtained from rice and oat media at 7 and 15 days of incubation were clustered in the upper right quadrant of PCA plot (encircled orange).

The loadings plot in Figure 5.9 B demonstrated that extract from rice and oat at 7 and 15 days produced low MWt metabolites ranging from 150 to 300 Da (encircled orange). Meanwhile, 30 days extracts from oat, rice and potato-dextrose contained metabolites with MWt from 150 to 300 Da, as encircled in red. Furthermore, the outlying extracts obtained from Wickersham medium after incubation at 7 days yielded lower MW metabolites discriminated by ion peaks at m/z 212.144, 360.150 Da, while after 30 days, higher MW compounds were yielded, which were separated by metabolites with ion peaks at m/z 591.427, 634.453, 678.479, 722.506 Da. All the above discriminating metabolites gave no compound hits except for ion peaks at m/z 360.150 Da from extracts obtained at 7th day of incubation and 678.479 Da after 30 days of incubation in Wickersham medium (Figure 5.10). These metabolites were putatively identified as turbomycin A and phakelliacerebroside A.

The model gave goodness of fit (R^2) of 0.811 and a good predictability score (Q^2) of 0.534 after seven components. Turbomycin A exhibited broad spectrum of

antibacterial activity against gram-positive and gram-negative bacteria, it was first isolated from cultured soil DNA and was produced from *Escherichia coli* (Gillespie *et al.*, 2002). There were no studies on the anticancer activities of this compound. Phakelliacerebroside A was isolated from the sponge *Phakellia fusca*, and there are no reported studies on the bioactivity of this compound (DNP database) as well.

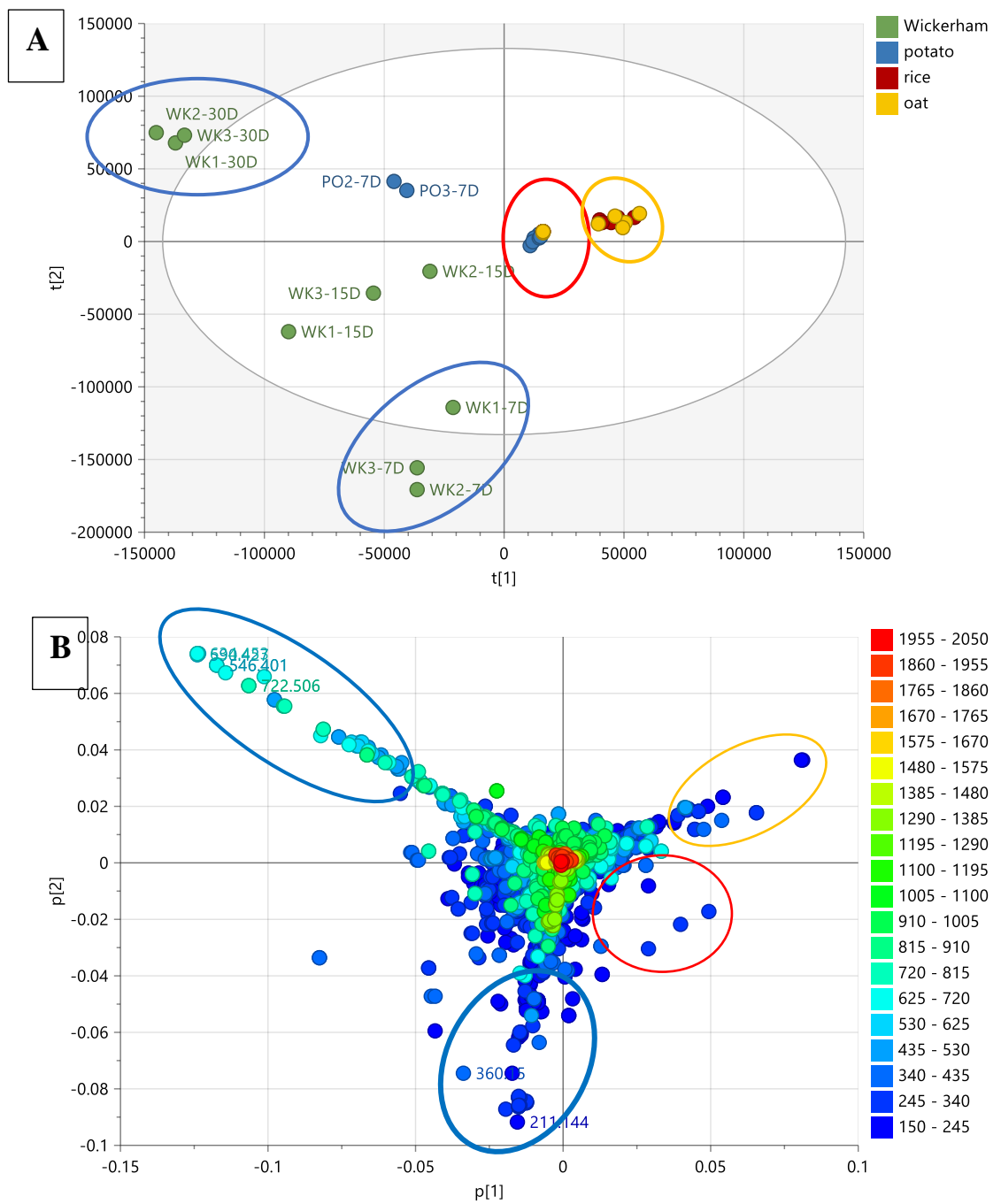
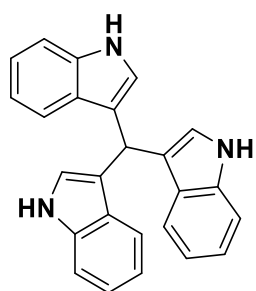
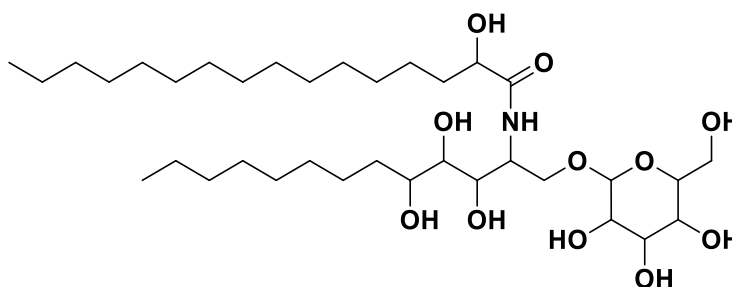


Figure 5.9: (A) PCA scores (B) loading plots of LC-HRMS data of *A. ustus* extracts from four media incubated at 7, 15, and 30 days. $R^2X= 0.811$ and $Q^2X = 0.534$. Encircled features represent the discriminating ion peaks for the outlying extracts obtained from Wickersham media incubated for 7 and 30 days.



Turbomycin A
 Mzmine ID: N_15143
 m/z 360.1502
 rt: 4.19
 MW: 361.1575



Phakelliacerebroside A
 Mzmine ID: N_8269
 m/z 678.4792
 rt: 24.78
 MW: 679.4865

Figure 5.10: Discriminating metabolites from fungal extracts obtained after 7 and 30 days of incubation in Wickersham media.

An OPLS-DA analysis was performed to provide a clearer illustration of the differences in metabolic profiles between fungal extracts isolated from various media (Figure 5.11). It afforded a fitness (R^2) and predictability (Q^2) scores of 0.85 and 0.67, respectively. This indicated good fitting and prediction of the generated model, which improved when compared to the PCA model above. The variation between groups R^2X_o [1] was 17.5% and within group $R^2X[1]$ was 10.5% that indicated low diversity of the samples within the respective groupings. Extracts from *A. ustus* grown on Wickersham media for 7, 15, and 30 days of incubation were closely clustered in the right side of the plot, which were not dispersed as observed on the PCA model and contained metabolites with MW ranging from 240 to 690 Da (encircled green), as shown in Figure 5.11B. *A. ustus* extracts from the rice media incubated at 7 and 15 days were overlapping in the lower left right quadrant containing metabolites with MWs range from 150 to 700 Da (encircled red). Whereas, extracts of *A. ustus* inoculated on oat media at 7th and 15th day of incubation were overlapping in the upper left right quadrant containing metabolites with a wider range of MWs from 250 to 700 Da (encircled orange). However, the metabolites for *A. ustus* extracts obtained from the rice and oat at 30th day of incubation overlapped in the lower left quadrant, indicating that they shared metabolites with a similar range of MWs. On the other

hand, extracts obtained from the potato dextrose media incubated at 7, 15, and 30 days were positioned in the upper left quadrant together with those afforded by the oat media. The discriminating features of *A. ustus* from each media were dereplicated in Table 5.2.

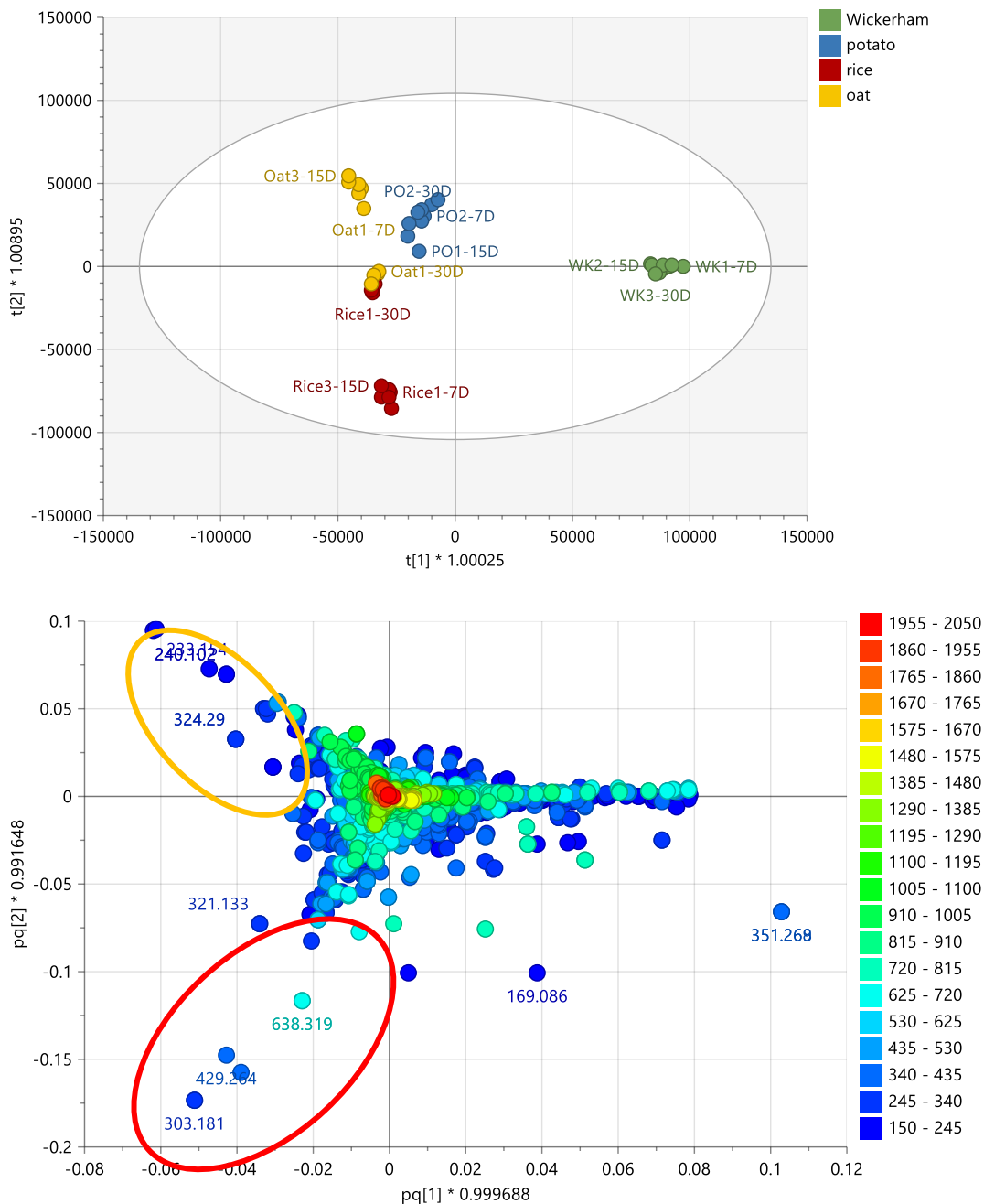


Figure 5.11: (A) OPLS-DA scores and (B) loading plots of LC-HRMS of *A. ustus* extract obtain from different media. The encircled box indicated the discriminating feature for each media extracts. $R^2 = 0.86$ and $Q^2 = 0.76$. The difference between group $R^2X_0[1]$ is equal to 17.5% and the difference within groups $R^2X[2]$ is 10.5%.

Table 5.2: Dereplication of discriminating metabolites of *A. ustus* for the different media. Structures are shown in Figure 5.12.

MZmine ID	p-value	m/z	Rt	MW	compound hits †	Predicted molecular formula (DBE)	Source
Wickersham medium extracts							
N_1780	0.0024	211.14432	5.58	212.1516	cyclo(leucylvalyl) (1)	C ₁₁ H ₂₀ N ₂ O ₂ (3)	<i>A.fumigatus</i>
P_168	0.1003	351.26853	26.49	350.2613	β-apo-12'-carotenal (2)	C ₂₅ H ₃₄ O* (9)	oxidn. of β-carotene
N_15143	0.0002	360.15027	4.20	361.1575	turbomycin A (3)	C ₂₅ H ₁₉ N ₃ (6)	<i>Escherichia coli</i>
N_3063	0.0336	546.40079	25.17	547.4081	no hits	C ₂₉ H ₅₇ NO ₈ (2)	-
N_2763	0.0341	590.42694	25.00	591.4342	no hits	C ₃₁ H ₆₁ NO ₉ (2)	-
N_3160	0.0336	634.45284	24.90	635.4601	no hits	C ₃₃ H ₆₅ NO ₁₀ (2)	-
N_8269	0.1708	678.47929	24.79	679.4866	phakelliocerebroside A (4)	C ₃₅ H ₆₉ NO ₁₁ (1)	<i>Phakellia fusca</i> (sponge)
Rice medium extracts							
P_193	0.0040	303.18148	9.63	302.1742	viridamine (5)	C ₁₆ H ₂₂ N ₄ O ₂ (4)	<i>Penicillium viridicatum</i> CSIR 354
P_401	0.0081	321.13339	23.17	320.1261	aculeatusquinone B (6)	C ₁₇ H ₂₀ O ₆ (8)	<i>A.aculeatus</i>
N_3162	0.0095	429.26441	19.63	430.2717	protoaustinoid A (7)	C ₂₆ H ₃₈ O ₅ (8)	<i>A.nidulans</i>
P_241	0.0001	638.31912	13.61	637.3118	no hits	C ₃₃ H ₄₃ N ₅ O ₈ (15)	
N_2936	0.0001	638.31912	13.61	639.3264	petrosifungin B (8)	C ₃₃ H ₄₅ N ₅ O ₈ (14)	<i>Penicillium brevicompactum</i>
Oat medium extracts							
N_4060	0.0433	233.15401	14.85	234.1613	aspergillusene A (9)	C ₁₅ H ₂₂ O ₂ (5)	<i>A.sydowii</i>
P_389	0.0292	268.19077	15.12	267.1835	menthyl pyrrolidone carboxylate (10)	C ₁₅ H ₂₅ NO ₃ (3)	various sources
N_17584	0.0104	268.19103	14.97	269.1983	N-undecanoylhomoserine lactone (11)	C ₁₅ H ₂₇ NO ₃ (1)	<i>Pseudomonas aeruginosa</i>
P_397	0.0128	227.10689	18.39	226.0996	3-hydroxy-5-methoxystilbene (12)	C ₁₅ H ₁₄ O ₂ (2)	<i>Penicillium commune</i>

N_1520	0.0029	324.29000		325.297	<i>N</i> -(2-hydroxyethyl) oleamide (13)	C ₂₀ H ₃₉ NO ₂ (2)	various sources
N_4049	0.0291	233.15399	14.73	234.1613	terrecyclol (14)	C ₁₅ H ₂₂ O ₂	<i>A. terreus</i>
P_391	0.0217	240.10207	12.04	239.0948	TMC 120B (aspergillitine) (15)	C ₁₅ H ₁₃ NO ₂ (9)	<i>A. ustus</i> , <i>A. pseudodeflectus</i> <i>A. versicolor</i>
N_3947	0.0217	240.10210	12.06	241.1094	TMC 120A (16)	C ₁₅ H ₁₅ NO ₂ (8)	<i>A. ustus</i> <i>A. calidoustus</i>
P_388	0.1188	465.30010	14.86	464.2928	ganodermalactone H (17)	C ₃₀ H ₄₀ O ₄ (11)	<i>Tomophagus</i> sp
Potato-dextrose medium extracts							
P_21	0.0252	169.0861	9.18	168.0789	3-(4-hydroxyphenyl)-1,2-propanediol (18)	C ₉ H ₁₂ O ₃ (4)	<i>A. flavus</i>
P_190	0.3907	231.1382	16.03	230.1310	tavacuran (19)	C ₁₅ H ₁₈ O ₂ (3)	marine sponge <i>Dysidea</i> sp., t nudibranchs: <i>Hypselodoris cantabrica</i> , <i>H. tricolor</i> and <i>H. villafranca</i>
N_17936	0.910	740.5239	28.40	741.5311	phosphatidylethanolamine (20)	C ₄₁ H ₇₆ NO ₈ P (4)	various sources
P_161	0.639	1053.6815	28.38	1052.6742	No hits	-	-
[†] For multiple hits, chosen compound hits were filtered for microbial or fungal species except otherwise. *All other hits were from plant species.							

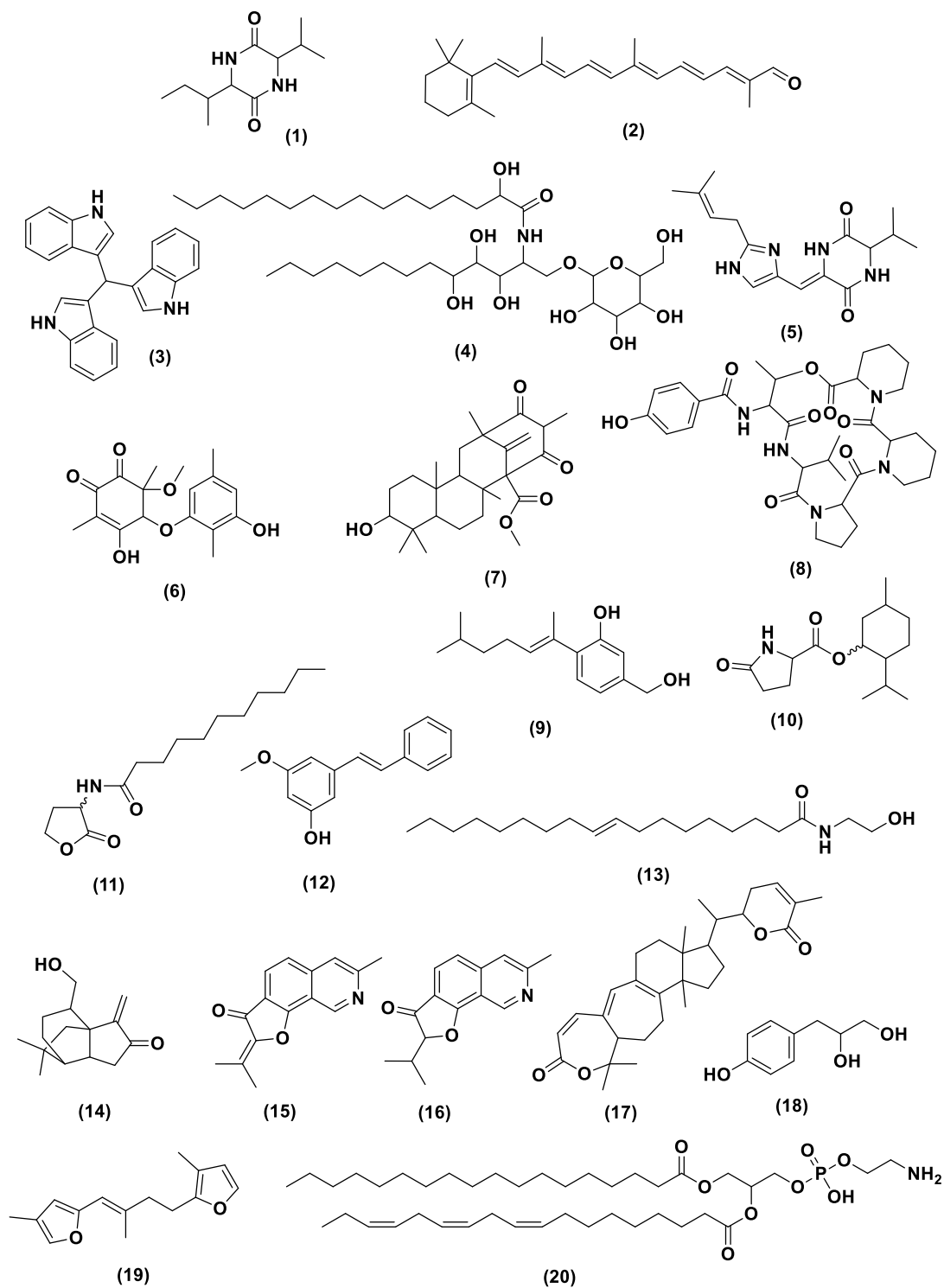


Figure 5.12: Structures of the discriminating metabolites from *A. ustus* extract obtained from different media and listed in Table 5.2

The OPLS-DA of the active versus the inactive extracts was also performed as presented in Figure 5.13. It gave fitness and predictability scores of 0.94 and 0.51, respectively, indicating good fitting and prediction of the generated model. The variation score between groups was 15.2 % while within groups, it was only 2.0% indicating a relatively good homogenous features for the respective classes. The OPLS-DA scores plot in Figure 5.13A positioned the active extracts on the right quadrants, as outliers. Meanwhile, the inactive extracts were dispersed on the left quadrants of the scores plot, as shown in Figure 5.13A. The outlying *A. ustus* extracts obtained from potato-dextrose media at 30th day of incubation were discriminated by metabolites encircled in red with *p*-values < 0.05 (Figure 5.13C), which indicated a strong model with a confidence interval of more than 95%. The bioactive metabolites gave a *m/z* value range between 190 to 1000 Da. From the dereplication results, discriminating metabolites with *p*-values of less than 0.05 are listed in Table 5.3. Eight of the ion peaks remained unidentified, structures of putatively identified compound hits are shown in Figure 5.14. Discriminating features with MWt range between 550 and 790 Da showed low DBE values of 1 to 4 that indicated the presence of aliphatic systems. Looking back on the OPLS-DA loadings plot of their ¹H NMR spectral data in Figure 5.8B, this was supported by resonances between 0.50 and 2.00 ppm and olefinic systems resonating between 5.00 and 5.50 ppm.

Dereplication putatively identified some of the compounds from the DNP database, as shown in Table 5.3. These included MZmine IDs N_17361, N_10906, N_1719 and N_7030 represented by ion peaks found at *m/z* 554.5147, 742.5387, 784.5858 and 652.588 dereplicated as *N*-2-hydroxyhexadecanoylsphinganine; phospholipid derivatives: stearylinoyleoylphosphatidyl-ethanolamine and -choline; and pakistamide A, respectively.

While discriminating feature MZmine ID N_8964 with MWt of 488.1735 500 Da showed the presence of sugar systems. The OPLS-DA loadings plot (in Figure 5.8B) of the NMR spectral data confirmed this by the presence of few numbers of glycosylated signals resonating between 3.00 and 4.00 ppm afforded by fungal extracts obtained potato dextrose medium incubated for 30 days. On the other hand, discriminating features with MWt of less than 380 Da showed higher DBE values.

This indicated the presence of aromatic systems. The NMR data of OPLS-DA loadings plot (in Figure 5.8B) also confirmed this by the presence of aromatic signals resonating between 6.00 and 8.00 ppm. (Hayes *et al.*, 1996). These discriminating features were identified as stellatic acid, 3-(4-hydroxyphenyl)-1,2-propanediol, and 2 α ,11-dihydroxy-7-drimen-6-one, respectively. Stellatic acid was first isolated from the fungus *A.stellatus*, which was cultivated on Czapak-Dox medium (Qureshi *et al.*, 1980). Also, stellatic acid was isolated from the fungus *Emericella varicolor* NBRC 32302 (Frisvad and Samson, 2004), it was moderately cytotoxic to murine leukaemia (P388) cells with an IC₅₀ value of 24.7 μ M (Matsuda *et al.*, 2015). Whereas, drimane sesquiterpene ester 2 α ,11-dihydroxy-7-drimen-6-one was also described from *A. ustus* var. *pseudodeflectus* growing on malt extract agar, which was obtained from Xenova culture 3811 of an Egyptian dessert soil. This compound showed endothelin receptor binding inhibitory action against the endothelin-A and endothelin-B receptors of rabbit and rat (Hayes *et al.*, 1996).

Furthermore, two drimane sesquiterpene ester were also isolated from *A. ustus* including deoxyuvidin B and 9,11-dihydroxy-7-drimen-6-one. Deoxyuvidin B was isolated from cultures of the fungus *A. ustus*, and previously isolated from the plant pathogen *Alternaria brassicae*. Deoxyuvidin B was also obtained from *A. ustus* cultures derived from marine sponge *Suberites domuncula*. The fungus was grown at 22°C for 21 days on biomalt agar and barley-spelt solid medium, It was shown to be non-cytotoxic against the L5178Y, HeLa, and PC12 cell lines (Liu *et al.*, 2009). Meanwhile, 9,11-dihydroxy-7-drimen-6-one was obtained from the Fungus X3811, which was confirmed as a strain of *A. ustus* var. *pseudodeflectus* (Hayes *et al.*, 1996). It was growing on malt extract agar (MEA) and glycerol nitrate agar (G25N).

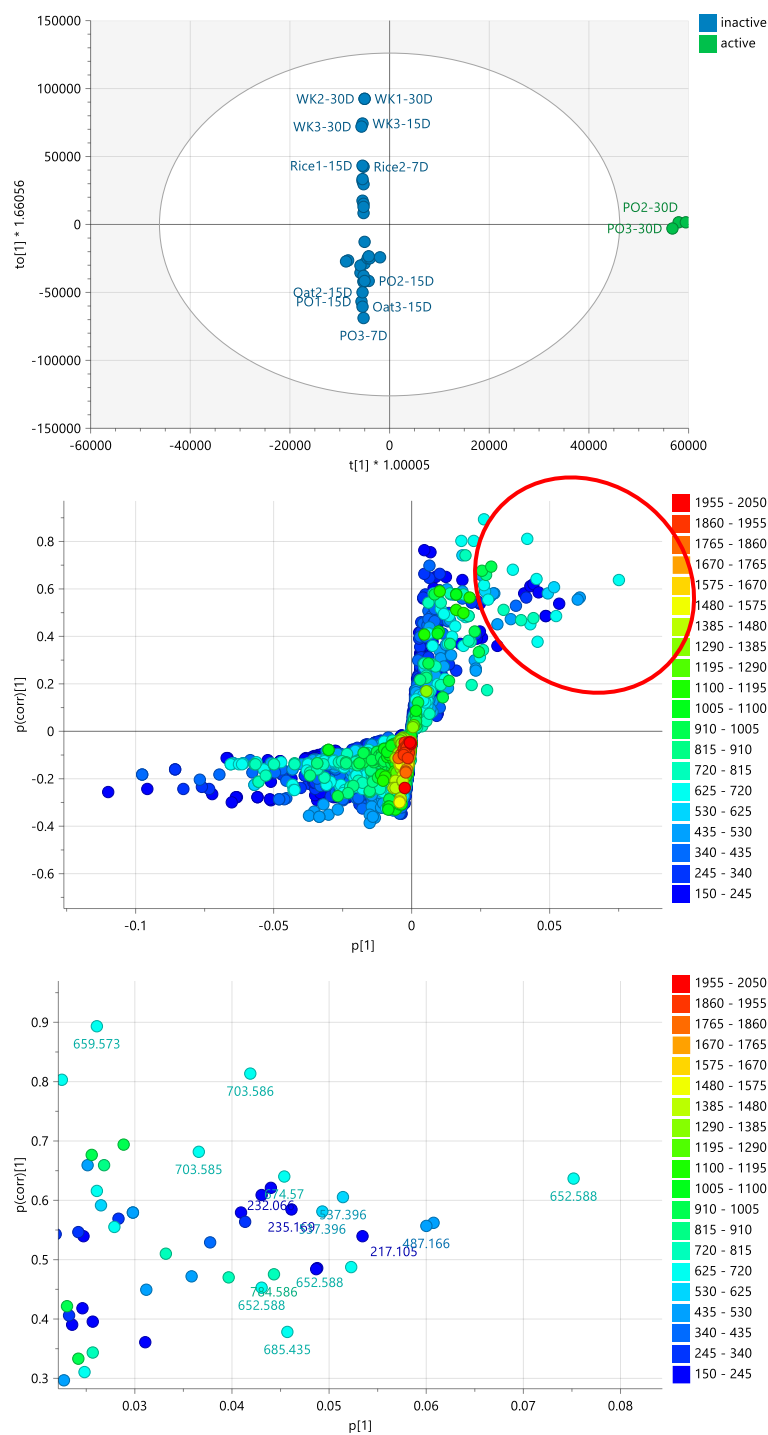


Figure 5.13: (A) OPLS-DA scores (B) OPLS-DA loadings S-plot of LC-HRMS data of *A. ustus* of different media extracts classified according to their bioactivity against breast cancer cells (ZR-75) (C) Expansion of the OPLS-DA loadings plot indicating the discriminating features for the active *A. ustus* extracts obtained from potato-dextrose media at 30th day, which are labelled with their m/z values and were listed below in Table 5.3. $R^2 = 0.94$ and $Q^2 = 0.51$. The difference between group $R^2X_0[1]$ is equal to 15.2% and the difference within groups $R^2X[2]$ is 2.0%.

Table 5.3: Dereplicated metabolites that define the discriminating features of anticancer bioactive potato dextrose media extracts. The compounds are arranged according to their *p*-values. Structures are shown in Figure 5.14.

MZmine ID	<i>p</i> -value	m/z	Rt	MW	compound hits †	Predicted molecular formula* (DBE)	Source
N_2454	2.30E-13	659.5727	37.53	660.5799	no hits	C ₄₁ H ₇₆ N ₂ O ₄ (5)	-
N_2730	3.40E-09	655.5396	34.10	656.5469	no hits	C ₄₁ H ₇₂ N ₂ O ₄ (7)	-
N_2533	3.56E-09	633.5587	37.84	634.566	ergosteryl palmitate (1)	C ₄₄ H ₇₄ O ₂ (8)	<i>A.itaconicus</i>
N_17361	9.02E-08	554.5147	33.10	555.522	<i>N</i> -2-hydroxyhexadecanoylsphinganine (2)	C ₃₄ H ₆₉ NO ₄ (1)	<i>Acetobacter spp.</i>
N_2789	3.04E-07	725.6303	32.11	726.6376	no hits	C ₄₄ H ₈₆ O ₇ (2)	-
N_6991	2.24E-05	674.5705	33.61	675.5777	no hits	C ₄₂ H ₇₇ NO ₅ (5)	-
N_24175	4.66E-05	232.0657	9.82	233.073	no hits	-	-
N_7030	5.30E-05	652.588	32.01	653.5953	pakistamide A (3)	C ₄₀ H ₇₉ NO ₅ (2)**	<i>Abutilon pakistanicum</i>
N_2107	0.000142	537.3958	37.56	538.403	no hits	C ₃₅ H ₅₄ O ₄ (9)	-
N_2873	0.000172	235.1695	11.04	236.1768	aspergiterpenoid A (4) brasilanone B (5) brasilanone C (6) brasilanone D (7) 4a,5-dihydromonascusic acid A (8)	C ₁₅ H ₂₄ O ₂ (4)	<i>Aspergillus sp</i> <i>A.terreus</i> <i>A.nidulans</i>
P_170	0.000206	214.0898	4.12	213.0826	<i>N</i> -butylbenzenesulfonamide (9)	C ₁₀ H ₁₅ NO ₂ S (4)	<i>Actinoallomurus sp</i> <i>Pseudomonas sp</i>
P_93	0.000259	327.0083	44.19	326.001	no hits	-	-
P_254	0.000315	537.3958	37.51	536.3885	palmitoylarucadiol (10) hyperforin (11) labdanecaryophyllic acid (12)	C ₃₅ H ₅₂ O ₄ (10)**	<i>Salvia miltiorrhiza</i> <i>Hypericum perforatum</i> <i>Calocedrus macrolepis</i>
N_8964	0.000354	487.1662	2.56	488.1735	β-L-rhamnopyranosyl-(1→4)-β-D-glucopyranosyl-(1→4)-D-galactose (13)	C ₁₈ H ₃₂ O ₁₅ (3)	<i>Streptococcus pneumoniae</i> <i>type 23F</i>

N_10906	0.001188	742.5387	30.34	743.546	stearoyllinoleoylphosphatidylethanolamine (14)	C ₄₁ H ₇₈ NO ₈ P (4)	membranes of eukaryotic and prokaryotic cells
N_398	0.002438	217.1046	5.87	218.1119	no hits	-	-
N_1719	0.002954	784.5858	37.88	785.5931	linoleoylstearylphosphatidylcholine. (15)	C ₄₄ H ₈₄ NO ₈ P (4)	membranes of eukaryotic and prokaryotic cells
P_34	0.017958	195.1229	4.85	194.1157	2,3,4-tri- <i>O</i> -methylxylitol (16)	C ₈ H ₁₈ O ₅ (0)	<i>Psalliota campestris</i>
N_2824	0.228314	369.2793	25.87	370.2866	stellatic acid (17)	C ₂₅ H ₃₈ O ₂ (7)	<i>A.stellatus, Emericella venezuelensis</i>
P_21	0.156459	169.0861	9.17	168.0788	3-(4-hydroxyphenyl)-1,2-propanediol (18)	C ₉ H ₁₂ O ₃ (4)	<i>A.flavus</i>
P_157	0.555233	253.1800	14.36	252.1728	2 α ,11-dihydroxy-7-drimen-6-one (19) deoxyuvidin B (20) 9,11-dihydroxy-7-drimen-6-one (21)	C ₁₅ H ₂₄ O ₃ (4)	<i>A. ustus</i>

[†]For multiple hits, chosen compound hits were filtered for microbial or fungal species (particularly for the genus *Aspergillus*) except otherwise.

*Follows the heuristic rules. **All other hits were from plant species.

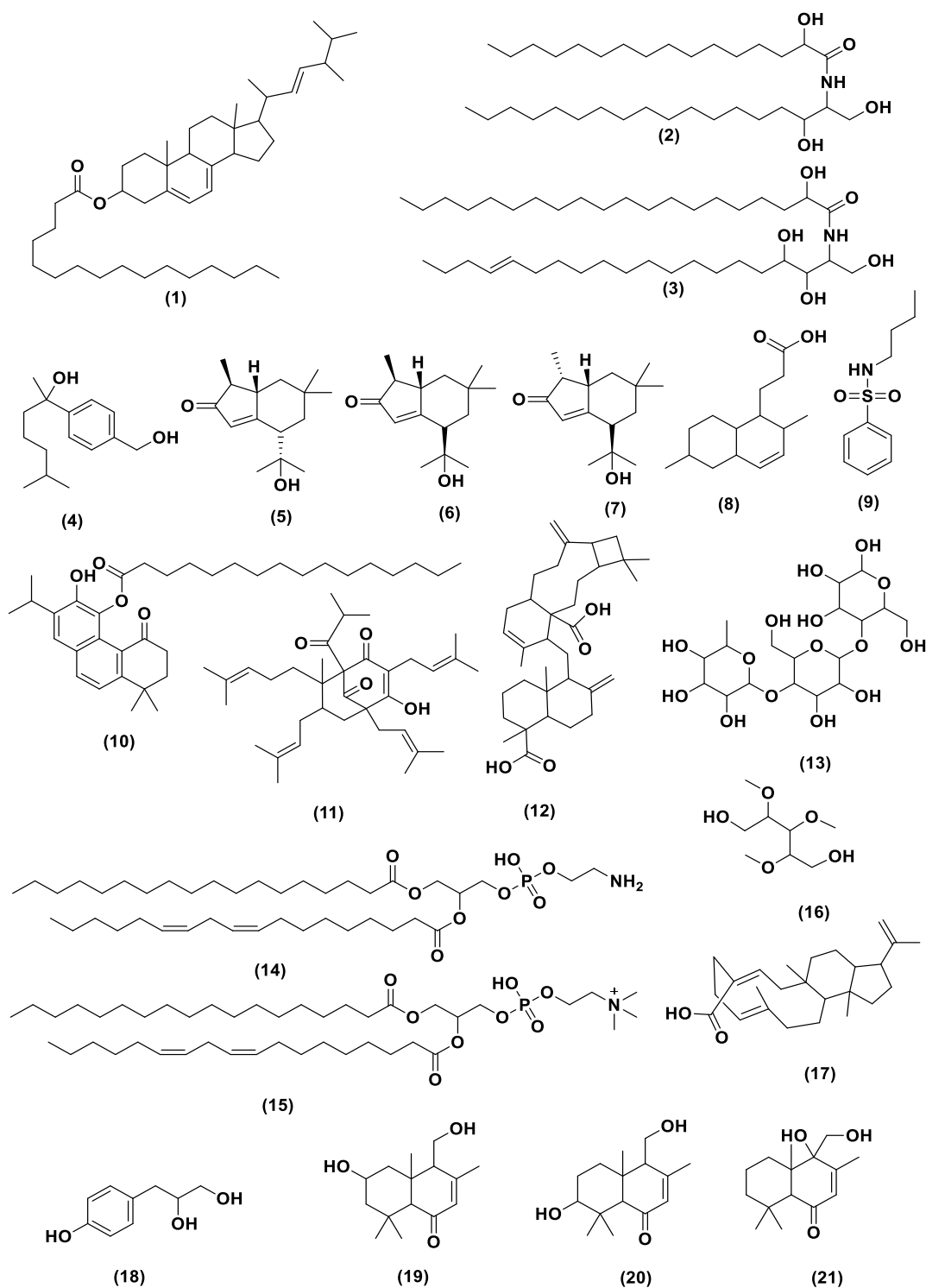


Figure 5.14: Structures of the discriminating bioactive metabolites from *A. ustus* extract obtained from potato dextrose media have been listed in Table 5.3.

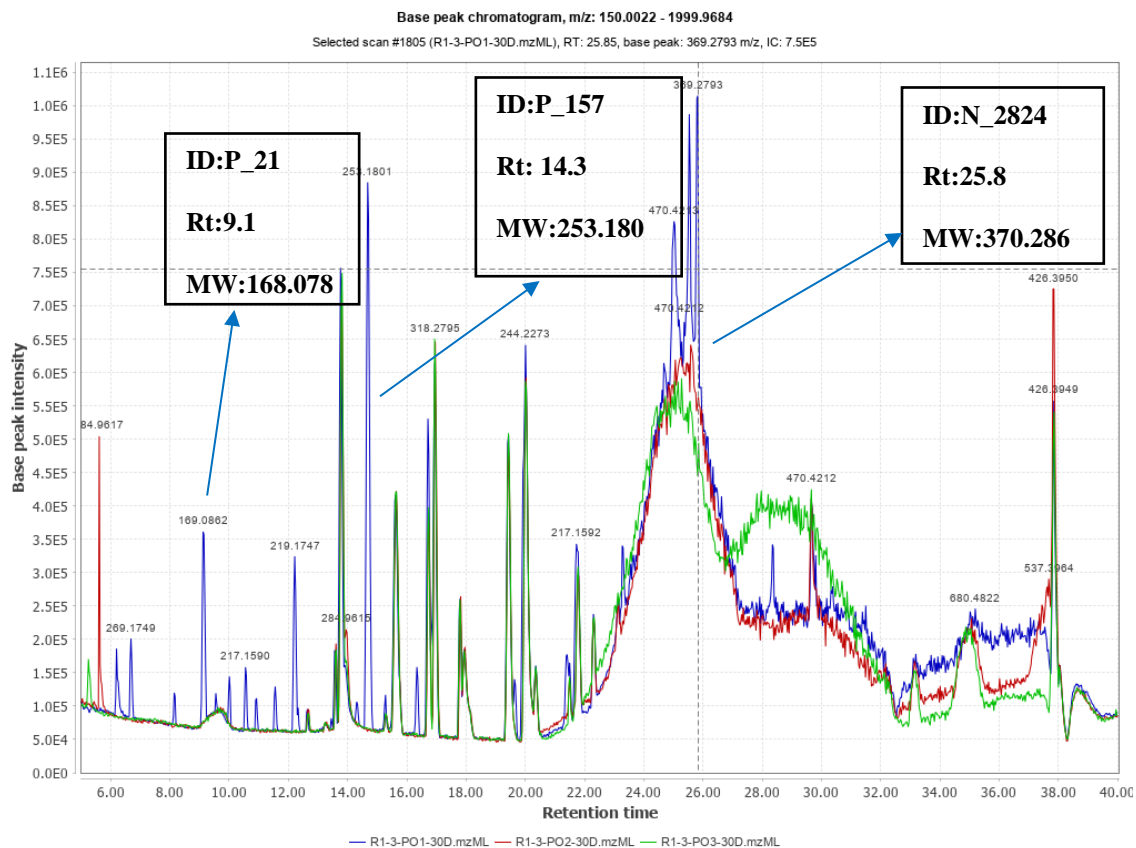


Figure 5.15: Total Ion Chromatogram (TIC) of the bioactive *A. ustus* extracts obtained from potato-dextrose media. The ion peaks that represent the discriminating features listed in Table 5.3 have been labelled.

5.2. Optimising the production of anticancer bioactive metabolites in *A. solani*

The fungal genus *Alternaria* are members of the Dematiaceae family of the Hyphomycetes. They may function as plant pathogens, weak facultative parasites, saprophytes, and endophytes (Thomma, 2003). Several *Alternaria* metabolites are poisonous to both plants and animals, and are classified as phytotoxins or mycotoxins, depending on their toxic properties (Strange, 2007, Duke and Dayan, 2011). The metabolites produced by *Alternaria* fungus may be divided into numerous groups, which include nitrogen-containing compounds, steroids, terpenoids, pyranones (pyrones), quinones, and phenolics. Several metabolites are exclusive to a single *Alternaria* species; however, the vast majority of metabolites are produced by several *Alternaria* species (Lou *et al.*, 2013).

A. solani afforded compounds such as tetrahydroaltersolanol B (**7**), hydroxybostrycin (**8**) as well as altersolanols A (**9**), B (**10**), C (**11**), D (**12**), E (**13**), F (**14**), G (**15**) and H (**16**). It was found that *A. solani* causes black spot disease on tomato leaves (Okamura *et al.*, 1993a, Okamura *et al.*, 1993b). Several anthraquinone metabolites isolated from *A. solani* and *Alternaria sp.*, included macrosporin (**6**), hydroxybostrycin (**8**), altersolanol A (**9**), altersolanol B (**10**), altersolanol C (**11**), altersolanol G (**15**), and alterporriol C (**18**), which demonstrated antibacterial activity against *Pseudomonas aeruginosa*, *Bacillus subtilis*, *Escherichia coli*, *Vibrio parahemolyticus*, *Micrococcus luteus* *Staphylococcus albus*, and *Staphylococcus aureus* (Zheng *et al.*, 2012, Okamura *et al.*, 1993a, Yagi *et al.*, 1993).

Additionally, phenolic phytotoxins were also isolated from *A. solani* causing early blight disease in potato and tomato. These phytotoxin were identified as zinniol (**19**), 8-zinniol 2-(phenyl)-ethyl ether (**20**), 8-zinniol methyl ether (**21**), 2-(2",3"-dimethyl-but-1-enyl)-zinniol (**22**) and homozinniol (**23**) (Moreno-Escobar *et al.*, 2005, Gamboa-Angulo *et al.*, 1997)

Table 5.4: Secondary metabolites previously isolated from *A. solani*.

Metabolite class	No.	Metabolite name	Reference
Pyranones	1	alternaric acid	(Patel <i>et al.</i> , 2011)
	2	solanapyrone A	(Ichihara <i>et al.</i> , 1983)
	3	solanapyrone B	
	4	solanapyrone C	
	5	solanapyrone D	
	6	solanapyrone E	
Quinones	7	macrosporin	(Stoessl <i>et al.</i> , 1979)
	8	tetrahydroaltersolanol B	(Zheng <i>et al.</i> , 2012)
	9	hydroxybostrycin	(Yagi <i>et al.</i> , 1993)
	10	altersolanol A = stemphylin	(Yagi <i>et al.</i> , 1993, Okamura <i>et al.</i> , 1993a, Zheng <i>et al.</i> , 2012)
	11	altersolanol B = dactylarin	
	12	altersolanol C = dactylariol	
	13	altersolanol D	
	14	altersolanol E	
	15	altersolanol F	
	16	altersolanol G	
	17	altersolanol H	
	18	alterporriol A/B	(Okamura <i>et al.</i> , 1993b, Suemitsu <i>et al.</i> , 1990)
	19	alterporriol C	(Suemitsu <i>et al.</i> , 1990)
Phenolics	20	zinniol	(Moreno-Escobar <i>et al.</i> , 2005)
	21	8-zinniol 2-(phenyl)-ethyl ether	
	22	8-zinniol methyl ether	
	23	2-(2",3"-dimethyl-but-1-enyl)-zinniol	
	24	homozinniol	(Gamboa-Angulo <i>et al.</i> , 1997)

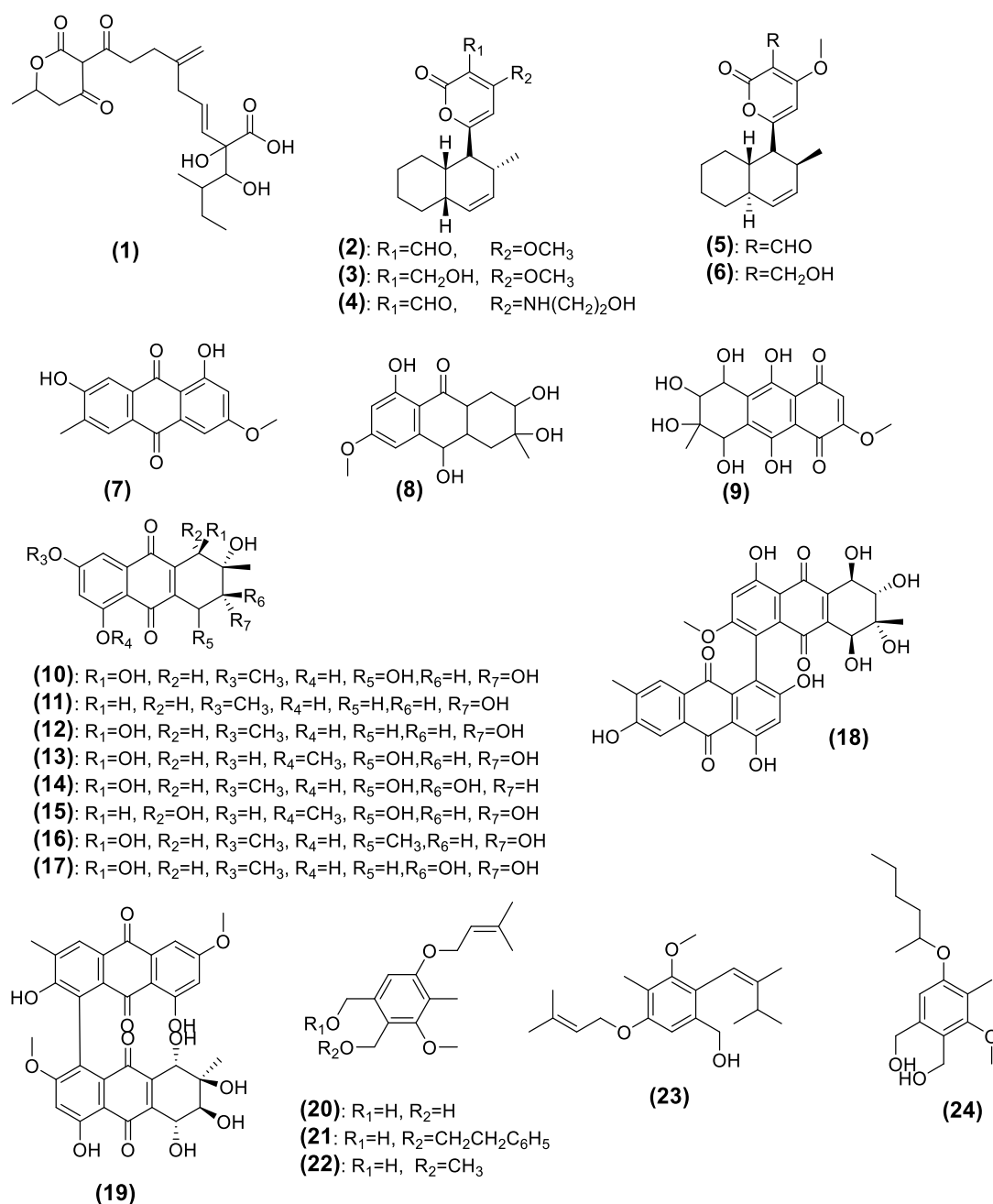


Figure 5.16: Secondary metabolites previously isolated from *A. solani*

5.2.1. Extract yields on different media.

A. solani isolated from the stem of Jordanian chamomile was grown on five different media. Again, like the previous endophytic fungus, the average yield of extracts afforded by the solid media was higher than when grown on liquid media. Amongst the liquid media, the highest yield of 94.0 mg was achieved by growing the fungus on

potato-dextrose media extract at 15 days of incubation. The extract yields of the liquid media started to decline on the 30th day of incubation, which indicated the end of the stationary phase and beginning of the death phase. On solid media, the highest extract yield of 455.6 mg was obtained from the fungus grown for 15 days on rice media. Extract yields obtained from the various media are presented in Table 5.5 and Figure 5.17. The log growth phase of *A. solani* was observed at 15th day on solid media and liquid media.

Table 5.5: Extract yields afforded by *A. solani* grown on five different media and collected at various incubation periods. All cultures were incubated at 27°C.

Liquid media			
Type of media	Incubation period		
	7 Days	15 Days	30 Days
Potato-dextrose	45.5	94.0	24.2
Wickersham media	42.3	84.5	23.2
Malt media	17.5	43.5	41.2
Solid media			
Rice media	214.8	270.1	311.7
Oat media	388.0	455.6	450.2

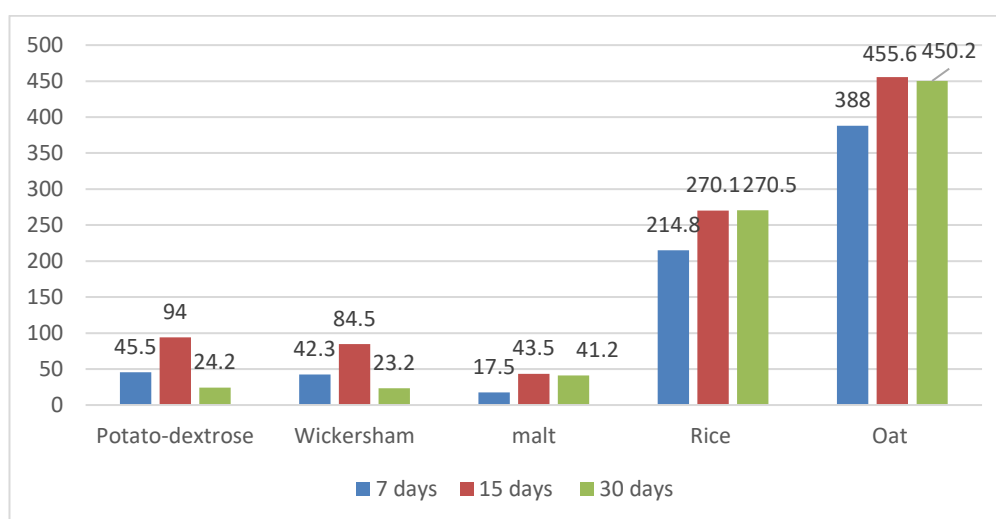


Figure 5.17: Histogram of extract weights of *A. solani* obtained from five different media and incubated at 7, 15, and 30 days.

5.2.2. Biological assay

Before selecting the optimal medium for large-scale fermentation, the biological activity of fungal extracts grown on different media were tested against breast cancer (ZR-75) cells. At first, media optimisation was done on four different media including potato-dextrose, Wickersham, rice and oat. Then, malt medium was used to compare the chemical profile to malt extract agar medium. As depicted in Figure 5.18, all extracts of *A. solani* from five different media at various incubation time were inactive against breast cancer (ZR-75) cells. However, multivariate analysis of the production of metabolites were done to attempt to explain the changes occurring in the fungus during the media optimisation experiment and to find the causes contributing for losing the bioactivity.

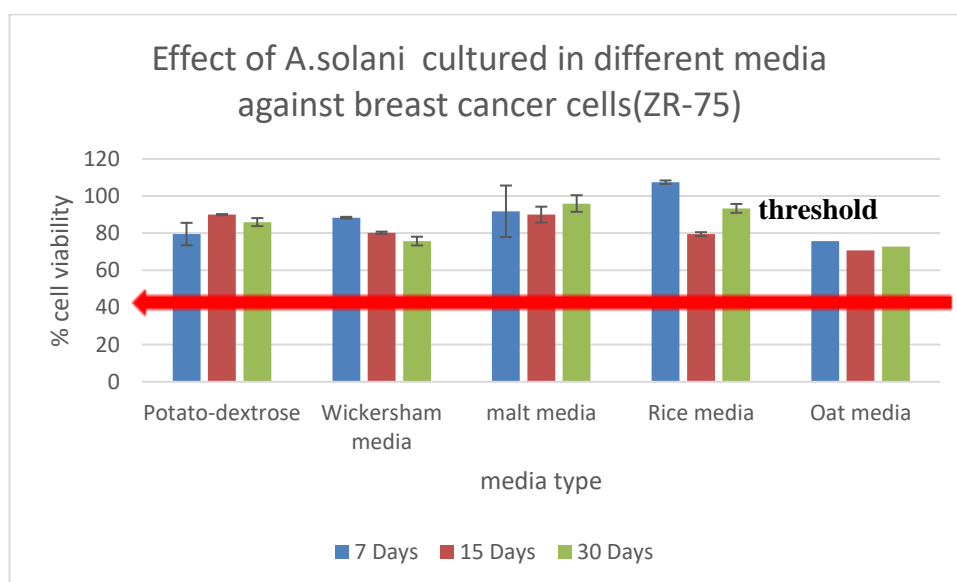


Figure 5.18: AlamarBlue® cell viability assay results of 30µg/mL of *A. solani* extracts. The red line indicates the bioactivity threshold.

5.2.3. NMR spectroscopy for *A. solani* extracts

5.2.3.1. Rice media

The proton NMR results provided a general indication of the major compound present in the various extracts. Stacked ^1H NMR spectra of *A. solani* extracts obtained from rice media at 7, 15, and 30 days of incubation was shown in Figure 5.19. When comparing the fungal extracts with the blank media (red box), major variations were noticeable at the glycosylated and aromatic resonance between 3.50 and 7.25 ppm. A new set of signals can be detected after 15 and 30 days of incubation, including hydroxylated peaks resonating between 3.50 and 4.50 ppm (green box), as well as aromatic peaks between 6.50 and 7.25 ppm (blue box).

The intensity of the peaks of extracts obtained from 15th and 30th days of incubation were higher than the peaks of extracts obtained from 7th days of incubation, which indicated that the log growth phase of *A. solani* was observed between 15th and 30th day.

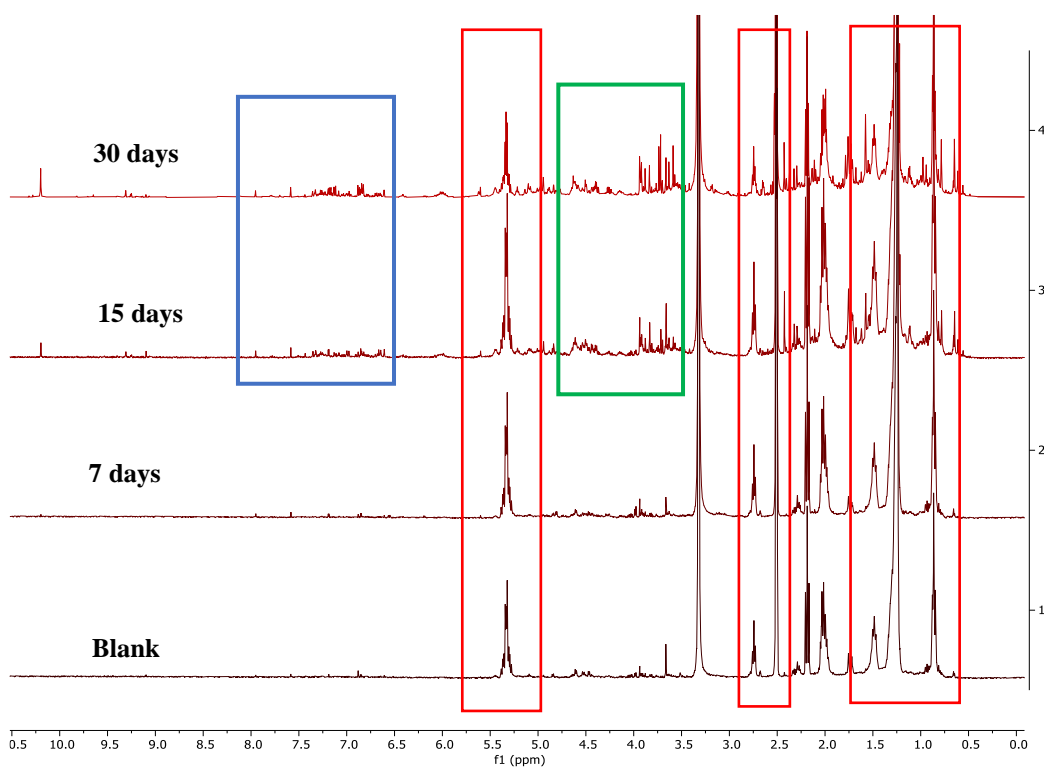


Figure 5.19: The ^1H NMR (measured in DMSO-d_6 , 500 MHz) data obtained from *A. solani* extracts after inoculation on solid-rice medium incubated for 7, 15, 30 days.

5.2.3.2. Oat media

As depicted by the red boxes in Figure 5.20, the ^1H NMR spectra obtained from oat blank medium and fungal extracts were relatively similar. Most of the solid oat medium peaks remained in the fungal extract except at 30 days of incubation. A small production of secondary metabolites at chemical shifts resonating between 6.50 and 7.25 ppm were observed as shown in Figure 5.20 (blue box).

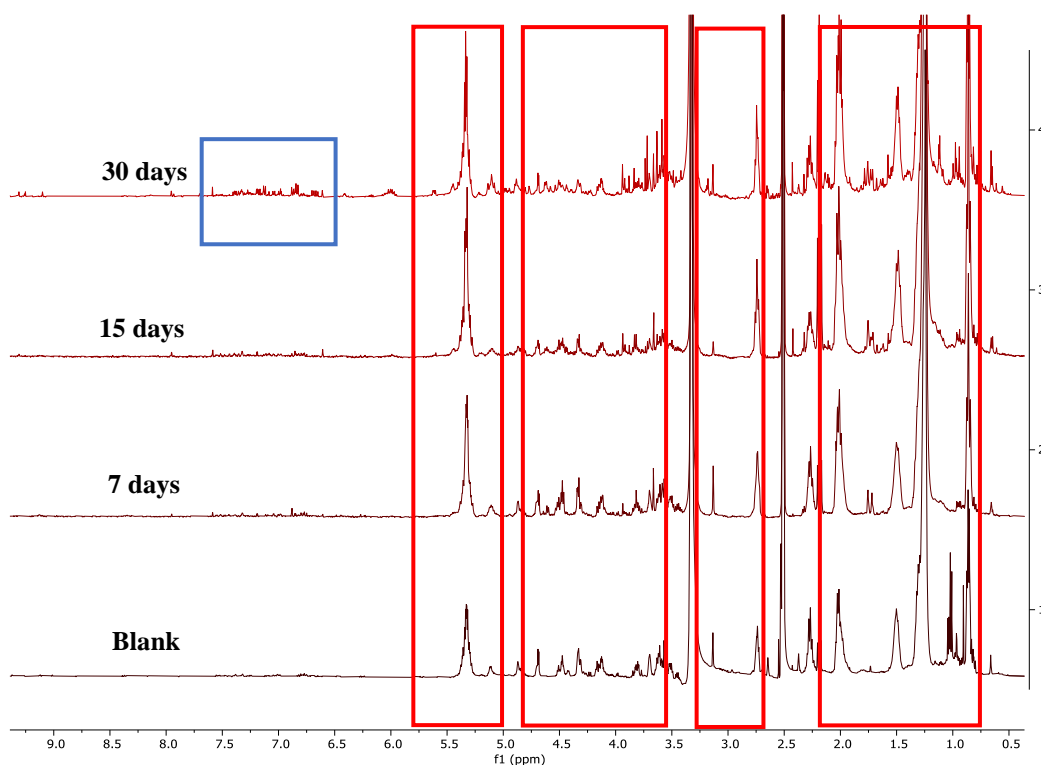


Figure 5.20: The ^1H NMR (measured in DMSO-d_6 , 500 MHz) data obtained from *A. solani* extracts after inoculation on solid-oat medium incubated for 7, 15, 30 days.

5.2.3.3. Potato-dextrose media

The ^1H NMR spectra of fungal extracts obtained from those inoculated on potato-dextrose and that for the blank medium showed no differences from each other. No changes in peak resonances were observed between the potato-dextrose medium peaks and those for the fungal extracts after 30 days of incubation, as shown by the red boxes in Figure 5.21. This suggested that the fungus was not utilising the nutrients in the medium, resulting in poor secondary metabolite synthesis with low growth rates.

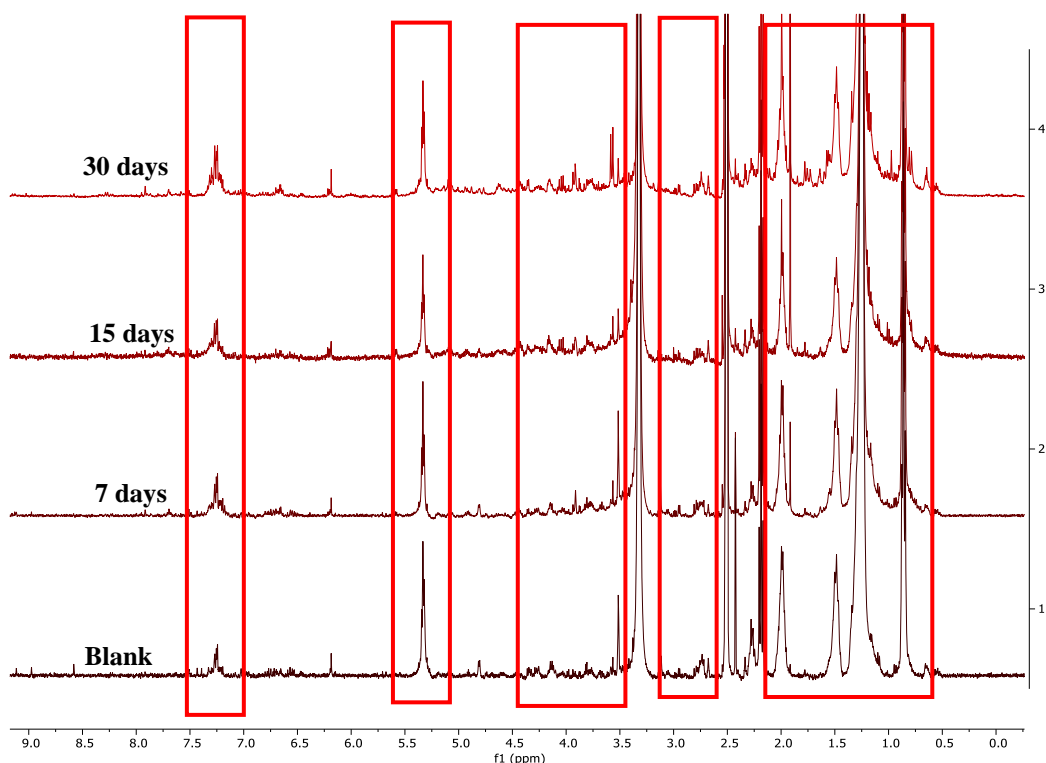


Figure 5.21: The ^1H NMR (measured in DMSO-d_6 , 500 MHz) data obtained from *A. solani* extracts after inoculation on potato-dextrose medium incubated for 7, 15, 30 days.

5.2.3.4. *Wickersham media*

The endophyte generated relatively few metabolites when grown in liquid Wickersham medium. As shown in Figure 5.22, the majority of ^1H NMR signals in liquid Wickersham culture extracts were derived from the medium components (highlighted in red boxes). Fatty acid signals were detected in the ^1H NMR spectrum, as illustrated in the Figure 5.22. Long-chain fatty acids have a high intensity signal at δ_{H} 1.00 to 1.50, which is characteristic of methylene units in these fatty acids. Aside from that, the presence of olefinic protons in unsaturated fatty acids was also identified in the region of δ_{H} 5.00 to 5.50 in addition to the proton signal at δ_{H} 2.10 to 2.40, which indicated the presence of α proton signals of the terminal carboxylic unit. After 30 days of incubation, the endophyte started to produce a small quantity of aromatic compounds, which were implied by proton signals resonating at δ_{H} 6.00 – 6.75, as shown in Figure 5.22 (blue box). However, the production of these molecules was very

minimal in comparison to the occurrence of fatty acids, as seen by their peak intensities.

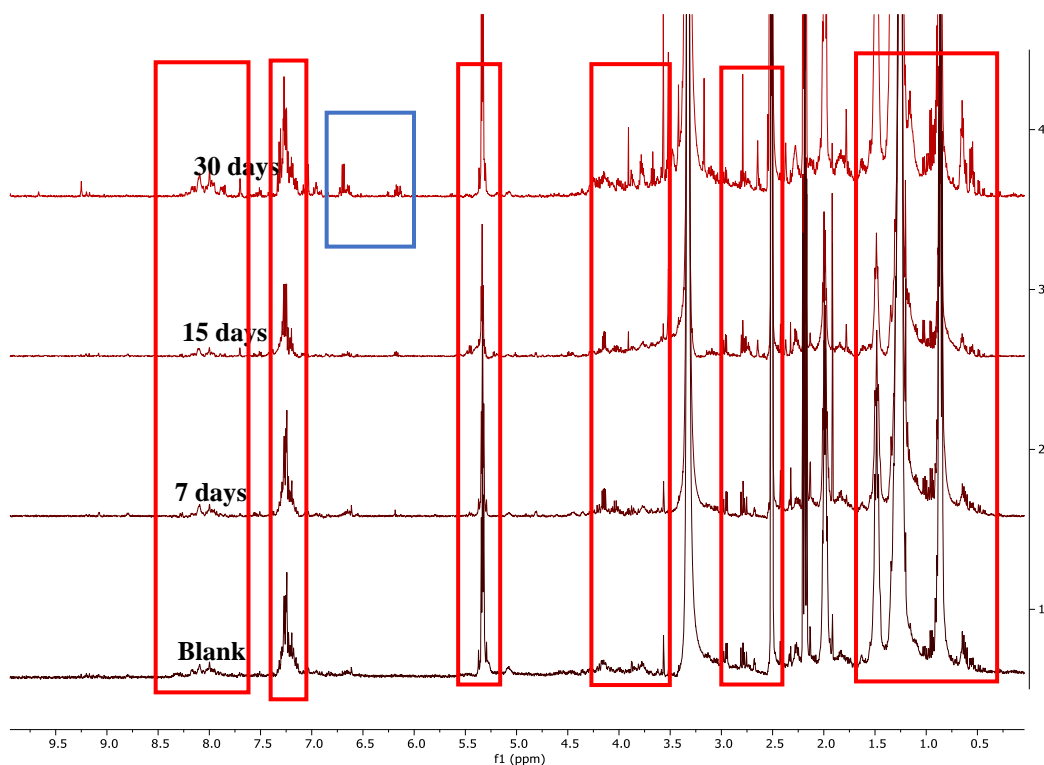


Figure 5.22: The ¹H NMR (500 MHz) data obtained from *A. solani* extracts after inoculation on Wickersham medium incubated for 7, 15, 30 days, measured in DMSO-d₆

5.2.3.5. Malt extract broth media

The stacked proton NMR spectra of *A. solani* extracts obtained at 7, 15 and 30 days of incubation periods on malt extract with media blanks are presented in Figure 5.23. after incubation for 15 and 30 days, a few low intensity peaks were observed in the aromatic region at 5.92 ppm (blue box). In addition, resonances for hydroxyl groups and olefinic hydrogens at 3.50 and 5.50 ppm, respectively (green and orange box), were also observed on the spectra of the fungal extracts.

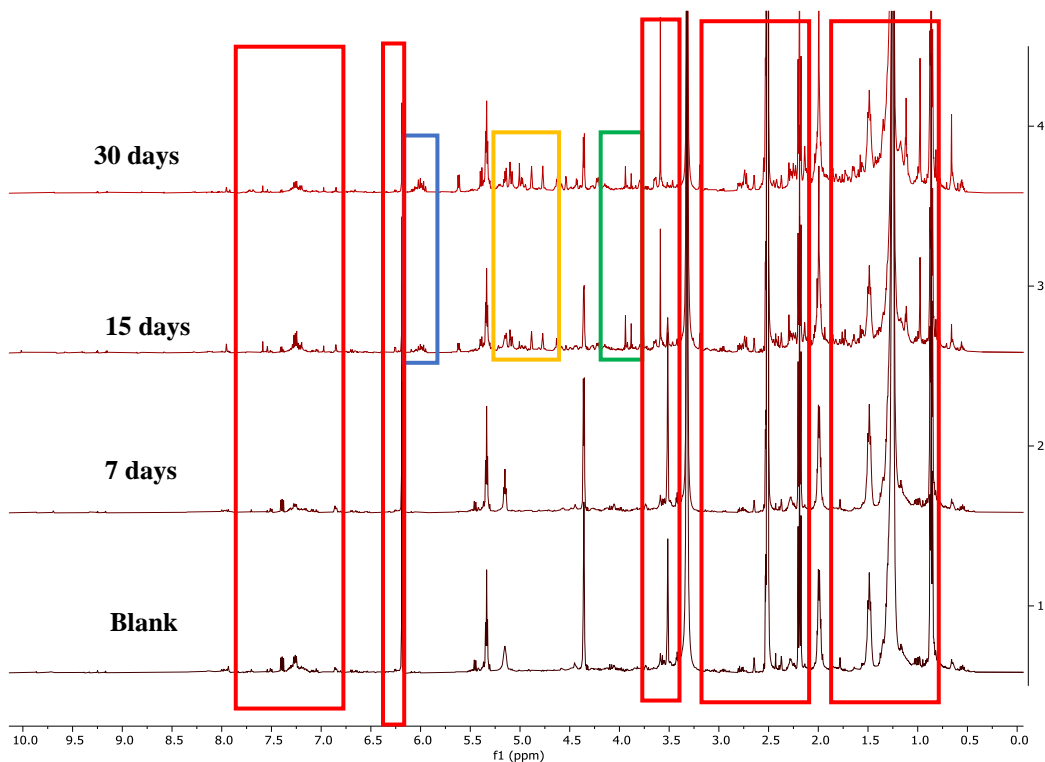


Figure 5.23: The ¹H NMR (500 MHz) data obtained from *A. solani* extracts after inoculation on malt extract broth medium incubated for 7, 15, 30 days, measured in DMSO-d₆

From the analysis of the proton NMR spectrum, it was quite evident that chemical profiles of *A. solani* extracts afforded upon inoculation on five different media were also quite different from the extract yielded by the MA media as shown in Figure 5.24. Metabolite production in the fungi was highly dependent on the type of media and stability of the production of the secondary metabolites by the fungus.

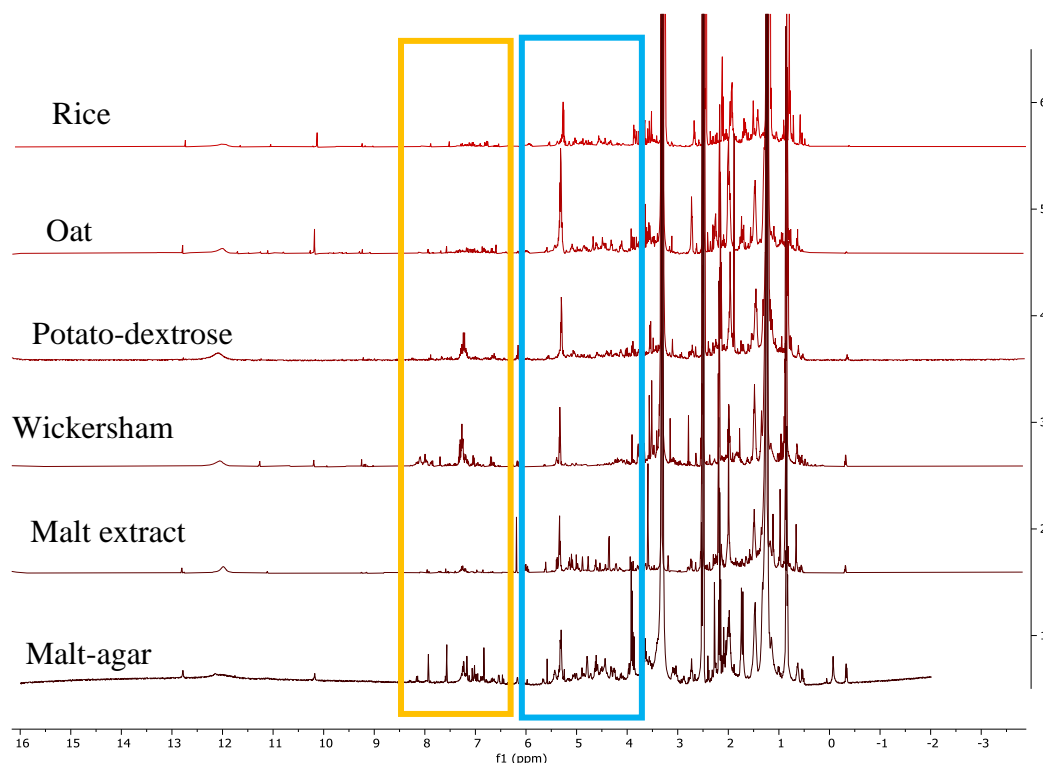


Figure 5.24: The stacked ¹H NMR (measured in DMSO-d₆, 500 MHz) data obtained from *A. solani* extracts from the screening step in comparison to the five different media used during the media optimisation step incubated for 30 days.

5.2.4. Multivariate analysis of NMR spectral data

As displayed in Figure 5.25, a PCA scores plot of the ¹H NMR spectrum data of *A. solani* extracts revealed similarities and differences across the incubated medium for 15 and 30 days. All media produced insufficient metabolites on the 7th day. So, extracts obtained at 7th day from each medium were excluded for multivariate analysis. As demonstrated in Figure 5.25A, extracts of *A. solani* obtained from Wickersham media incubated for 30 days were separated in the upper left quadrant, indicating their relatively unique chemical profiles. From the loadings plot in Figure 5.25 B, the discriminating chemical shifts for extracts obtained from the fungus incubated in Wickersham for 30 days exhibited signal resonating mainly in the aliphatic region between 0.0 and 2.0 ppm and contained glycosylated metabolites implied by signals at 3.0 to 4.0 ppm (encircled green). Meanwhile, the ¹H NMR spectral data of extracts obtained from the fungi incubated in potato-dextrose and oat for 30 days were dispersed in the upper right quadrant of the PCA scores plot, which showed high

intensity of peaks at the aliphatic region between 0.0 and 2.00 ppm and a relatively lesser number of glycosylated metabolites between 3.00 and 4.00 ppm (encircled blue). On the other hand, extracts obtained from the fungus incubated in rice for 15 and 30 days were clustered in the lower right quadrant. Whereas, extracts from the fungi incubated in Wickersham, potato dextrose and oat for 15 days were slightly dispersed in the lower left quadrants of the plot. Poor production of secondary metabolites were observed for these extracts. This was confirmed by the ^1H NMR spectra of these extracts, which were very similar to that of the medium blank. The model gave a goodness of fit at 0.99 and good predictivity score of 0.95 after 7 components. The difference between R^2 and Q^2 values less than 0.3, confirming that the model was not over fitted.

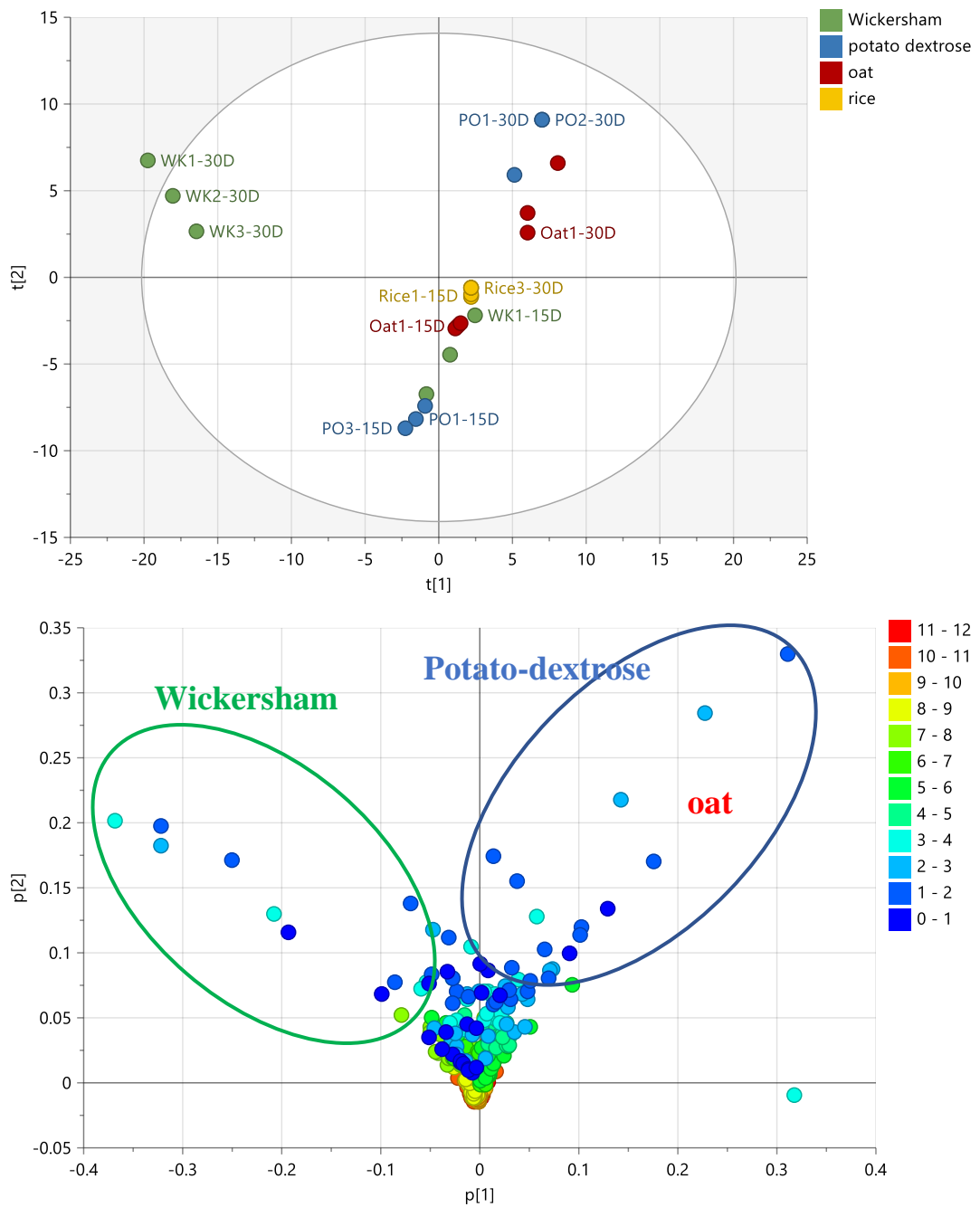


Figure 5.25: (A) PCA scores (B) loading plots of ^1H NMR spectral of *A. solani* extracts from four media incubated at 15 and 30 days. $R^2 = 0.99$ and $Q^2 = 0.95$ after 7 components.

The OPLS-DA scores plot of the proton NMR spectral data of *A. solani* extracts was performed to provide the differences in metabolic profiles between *A. solani* extracts obtained from the different media at 15 and 30 days of incubation (Figure 5.26A). According to the OPLS-DA loadings plot (5.26B), the right side of plot entailing the fungal extracts from the Wickersham media after incubation for 15 and 30 days were dominated with resonances between 0.00 and 2.00 ppm indicating the occurrence of aliphatic compounds and showed the occurrence of resonance between 3.0 and 5.0 ppm indicating the presence of hydroxylated, glycosylated compounds (encircled green). While extracts obtained from oat media at 15th and 30th days were found in the lower left quadrant and exhibited a resonance between a 1.00 to 5.50 ppm. This is indicative of acetylated compounds and fatty acids. R^2 and Q^2 values were 0.99 and 0.79, respectively. This indicated a model with excellent fitness and predictability. However, $R^2Xo[1]$ provided a variation score of 29.6%, whereas the difference within groups $R^2X[2]$ provided a score of 5.6%. The difference between the variation scores between groups is greater than the difference between the variation scores within groups, indicating that there is strong separation between media extracts.

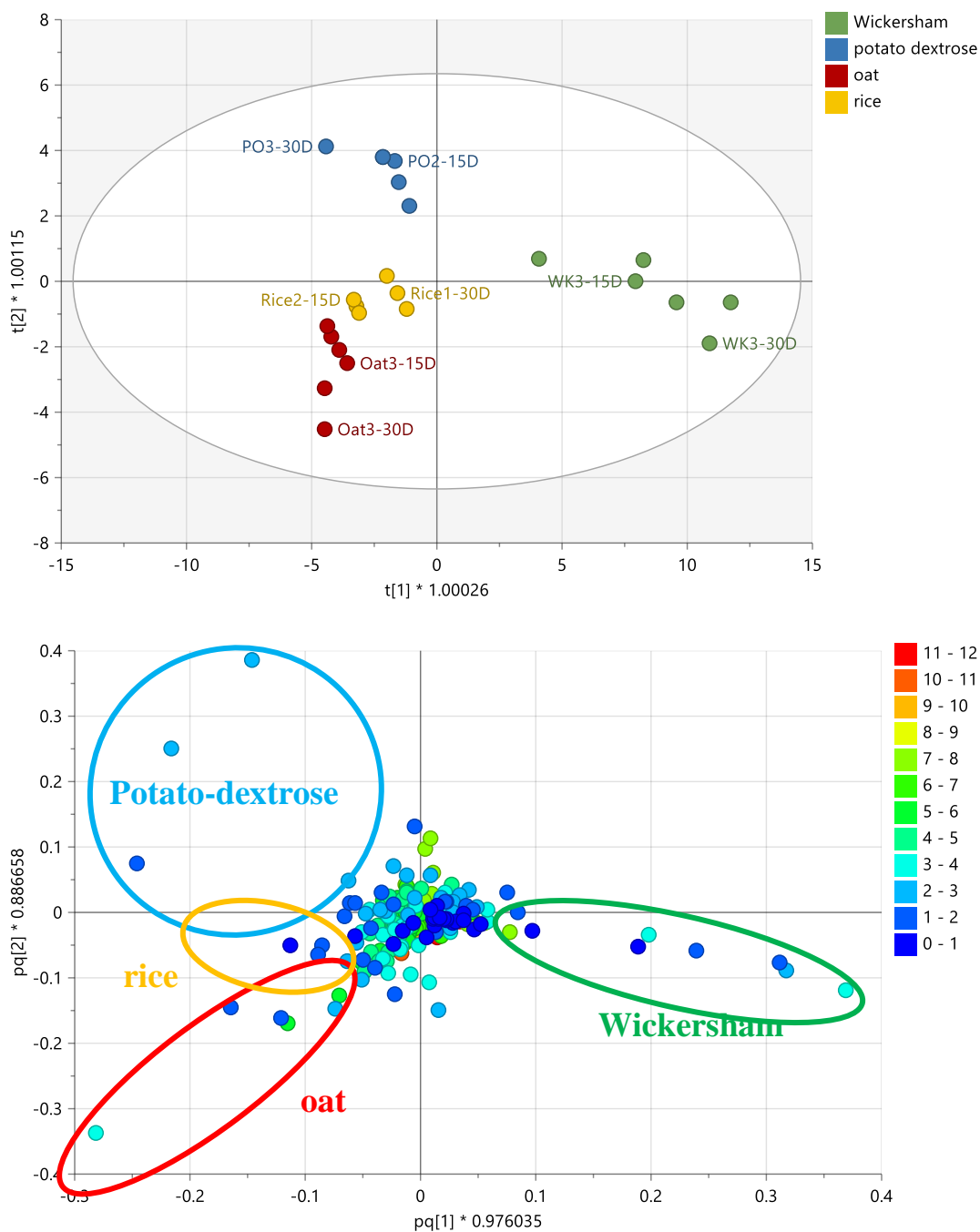


Figure 5.26: (A) OPLS-DA scores **B)** loadings plots of ¹H NMR spectral of *A. solani* extracts obtained from different media. R^2 and Q^2 values were 0.99 and 0.79, respectively. The difference between group $R^2X_o[1]$ is equal to 29.6% and the difference within groups $R^2X[2]$ is 5.6%. Encircled features on the loadings plot indicate the discriminating chemical shifts

Multivariate analysis of proton NMR of the fungal extracts grown on malt-broth medium at 7, 15 and 30 days and MA medium were done to understand the reasons for losing of the bioactivity of *A. solani* extracts. The PCA scores plot of the NMR spectral data (Figure 5.27A) showed differences between the extracts grown on malt-broth for 7, 15 and 30 days and MA medium. MA media was found on the right side of plot while malt-broth medium found on the left side of the plot (Figure 5.27A), which indicated different chemical profile between both extracts. The PCA-loadings plot revealed the type of functional groups and chemical profiles for each group of extracts. As depicted in Figure 5.27B, higher number of produced metabolites in MA medium when compared to malt medium. High intensity of metabolites resonated between 0.0-2.0 ppm. Metabolites afforded by MA medium were highly glycosylated, which were indicated by ^1H signals from 3.00 to 4.00 ppm. On the other hand, resonances for olefinic and aromatics from 5.00 to 8.00 ppm were observed amongst extracts obtained from fungi inoculated on malt-broth. While fungal extracts grown on malt-broth seem to produce fewer secondary metabolites than those inoculated on MA medium. In the generated model, R^2 was 1.0 and Q^2 was 1.0, suggesting a model with excellent fitting and predictability. In summary, a different chemical profile between MA and malt medium was illustrated, which can explain the loss of the bioactivity of *A. solani*.

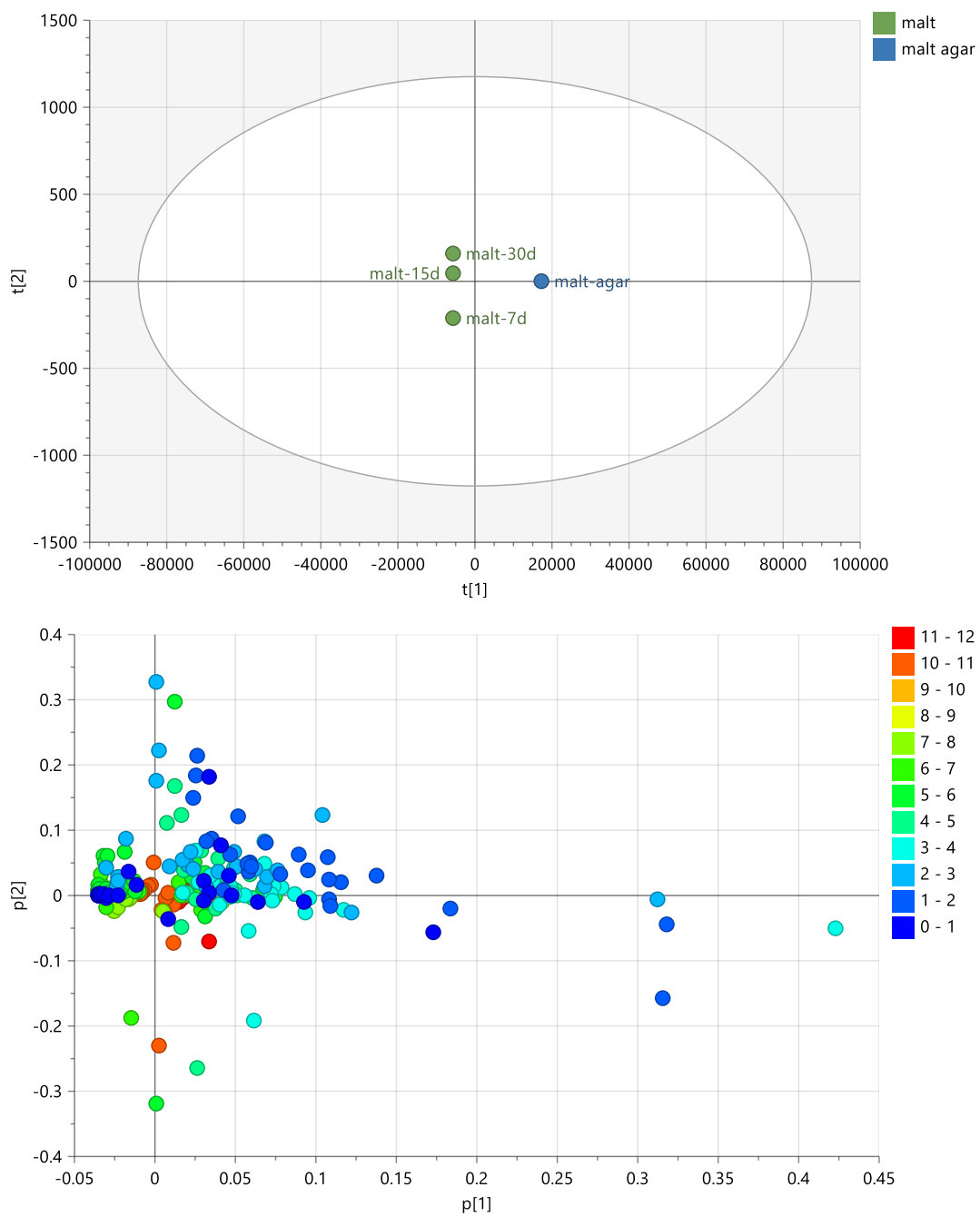


Figure 5.27: (A) PCA scores (B) loading plots of ^1H NMR spectral of *A. solani* extracts from malt medium incubated at 15 and 30 days and MA medium. $R^2 = 1.0$ and $Q^2 = 1.0$ after 3 components.

5.2.5. Multivariate analysis of LC-HRMS data

LC-HRMS analysis was accomplished for the extracts obtained from four media including oat, rice, Wickersham and potato-dextrose media. LC-HRMS analysis was not performed on extract obtained from malt because the MS device stopped working before the pandemic. The PCA model was generated from the LC-MS data, which included the extracts of *A. solani* obtained from four different media after 15 and 30 days of incubation. Extracts obtained from 7 days of incubation were excluded for all media due to poor metabolites production. PCA scores plots grouped the extracts into four clusters as shown in Figure 5.28A. The extracts were categorised to determine the discriminating metabolites for each of the respective extract clusters on the loadings plot on Figure 5.28B. Extracts of *A. solani* obtained from oat media at the 30th day were in the right side of the scores plot. Extracts afforded by oat media which were incubated for 30 days, implied to have a relatively different chemical profiles from the other extracts. The loadings plot provided targeted metabolites with a MWt range between 150 and 500 Da (encircled green). Furthermore, the outlying extracts were discriminated by MZmine IDs P_3862, and P_663 with ion peaks at m/z 182.081, and 329.005 Da, respectively. Only P_3862 was putatively identified as 4-hydroxy-2-methoxyacetanilide (Figure 5.29), which had cytochrome P450 (CYP) 3A4 inhibitory activity with IC₅₀ values of 0.41 µg/mL (El-Beih *et al.*, 2007). While the other did not give any hits and remains unidentified.

Meanwhile, extracts from Wickersham media incubated at 15 days were in the lower left quadrant of the plot, which exhibited wider range of metabolites with MWt between 250 and 1000 Da on the corresponding loadings plot (encircled orange). Fungal extracts obtained from rice media incubated for 30 days were positioned in the upper side in the plot. The rest of the *A. solani* extracts from other media were dispersed in the upper and lower left quadrant. Metabolites with high molecular mass were observed in these extracts (encircled red). At four components, the R² and Q² values were at 0.67 and 0.37, respectively, which indicated excellent fitness but poor predictability of the model.

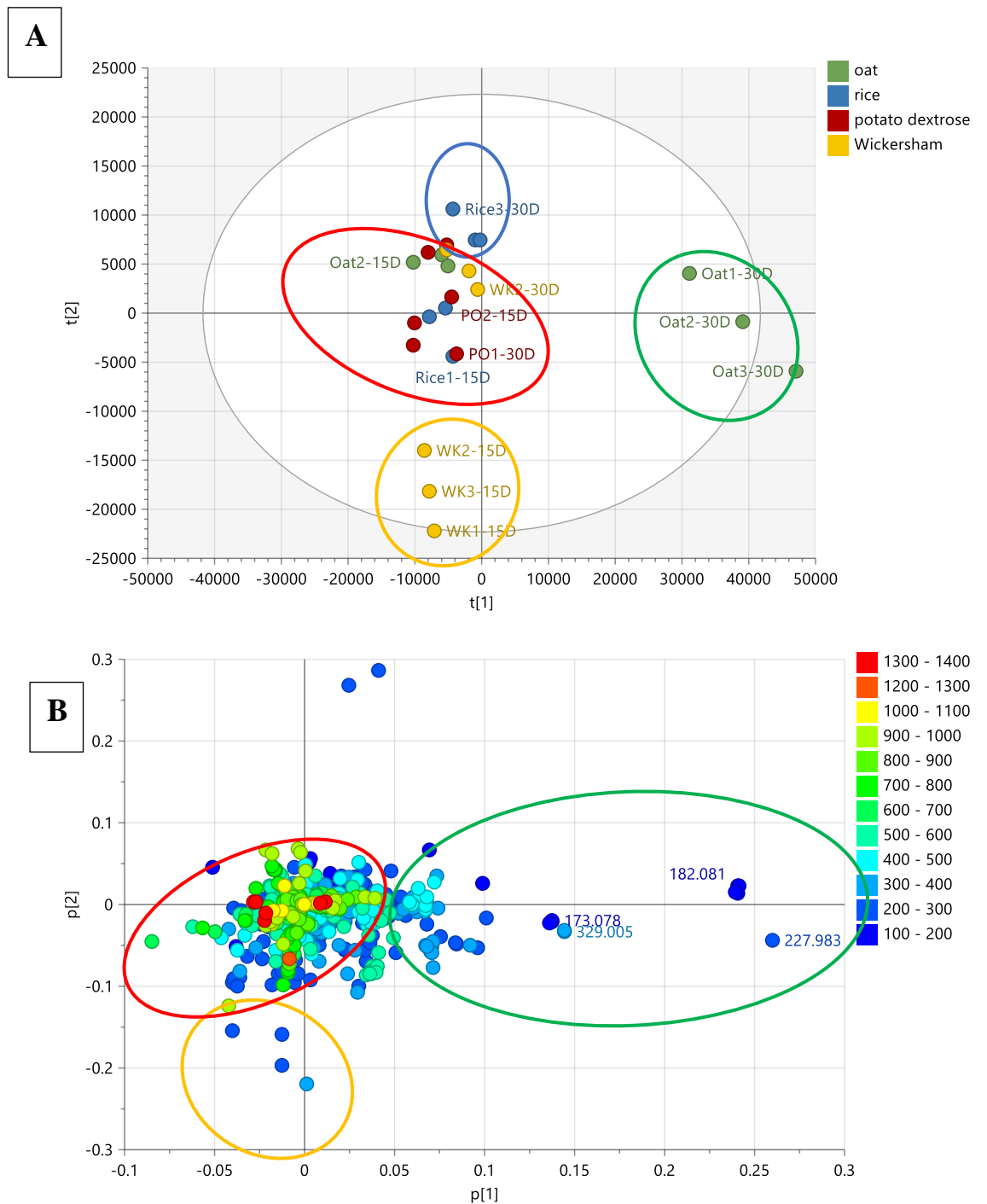
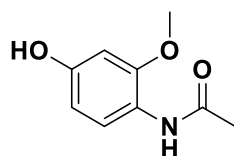


Figure 5.28: (A) PCA scores (B) loading plots of LC-HRMS of *A. solani* extracts from four media incubated at 15, 30 days. $R^2X = 0.67$ and $Q^2X = 0.38$. Encircled features represent the discriminating ion peaks for the extracts obtained from different media.



4-Hydroxy-2-methoxyacetanilide
Mzmine P_3862
Rt 1.94
MW 181.0740 Da

Figure 5.29: Discriminating metabolite from extracts of *A. solani* inoculated on oat media and incubated for 30 days.

According to the OPLS-DA scores plot (Figure 5.30A), extracts obtained from the oat media at 15th and 30th day of incubation were overlapping on lower right quadrant of the scores plot. Whereas extracts obtained from rice and Wickersham for 15 and 30 days were positioned in the upper and lower left quadrant of the plot, respectively. On the other hand, potato dextrose extracts at 15 and 30 days were found in the left side of the plot. The R^2 and Q^2 values were at 0.80 and 0.52, respectively, which indicated a good fit and predictability of the model. The variation between groups R^2X_o [1] was 18.0% and within group $R^2X[1]$ was 4.7%. This indicated good separation between the extracts obtain from different media while the low separation score within groups indicated a significant similarity in chemical profiles between the 15- and 30-days extracts obtained from the respective media.

Loadings plot (Figure 5.30B) was generated from the OPLS-DA scores plot. four discriminating metabolites with ion peaks at m/z 267.0724, 182.0813 and 173.0782 Da were found in *A. solani* extracts from oat media at 15th and 30th days (Table 5.6). These metabolites were dereplicated from the DNP database. From the dereplication data, these metabolites with MZmine ID of N_171, and P_3862 were identified as deaminated neuraminic acid and 3-methylether-*N*-acetyl-4-amino-1,3-benzenediol, respectively, while P_1467 was not identified with no molecular formula prediction. These two known compounds were confirmed ¹H NMR spectra of oat extracts, which includes producing aromatic and glycosylated secondary metabolites at 30th days. Whereas, the discriminating features for Wickersham media extracts were P_6007, and P_2242 with m/z value of 244.2271 and 214.0896 Da and were identified as

tetradeca-4-sphingenine and *N*-butyl benzenesulfonamide. Other discriminating feature from *A. solani* extracts from four different media were listed in Table 5.6.

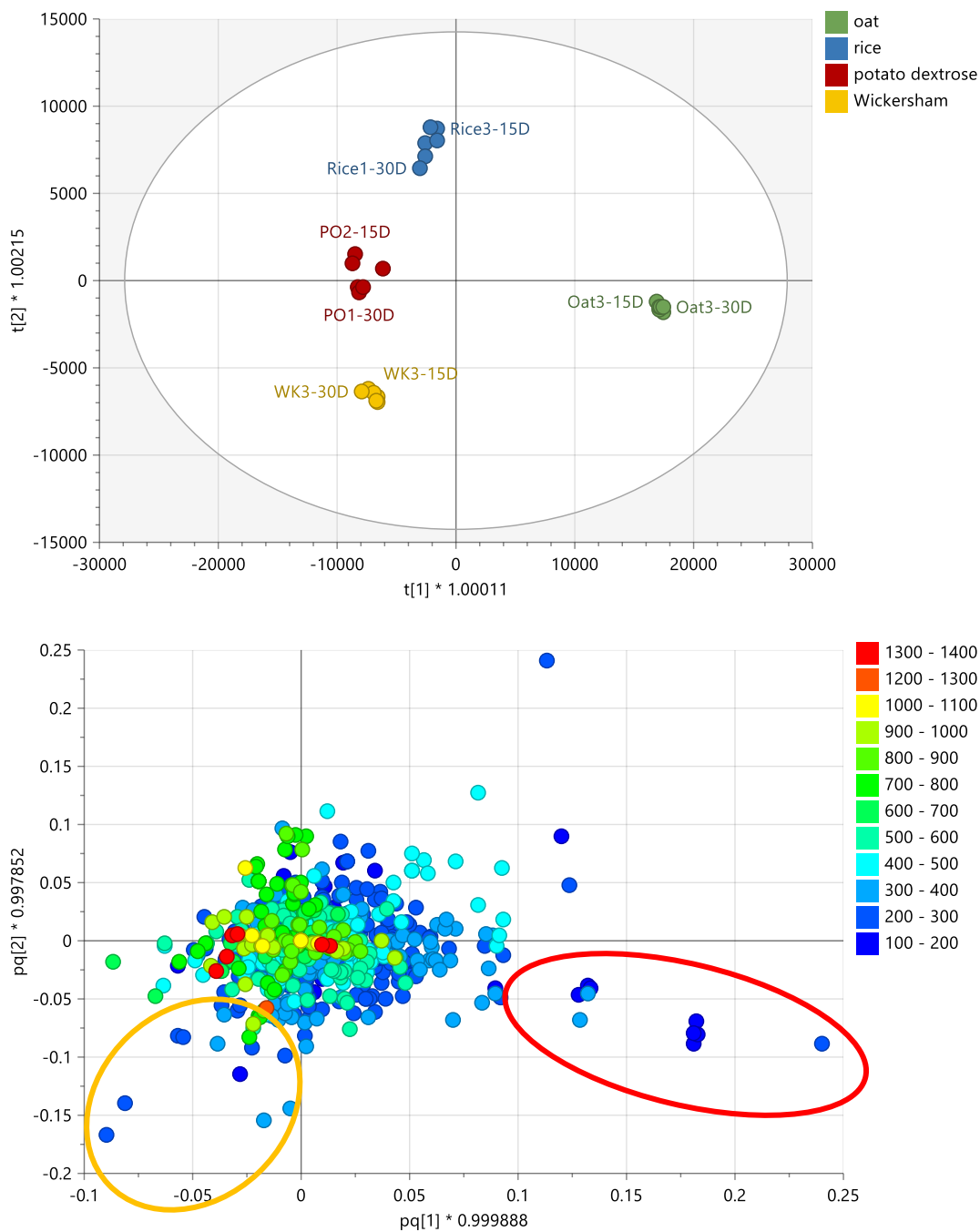


Figure 5.30: A) OPLS-DA scores and B) loading plots of LC-HRMS of *A. solani* extract obtain from different media. The encircled box indicated the discriminating feature for each media extracts. $R^2 = 0.80$ and $Q^2 = 0.52$. The difference between group $R^2X_0[1]$ is equal to 18.0% and the difference within groups $R^2X[2]$ is 4.7%.

Table 5.6: Dereplication of discriminating metabolites of *A. solani* for different media. Structures of compound hits are shown in Figure 5.31.

Primary ID	p-value	m/z	Rt	mw	Compound hits [†]	Molecular formula* (DBE)	source
oat media							
N_320	0.0021	429.1252	8.84	430.1325	3'-O- α -D-glucopyranosylinosine (1)	C ₁₆ H ₂₂ N ₄ O ₁₀ (4)	crustacean <i>Ligia exotica</i>
N_318	0.0062	377.0859	9.18	378.0932	altersolanol N (2) 3-acetylaltersolanol M (3) flavimycin A (4) 3-deoxy-5,6-dihydroxy secosterigmatocystin (5) sporormiellin C (6)	C ₁₈ H ₁₈ O ₉ (10)	<i>Stemphylium globuliferum</i> <i>A. flavipes</i> <i>Phomopsis spp</i> <i>Sporormiella minima</i>
N_171	0.0348	267.0724	5.76	268.0797	deaminated neuraminic acid (Structure is not defined)	C ₉ H ₁₆ O ₉ (2)	<i>Klebsiella ozaenae</i>
P_1467	0.0532	173.0783	3.70	172.0710	no hits	no prediction	-
N_230	0.0540	387.1149	5.77	388.1221	no hits	C ₁₃ H ₂₄ O ₁₃ (2)	-
P_3862	0.0678	182.0813	1.95	181.0740	3-methylether- <i>N</i> -acetyl-4- amino-1,3-benzenediol (7)	C ₉ H ₁₁ NO ₃ (4)	Isol. from a fungal endophyte of spruce needles and from a soil fungus.
P_663	0.0670	329.0049	2.30	328.9976	no hits	-	-
Wickersham media							
P_657	0.0071	327.0080	2.25	326.0007	no hits	no prediction	-
P_2239	0.0027	286.9581	2.23	285.9508	no hits	no prediction	-
P_2242	0.0060	214.0896	2.24	213.0824	<i>N</i> -butyl benzenesulfonamide (8)	C ₁₀ H ₁₅ NO ₂ S (3)	<i>Actinoallomurus sp. K216</i> <i>Pseudomonas sp.</i>
P_6007	0.0044	244.2271	20.46	243.2198	tetradeca-4-sphinganine (9)	C ₁₄ H ₂₉ NO ₂ (1)	germination-accelerating factor for fungus
P_752	0.0144	493.4059	26.09	492.3986	benzoylcholestan-3 α -ol (10)	C ₃₄ H ₅₂ O ₂ (9)	<i>various marine species</i>
P_17	0.0215	272.2220	40.52	271.2147	clavaminol L (11)	C ₁₅ H ₂₉ NO ₃ (1)	<i>Clavelina phlegraea</i>
P_1271	0.0041	686.4390	34.76	685.4317	no hits	C ₄₃ H ₅₉ NO ₆ (15)	no reports

N_268	0.0509	766.5414	38.02	767.5487	phosphatidylethanolamine (12)	C ₄₃ H ₇₈ NO ₈ P (4)	membranes of eukaryotic and prokaryotic cells <i>Trichoderma cf. strigosum</i>
P_1	0.0637	264.2321	13.84	263.2249	victoxinine (13)	C ₁₇ H ₂₉ NO (8)	<i>Helminthosporium victoriae</i> , <i>Helminthosporium carbonum</i> , <i>Helminthosporium sativum</i>
N_295	0.0746	714.5098	37.99	715.5171	no hits	C ₄₆ H ₆₉ NO ₅ (13)	-
rice media							
P_697	0.000002	427.3975	37.83	426.3902	no hits	C ₂₀ H ₄₆ N ₁₀ (3)	no reports
N_315	0.0996	711.2211	3.87	712.2284	no hits	-	-
P_2240	0.0059	470.4205	37.84	469.4132	no hits	C ₂₈ H ₅₅ NO ₄ (2)	no reports
N_191	0.0385	471.1359	3.95	472.143	α-D-glucopyranuronosyl-(1→2)-β-D-xylopyranosyl-(1→4)-D-xylose* (14)	C ₁₇ H ₂₈ O ₁₅ (4)	<i>Picea glauca</i>
potato dextrose extracts							
P_754	0.0435	270.2425	26.41	269.2352	2-amino-4,8-hexadecadiene-1,3-diol (15)	C ₁₆ H ₃₁ NO ₂ (1)	<i>fatty acid component in Penicillium chrysogenum</i>
P_1339	0.0571	298.2375	33.17	297.2302	(S)-N-tridecanoylhomoserine lactone (16)	C ₁₇ H ₃₁ NO ₃ (2)	<i>Methylobacterium mesophilicum</i>
N_307	0.0344	1035.3271	5.44	1036.3344	no hits	C ₃₆ H ₄₈ N ₁₈ O ₁₉ (22)	-
P_3408	0.0389	224.1281	3.21	223.1208	alternamic acid (+)-cerulenin (17)	C ₁₂ H ₁₇ NO ₃ (4)	<i>Alternaria mali</i> <i>Cephalosporium caerulens</i> <i>Helicoceras oryzae</i>
P_3391	0.0733	471.4239	29.61	470.4166	no hits	-	-
P_2081	0.0799	784.5842	37.96	783.5770	linoleoylphosphatidylcholine (18) stearoylphosphatidylcholine (19)	C ₄₄ H ₈₂ NO ₈ P	structural component of intracellular membranes and the plasma membrane
[†] For multiple hits, chosen compound hits were filtered for microbial or fungal species (particularly for the genus <i>Aspergillus</i>) except otherwise. *Follows the heuristic rules. **All other hits were from plant species.							

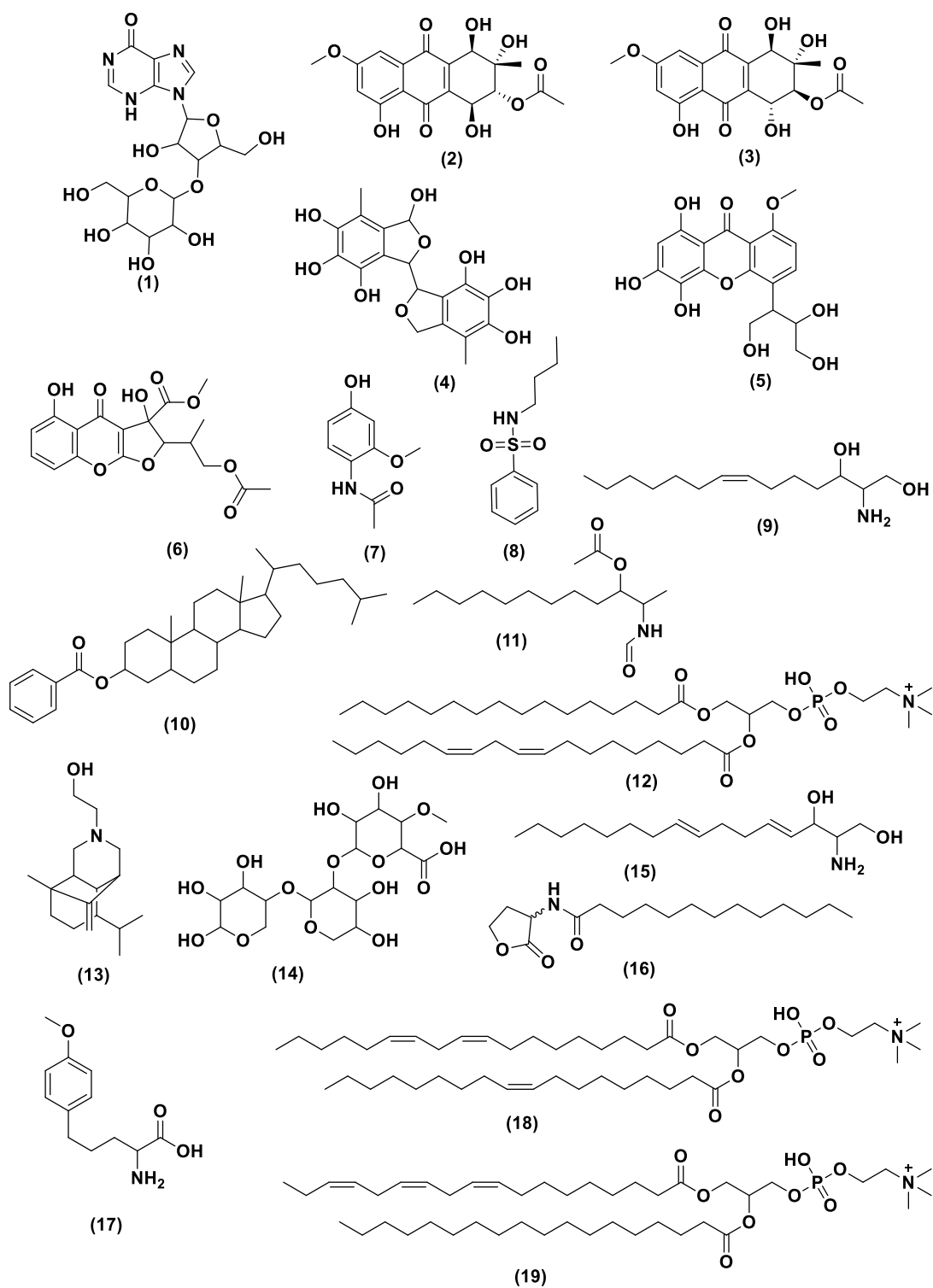


Figure 5.31: Structures of the discriminating bioactive metabolites from *A. solani* extract obtained from potato dextrose media have been listed in Table 5.6.

5.3. Summary

5.3.1. *A. ustus* optimisation

Several compounds have been isolated from *A. ustus* and their biological activity have been studied (Liu *et al.*, 2009, Lu *et al.*, 2009, Ebel, 2010, Dai *et al.*, 2010). The chemical compounds recorded to be isolated from *A. ustus* exhibited cytotoxic activity against L5178Y, HeLa, and PC12 cells cell line (Liu *et al.*, 2009).

After isolation of *A. ustus* from the screening chapter, further work was performed on *A. ustus* to choose the ideal medium that produces higher yields of metabolites and greater biological activity. *A. ustus* is a slow-growing fungus. No growth was observed up to the 15th day of incubation, and it required at least 21 days to reach its logarithmic phase. The average yield afforded by the solid media is higher than growing the fungus on a liquid media. However, only potato-dextrose media was strongly active against breast cancer (ZR-75) cell line, where cell viability was almost zero at 30 days of incubation, even those extract not providing the highest yield. Therefore, the recommended media for a scale up would be potato-dextrose media for a 30-day incubation period.

The NMR spectral data of the extract obtained from the potato-dextrose extract broth afforded distinct peaks not found in the blank. Multivariate analysis of the NMR spectral data of *A. ustus* extracts did not designate any outlier but did show a clear trend on the change of metabolic profile between incubation periods when the fungus is inoculated on a liquid media. The OPLS-DA loadings plot of the mass spectral data of the extracts indicated 21 discriminating ion peaks eleven of these compounds did not give any hit from the DNP database.

The putatively identified compounds were a derivative of phospholipid, which include ion peaks with MZmine IDs N_17361, N_10906, N_1719 and N_7030 was found at m/z 554.5147, 742.5387, 784.5858 and 652.588 were dereplicated from the DNP database as *N*-2-hydroxyhexadecanoylsphinganine; phospholipid derivatives: stearyl linoleoylphosphatidyl-ethanolamine and -choline; and pakistamide. While other ion peaks at m/z 369.2793, 169.0861 and 253.1800 were putatively identified as

terpenoid derivatives including stellatic acid, 3-(4-hydroxyphenyl)-1,2-propanediol and 2,11-dihydroxy-7-drimen-6-one; 2 α -form, respectively. The next step will be to do large scale fermentation of *A. ustus* at 30 days of incubation in potato-dextrose medium in order to produce higher yields of the targeted bioactive metabolites.

5.3.2. *A. solani* optimisation

Isolation and purification work of any of the metabolites were not pursued for *A. solani* due to loss of bioactivity during media optimisation. However, multivariate analysis of the production of metabolites were done to attempt to explain the changes occurring in the fungal strains during the media optimisation. Differences in metabolic production profile were also defined. The chemical profiles of *A. solani* obtained from MAmedia in the screening and from five different media in the media optimisation were compared. The chemical profiles of the fungal extracts derived from different media were different. However, any other variation would affect the chemical profile of the afforded extracts.

6. *A. ustus* scale up and isolation of anticancer compounds.

A. ustus was chosen for further scaleup work because its extracts provided the most potent activity against the tested cancer cell lines.

6.1. Literature background on the endophytic fungi *A. ustus*

A. ustus is a widespread filamentous fungus that may be found in food, soil, and indoor environments (Mousavi *et al.*, 2016). *A. ustus* is a member of the phylum Ascomycota. Numerous *Aspergillus* species are found in or on a wide variety of plants endophyte and marine invertebrates (Seyedmousavi *et al.*, 2015, Mousavi *et al.*, 2016). Plant-derived *A. ustus* have been proven to be very good sources of bioactive natural products, but marine-derived *A. ustus* do produce chemically diverse new natural products with interesting biologically active secondary metabolites (Debbab *et al.*, 2010). A comparison between plant- and marine-derived *A. ustus* was tabulated based on their host organisms, isolated secondary metabolites, bioactivity, and cytotoxicity, as depicted in Table 6.1.

Table 6.1: Reported sources, biological activity, and isolated compounds for *A. ustus*.

Type of Host	Host Organism (references)	Isolated Compounds	Bioactivity	Cytotoxicity
plant-derived	<p>Pods pea seeds (Cutler <i>et al.</i>, 2002)</p>	<p>pergillin</p> <p>ophiobolin G</p> <p>ophiobolin H</p>	<p>(Lu <i>et al.</i>, 2009)</p> <p>both inhibited growth of <i>Bacillus subtilis</i> cultures</p> <p>inhibition of endothelin-type B receptors (B16 cell lines and antifungal activity against <i>Candida albicans</i>)</p>	nontoxic
marine-derived	<p>rhizosphere soil of mangrove plants (Lu <i>et al.</i>, 2009)</p> <p>marine sponge <i>Suberites domuncula</i> (Liu <i>et al.</i>, 2009)</p> <p>marine green alga <i>Codium fragile</i> (Liu <i>et al.</i>, 2013)</p>	<p>meroterpenoid - mycotoxins, drimane sesquiterpene esters (ustusolates A to E)</p> <p>ophiobolins derivatives</p> <p>drimane sesquiterpenes derivatives</p> <p>terretonin, ophiobolin, and drimane terpenes derivatives</p>	<p>cytotoxicity of the new compounds against A549 and HL-60 human tumour cells were determined by the SRB20 and MTT</p> <p>murine lymphoma cell line L5178Y, HeLa, and PC12 cells</p>	<p>moderate cytotoxicity</p> <p>cytotoxic</p>

Bioactive compounds were isolated from the marine algae *Codium fragile* and an associated fungus *A. ustus* (Liu *et al.*, 2013). In the literature, *A. ustus* has been shown to be a prolific generator of terpenes, which include meroterpenes, sesterterpenes, and sesquiterpenes (Ebel, 2010, Liu *et al.*, 2013). Terpenes produced from marine sources exhibit a higher degree of molecular and structural diversity with unique carbon skeletons such as terretonin, ophiobolin, and drimane of secondary metabolites described from *A. ustus* (Ebel, 2010, Liu *et al.*, 2013). It was stated in the literature that eight novel compounds were discovered as shown in Figure 6.1 (Liu *et al.*, 2013), including one meroterpene; 1,2-dihydroterretonin F (**2**), and five new sesterterpenes; 6 α -21-deoxyophiobolin G, 6 α -16,17-dihydro-21-deoxyophiobolin G (**4**), ophiobolin V (**6**), ophiobolin W (**7**) and ophiobolin U (**5**). Furthermore, two new sesquiterpenes of 6-strobilactone-B esters of (*E,E*)-6,7-epoxy-2,4-octadienoic acids (**13**&**13'**). These secondary metabolites were assayed for antibacterial and brine shrimp toxicity, as well as antifungal, only compound **5** exhibited an activity against *E. coli* and *S. aureus* and compounds **2**, **5**, and **13** demonstrated cytotoxic activity on *Artemia salina* at 100 μ g/mL. whereas none of these compounds showed antifungal activities against *Colletotrichum lagenarium* and *Fusarium oxysporum*. However, other secondary metabolites were already known compounds and have been earlier described, which includes terretonin F (**1**), 6 α -21,21-*O*-dihydroophiobolin G (**8**), (5 α ,6 α)-ophiobolin H (**9**), ophiobolin H (**10**), ophiobolin F (**11**), 3 β ,9 α ,11-trihydroxy-6-oxodrim-7-ene (**12**), ustusolate D (**14**), and (29*E*,49*E*,69*E*)-6-(19-carboxyocta-29,49,69-triene)-11,12-epoxy-9,11-dihydroxydrim-7-ene (**15**) (Figure 6.1).

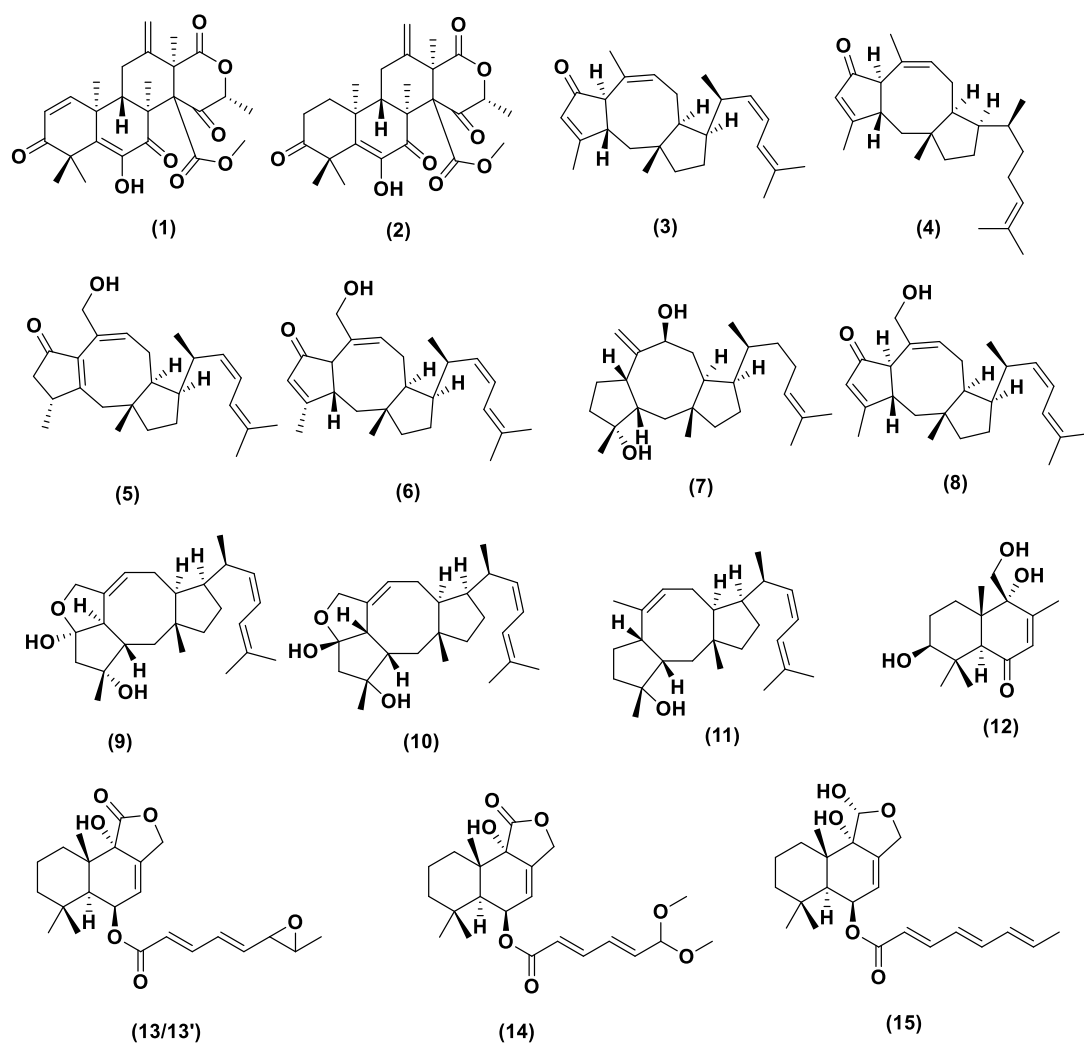


Figure 6.1: Secondary metabolites previously isolated from *A. ustus* obtained from the marine algae *Codium fragile* (Liu *et al.*, 2013).

Drimane sesquiterpenoids are well-known as bioactive metabolites, which were obtained from *A. ustus* isolated from the marine sponge *Suberites domuncula* (Liu *et al.*, 2009). They have gained widespread attention for their biological activities, which include antibacterial, antifungal, antifeedant, plant growth regulator, cytotoxic, phytotoxic, and molluscicidal effects (Ogawa *et al.*, 2004). As described in the literature (Liu *et al.*, 2009), deoxyuvidin B (**20**), strobilactone B (**21**), and RES-1149-2 (**25**) were identified as known compounds. On the other hand, seven new drimane sesquiterpenoids were discovered, including hydroxylated derivatives; 3 β ,9 α ,11-trihydroxy-6-oxodrim-7-ene (**17**), 2 α ,9 α ,11-trihydroxy-6-oxodrim-7-ene (**18**), 2 α ,11-

dihydroxy-6-oxodrim-7-ene (**19**), ester derivatives of drimane sesquiterpenes that includes mono-6-strobilactone-B ester of (*E,E*)-2,4-hexa-dienedioic acid (**22**), 6-strobilactone-B ester of (*E,E*)-6-oxo-2,4-hexadienoic acid (**23**), 6-strobilactone-B ester of (*E,E*)-6,7-dihydroxy-2,4-octadienoic acid (**24**) (Figure 6.2). All these drimane sesquiterpenes derivatives were tested against L5178Y, HeLa and PC12 cells to determine cytotoxicity by MTT assay. Compounds **22**, **23**, and **25** exhibited cytotoxic activity against L5178Y, HeLa, and PC12 cells, with **22** being the most active with an EC₅₀ value of 0.6 µg/mL against L5178Y cell line (Liu *et al.*, 2009).

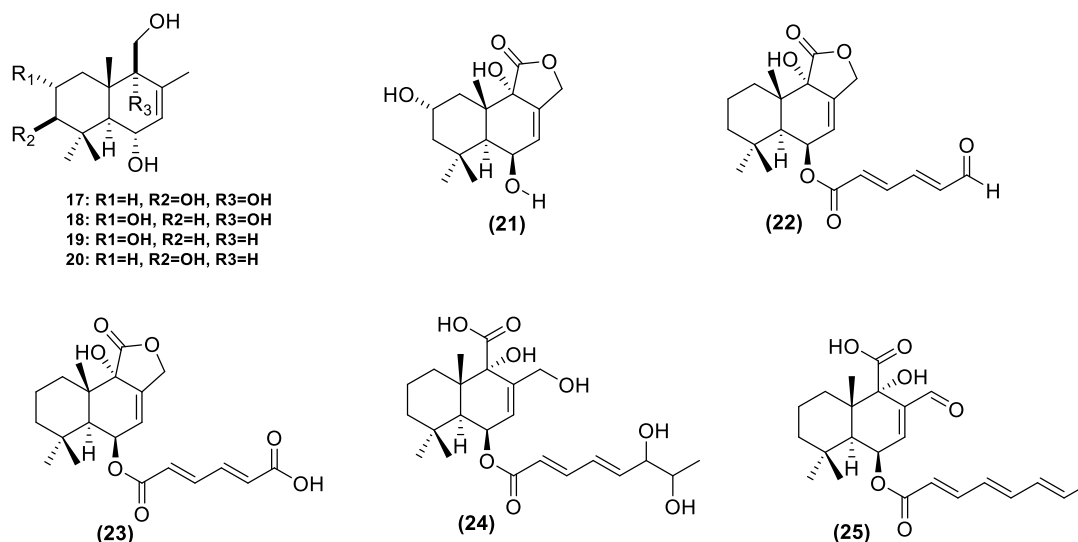


Figure 6.2: Secondary metabolites isolated from *A. ustus* obtained from the sponge *Suberites domuncula* (Liu *et al.*, 2009).

6.2. Fractionation of the extract and multivariate analysis

The potato-dextrose extract from the *A. ustus* was fractionated by FC through a Büchi Sepacore® system. Each fraction was collected in a 100ml Erlenmeyer flask and TLC analysis was performed on all fractions. Fractions with similar TLC profiles were pooled together, then was dried using a rotary evaporator and placed in tared vials (Figure 6.3).

The overall percentage yield of the collected dried fractions was 94.3% percent of the weight of the loaded extract (Table 6.2). The dried fractions were spotted on a normal phase Si-60 TLC plate along with the crude extract for monitoring purposes using a

solvent system of 97:3% DCM:MeOH and sprayed with anisaldehyde-sulphuric acid reagent.



Figure 6.3: Collected fractions by FC showing change in colours between fractions indicating the occurrence of various metabolites in the respective fractions.

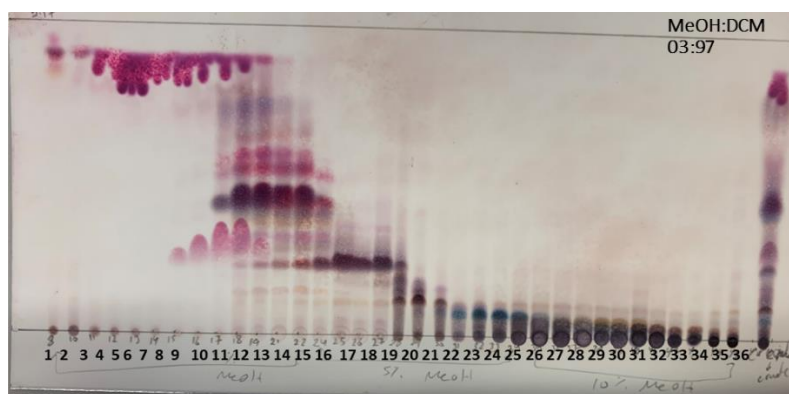


Figure 6.4: Summary TLC plate for the pooled fractions using a solvent system 97:03 % of DCM:MeOH after spraying with anisaldehyde-sulphuric acid reagent

Table 6.2: Weights of extracts after pooling similar fractions.

Fraction no.	Weight of fraction (mg)	Fraction no.	Weight of fraction (mg)
1	125.1	20	213.6
2	57.4	21	162.8
3	371.6	22	138.5
4	750.6	23	104.9
5	587.5	24	72.7
6	484.3	25	63.0
7	414.9	26	55.5
8	254.0	27	49.0
9	394.4	28	48.5
10	436.8	29	44.4
11	708.3	30	41.4
12	343.0	31	63.9
13	372.3	32	97.2
14	134.6	33	94.8
15	82.0	34	1018.0
16	32.7	35	37.3
17	64.3	36	25.4
18	820.3	37	87.6
19	579.0	Total amount	9432.1

6.3. Biological assay results of fractions

Each of the fractions was assayed against breast cancer cell line ZR-75 (Figure 6.5). Fractions F10 to F32 were found active. IC₅₀ values were calculated for each of the active fraction to determine the most potent fractions against ZR-75 (Figure 6.6). Fractions F10 to F16 were the most potent with IC₅₀ values of less than 5.5 µg/mL. On the other hand, F17 to F23 exhibited lower potency with IC₅₀ values at only less than 15 µg/mL.

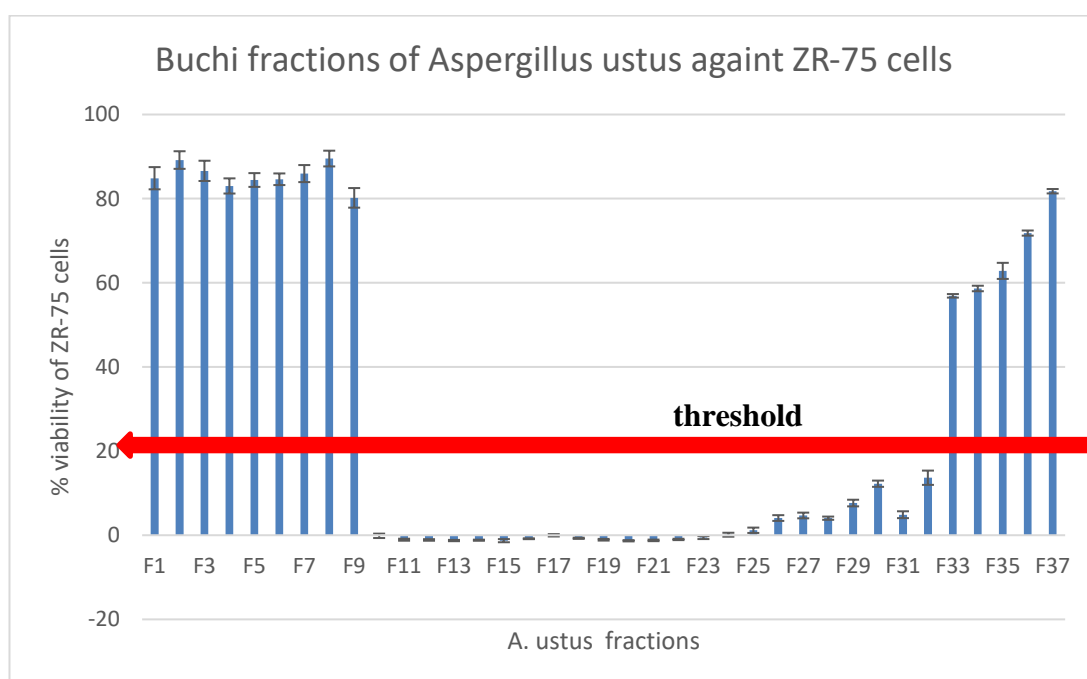


Figure 6.5: Biological activity for Büchi fractions of *A. ustus* at 30 µg/mL against breast cancer cell line ZR-75. The red line indicates the bioactivity threshold, which must be below 20% of cell viability.

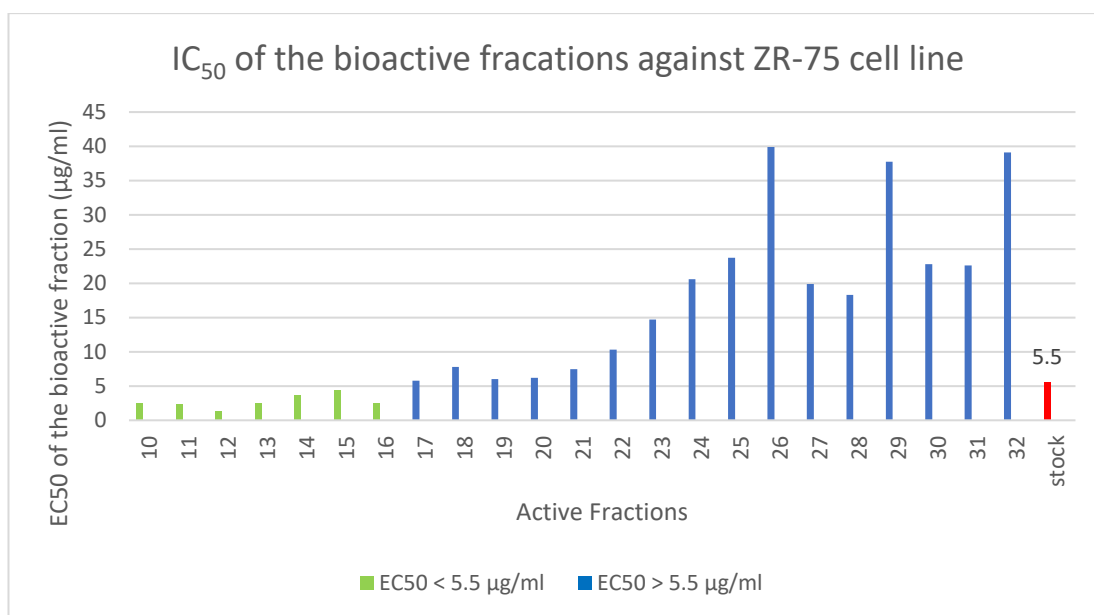


Figure 6.6: IC₅₀ for the bioactive fractions from *A. ustus*.

6.4. NMR spectroscopy of *A. ustus* fractions

Proton NMR measurements were performed on the pooled fractions to get an overview of the chemical profile and types of functional groups occurring in the metabolites predicted for each fraction. The ¹H NMR for the bioactive fraction with IC₅₀ values less than 5.5 µg/mL were stacked as shown in Figure 6.7. Meanwhile the bioactive fraction with IC₅₀ values less than 15 µg/mL but greater than 5.5 µg/mL were also stacked as shown in Figure 6.8. The ¹H NMR spectra revealed an olefinic system between 7.25 to 5.90 ppm that could be related to esterified di- or sesquiterpenes strobilactones and drimanes that could be present in the fractions with IC₅₀ values less than 5.5 µg/mL (enclosed in a blue box) as shown in Figure 6.7. in addition to the presence of high intensity peaks at the aliphatic region.

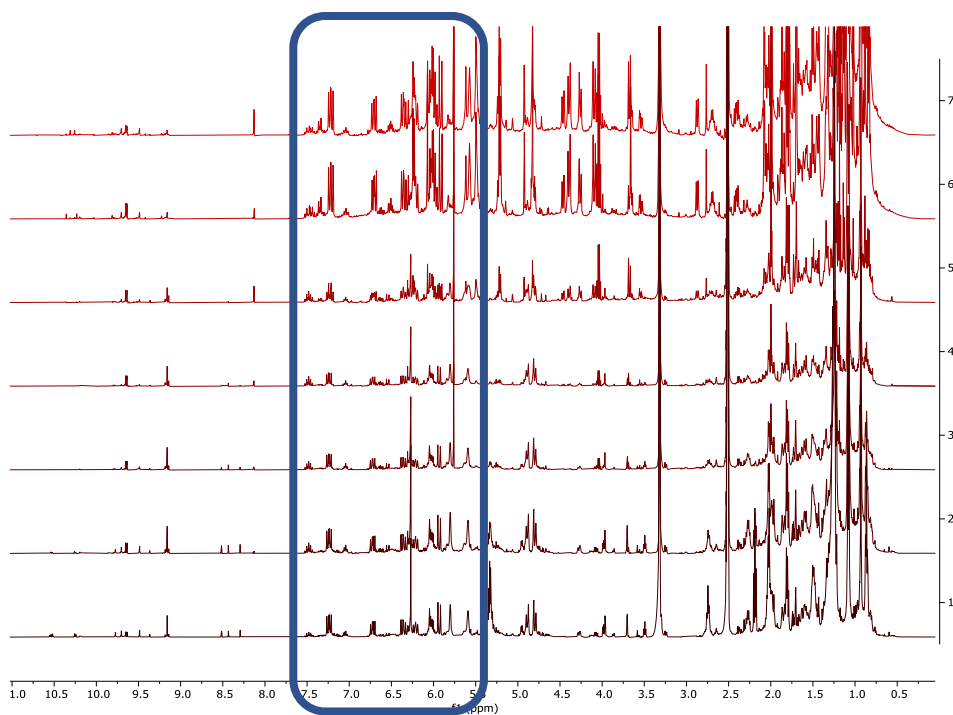


Figure 6.7: Stacked ¹H NMR spectra of the bioactive MPLC fractions with $IC_{50} < 5.5 \mu\text{g/mL}$. The highlighted blue box suggested the present of di or sesquiterpenes group.

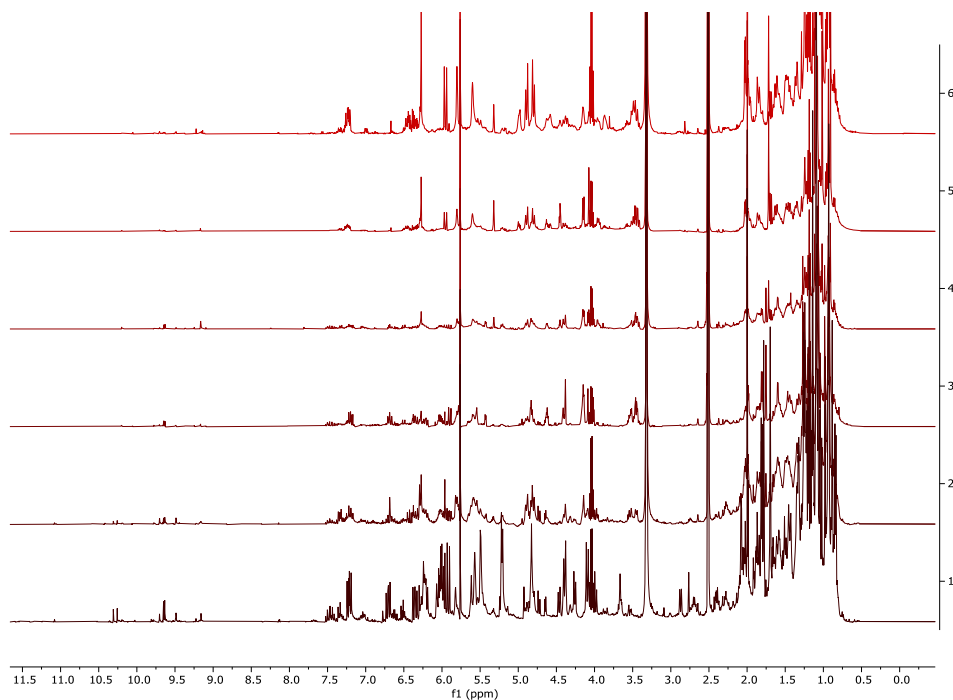


Figure 6.8: Stacked ¹H NMR spectra of the bioactive MPLC fractions with IC_{50} between 5.5-15 $\mu\text{g/mL}$.

The PCA scores scatter plot differentiates the bioactive fraction against breast cancer cell line apart from the inactive fractions (Figure 6.9A). The bioactive fractions 12 to 23 grouped together at the lower left quadrant, suggesting that they have a similar chemical profile. Meanwhile, the loadings plot of NMR data showed that these bioactive fractions 12 to 23 have metabolites that contains olefinic at 4.00 to 6.00 ppm and aliphatic groups from 1.00 to 2.00 ppm (Figure 6.9B). In the generated model at pareto scaling, the R^2 was 0.91 and Q^2 was -0.04 at twelve components, which indicated a good fit model but poor predictability. Although, the active fractions tend to cluster together, the inactive fractions were quite dispersed throughout the plot generating a low predictability score.

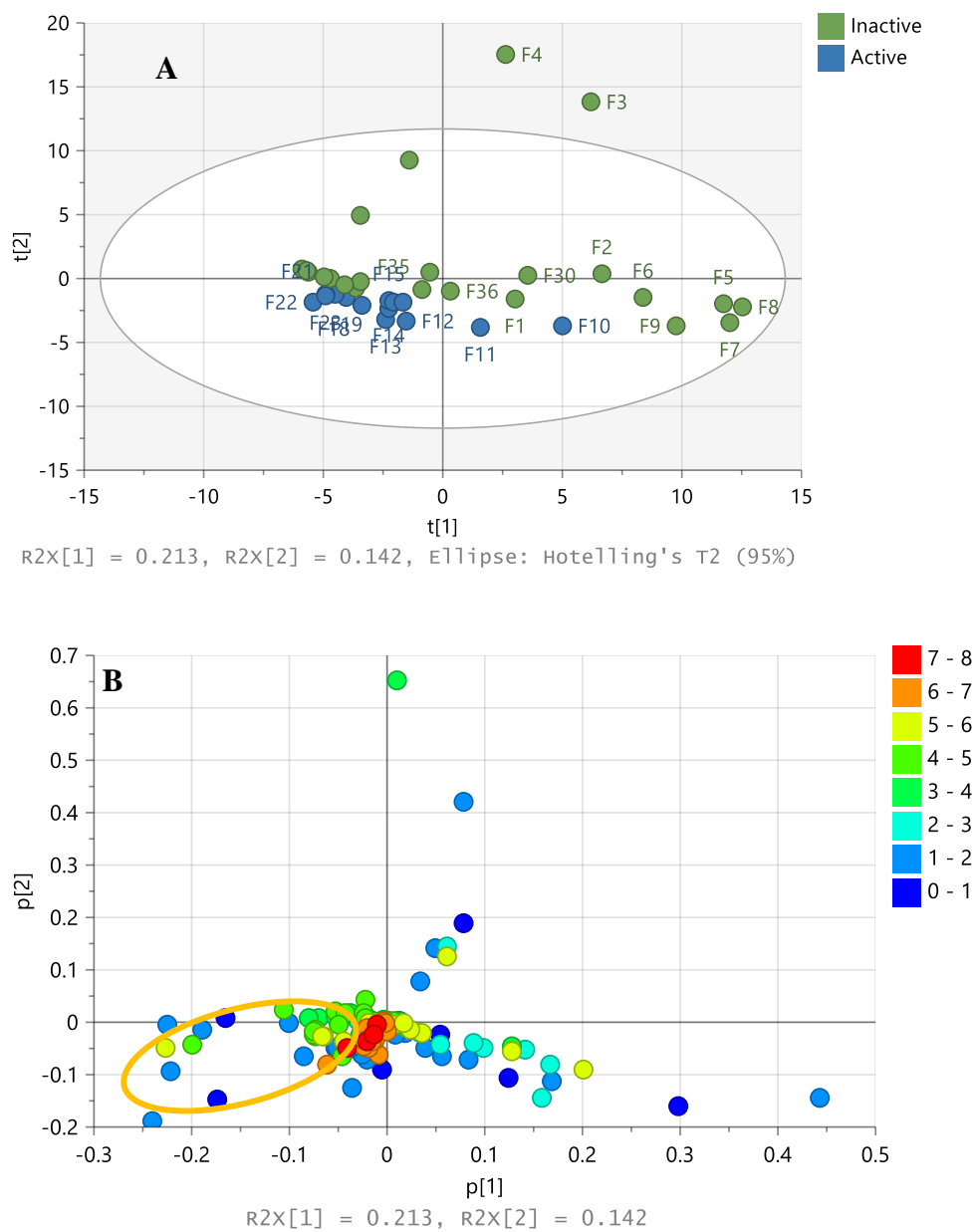


Figure 6.9: (A) PCA scores and (B) loadings plots of the NMR spectral data of the fractions. The R^2 and Q^2 values were 0.91 and -0.04, respectively.

An OPLS-DA was also performed to indicate the discriminating signals for the active fractions. The active fractions were positioned on the right quadrants of the OPLS-DA scores plot (Figure 6.10 A), where fractions 10 and 11 were separated on the upper right quadrant, fractions 18 and 22 were found in the lower right quadrant and the rest of the fractions were clustered in the middle. The inactive fractions were arranged at the left quadrants of the OPLS-DA scatter plot. The loadings plot showed the occurrence of wider range of resonance between 1.00 and 8.00 ppm for the active fractions, which indicated a high possibility of unique chemical profile. While the inactive fractions exhibited a higher ratio of olefinic and glycosylated peaks that resonated mainly between 3.00 and 5.00 ppm. R^2 and Q^2 values were 0.93 and 0.80, respectively, which indicated good fitness and predictability that is better than the PCA model. On the other hand, $R^2X_o[1]$ generated a variation score of 10.3% between groups while within groups, the variation score is only 1.5%, which indicated low diversity of the samples within the respective groupings. This is an excellent separation between the active and inactive clusters where the variation score between groups is greater than within groups. These differences between the two groups were also demonstrated by the loadings plot. A permutation test was performed to further validate the model (Figure 6.11). In the generated model, the R^2 was 0.93 and Q^2 was 0.80, while the R^2Y intercept was 0.98 and the Q^2Y intercept was -2.01. These values indicated both good fit and prediction as the R^2 value was close to 1 and the Q^2 value was greater than 0.5, respectively. The difference between R^2 and Q^2 values was 0.18, suggesting that there was no evidence of overfitting. The validity of the model was further confirmed by the negative value of Q^2 , being -2.01.

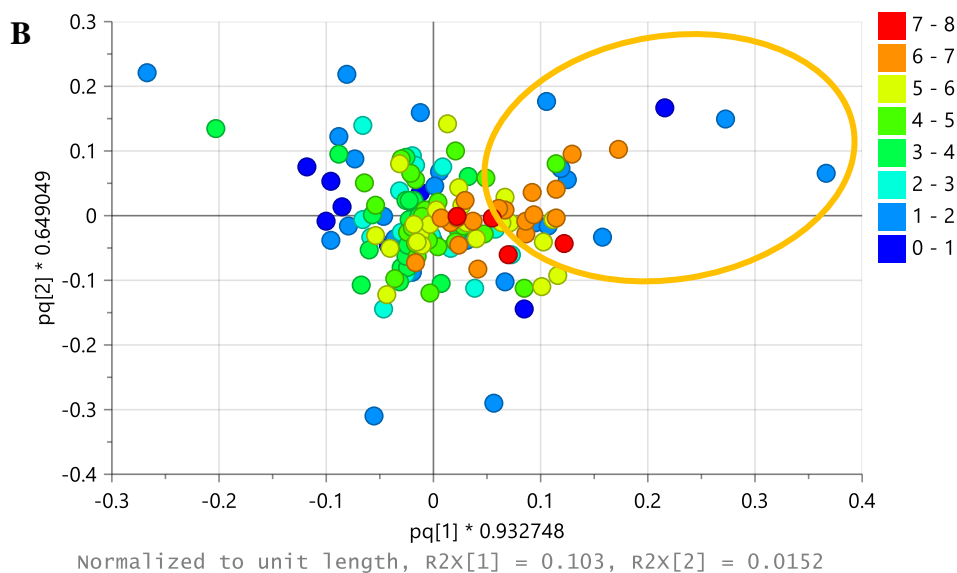
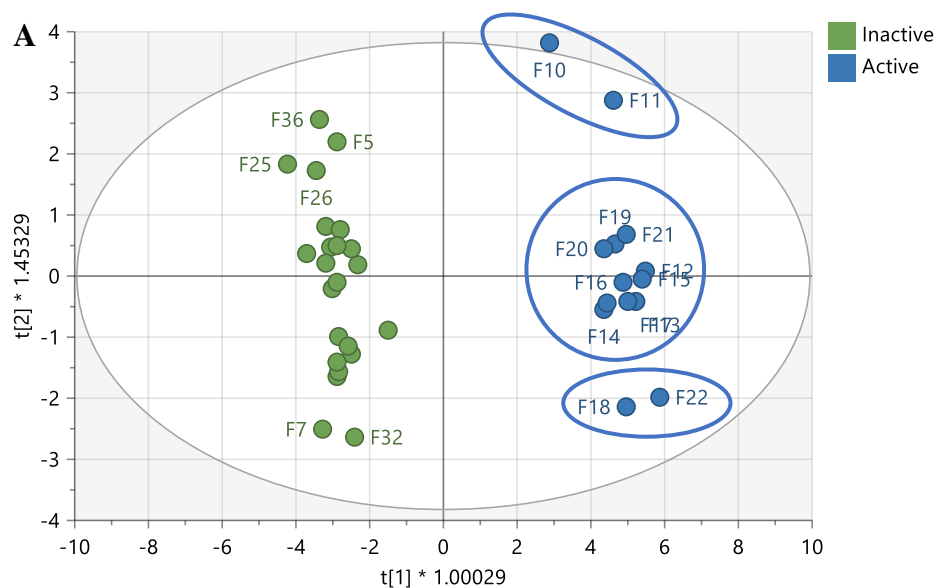


Figure 6.10: OPLS-DA scores (A) and loadings (B) plots of the NMR spectral data of the MPLC fractions grouped according to their bioactivity against breast cancer cell line ZR-75. R^2 and Q^2 values were 0.93 and 0.80, respectively. The difference between group $R^2X_0[1]$ is equal to 10.3% and the difference within groups $R^2X[2]$ is 1.5%. Encircled features on the loadings plot indicate the discriminating chemical shifts for the biologically active fractions.

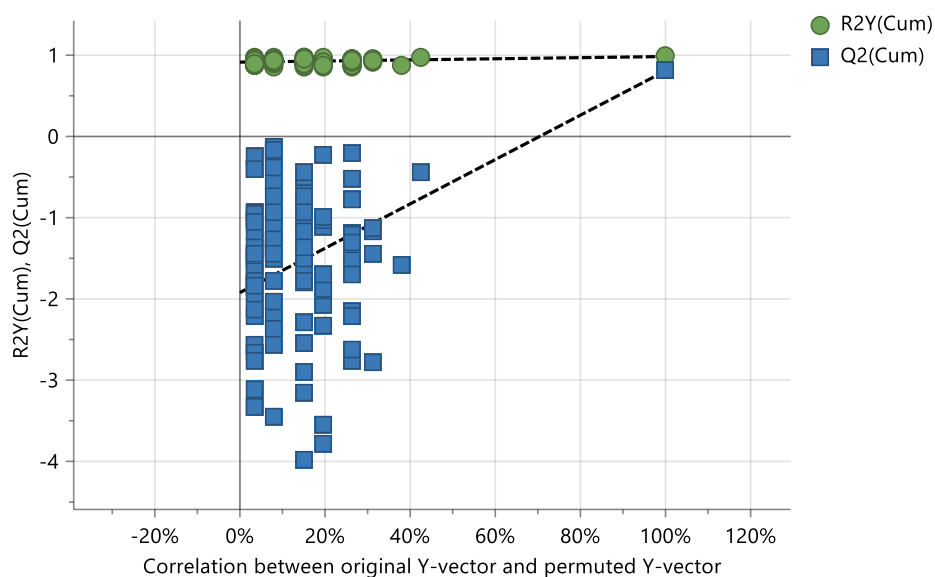


Figure 6.11: Permutation test (100 permutations) for *A. ustus* fractions for the OPLS-DA model of their activity against breast cancer cell line ZR-75.

Analysis on MetaboAnalyst® was also performed. The heatmap confirmed that bioactive fractions F10 to F18 were having metabolites with chemical shifts ranging from 1.07 to 1.70 ppm, which suggested the presence of aliphatic compounds. However, a high intensity of metabolites with chemical shifts ranging between 5.90 and 7.25 were also observed for these bioactive fractions, which also indicated the occurrence of olefinic compounds (Figure 6.12). Results of the heatmap analysis was compatible to those found from the OPLS-DA loadings plot. Additionally, the heatmap showed that the active fractions exhibited higher intensity of a more diverse number of chemical shifts. VIP (Variable Importance in Projection) summarising the important of variables both to explain X and to correlated to Y. Important variables have VIP scores greater than 1. Variables with VIP scores less than 1 are less important and may be excluded from the model (Akarachantachote *et al.*, 2014). OPLS-DA indicated the top VIP, which confirmed the above results as shown in Figure 6.13. Discriminating chemical shifts indicated the presence of aromatic systems resonating between 6.00 to 8.00 ppm with aliphatic signals between 1.00 and 2.00 ppm, as highlighted in the orange box (Figure 6.13).

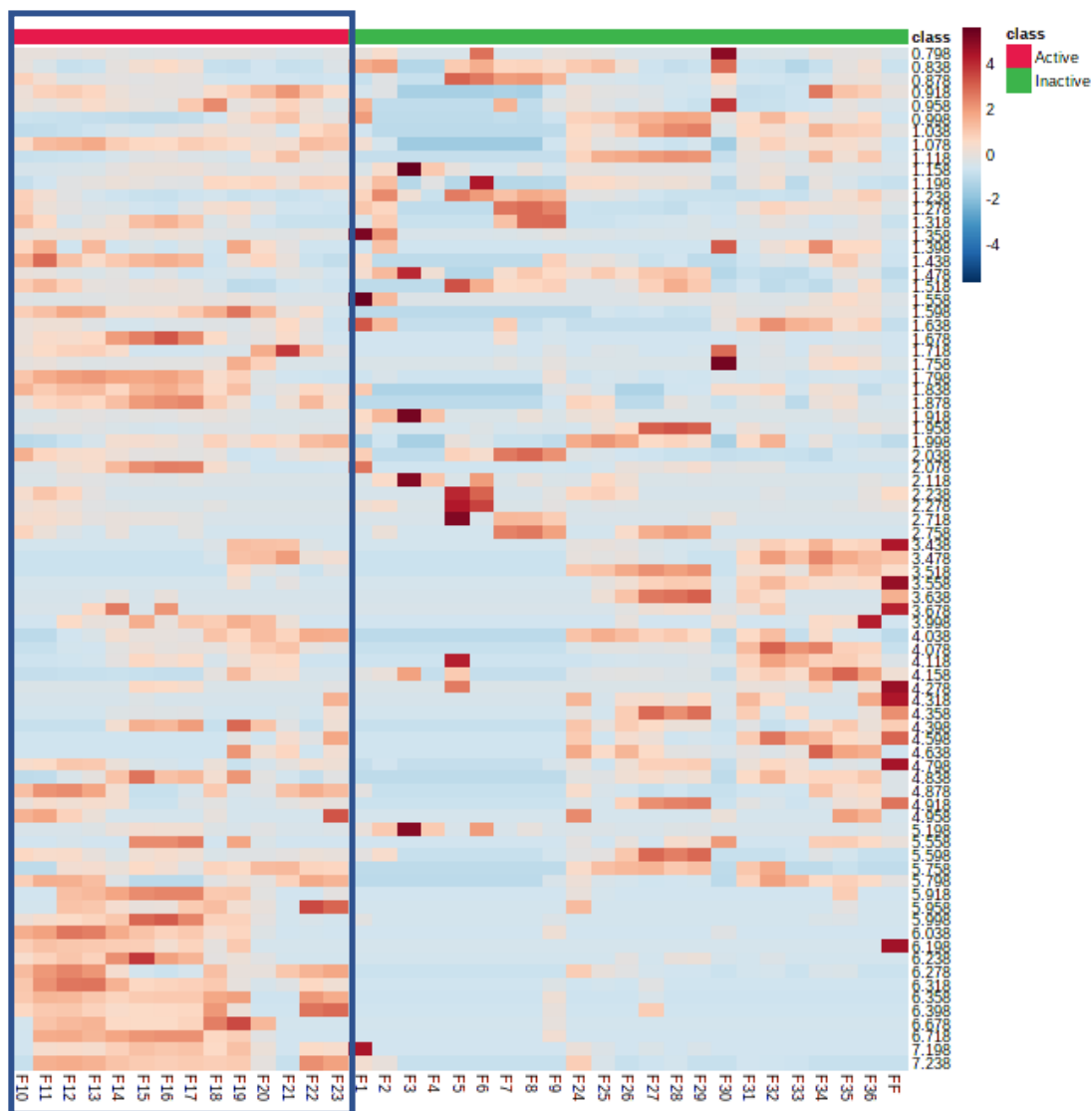


Figure 6.12: Heatmap analysis of the NMR spectral data of the *A. ustus* fractions generated by MetaboAnalyst®. The boxed fractions are those biologically active against the breast cancer cell line ZR-75 along with the discriminating chemical shifts unique to the anticancer fractions.

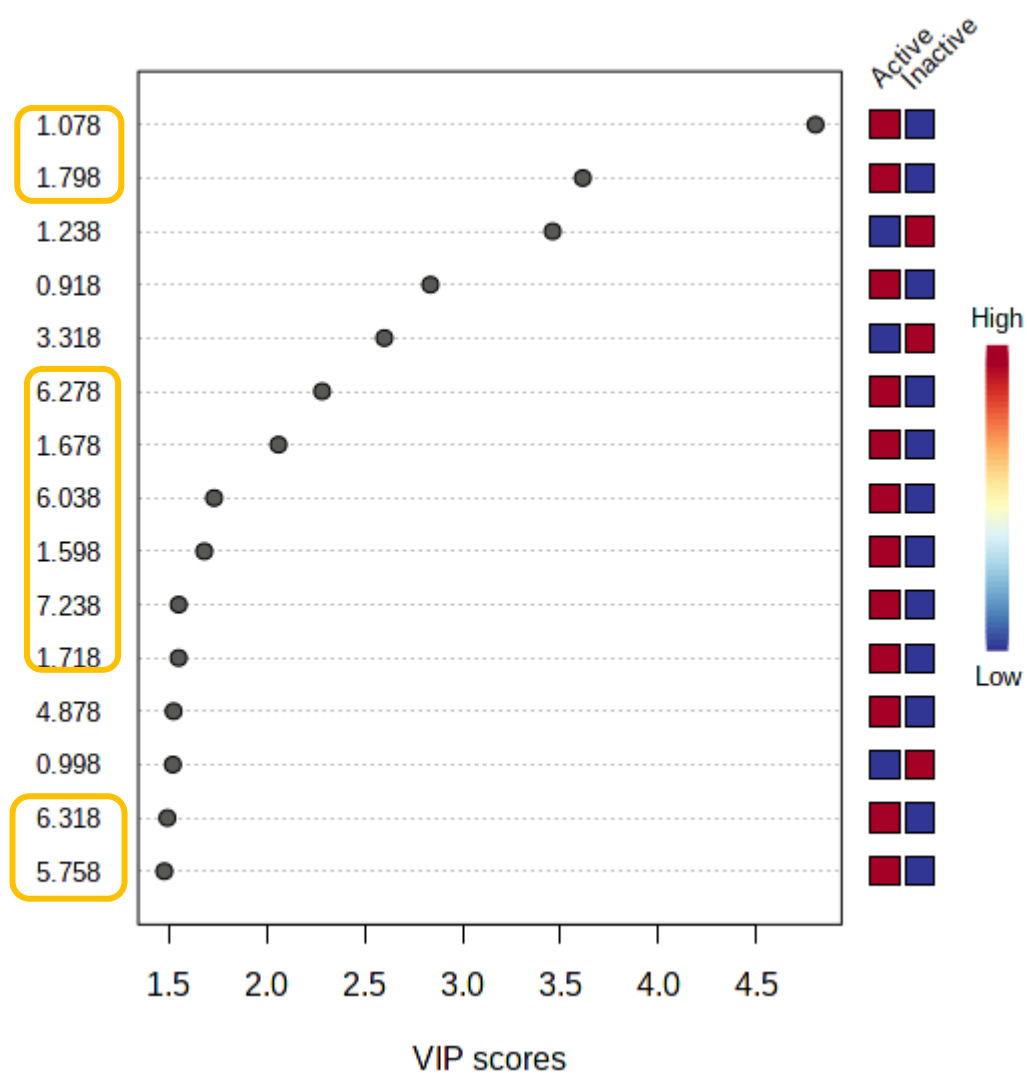


Figure 6.13: VIP scores of *A. ustus* fractions from MetaboAnalyst®. The highlighted yellow boxes show the discriminating chemical shift of the metabolites found in the bioactive fractions against the breast cancer cell line ZR-75.

6.5. LC-HRMS analysis of *A. ustus* fractions

Like the results of the multivariate analysis of the NMR spectral data, the active fractions were observed closer to each other on the presented scores plot (Figure 6.14A) except for the outlying fraction F16 but mostly positioned on the left quadrants. The loadings plot (Figure 6.14B) indicated a higher density of discriminating metabolites with MWs between 280 and 370 Da for the inactive fractions. On the other hand, the outlying active fraction F16 was discriminated by metabolites with ion peaks at m/z 369.290 for P_647, 253.185 for P_439, 215.147 for P_443, and 297.160 for N_158/N_199, these metabolites were listed in Table 6.3. P_443 was dereplicated as the Asteraceae metabolite senarguine B while anmindenol A was from the marine-derived *Streptomyces*. N_158/N_199 was the only discriminating metabolite (2,5-bis(4-hydroxybenzyl) piperazine and fumigaclavine A putatively identified as an *Aspergillus* metabolite. P_439 did not give any reasonable molecular formula prediction following the heuristic filter. While P_647 afforded sponge metabolite hits.

The model gave a goodness of fit R^2 at 0.71 but a very poor predictability Q^2 of 0.35 after five components. The OPLS-DA of the active versus the inactive fractions gave fitness and predictability scores of 0.89 and 0.72, respectively. R^2 and Q^2 values improved when compared to PCA model. This indicated good fit and prediction of the generated OPLS-DA model. However, in the OPLS-DA model, F16 was not an outlier on the shown scores plot on Figure 6.15A. The variation score between groups was significantly higher at 9.87% while within groups, it was only 0.92%. The considerable difference of the variation scores indicated a good separation between the active and inactive fractions with decreased disparity between the samples within the respective groups. The discriminating features for the active fractions were more diverse with ion peaks ranging between 280 and 720 Da as illustrated on the loadings, S- and VIP plots on Figures 6.15B, 6.15C and 5.16, respectively. The discriminating features for the inactive fractions were generally at lower MWts observed only between 280 and 370 Da.

However, none of these discriminating features listed on Table 6.3 were presented by major TIC peaks shown on Figure 6.17. This simply indicated that none of major

components were responsible for the anticancer activity. Multivariate analysis indicated that the minor components were responsible for the biological activity against the breast cancer cell line ZR-75. Targeting this low-yielding metabolites by chromatographic separation and purification work could be a challenge. Multivariate analysis can define targets at μg level concentrations, which may pose inaccessible for any chromatographic isolation work (Mazlan *et al.*, 2020a, Mazlan *et al.*, 2020b). The heatmap generated from MetaboAnalyst® on Figure 6.18 also displayed a more diverse mass ion peak range for the active fractions in comparison with the inactive samples. Structures of the discriminating of target bioactive metabolites against breast cancer (ZR-75) predicted by OPLS-DA loadings S-plots are listed in Table 6.4 were presented in Figure 6.17.

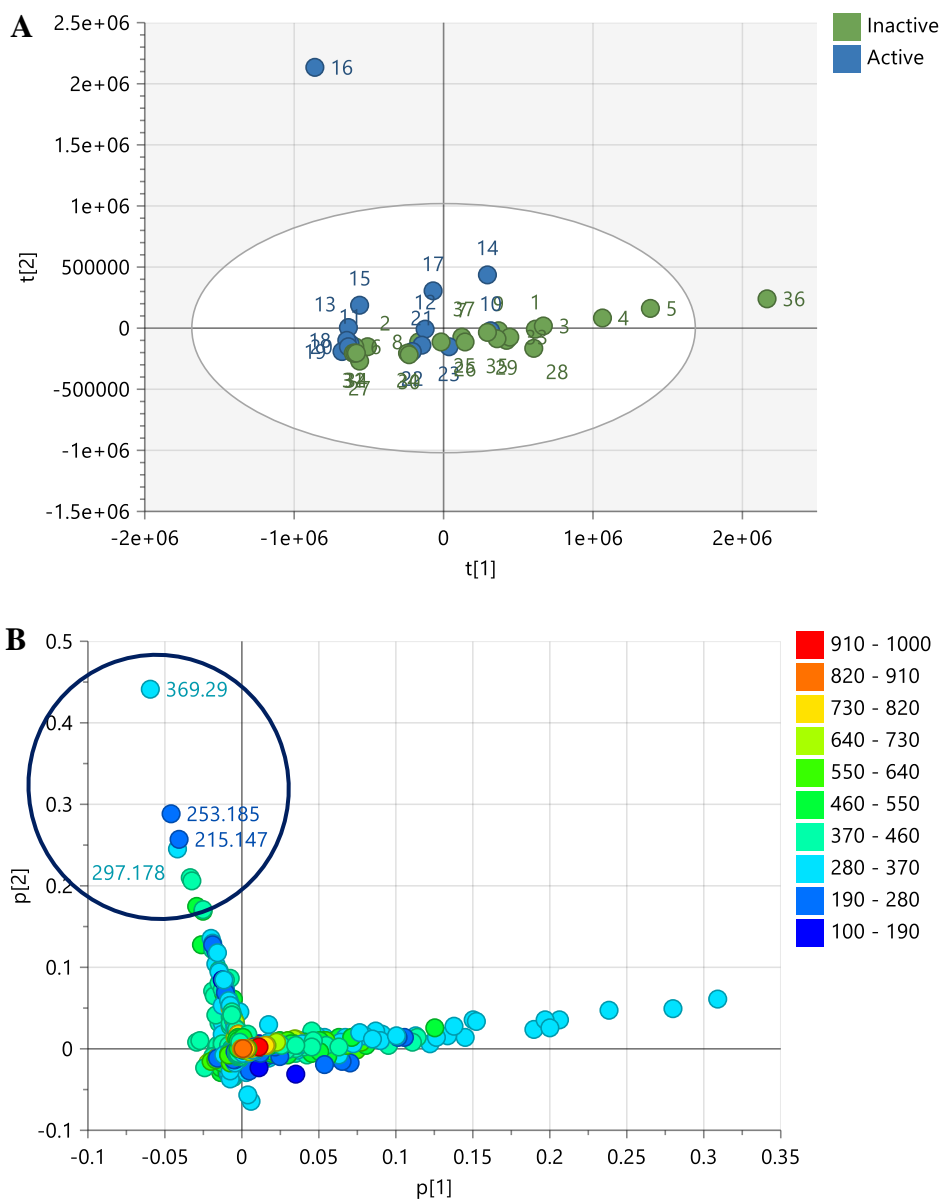
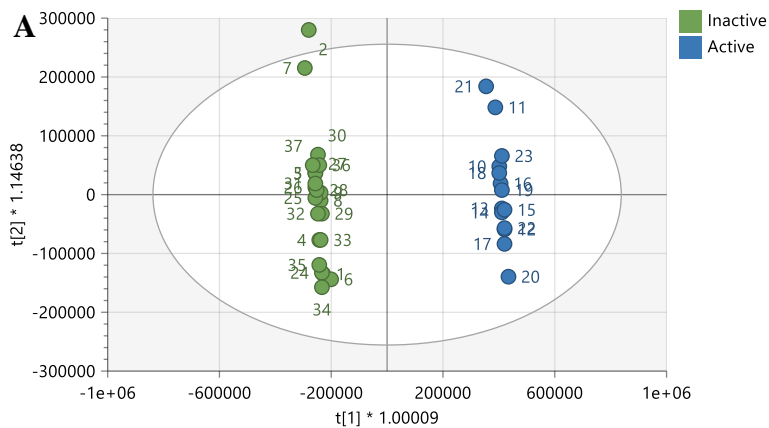
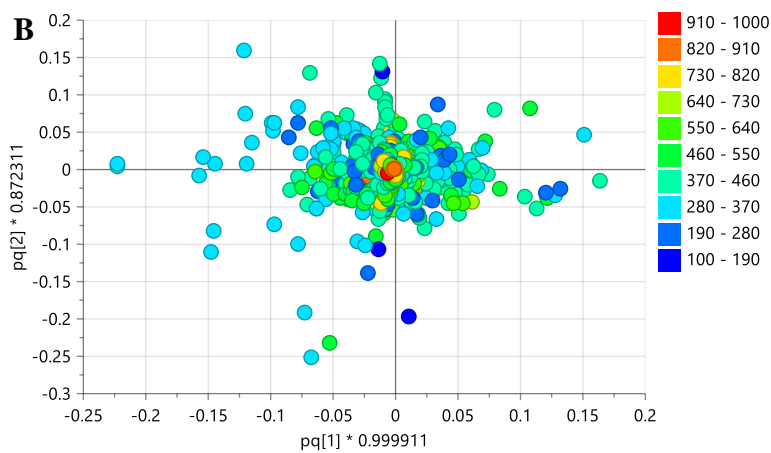


Figure 6.14: PCA scores (**A**) and loadings (**B**) plots of the LC-HRMS data of *A. ustus* fractions. Encircled features represent the discriminating ion peaks for the outlier F16. The R^2 and Q^2 values were 0.71 and 0.35, respectively.



Scaled proportionally to R2X, R2X[1] = 0.0987, R2X[2] = 0.00919,
 Ellipse: Hotelling's T2 (95%)



Normalized to unit length, R2X[1] = 0.0987, R2X[2] = 0.00919

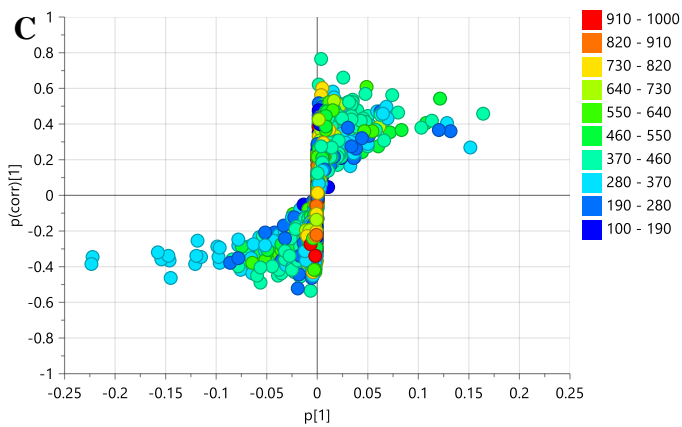


Figure 6.15: (A) OPLS-DA scores, (B) loadings, and (C) S-plots of the LC-HRMS data of *A. ustus* fractions.

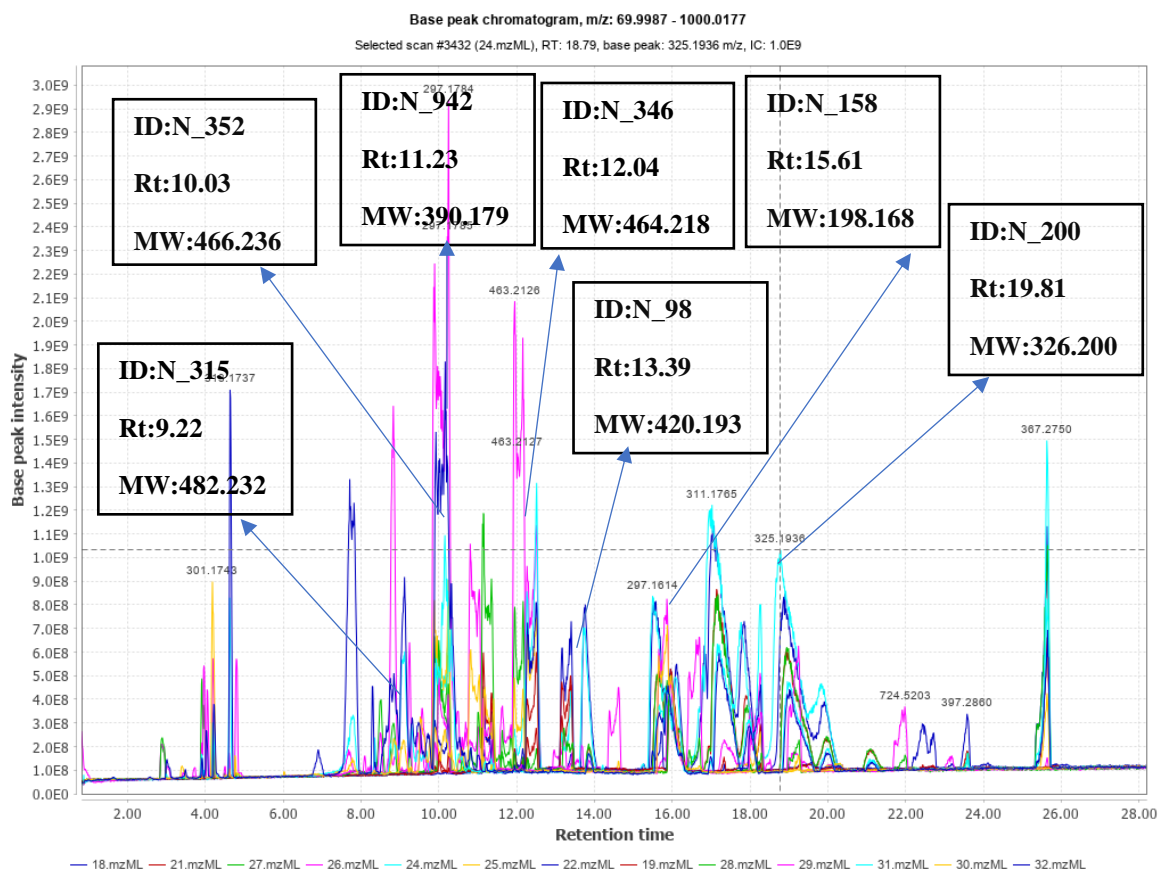


Figure 6.16: Total Ion Chromatogram (TIC) of the active fraction. The ion peaks that represent the discriminating features listed in Table 6.3 have been labelled.

Table 6.3: Dereplication of target bioactive metabolites against breast cancer (ZR-75) as predicted by OPLS-DA loadings S-plots. Structures of compounds are shown in Figure 6.17. For multiple compound hits, hits were filtered according to a fungal genus prioritising the genus *Aspergillus*.

Primary ID	p-value	m/z (Da)	Rt (min)	MW (Da)	Compound hits	Name	Source(from DNP and biological source)
N_346	0.0255	463.2109	12.04	464.2182	asparaginyln-D-tryptophylphenylalaninamide (1)	C ₂₄ H ₂₈ N ₆ O ₄	<i>Aplysia kurodai</i> <i>Euhadra congenita</i> <i>Lymnaea stagnalis</i>
N_352	0.0115	465.2297	10.39	466.2369	sartoryglabrin C (2)	C ₂₉ H ₃₀ N ₄ O ₂	<i>Neosartorya glabra</i>
N_942	0.0034	389.1719	11.23	390.1792	nitrosporin (3)	C ₂₀ H ₂₆ N ₂ O ₆	<i>Streptomyces nitrosporeus</i>
P_440	0.0213	409.2854	20.71	408.2781	echinine (4)	C ₂₆ H ₃₆ N ₂ O ₂	<i>A.glaucus</i>
N_98	0.0089	419.1862	13.39	420.1935	2'-O-methylprenylterphenyllin (5) prenylterphenyllin C (6)	C ₂₆ H ₂₈ O ₅	<i>Aspergillus</i> sp. YXf3 <i>A.taichungensis</i>
N_315	0.0273	481.2256	9.22	482.2328	19-keto-13(24),17-cheilanthadiene-25S - triol-24E-sulfate (7)	C ₂₅ H ₃₈ O ₇ S	<i>Coscinoderma</i> sp.
P_140	0.0002	391.2736	21.08	390.2663	chilocorine A (8) chilocorine B (9)	C ₂₆ H ₃₄ N ₂ O	<i>Chilocorus cacti</i>
P_174	0.0074	367.2736	21.74	366.2663	granulatamide B (10)	C ₂₄ H ₃₄ N ₂ O	<i>Eunicella granulata</i>
P_196	0.0018	367.2736	20.63	366.2663	granulatamide B (10)	C ₂₄ H ₃₄ N ₂ O	<i>Eunicella granulata</i>
N_345	0.0133	297.1780	9.95	298.1851	no hits	C ₁₅ H ₂₆ N ₂ O ₄ (DBE =4)	-
P_443	0.0279	215.1470	17.98	214.140	senarguine B (11) anmindenol A (12)	C ₁₅ H ₁₈ O	<i>Senecio argunensis</i> marine-derived <i>Streptomyces</i>
N_158	0.0287	297.161	15.61	298.1683	2,5-bis(4-hydroxybenzyl) piperazine (13) fumigaclavine A (14)	C ₁₈ H ₂₂ N ₂ O ₂	<i>A.flavus</i> <i>A.fumigatus</i>

Primary ID	<i>p</i> -value	<i>m/z</i> (Da)	Rt (min)	MW (Da)	Compound hits	Name	Source(from DNP and biological source)
P_439	0.0294	253.1850	9.99	252.1781	no reasonable prediction based on heuristic filter		
N_199	0.0378	297.1609	15.77	298.1682	2,5-bis(4-hydroxybenzyl) piperazine (13) fumigaclavine A (14)	C ₁₈ H ₂₂ N ₂ O ₂	<i>A.flavus</i> <i>A.fumigatus</i>
N_200	0.0367	325.1931	19.81	326.2004	ajmaline (15) all hits coming from plant families Apocynaceae	C ₂₀ H ₂₆ N ₂ O ₂	<i>Rauwolfia serpentina</i> <i>Rauwolfia</i> spp <i>Melodinus balansae</i> <i>Tonduzia longifolia</i>
P_647	0.1110	369.2900	20.30	368.2830	halichonadine J (16) <i>N</i> -(2-phenylethyl)- <i>N'</i> -2-trachyopsanylurea (17) <i>N</i> -phenylethyl-2-formamido-6-axene (18)	C ₂₄ H ₃₆ N ₂ O	sponge <i>Halichondria</i> <i>Axinyssa aplysinoides</i>

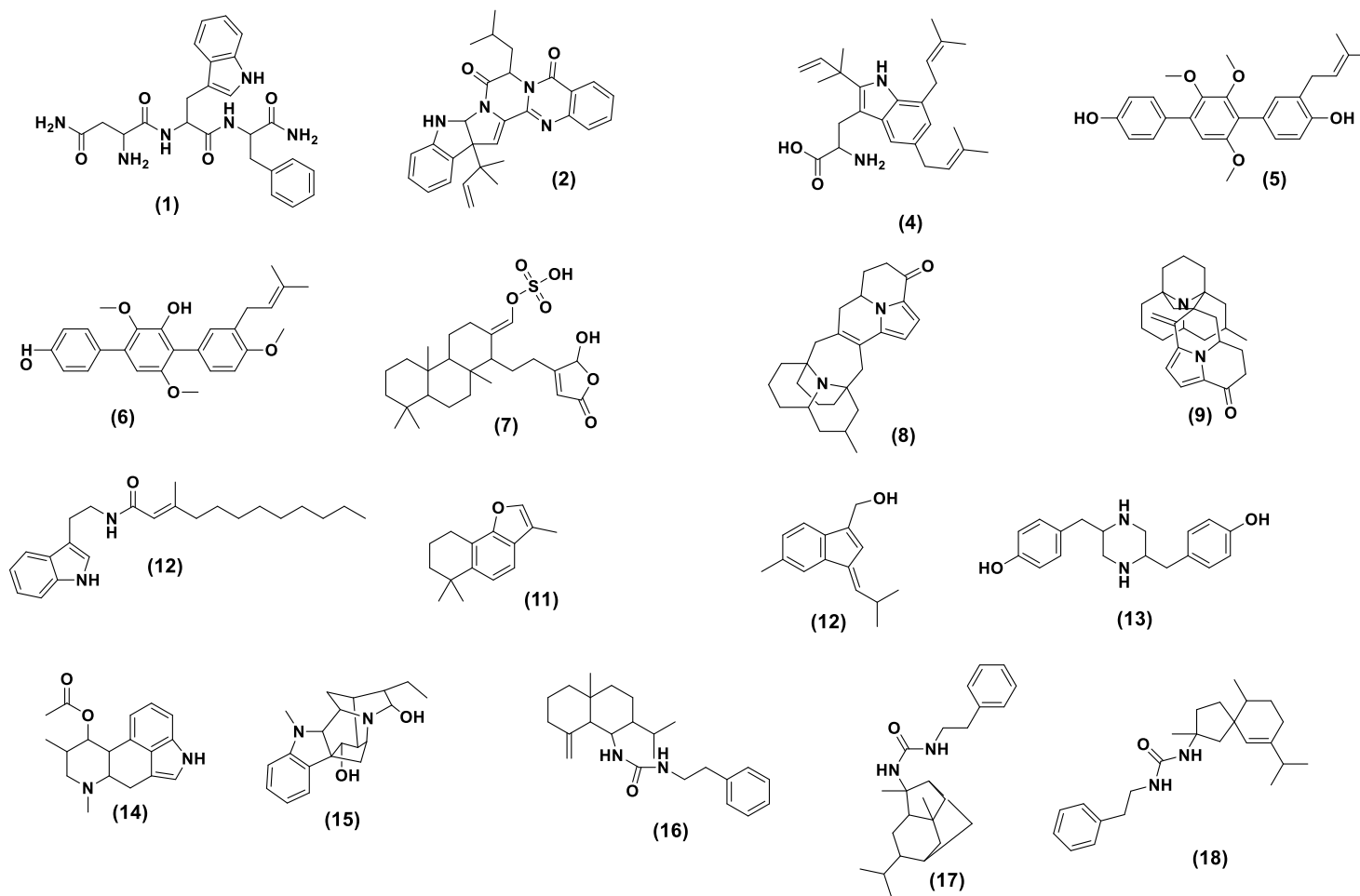


Figure 6.17: Structures of the discriminating bioactive metabolites against breast cancer (ZR-75) as predicted by OPLS-DA loadings S-plots as listed in Table 6.3



Figure 6.18: Heatmap analysis of the mass spectral data of the *A. ustus* fractions generated by MetaboAnalyst®. The boxed fractions are those biologically active against the breast cancer cell line ZR-75 along with the discriminating ion peaks unique to the anticancer fractions.

6.6. HRMS analysis of *A. ustus* subfractions

HRMS data by direct infusion of the *A. ustus* subfractions of the biologically active fraction F11 were subjected to multivariate analysis to validate the targeted anticancer metabolites that were found elusive on the TIC of the crude flash chromatographic fractions. F11 was initially chosen for further chromatographic isolation work due to its high yield. Considering the low polarity of fraction F11, it was possible that highly non-polar or lipophilic compounds were not being eluted through the column to the mass spectrometer. To resolve this limitation, direct infusion method was used over LC for mass spectral analysis. PCA scores plots grouped the subfractions into four groups as shown in Figure 6.19A. The subfractions were categorised to determine the discriminating metabolites for each of the respective subfraction clusters on the loadings plot on Figure 6.19B. F11-17 was in the upper left quadrant of the scores plot. The loadings plot provided targeted metabolites with a MWt range between 300 and 500 Da (encircled blue). Meanwhile, F11-29-6 and F11-23 were distributed in the right side of the plot, which exhibited overlapping features on the corresponding loadings plot (encircled red). F11-11 and F11-12 were positioned in the lower left quadrant. Metabolites with high molecular mass were observed in both subfractions (encircled green). On the other hand, F12-11-2 and F12-6-5 overlappingly clustered indicating a strong similarity in their mass spectral data profile (encircled orange). At six components, the R^2 and Q^2 values were at 1.0 and 0.999, respectively, which indicated excellent fitness and predictability of the model.

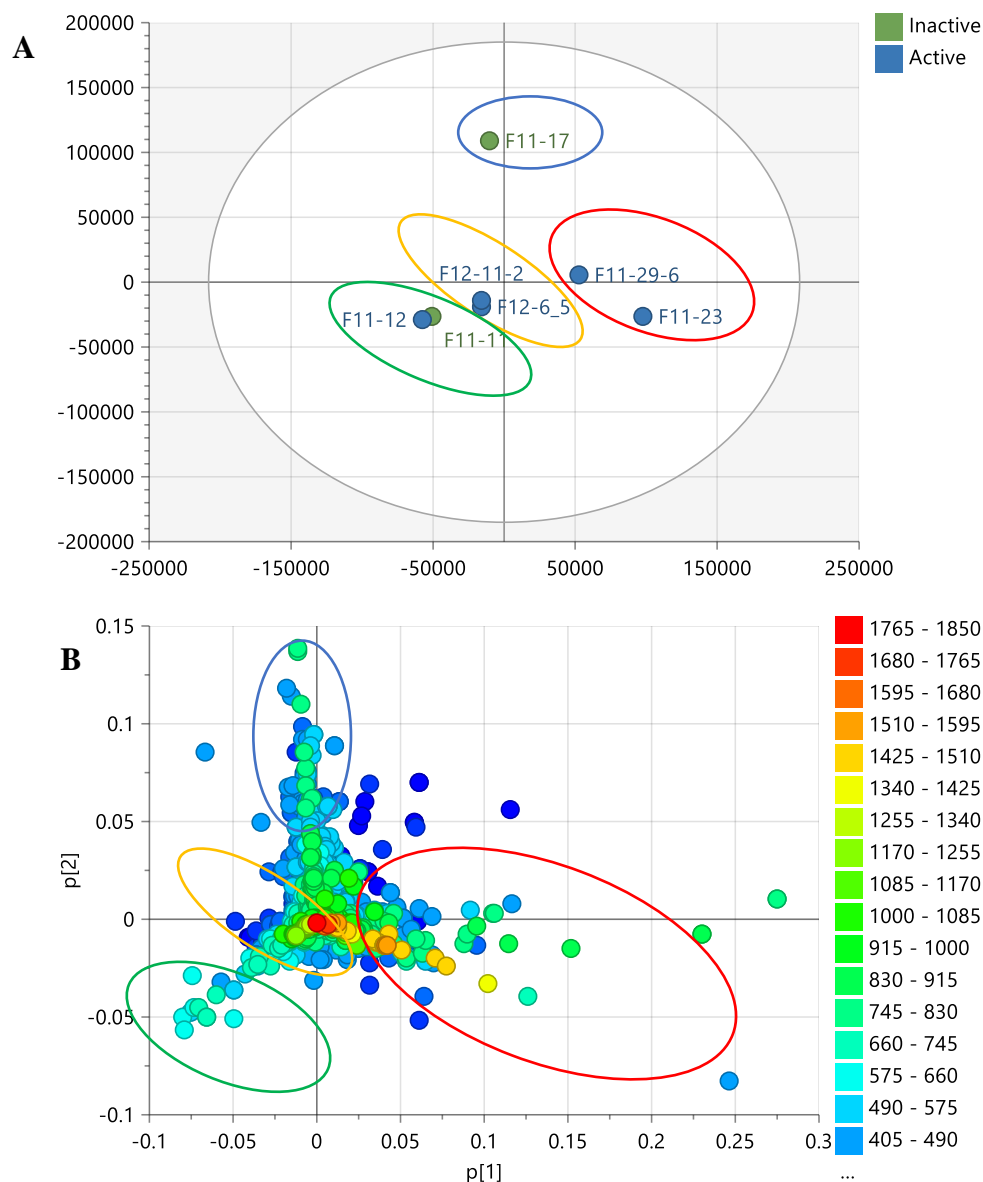


Figure 6.19: (A) PCA scores and (B) loadings plot of the LC-HRMS data of *A. ustus* purified subfractions. The discriminating features from each subfraction were encircled in the figure, F11-29-6 and F11-23 encircled in red, F11-17 encircled in blue, F12-11-2 and F12-6-5 encircled in orange and F11-11 and F11-12 encircled in green.

According to the OPLS-DA scores plot (Figure 6.20A), the active subfractions were positioned in the right side of the plot, while the inactive compounds were in the left

side. The R^2 and Q^2 values were at 1.0 and 0.978, respectively, which indicated good fit and predictability of the model. The variation between groups R^2X_0 [1] was 22.5% and within group $R^2X[2]$ was 16.8%. This indicated good separation between the active and inactive clusters.

Loadings plot (Figure 6.20B) was generated from the OPLS-DA scores plot, in which, the possible types of discriminating bioactive metabolites can help identify the target anticancer compounds. Two discriminating metabolites with ion peaks at m/z 471.20 and 419.17 were found to be abundant in F11-29-6 and F12-11-2. These metabolites were dereplicated from the DNP database. From the dereplication data, F11-29-6 was identified as terretonin F (Oleinikova *et al.*, 2016) with an MZmine ID of P_903, MW of 470.19 Da, and a molecular formula of $C_{26}H_{30}O_8$. While F12-11-2 (N_1001) was recognised as 11,12-epoxy-7-drimene-6,9,11-triol; (6 β ,9 α ,11 α OH)-11-ketone with a MW of 420.21 Da and molecular formula of $C_{23}H_{32}O_7$. These two known compounds were earlier isolated from *A. ustus* obtained from the marine sponge *Suberites domuncula* and described to exhibit anticancer activity (Oleinikova *et al.*, 2016, Liu *et al.*, 2009). Terretonin F was isolated for the first time from the marine fungus *A. insuetus*, which was obtained from *Petrosia ficiformis* sponge. Terretonin F was found to have activity as an inhibitor of the mammalian mitochondrial respiratory chain (Lopez-Gresa *et al.*, 2009).

Other discriminating features for anticancer activity were P_1346 and P_1635 with MWs of 386.207 and 374.171 Da as well as molecular formulas of $C_{23}H_{30}O_5$ and $C_{21}H_{26}O_6$, respectively. These sub-fractions were putatively identified as Antibiotic RES 1149-2 and ustusolate E. and both exhibited anticancer activity against breast cancer cells (ZR-75). Antibiotic RES 1149-2 was earlier isolated from *A. ustus* var. *pseudodeflectus* of a Xenova culture 3811 soil sample (Hayes *et al.*, 1996). Both compounds antibiotic RES 1149-2 and ustusolate E were cultivated from the fungus *A. ustus*, which on the other hand was obtained from the Mediterranean sponge *Suberites domuncula* (Liu *et al.*, 2009).

The inactive subfractions, F11-11 and F11-17 were observed on the left quadrants of the scores plot. These subfractions reduced the cell viability by only about 20%. The

discriminating feature was defined on the loadings plot as glycerol 1,2-di-(9Z,12Z-octadecadienoate) with an MZmine ID of P_2370, a MW of 616.505 Da and molecular formula of $C_{38}H_{68}O_5$, which was later isolated and confirmed by NMR data F11-11 was from an unknown source. F11-17 was elucidated as ophiobolin K, which was earlier described and isolated from various *Aspergillus* spp. It was detected with MZmine ID of P_2564, a MW of 384.2663 Da and molecular formula of $C_{25}H_{36}O_3$.

The S-plot was also generated from OPLS-DA model (Figure 6.20C). The right side of the plot showed the metabolites from the active subfractions, whereas the inactive compounds were in the left side. As a result, the targeted bioactive metabolites were dereplicated and listed in Table 6.4.

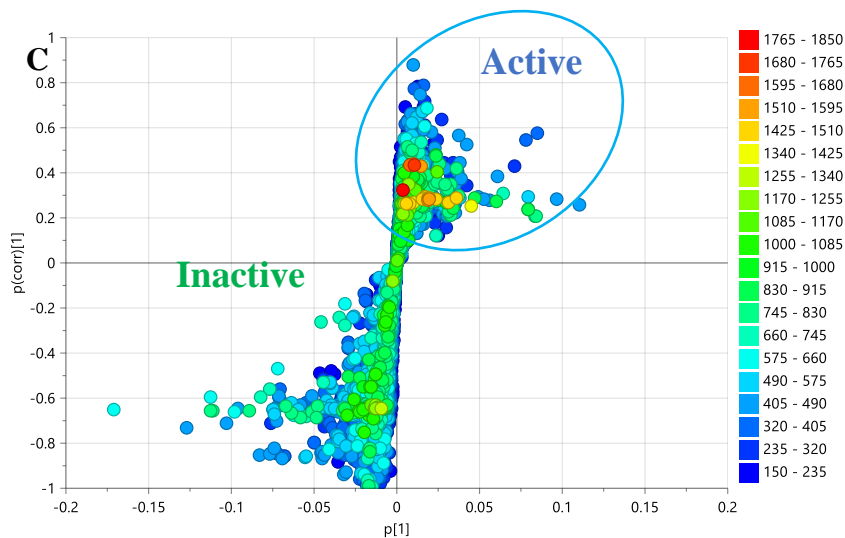
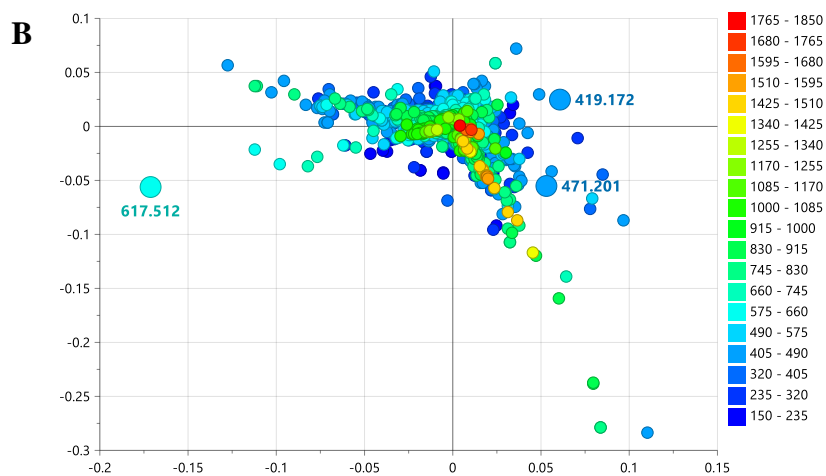
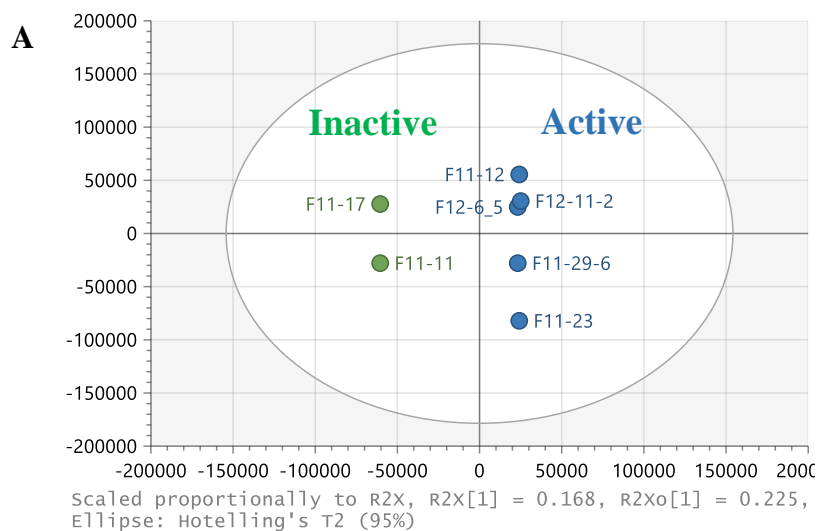


Figure 6.20: (A) OPLS-DA scores, (B) loadings and (C) S-plots of the LC-HRMS data of *A. ustus* subfractions of the active fraction F11.

Table 6.4: Dereplication of target bioactive metabolites against breast cancer (ZR-75) as predicted by OPLS-DA loadings S-plots of the LCMS data by direct infusion. The highlighted rows correspond to isolated compounds from *A. ustus*.

No.	Primary ID	<i>m/z</i> (Da)	MW (Da)	compound	molecular formula prediction	Source (from DNP and biological source)
1	P_2137	424.2542	423.2469	valylamienomycylglutamine	C ₂₀ H ₃₃ N ₅ O ₅	<i>Venezuelae-xanthophaeus</i>
2	P_2370	617.5122	616.5049	glycerol 1,2-dialkanoates; glycerol 1,2-di-(9Z,12Z-octadecadienoate)	C ₃₉ H ₆₈ O ₅	unknown
3	N_33	419.1722	420.1795	ochraceopone C	C ₂₂ H ₂₈ O ₈	<i>A.ochraceopetaliformis</i>
4	N_968	485.2832	486.2904	9Z-octadecenoyl-3-(chloromethylene)-2,3-dihydro-1-benzoxepin-7-MeOH	C ₃₀ H ₄₃ ClO ₃	<i>Mycena galopus</i>
5	N_39	469.1873	470.1945	parasiticolide A	C ₂₆ H ₃₀ O ₈	<i>A.variecolor, A.parasiticus Eurotium chevalieri</i>
6	P_903	471.2009	470.1936	terretonin F	C ₂₆ H ₃₀ O ₈	<i>A.insuetus</i>
7	P_2301	409.1988	408.1916	xenorhabdin 13	C ₂₁ H ₃₂ N ₂ O ₂ S ₂	<i>Pseudoalteromonas sp. SANK 73390</i>
8	N_36	247.1340	248.1413	aspergentisyl B	C ₁₅ H ₂₀ O ₃	<i>A.glaucus HBI-19</i>
9	P_1030	170.1541	169.1468	haloxynine	C ₁₀ H ₁₉ NO	<i>Haloxylon salicornicum Anabasis aphylla, Lupinus luteus, Lupinus palmeri Lupinus spp.)</i>
10	P_1595	170.1540	*	octahydro-2 <i>H</i> -quinolizine-1-MeOH; (-)-form	C ₁₀ H ₁₉ NO	
11	N_42	363.1460	364.1532	fudecadione B	C ₁₉ H ₂₄ O ₇	<i>Aspergillus sp. fA75 Penicillium sp. BCC 17468</i>
12	P_2564	385.2736	384.2663	ophiobolin K	C ₂₅ H ₃₆ O ₃	<i>A. ustus A.insuetus IBT 28443</i>

No.	Primary ID	<i>m/z</i> (Da)	MW (Da)	compound	molecular formula prediction	Source (from DNP and biological source)
13	P_1346	387.2148	386.2075	Antibiotic RES 1149-2	C ₂₃ H ₃₀ O ₅	<i>A. ustus</i> var. <i>pseudodeflectus</i> X3811 <i>Aspergillus</i> sp. RES-1149
14	P_795	387.2149	386.2076	Antibiotic RES 1149-1 12- <i>O</i> -acetylaspergillol asperugin B	C ₂₃ H ₃₀ O ₅	<i>Aspergillus</i> sp. RES-1149 <i>A. versicolor</i> <i>A. rugulosus</i>
15	N_707	385.2034	386.2107			
16						
17	P_1635	375.1786	374.1713	ustusolate E	C ₂₁ H ₂₆ O ₆	<i>A. ustus</i>
18				9- <i>O</i> -acetyldiorcinol B		<i>Aspergillus</i> sp. No. 16-20-8-1 marine-derived <i>A. tennesseensis</i> OUCMB I 140430
19	N_1001	419.2083	420.2156	11,12-epoxy-7-drimene-6,9,11-triol; (6β,9α,11αOH)-form, 11-ketone (lactone), 6- <i>O</i> -(6 <i>R</i> *,7 <i>R</i> *-dihydroxy-2 <i>E</i> ,4 <i>E</i> -octadienoyl)	C ₂₃ H ₃₂ O ₇	<i>A. ustus</i>

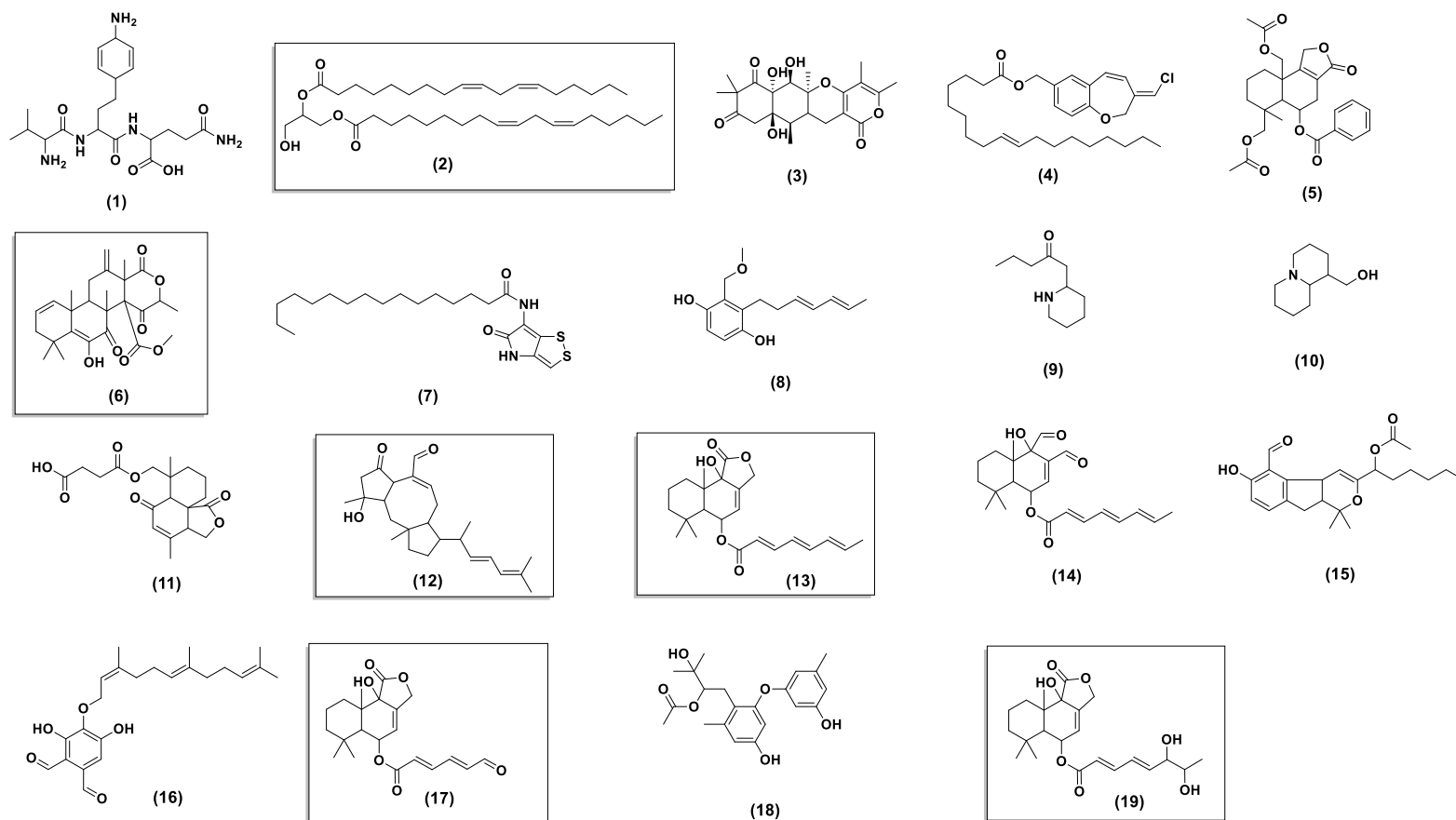


Figure 6.21: Structures of the discriminating of target bioactive metabolites against breast cancer (ZR-75) as predicted by OPLS-DA loadings S-plots as listed in Table 6.4. compounds in the black box correspond to isolated compounds from *A. ustus*.

6.6. Pure compounds isolation

Fractions F11 (708 mg) and F12 (343 mg) were separately dissolved in 2ml of EtOAc and added dropwise to 2g of celite with thorough mixing. The loaded sample was left to dry under the fume hood for 48h prior to loading on a pre-packed 12g silica column for a Grace Reveleris FC system. The solvent system was optimised for fractionation. Fraction 11 was a complex combination of several compounds, as seen in Figure 6.22. Due to the presence of non-chromophoric compounds, fraction 11 (708 mg) was fractionated using a Reveleris FC equipped with an evaporative light scattering detector (ELSD). Gradient elution was used with n-Hexane and EtOAc as a solvent system, starting with 100% n-Hexane and finishing up with 100% EtOAc in 2h at a flow rate of 40 mL/min obtaining 30 pooled subfractions from fraction F11 (Table 6.5 and Figure 6.22). Fractions were prioritised for further isolation work (Figure 6.23) depending on the non-complexity but novelty of their chemical profile, fraction yield, and potency of their anticancer activity.

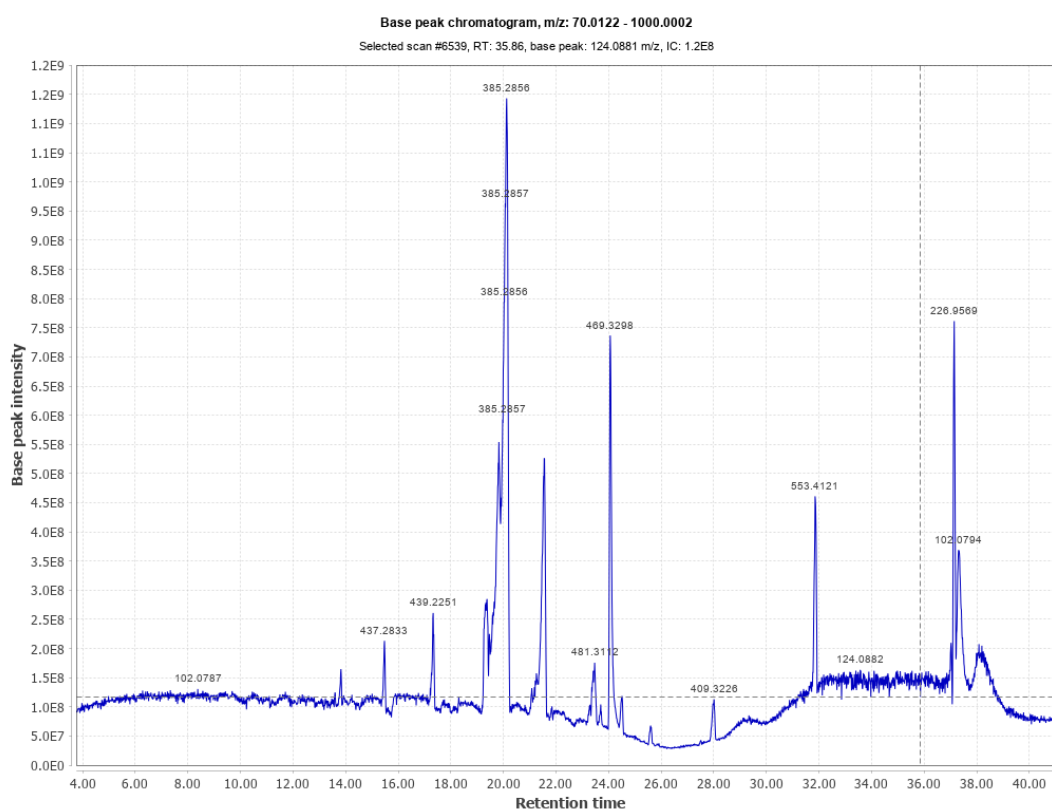


Figure 6.22: Total Ion Chromatogram (TIC) of fraction 11.

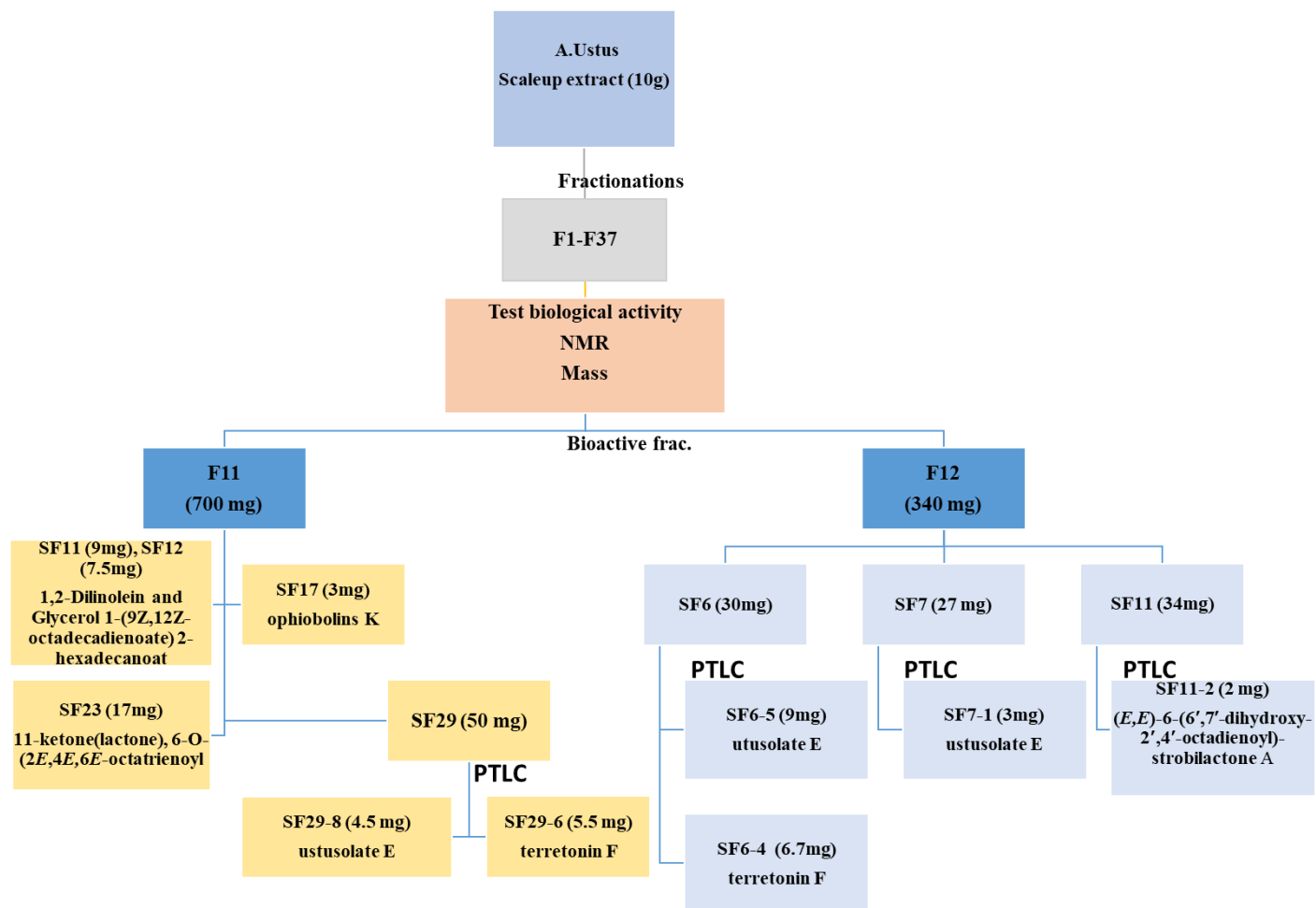


Figure 6.23: Schematic diagram for isolating the pure compounds from *A. ustus* extract.

Table 6.5: Weight of subfractions 1 to 12 of fraction 11 obtained by Reveleris FC using 0% to 20% of EtOAc in combination of n-Hexane.

Subfractions no.	Weight (mg)
F11-1	2.2
F11-2	6.7
F11-3	0.9
F11-4	0.8
F11-5	0.5
F11-6	2.1
F11-7	0.5
F11-8	10.8
F11-9	5.4
F11-10	7.1
F11-11	9.2
F11-12	7.5

The subfractions were examined by ^1H NMR (Figure 6.24). Subfractions with low yields were not subjected to ^1H NMR measurements.

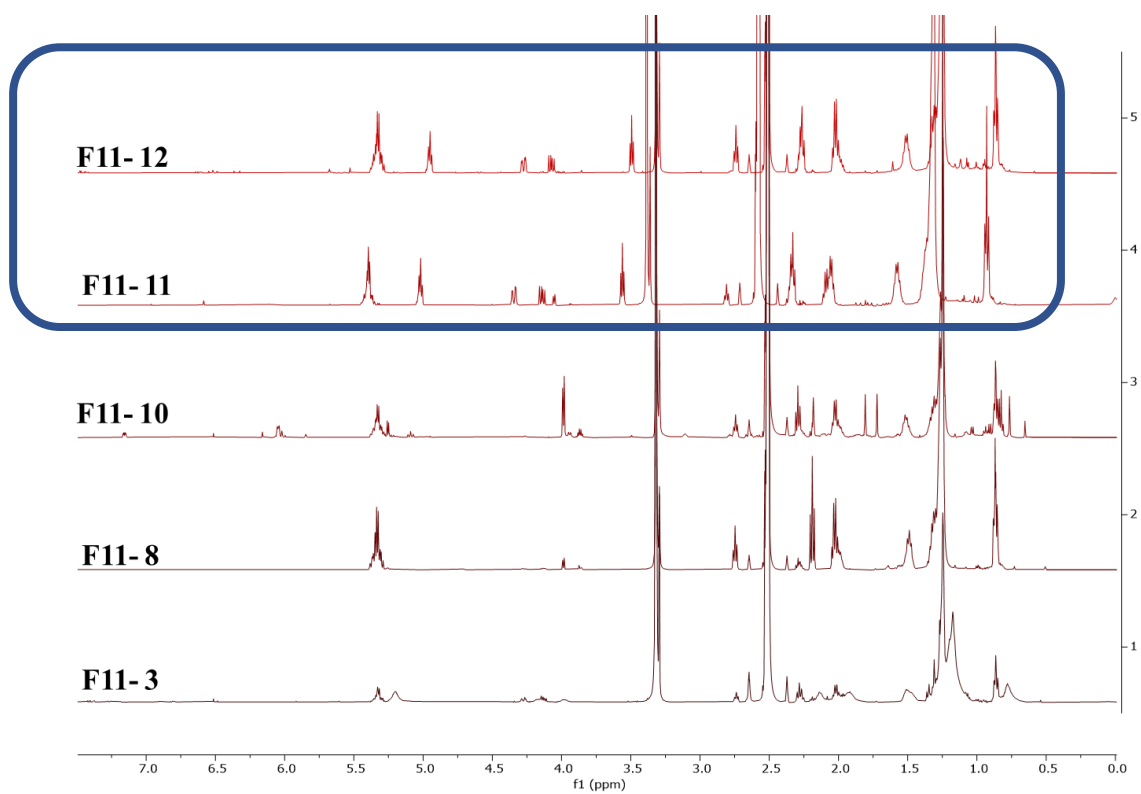


Figure 6.24: Stacked ^1H NMR spectra of subfractions from the fraction 11. The highlighted subfractions were subjected for further analysis.

6.6.1. Linoleic acid derivatives

SF11 and SF12 were the purest as shown in Figure 6.25 and were further subjected to structural elucidation using several 2D-NMR analysis such as HSQC, COSY, and HMBC.

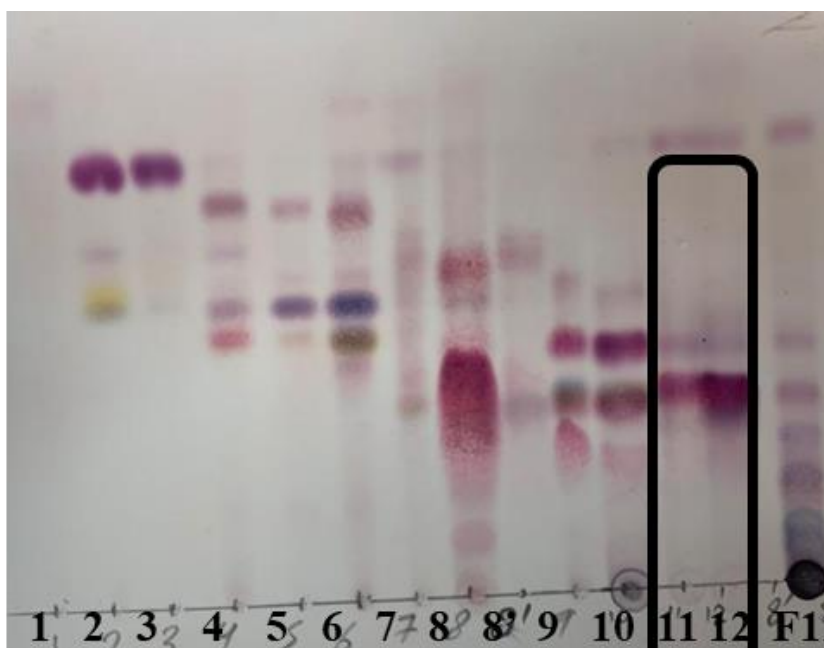


Figure 6.25: Summary TLC plates for the fractionation of F11 using solvent system 75:25% of n-Hexane and EtOAc. TLC for subfractions 11 and 12 were shown in the black box.

6.5.1.1. Compound F11-12 structure elucidation.

3'-hydroxy-2'-(palmitoyloxy) propyl (9Z,12Z)-octadeca-9,12-dienoate

Chemical Formula: C₃₇H₆₈O₅

Exact Mass: 592.5067

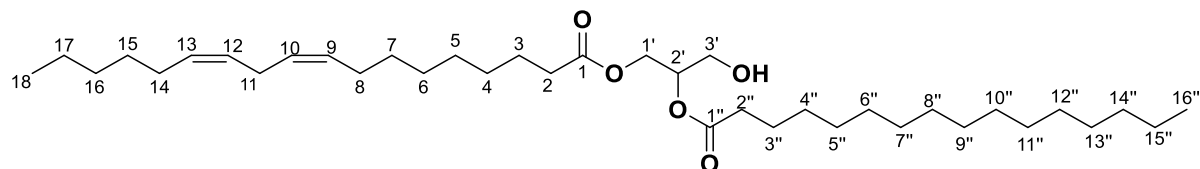


Figure 6.26A: Chemical structure of compound F11-12

Formula	Calculated Mass	Target Mass	Double Bond Equivalence	Absolute Error (ppm)	Error (mDa)	Error (ppm)	Fitness
C ₃₇ H ₆₈ O ₅ Na	615.49644	615.49676	3.5	0.51	0.31	0.51	0.137

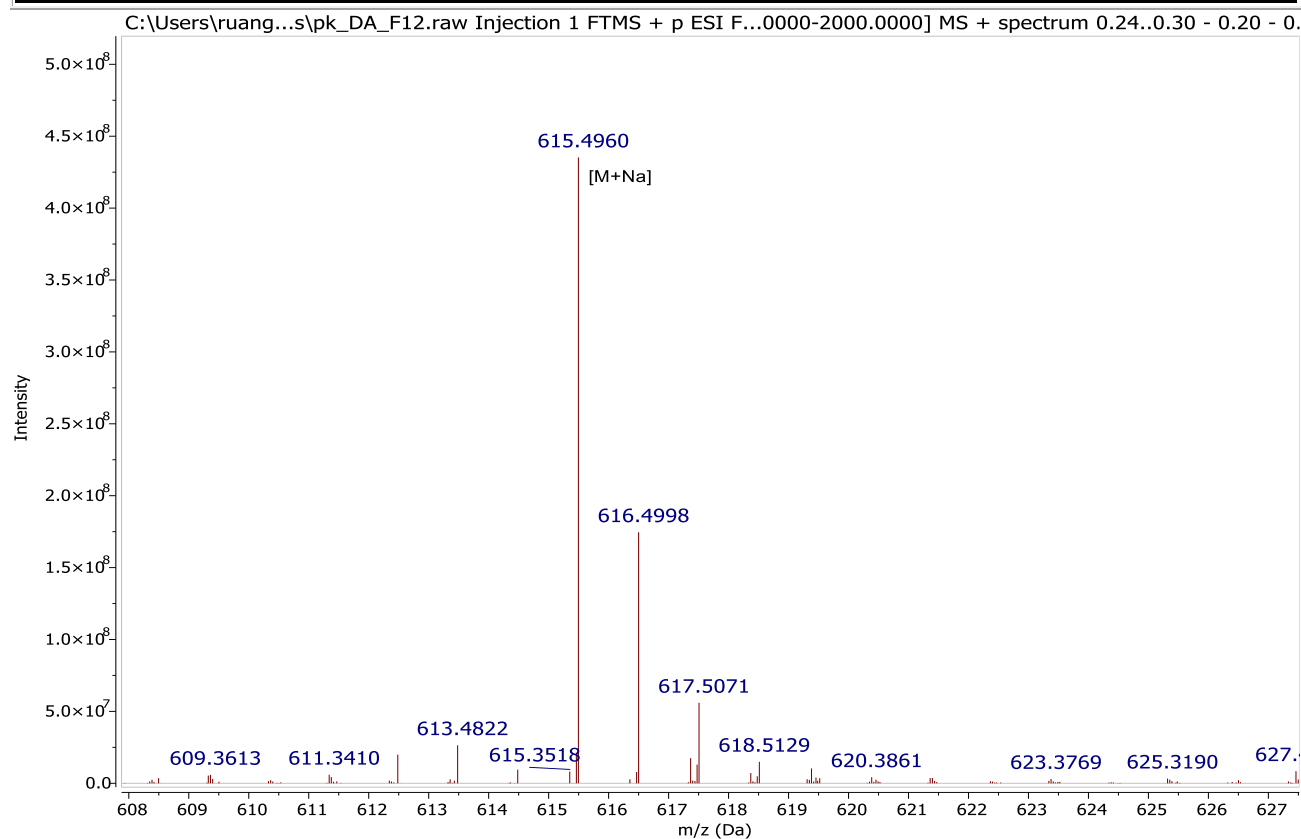


Figure 6.26B: Mass spectral data of F11-12 for the ion peak at m/z 615.496 [M+Na]⁺.

Compound 11-12 was purified from fraction 11 as a yellow amorphous solid with a yield of 7.5 mg, the compound was eluted from the non-polar eluate at higher percentage of n-Hexane 80% and 20% EtOAc. HR-ESIMS data gave a MWt of 592.5067 Da and molecular formula of $C_{37}H_{68}O_5$, which was inferred from the sodium ion peak at m/z 615.496 (Figure 6.27). The number of hydrogens is almost twice the number of carbons fewer than six, which is typical for a fatty acid formula. The molecular formula indicates that F11-12 has four DBE.

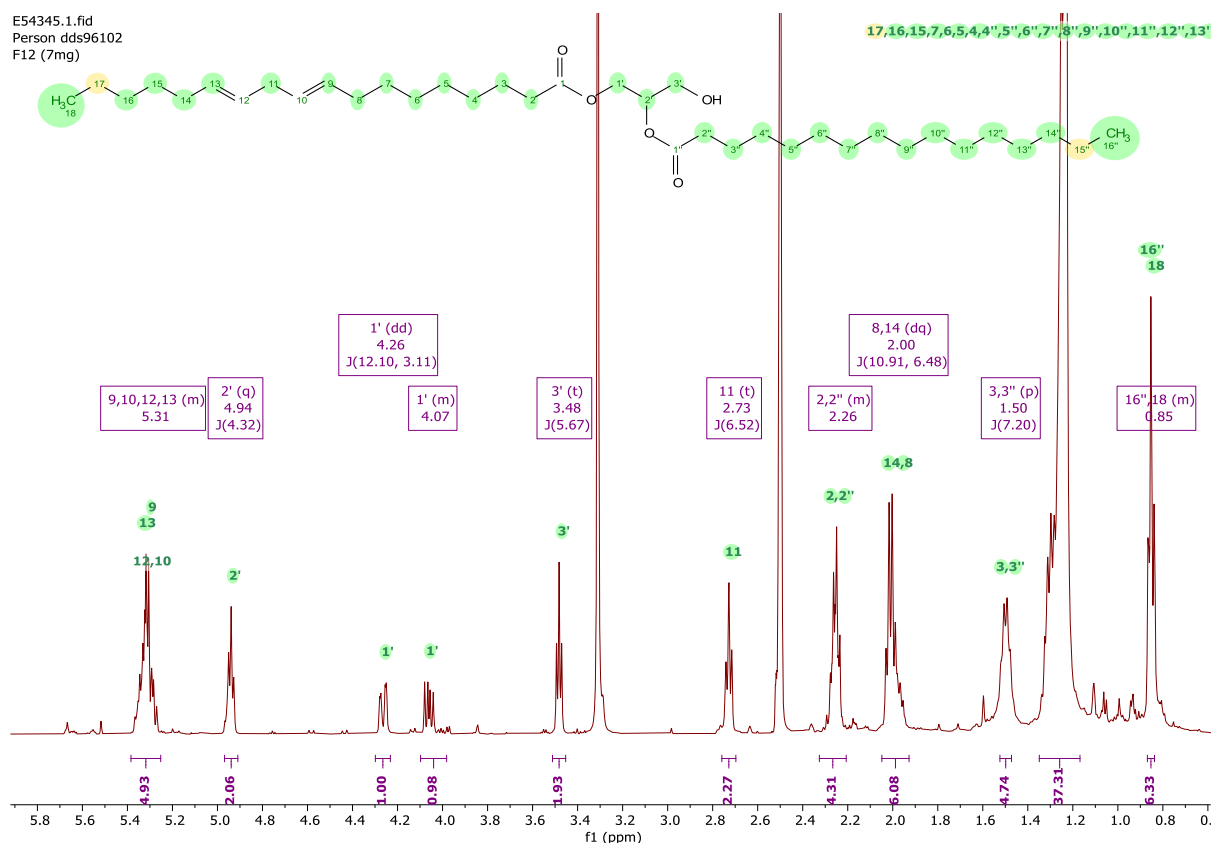


Figure 6.27: 1H NMR spectrum of compound F11-12 in $DMSO-d_6$ measured at 500 MHz.

The 1H NMR spectrum of F11-12 (Figure 6.27) disclosed the presence of distinctive unconjugated *cis* olefinic multiplet at 5.31 ppm, as well as four proton signals for a glycerol moiety ranging from 3 to 5 ppm, two of them for geminal carbons. However, the integration for the hydroxylated protons had a ratio of 2:2:1, implying the five protons of a glycerol moiety. The occurrence of an alkyl triplet signal at 2.74 ppm ($J= 6.5Hz$) is typical for a methylene unit located between two double bonds. Meanwhile, the other methylene multiplet signal at 2.27 is attached to the carbonyl group. On the other hand, a high intensity broad

signal was observed at 1.25 ppm along with a terminal methyl proton at 0.85 ppm. The integration was twice the predicted alkyl chain length and methyl units, revealing a likely combination of fatty acids with two distinct branching units (Figure 6.28).

The COSY spectrum determined the correlation between the neighbouring protons and defined the different spin systems in the main compound as shown in Figure 6.28. The glycerol protons were connected to each other through coupling between H2' with H1'A, H1'B and H3' forming a CH₂-CH-CH₂OH fragment and this resulted in a complete spin system highlighted by an orange box. On the other hand, the olefinic unconjugated unit coupled with the methylene moiety at 2.74 ppm (H12), as well as coupled to the alkyl unit at 2.05 ppm, which further coupled to the long alkyl chain then correlated with the terminal methyl at 0.85 ppm, resulting in a second spin system as indicated by blue lines on the COSY spectrum (Figure 6.28). The third spin system was highlighted with green lines, coupling the alkyl unit at 2.27 ppm towards the methylene unit at 1.51 ppm that was further connected to the long alkyl chain at 1.25 ppm.

The proton signals were categorised into methines, methylenes, and methyl units using the HSQC spectrum as shown in Figure 6.29. Two terminal methyl moieties were overlapping with the broad alkyl chain, suggesting a triglyceride molecule with two or three distinct fatty acids chain connected to the glycerol unit.

The HMBC correlations in Figure 6.30 were utilised to characterise the distinct structural units associated to the glyceride moiety and to verify the connectivity of the substructures. The quaternary carbons were only detected using HMBC because measuring a ¹³C NMR spectra for F11-12 was not practical to achieve owing to its low yield. HMBC correlations between carbonyl unit at 172.5 ppm (C1) towards the glycerol proton 4.07 ppm (H1') and the methylene groups (H2, H3, H2'', H3''), indicated a triglyceride structure containing two fatty acids. Alternatively, the glyceryl methylene at C3' correlated between carbons within the glycerol moiety, indicating that the system lacked a third fatty acid system. The ¹H and ¹³C data were fully assigned and presented in Table 6.6. The structure of F11-12 was fully elucidated as 3'-hydroxy-2'-(palmitoyloxy) propyl (9Z,12Z)-octadeca-9,12-dienoate. This compound was earlier isolated from the coralloid roots of *Cycas revoluta* (Cycadaceae) and was reported to have pronounced hormogonium-inducing factor (HIF) activity (Hashidoko *et al.*, 2019)

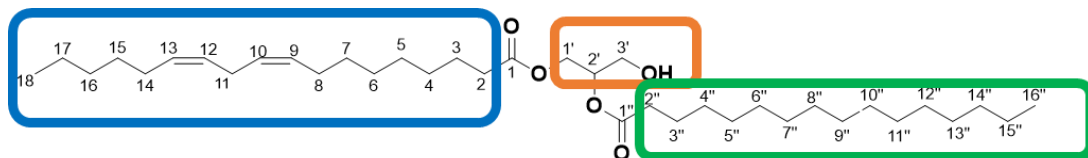
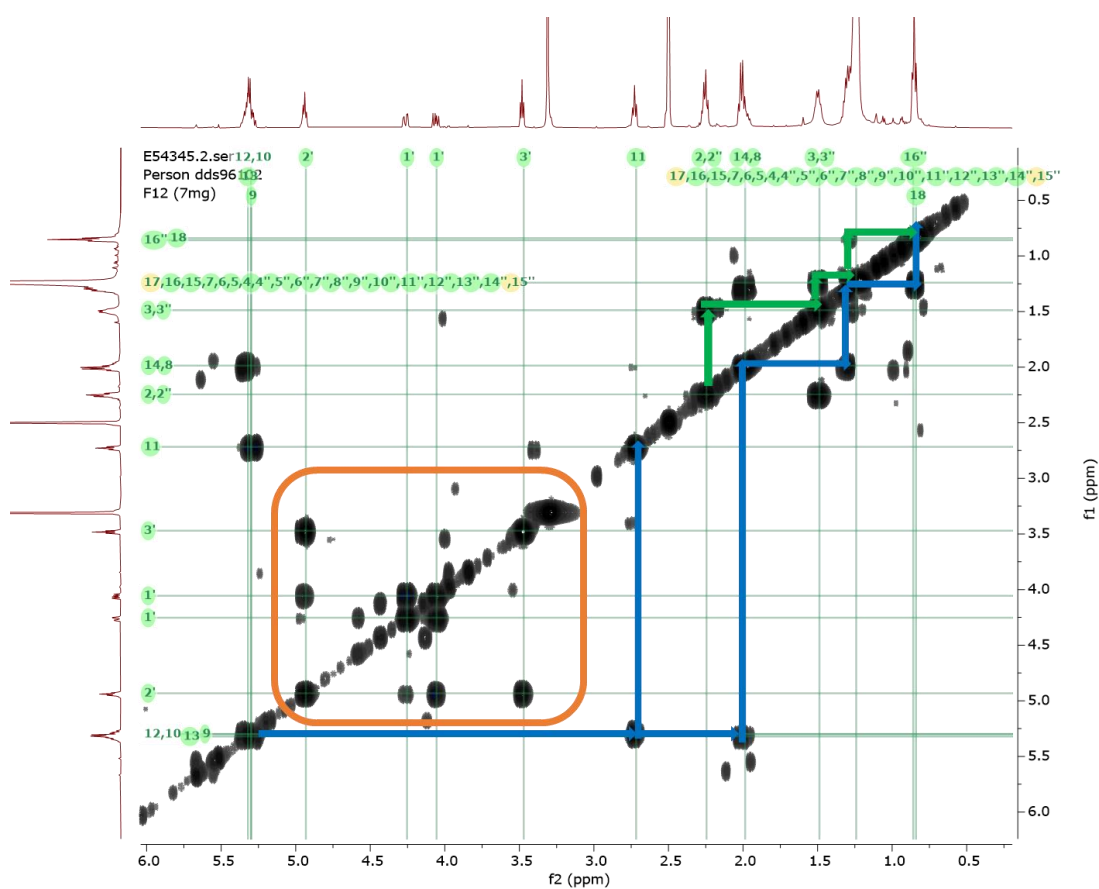


Figure 6.28: (^1H - ^1H) COSY correlation NMR spectrum of compound F11-12 in $\text{DMSO-}d_6$ measured at 500 MHz.

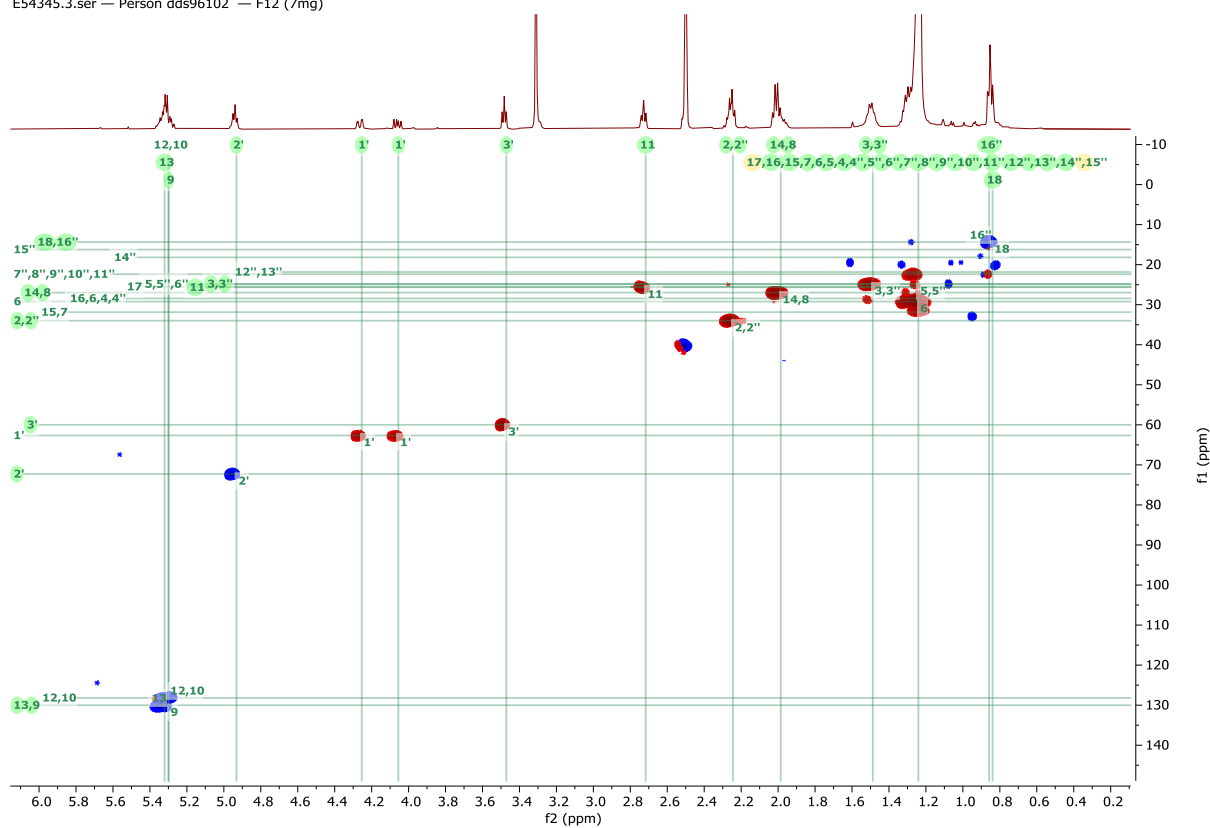


Figure 6.29: HSQC NMR spectrum of compound F11-12 in DMSO-*d*₆ measured at 500. Red correlations are CHs and CH₃s while blue are CH₂s.

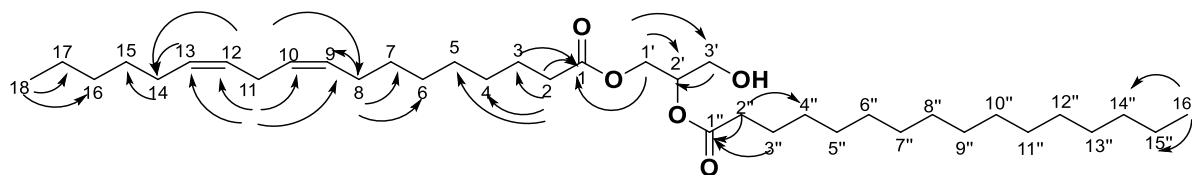
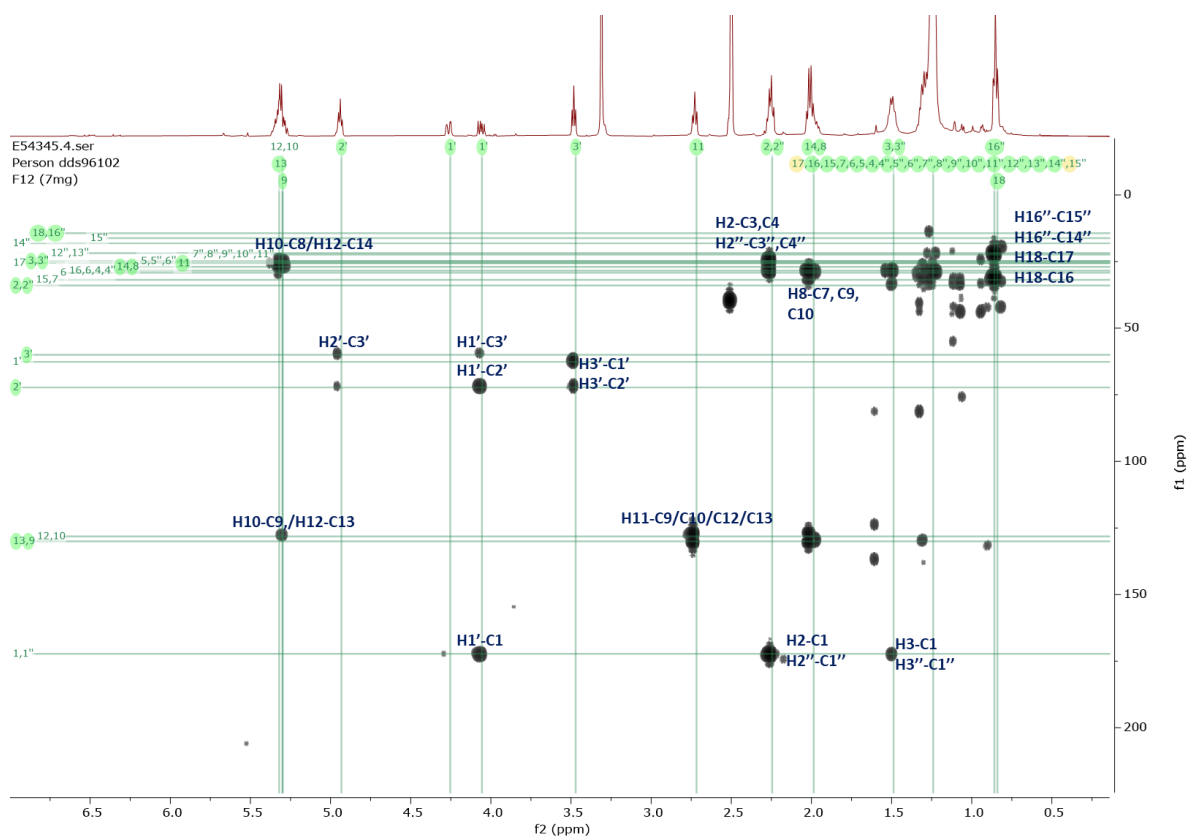


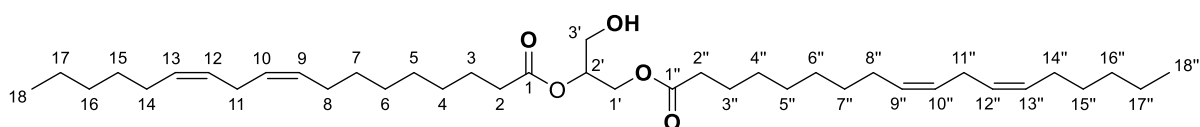
Figure 6.30: HMBC NMR spectrum and observed ^1H to ^{13}C correlations of compound F11-12 in $\text{DMSO-}d_6$ measured at 500 MHz.

Table 6.6: NMR spectral data for compound F11-12 in DMSO-*d*₆ measured at 500 MHz.

Atom no.	¹³ C	¹ H	<i>J</i> in Hz	HMBC (¹ H to ¹³ C)
1	172.5 C	4.07 dd		
2	34.0 CH ₂	2.27 m		C1, C3, C4, C5
3	24.9 CH ₂	1.51 quin	7.2	C1
4	28.3 CH ₂	1.25 q	10.5	
5	25 CH ₂	1.25 q	10.5	
6	29.2 CH ₂	1.25 q	10.5	
7	28.3 CH ₂	1.25 q	10.5	
8	32.0 CH ₂	2.02 dq	10.9, 6.4, 6.5	C7, C9, C10
9	130.0 CH	5.31 m		
10	127.1 CH	5.31 m		C8
11	25.7 CH ₂	2.74 t	6.5	C9, C10, C12, C13
12	127.1 CH	5.31 m		C14
13	130.2 CH	5.31 m		
14	27.0 CH ₂	2.02 dq		C13, C12, C15
15	31.8 CH ₂	1.25 q		
16	28.3 CH ₂	1.25 q		
17	25.5 CH ₂	1.25 q		
18	14.4 CH ₃	0.85 td		C16, C17
1'A	62.8 CH ₂ B	4.07 dd	12.1, 3.1	C1, C2', C3'
1'B	62.8 CH ₂ A	4.28 dd	12.1, 3.1	C1, C2', C3'
2'	72.3 CH	4.96 q	4.3	C3'
3'	60.0 CH ₂	3.50 t	5.6	
3-OH		3.50 t		
1''	172.5 C	---		
2''	34.0 CH ₂	2.27 m		C1'', C4'', C5''
3''	24.9 CH ₂	1.51 quin	7.2	C1''
4''	28.4 CH ₂	1.25 q	10.5	
5''	24.8 CH ₂	1.25 q	10.5	
6''	24.8 CH ₂	1.25 q	10.5	
7''	22.4 CH ₂	1.25 q	10.5	
8''	22.4 CH ₂	1.25 q	10.5	
9''	22.4 CH ₂	1.25 q	10.5	
10''	22.4 CH ₂	1.25 q	10.5	
11''	22.4 CH ₂	1.25 q	10.5	
12''	21.8 CH ₂	1.25 q	10.5	
13''	21.8 CH ₂	1.25 q	10.5	
14''	18.2 CH ₂	1.25 q	10.5	
15''	16.2 CH ₂	1.25 q	10.5	
16''	14.4 CH ₃	0.85 td	6.9, 2.2	

Legend: s= singlet, d = doublet, t = triplet, q = quartet, m =multiplet, quin=quintet

6.5.1.2. Compound F11-11 structure elucidation.



3'-hydroxy-1',2'-diyl (9Z,9'Z,12Z,12'Z)-bis(octadeca-9,12-dienoate)

Chemical Formula: C₃₉H₆₈O₅

Exact Mass: 616.5125

Formula	Calculated Mass	Target Mass	Double Bond Equivalence	Absolute Error (ppm)	Error (mDa)	Error (ppm)	Fitness
C ₃₉ H ₆₉ O ₅	617.51450	617.51251	5.5	3.22	-1.99	-3.22	0.999

Figure 6.31: Chemical structure of compound F11-11

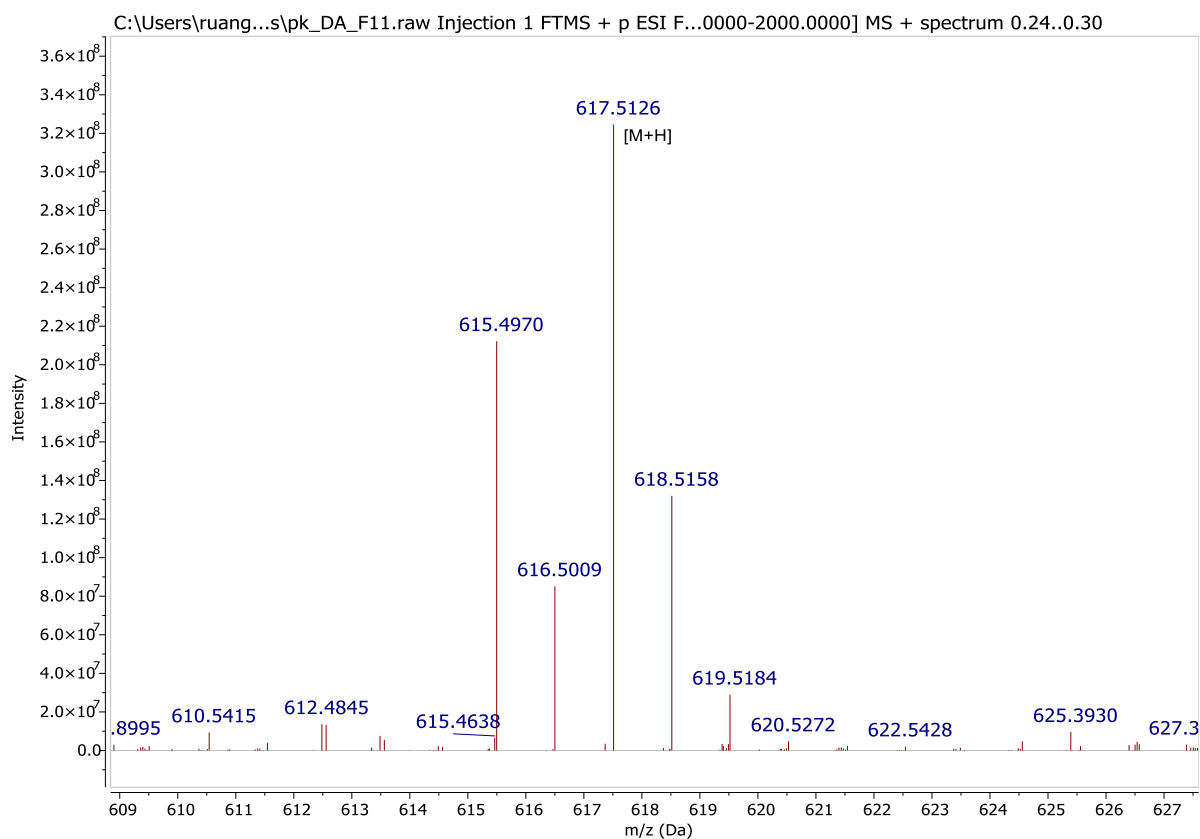


Figure 6.32. Mass spectral data of F11-11 on the ion peak at m/z 617.513 [M+H]⁺.

Compound F11-11 was isolated as a yellow amorphous powder with a yield of 9 mg. HR-ESIMS (Figure 6.32) data afforded an ion peak at m/z 617.513 $[M+H]^+$, suggesting a MWt of 616.5125 Da that is 24 mass units more than that of F11-12. The molecular formula afforded by HRMS is $C_{39}H_{68}O_5$. When compared to F11-12, the DBE of six suggested either two additional double-bonds or a combination of an extra fatty acid carbonyl unit attached to the 2'-OH and another double bond.

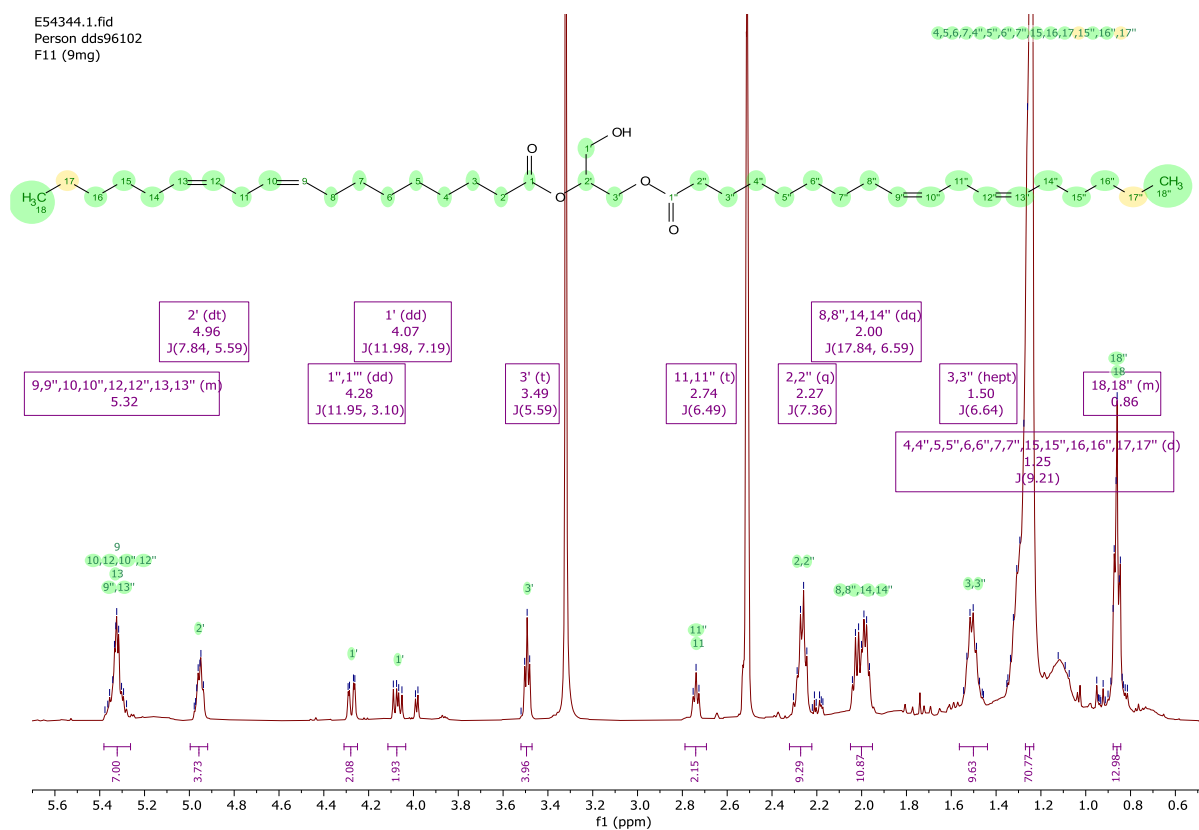


Figure 6.33: 1H NMR spectrum of compound F11-11 in $DMSO-d_6$ measured at 500 MHz.

The 1H NMR spectrum of F11-11 in Figure 6.33 was very similar to that of F11-12. Minor changes were observed in the integration of the unconjugated olefinic system at 5.31 ppm, which suggested 4 double bonds. The 1H - 1H COSY NMR spectrum of F11-11 in Figure 6.34 confirmed the presence of the three spin systems as in F11-12. The resonances between 3 and 5 ppm did correlate, which was characteristic of a glycerol unit, as noted in orange box in

Figure 6.34. Proton coupling in the linoleic moiety like that in F11-12 was also observed and indicated by the blue and green lines in the spectra.

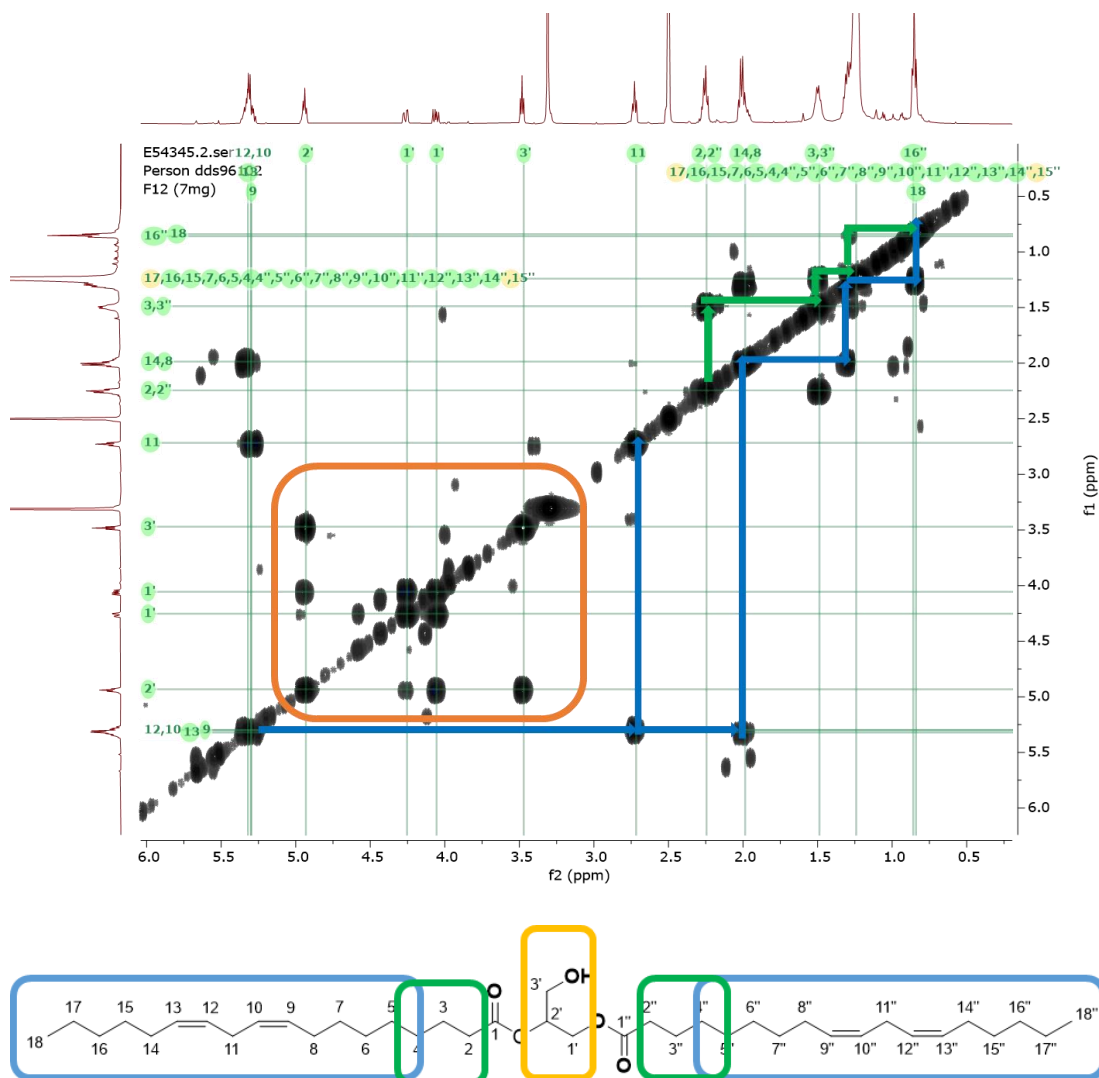


Figure 6.34: (^1H - ^1H) COSY correlation of the NMR spectrum of compound F11-11 in $\text{DMSO-}d_6$ measured at 500 MHz.

HMBC spectra (Figure 6.36) also revealed comparable correlations to those in F11-12. The HMBC correlations established the structure of F11-11 and corroborated the glycerol moiety's connection to the carboxy unit. $\text{CH}_2\text{B-1'}$ showing a cross peak with C2' methine at and C1 of

the carboxyl group at 173.0 ppm. As well the glycerol proton at H2' correlate with the carboxyl group at 173.0 ppm, which indicated the presence of two identical fatty acid connected to glycerol moiety at H1' and H2'. F11-11 was therefore identified as 1',2'-diyl (9Z,9'Z,12Z,12'Z)-bis(octadeca-9,12-dienoate), also known as 1',2' dilinolein (Liu *et al.*, 2013).

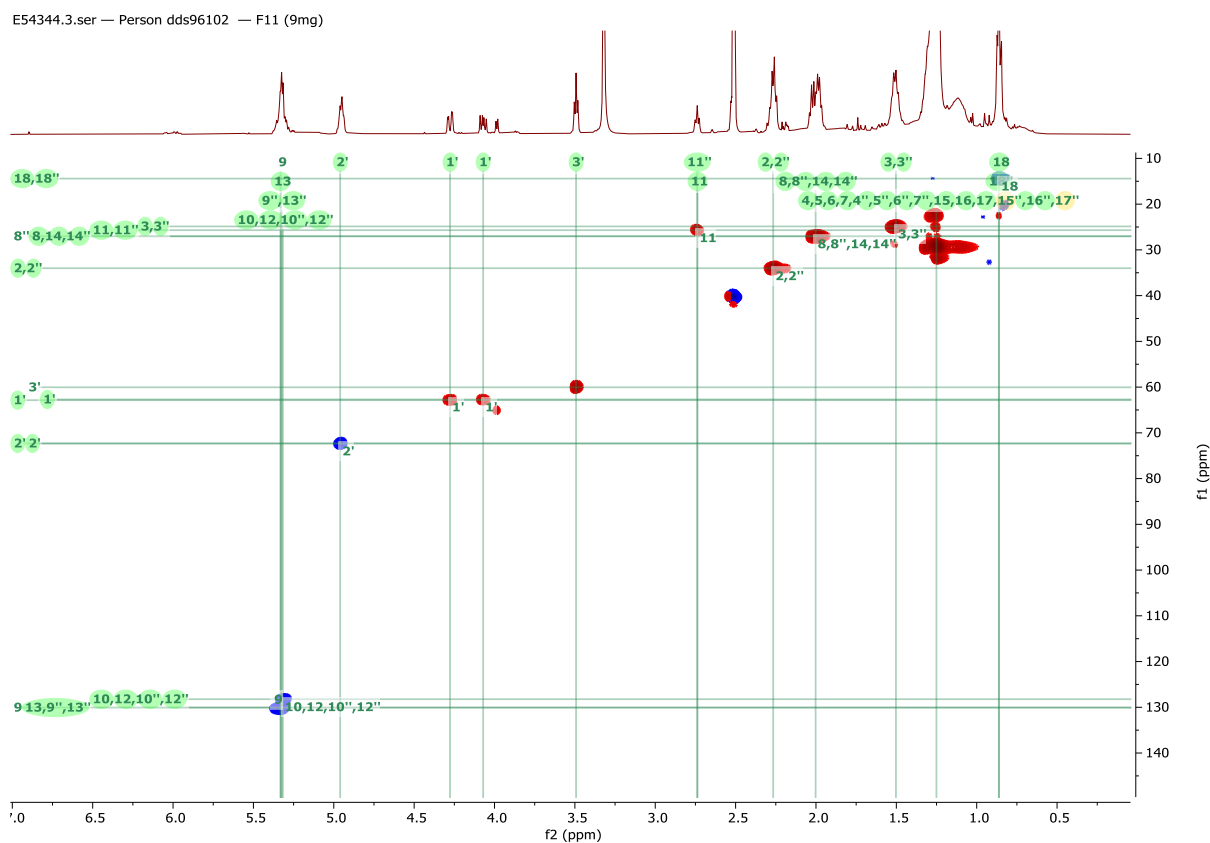


Figure 6.35: HSQC NMR spectrum of compound F11-11 in DMSO-*d*₆ measured at 500 MHz. Red correlations are CHs and CH₃s while blue are CH₂s group.

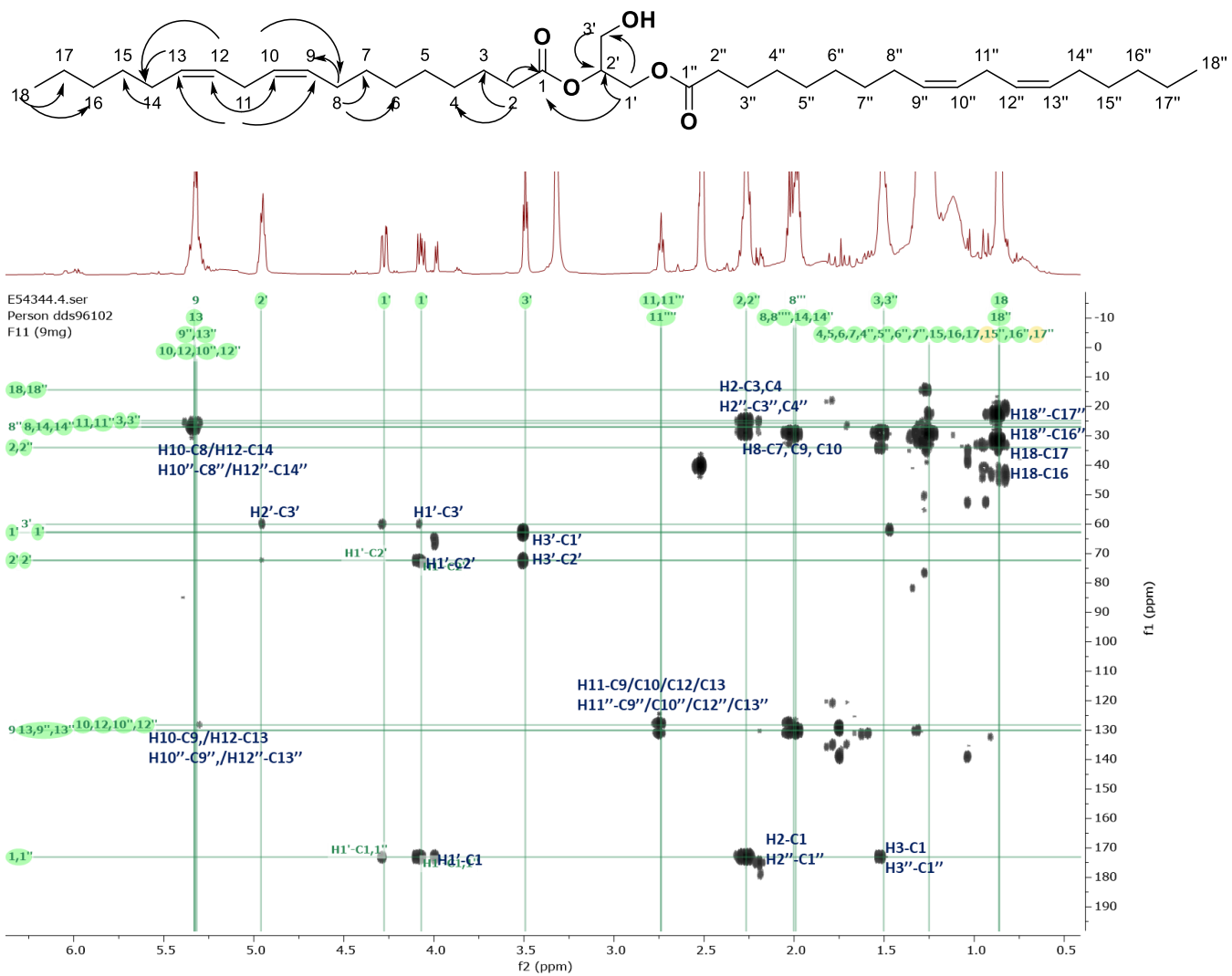


Figure 6.36: HMBC NMR spectrum of compound F11-11 in DMSO-*d*₆ measured at 500 MHz.

Table 6.7: NMR spectral data for compound F11-11 in DMSO-*d*₆ measured at 500 MHz.

Atom no.	¹³ C Multiplicity	¹ H Multiplicity	<i>J</i> in Hz	HMBC
1	173.0			
2	34.0 CH ₂	2.26 q	7.4	C1, C3, C4, C5
3	24.9 CH ₂	1.50 hept	6.6	C1
4	28.3 CH ₂	1.25 d	9.2	
5	25 CH ₂	1.25 d	9.2	
6	29.2 CH ₂	1.25 d	9.2	
7	28.3 CH ₂	1.25 d	9.2	
8	27.0 CH ₂	2.00 dq	17.8, 6.6	C7, C9, C10
9	130.0 CH	5.31 m		
10	128.2 CH	5.31 m		C8
11	25.7 CH ₂	2.73 t	6.5	C9, C10, C12, C13
12	128.2 CH	5.31 m		C14
13	130.0 CH	5.31 m		
14	27.0 CH ₂	2.00 dq	17.8, 6.6	C13, C12, C15
15	31.8 CH ₂	1.25 q		
16	28.3 CH ₂	1.25 q		
17	25.5 CH ₂	1.25 q		
18	14.4 CH ₃	0.85 td		C16, C17
1'A	62.8 CH ₂ B	4.07 dd	12.0, 7.2	C1, C2', C3'
1'B	62.8 CH ₂ A	4.27 dd	12.0, 7.2	C1, C2', C3'
2'	72.3 CH	4.96 dt	7.8, 5.6	C3'
3'	60.0 CH ₂	3.49 t	5.6	
3-OH		3.49 t		
1''	173.0			
2''	34.0 CH ₂	2.26 q	7.4	C1'', C3'', C4'', C''
3''	24.9 CH ₂	1.50 hept	6.6	C1''
4''	28.3 CH ₂	1.25 d	9.2	
5''	25 CH ₂	1.25 d	9.2	
6''	29.2 CH ₂	1.25 d	9.2	
7''	28.3 CH ₂	1.25 d	9.2	
8''	27.0 CH ₂	2.00 dq	17.8, 6.6	C7'', C9'', C10''
9''	130.0 CH	5.31 m		
10''	128.2 CH	5.31 m		C8''
11''	25.7 CH ₂	2.73 t	6.5	C9'', C10'', C12'', C13''
12''	128.2 CH	5.31 m		C14''
13''	130.0 CH	5.31 m		
14''	27.0 CH ₂	2.00 dq	17.8, 6.6	C13'', C12'', C15''
15''	31.8 CH ₂	1.25 q		
16''	28.3 CH ₂	1.25 q		
17''	25.5 CH ₂	1.25 q		
18''	14.4 CH ₃	0.85 td		C16'', C17''

Legend: s= singlet, d = doublet, t = triplet, q = quartet, m =multiplet, hept=heptet.

6.6.2. Ophiobolins

While continuing the fractionation and purification work with F11 by Reveleris® FC, subfractions 13 to 18 (Table 6.8) were afforded by increasing the percentage of EtOAc to 40%. ¹H NMR was accomplished for subfractions 13 to 18 (Figure 6.37). Subfraction 17 was subjected to further 2D NMR analysis because it was the purest compound.

Table 6.8: Weights of subfractions 13 to 18 from the bioactive fraction F11.

Subfractions no.	Weight (mg)
F11-13	3.4
F11-14	1.5
F11-15	1.6
F11-16	5.8
F11-17	3
F11-18	2.7

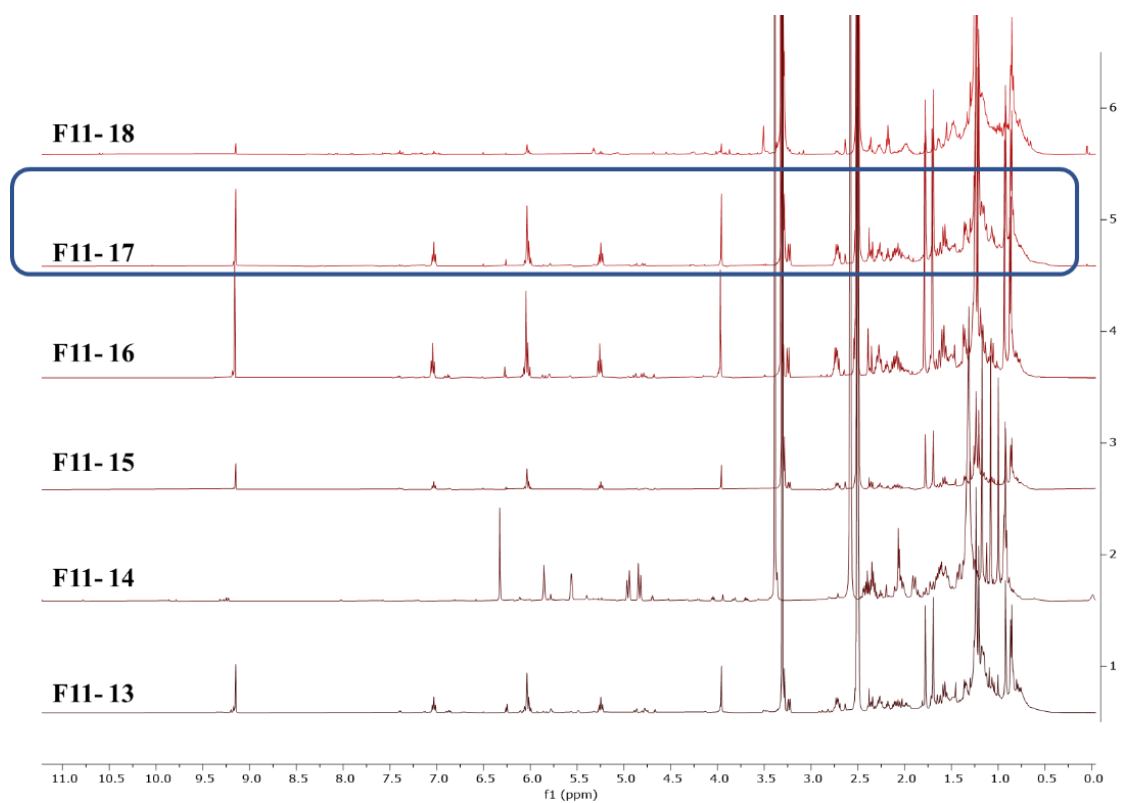


Figure 6.37: Stacked ¹H NMR for subfractions 13 to 18. Fractions concentration was at 5mg/600μl in DMSO-*d*₆ measured at 500MHz. The highlighted subfraction was subjected to further structural elucidation work.

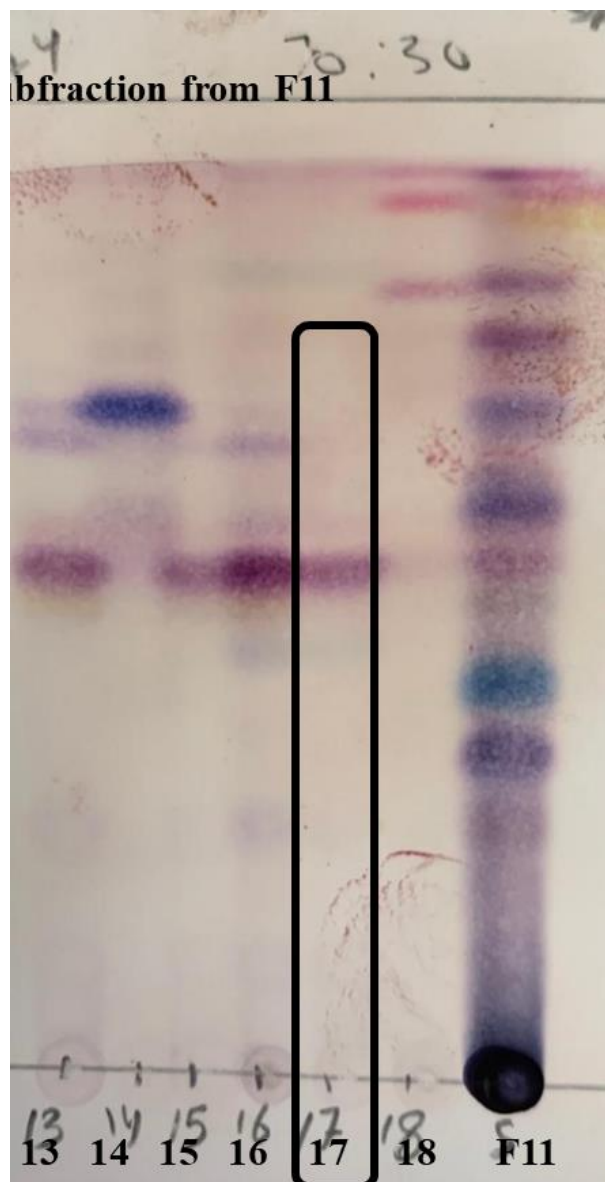
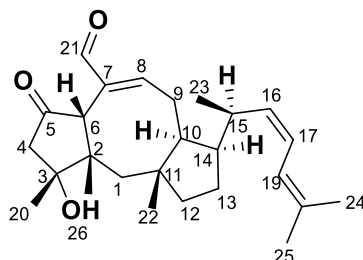


Figure 6.38: TLC for subfractions 13 to 18 obtained from Reveleris FC using solvent system 70:30% of n-Hexane and EtOAc.

Compound F11-17 structure elucidation.

Chemical Formula: C₂₅H₃₆O₃

Exact Mass: 384.2666



ophiobolin K

Figure 6.39: Chemical structure of compound F11-17

Formula	Calculated Mass	Target Mass	Double Bond Equivalence	Absolute Error (ppm)	Error (mDa)	Error (ppm)	Fitness
C ₂₅ H ₃₆ O ₃ N a	407.25621	407.2563 6	7.5	0.36	0.15	0.36	0.998

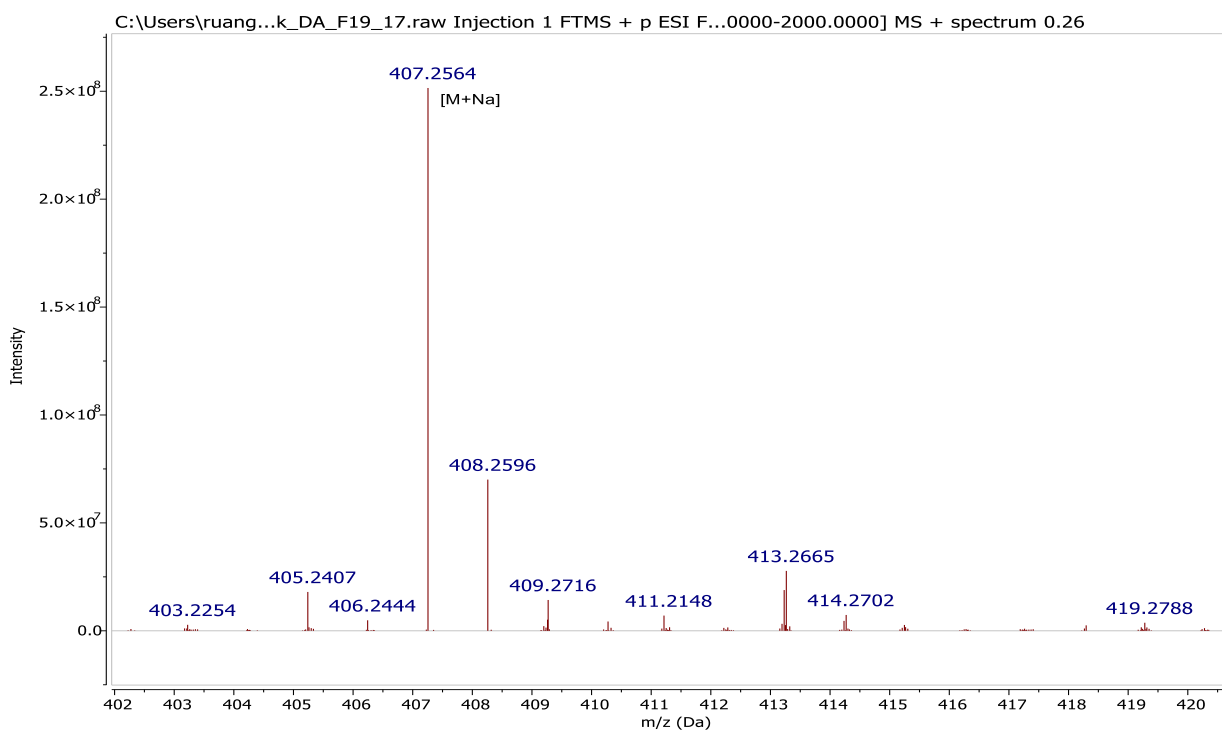


Figure 6.40. Mass spectral data of F11-17 on the ion peak at m/z 407.256 [M+Na]⁺.

Compound F11-17 was isolated from fraction 11 as a yellow amorphous solid with a yield of 3 mg. The compound was purified with FC at 40% EtOAc and 60% n-Hexane. High resolution mass spectral analysis gave a MWt of 384.2666 for an ion peak at m/z 407.256 $[M+Na]^+$ (Figure 6.40), which was determined to have a molecular formula of $C_{25}H_{36}O_3$. The molecular formula indicated that the molecule has 8 DBE, which was attributed due to the presence of tricyclic system with three olefinic bonds and two carbonyl groups.

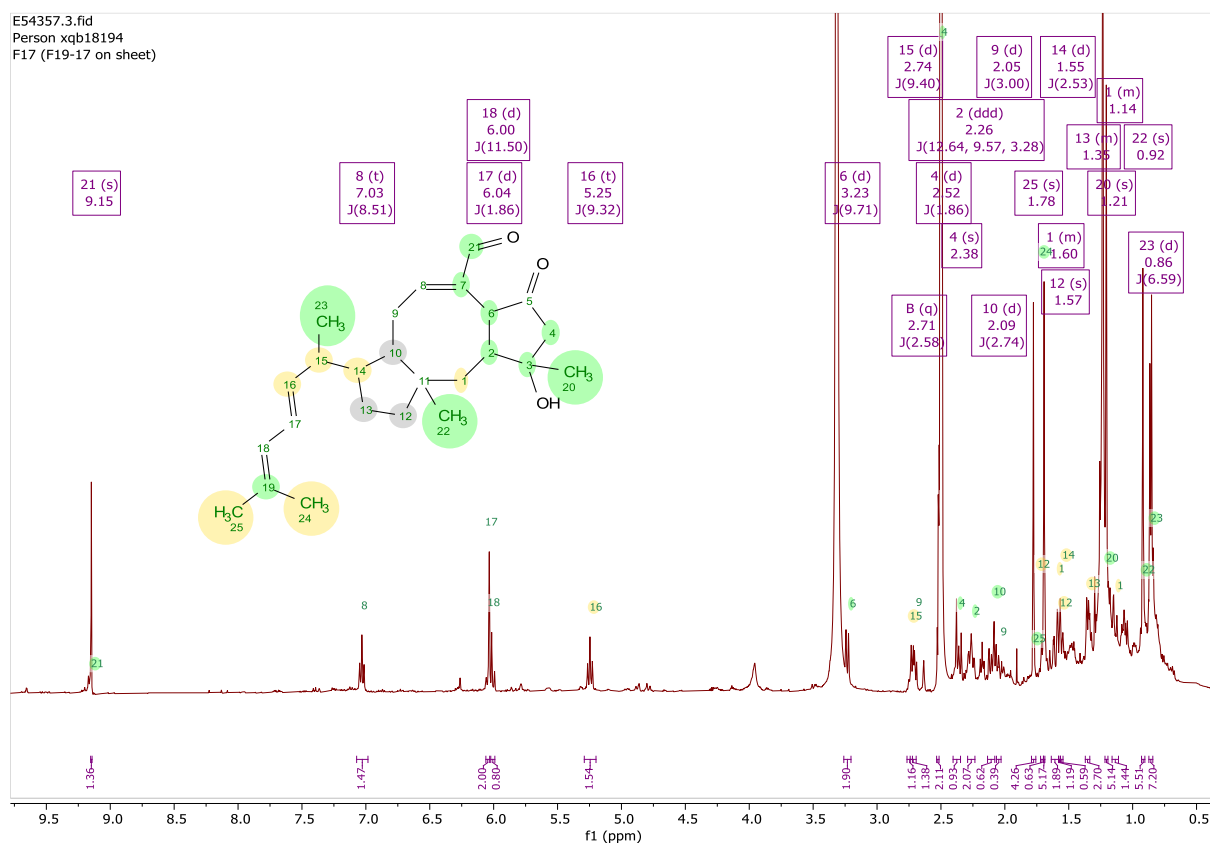


Figure 6.41: 1H NMR spectrum of compound F11-17 in $DMSO-d_6$ measured at 500 MHz.

The 1H NMR spectra shown in Figure 6.41 exhibited an aldehyde proton singlet at δ_H 9.15 s, four olefinic protons at (δ_H 7.03, t, $J=8.51$, H8), (δ_H 6.04, d, $J=11.4$, 1.8, H17, H18), (δ_H 5.24, t, $J=9.3$, H16), four singlet methyl including two vinylic methyl (δ_H 1.70, H24) and (δ_H 1.78, H25), one methyl group connected to an oxygen bearing carbon at (δ_H 1.21, H20), and an angular methyl (δ_H 0.93, H22), and a methyl doublet (δ_H 0.86, H23).

Detailed interpretation of both 1D and 2D NMR, in association with the DBE number of the compound disclosed an ophiobolin-based sesterterpenoid skeleton (Mandal *et al.*, 2009, Singh

et al., 1991). Based on the HSQC spectrum (Figure 6.42) and HMBC correlations, (Figure 6.43), there were 25 carbons that comprised of five alkyl methines, five methylene carbons, five methyl carbons, aldehyde carbon (δ_C 192.9), four olefinic methine carbons, and five non-protonated carbons, which included two olefinic (δ_C 140.7, 134.6), an oxygenated quaternary (δ_C 76.0), a carbonyl ketone (δ_C 217.0) and a quaternary aliphatic carbon (δ_C 43.5).

The COSY spectrum (Figure 6.44) exhibited cross-peaks of H1 with H2, H2 with H6 and H8 with H9, as well as HMBC correlations from H21 (δ_H 9.15) to C6 (δ_C 48.9) and C7 (δ_C 140.7) and C8 (δ_C 158.7) that established an eight-membered ring B with a fragment of C7=C8-C9-C10. The observed COSY correlations from H16 (δ_H 5.58) with H15 (δ_H 5.36), H17 (δ_H 5.36) and H18 (δ_H 4.15), as well as the HMBC correlations from H24 (δ_H 1.24), and H25 (δ_H 1.21) to C17/C18/C10 and from H23 to C16, confirmed the terminal side chain connected to ring C at C14.

The ^1H - ^1H COSY spectrum disclosed the spin system in F11-17, one of the isolated spin systems was assigned following the indicated blue lines in Figure 6.44, which revealed the coupling between H16 with H15, H17 and H18 on the terminal side chain, while H8 coupled with H9, and H10 in the eight member-ring. The second spin system was assigned to the geminal proton at C4, and coupling between H2 with H4, which was depicted with orange lines in Figure 6.44.

Further evidence for a tricyclic ophiobolin skeleton was confirmed by HMBC correlations between H4 β methyl and H20 to both C2 and C3 as well as H1 β to C6 and C11, C11 also correlated with H22 and H14. Similar correlation between H6 and C5 carbonyl, and H22 to C1. These ^1H - ^{13}C correlations were an ophiobolin skeleton system (Singh *et al.*, 1991).

The relative configuration of the compound was revealed by a ROESY experiment (Figure 6.45) as well as by comparing the NMR to literature data (Singh *et al.*, 1991). The ROESY correlations of H22 (δ_H 0.93) with H2 (δ_H 2.27), H6 (δ_H 3.23), and H9 β (δ_H 2.05), as well as of H9 β (δ_H 2.05) with H20 (δ_H 1.21) indicated these groups are cofacial, and these groups were assigned as β -oriented. So, correlation between H6 with H2 supported the enhancement of cis-fused A/B ring system (Singh *et al.*, 1991). In addition, the through space correlation of H9 α (δ_H 2.71) with H8 (δ_H 7.03), H10 ($\sim\delta_H$ 2.10) and H15($\sim\delta_H$ 2.72), suggested an α -orientation, while on the other way around, the ROESY data revealed a synonymous link

between H8 and the CHO group. A Z-configuration was confirmed between H16 and H17 due to the coupling constant of 9.3 Hz, which was further substantiated by the ROESY correlation between H15 with H18.

A full assignment of the spectral data of F11-17 as presented in Table 6.9 and in comparison with those of the literature data (Table 6.10) resulted in the elucidation of the ophiobolin K structure (Singh *et al.*, 1991). Ophiobolin K exhibited nematocidal activity (ED₅₀ 10 µg/mL) against the free-living nematode *Caenorhabditis elegans* (Singh *et al.*, 1991). More recently, ophiobolin K was isolated from the endophytic fungus *A. calidoustus*, an endophytic fungus from the medicinal plant *Acanthospermum australe* (Asteraceae) and was reported for its antifungal activity against fungal plant pathogens, protozoal activity against *Trypanosoma cruzi*, and cytotoxic activity against human tumour cell lines (Rodrigues de Carvalho *et al.*, 2016).

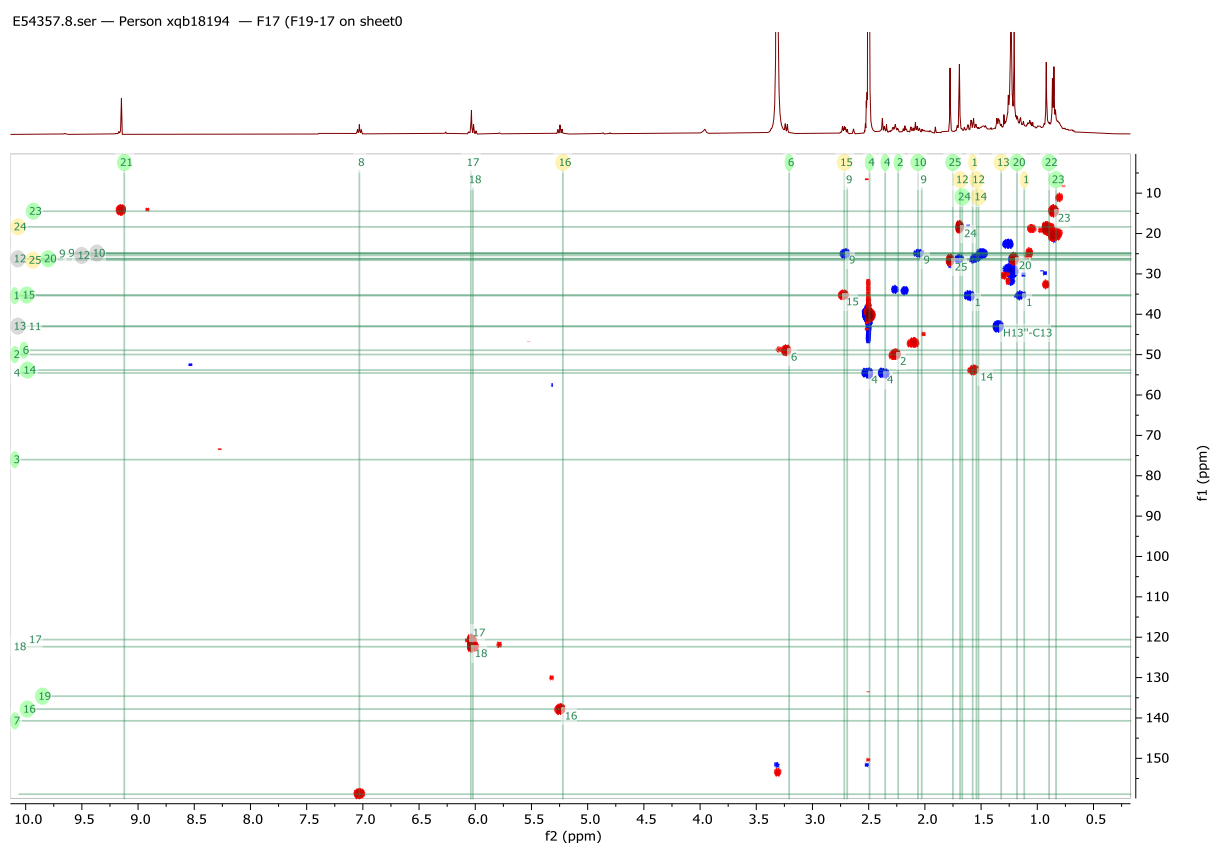
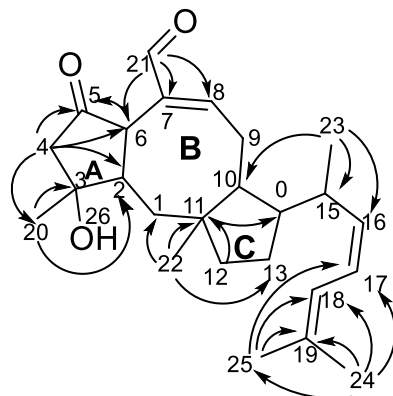


Figure 6.42: HSQC NMR spectrum of compound F11-17 in DMSO-*d*₆ measured at 500 MHz. Red cross peaks are CHs and CH₃s while blue are CH₂s.



E54357.6.ser — Person xqb18194 — F17 (F19-17 on sheet)

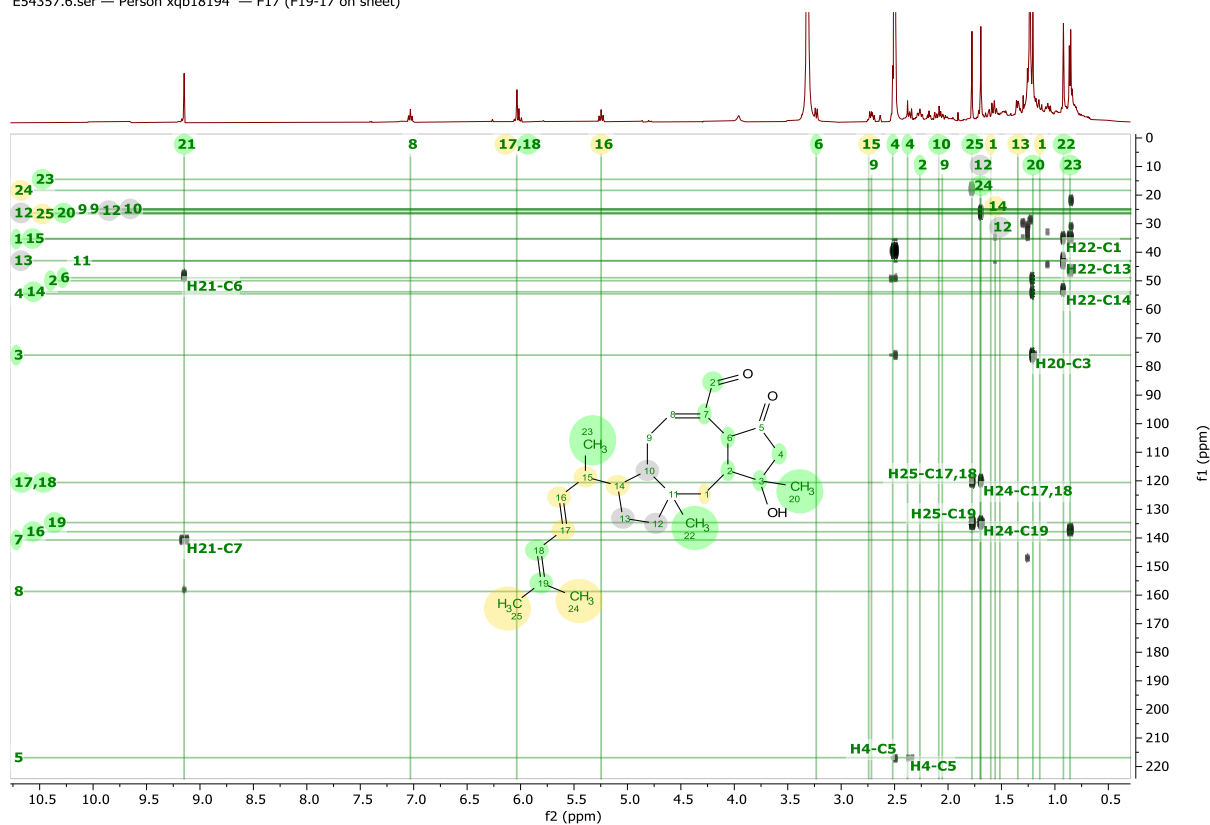


Figure 6.43: HMBC NMR spectrum of compound F11-17 in DMSO-*d*₆ measured at 500 MHz.

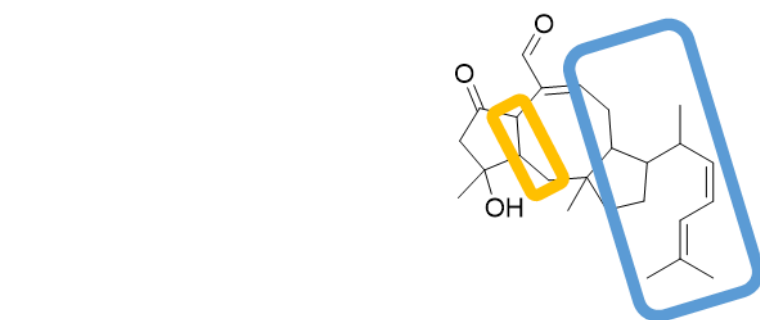
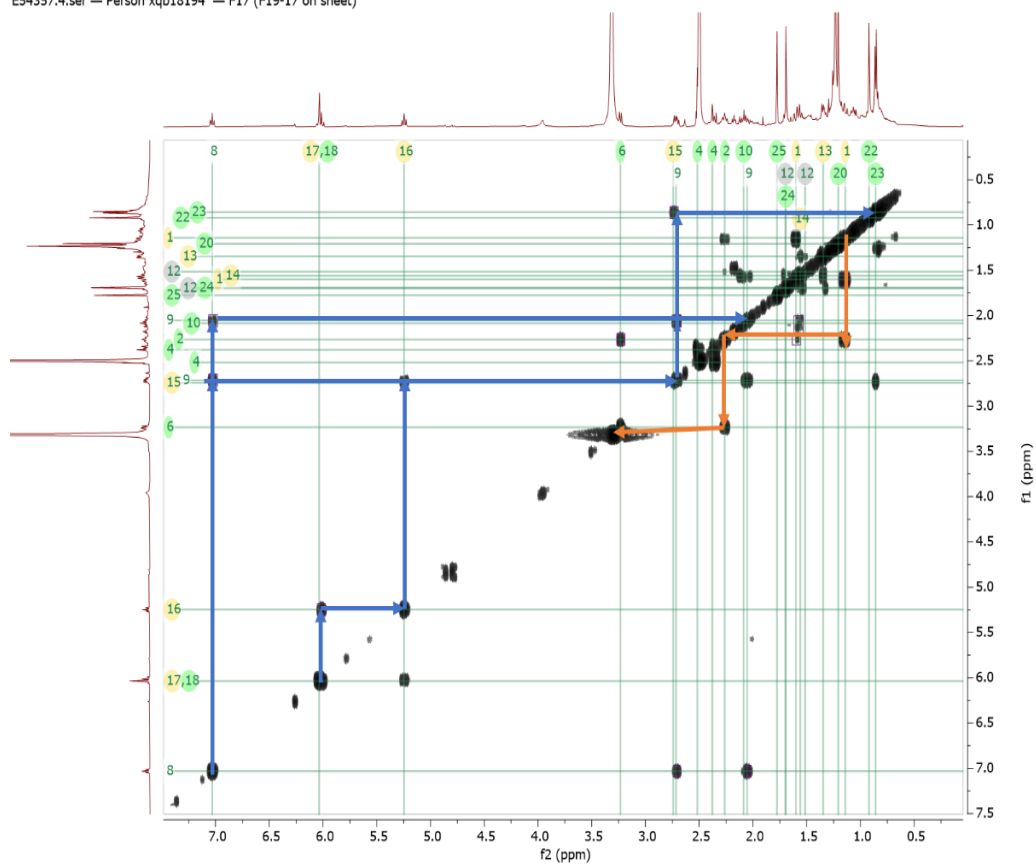


Figure 6.44: (^1H - ^1H) COSY correlation NMR spectrum of compound F11-17 in $\text{DMSO-}d_6$ measured at 500 MHz.

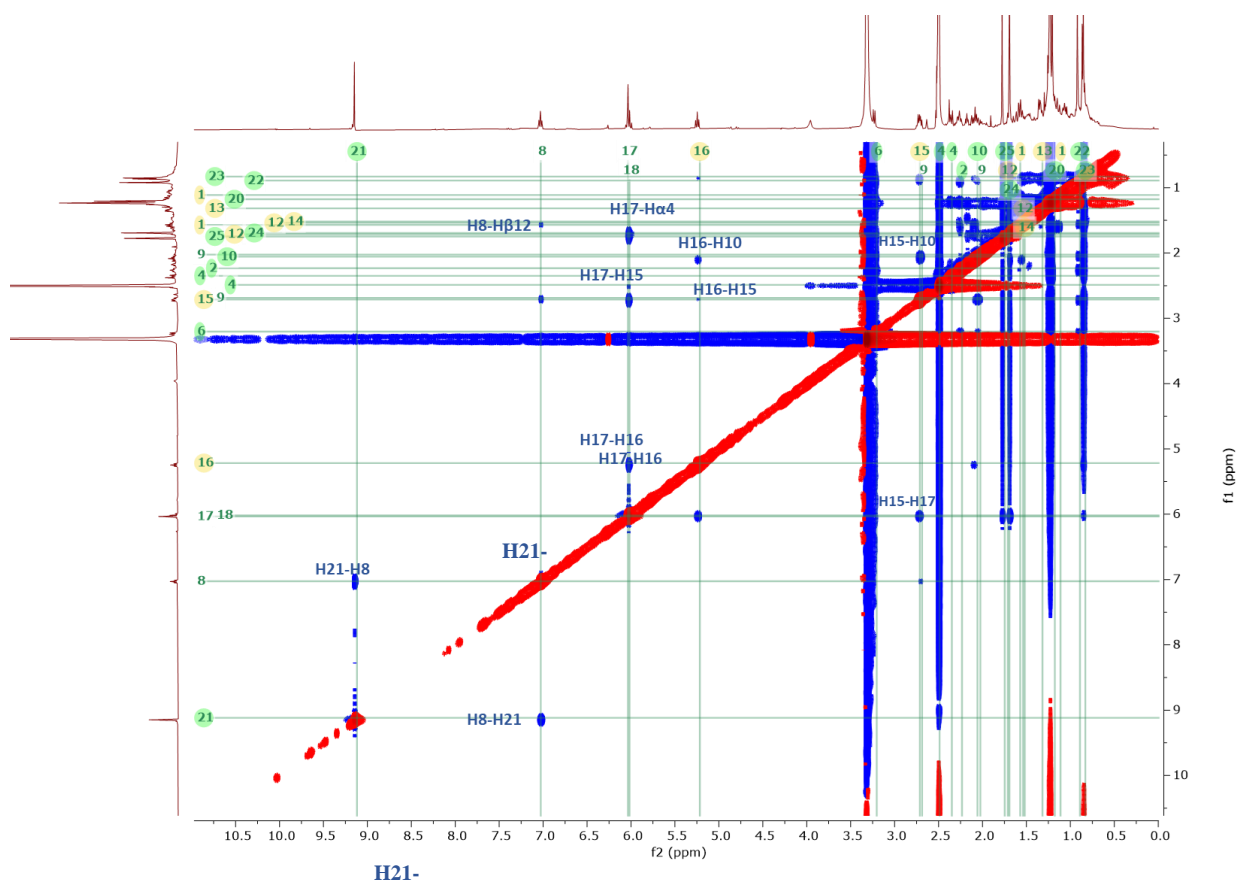


Figure 6.45: ROESY NMR spectrum and the essential correlation of F11-17 in DMSO-*d*₆ measured at 600 MHz.

Table 6.9: NMR spectral data for compound F11-17 in DMSO-*d*₆ measured at 500 MHz..

Atom no.	¹³ C*	¹ H	<i>J</i> in Hz	HMBC ¹ H to ¹³ C	Roesy
1α 1β	35.3 CH ₂	1.15 m 1.59 m			
2	49.9 CH	2.27 ddd	12.6, 9.5, 3.2		H20, H22
3	76.0 C	---			
4α 4β	54.4 CH ₂	2.53d 2.37 s	1.8	C2, C3, C5, C6, C20	H4 β -H20
5	217.0 CO	---			
6	48.9 CH	3.23 d	9.7	C5	H2
7	140.7 C	---			
8	158.7 CH	7.03 t	8.5		H9 α , H21
9α 9β	25.0 CH ₂	2.72 m 2.05 m			
10	46.9 CH	2.10 d	2.74		H9 α , H15
11	43.5 C	---			
12α 12β	26.2 CH ₂	1.70 m 1.56 m		C11	
13	42.9 CH ₂	1.35 m			
14	53.8 CH	1.57 d	8.1	C11	
15	35.2 CH	2.72 d	9.4		H9 α H10, H17
16	137.8 CH	5.24 t	9.3		H4 α , H10, H15
17	122.4 CH	6.04 d	1.8		H4 α , H15, H16
18	122.3 CH	6.02 d	11.5		
19	134.6 C	---			
20	26.2 CH ₃	1.21 s		C2, C3, C4	H4 β
21	194.9 CH	9.15 s		C6, C7, C8	H8
22	18.7 CH ₃	0.93 s		C1, C11, C13, C14	H9 β , H2, H6
23	20.4 CH ₃	0.86 d	6.6	C10, C15, C16	H15, H16
24	18.3 CH ₃	1.70 s		C17, C18, C19, C25	H17
25	26.6 CH ₃	1.78 s		C17, C18, C19, C24	H17
26	OH	---			

Legend s= singlet, d = doublet, t = triplet, q = quartet, m =multiplet, hept=heptet.
*Data taken from HSQC, HMBC and Roesy experiments.

Table 6.10: NMR data of F11-17 compared to that of ophiobolin K from the literature (Singh *et al.*, 1991).

ophiobolin K in CDCl ₃ (300 MHz)				F11-17 in DMSO- <i>d</i> ₆ (500 MHz)		
Atom no.	¹³ C	¹ H	<i>J</i> in Hz	¹³ C*	¹ H	<i>J</i> in Hz
1α	35.0 CH ₂	1.20m		35.3 CH ₂	1.15 m	
1β		1.75 m			1.59 m	
2	50.2 CH	2.39 brdt	12.9, 3.1	49.9 CH	2.27 ddd	12.6, 9.5, 3.2
3	76.9 C	---		76.0 C	---	
4α	54.9 CH ₂	2.78 d	19.2	54.4 CH ₂	2.53 d	20.0
4β		2.48 d	19.2		2.37 s	
5	217.7 CO	---		217.0 CO	---	
6	48.5 CH	3.25 brd	10.5	48.9 CH	3.23 d	9.7
7	141.3 C	---		140.7 C	---	
8	164.0 CH	7.11 t	8.6	158.7 CH	7.03 t	8.5
9α	25.4 CH ₂	2.10 m		25.0 CH ₂	2.05 m	
9β		2.94 dd	12.6, 8.3		2.72 d	8.2
10	47.1 CH	2.06 m		46.9 CH	2.10 d	2.74
11	43.8 C	---		43.5 C	---	
12α	26.5 CH ₂	1.60		26.2 CH ₂	1.70 m	
12β		1.25 m			1.56 m	
13	42.5 CH ₂	1.40 m 1.40 m		42.9 CH ₂	1.35 m	
14	53.3 CH	1.56 m		53.8 CH	1.57 d	8.1
15	35.8 CH	2.70 m		35.2 CH	2.72 d	9.4
16	137.1 CH	5.17 t	9.6	137.8 CH	5.24 t	9.3
17	122.4 CH	6.02 dt	10.5, 0.9	122.4 CH	6.04 d	11.4, 1.8
18	119.9 CH	5.96 dd	10.5, 1.0	120.0 CH	6.04 d	11.4, 1.8
19	136 C	---		134.6 C	---	
20	25.6 CH ₃	1.34 s		26.2 CH ₃	1.21 s	
21	196.2 CH	9.19 s		192.9 CH	9.15 s	
22	18.7 CH ₃	0.95 s		18.7 CH ₃	0.93 s	
23	20.4 CH ₃	0.90 d	6.7	20.4 CH ₃	0.86 d	6.6
24	18.1 CH ₃	1.72 brs		18.3 CH ₃	1.70 s	
25	26.5 CH ₃	1.8 brs		26.6 CH ₃	1.78 s	
26	OH	---		OH	---	

Legend: br = broad, s = singlet, d = doublet, t = triplet, q = quartet, m = multiplet.
*Data taken from HSQC, HMBC and ROESY experiments.

6.6.3. Drimane sesquiterpene derivatives

Drimane sesquiterpene derivatives were obtained from *A. ustus* fractions by further fractionation of F11 (Table 6.11) using the eluting solvents of 50% to 100% of EtOAc in combination with n-Hexane. Fraction 11 produced two derivatives SF11-23 and SF11-29-8. Meanwhile fraction 12 also produced three derivatives, two of them were like SF11-29-8 (SF6-5 and SF7-1) and one other derivative SF12-11-2.

Table 6.11: Weight of subfractions 19 to 32 from fraction 11 obtained by Reveleris FC using 50% to 100% of EtOAc in combination with n-Hexane. TLC chromatograms are shown in Figure 6.46.

Subfractions no.	Weight (mg)
F11-19	23.6
F11-20	36.9
F11-21	14.5
F11-22	10.6
F11-23	17.8
F11-24	9.6
F11-25	8.7
F11-26	4.5
F11-27	6.9
F11-28	10.4
F11-29	56.3
F11-30	12.4
F11-31	10.3
F11-32	10.2

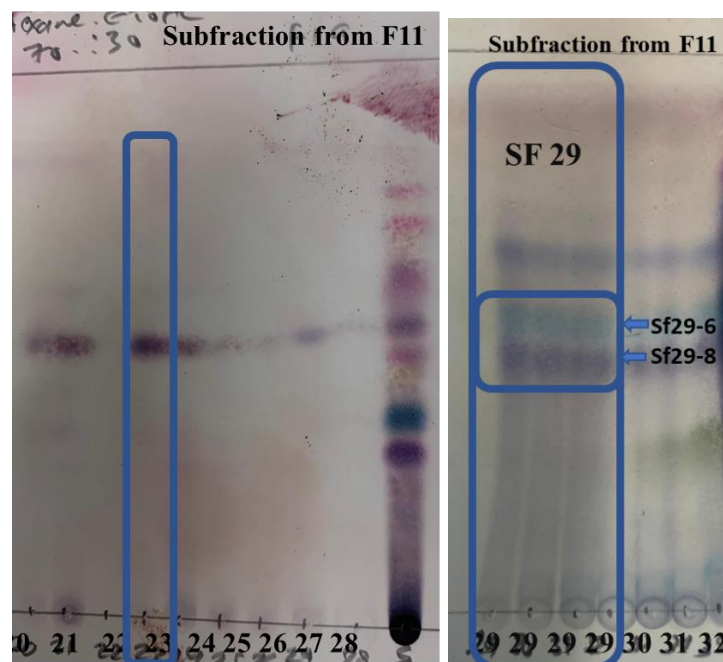


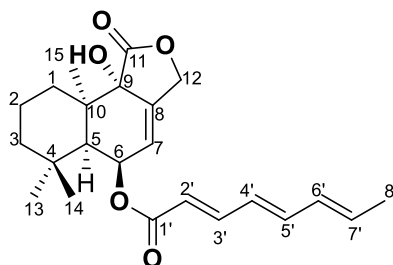
Figure 6.46: TLC for subfractions 20 to 32 from fraction 19 using solvent system 70:30% n-Hexane and EtOAc. Boxed in blue was SF 23, which was directly selected for 2D NMR structure elucidation work and SF 29 that was subjected to further preparative TLC purification steps.

6.5.3.1. Compound F11-23 structure elucidation.

9 α -hydroxy-6 α -[(2*E*,4*E*,6*E*)-octa-2,4,6-trienyloxy]-5 α -drim-7-en-11,12-olide

Chemical Formula: C₂₃H₃₀O₅

Exact Mass: 386.2081



Antibiotic RES 1149-2

Figure 6.47 :Chemical structure of compound F11-23

Formula	Calculated Mass	Target Mass	Double Bond Equivalence	Absolute Error (ppm)	Error (mDa)	Error (ppm)
C ₂₃ H ₃₀ O ₅ Na	409.19909	409.19791	8.5	2.90	-1.19	-2.90

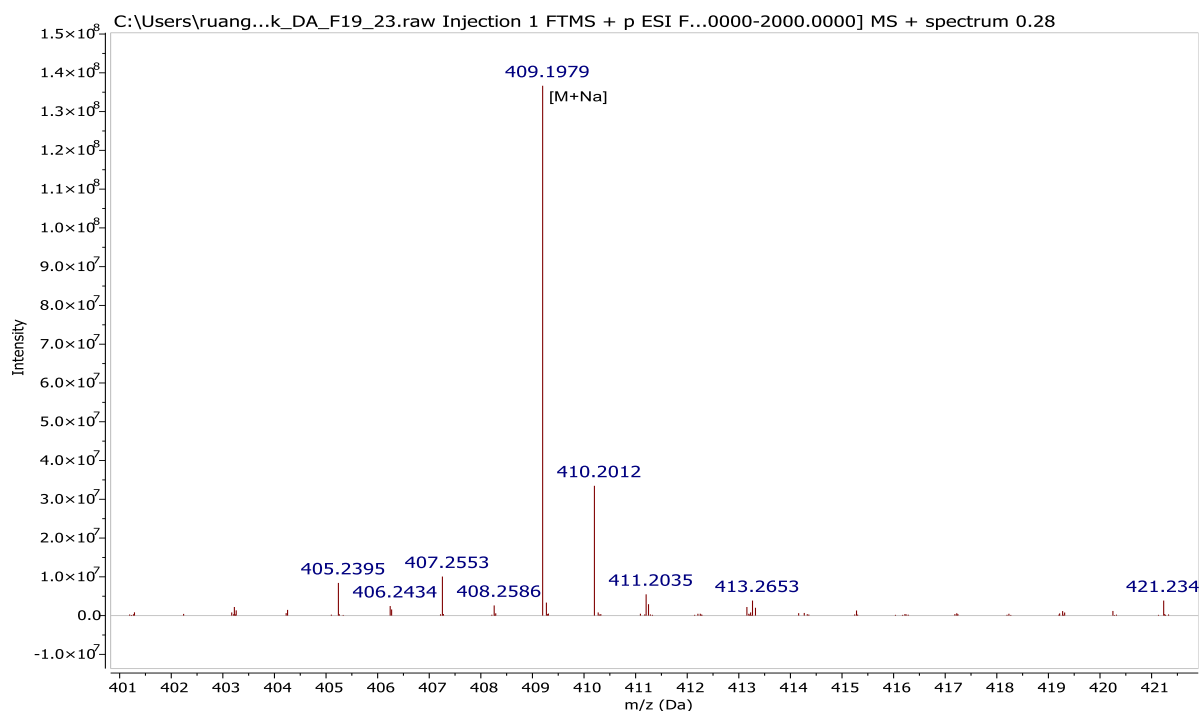


Figure 6.48. Mass spectral data of F11-23 for the ion peak at m/z 409.198 [M+Na]⁺.

Compound F11-23 was isolated from subfraction 19 as a white amorphous solid with a yield of 17 mg. The compound was eluted along with the semi-polar fractions at 50% EtOAc and 50% n-Hexane. Mass spectrometric data suggested a DBE of 9, proposing three rings, along with four double bonds from the olefinic system and two carbonyl groups. HREIMS suggested a MW of 386.21 Da and molecular formula of $C_{23}H_{30}O_5$ at an ion peak m/z 409.198 $[M+Na]^+$. The structure was confirmed as 9 α -hydroxy-6 β -[(2E,4E,6E)-octa-2,4,6-trienyloxy]-5 α -drim-7-en-11,12-olide by inspection of both 1H and 2D NMR data as well as in comparison to the literature data (Table 6.12).

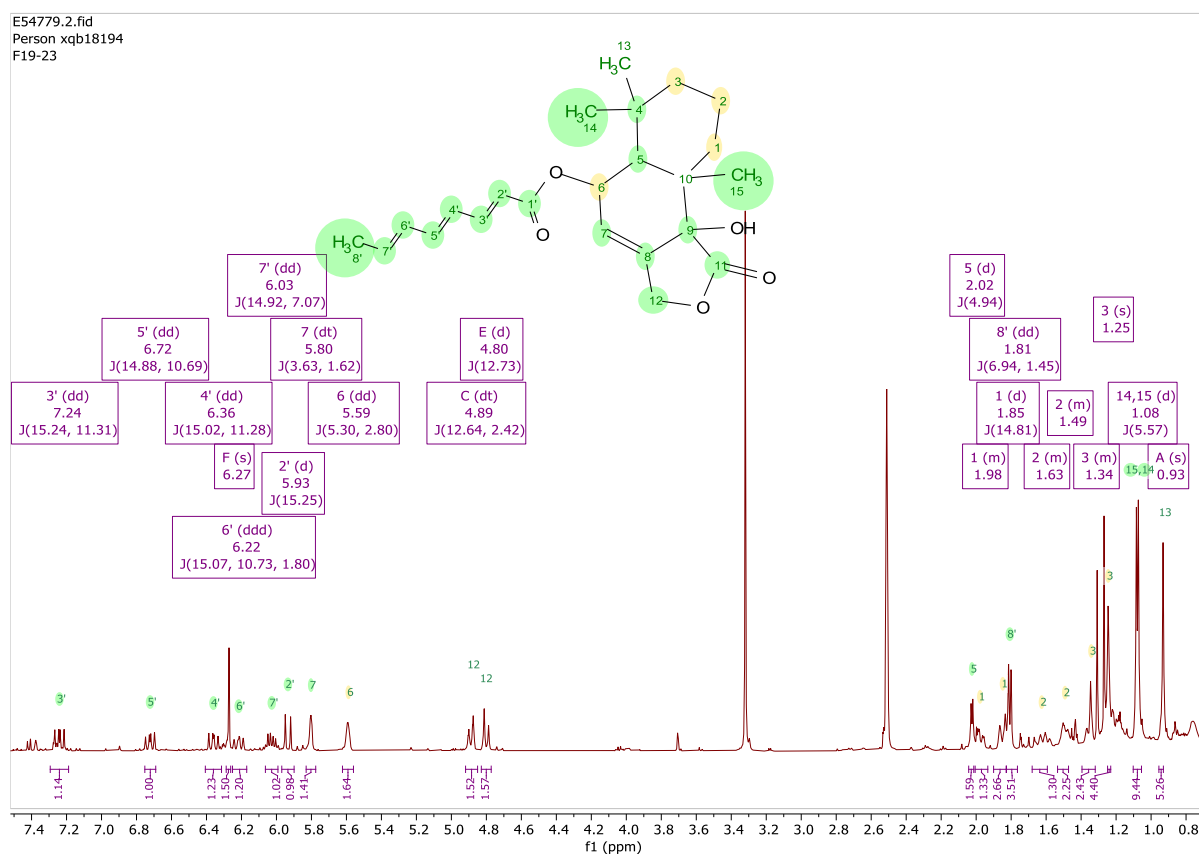


Figure 6.49: 1H NMR spectrum of compound F11-23 in $DMSO-d_6$ measured at 500 MHz. The 1H NMR spectrum (Figure 6.49) disclosed the presence of four methyl groups at δ_H 0.93s (H13), 1.09d (H14), 1.08d (H15), and 1.81dd (H8') 1.3 Hz, H3-12), an oxymethylene unit at δ_H 4.88 dt and 4.81 d (H12) with $J = 12.6, 2.4$ Hz and 12.7 respectively. One exchangeable proton at δ_H 6.28s (9-OH). The presence of three methylene groups at δ_H 1.99m and

1.87d(H1), 1.61m and 1.50m (H2), 1.35m and 1.22d (H3). However, the occurrence of a conjugated trans olefinic system was shown by ¹H NMR, which revealed six trans-coupled olefinic protons at δ_{H} 5.90d, 7.23d, 6.36d, 6.72, 6.22ddd, and 6.04dd connected to a methyl terminal unit at δ_{H} at 1.81ppm.

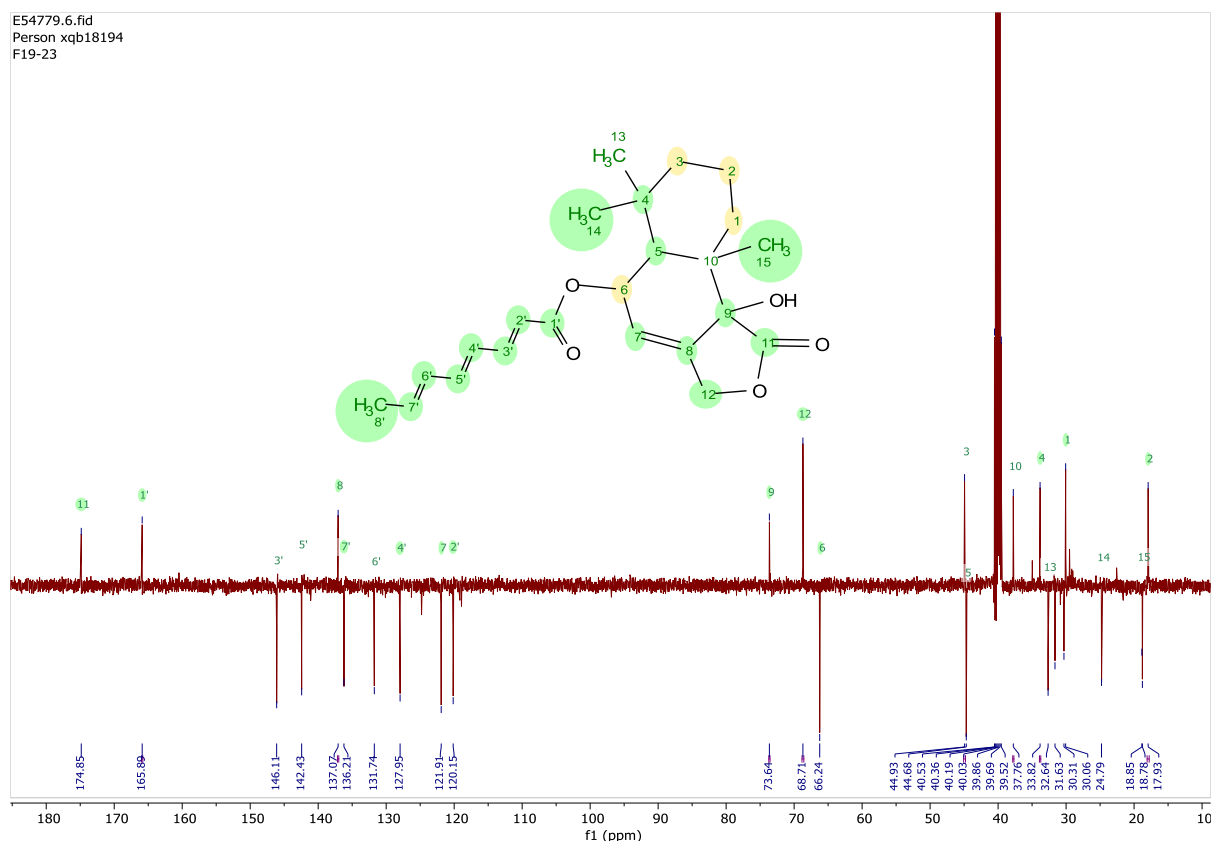


Figure 6.50: ¹³C JMOD NMR spectrum of compound F11-23 in DMSO-*d*₆ measured at 500 MHz

The ¹³C JMOD spectrum (Figure 6.50) showed 23 signals assigned for two ester carbonyl groups at (δ_{C} 174.8 C, and 165.2 54 C), six olefinic protons, 3 quaternary carbons and 12 aliphatic. The ¹³C and ¹H NMR spectra exhibited 23 carbon and 30 proton signals, respectively.

¹³C-JMOD along with HSQC spectra (Figure 6.51) revealed the presence of four methyl resonances, four methylene resonances, nine CH and six quaternary carbons. All the other proton resonances correlated to respective carbon signals except for the singlet at 6.28 ppm, suggesting that this was due to an exchangeable hydroxyl proton.

Considering the chemical shift data indicated that the CH₂ at 68.7 ppm, the CH at 66.1 ppm and quaternary carbons at 73.7, 165.2 and 174.8 ppm were oxygenated. The presence of six double bonds was deduced from the presence of eight olefinic carbons (120.3, 128.0, 131.8, 136.2, 136.2, 142.4, 146.1) and two carbonyl carbons.

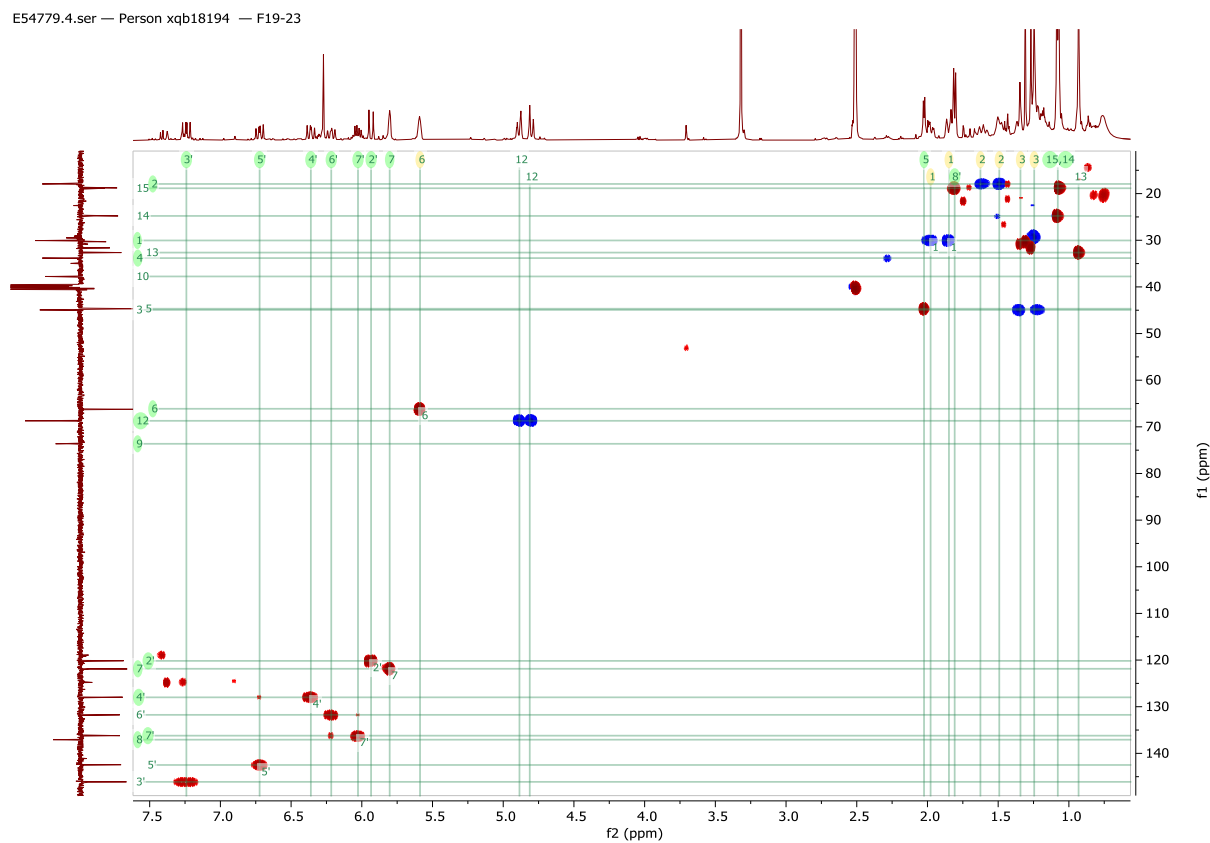


Figure 6.51: HSQC NMR spectrum of compound F11-23 in DMSO-*d*₆ measured at 500 MHz. Red cross peaks are CH and CH₃ while blue are CH₂ groups.

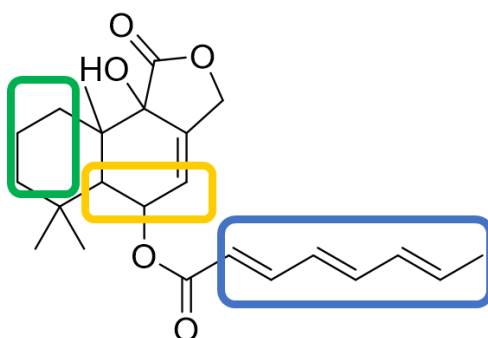
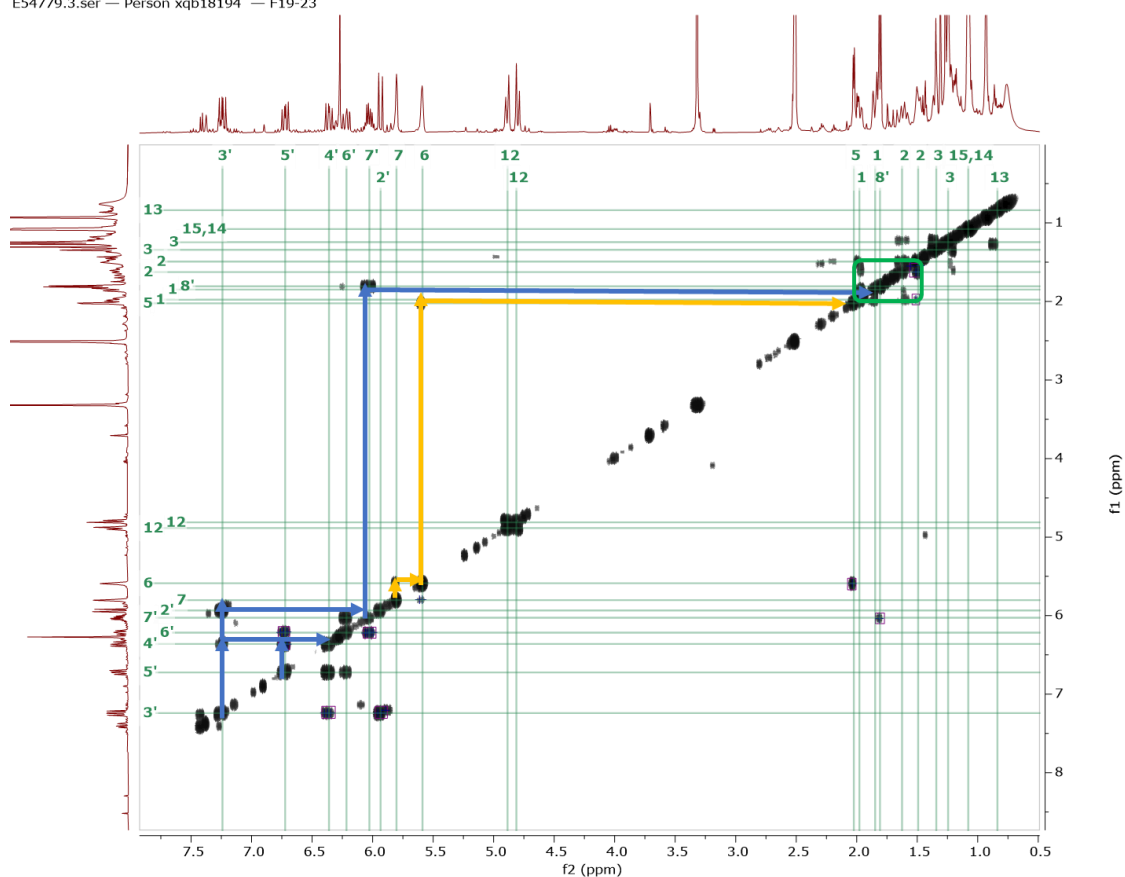


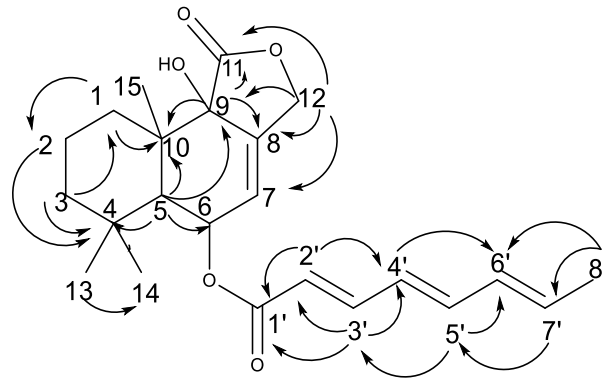
Figure 6.52: (^1H - ^1H) COSY correlation NMR spectrum of compound F11-23 in $\text{DMSO-}d_6$ measured at 500 MHz.

Using a COSY spectrum (Figure 6.52) determined the various spin system for the major compound for Fraction 11-23 as shown in Figure 6.52. The COSY spectrum revealed that $\text{H}3'$ coupled with $\text{H}2'$ and $\text{H}4'$, $\text{H}5'$ coupled with $\text{H}4'$, and $\text{H}6'$, meanwhile the olefinic unit at $\text{H}7'$ (6.04 ppm) coupled to $\text{H}8'$ (1.81 ppm, dd, $J = 6.9, 1.4\text{Hz}$), which was typical for a methyl unit

attached to a double bond system. This makes up a complete spin system as indicated by the blue lines on the spectrum (Figure 6.52).

The ^1H - ^1H COSY experiment revealed that these protons connected to form a $\text{CH}-\text{CH}=\text{CH}-\text{CH}=\text{CH}-\text{CH}-\text{CH}_3$ moiety corresponding to the correlations between C2' through C8'. The structure was further confirmed by HMBC correlations (Figure 6.53), such as from H6 to C1' that placed the double bond closer to the ester linkage with a J value of 15.2 Hz between the coupling protons H2' and H3'. The coupling constant indicated that the olefinic system followed an *E* configuration, which further confirmed a *2E,4E,6E*-octatrienoyloxy group, located at position 6 of the drimane skeleton through the correlations between H3' to C1', C2', C4', C5', H4' to C3', C6' and H8' to C6', C7'.

While other spin system showed correlation between C6 at 5.59 and C7 at 5.81 ppm, as presented by the orange lines in Figure 6.52. On the other hand, the alkyl units in the drimane sesquiterpene nucleus (Figure 6.54) showed a correlation highlighted by the green box drawn on the structure in Figure 6.52. The connection of C11 and 9-OH was established by the HMBC correlations from C5 to C2, C3, C4, C6, C9, C10 and C14, while the location of the – OCH_3 unit at C6 was deduced *via* a correlation between the methoxy proton singlet and C6.



E54779.5.ser — Person xqb18194 — F19-23

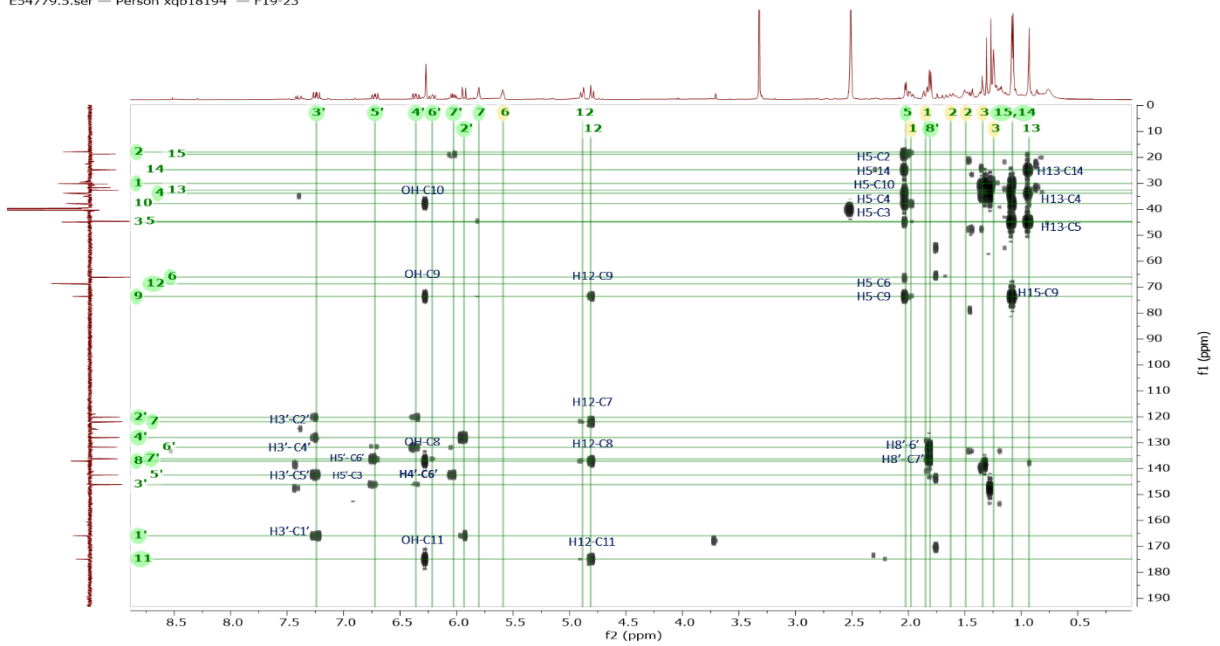


Figure 6.53: HMBC NMR spectrum correlation of compound F11-17 in DMSO- d_6 measured at 500 MHz.

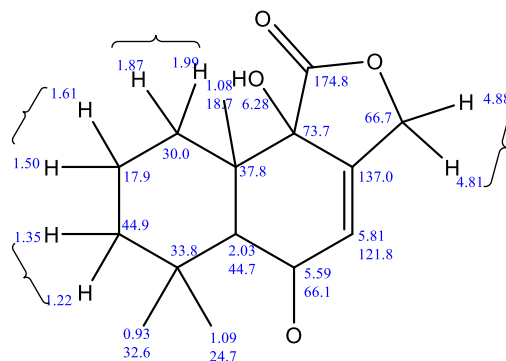


Figure 6.54: Drimane sesquiterpene nucleus structure

The lactone linkage was formed due to the correlations between the methylene protons at 4.88 and 4.81 ppm, the carbonyl at 174.8 ppm, quaternary carbons at 73.7 and 137.0 ppm. The coupling from H5 at 2.03 ppm and the ^{13}C resonance at 73.7 and 37.8 ppm were also useful in establishing the drimane carbon skeleton. A singlet proton peak at 6.28 correlated with C8, C9, C10, C11 and H12 also correlated to C7, C8, C9, C11, which led to confirm the sesquiterpene nucleus in Figure 6.54. The drim-7-en-11,12-olide and octatrienoyl fragments were linked by a further coupling between the ester carbonyl at 165.2 and the proton at 5.59 ppm. The carbon skeleton of the compound, particularly for the contiguous quaternary centres around C10.

The relative configuration of F11-23 was identified by a ROESY experiment (Figure 6.55). The 2D ROESY experiments of F11-29-8 exhibited the same correlations between H-1 α /H-2 α with H15, between H5 with H-3 α , H13, H6, and between 9-OH with H5, H12 α indicating that they both share the same relative configuration. ROESY interactions between the A/B rings were used to infer the A/B ring trans-junction between H5/H6 to H13 and H15 to H14. Thus, the structure for F11-23 was elucidated as 9 α -hydroxy-6 α -[(2*E*,4*E*,6*E*)-octa-2,4,6-trienoyloxy]-5 α -drim-7-en-11,12-olide. Full ^1H and ^{13}C assignments, which were compatible to those reported in the literature were presented in Tables 6.12 and 6.13 (Hayes *et al.*, 1996).

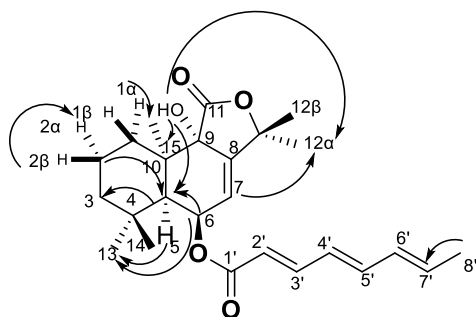
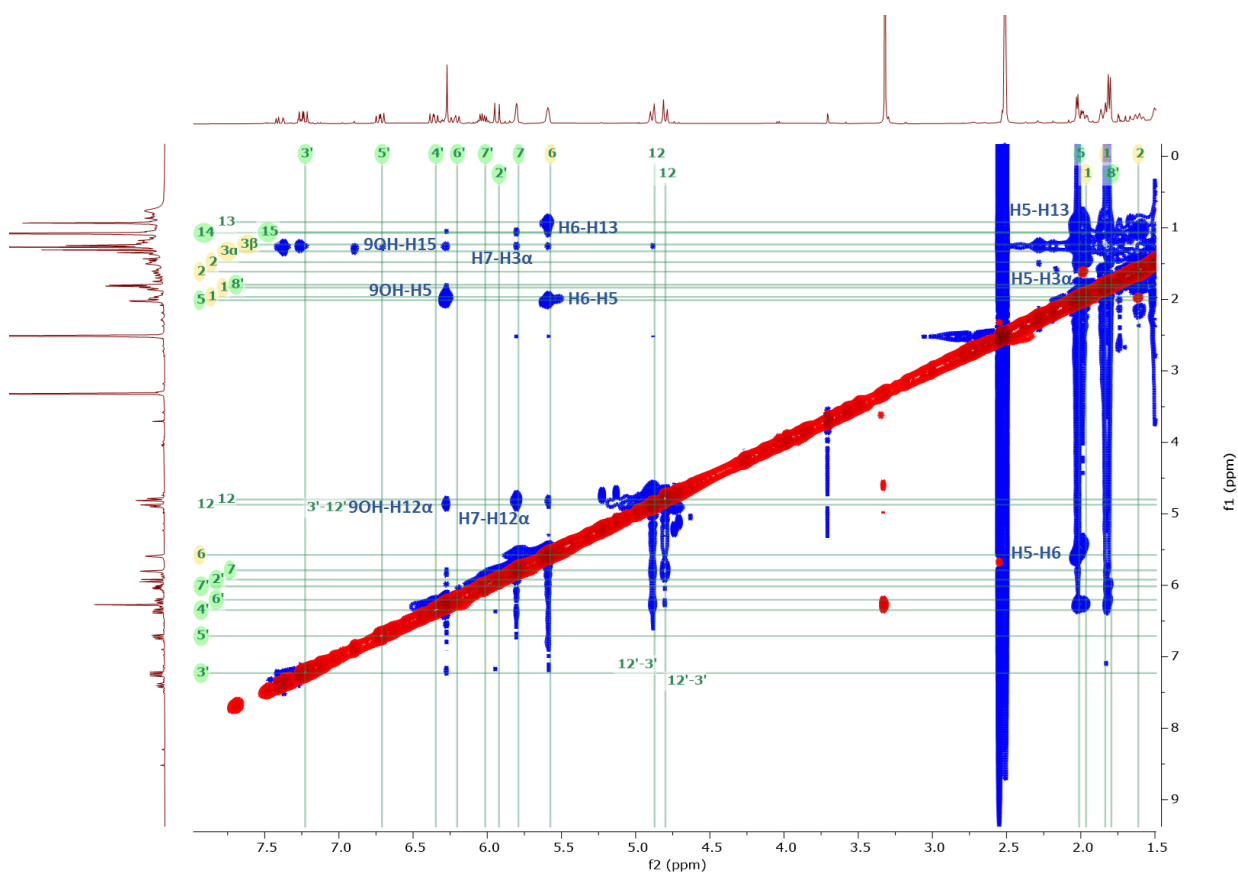


Figure 6.55: ROESY spectrum and essential correlation of compound F11-23 in DMSO- d_6 measured at 600 MHz.

Table 6.12: NMR data of F11-23 compared to the literature data (Hayes *et al.*, 1996).

Atom no.	literature in DMSO- <i>d</i> ₆			F11-23 in DMSO- <i>d</i> ₆		
	¹³ C (100MHz)	¹ H (500MHz)	<i>J</i> in Hz	¹³ C (500MHz)	¹ H (500MHz)	<i>J</i> in Hz
1α 1β	29.4 CH ₂	1.97 dd 1.84 d	13.7, 4.2 13.7	30.0 CH ₂	1.99 dd 1.87 d	13.8, 4.3 14.8
2α 2β	17.3 CH ₂	1.60 m 1.47 m		17.9 CH ₂	1.61 m 1.50 m	
3α 3β	44.3 CH ₂	1.34 d 1.20 m	12.7	44.9 CH ₂	1.35 m 1.22 m	
4	33.2 C	---		33.2 C	---	
5	44.1 CH	2.02 d	4.8	44.7 CH	2.03 d	4.9
6	65.7 CH	5.57 m		66.1 CH	5.59 dd	5.3, 2.8
7	121.3 CH	5.77 t	1.7	121.8 CH	5.81 dt	3.6, 1.6
8	136.5 C	---	---	137.0 C	---	---
9	73.0 C	6.20 brs (9-OH)	---	73.7 C	6.28 brs (9-OH)	---
10	37.2 C	---	---	37.8 C	---	---
11	174.2 C	---	---	174.8 C	---	---
12α 12β	68.1 CH ₂	4.88 dt 4.75 d	12.6,2.2 12.6	68.7 CH ₂	4.88 dt 4.81 d	12.6, 2.4 12.7
13	32.0 CH ₃	0.90 s	---	32.6 CH ₃	0.93 s	---
14	24.1 CH ₃	1.06 s	---	24.7 CH ₃	1.09 d	5.5
15	18. CH ₃	1.05s	---	18.7 CH ₃	1.08 d	5.5
1'	165.2 C	---	---	165.7 C	---	---
2'	119.5 CH	5.90 d	15.2	120.3 CH	5.90 d	15.2
3'	145.4 CH	7.23 dd	14.8, 11.3	146.1 CH	7.23 dd	15.24, 11.3
4'	127.3 CH	6.63 dd	15.1, 11.3	128.0 CH	6.36 dd	15.0, 11.2
5'	141.7 CH	6.68 dd	14.9, 10.7	142.4 CH	6.72 dd	14.8, 10.6
6'	131.1 CH	6.17 m	---	131.8 CH	6.22 ddd	15.0, 10.7, 1.8
7'	135.5 CH	6.00dq	14.9, 6.9	136.2 CH	6.04 dd	14.9, 7.0
8'	18.2 CH ₃	1.78 d	6.9	18.8 CH ₃	1.81 dd	6.9, 1.4

Legend: br s= broad singlet, s = singlet, d = doublet, t = triplet, q = quartet, m =multiplet

Table 6.13: NMR spectral data for compound F11-23 in DMSO-*d*₆ measured at 500 MHz.

F11-23					
Atom no.	¹³ C	¹ H	<i>J</i> in Hz	HMBC (¹ H to ¹³ C)	Roesy
1α 1β	30.0 CH ₂	1.87 d 1.99 dd	14.8 13.8, 4.3	C2, C9, C10	H1 β – H2 β H1 α – H2 α H1 β – H3 β H1 α -H15
2α 2β	17.9 CH ₂	1.61 m 1.50 m	---	C4	H2 α -H15 H2 α -H5
3α 3β	44.9 CH ₂	1.22 d 1.35 d	3.8	C1, C4	
4	33.8 C	---	---		
5	44.7 CH	2.03 d	4.9	C2, C3, C4, C6, C9, C10, C14	H3 α , H6, H13
6	66.1 CH	5.59 dd	5.3, 2.8		H5, H13
7	121.8 CH	5.81 dt	3.6, 1.6		H3 α , H12, H15
8	137.0 C	---	---		
9	73.7 C	6.28 brs	---	C8, C9, C10, C11	
10	37.8 C	---	---		
11	174.8 C	---	---		
12α 12β	68.7 CH ₂	4.88 dt 4.81 d	12.6, 24 12.7	C7, C8, C9, C11	
13	32.6 CH ₃	0.93 s	---	C4, C5, C14	
14	24.7 CH ₃	1.09 d	5.5	C1, C4, C5, C9, C10	
15	18.7 CH ₃	1.08d	5.5		
1'	165.7 C	---	---		
2'	120.3 CH	5.90 d	15.2	C1', C4'	
3'	146.1 CH	7.23 dd	15.24, 11.3	C1', C2', C4', C5'	H15
4'	128.0 CH	6.36 dd	15.0, 11.2	C6'	
5'	142.4 CH	6.72 dd	14.8, 10.6	C3', C6'	H3
6'	131.8 CH	6.22 ddd	15.0, 10.7, 1.8		
7'	136.2 CH	6.04 dd	14.9, 7.0	C5'	H8'
8'	18.8 CH ₃	1.81 dd	6.9, 1.4	C6', C7'	
9-OH	---	6.28	---	C8, C9, C10, C11	H5, H12 α , H15

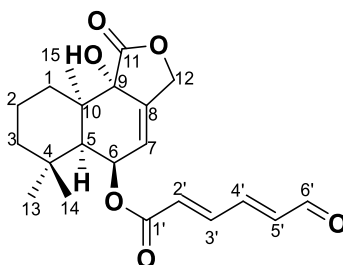
Legend: br s= broad singlet, s = singlet, d = doublet, t = triplet, q = quartet, m =multiplet.

6.5.3.2. Compound F11-29-8 structure elucidation.

9 α -hydroxy-6 α -(6-oxohex-2*E*,4*E*-dienyloxy)-5 α -drim-7-en-11,12-olide

Chemical Formula: C₂₁H₂₆O₆

Exact Mass: 374.1724



ustusolate E

Figure 6.56: Chemical structure of compound F11-29-8

Formula	Calculated Mass	Target Mass	Double Bond Equivalence	Absolute Error (ppm)	Error (mDa)	Error (ppm)
C ₂₁ H ₂₆ O ₆ Na	397.16271	397.16213	8.5	1.45	-0.58	-1.45

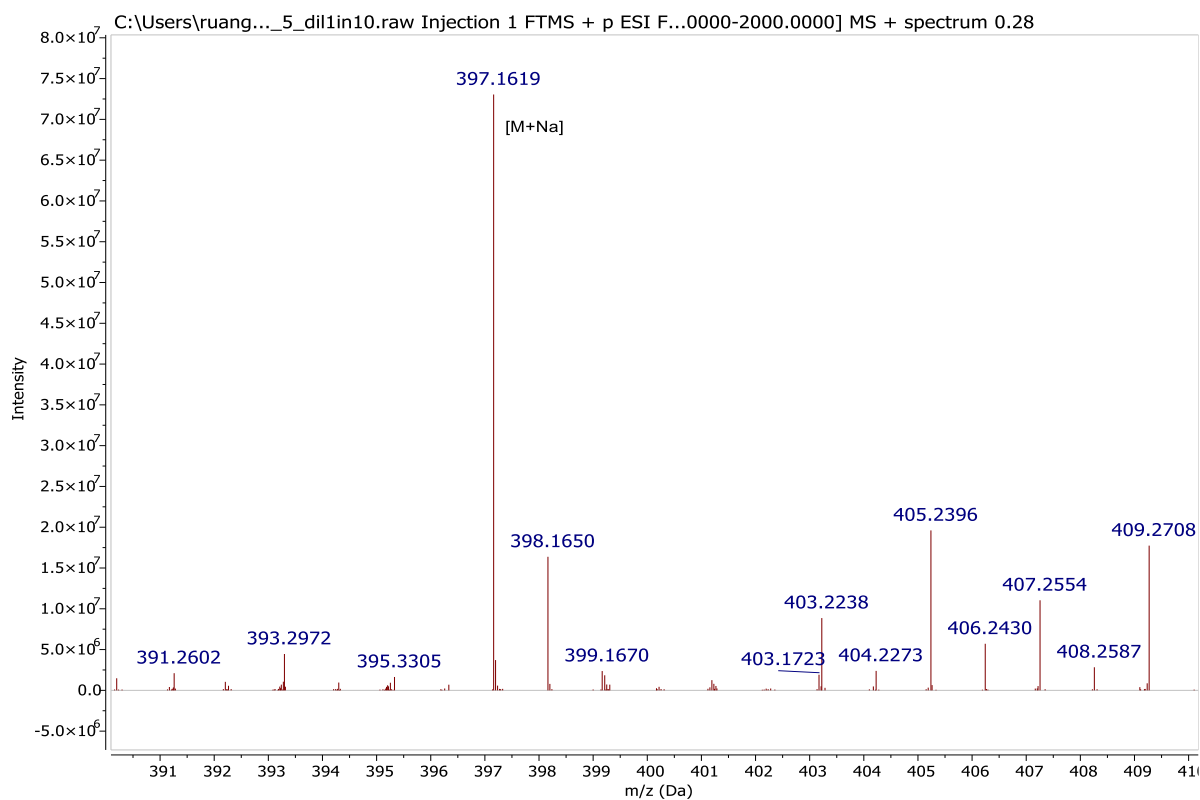


Figure 6.57. Mass spectral data of F11-29-8 at the ion peak m/z 397.162 [M+Na]⁺.

Compound F11-29-8 was isolated from fraction 11 as an off-white amorphous powder using FC and further purification was performed by preparative-TLC affording a yield of 4.5 mg. The compound was eluted along with the polar fractions at 80% EtOAc and 20% n-Hexane. HRESIMS (Figure 6.57) gave an exact mass of m/z 374.17 Da for $[M + Na]^+$, suggesting a molecular formula of $C_{21}H_{26}O_6$.

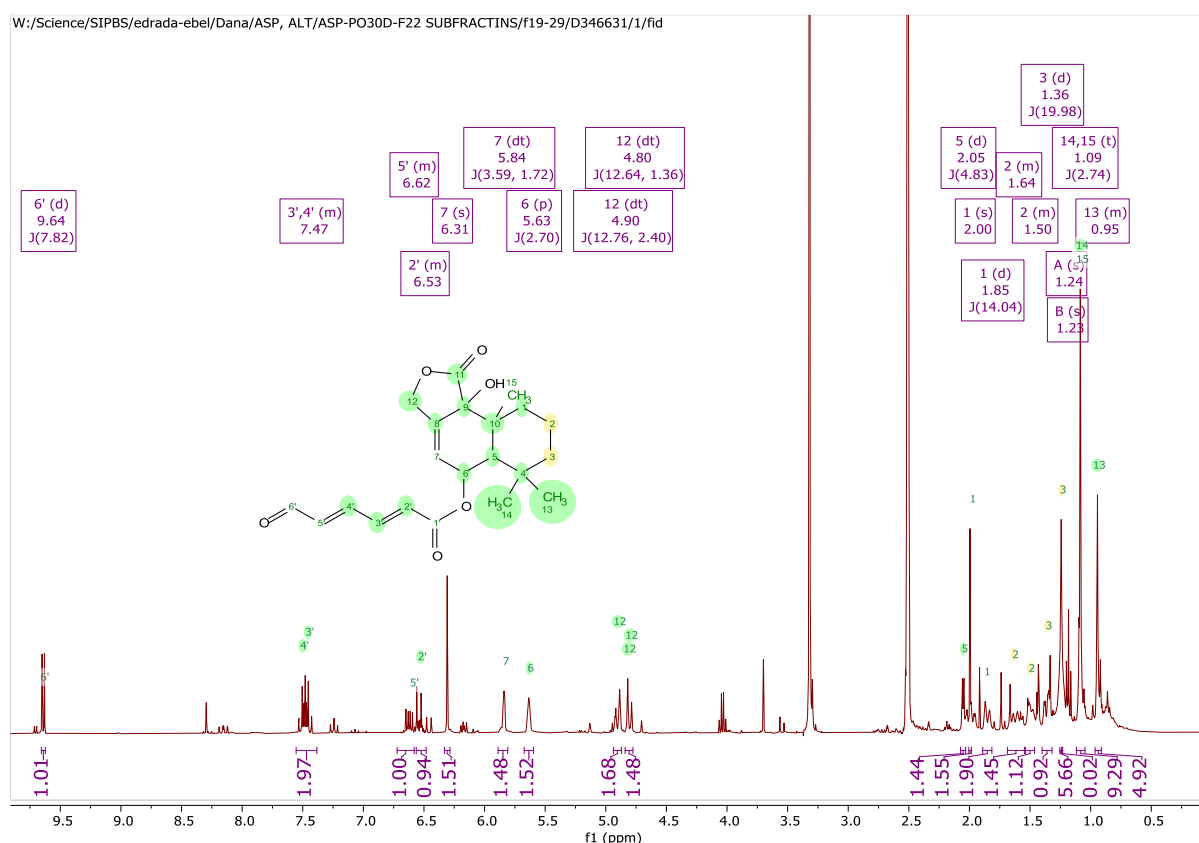


Figure 6.58: 1H NMR spectrum of compound F11-29-8 in $DMSO-d_6$ measured at 500 MHz.

1H and ^{13}C NMR spectra suggested that the structure of F11-29-8 was closely related to F11-23, except for the absence of one olefinic methine proton and the presence of an aldehyde doublet signal at δ_H 9.64. The occurrence of four conjugated trans-olefinic system was shown in the 1H NMR spectrum (Figure 6.58) at δ_H 6.56m, 7.47m, 7.48m and 6.63m coupled with the aldehyde terminal, instead of the six conjugated olefinic proton pairs detected previously

in F11-23. Furthermore, this corroborated the apparent downshift signal for H2', H3', H4', and H5' due to the aldehyde functionality's deshielding effect. Minor changes in the ¹H NMR chemical shift were seen in the drimane sesquiterpene core, with the methyl unit at position 13 being moved more downfield at 0.95 ppm and an exchangeable proton was relocated at 6.30 ppm (9-OH).

The ¹H-¹H COSY experiment (Figure 6.59) established the fragment CH=CH-CH=CH-CHO. These findings pointed to a 6-oxohex-2E,4E-dienoyl as an aldehyde acyl moiety and this was confirmed by the COSY correlations of H2' to H3' and H4' to H6' (aldehyde group) through H-5' as well as the HMBC correlations (Figure 6.60) from H5'/H4' to C6', H3' to C1 and H4' to C2'. HSQC spectra (Figure 6.61) suggested four conjugated olefinic resonances, four methylene resonances, one oxygenated methine, and three methyl resonances.

The 2D ROESY experiments on F11-29-8 (Figure 6.62) exhibited the same relative configurations by comparison of the NMR data for F11-23. F11-29-8 was elucidated as 9 α -hydroxy-6 α -(6-oxohex-2E,4E-dienoyloxy)-5 α -drim-7-en-11,12-olide or ustusolate E. ¹H and ¹³C spectral datasets are presented on Table 6.14, which were found compatible to those found in the literature (Liu *et al.*, 2009). Ustusolate E was isolated from a marine-derived *A. ustus* and was described to exhibit moderate cytotoxicity against lung cancer cell A549 and leukemia cell HL-60 with IC₅₀ value of 10.5 and 9.0 μ M, respectively (Lu *et al.*, 2009).

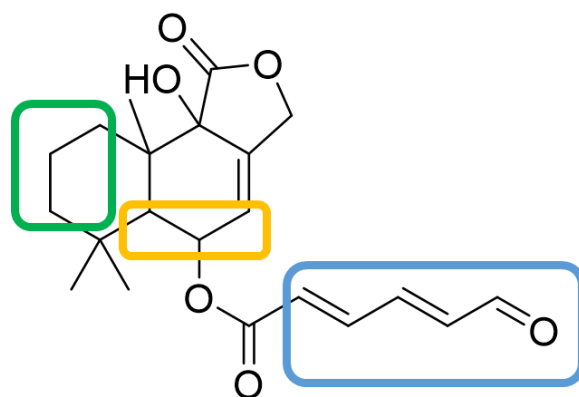
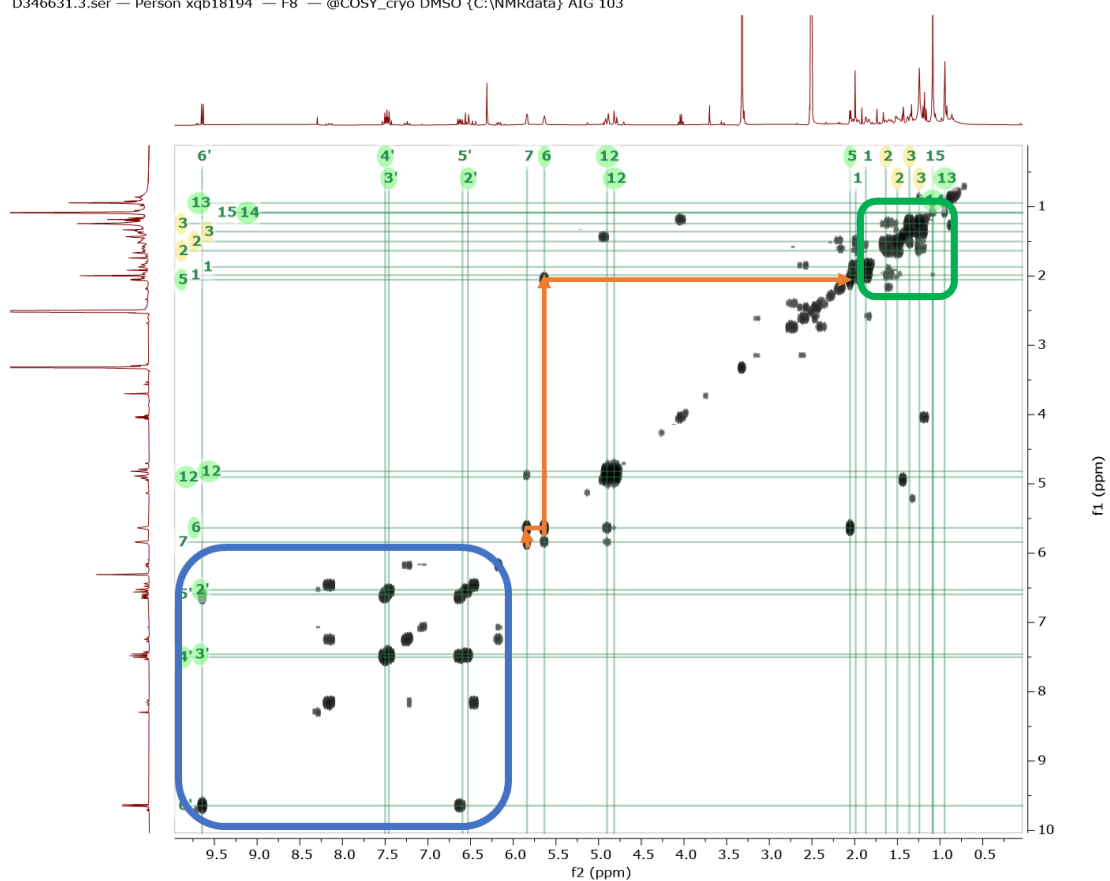


Figure 6.59: ^1H - ^1H -COSY correlation NMR spectrum of compound F11-29-8 in $\text{DMSO-}d_6$ measured at 500 MHz.

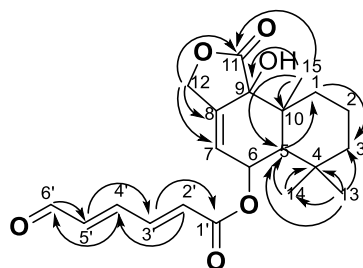
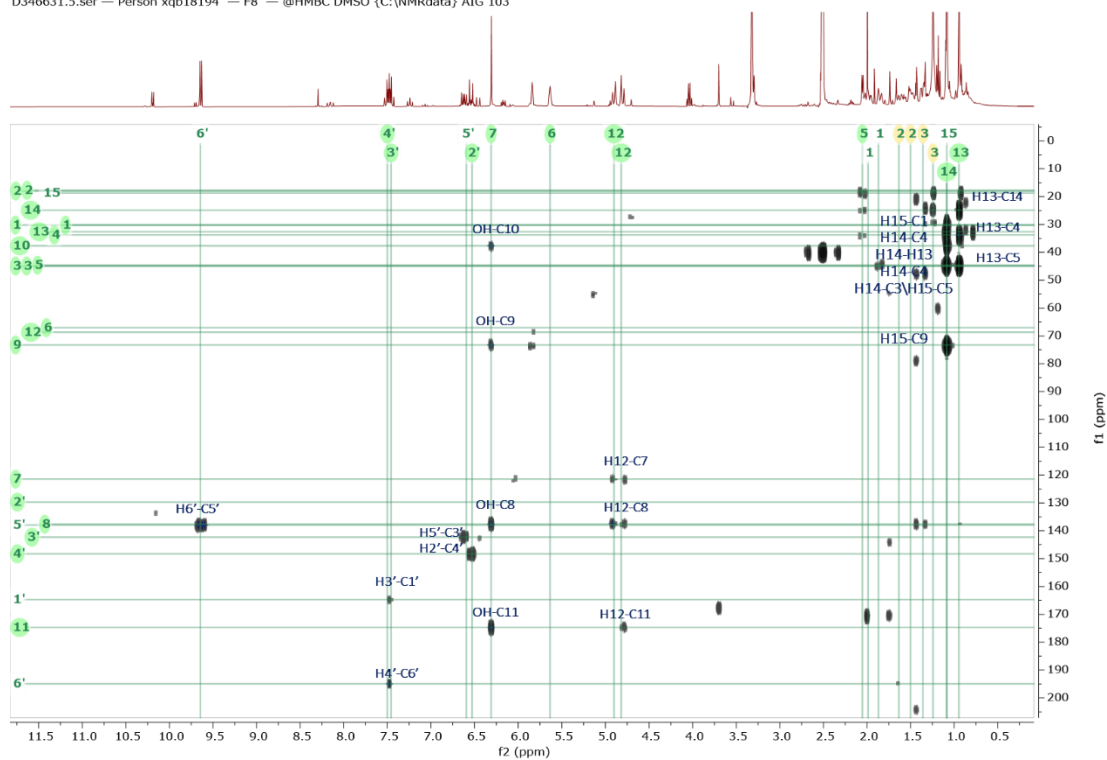


Figure 6.60: HMBC NMR spectrum and essential correlations to determine the structure of compound F11-29-8 in DMSO- d_6 measured at 500 MHz.

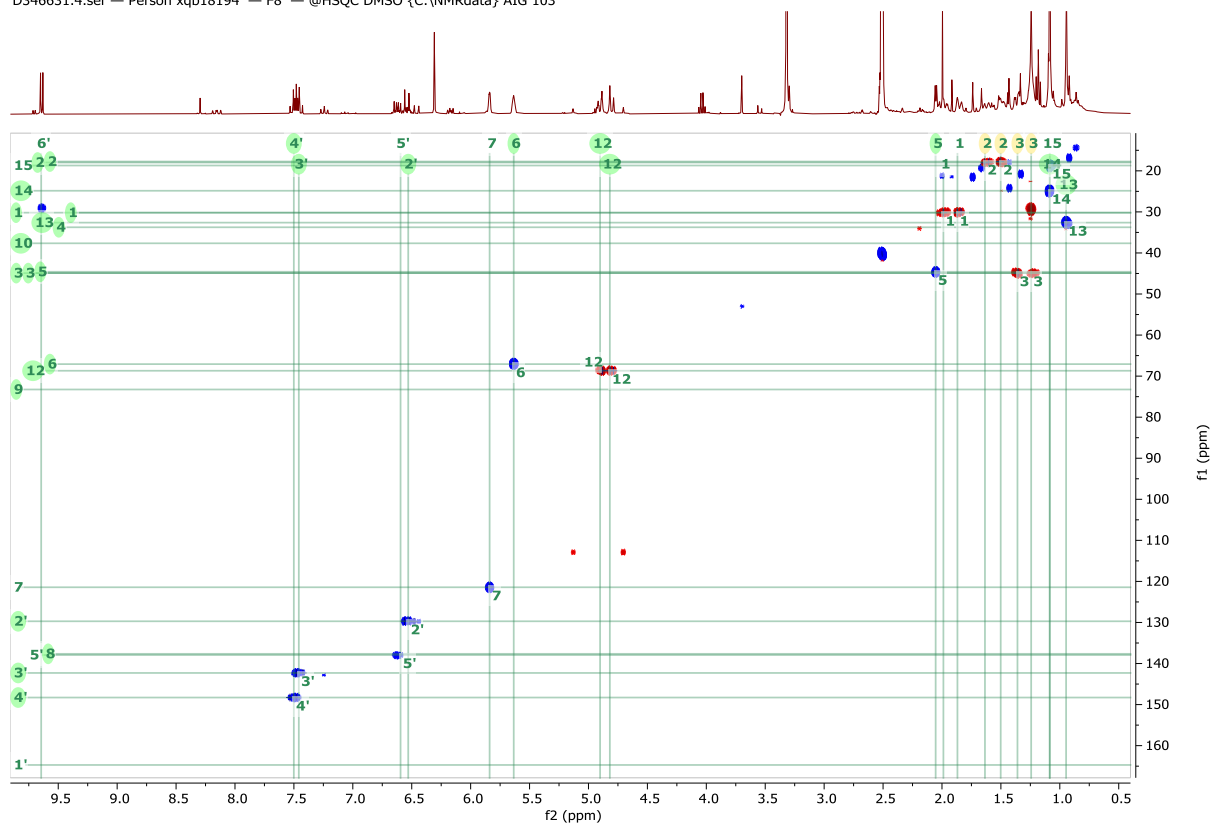


Figure 6.61: HSQC NMR spectrum of compound F29-19-8 in DMSO-*d*₆ measured at 500 MHz. Red correlations are CHs and CH₃s while blue are CH₂s.

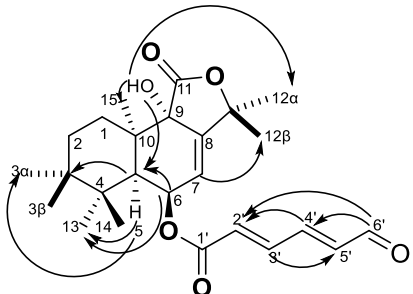
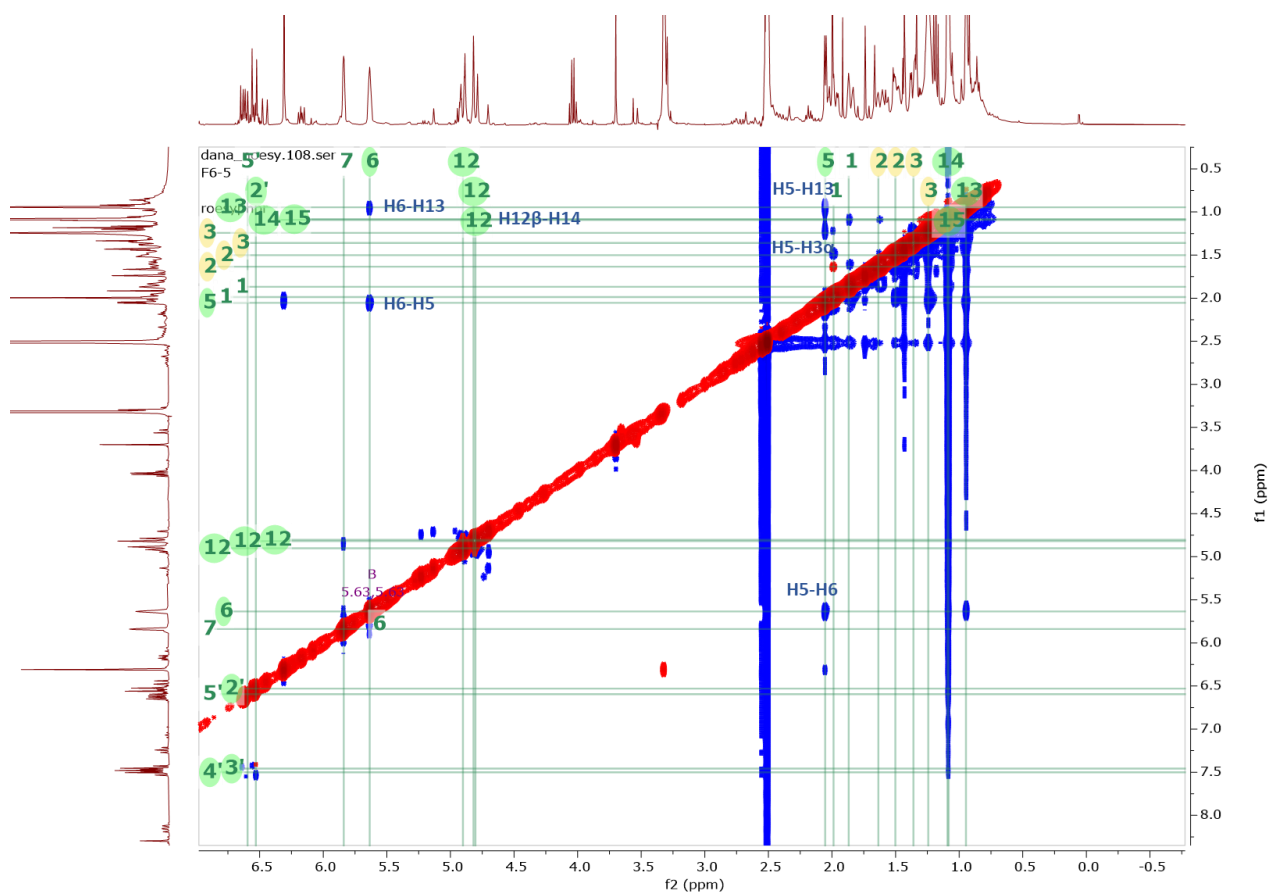


Figure 6.62: ROESY spectrum and essential correlation of compound F11-29-8 in DMSO-*d*₆ measured at 600 MHz.

Table 6.14: NMR spectral data for compound F11-29-8 DMSO-*d*₆ measured at 500 MHz..

Atom no.	¹³ C*	¹ H	<i>J</i> in Hz	HMBC (¹ H to ¹³ C)	Roesy
1 α	30.2 CH ₂	1.87 d	---	C3, C5	H1β – H2β
1 β		1.99 s			H1α – H2α
2 α	18.0 CH ₂	1.64 m	---		
2 β		1.51 m			
3 α	44.9 CH ₂	1.22 s	---	C14	H3α -H5
3 β		1.35 m			
4	33.7 C	---			
5	44.5 CH	2.05 d	4.8	C14	H3α, H13, H6
6	66.0CH	5.63 s	---		H5, H13
7	121.4 CH	5.84 m	---		H12β, H14
8	137.6 C	---	---		
9	73.4 C	6.30 brs	---		
10	37.6 C	---	---		
11	174.7 C	---	---		
12	68.7 CH ₂	4.88 dt 4.82 dt	12.7, 2.3 12.6, 1.3	C7, C8, C11	H12β-H14
13	32.6 CH ₃	0.95 S	---	C3, C4, C5, C 14	H5
14	24.8 CH ₃	1.09 d	1.4	C3, C4, C5, C13	
15	18.7 CH ₃	1.08d	1.6	C4, C5, C9, C10, C11	
1'	165.0 C	---	---		
2'	129.6 CH	6.56 m	---	C1', C4'	Me-15, H4'
3'	142.3 CH	7.47m	---		Me-15,
4'	148.4 CH	7.48 m	---	C1', C6'	Me-15, H2', H6'
5'	138.0 CH	6.63 m	---	C3'	H3'
6'	194.9	9.64 d	7.9	C5'	H4', H2'
9-OH	---	6.30 s		C8, C9, C10, C11	H5, H12α, H15

Legend: br s=broad singlet, s= singlet, d = doublet, t = triplet, q = quartet, m =multiplet, quin=quintet.

*Data taken from HMQC and HMBC experiments

6.5.3.3. Compound F12-11-2 structure elucidation.

(*E,E*)-6-(6',7'-dihydroxy-2',4'-octadienyl)-strobilactone A

Chemical Formula: C₂₃H₃₂O₇

Exact Mass: 420.21448

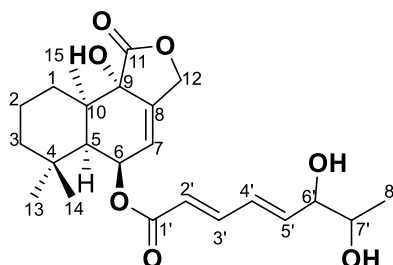


Figure 6.63: Chemical structure of compound F12-11-2

Formula	Calculated Mass	Target Mass	Double Bond Equivalence	Absolute Error (ppm)	Error (mDa)	Error (ppm)	Fitness
C ₂₃ H ₃₁ O ₇	419.20753	419.20854	8.5	2.40	1.01	2.40	0.817

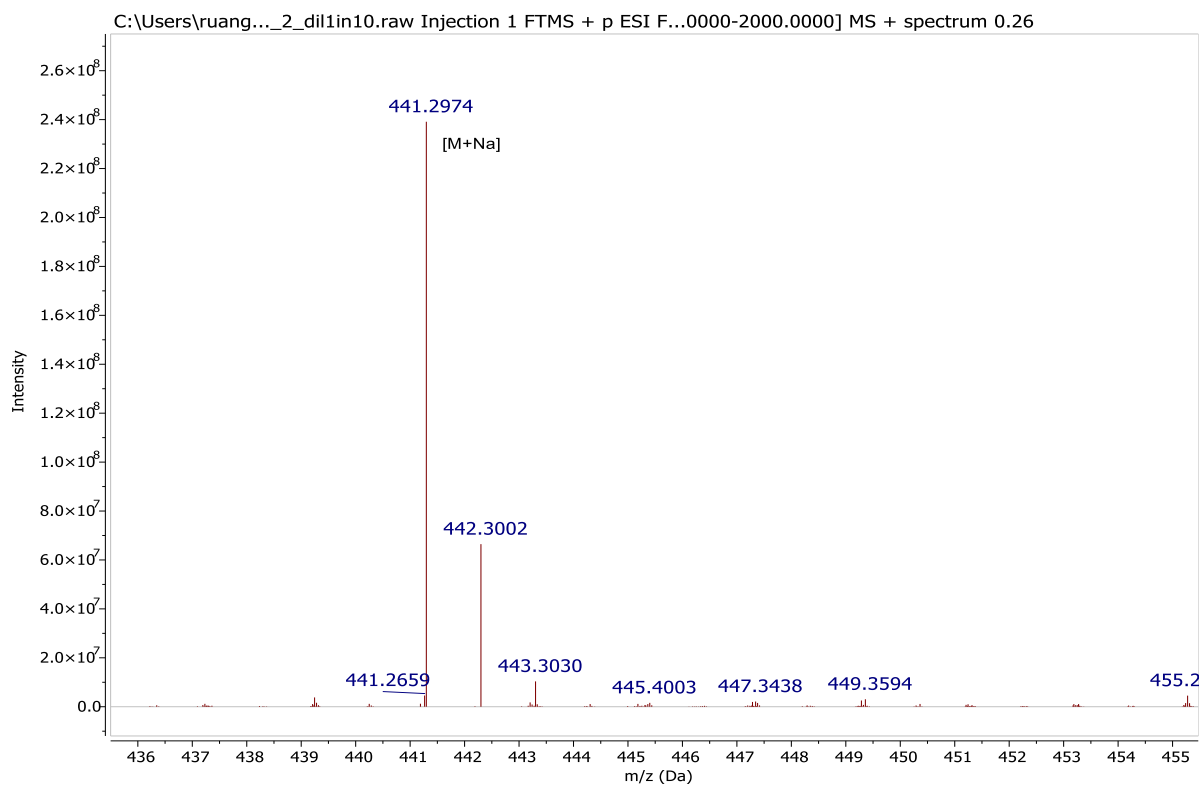


Figure 6.64. Mass spectral data of F12-11-2 at the ion peak m/z 419.2085 [M-H]⁻.

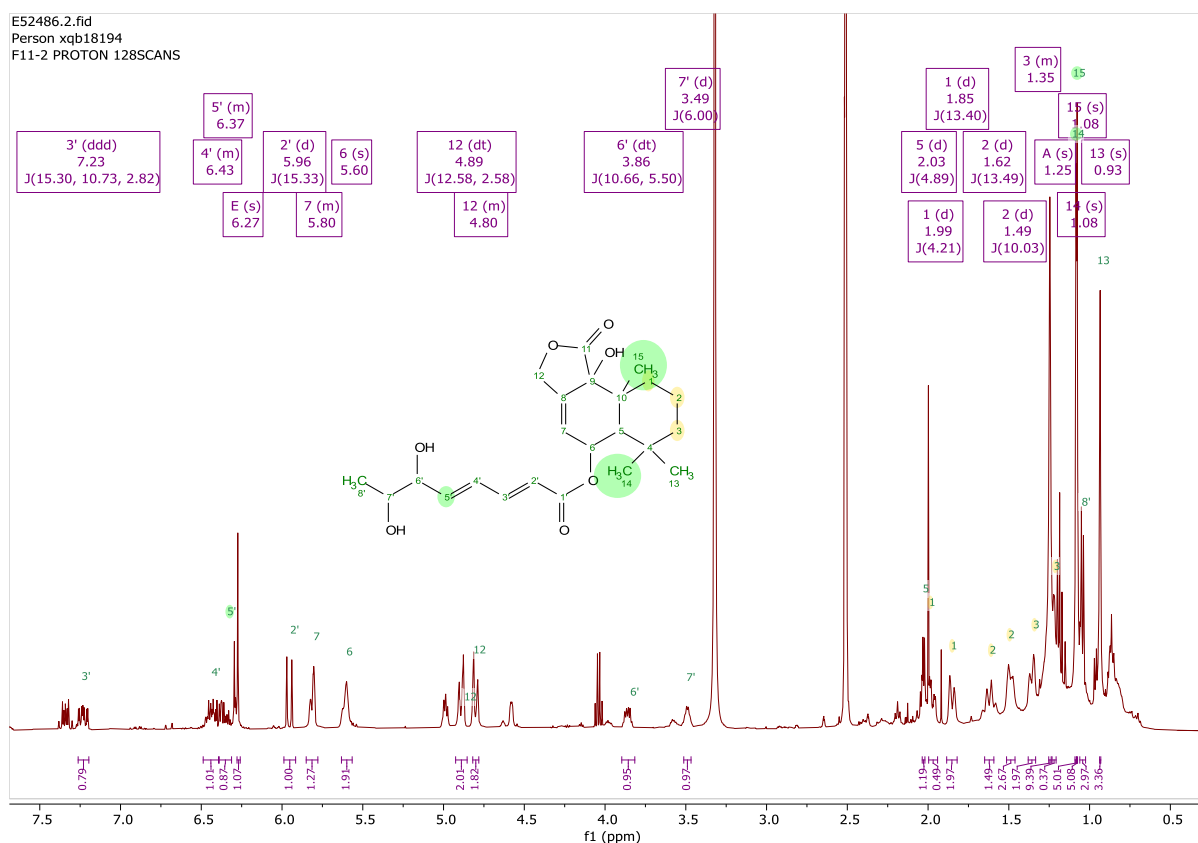


Figure 6.65: ^1H NMR spectrum of compound F12-11-2 in $\text{DMSO-}d_6$ measured at 500 MHz.

F12-11-2 (2 mg) was obtained from fraction 12 and then purified using preparative-TLC. It is a yellow amorphous solid with the molecular formula $\text{C}_{23}\text{H}_{32}\text{O}_7$, indicating eight degrees of unsaturation by its HRESI-MS spectrum. In addition to its low yield, F12-11-2 has a very poor solubility in polar solvents used for ESI-MS analysis. The ion peak at m/z 419.2085 $[\text{M}-\text{H}]^-$ was detectable by MZmine (metabolite ID: N_1001 in Table 6.4) amongst the discriminating feature for the bioactive fractions and it was also possible to extract the base peak (Figure 6.64), but it was not feasible to obtain a quantifiable mass spectrum.

The ^1H and 2D NMR data of the compound were comparable to previous fractions. The nucleus structure of F12-11-2 was found to be identical to that of the drimane sesquiterpenes when their NMR data was compared. The main difference was in the side chain with the presence of four olefinic carbons, two hydroxylated methines and a methyl group that constituted a terminal butane-2,3-diol moiety. Side-chain signals observed from the ^1H spectrum (Figure 6.65) included proton resonances at δ_{H} 5.96 (1H, ddd, $J = 15.3$, Hz, H2'),

7.23(1H, dd, $J = 15.3, 10.7, 2.8$ Hz, H3'), 6.44 (1H, m, H4'), 6.31 (1H, m, H5'), 3.86 (1H, dt, $J = 10.6, 5.5$ Hz, H6'), 3.48 (1H, d, $J = 6.0$ Hz, H7'), and 1.04 (3H, d, $J = 6.3, 1.0$ Hz, H8').

The ^1H - ^1H COSY (Figure 6.66) correlations of H3'/H2', H3'/H4', H5'/H6', H6'/OH6', and H7'/OH7', OH7'/H8', as well as the HMBC (Figure 6.67) correlations of H2' to C1' and C4', H4' to C6', and H8' to C7' suggested that the side chain was (2'*E*,4'*E*)-6',7'-dihydroxyocta-2',4'-dienoyl. This moiety was attached to drimane core at H6 and the carbonyl carbon at C1'. The ^1H with the corresponding ^{13}C data was fully assigned with the HSQC spectrum (Figure 6.68) and presented on Table 6.15. The structure of F12-11-2 was elucidated as (*E,E*)-6-(6',7'-dihydroxy-2',4'-octadienoyl)-strobilactone A was comparable to the published data (Table 6.16) (Liu *et al.*, 2009). The compound was earlier described from the sponge-derived *A. ustus*, and tested against a panel of tumour cell lines, including lymphoma cell L5178Y, cervical cancer HeLa, and neural foetal PC12 cells but was found inactive.

A ROESY experiment (Figure 6.69) was used to evaluate the relative configurations of drimane nuclei, which revealed correlation between H3 α to H5, H15 to H14, H5/H6 to H13, and 9-OH to H5 and H12 α , indicating that they all share the same relative configuration. This suggests all have α configuration.

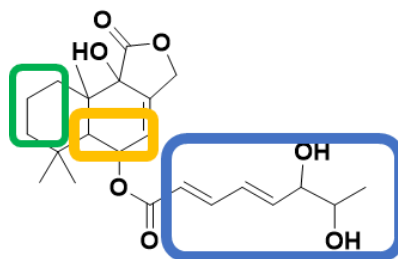
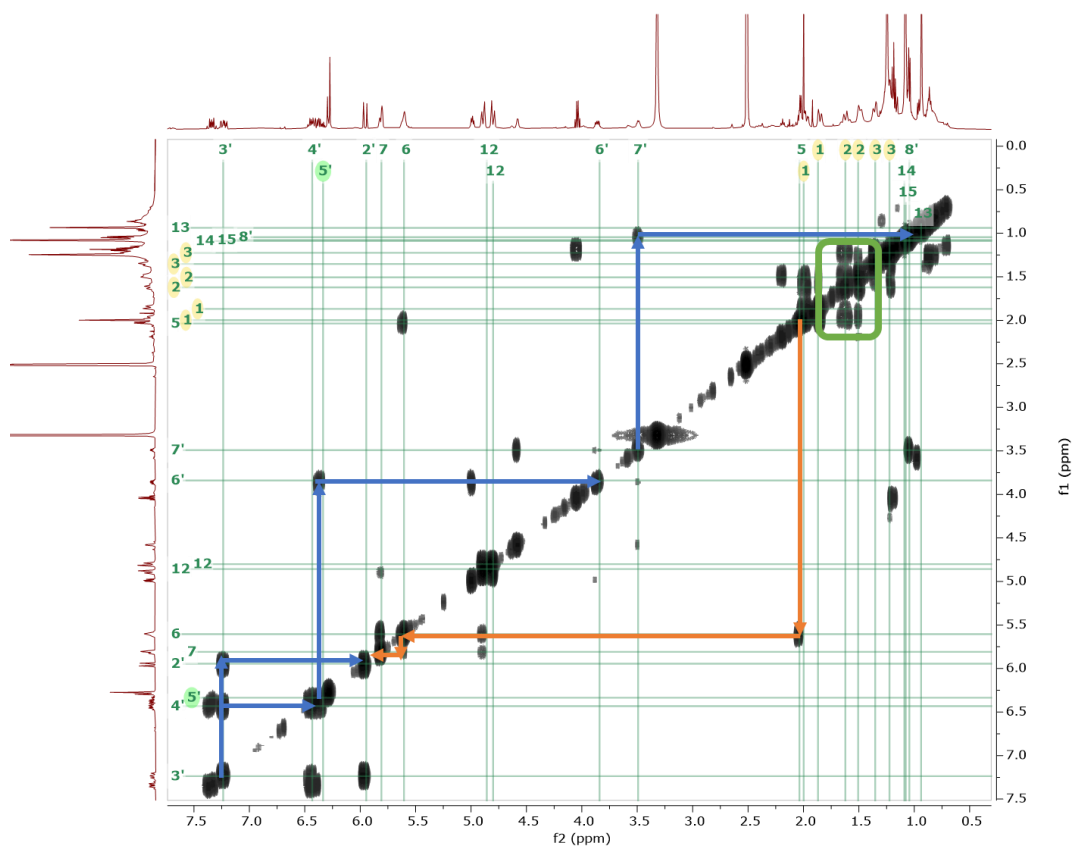
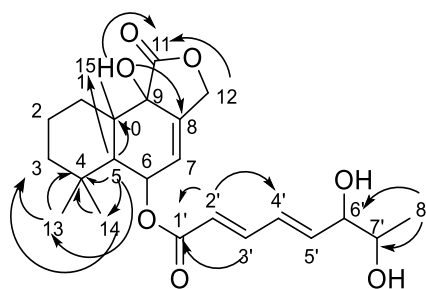


Figure 6.66: (^1H - ^1H) COSY correlation NMR spectrum of compound F12-11-2 in $\text{DMSO-}d_6$ measured at 500 MHz.



E52486.5.ser — Person xqb18194 — F11-2

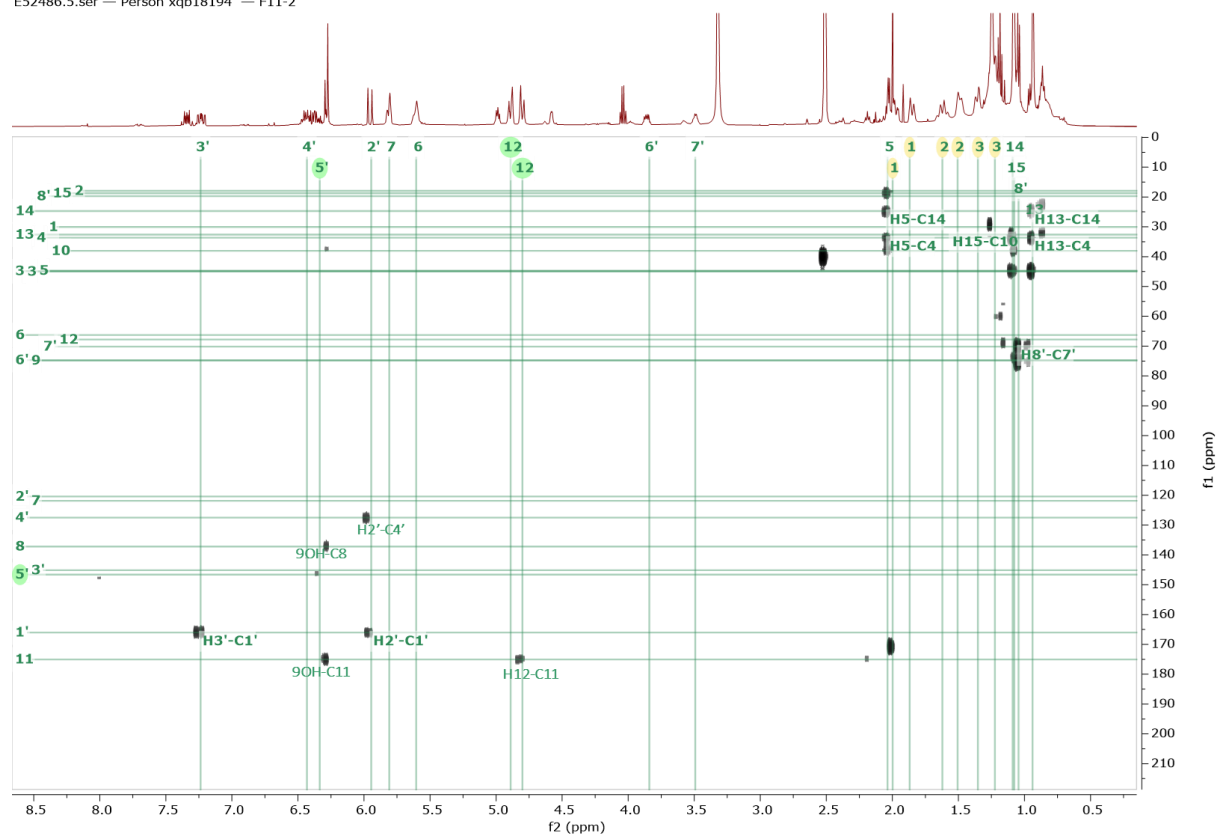


Figure 6.67: HMBC NMR spectrum of compound F12-11-2 in DMSO- d_6 measured at 500 MHz.

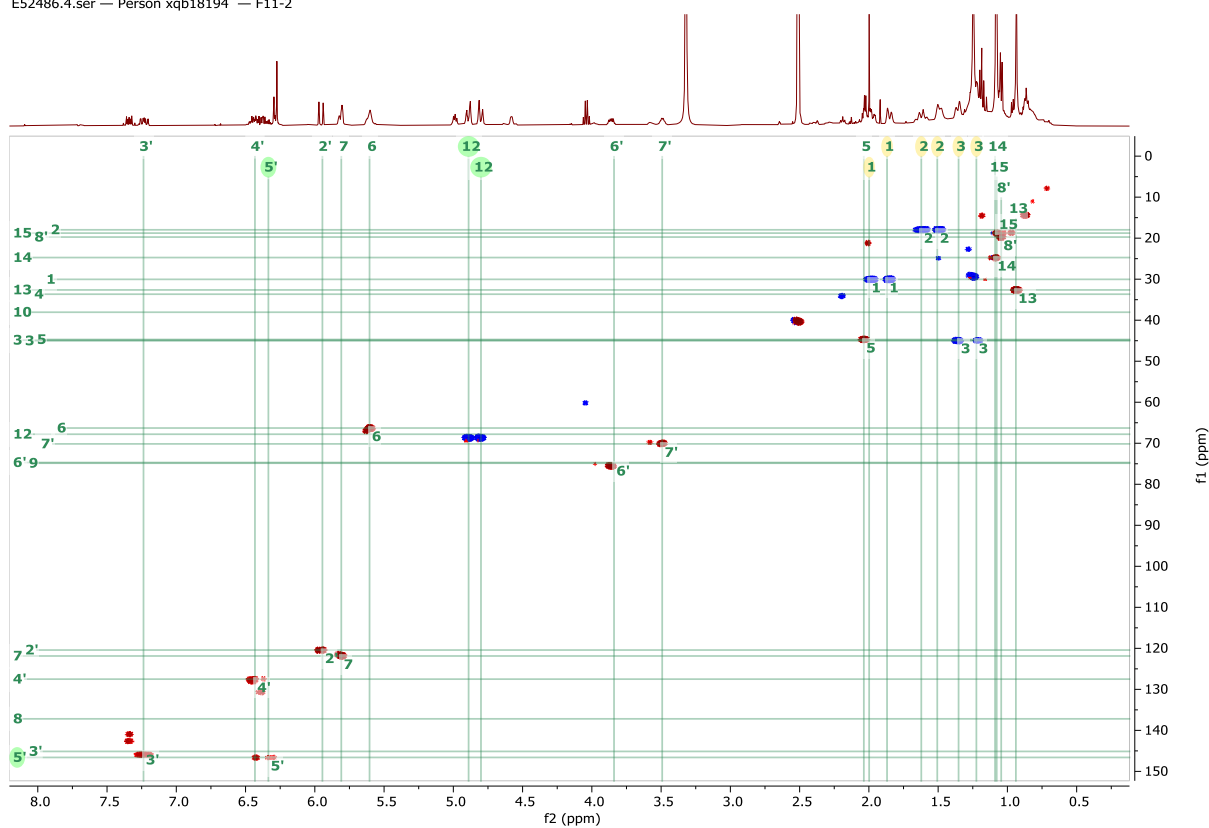


Figure 6.68: HSQC NMR spectrum of compound F12-11-2 in DMSO-*d*₆ measured at 500 MHz. Red correlations are CH and CH₃ while blue are CH₂.

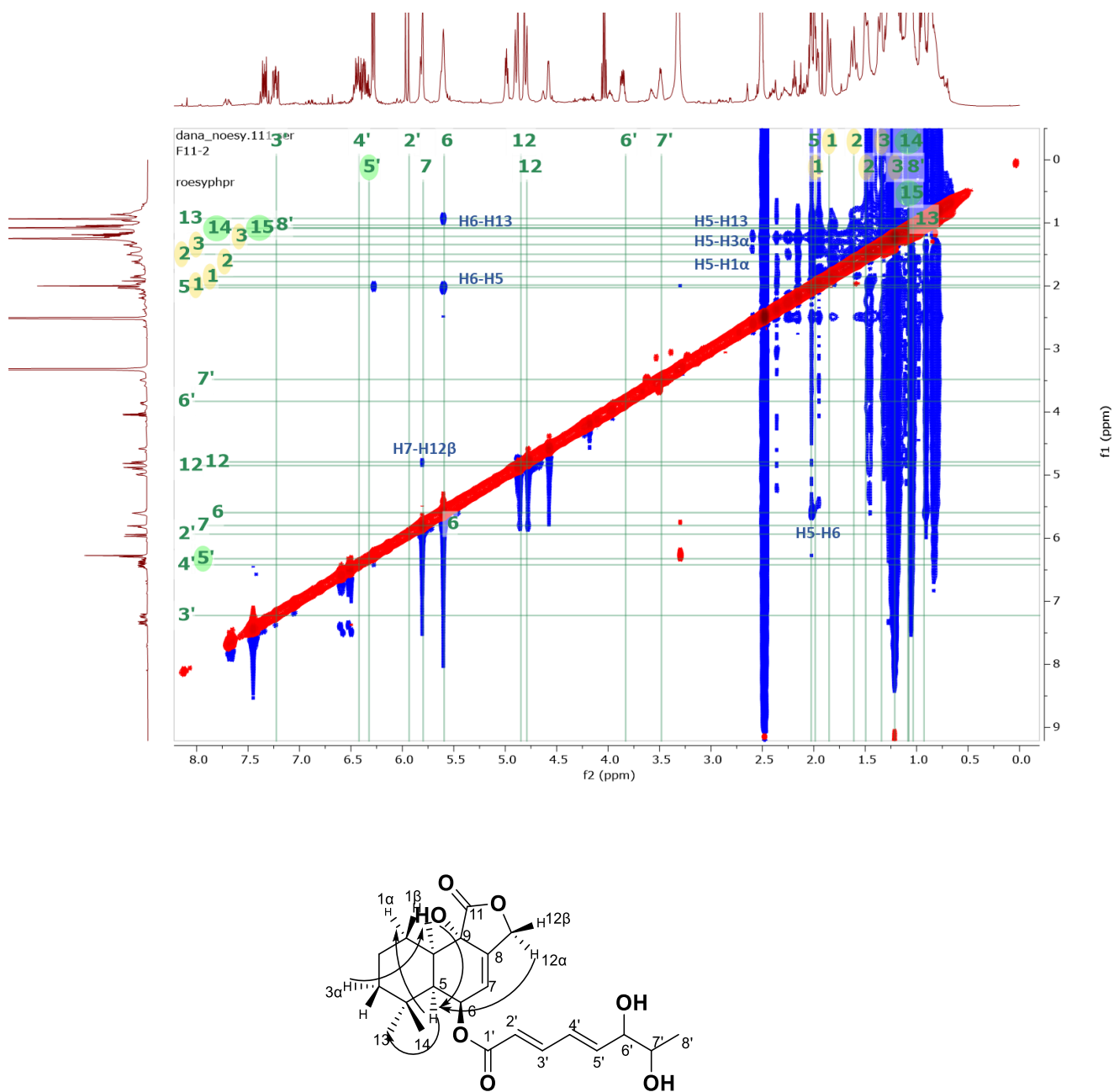


Figure 6.69: ROESY spectrum and essential correlation of F12-11-2 in DMSO-*d*₆ measured at 600 MHz.

Table 6.15: NMR spectral data for compound F12-11-2 in DMSO-*d*₆ at 500 MHz.

Atom no.	¹³ C*	¹ H	<i>J</i> in Hz	HMBC (¹ H to ¹³ C)	Roesy
1 α	30.0 CH ₂	1.87 d	13.4		H1β – H2β
1β		1.99 d	4.2		
2 α	17.9 CH ₂	1.61 d	13.5		
2β		1.50 d	10.0		
3 α	45.0 CH ₂	1.20 d	3.0		H3α -H15
3β		1.35 m			
4	33.7 C	---			
5	44.7 CH	2.04 dd	7.8, 4.8	C4, C10, C14, C15	H1α, H3α, H6, H13
6	66.2 CH	5.60 s	---		H5, H6, H13,
7	121.8 CH	5.81 m	---		
8	137.1 C	---	---		
9	73.7 C	6.27 s	---		
10	38.1 C	---	---		
11	175.0 C	---	---		
12	68.7 CH ₂	4.89 dt 4.81 m	12.5, 2.5	C11	H12β
13	32.6 CH ₃	0.94 s		C3, C4, C5, C14	
14	24.7 CH ₃	1.09 d	3.4	C3, C4, C5	
15	18.7 CH ₃	1.08d	3.4		
1'	166.0 C	---	---		
2'	120.4 CH	5.96 d	15.3	C1', C4'	
3'	145.9 CH	7.23 ddd	15.3, 10.7, 2.8	C1'	
4'	127.5 CH	6.44 m			
5'	146.6 CH	6.34 m			
6'	75.5 CH	3.86 dd	10.6, 5.5		
7'	70.0 CH	3.48 d	6.0		
8'	19.7 CH ₃	1.04 dd	6.3, 1.0	C6', C7'	
9-OH	---	6.27 s	---	C8, C10, C11	H5, H12α,
6'-OH	---	3.86 dd	---		
7'-OH	---	3.48 d	---		

Legend s= singlet, d = doublet, t = triplet, q = quartet, m =multiplet, quin=quintet.
*Data taken from HMQC and HMBC experiments

Table 6.16: NMR spectral data of compound F12-11-2 compared to that of literature (Liu *et al.*, 2009).

literature in DMSO- <i>d</i> ₆ (600 MHz)				F12-11-2 in DMSO- <i>d</i> ₆ (500 MHz)		
Atom no.	¹³ C	¹ H	<i>J</i> in Hz	¹³ C*	¹ H	<i>J</i> in Hz
1 α	29.3 CH ₂	1.81 d	13.4	30.0 CH ₂	1.87 d	13.4
1 β		1.93 dd	13.6, 4.4		1.99 d	4.2
2 α	17.2 CH ₂	1.56 m		17.9 CH ₂	1.61 d	13.5
2 β		1.46 brd	12.5		1.50 d	10.0
3 α	44.2 CH ₂	1.18 td	12.8, 2.5	45.0 CH ₂	1.20 d	3.0
3 β		1.32 d	12.5		1.35 m	
4	33.9 C	---		33.7 C	---	
5	43.9 CH	1.97 d	4.8	44.7 CH	2.04 dd	7.8, 4.8
6	65.6 CH	5.58 br s		66.2 CH	5.60 s	---
7	121.1 CH	5.76 t	1.5	121.8 CH	5.81 m	---
8	136.2 C	---	---	137.1 C	---	---
9	72.8 C	6.20 brs	---	73.7 C	6.27 s	---
10	36.9 C	---	---	38.1 C	---	---
11	174.1 C	---	---	175.0 C	---	---
12	68.1 CH ₂	4.87 dt 4.76 d	12.7,2.3 12.8	68.7 CH ₂	4.89 dt 4.81 m	12.5, 2.5
13	31.9 CH ₃	0.90 s	---	32.6 CH ₃	0.94 s	2.0
14	24.0 CH ₃	1.04 s	---	24.7 CH ₃	1.09 s	
15	18.1 CH ₃	1.04s	---	18.7 CH ₃	1.08s	
1'	165.2 C	---	---	166.0 C	---	---
2'	119.7 CH	5.91 d	15.4	120.4 CH	5.96 d	15.3
3'	145.2 CH	7.20 dd	15.4,11.2	145.9 CH	7.23 ddd	15.3, 10.7, 2.8
4'	126.9 CH	6.40 dd	15.5, 11.2	127.5 CH	6.44 m	
5'	145.9 CH	6.31 dd	15.5, 5.0	146.6 CH	6.34 m	
6'	74.7 CH	3.84 br s	---	75.5 CH	3.86 dt	10.6, 5.5
7'	69.4 CH	3.47 br s	14.9, 6.9	70.0 CH	3.48 d	6.0
8'	19.0 CH ₃	1.02	6.0	19.7 CH ₃	1.04 dd	6.3, 1.0
9-OH	---	6.20 br s	---	---	6.27 s	---
6'-OH	---	3.84 br s	---	---	3.86 dd	---
7'-OH	---	3.4br s	---	---	3.48 d	---

Legend: br = broad, s = singlet, d = doublet, t = triplet, q = quartet, m = multiplet, quin=quintet. *Data taken from HMQC and HMBC experiments.

6.6.4. Terretonin

A terretonin derivative was isolated from subfraction 29 of F11 of *A. ustus* with a yield of 5.5 mg. It produced a quenching spot under short UV light (254nm) and major blue band upon spraying with anisaldehyde/sulfuric acid (Figure 6.70).

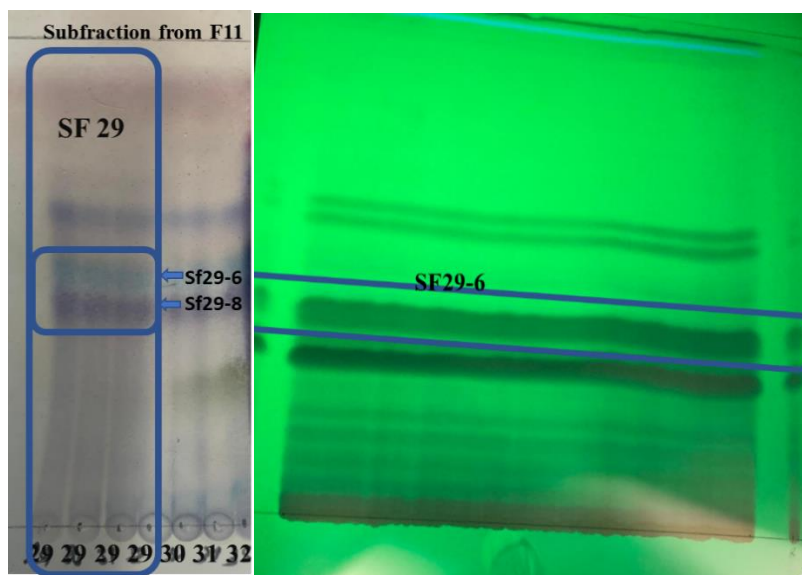
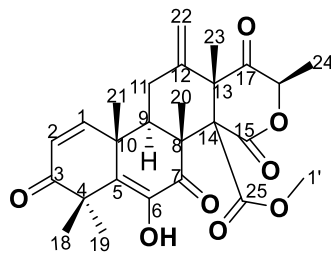


Figure 6.70: PTLC methods for purification of SF29-6 from subfraction F11-29 using solvent system 50:50 % of n-Hexane and EtOAc.

Compound F11-29-6 structure elucidation.



terretonin F

Chemical Formula: $C_{26}H_{30}O_8$

Exact Mass: 470.1941

Figure 6.71: Chemical structure of compound F11-29-6.

Formula	Calculated Mass	Target Mass	Double Bond Equivalence	Absolute Error (ppm)	Error (mDa)	Error (ppm)	Fitness
$C_{26}H_{30}O_8Na$	493.18384	493.18388	11.5	0.08	0.04	0.08	0.999

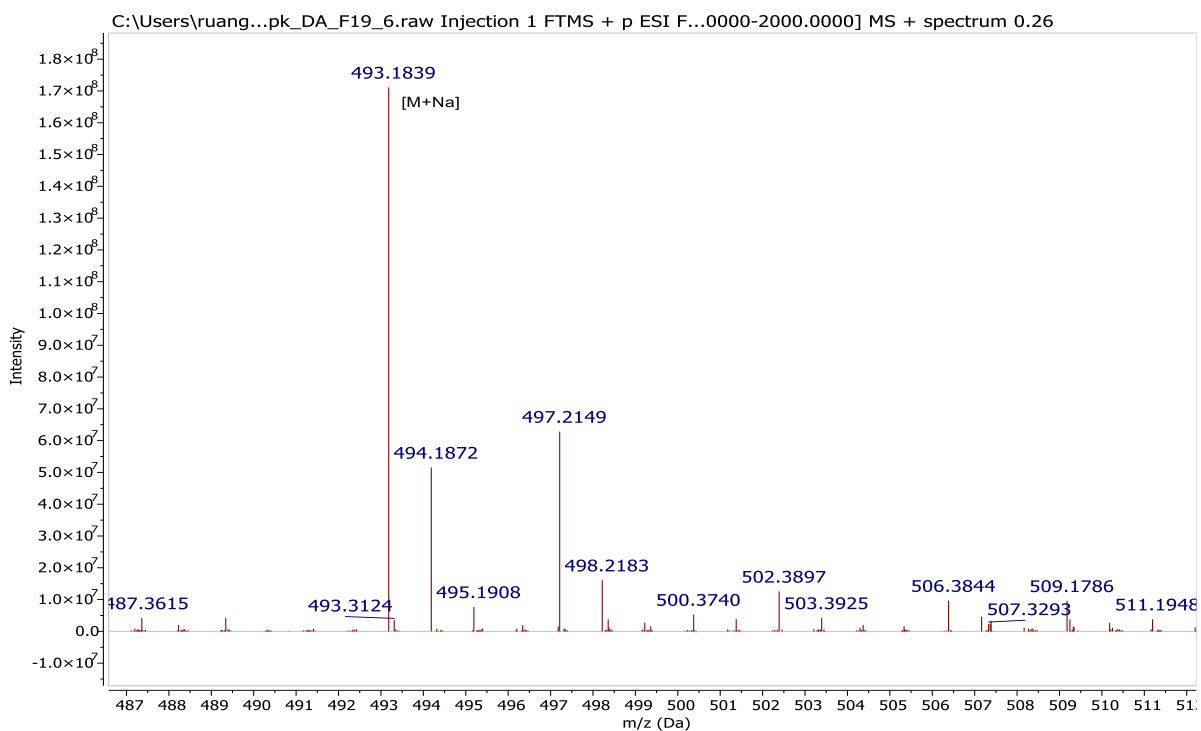


Figure 6.72. Mass spectral data of F11-12 at the ion peak m/z 493.183 $[M+Na]^+$.

Terretonin F was obtained by further purification of subfraction F11-29. The compound was eluted on preparative TLC plate, which gave intensive violet band upon spraying with anisaldehyde/sulfuric acid and heating. It was moderately polar white amorphous solid with a yield of 6.7 mg. HR-ESIMS data gave a MWt of 470.1941 Da and molecular formula of $C_{26}H_{30}O_8$, which was deduced from the sodiated molecular ion peak at m/z 493.183 (Figure 6.72). A twelve degree of unsaturation was determined from the obtained molecular formula.

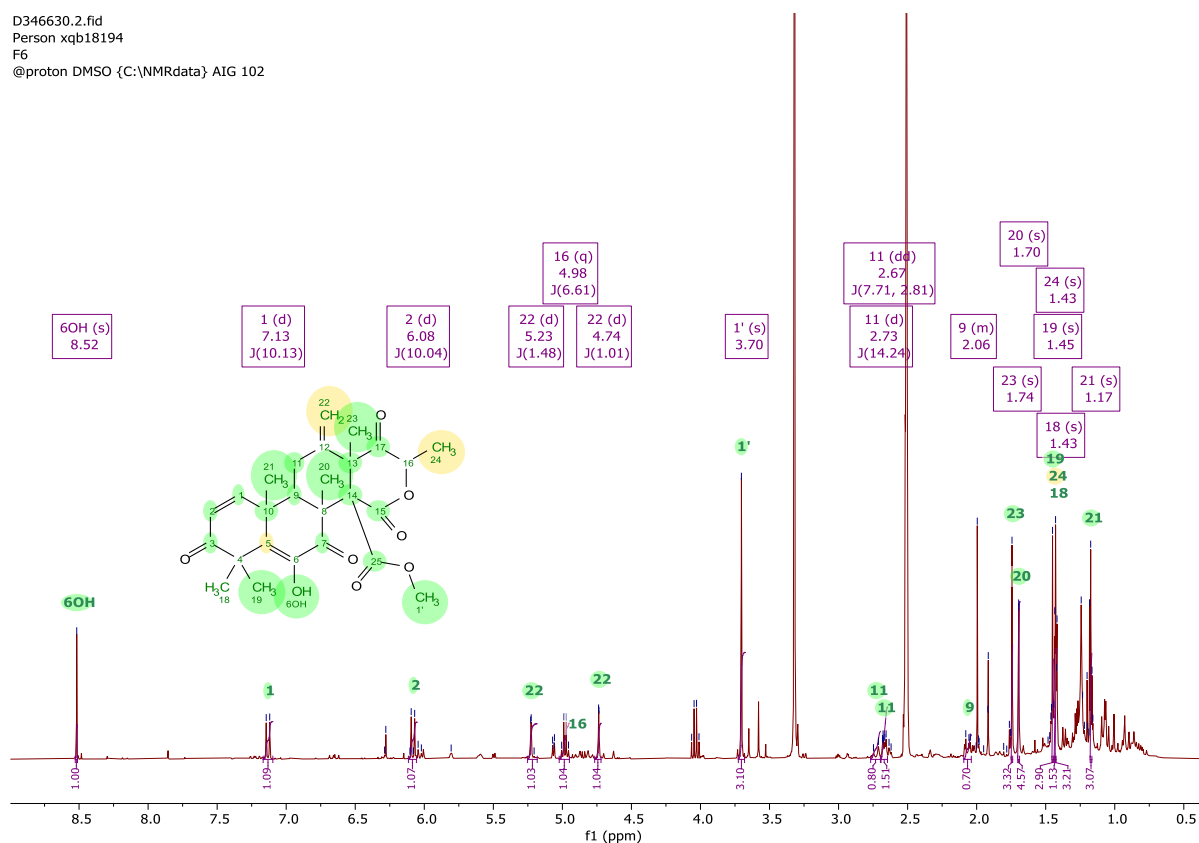


Figure 6.73: ^1H NMR spectrum of compound terretonin F in $\text{DMSO-}d_6$ measured at 500 MHz.

The ^1H NMR (Figure 6.73) and HSQC (Figure 6.74) spectra revealed the presence of six methyl singlets signals at δ_{H} 1.17 (H21), 1.43 (H18), 1.5 (H19), 1.70 (H20), 1.43 (H24) and 1.74 (H23), one singlet methoxy peak at δ_{H} 3.71 (s, H1'), one quartet resonating at δ_{H} 4.98 (q, 6.6 Hz, H16) attributed to an oxymethine moiety, and a pair of doublets at δ_{H} 5.73 (d, 1.0 Hz, H22a) and 5.23 (d, 1.4 Hz, H22b) attributable to an exomethylene moiety, one methylene signals at δ_{H} (2.66, H11ax, 2.71, H11eq), a pair of doublets at δ_{H} 5.73 (d, 1.0 Hz, H22a) and 5.23 (d, 1.4 Hz, H22b) for an exomethylene moiety, two conjugated olefinic protons at δ_{H}

6.08 (d, 10 Hz, H2) and 7.14 (d, 10.1 Hz, H1), and one exchangeable proton at δ_{H} 8.52 (s, OH6).

The ^{13}C NMR spectrum exhibited 26 resonances including eleven sp² carbons, six of them at δ , 153.4 (C1) and 126.3 (C2) 133.2 (C5), 143.6 (C12), 141.3 (C6), 143.2 (C12), and 113.3 (C22) belonging to three double bonds. Two sp² carbon resonances at δ 170.2 (C15) and 167.5 (C25) indicated the presence of two ester carbonyls. The other three sp² carbon ascribed to the ketone group at δ 203.0 (C3) and 203.4 (C17), and 194.4 (C7). The remaining four degree of unsaturation were ascribed to the four rings.

The analysis ^1H - ^1H COSY (Figure 6.75) along with HMBC (Figure 6.76) correlation further confirmed the structure of F11-29-6. The assignment of ring A was deduced from the coupling between H1 and H2, and correlations between H1 toward C3, C5, C9 and H2 with C10. Isolated spin system from the two olefinic protons ascribed to the vinylidene moiety near a carbonyl unit. The fusion between rings A and B through C5 and C10 was proved by HMBC correlations between H21(1.17) and C1, 5, 9, and 10. On the other hand, the occurrence of an HMBC correlation from H20 (1.70) between C7,8,9, and 14 verified the direct fusion between rings B and C through C8 and C9.

COSY (Figure 6.75) cross peaks of exomethylene moiety and H9 and the assignment of HMBC correlations (Figure 6.76) of corresponding protons (H22a/22b [5.23, 5.73]) with C11 and C13 facilitated in the putting together the substructure for ring C. The HMBC correlation confirmed the linkage between rings C and D through C13 and C14 from the methyl H23 (1.74) to C12, C13, C14 and C15. The HMBC cross peak between H16 (4.98) and the lactone carbonyl C15 (170.2) was used to identify the keto-lactone unit of ring D, as well as the connectivity of the methyl unit at H24 (1.38) with the ketone carbonyl on C17 (203.4).

Signal at δ_{C} 78.8 (C16) was typical for a sp³ carbon linked to an oxygen. COSY cross peaks indicated that the methine group at (δ 4.98, H16, q, $J = 6.6$ Hz) was substituted by a methyl unit at δ_{H} 4.87 (m, H16). ROESY cross peaks (Figure 6.77) was used to identify the relative configuration of terretonin F. The correlations between H11 β with H1 (δ_{H} 7.14), H20 (δ_{H} 1.70), H21 (δ_{H} 1.17), H22 (δ_{H} 5.23, 4.73), and H23 (δ_{H} 1.74), as well as H1 (δ_{H} 7.14) with H9 (δ_{H} 2.08) and H2 (δ_{H} 6.08), suggesting that all these protons were positioned on the same side of the molecule, which is the β orientation. In addition, the through-space correlation of

methyl H24 with H20, H21 suggested as well a β orientation of the methyl unit. Full assignments of the NMR spectral data of F11-29-6 are presented on Table 6.17, which were compatible those found for terretonin F (Table 6.18) (Lopez-Gresa *et al.*, 2009). Terretonin F was first isolated from a marine-derived fungus *A. insuetus*, associated with the sponge *Petrosia ficiformis*. Terretonin F showed activity as an inhibitor of the mammalian mitochondrial respiratory chain (Lopez-Gresa *et al.*, 2009) that is of importance in degenerative diseases such as Parkinson's and Huntington's diseases.

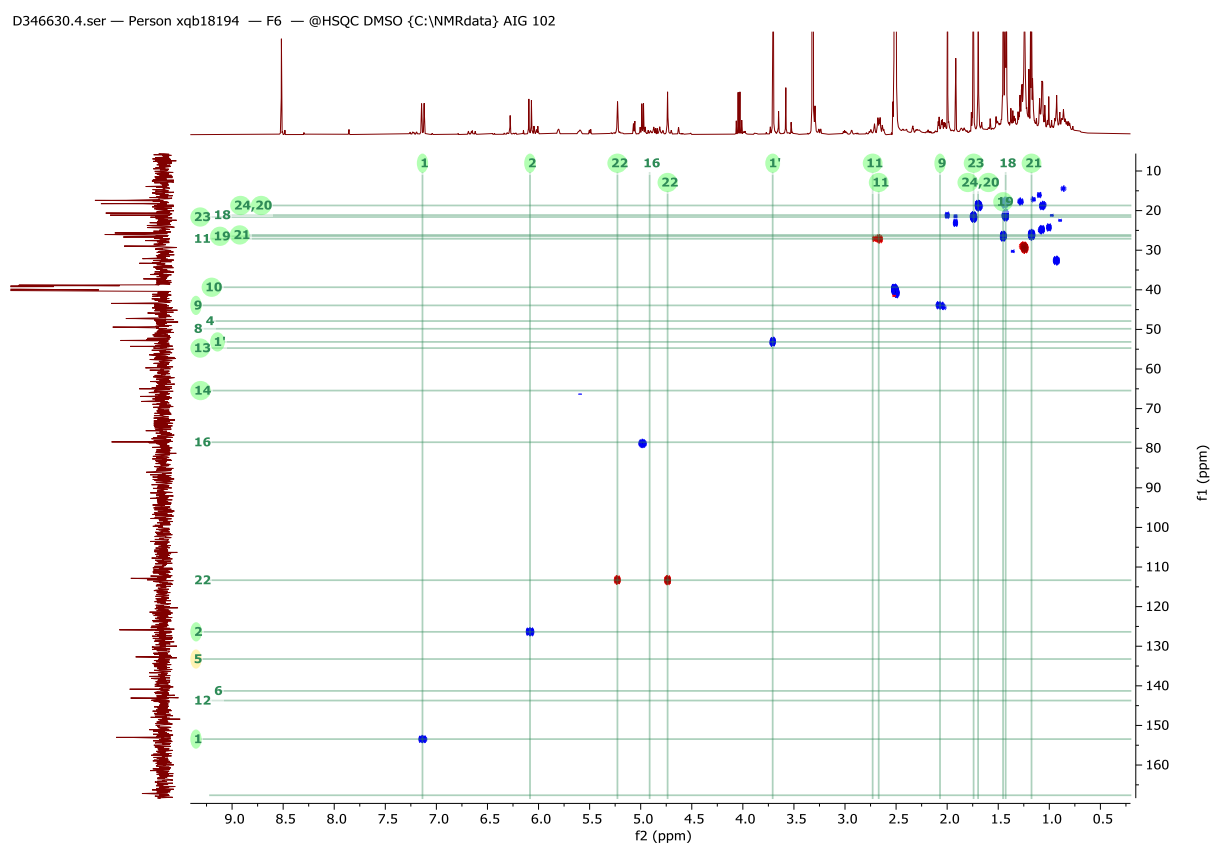


Figure 6.74: HSQC NMR spectrum of compound terretonin F in DMSO-*d*₆ measured at 500 MHz. Red cross peaks are CH and CH₃ while blue are CH₂.

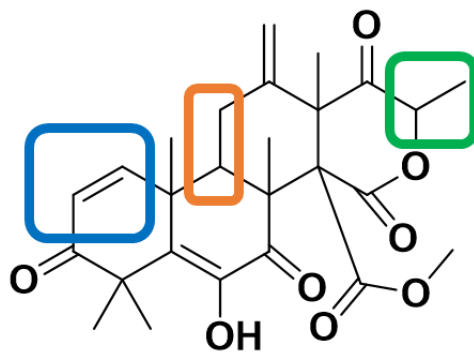
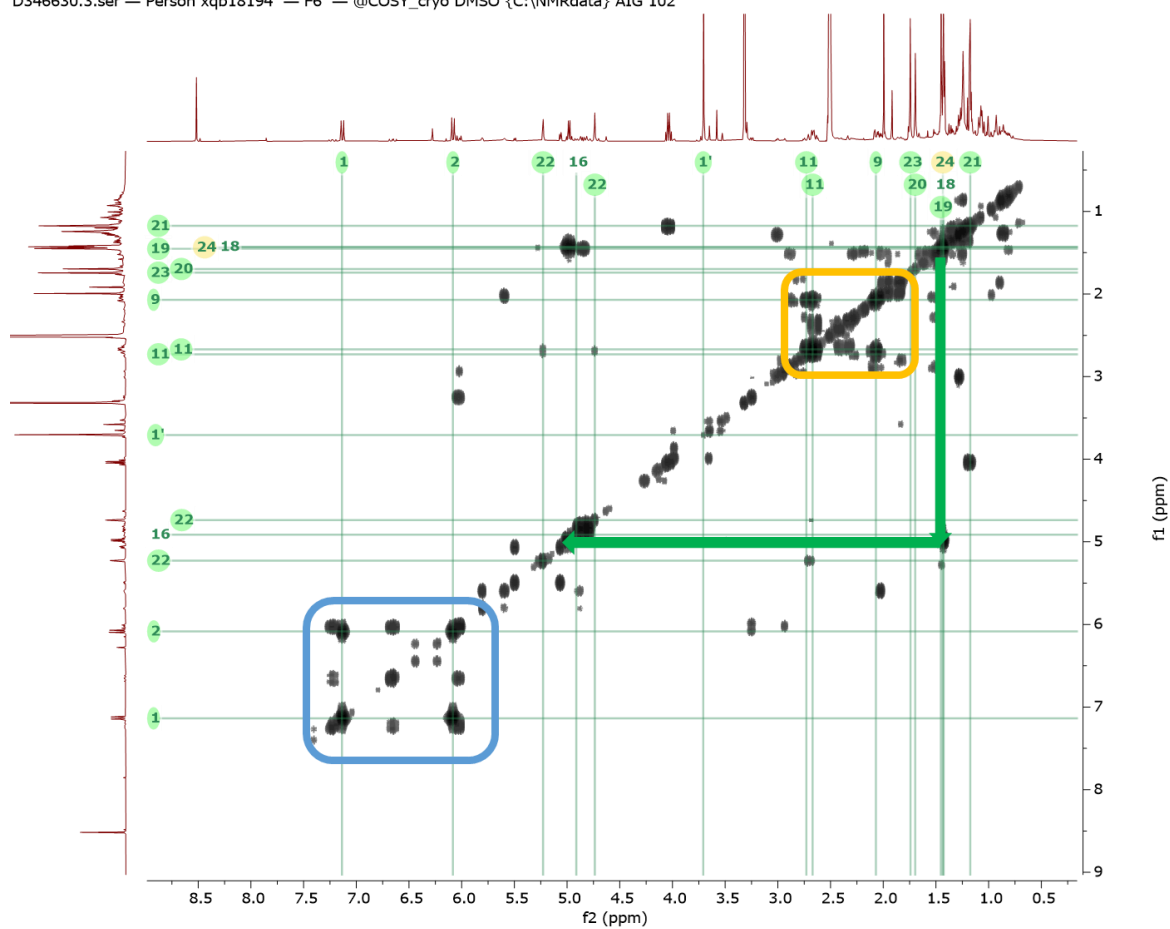
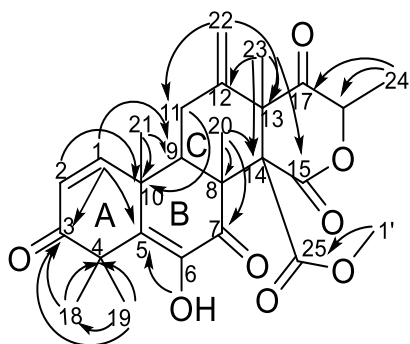


Figure 6.75: (^1H - ^1H) COSY correlation NMR spectrum of terretinin F in $\text{DMSO-}d_6$ measured at 500 MHz.



D346630.5.ser — Person xqb18194 — F6 — @HMBC DMSO {C:\NMRdata} AIG 102

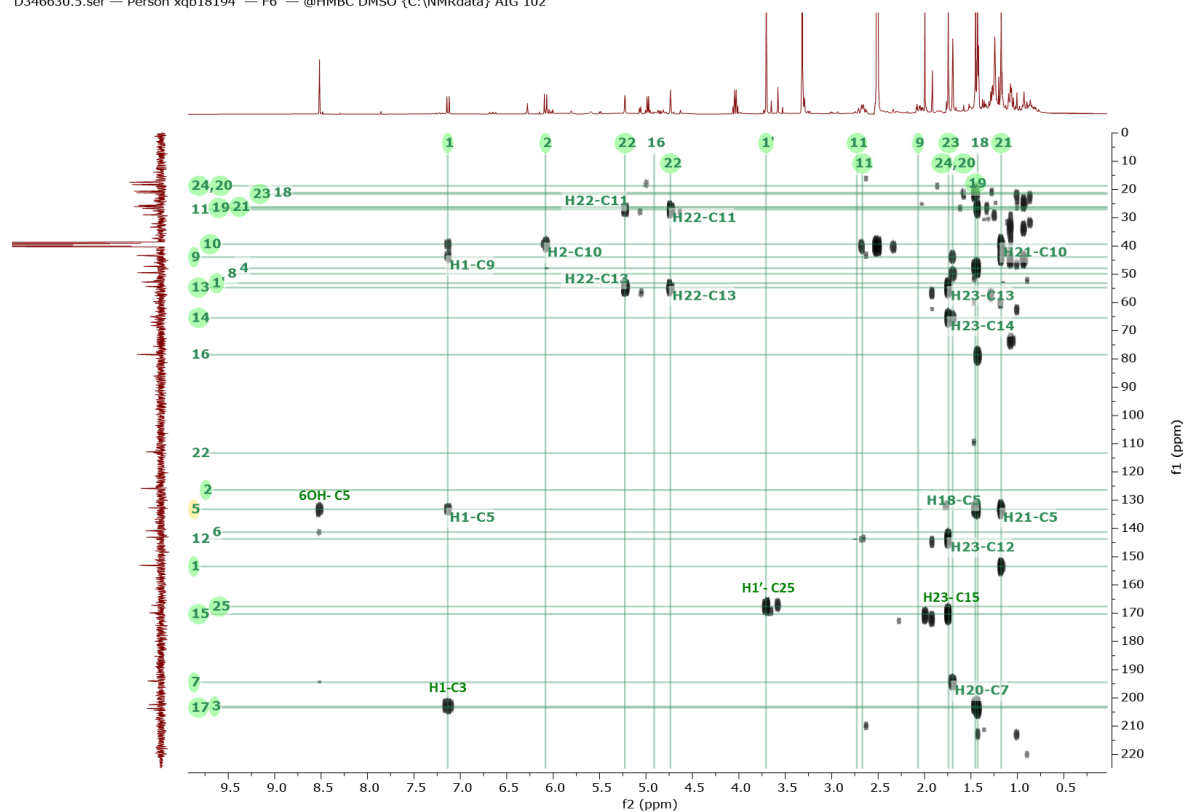


Figure 6.76: HMBC NMR spectrum of compound terretinin F in DMSO-*d*₆ measured at 500 MHz.

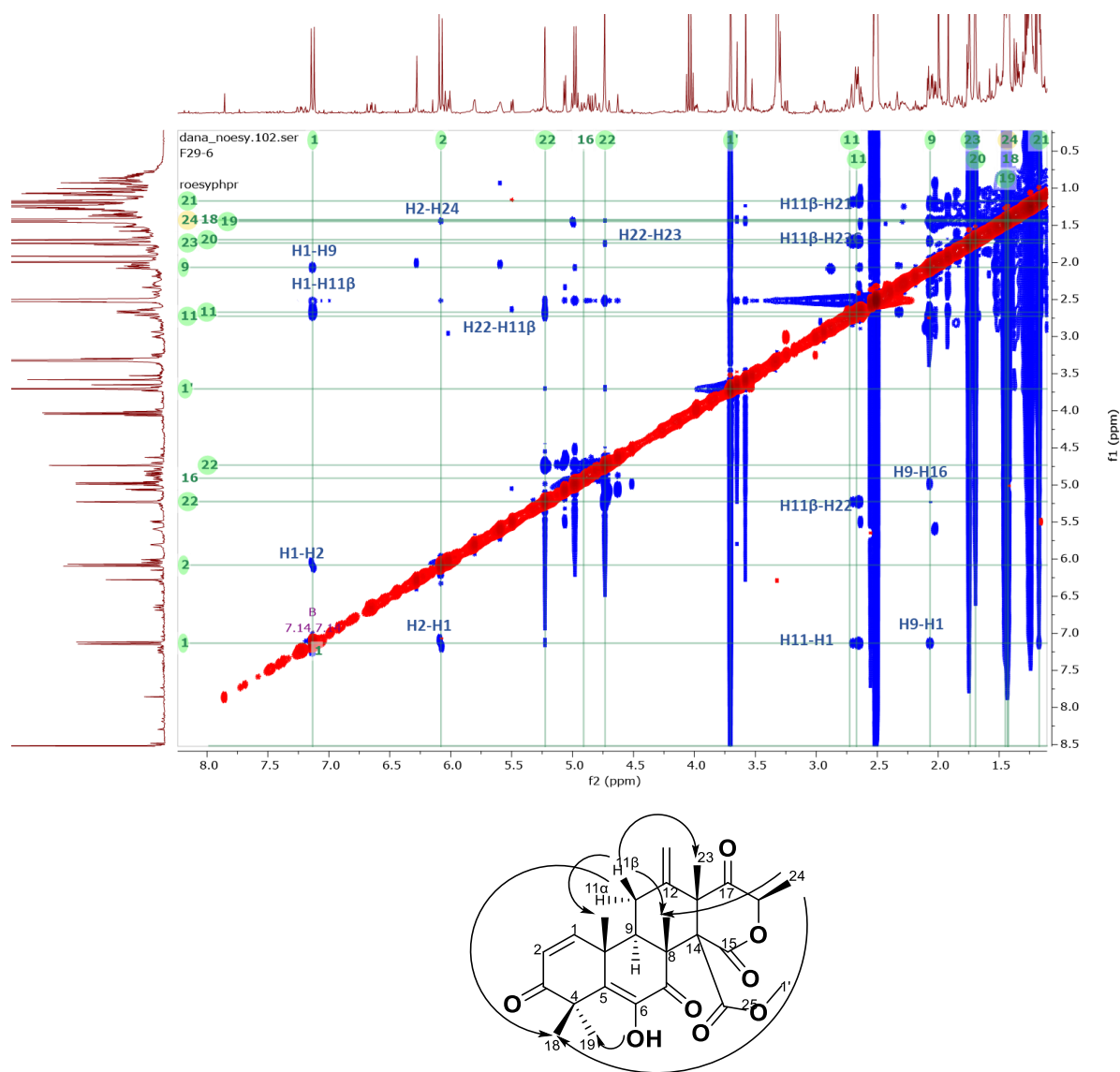


Figure 6.77: ROESY spectrum and their essential correlation of compound terretonin F in DMSO- d_6 measured at 600 MHz.

Table 6.17: NMR data of F11-29-6 in DMSO-d₆ measured at 500 MHz..

Atom no.	¹³ C*	¹ H	<i>J</i> in Hz	HMBC	ROESY
1	153.4CH	7.14 d	10.1	C3, C5, C9	H2, H9, H11(eq), H21
2	126.3 CH	6.08 d	10.0	C10	H21,H22, H24, H1'
3	203.0 qC				
4	47.9 qC				
5	133.2 qC				
6	141.3 qC				
7	194.4 qC				
8	49.8 qC				
9	44.0 CH	2.08 m			H1, H16
10	39.2 qC				
11	27.1 CH ₂	2.71 dd ax 2.66 dd eq	14.2 7.7, 2.8	C10	H11(eq), H1, H21, H22, H23
12	143.6 qC				
13	54.8 qC				
14	65.4 qC				
15	170.2 qC				
16	78.8 CH	4.98 q	6.6		
17	203.4 qC				
18	21.1 CH ₃	1.43 s		C3, C4, C19	
19	26.5 CH ₃	1.45 s		C3, C4, C18	
20	18.7 CH ₃	1.70 s		C7, C8, C9, C14	H11(eq), H21
21	26.1 CH ₃	1.17 s		C1, C5, C9, C10	H11(eq), H20, H18
22	113.3 CH ₂	5.23 d 4.73 d	1.4 1.0	C11, C13	H11(eq), H23
23	21.6 CH ₃	1.74 s		C12, C13, C14, C15	
24	18.0 CH ₃	1.43 s		C16, C17	H20, H21, H18
25	167.5 qC				
1'	53.2 CH ₃	3.71 s		C25	H23
6-OH		8.52 s		C5	H19

Legend: br = broad, s = singlet, d = doublet, t = triplet, q = quartet, m = multiplet, quin = quintet.
*Data taken from HMQC and HMBC experiments.

Table 6.18: NMR data of F11-29-6 compared to that to literature(Lopez-Gresa *et al.*, 2009).

terretonin F (literature) in CDCl ₃				F11-29-6 in DMSO- <i>d</i> ₆		
Atom no.	¹³ C (125 MHz)	¹ H (500 MHz)	<i>J</i> in Hz	¹³ C (500 MHz)	¹ H (500 MHz)	<i>J</i> in Hz
1	150.6 CH	6.80, d	10.2	153.4CH	7.14 d	10.1
2	127.4 CH	6.11, d	10.2	126.3 CH	6.08 d	10.0
3	204.1 qC			203.0 qC		
4	48.0 qC			47.9 qC		
5	133.2 qC			133.2 qC		
6	140.0 qC			141.3 qC		
7	194.5 qC			194.4 qC		
8	49.3 qC			49.8 qC		
9	44.1 CH	2.18 dd	13.8, 3.0	44.0 CH	2.08 m	
10	39.1 qC			39.2 qC		
11	28.0 CH ₂	2.66ax t 2.48 eq dd	13.8 13.8, 3.0	27.1 CH ₂	2.71 dd ax 2.66 dd eq	14.2 7.7, 2.8
12	143.0 qC			143.6 qC		
13	54.8 qC			54.8 qC		
14	65.6 qC			65.4 qC		
15	169.9 qC			170.2 qC		
16	78.8 CH	4.78 q	6.7	78.8 CH	4.98 q	6.6
17	209.9 qC			203.4 qC		
18	20.9 CH ₃	1.54 s		21.1 CH ₃	1.43 s	
19	26.4 CH ₃	1.58 s		26.5 CH ₃	1.45 s	
20	18.9 CH ₃	1.80 s		18.7 CH ₃	1.70 s	
21	25.7 CH ₃	1.27 s		26.1 CH ₃	1.17 s	
22	111.3 CH ₂	5.10, 4.93 brs		113.3 CH ₂	5.23 d 4.73 d	1.4 1.0
23	21.8 CH ₃	1.86 s		21.6 CH ₃	1.74 s	
24	17.8 CH ₃	1.55 d	6.7	18.0 CH ₃	1.43 s	
25	166.9 qC			167.5 qC		
1'	53.3 CH ₃	3.82 s		53.2 CH ₃	3.71 s	
6-OH		6.68 s			8.52 s	

Legend: s= singlet, d = doublet, t = triplet, q = quartet, m =multiplet, ax = axial, eq =equatorial.

6.7. Biological assay results of the pure compounds

All the purified compounds were tested for their anticancer activity against breast cancer cells (ZR-75). All compounds including F11-12 (3'-hydroxy-2'-(palmitoyloxy) propyl (9Z,12Z)-octadeca-9,12-dienoate), F11-23 (9 α -hydroxy-6 α -[(2E,4E,6E)-octa-2,4,6-trienyloxy]-5 α -drim-7-en-11,12-olide), F11-29-8 (ustusolate E), F12-11-2 (strobilactone A) and F11-29-6 (terretonin F) demonstrated very good bioactivity against the tested breast cancer (ZR-75) cell line, with cells viability less than 40% at 30 μ g/mL. Except for (F11-17) ophiobolin K and F11-11 (1,2 diolinolein) were found inactive, obtaining cell viability greater than 80% (Figure 6.78). IC₅₀ of the bioactive compounds was less than 6 μ M, as shown in Table 6.19 and Figure 1 in appendix 3 .

Moreover, all the isolated purified compounds were assayed for their toxicity against normal HS-27 and determined their IC₅₀ values, the results are shown in Table 6.19 and Figure 2 in appendix 3. The toxicity of the compounds was established by measuring the IC₅₀ on the normal HS-27 cells; if the IC₅₀ is more than 90 μ g/mL, the compounds are regarded non-cytotoxic; otherwise, if the IC₅₀ value falls between 2 and 89 μ g/mL, the drug is classified as moderately cytotoxic, and if it is less than 2 μ g/mL, the compounds are classified as cytotoxic (Mazlan *et al.*, 2020b). Compounds with *SI* values greater than 10 or when IC₅₀ values against the normal HS-27 cell line could not be determined from the dilution curve, it suggested that the compound is selective (Vonthron-Sénécheau *et al.*, 2003).

Thus, the toxicity and selectivity indexes were calculated for the isolated compounds and mentioned in Table 6.22. All the drimane sesquiterpenes derivatives including F11-23, F11-29-8 and F12-11-2 were found active against breast cancer cells (ZR-75) with IC₅₀ equals to 5.93, 5.54, 4.62 μ M. On the other hand, the above compounds had an IC₅₀ on the normal Human foreskin fibroblast (HS-27) cells equals to 78.77, 136.50 and 46.50 μ M and *SI* of 13.28, 24.63 and 10 respectively. As a result, all the drimane derivatives are considered moderately toxic and selective.

Furthermore, F11-12 was the most potent compound against ZR-75 cells with IC₅₀ 2.47 μ M, and an IC₅₀ of 100 μ M on HS-27 cells. F11-12 was considered not toxic on HS-27 and selective on ZR-75 cells. Finally, terretonin F (F11-29-6) was found active against ZR-75 cells

with IC_{50} of 4.66 μ M, and an IC_{50} on the normal HS-27 cells of 356.2 μ M resulting to an SI of 76.43. Terretinin F was considered selective and not toxic.

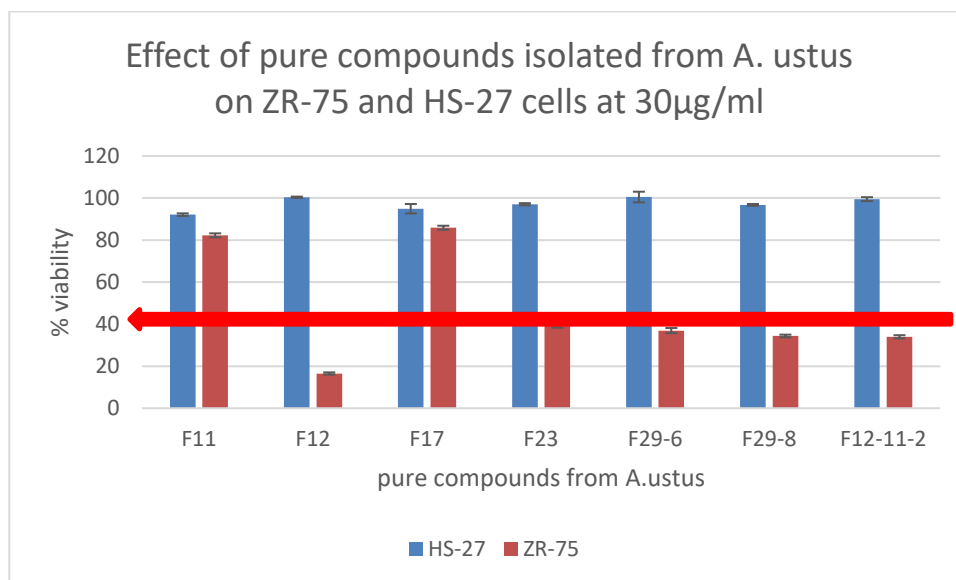


Figure 6.78: Effect of pure compounds isolated from *A. ustus* on ZR-75 and HS-27 cells at 30 μ g/mL. The red line indicates the bioactivity threshold.

Table 6.19: IC₅₀ concentrations (μM) for the bioactive isolated compound against respective cell lines. If *SI* greater than 10 or the IC₅₀ of the tested normal cell was not obtainable, then the compound considered selective.

compound code	Name	IC ₅₀ (μM) ZR-75	IC ₅₀ (μM) HS-27	IC ₅₀ (μg/mL) HS-27	Toxicity	<i>SI</i>	Selectivity
F11-11	1, 2 dilinolein	inactive	inactive	inactive	-	-	inactive
F11-12	3'-hydroxy-2'-(palmitoyloxy) propyl (9Z,12Z)-octadeca-9,12-dienoate	2.47	100	>100	not cytotoxic	40.45	(selective)
F11-17	ophiobolin K	inactive	inactive	inactive	-	-	inactive
F11-23	9α-hydroxy-6α -[(2 <i>E</i> ,4 <i>E</i> ,6 <i>E</i>)-octa-2,4,6-trienoyloxy]-5 α-drim-7-en-11,12-olide	5.93	78.77	30-100	moderate cytotoxic	13.28	selective
F11-29-8	ustusolate E	5.54	136.5	30-100	moderate cytotoxic	24.63	selective
F11-29-6	terretonin F	4.66	356.2	>100	not cytotoxic	76.43	selective
F12-11-2	(<i>E,E</i>)-6-(6',7'-dihydroxy-2',4'-octadienoyl)-strobilactone A	4.62	46.50	30-100	moderate cytotoxic	10	selective
Legend: <i>SI</i>=selectivity index. n.b= not obtainable, If IC₅₀ (μM) of HS-27 > 90 μg/mL=not cytotoxic, 2-89 μg/mL=moderate cytotoxicity and if less than 2 μg/mL = cytotoxic							

6.8. Summary

The most ideal condition for the large-scale fermentation of *A. ustus* was achieved at 30 days of incubation in liquid potato-dextrose medium. Multivariate analysis of the NMR and mass spectral datasets showed that the extracts obtained from the potato-dextrose cultures were more chemically complex and diverse. Moreover, the potato-dextrose culture extracts exhibited activity against breast cancer after 30 days of incubation. Further isolation work yielded seven compounds, six of which were pinpointed by multivariate analysis to exhibit the putative bioactivity. The isolated target compounds were all known compounds, which consisted of three drimane sesquiterpenes derivatives including 9 α -hydroxy-6 α -[(2*E*,4*E*,6*E*)-octa-2,4,6-trienoyloxy]-5 α -drim-7-en-11,12-olide (F11-23), ustusolate E (F11-29-8) and *E,E*-6-(6',7'-dihydroxy-2',4'-octadienyl)-strobilactone A (F12-11-2).

Terretonin F (F11-29-6), ophiobolin K (F11-17). Additionally, two linoleic acid derivatives including 1',2' diolinolein (F11-11) and 3'-hydroxy-2'-(palmitoyloxy) propyl (9*Z*,12*Z*)-octadeca-9,12-dienoate (F11-12). F11-12 was not detected amongst the target metabolites predicted by multivariate analysis. All the isolated compounds were assayed ZR-75 and HS-27 cell lines. Except for ophiobolin K and 1',2' diolinolein all other compounds exhibited very good bioactivity against the tested breast cancer cell line ZR-75. All the drimane sesquiterpenes derivatives including F11-23, F11-29-8 and F12-11-2 were found active against breast cancer cells (ZR-75) with IC₅₀ equals less than 6 μ M. All the drimane derivatives were found moderately toxic on HS-27 cells and selective on ZR-75 cells.

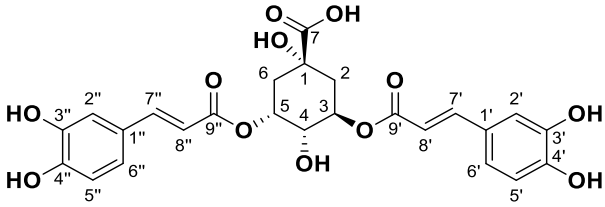
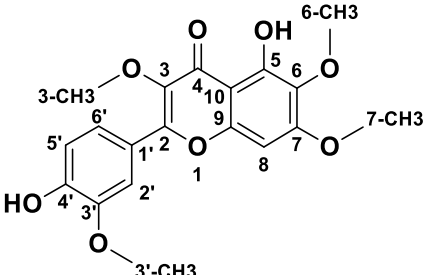
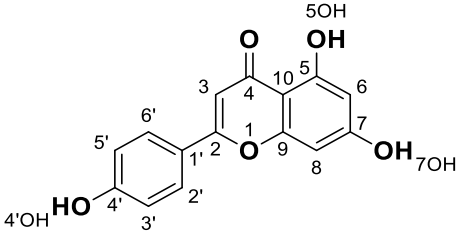
Furthermore, F11-12 was found the most potent compound against ZR-75 cells with IC₅₀ of 2.47 μ M. F11-12 was considered not toxic on HS-27 and selective on ZR-75 cells. Finally, terretonin F (F11-29-6) was found active against ZR-75 cells with IC₅₀ equals to 4.66 μ M, and the IC₅₀ on the normal HS-27 cells was equal to 356.2 μ M with SI of 76.43. therefore, terretonin F was considered selective and not toxic.

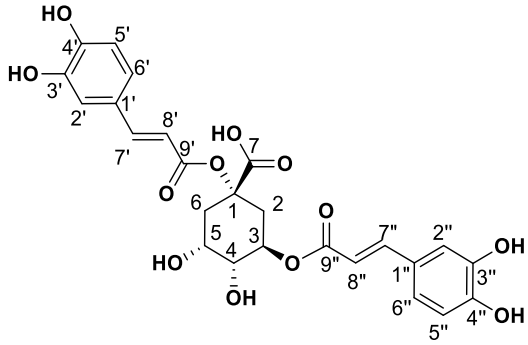
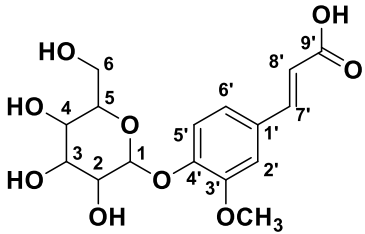
7. General Discussion

7.1. Anticancer and antioxidant compounds from two varieties of chamomile.

Below on Table 7.1 is a summary of biologically active compounds isolated from Jordanian and European chamomile investigated in this study.

Table 7.1: Compounds isolated from the Jordian and European chamomile varieties.

Isolated compounds	Chemical Formula, MW and name	Chamomile variant
	Chemical Formula: $C_{25}H_{24}O_{12}$ Exact Mass: 516.1264 3,5- <i>O</i> -dicaffeoylquinic acid ChJ-F8 active	Jordanian
	Chemical Formula: $C_{19}H_{18}O_8$ MWt: 374.1000 chrysosplenetin ChE-F2 active	European
	Chemical Formula: $C_{15}H_{10}O_5$ Exact Mass: 270.0525 apigenin ChE-F8 active	European

	<p>Chemical Formula: $C_{25}H_{24}O_{12}$ MWt: 516.1261 1,3 dicaffeoyl quinic acid 1,3-<i>O</i>- dicaffeoylquinic acid ChE-F12 active</p>	<p>European</p>
	<p>Chemical Formula: $C_{16}H_{20}O_9$ MWt: 356.1179 4'→1-<i>O</i>- feruloylglucose glucoferulic acid (lavandoside) ChE-F11 active</p>	<p>European</p>

7.1.1. Metabolomic-guided isolation of target anticancer active metabolites

The dereplicated secondary metabolites produced by Jordanian and European chamomiles were quite comparable in terms of their chemistry as all analogues belong to the quinic acids family of compounds. However, the proton NMR of the bioactive EtOAc extracts of Jordanian and European varieties have different chemical profile because of a higher concentration of flavonoid type of compounds despite the presence of lower yielding quinic acid derivatives. The EtOAc extracts for Jordanian chamomile revealed the presence of metabolites with chemical shifts resonating between 6.00 and 7.00 ppm (aromatic compounds) which was an indication of the presence of phenylpropanoids. Meanwhile, the NMR spectral data of European chamomile extracts exhibited a higher density of resonances between 2.0 and 4.0 ppm, indicating the presence of glycosylated and hydroxylated active metabolites, which was evidence of the presence of flavonoids.

However, the antioxidant active metabolite with a chemical formula $C_{24}H_{25}O_{24}$ found at the ion peak m/z 517.1341 $[M+H]^+$, 515.1196 $[M-H]^-$ was a common target from both varieties.

Discriminating metabolites from the Jordanian EtOAc extract yielded medium MWt compounds that were derivatives of caffeoyl quinic acid, which have been described for their antioxidant activity (Forino *et al.*, 2015). These included N_3285 and N_3284 with ion peaks found at m/z 353.0880 and 515.1196 Da. Furthermore, discriminating metabolites with MZmine ID P_7541, P_21550, N_3306, P_845 with m/z values of 449.1079, 465.1028, 465.1029, 463.0887, 495.1133 Da were dereplicated as flavonoid derivatives. Numerous flavonoids have been shown to have anticancer properties. However, the molecular mechanisms behind this effect have not been completely understood (Kopustinskiene *et al.*, 2020). The latter metabolites were found in the European chamomile EtOAc extract, which supported the evidence for its anticancer activity against breast cancer cells. A correlation between total phenolic content and antioxidant activity have been earlier reported (Al-Rimawi *et al.*, 2016), but not with total flavonoid content.

Ion peaks $[M-H]^-$ at m/z 515.127, and 515.118 Da were pinpointed as the discriminating features for the active EtOAc extracts and 1031.260 is a complex of 515.127 Da. Amongst the targeted compounds from the crude EtOAc extract of both varieties, only two compounds could be isolated, which were F11-ChE and F8-ChJ that were both present in European and Jordanian chamomile. Both compounds elucidated as 1,3-Dicaffeoyl quinic acid and 3,5-Dicaffeoyl quinic acid, respectively have been widely reported for their significant antioxidant activity and scavenging properties (Danino *et al.*, 2009, Hong *et al.*, 2015).

However, four of the isolated targeted discriminating features for the European variety with ion peaks $[M-H]^-$ at m/z 373.093, 269.045, 515.127, and 355.103 Da were associated with the active fractions corresponding to chrysosplenetin, apigenin, 1,3-Dicaffeoyl quinic acid and glucoferullic acid, respectively. While one compound was isolated from

Jordanian chamomile crude extracts, which was 3,5-Dicaffeoyl quinic acid. Both variants yielded Dicaffeoyl quinic acid isomers, which were the most abundant in both varieties and led to the antioxidant activity of their extracts (Danino *et al.*, 2009, Hong *et al.*, 2015). The ^1H NMR spectra of F11-ChE was comparable to that of F8-ChJ, which are structural isomers with the identical MWt, with only a variation in elution time of 0.3 seconds between them. Even though the spectral data of F11-ChE and F8-ChJ were almost comparable, they were not identical. The compounds are structural isomers with identical MWt, and there was a variation of 0.3 seconds in their retention times. Differences were also detected in the respective ^1H NMR of both compounds. When the ^1H NMR spectra of F11-ChE and F8-ChJ were compared, it was observed that there was a more obvious separation of the trans olefinic ^1H signals for the two caffeoyl units. The chemical shift of H3 (4.96 ppm) and H5 (5.11 ppm) were more shifted downfield, which suggested the esterification of two quinic acid moieties at positions 3 and 5. Whereas, the chemical shift of the methine proton on C3 was shielded upfield in F11-ChE, it was determined that the caffeoyl unit on 3-OH disappeared, and the esterification of the hydroxyl unit on C1 had taken its place.

In this study, a metabolomics approach has been applied in investigating the differences in the production of secondary metabolites of two chamomile varieties grown under different environmental conditions. Changes in metabolite production were perceived between two varieties. Different environmental conditions between Jordanian and European chamomile affected the type of the isolated compounds.

Even though the climate in Jordan varies from a more Mediterranean to a desert environment, the country is typically quite dry. Winter temperatures vary between 9 and 13 °C and summer temperatures range between 25 and 35 °C (Matouq *et al.*, 2013). Meanwhile, the climate in the United Kingdom is temperate oceanic, with more rainfall throughout the whole year. Seasonal variations in temperature are common; nonetheless, the temperature rarely goes below -10 °C or climbs over 35 °C. In the literature, it was stated that warm and dry weather in *Quercus ilex* leaves increases the concentration of

polyphenols (Nogués *et al.*, 2014, Rivas-Ubach *et al.*, 2014), which explained the production of di-caffeoyl quinic acid in high concentration in Jordanian chamomile.

As a result, significant changes in the synthesis of primary and secondary metabolites were seen between specimens of the same plant species grown under various environmental circumstances. (Sampaio *et al.*, 2016, Zanatta *et al.*, 2021). Polyphenols are the most adaptable secondary metabolites, enabling plants to react quickly to a variety of unanticipated stressors, which could be influenced by various environmental factors (Di Ferdinando *et al.*, 2014). The respective category of secondary metabolites, which is influenced by environmental conditions, serves as a chemical interface between the plant and its environment. These interaction could generate variations in metabolic profile for same species (Sampaio *et al.*, 2016).

Other factors that affects secondary metabolites productions of same species appears to be related to induction of seasonal stress factors in the plant, such as (i) drought stress, which can cause a reduction in photosynthetic rate with a consequent increase in production of reactive oxygen species (ROS), resulting in an increase in the production of phenolic compounds (natural antioxidants) during the dry season as a defence mechanism (Ramakrishna and Ravishankar, 2011, Arbona *et al.*, 2013, Reddy *et al.*, 2004). (ii) Thermal stress caused by a wide temperature variation range throughout the year, particularly during drier periods, which can affect metabolic regulation, permeability to water and CO₂, as well as the rate of intracellular reactions as well as improve antioxidant properties by increasing the availability of carbohydrates thermal stress (Ramakrishna and Ravishankar, 2011, Morison and Lawlor, 1999).

7.1.2. Proposed biosynthetic pathways of the isolated phenolic compounds

In this study, two flavone types of compounds and three phenylpropanoid derivatives were isolated from two chamomile varieties. The biosynthesis of these flavones is proposed (Scheme 7.1) from the reaction between *p*-coumaryl and three molecules of malonyl-

coenzyme A (CoA; *via* the fatty acid pathway) to produce naringenin-chalcone compound. Then chalcone isomerase (CHI) was catalysed and naringenin was produced as a key substrate. In next step flavone synthase (FNS) was involved to produce apigenin (ChE-F8). While other flavonoid was resulted from the hydroxylation of naringenin through F3H (flavanone 3-hydroxylase), F3'H (flavonoid 3'-hydroxylase) and F6H (flavanone 6-hydroxylase) at position 3',3 and 6 to produce trihydroxyquercetin. Then, trihydroxyquercetin was methylated using at its 3', 3,6 and 7-hydroxyl group to form 4',5 dihydroxy-3',3,6,7 tetramethoxy flavone (ChE-F2) as proposed in Scheme 7.1 (Berim and Gang, 2013, Kim, 2006).

The hydroxylation of *p*-coumaric acid at the 3-position of the benzyl ring by the enzyme 3-hydroxylase (C3H) results in caffeic acid. Ferulic acid is produced from caffeic acid by the enzyme caffeate O-methyltransferase (COMT) (Do *et al.*, 2007). The 4-hydroxy group of ferulic acid is then glycosylated, resulting in the synthesis of ferulic acid 4-O-glucoside (ChE-F12). The glucose group was transferred from UDP-glucose to ferulic acid (Han *et al.*, 2016, Alcazar Magana *et al.*, 2021).

On the other hand, the biosynthesis of two phenylpropanoid derivatives were from converting *p*-coumaric acid into caffeic acid. The resultant caffeic acid is then converted to caffeoyl-CoA through ligation of coenzyme A (CoA) by 4-CoA ligase (4CL). Then, subsequently transesterified with quinic acid by HQT (hydroxycinnamoyl CoA quinate hydroxycinnamoyl transferase) / HCT (hydroxycinnamoyl-CoA shikimate/quinate hydroxycinnamoyl transferase) to generate 3- caffeic quinic acids. Further esterification of the quinic acid with caffeoyl CoA by HQT at position number 5, resulted in 3, 5-O-dicaffeoyl quinic acid (ChJ-F8). While esterification at positioned 1, resulted in 1,3-O-dicaffeoyl quinic acid ((ChE-F11) (Alcazar Magana *et al.*, 2021).

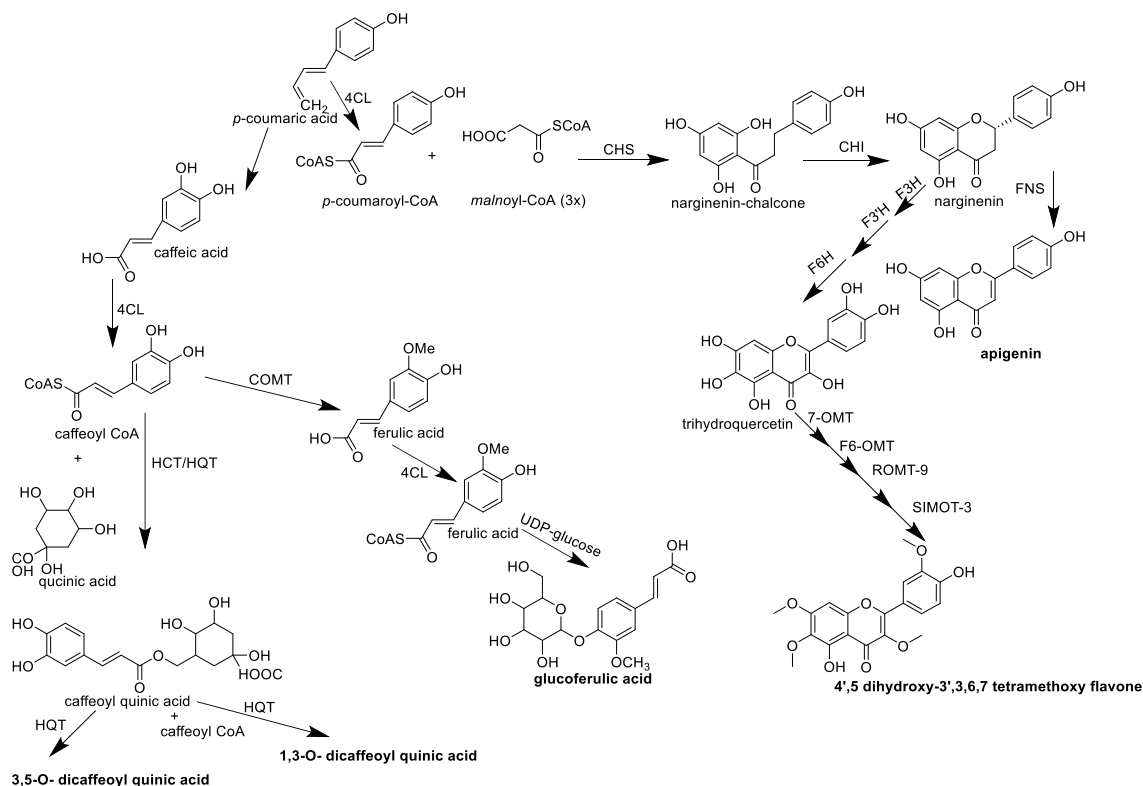


Figure 7.1: Schematic diagram of proposed biosynthesis of the isolated compounds from chamomile varieties. Enzyme abbreviations: CHS, chalcone synthase; CHI, chalcone isomerase; FNS, flavone synthase; F3H, flavanone 3-hydroxylase; F3'H, flavonoid 3'-hydroxylase; F6H, flavanone 6-hydroxylase; FLS, flavonol synthase; 7-OMT, 3-methylquercetin 7-O-methyltransferase; F6-OMT-, F6-O-methyltransferase; ROMT-9, rice O-methyltransferase-9; 4CL, 4-hydroxycinnamoyl-CoA ligase; HCT, hydroxycinnamoyl-CoA shikimate/quinic acid hydroxycinnamoyl transferase; HQT, hydroxycinnamoyl CoA quinate hydroxycinnamoyl transferase; C3'H, p-coumaroyl ester 3'-hydroxylase (Alcazar Magana *et al.*, 2021, Han *et al.*, 2016, Do *et al.*, 2007, Berim and Gang, 2013, Kim, 2006)

7.1.3. Role of isolated phenolics and flavonoids compound from chamomile varieties as anticancer and antioxidant activity

Polyphenols are a class of secondary metabolites found in plants that have been widely investigated. Polyphenols are distinguished by the presence of numerous phenol (benzene) rings in their structure (Sung *et al.*, 2016). Flavonoids, phenolic acids, stilbenes, lignans are all polyphenols. Polyphenols have a wide range of biological roles, including anticancer action, due to their structural diversity (Madunic *et al.*, 2018). Their basic structures are C₆-C₃-C₆ carbon framework with various substitution that result in a variety of subclass compounds such as flavones, flavonols, flavanones, isoflavones, flavanols or catechins, and anthocyanins (Birt and Jeffery, 2013).

Flavonoids exert their anticancer effect by inducing apoptosis in cancer cells (Kopustinskiene *et al.*, 2020). Although studies have demonstrated that a high flavonoid consumption is related with a lower risk of several forms of cancer. Aside from anticancer action, flavonoid-mediated health advantages include anti-oxidant activity through the elimination of free radicals, which may damage lipids, proteins, and DNA (Sak, 2014, Sung *et al.*, 2016, Simon *et al.*, 2000). In this study, antioxidant and anticancer activity on breast cancer cells were examined and it was found that chrysopterin and apigenin significantly inhibited ZR-75 cells with IC₅₀s of 1.94 and 1.41 μM respectively without exerting antioxidant activity. While 3,5-*O*-dicafeoyl quinic acid, 1,3-*O*-dicafeoyl quinic acid and glucoferulic acid demonstrated antioxidant activity on DPPH assays with EC₅₀s of 147, 603 and 463 μM, no effect on ZR-75 cells was exhibited.

The most prevalent and investigated flavonoid is 4',5,7-trihydroxyflavone, also known as apigenin, with a molecular mass of 270.24 g/mol. Apigenin is abundant in parsley, celery, chamomile, oranges, thyme, onions, honey, spices, and plant-based drinks (Bak *et al.*, 2016, Zhou *et al.*, 2016). Previous studies showed that apigenin inhibits the growth of progesterone-dependent BT-474 breast cancer cells xenograft tumours in nude mice by increasing apoptosis and decreasing HER2/neu expression (Mafuvadze *et al.*, 2012). It was reported by other studies that apigenin-induced apoptosis in MDA MB-453, SKBR3,

and BT-474 breast cancer cells lines (Seo *et al.*, 2015b, Seo *et al.*, 2015a, Seo *et al.*, 2014). The observed inhibition of cell proliferation in these HER2-overexpressing in breast cancer was related with a caspase-dependent extrinsic apoptotic mechanism and suppression of the STAT3/VEGF signalling pathway. Furthermore, apigenin showed cytotoxic effects in MCF-7 cells were accompanied by morphological changes, reduced motility, and decreased intracellular communication due to structural abnormalities and decreased intracellular α -tubulin (Bai *et al.*, 2014). The anti-cancer activity of apigenin has been studied extensively in several research as a possible cancer-chemopreventive drug against a diverse range of cancer forms (Birt *et al.*, 1986)

Apigenin has been demonstrated orally to suppress the metastasis of ovarian cancer cell xenograft tumours in mice, and it has also been proven to suppress the invasion and migration of ovarian cancer cells when administered *in vitro*. Apigenin's downregulation of MMP-9 in exposed cells and tissues was attributed to these effects.(He *et al.*, 2012)

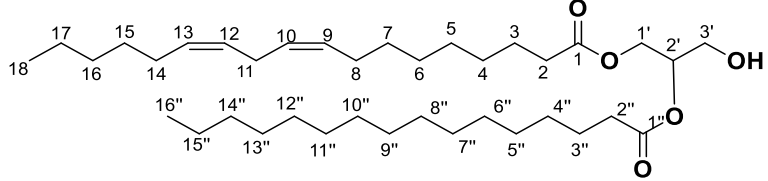
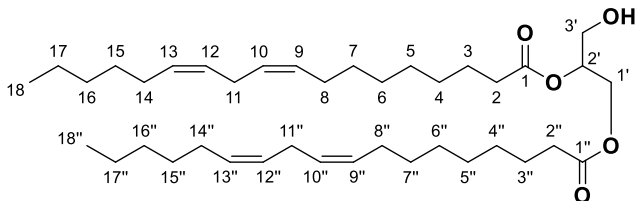
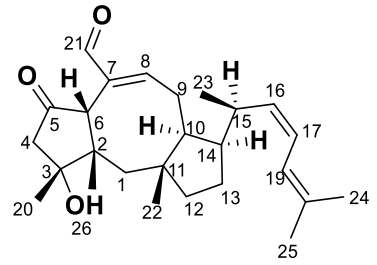
On the other hand, chrysofenetin showed antiproliferative effect on the MCF-7 breast cancer cell line With an IC₅₀ value of 0.29 μ M. It exhibited dual inhibitory activity against topoisomerase I and II. It inhibited topoisomerase II by 83–96% in the 12.5–100 μ M range. Molecular docking studies were conducted to better understand chrysofenetin's binding mechanism, interactions, and affinity for DNA and topoisomerases I and II. These experiments established that the 4-chromone core and the hydroxyl and methoxy groups are required for intercalation with DNA and inhibition of topoisomerase I and II (Sohretoglu *et al.*, 2020). Another mechanism underlying to its antiproliferative activity is the activation of the mitotic spindle checkpoint through microtubule depolymerisation which leads to cell apoptosis. The property of microtubule disassembling and their lower toxicity allow them to be considered chemopreventive agents (Sinha *et al.*, 2015).

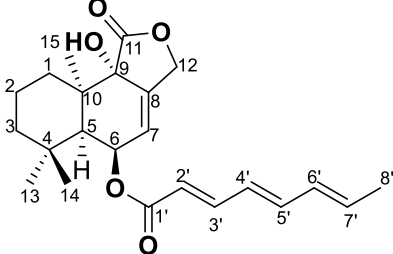
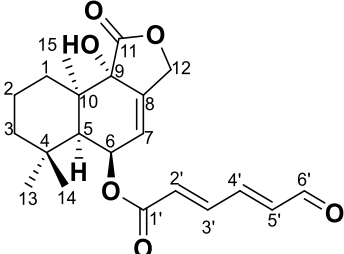
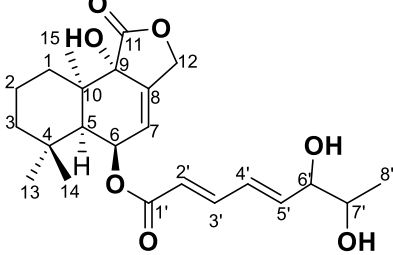
The phenolics and flavonoids demonstrated outstanding anti-inflammatory and anticancer activities (Chahar *et al.*, 2011, Talhouk *et al.*, 2007). Phenolic compounds, which are plant secondary metabolites, are well-known antioxidants and play an important roles in disease resistance (Tungmunnithum *et al.*, 2018)

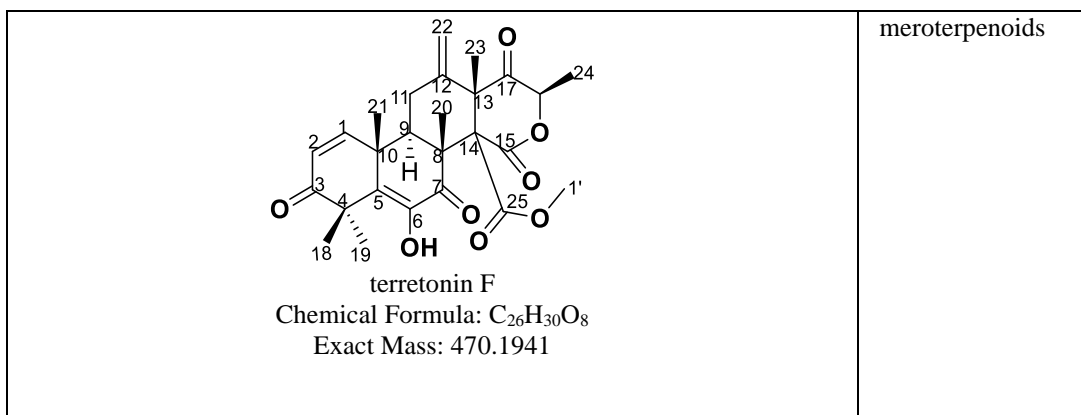
According to the literature, 1,3-diCQA (1,3-*O*-dicafeoyl quinic acid) demonstrated significant antioxidant and free radical scavenging properties. The IC₅₀ value (40 μM) of 1,3-diCQA was two-fold lower than that of Trolox (positive control), suggesting that 1,3-diCQA had higher antioxidant activity than Trolox (Danino *et al.*, 2009). Furthermore, it was stated that 3,5-DiCQA (3,5-*O*-dicafeoyl quinic acid) demonstrated significant antioxidant activity, which assayed on DPPH with of an IC₅₀ of 4.26 g/mL, ABTS radical scavenging assay with TEAC value of 0.9974, and FRAP activity with 3.84 mmole of Trolox equivalent/g activities (Hong *et al.*, 2015). Also, glucoferulic acid has also been reported in the literature to exhibit antioxidant activity (Kikuzaki *et al.*, 2002)

7.2. Anticancer compounds from the fungal endophyte of Jordanian chamomile.

Table 7.2: Compounds isolated from the *A. ustus* extracts

Isolated compounds	Type
 <p>3'-hydroxy-2'-(palmitoyloxy) propyl (9Z,12Z)-octadeca-9,12-dienoate Chemical Formula: C₃₇H₆₈O₅ Exact Mass: 592.5067 active</p>	linoleic acid derivatives
 <p>3'-hydroxy-1',2'-diyl (9Z,9'Z,12Z,12'Z)-bis(octadeca-9,12-dienoate) Chemical Formula: C₃₉H₆₈O₅ Exact Mass: 616.5125 inactive</p>	linoleic acid derivatives
 <p>ophiobolin K Chemical Formula: C₂₅H₃₆O₃ Exact Mass: 384.2666 inactive</p>	sesterpenes

 <p>9α-hydroxy-6α -[(2<i>E</i>,4<i>E</i>,6<i>E</i>)-octa-2,4,6-trienoyloxy]-5 α-drim-7-en-11,12-olide (Antibiotic RES 1149-2) Chemical Formula: C₂₃H₃₀O₅ Exact Mass: 386.2081 active</p>	sesquiterpenes
 <p>9α-hydroxy-6α -(6-oxohex-2<i>E</i>,4<i>E</i>-dienoyloxy)-5α-drim-7-en-11,12-olide (ustusolate E) Chemical Formula: C₂₁H₂₆O₆ Exact Mass: 374.1724 active</p>	sesquiterpenes
 <p>(<i>E,E</i>)-6-(6',7'-dihydroxy-2',4'-octadienyl)-strobilactone A Chemical Formula: C₂₃H₃₂O₇ Exact Mass: 420.21448 active</p>	sesquiterpenes



7.2.1. LC and direct infusion mass spectroscopic-based metabolomic profiling of terpenoids

The most often used approach in metabolomics research is MS, which is frequently used in combination with a separation technique such as LC (Madji Hounoum *et al.*, 2016). Alternatively, direct infusion MS may be also used to perform MS-based metabolomics without the separation phase (Gonzalez-Dominguez *et al.*, 2017). None of the known approaches can analyse all metabolites simultaneously. Not all mass spectrometric techniques and methods can detect all metabolites since certain metabolites do not ionise depending on the ion source or detected depending in the mass analyser or that their concentration is too low that is below the limit of detection. The dynamic range of the majority of mass spectrometers is between 3 and 4 orders of magnitude, although metabolite concentrations in biological samples are often substantially higher (Scalbert *et al.*, 2009). The number of metabolites covered by the different MS analytical techniques varies greatly, depending on whether the it is targeted or a non-targeted approach (Wishart, 2008) .

The benefit of LC-MS is that it does not need derivatisation for the detection of polar or high MWt metabolites, allowing for quick analysis of small samples. For LC-MS, a variety of detectors are available, ranging from ultra-high resolution MS (FT-ICR) or

Orbitrap FT to high resolution MS (TOF) and low resolution MS (ion traps, triple quads) to hybrid systems (Dwivedi *et al.*, 2008)

Direct infusion mass spectrometry, which also includes nanospray and microchip ionization methods, enables the quick and simple examination of a broad variety of metabolites at high speeds (Poho *et al.*, 2019). The benefit is that samples can be processed quickly. Direct infusion MS is used for detecting and characterising a wide range of metabolites from several functional categories. This depends on their polarity. We have the polar metabolites such as glycolytic intermediates, nucleotides, nucleotides including pyridine, and amino acids (Gonzalez *et al.*, 1997). On the hand, there are also non-polar components, which includes lipids and terpenoids. Employing an LC will limit or enhance their elution depending on the column absorbent.

However, direct infusion MS experiments may suffer from matrix effects, reducing sensitivity and causing ion suppression (Annesley, 2003). Direct infusion MS has low selectivity because isobaric molecules cannot be separated only by mass-to-charge ratio. Direct infusion MS has been utilised in metabolomics to analyse lipids in serum and plasma, and less commonly in other biological matrices including tissue samples (Gonzalez-Dominguez *et al.*, 2017, Draper *et al.*, 2013).

As result high-resolution mass spectrometry (HRMS) is often used for untargeted metabolomics (Kaufmann *et al.*, 2011). HRMS can determine the masses of thousands of metabolites at the same time, allowing for a more comprehensive picture of the sample's composition to be obtained. HRMS has additional benefits such as a wide dynamic range, a high mass extraction window, high mass accuracy, and strong discrimination between compounds and interferences (Marshall and Hendrickson, 2008, Xian *et al.*, 2012).

A study has been performed to compare the direct infusion MS and LC-MS techniques by assessing human foreskin fibroblasts (HFF) and human induced pluripotent stem cells (hiPSC) reprogrammed from HFF using both methods in positive ion mode. The study stated that higher number of metabolites were detected in LC-MS when compared to direct infusion. This is because LC-MS has a higher selectivity and less ion suppression.

However, the findings demonstrate that chip-MS is a rapid and straightforward approach that enables high sample throughput from small sample volumes and can identify and categorise major metabolites and cells based on their metabolic profiles (Poho *et al.*, 2019). So, these results confirmed that there is no advantage of using direct infusion over LC-MS as most biomarkers identified using direct infusion MS were also detected using LC-MS. As results, there are other purposes why the isolated compounds were showing in direct infusion but not in LC-MS.

LC-MS has the benefits of high selectivity and sensitivity. However, this procedure requires much more time for analysis than direct infusion (Dwivedi *et al.*, 2008). Other limitation is that LC-MS cannot detect all metabolites. In my study, LC-MS was not able to elute terpenoid compounds due their very low polarity and using reversed-phased columns, which is not compatible to the low polarity of the terpenoids rendering them undetectable. And in this case, LC-MS was more a disadvantage making direct infusion the better method of analysis.

In the screening, the anticancer extracts of R1-2 and R1-3 showed a unique set of discriminating metabolites from the root endophytes, which were discriminated by the “end point” metabolites N_3, N_11, N_4049, and, N_77 with ion peaks found at m/z 325.185, 339.200, 389.610, and 956.594 Da, respectively. N_11 was putatively identified as 4-methylbenzenesulfonyl-1-dodecanol. Four structurally-related bisphenol S (BPS) surfactants (decylbenzenesulphonic acid, undecylbenzenesulphonic acid, 2-dodecylbenzenesulphonic acid and tridecylbenzenesulphonic acid) have been identified as plasticiser pollutants from the Arctic region of Kongsfjorden (Nejuma *et al.*, 2017). Whereas, N_4049 was putatively identified as 6-*O*-(5-carboxy-2*E*,4*E*-pentadienoyl)11,12-epoxy-7-drimene-6 β ,9 α ,11 α -triol obtained from the marine-derived *A. ustus* and described to exhibit cytotoxic activity against tumour cell lines, including L5178Y, HeLa, and PC12 cells (Liu *et al.*, 2009). However, these low-yielding metabolites that were less than microgram levels were not feasible to be isolated.

All the isolated compounds from *A. ustus* subfractions were extracted from F11 and F12 and were detected by HRMS only by direct infusion method. It was likely that non-polar or lipophilic molecules were not eluting through the LC-MS mass spectrometer column due to low polarity of fraction F11 and 12. Thus, for this limitation, the direct infusion MS was used for the analysis of non-polar compounds and lipids (Poho *et al.*, 2019).

Direct infusion MS validated the targeted anticancer metabolites. Two discriminated metabolites with ion peaks at m/z 471.20 and 419.17 in F11-29-6 and F12-11-2. F11-29-6 was identified as terretonin F (Oleinikova *et al.*, 2016) with a MZmine ID of P_903, MW of 470.19 Da, and chemical formula of $C_{26}H_{30}O_8$. The chemical formula of F12-11-2 (N 1001) is $C_{23}H_{32}O_7$ with MW of 420.21 Da. These two compounds were previously described as having anticancer activity (Oleinikova *et al.*, 2016, Liu *et al.*, 2009). P_1346 and P_1635 have MWs of 386.207 and 374.171 Da and molecular formula of $C_{23}H_{30}O_5$ and $C_{21}H_{26}O_6$, respectively. P_1346 and P_1635 were assigned the trivial names antibiotic RES 1149-2 (F11-23) and ustusolate E (F11-29-8), respectively and had anticancer activity against breast cancer cells (ZR-75).

Two inactive subfractions were isolated and defined as glycerol 1,2-di-(9Z,12Z-octadecadienoate) with an MZmine ID of P_2370, a MW of 616.505 Da and molecular formula of $C_{38}H_{68}O_5$, which was later isolated and confirmed by NMR data F11-11 was from an unknown source. F11-17 was elucidated as ophiobolin K (F11-17), which was earlier described and isolated from various *Aspergillus* spp. It was detected with MZmine ID of P_2564, a MW of 384.2663 Da and molecular formula of $C_{25}H_{36}O_3$. Ophiobolin K showed nematocidal activity (ED_{50} 10 $\mu\text{g/mL}$) against *Caenorhabditis elegans* (Singh *et al.*, 1991). Furthermore, ophiobolin K was isolated from *A. calidoustus* obtained from *Acanthospermum australe* (Asteraceae) and was reported for its antifungal activity against fungal plant pathogens, protozoal activity against *Trypanosoma cruzi*, and cytotoxic activity against human tumoral cell lines (Rodrigues de Carvalho *et al.*, 2016).

However, one of the isolated active compounds against ZR-75 cells was not a discriminating feature in HRMS analysis, which was identified as 3'-hydroxy-2'-

(palmitoyloxy) propyl (9Z,12Z)-octadeca-9,12-dienoate (F11-12). This compound was found in the active side of OPLS-DA plot. The secondary metabolite was earlier isolated from the coralloid roots of *Cycas revoluta* (Cycadaceae). Also, it was reported to have pronounced hormogonium-inducing factor (HIF) activity (Hashidoko *et al.*, 2019).

7.2.2. Proposed biosynthetic pathways of the isolated fungal compounds

7.2.2.1 *Linoleic acid and its derivatives*

According to the suggested biosynthetic pathway of linoleic acid derivatives as seen in Figure 7.2, the process begins with one mole of acetyl-CoA and seven moles of malonyl-CoA, which serve as precursors for the production of fatty acids (Akpınar-Bayızit, 2014). After entering the FA cycle, where the acyl substrate (either as the acetyl molecule or ACP-bound) and malonyl undergo condensation in the presence of ketoacyl synthase (Gajewski *et al.*, 2017)

The resulting ketoacyl intermediate is then processed in a repetitive sequence of reaction steps that includes reduction with ketoacyl reductase (KR), dehydrogenation with a dehydratase (DH) enzyme, and another reduction step with enoyl reductase (ER) in the presence of NADPH, resulting in a fully reduced acyl chain. The formed acyl-chain serve as the precursor for the subsequent cycle. The procedure is continued until the final FA is cleaved from its thio-CoA moiety by thioesterase with hydrolysis. The C16 (palmitic acid) FA product is elongated to C18 (stearic acid) using an elongase enzyme, and then a series of desaturation reactions proceeds to add double bonds to the FA structure. Beginning with Δ^9 desaturase would form oleic acid (18:1(9)) then followed with Δ^{12} desaturase to generate linoleic acid (18:2(9,12)). The proposed biosynthesis of 2,3-dihydroxypropyl (9Z,12Z)-octadeca-9,12-dienoate, which is known as glycerol linoleate. Esterification reaction of linoleic acid in the presence of glycerol. The proposed biosynthesis of 1,2 diolinolein (F11-11) shown in Figure 7.2 could be accomplished by esterification of glycerol linoleate with linoleoyl CoA in the presence of monoacylglycerol

acyltransferase (MGAT). While 3'-hydroxy-2'-(palmitoyloxy) propyl (9Z,12Z)-octadeca-9,12-dienoate (F11-12) produced from esterification of glycerol linoleate with palmitoyl CoA in the presence of monoacylglycerol acyltransferase (MGAT).

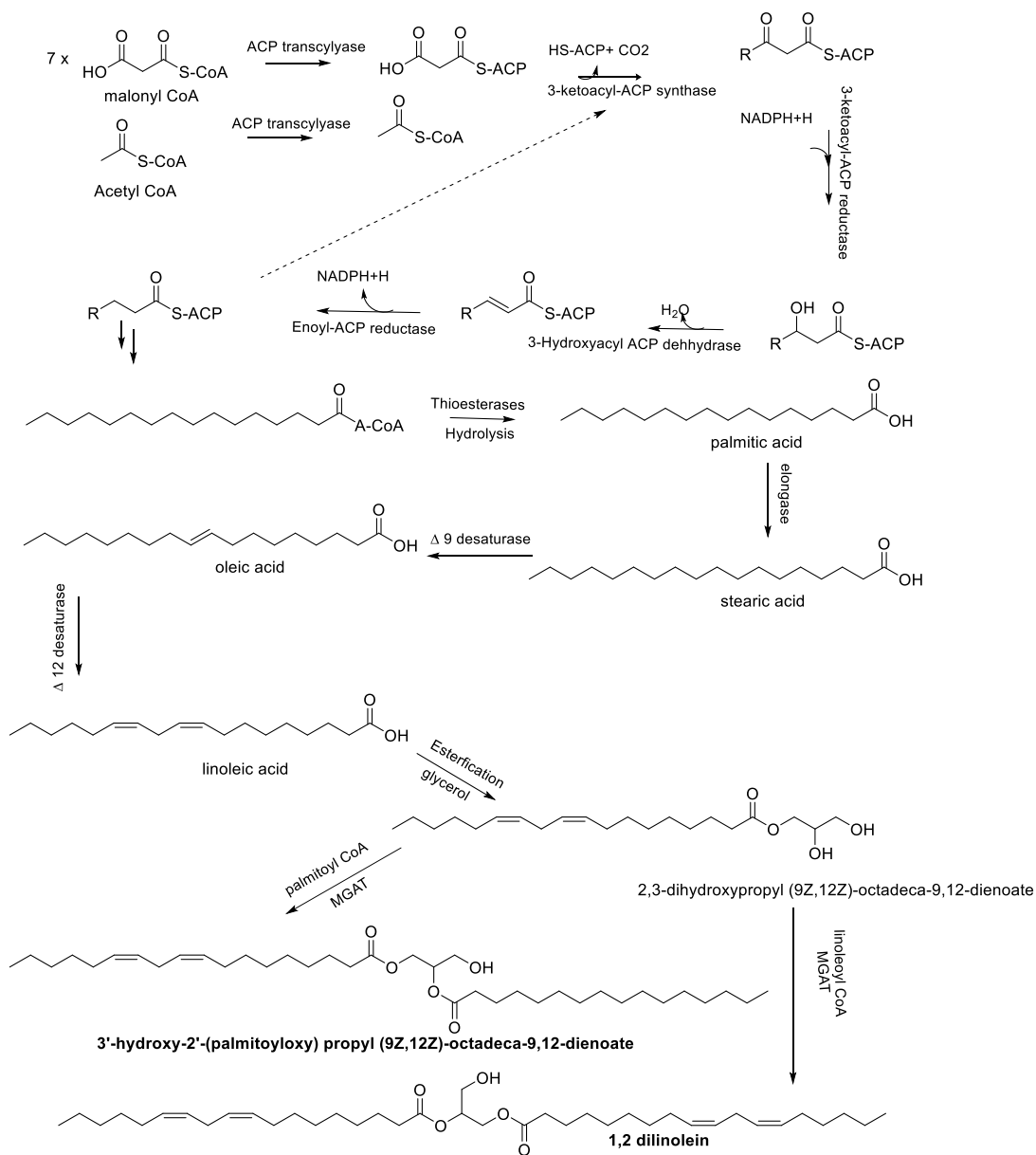


Figure 7.2:The proposed biosynthetic pathway of linoleic acid derivatives. (Gajewski *et al.*, 2017, Akpinar-Bayizit, 2014). Enzyme abbreviations; MGAT: monoacylglycerol acyltransferase.

7.2.2.2. Terpenoids

Terpenes are the most abundant class of natural compounds in terms of structural diversity. Several terpenoids with anticancer potential were isolated from *Aspergillus* spp (Nadumane *et al.*, 2016). Terpenes are composed of an isoprene, 2-methylbuta-1,3-diene (C₅H₈). Thus, terpenoids are categorised as hemiterpenes (C₅), monoterpenes (C₁₀), sesquiterpenes (C₁₅), diterpenes (C₂₀), sesterpenes (C₂₅), triterpenes (C₃₀), tetraterpenes (C₄₀), and polyterpenes (C₄₀) based on their C₅ units (Zwenger and Basu, 2008).

Drimane-type natural products are a class of sesquiterpenoids that are present in a variety of plant species, including terrestrial plants, endophytic fungi, and sponges (Figure 7.3). All terpenoid is mediated by two biosynthetic pathways to produce basic five carbon precursors from isopentenyl diphosphate (IPP) and (dimethylallyl diphosphate) DMAPP. They are synthesised from the main precursor to all sesquiterpenoids, farnesyl diphosphate (FPP), which is then catalyzed by drimenol synthase to generate a variety of unique related-natural compounds The first is the mevalonic acid (MVA) route, which is found mostly in fungi and higher plants, and the second is the 2-C-methyl-D-erythritol 4-phosphate (MEP) system, which is found primarily in bacteria (Dairi *et al.*, 2011).

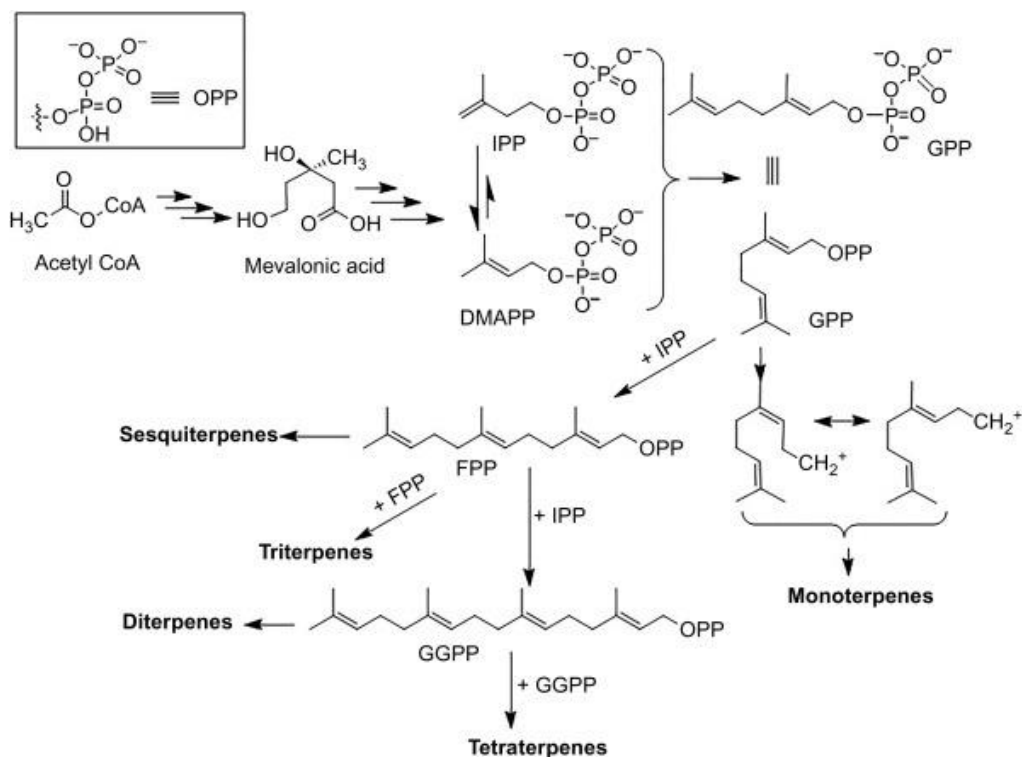


Figure 7.3: The proposed biosynthetic pathway of terpenoids derivatives (Dairi *et al.*, 2011). Abbreviation; isopentenyl pyrophosphate (IPP), dimethylallyl pyrophosphate (DMAPP), farnesyl diphosphate (FPP).

In this study, three drimane sesquiterpenes, one meroterpenes and one sesterpenes derivatives were isolated from *A. ustus*. Sesterterpene ophiobolin biosynthesis involving multiple gene clusters in *A. ustus* has also been demonstrated (Chai *et al.*, 2016). The proposed biosynthetic pathway of terpenoids derivatives were illustrated in Figure 7.4.

Initially, two moles of isopentenyl pyrophosphate (IPP) were reacted with one mole of dimethylallyl pyrophosphate (DMAPP) to generate farnesyl pyrophosphate to form drimane sesquiterpenes (FPP). An enzyme called terpene cyclase B (DrtB) was used to catalyse the production of drimenol from FPP. DrtB exhibited similar activity to that reported in plant-derived drimenol cyclases. A cytochrome P450 (DrtD) was shown to be capable of catalysing numerous hydroxylations of C6, C9, and C12, as well as additional

oxidation of hydroxy groups at C-6 and C-11, resulting in the formation of ketone and aldehyde (Wenyu *et al.*, 2022).

C11 and C12 were oxidised using a FAD-binding oxidoreductase (DrtC) to form a carboxylic acid, which was subsequently condensed with the γ -OH to yield the γ -butyrolactone ring. The polyketide synthase (DrtA) was capable of synthesising PKS chains of varied lengths (C6 and C8) that were subsequently dehydrated to varying degrees by the short-chain dehydrogenase (DrtF). Finally, the acyltransferase (DrtE) incorporated the PKS chains into the drimane skeleton to generate the various sesquiterpene esters including Antibiotic RES 1149-2, strobilactone A and ustusolate E (Wenyu *et al.*, 2022, Huang *et al.*, 2021)

While the production of ophiobolin K required 4 moles of IPP and one mole of DMAPP, this reaction was catalysed by OblA_{Au}. The ophiobolin backbone was synthesised through a sequence of oxidation reactions at C5 and C21, which were catalyzed by OblBA_{Au} and resulted in the formation of ophiobolin C. Then dehydrogenation reaction in the sidechain by OblCA_{Au} to produce ophiobolin K as shown in Figure 7.3 (Yan *et al.*, 2022).

On the other hand, terretonin F was formed by alkylation of 3,5-dimethylorsellinic acid (DMOA) with FPP to generate FPP-DMOA, which was subsequently cyclised and subjected to several oxidations steps to get preterretonin A. Trt9 oxidises preterretonin A at the C3 position. Further hydroxylated at C16 and subjected to multistep oxidation by the P450 (Trt6). The intermediate formed is transformed to terretonin F by water's nucleophilic attack on the C17 ketone with consequent lactonisation (Matsuda and Abe, 2016).

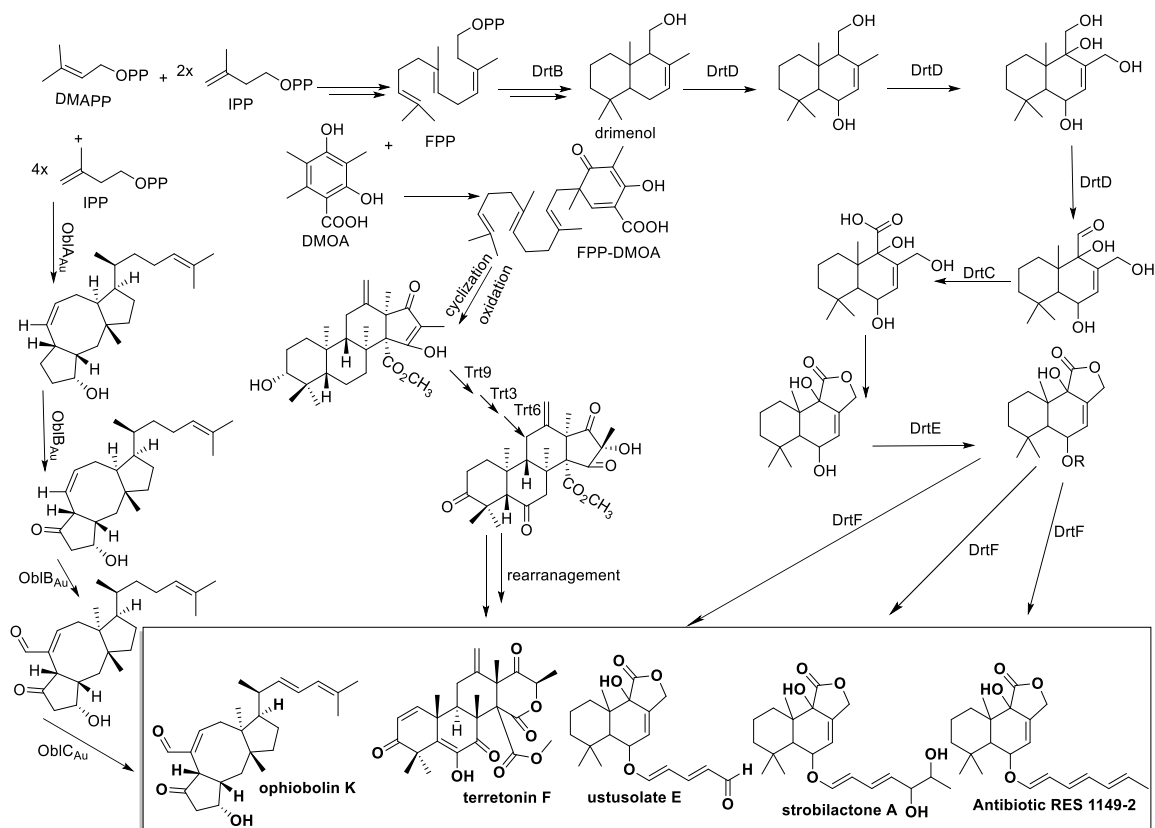


Figure 7.4: The proposed biosynthetic pathway of terpenoids derivatives (Yan *et al.*, 2022, Wenyu *et al.*, 2022, Huang *et al.*, 2021, Matsuda and Abe, 2016). The isolated compounds from *A. ustus* are in the black box. Abbreviation: isopentenyl pyrophosphate (IPP), dimethylallyl pyrophosphate (DMAPP), farnesyl diphosphate (FPP), terpene cyclase B (DrtB), cytochrome P450 (DrtD), FAD-binding oxidoreductase (DrtC), polyketide synthase (DrtA), dehydrogenase (DrtF), the acyltransferase (DrtE), 3,5-dimethylorsellinic acid (DMOA), cytochrome P450 (Trt6), OblAAu, OblBAu and OblCAu are oxidases

7.2.3. Related bioactivities of isolated compounds and their known derivatives

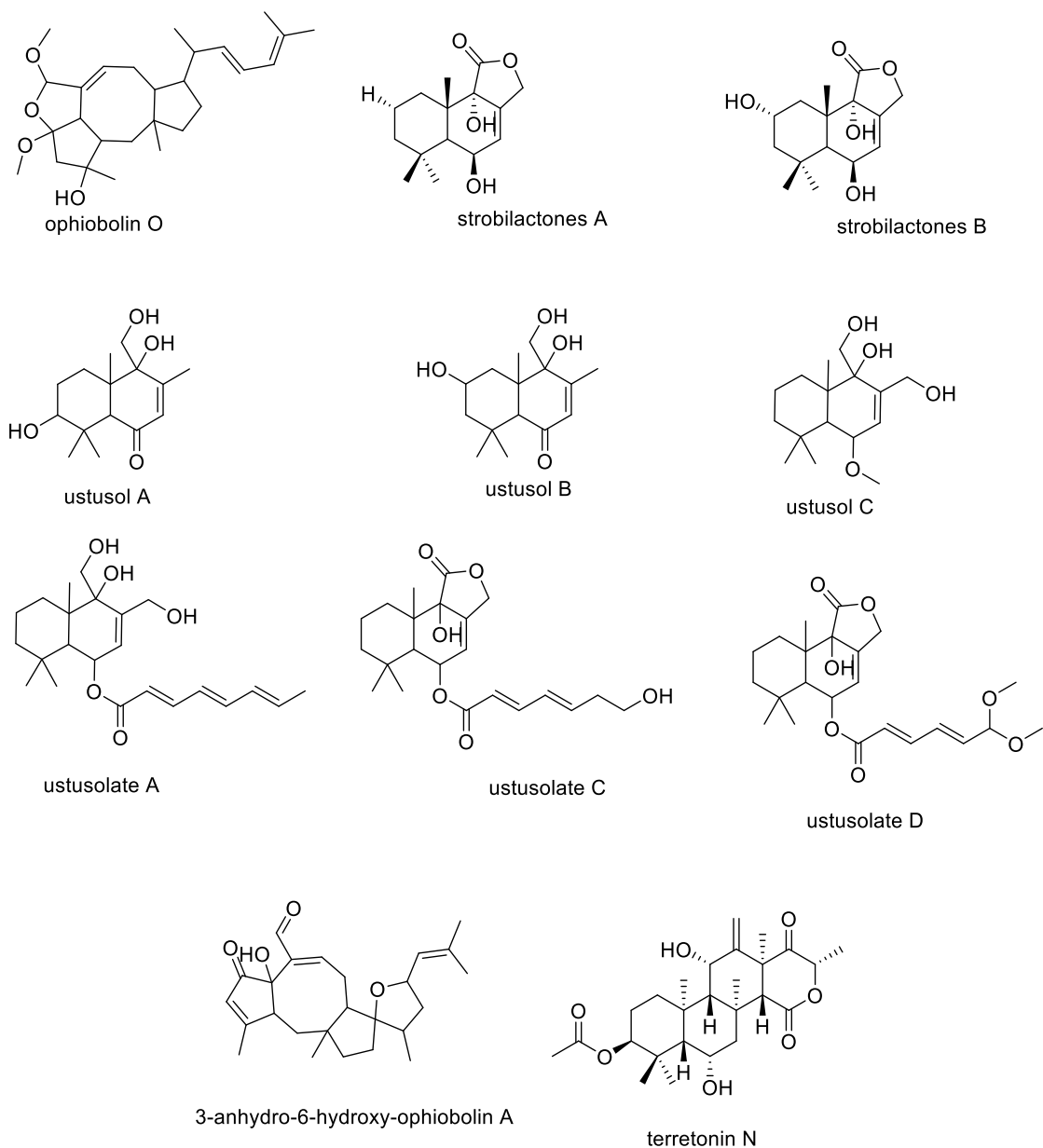


Figure 7.5: The chemical structures of bioactive congeners that are structurally related to the isolated compounds.

Isolated compounds F11-23 and F11-29-8 were identical to antibiotic RES 1149-2 and ustusolate E, respectively. Both compounds antibiotic RES 1149-2 and ustusolate E were obtained from cultures of the fungus *A. ustus*, which was isolated from the Mediterranean sponge *Suberites domuncula* showed cytotoxic activity against a panel of tumour cell lines, including mouse lymphoma (L5178Y), human cervical carcinoma (HeLa), and rat pheochromocytoma (PC12) cells, with ustusolate E being the most active (EC₅₀ against L5178Y cell line: 0.6 µg/mL) (Liu *et al.*, 2009). Ustusolate A showed weak cytotoxicity against human leukemia (HL-60) and human lung cancer (A549) cell lines with an IC₅₀ value of 20.6 and 30.0 µM, respectively.

Strobilactones A and B were isolated from the mushroom *Strobilurus ohshimae* from Japan. Strobilactones A and B inhibited cell proliferation in the human colon cancer cell line (COLO 20) at IC₅₀ of 40 g/mL and 35 g/mL, respectively. Strobilactones B had moderate antibacterial activity against *S. aureus* NBRC 13276 and *P. aeruginosa* ATCC 15442, with zones of inhibition of 12 mm in diameter at a 100 g/disk concentration. These findings demonstrated that the polarity of a compound seems to be critical for its antibacterial activity as strobilactones B is more polar than strobilactones A (Shiono *et al.*, 2007). Strobilactones A and B structures have the drimane sesquiterpene nucleus. All the isolated drimane sesquiterpenes were sharing the same structural core (strobilactones A) and only differ inside chain attached to C6 by an ester linkage.

Another *A. ustus* culture isolated from the rhizosphere soil of the mangrove plant *Bruguiera gymnorrhiza* in China also yielded eight drimane sesquiterpenes known as ustusols A to C and ustusolates A to E and RES-1149-2 (Lu *et al.*, 2009). In previous studies, RES-1149-2 was characterised as a metabolite from *A. ustus* var. *pseudorefectus* that was isolated from a soil sample. It was discovered to serve as a selective endothelin type B receptor antagonist with an IC₅₀ of 20 µg, which may have critical role in inflammatory lung diseases and diseases of the airways (Ogawa *et al.*, 1996, Uosaki *et al.*, 1996).

Drimane sesquiterpenes were also isolated from the EtOAc extract of another marine-derived fungus *A. ustus* 094102. The fungus was obtained from the rhizosphere soil of the mangrove plant *Bruguiera gymnorrhiza*, found along the South China Sea coastline. The cytotoxic effects on A549 and HL-60 cell lines were evaluated by SRB (sulforhodamine B assay) and MTT methods that involves both colorimetric assay for assessing cell viability, proliferation, and cytotoxicity. Ustusolates C and E exhibited moderate cytotoxicity against A549 and HL-60 cells with IC₅₀ values of 10.5 and 9.0 μM, respectively, and ustusolate A showed weak cytotoxicity against HL-60 and A549 cells with IC₅₀ values of 20.6 and 30.0 μM, respectively (Lu *et al.*, 2009) Meanwhile ustusolate C and D were almost identical as they share the same skeleton except for the side chain. Instead of having an aldehyde moiety at position C6', a hydroxyethyl moiety was attached to the methine group at C5'. On the other hand, ustusolate D has a methine at position 6' attached to two methoxy group.

The isolated compound F12-11-2 is identical to (*E,E*)-6-(6',7'-dihydroxy-2',4'-octadienoyl)-strobilactone A, which was obtained from marine-derived fungus *A. insuetus* (OY-207) that was isolated from the Mediterranean sponge *Psammocinia sp.* It exhibited anti-fungal activity towards *Neurospora crassa* with MIC values of 162 μM and mild cytotoxicity towards MOLT-4 human leukemia cells (Cohen *et al.*, 2011).

The ophiobolins are class of sesterterpenes that isolated from different fungal genera including *Bipolaris*, *Aspergillus*, *Sarocladium* and *Drechslera* (Yun *et al.*, 2012, Au *et al.*, 2000, Boehle *et al.*, 2002, Bencsik *et al.*, 2014) . The isolation of ophiobolins from *Aspergillus spp.* was ascribed to three distinct species: *A. calidoustus*, *A. insuetus*, and *A. keveii*, all belonging to the *Aspergillus* section *Usti*. (Chen *et al.*, 2012). Ophiobolins have a MWt of around 400 Da. All ophiobolin derivatives are tricyclic with a 5-8-5 ring structure. Ophiobolin A inhibited the growth of lung cancer A-549, colon cancer HT-29, melanoma Mel-20, leukemia P-388, and ovarian cancer OVCAR-3, with IC₅₀ values of 0.1, 0.1, 0.06 and 0.3 μM, respectively (Ahn *et al.*, 1998, Singh *et al.*, 1991, Bhatia *et al.*, 2016, Bury *et al.*, 2013a, Bury *et al.*, 2013b).

Ophiobolin O, a naturally occurring compound isolated from *A. ustus* 094102, inhibited breast cancer MCF-7 and leukemia P-388 cell lines with IC₅₀ values of 17.9 and 4.7 μM, respectively. Ophiobolin O caused G₀/G₁ phase arrest in MCF-7 cells and triggered apoptosis in MCF-7 cells. Ophiobolin O also activated JNK, p38 MAPK, and ERK, while degrading Bcl-2 phosphorylation (Ser70) (Yang *et al.*, 2012). Ophiobolin O and K were almost identical except for the functional groups at positions 5 and 21, which were different. A furan ring was present in ophiobolin O, as well as the presence of two anomeric carbons (C5 and C21). Meanwhile, carbonyl moiety was present at position 5 and 21 in ophiobolin K (Zhang *et al.*, 2012). MCF-7 and ZR-75 are human breast cancer cells that belong to the Luminal A subtype and are both positive for the oestrogen receptor (ER). However, only ZR-75 cells are positive for the progesterone receptor (PR), while MCF-7 cells are not (Ding *et al.*, 2021). ZR-75 cells exhibit a hypertriploid chromosomal number, express oestrogen receptors, and generate large quantities of mucin mRNA (MUC-1) in the blood. MCF-7 is estrogen-dependent, which were more commonly employed in the research of 18F-FES (F-fluoroestradiol) than ZR-75-1 cells, although ZR-75-1 cells were more consistent with the cells found in the majority of breast cancer patients (Chang *et al.*, 2016, Ding *et al.*, 2021).

Further research on ophiobolin derivatives revealed 3-anhydro-6-hydroxyophiobolin A to be active against lung cancer (HepG2) and leukemia (K-562) cell lines with IC₅₀ values of 6.5 and 4.1 μM, respectively. It promotes apoptosis in human k562 leukemic cells by lowering the levels of the c-myc and bcl-2 proteins, making it a prospective candidate for the development of new anti-cml (chronic myelogenous leukemia) therapeutics, according to the findings of the study (Wang *et al.*, 2013). Both 3-anhydro-6-hydroxyophiobolin A and ophiobolin K share the same a tricyclic ophiobolin skeleton. The difference in the skeleton were addition of double bond at position 3\4 and hydroxy group at C6 in 3-anhydro-6-hydroxyophiobolin A. Also, different substitution at position 15 was observed in 3-anhydro-6-hydroxyophiobolin A. There has been no report about the anticancer activity for terretonin F. Terretonin F was isolated from the marine-derived fungus *A. insuetus*, which was obtained from the sponge *Petrosia ficiformi*. It was only

reported to inhibit the integrated chain of NADH oxidase activity with an IC₅₀ value of 1.2 µM. Therefore inhibiting the mitochondrial respiratory chain that is of importance in degenerative diseases such as Parkinson's and Huntington's diseases. (Lopez-Gresa *et al.*, 2009). Terretonin N was isolated from the thermophilic fungus *A. terreus* TM8 and demonstrated significant antiproliferative activity against ovarian cancer cells (SKOV3) and metastatic prostate cells (PC-3), with IC₅₀ values of 1.2 g/mL and 7.4 g/mL, respectively. The investigated fungal metabolites elevated early and late apoptotic rates with little or no necrotic apoptotic pathway. The outcomes of this study supported terretonin N's potential biological properties as an anticancer agent through stimulation of apoptosis. (Ghfar *et al.*, 2021).

Terretonin F and N were structurally related, both having four rings. Terretonin F has 12 degrees of unsaturation whereas terretonin N has 8. The additional four degrees of unsaturation in terretonin F accounted for two double bonds between C1/C2 and C5/C6, and two carbonyl moieties at positions 3 and 7. Furthermore, a methyl ester moiety was substituted at C14 in terretonin F and at C3 in terretonin N. In addition, a hydroxy moiety was bounded to C11 in terretonin N.

7.3. Relationship between Jordanian chamomile and its endophyte

Endophytes are harmless to their hosts' tissues and have a beneficial relationship with plants (Grayer and Kokubun, 2001). Endophytic interactions are not usually the case. These interactions can also be parasitic (Kaul *et al.*, 2012). Endophytes have been found in stems, leaves and roots of the plant (Taylor and Taylor, 2000). So, there's a possibility of horizontal genetic information transmission between hosts and endophytes (Stierle *et al.*, 1993). As a result, it is possible that the same biosynthetic pathway has evolved in both the host plant and the endophyte, resulting in the synthesis of secondary metabolites that are comparable in both species (Bömke and Tudzynski, 2009, Alvin *et al.*, 2014).

Endophytic fungi and bacteria are living creatures that do not have chlorophyll and so, they do not have the capacity to photosynthesise. Therefore, they spend the majority of their life cycles colonising host species, particularly plants, in search of carbon and energy

sources, without exhibiting any visible signs of illness (Grayer and Kokubun, 2001, Nisa *et al.*, 2015). However, plants benefit from the secondary metabolites that are generated by endophytes. It is considered that the capacity of a plant to adapt to biotic and abiotic stress factors is influenced by the secondary metabolites generated by the endophytes in the plant's environment (Giordano *et al.*, 2009). Thus, a plant's biological defence against pathogens is maintained by its symbiotic interaction with endophytes (Alvin *et al.*, 2014). This can be accomplished by the endophyte releasing antibacterial, antifungal, antiviral, or insecticidal secondary metabolites that directly attack the pathogens and lyse the affected cells, or by inducing the host plant's defence mechanism and promoting its growth in order to compete for cell apoptosis, thereby enhancing the host plant's growth and competitiveness in nature (Alvin *et al.*, 2014, Nisa *et al.*, 2015, Strobel and Daisy, 2003, Kloepper and Ryu, 2006). Additionally, the secondary metabolites produced by endophytes may aid the host plant in adapting to harsh environmental circumstances. The synthesis of phytohormones accelerates the development of plants colonised by specific endophytes (Owen and Hundley, 2004).

In this study, the Jordanian chamomile plant was used. Chamomile is a flowering plant, which was used in traditional folk medicine for centuries, and it is widely distributed around the globe (Singh *et al.*, 2011). Among medicinal plants, it is commonly referred to as the star (Schilcher, 1987). Chamomile contains around 120 different secondary metabolites. The most important metabolites include sesquiterpenes, flavonoids, coumarins, and polyacetylenes, those compounds families have proved different biological activities (Pirzad *et al.*, 2006).

Chamomile contains 0.2-2% of volatile oil, the major components are essential oil and flavonoids, which have several biological activities. Apigenin and its glycosides are the most promising flavonoids (Schilcher, 1987). German chamomile flowers contain a higher concentration of terpenoids and chamazulene (a deep blue volatile principle) than Roman chamomile flowers, while Roman chamomile flowers generate ester-like compounds. (Srivastava *et al.*, 2010).

In this study, Jordanian chamomile produced 3,5-di-*O*-caffeoylquinic acid (F8-ChJ) which exhibited the most potent antioxidant activity with EC₅₀ value of 147 μM. Two endophytes, *A. ustus* and *A. solani*, were isolated from *M. chamomilla* based on their chemical profile and biological activity. *A. ustus* extracts produced compounds that have anticancer activity against breast cancer cells (ZR-75). In the literature, five fungal endophytes have been isolated from *M. chamomilla* from North-eastern of Iran, which included *Phoma haematocycla*, *Paramyrothecium roridum*, *Stemphylium amaranthi*, *Xylariaceae sp.*, *Epicoccum nigrum* and *Didymella tanacetii*. The isolated endophytic fungi were tested for their ability to produce L-asparaginase, which is used as first line of treatment in acute lymphoblastic leukaemia (Theantana *et al.*, 2009).

Endophytes can produce bioactive compounds that plants employ to defend themselves against pathogens, and some of these substances have been shown to be effective in the identification of new drugs. Recent investigations have identified hundreds of natural compounds from endophytes, including alkaloids, terpenoids, flavonoids, and steroids. The majority of bioactive compounds extracted from endophytes have been shown to have antibacterial, immunosuppressive, anticancer, and biological control activity (Joseph and Priya, 2011).

8. Conclusion and Future Work

The present project aimed to investigate the differences in the production of secondary metabolites of two chamomile varieties grown under different environmental conditions. The Jordanian chamomile was collected with exact geographical information; however, no precise collection location could be obtained for the European chamomile. In Jordan, chamomile is only grown in gardens for individual use and not cultivated for commercial applications. Unlike the European chamomile, which has been widely cultivated in such countries like Germany and UK and sold commercially as herbal remedy for alternative medicine. In addition to that is the isolation of anticancer-active metabolites against breast cancer from plant endophytic fungi obtained from *M. chamomilla*. A metabolomics-guided isolation approach was applied, using NMR and HR-LC/MS as analytical platforms to pinpoint possible bioactive discriminating metabolites. Further fermentation and growth parameters were optimised on the endophytic fungi to improve the production yield of the respective bioactive target metabolites. The DNP database was employed as a dereplication tool using an Excel MACRO that allowed the identification of known metabolites.

8.1 Metabolomic profiling of potential anticancer and antioxidant metabolites from European and Jordanian chamomile for targeted isolation work

M. chamomilla is one of traditional folk medicinal plants used for centuries. It was used for the treatment of several disease including stomachache, flatulence, carminative, gingivitis, diuretic, anti-inflammatory, aromatic, and acute respiratory infection. Both European and Jordanian chamomile were obtained from same species but the different geographical location. Different chemical profile and biological activities were expected, which was confirmed after analysis of their similar NMR, HR-LC/MS data, and biological results.

After fractionation of EtOAc of two chamomile varieties, both European and Jordanian chamomile fractions produced dicaffeoyl quinic acid isomers that exhibited an antioxidant

activity with EC₅₀ values of 603 (F11-ChE) and 147 (F8-ChJ) μM. However, the Jordanian variant exhibited the most potent antioxidant activity because dicaffeoyl quinic acid was present as a major compound in high concentration. This was rationalised due to the warm and dry weather in Jordan which lead to increase the concentration of polyphenols (Nogués *et al.*, 2014).

Nevertheless, it was clear that the European chamomile were producing more classes of metabolites, as shown by the metabolomic data analysis. The isolated target compounds were all known compounds. The results revealed that chrysosplenetin (F2-ChE) and apigenin (F8-ChE) compounds from European fractions had anticancer activity against ZR-75 cells with IC₅₀ values of 1.94 and 1.41 μM, respectively. Those compounds were also assayed for their toxicity against human foreskin fibroblast cells (HS-27) and both were not toxic and selective. In addition, glucoferulic acid (F12-ChE) from European chamomile displayed antioxidant activity with EC₅₀ values equal to 436 μM. Changes in metabolite production were perceived between two varieties.

According to the results, the compounds chrysosplenetin (F2-ChE) and apigenin (F8-ChE) from European fractions exhibited anticancer activity against ZR-75 cells with respective IC₅₀ values of 1.94 and 1.41 μM. These compounds were also tested for their toxicity against human foreskin fibroblast cells (HS-27), both were selective and nontoxic. In addition, glucoferulic acid (F12-ChE) demonstrated antioxidant activity with an EC₅₀ value of 436 μM. It was observed that there were differences in the production of metabolites between the two varieties. The different environmental condition to which the Jordanian and European chamomile were exposed to affect the type of the isolated compounds

8.2. Metabolomic profiling of potential anticancer metabolites from *M. chamomilla* associated endophyte

The preliminary bioassay screening of the initial crude extract showed inhibition against breast cancer cell growth at greater than 80%. The extract gave an IC₅₀ value of 1.3 μg/mL.

ITS gene sequencing was performed to determine the taxonomy of the fungi that produced extracts with anticancer properties. These fungi included *A. ustus* and *A. solani*. *A. ustus* was then further optimised on four different media namely, Wickersham broth, potato-dextrose, oat and rice. According to the AlamarBlue® assay results, in addition to its chemical profile, the uniqueness of the extracts was determined by multivariate analysis. *A. ustus* was scaled-up on potato-dextrose medium, incubated for 30 days at 27C°. The scaled-up crude extracts of *A. ustus* was fractionated by MPLC. Multivariate analysis of ¹H NMR between active versus inactive fractions identified several distinct chemical fingerprints belonging to the active fractions. Also, integrating HR-LCMS data with chemometric analysis, such as PLS-DA, OPLS-DA, S-plots along with the bioactivity results of the fractions of *A. ustus* were used to identify the presence of active metabolites in the samples.

Further fractionation was performed on Fractions -11 and -12 from the extract derived from the potato-dextrose with an average breast cancer cell inhibition of more than 95% at 30µg/mL with IC₅₀ value of less than 5.5 µg/mL. Multivariate analysis was applied again to predict the most statistically probable bioactive metabolites of *A. ustus* and were targeted for further isolation and elucidation work. An available online processing platform such as MZmine and an in-house excel Macro was coupled to DNP to readily identify the bioactive metabolites. Seven compounds were isolated, three drimane sesquiterpenes derivatives including 9α-hydroxy-6α-[(2*E*,4*E*,6*E*)-octa-2,4,6-trienoyloxy]-5α-drim-7-en-11,12-olide (F11-23), ustusolate E (F11-29-8) and *E,E*-6-(6',7'-dihydroxy-2',4'-octadienoyl)-strobilactone A (F12-11-2). Terretonin F (F11-29-6), ophiobolin K (F11-17). Additionally, two linoleic acid derivatives including 1',2'-diolinolein (F11-11) and 3'-hydroxy-2'-(palmitoyloxy) propyl (9*Z*,12*Z*)-octadeca-9,12-dienoate (F11-12). All the predicted bioactive compounds were generated by an OPLS-DA S-plot of the mass spectral data obtained by direct infusion. Interestingly, these targeted and isolated compounds exhibited good activity against the tested breast cancer cell with IC₅₀ values less than 6 µM. Only the isolated bioactive compound F11-12 was not detected amongst the target metabolites predicted by multivariate analysis. Therefore,

HR-LCMS and NMR-based metabolomics were effective in predicting active compounds from *A. ustus* against breast cancer cells.

Metabolomics approach was also accomplished on analysing the optimum condition for medium-scale fermentation of *A. solani*. Five different media were utilised including, Wickersham broth, potato-dextrose, oat, rice, and malt extract. However, *A. solani* was discontinued for further scale-up and isolation work due to loss of bioactivity during media optimisation. Multivariate analysis of the production of metabolites were done to attempt to explain the changes occurring in the fungal strains during the media optimisation. The chemical profiles of *A. solani* extract grown on MAmedia for preliminary screening were compared to those obtained from the other five different media employed for media optimisation work. However, chemical profiles of the extracts of the fungi incubated on the various media were all found to be different. Media variation affected the chemical profile of the afforded extracts.

8.3. Future work

Some of the putatively active target compounds could not be isolated due to their low yield in the crude extracts, as a result, the scale-up fermentation volume or starting biomass should be increased. The use of hyphenated NMR, such as cryoprobe NMR, may be used to analyse pure compounds weighing less than 1 mg. Measurement of optical rotation for some of the isolated were needed such as glyceryl linoleate derivatives and F12-11-2 will be needed to help determine the relative stereochemistry of the isolated lipids, which was not possible to be currently done at the University of Strathclyde. Despite the outstanding *in vitro* activities of the isolated compounds, it is believed that the *in vivo* potential of the chosen active metabolites will ultimately lead to a greater understanding of their exact mechanisms of action.

Nowadays, the identification of novel secondary metabolites produced by endophytes is becoming to be a more difficult task. To optimise the production of novel bioactive fungal

metabolites, different other strategies could have been used. Interactions between bacteria and fungus inside the host plant create competition for nutrients and spaces, that stimulates the biosynthesis of bioactive secondary metabolites. Numerous investigations have shown that the interaction between bacteria and fungi could generate active secondary metabolites. A co-cultivation method that applies stress conditions between fungus or fungi and bacteria could have also been employed to improve the production yield of the target metabolite (Kalaitzis, 2013, Nah *et al.*, 2013, Stevens *et al.*, 2013, Zhang *et al.*, 2017). In a co-culture system, the two species will develop in symbiosis or compete until they reach an equilibrium phase. This will include interactions between the two species that will lead to produce metabolites that are not produced in a one-strain environment (Zhang *et al.*, 2017). Although, *A. solani* showed evidence for an unstable production of its secondary metabolites with loss of bioactivity during the scale-up process, small new scale-up fermentations could be repeated using a variation of other culture conditions to verify the stability the production of its anticancer metabolites.

9. References

- ABE, M., YAMANO, T., YAMATODANI, S., KŌZU, Y., KUSUMOTO, M., KOMATSU, H. & YAMADA, S. 2014. On the new peptide-type ergot alkaloids, ergosecaline and ergosecalinine. *Bull Agric Chem Soc Japan*, 23, 246-248.
- ABRAHAM, E. P., CHAIN, E., FLETCHER, C. M., FLOREY, H. W., GARDNER, A.D., HEATLEY, N. G. & JENNINGS, M. A. 1992. Further observations on penicillin. 1941. *Eur J Clin Pharmacol*, 42, 3-9.
- AHN, J.-W., LEE, M.-K., CHOI, S.-U., LEE, C.-O. & KIM, B.-S. 1998. Cytotoxic ophiobolins produced by *Bipolaris* sp. *J Microbiol Biotech*, 8, 406-408.
- AKARACHANTACHOTE, N., CHADCHAM, S. & SAITHANU, K. 2014. Cutoff threshold of variable importance in projection for variable selection. *Int J Pure App Math*, 94, 307 - 322.
- AKPINAR-BAYIZIT, A. 2014. Fungal lipids: The biochemistry of lipid accumulation. *Int J Chem Eng Appl*, 5, 409-414.
- AL-RIMAWI, F., RISHMAWI, S., ARIQAT, S. H., KHALID, M. F., WARAD, I. & SALAH, Z. 2016. Anticancer activity, antioxidant activity, and phenolic and flavonoids content of wild *Tragopogon porrifolius* plant extracts. *Evid Based Complement Alternat Med.*, 2016, 9612490.
- ALAMGIR, A. 2017. *Therapeutic use of medicinal plants and their extracts: volume 1*, Springer Cham.
- ALCAZAR MAGANA, A., KAMIMURA, N., SOUMYANATH, A., STEVENS, J. F. & MAIER, C. S. 2021. Caffeoylquinic acids: chemistry, biosynthesis, occurrence, analytical challenges, and bioactivity. *Plant J*, 107, 1299-1319.
- ALVIN, A., MILLER, K. I. & NEILAN, B. A. 2014. Exploring the potential of endophytes from medicinal plants as sources of antimycobacterial compounds. *Microbiol Res*, 169, 483-95.
- ALWAHSH, M., KHAIRUDDEAN, M. & CHONG, W. 2015. Chemical constituents and antioxidant activity of *Teucrium barbeyanum* Aschers. *Rec Nat Prod*, 9, 159-163.
- ALY, A.H., DEBBAB, A., CLEMENTS, C., EDRADA-EBEL, R., ORLIKOVA, B., DIEDERICH, M., WRAY, V., LIN, W. & PROKSCH, P. 2011A. NF kappa B inhibitors and antitrypanosomal metabolites from endophytic fungus *Penicillium* sp. isolated from *Limonium tubiflorum*. *Bioorg Med Chem*, 19, 414-421.
- ALY, A.H., DEBBAB, A., KJER, J. & PROKSCH, P. 2010. Fungal endophytes from higher plants: a prolific source of phytochemicals and other bioactive natural products. *Fungal Divers*, 41, 1-16.
- ALY, A.H., DEBBAB, A. & PROKSCH, P. 2011b. Fungal endophytes: unique plant inhabitants with great promises. *Appl Microbiol Biotechnol*, 90, 1829-45.
- ALY, A.H., EDRADA-EBEL, R., WRAY, V., MUELLER, W. E. G., KOZYTSKA, S., HENTSCHEL, U., PROKSCH, P. & EBEL, R. 2008. Bioactive metabolites from the endophytic fungus *Ampelomyces* sp. isolated from the medicinal plant *Urospermum picroides*. *Phytochemistry*, 69, 1716-1725.

- ANNESLEY, T. M. 2003. Ion suppression in mass spectrometry. *Clin Chem*, 49, 1041-1044.
- ARBONA, V., MANZI, M., OLLAS, C. D. & GÓMEZ-CADENAS, A. 2013. Metabolomics as a tool to investigate abiotic stress tolerance in plants. *Intl J Mol Sci*, 14, 4885-4911.
- AU, T. K., CHICK, W. S. H. & LEUNG, P. C. 2000. The biology of ophiobolins. *Life Sci*, 67, 733-742.
- BAI, H., JIN, H., YANG, F., ZHU, H. & CAI, J. 2014. Apigenin induced MCF-7 cell apoptosis-associated reactive oxygen species. *Scanning*, 36, 622-31.
- BAK, M. J., DAS GUPTA, S., WAHLER, J. & SUH, N. 2016. Role of dietary bioactive natural products in estrogen receptor-positive breast cancer. *Semin Cancer Biol*, 40-41, 170-191.
- BALDWIN, E. & OSHEROFF, N. 2005. Etoposide, topoisomerase II and cancer. *Curr Med Chem Anti-Cancer Agents*, 5, 363-372.
- BALUNAS, M. J. & KINGHORN, A.D. 2005. Drug discovery from medicinal plants. *Life Sci*, 78, 431-441.
- BARAN, R., KOCHI, H., SAITO, N., SUEMATSU, M., SOGA, T., NISHIOKA, T., ROBERT, M. & TOMITA, M. 2006. MathDAMP: a package for differential analysis of metabolite profiles. *BMC Bioinform*, 7, 1-9.
- BARTON, D., METH-COHN, O. & NAKANISHI, K. 1999. *Comprehensive natural products chemistry*, Elsevier Science Ltd.
- BECKER, S., KORTZ, L., HELMSCHRODT, C., THIERY, J. & CEGLAREK, U. 2012. LC-MS-based metabolomics in the clinical laboratory. *J Chromatogr B*, 883, 68-75.
- BEHIE, S. W., MOREIRA, C. C., SEMENTCHOUKOVA, I., BARELLI, L., ZELISKO, P. M. & BIDOCHKA, M. J. 2017. Carbon translocation from a plant to an insect-pathogenic endophytic fungus. *Nat Comm*, 8, 14245.
- BENCSEK, O., PAPP, T., BERTA, M., ZANA, A., FORGO, P., DOMBI, G., ANDERSSON, M. A., SALKINOJA-SALONEN, M., VAGVOLGYI, C. & SZEKERES, A. 2014. Ophiobolin A from *Bipolaris oryzae* perturbs motility and membrane integrities of porcine sperm and induces cell death on mammalian somatic cell lines. *Toxins*, 6, 2857-71.
- BERG, G. & HALLMANN, J. 2006. Control of plant pathogenic fungi with bacterial endophytes. In: SCHULZ, B. J. E., BOYLE, C. J. C. & SIEBER, T. N. (eds.) *Microbial Root Endophytes*. Berlin, Heidelberg: Springer Berlin Heidelberg.
- BERIM, A. & GANG, D. R. 2013. The roles of a flavone-6-hydroxylase and 7-O-demethylation in the flavone biosynthetic network of sweet basil. *J Biol Chem*, 288, 1795-805.
- BHATIA, D. R., DHAR, P., MUTALIK, V., DESHMUKH, S. K., VEREKAR, S. A., DESAI, D. C., KSHIRSAGAR, R., THIAGARAJAN, P. & AGARWAL, V. 2016. Anticancer activity of Ophiobolin A, isolated from the endophytic fungus *Bipolaris setariae*. *Nat Prod Res*, 30, 1455-8.

- BHIMBA, B. V., AGNEL, D. F. D. A., MATHEW, J. M., JOSE, G. M., JOEL, E. L. & THANGARAJ, M. 2012. Anticancer and antimicrobial activity of mangrove derived fungi *Hypocrea lixii* VB1. *Chin J Nat Med*, 10, 77-80.
- BIRT, D. F. & JEFFERY, E. 2013. Flavonoids. *Adv Nutr*, 4, 576-577.
- BIRT, D. F., WALKER, B., TIBBELS, M. G. & BRESNICK, E. 1986. Anti-mutagenesis and anti-promotion by apigenin, robinetin and indole-3-carbinol. *Carcinogenesis*, 7, 959-963.
- BLUNT, J., MUNRO, M. & UPJOHN, M. 2012. The role of databases in marine natural products research. *Handbook Mar Nat Prod*, 1, 389-422.
- BOEHLE, A., KURDOW, R., BOENICKE, L., SCHNIEWIND, B., FAENDRICH, F., DOHRMANN, P. & KALTHOFF, H. 2002. Wortmannin inhibits growth of human non-small-cell lung cancer in vitro and in vivo. *Langenbeck's Arch Surgery*, 387, 234-239.
- BÖMKE, C. & TUDZYNSKI, B. 2009. Diversity, regulation, and evolution of the gibberellin biosynthetic pathway in fungi compared to plants and bacteria. *Phytochemistry*, 70, 1876-1893.
- BRAY, F., FERLAY, J., SOERJOMATARAM, I., SIEGEL, R. L., TORRE, L. A. & JEMAL, A. J. C. A. C. J. F. C. 2018. Global cancer statistics 2018: GLOBOCAN estimates of incidence and mortality worldwide for 36 cancers in 185 countries. 68, 394-424.
- BURMEISTER, A. R. 2015. Horizontal Gene Transfer. *Evol Med Public Health*, 2015, 193-4.
- BURY, M., GIRAULT, A., MEGALIZZI, V., SPIEGL-KREINECKER, S., MATHIEU, V., BERGER, W., EVIDENTE, A., KORNIENKO, A., GAILLY, P., VANDIER, C. & KISS, R. 2013A. Ophiobolin A induces paraptosis-like cell death in human glioblastoma cells by decreasing BKCa channel activity. *Cell Death Dis*, 4, e561.
- BURY, M., NOVO-UZAL, E., ANDOLFI, A., CIMINI, S., WAUTHOZ, N., HEFFETER, P., LALLEMAND, B., AVOLIO, F., DELPORTE, C., CIMMINO, A., DUBOIS, J., VAN ANTWERPEN, P., ZONNO, M. C., VURRO, M., POU MAY, Y., BERGER, W., EVIDENTE, A., DE GARA, L., KISS, R. & LOCATO, V. 2013b. Ophiobolin A, a sesterterpenoid fungal phytotoxin, displays higher in vitro growth-inhibitory effects in mammalian than in plant cells and displays in vivo antitumor activity. *Int J Oncol*, 43, 575-85.
- BYLESJÖ, M., RANTALAINEN, M., CLOAREC, O., NICHOLSON, J. K., HOLMES, E. & TRYGG, J. 2006. OPLS discriminant analysis: combining the strengths of PLS-DA and SIMCA classification. *J Chemom*, 20, 341-351.
- CARLOTTO, J., DA SILVA, L. M., DARTORA, N., MARIA-FERREIRA, D., SABRY, D. D. A., FILHO, A. P. S., DE PAULA WERNER, M. F., SASSAKI, G. L., GORIN, P. A. J., IACOMINI, M., CIPRIANI, T. R. & DE SOUZA, L. M. 2015. Identification of a dicaffeoylquinic acid isomer from *Arctium lappa* with a potent anti-ulcer activity. *Talanta*, 135, 50-57.

- CHADHA, N., MISHRA, M., RAJPAL, K., BAJAJ, R., CHOUDHARY, D. K. & VARMA, A. 2015. An ecological role of fungal endophytes to ameliorate plants under biotic stress. *Arch Microbiol*, 197, 869-881.
- CHAGAS-PAULA, D. A., ZHANG, T., DA COSTA, F. B. & EDRADA-EBEL, R. 2015. A metabolomic approach to target compounds from the Asteraceae family for dual COX and LOX inhibition. *Metabolites*, 5, 404-430.
- CHAHAR, M. K., SHARMA, N., DOBHAL, M. P. & JOSHI, Y. C. 2011. Flavonoids: A versatile source of anticancer drugs. *Pharmacog Rev*, 5, 1.
- CHAI, H., YIN, R., LIU, Y., MENG, H., ZHOU, X., ZHOU, G., BI, X., YANG, X., ZHU, T., ZHU, W., DENG, Z. & HONG, K. 2016. Sesterterpene ophiobolin biosynthesis involving multiple gene clusters in *Aspergillus ustus*. *Sci Rep*, 6, 27181.
- CHANG, H.-T., CHOU, C.-T., LIN, Y.-S., SHIEH, P., KUO, D.-H., JAN, C.-R. & LIANG, W.-Z. 2016. Esculetin, a natural coumarin compound, evokes Ca²⁺ movement and activation of Ca²⁺-associated mitochondrial apoptotic pathways that involved cell cycle arrest in ZR-75-1 human breast cancer cells. *Tumor Biol*, 37, 4665-4678.
- CHEN, G.-D., LI, Y.-J., GAO, H., CHEN, Y., LI, X.-X., LI, J., GUO, L.-D., CEN, Y.-Z. & YAO, X.-S. 2012. New azaphilones and chlorinated phenolic glycosides from *Chaetomium elatum* with caspase-3 inhibitory activity. *Planta Med*, 78, 1683-1689.
- CHOW, Y. & TING, A.S. 2015. Endophytic L-asparaginase-producing fungi from plants associated with anticancer properties. *J Adv Res*, 6, 869-876.
- COHEN, E., KOCH, L., THU, K. M., RAHAMIM, Y., ALUMA, Y., ILAN, M., YARDEN, O. & CARMELI, S. 2011. Novel terpenoids of the fungus *Aspergillus insuetus* isolated from the Mediterranean sponge *Psammocinia* sp. collected along the coast of Israel. *Bioorg Med Chem*, 19, 6587-6593.
- COVINGTON, B. C., MCLEAN, J. A. & BACHMANN, B. O. 2017. Comparative mass spectrometry-based metabolomics strategies for the investigation of microbial secondary metabolites. *Nat Prod Rep*, 34, 6-24.
- CRAGG, G. M. 1998. Paclitaxel (Taxol®): a success story with valuable lessons for natural product drug discovery and development. *Med Res Rev*, 18, 315-331.
- CUTLER, H. G., CRUMLEY, F. G., COX, R. H., SPRINGER, J. P., ARRENDALE, R. F., COLE, R. J. & COLE, P. D. 2002. Ophiobolins G and H: new fungal metabolites from a novel source, *Aspergillus ustus*. *J Agric Food Chem*, 32, 778-782.
- DAI, J., KROHN, K., FLOERKE, U., PESCIPELLI, G., KERTI, G., PAPP, T., KOEVER, K. E., BENYEI, A.C., DRAEGER, S., SCHULZ, B. & KURTAN, T. 2010. Curvularin-type metabolites from the fungus *Curvularia* sp. isolated from a marine algA. *Eur J Org Chem*, 6928-6937, S6928/1-S6928/5.
- DAIRI, T., KUZUYAMA, T., NISHIYAMA, M. & FUJII, I. 2011. Convergent strategies in biosynthesis. *Nat Prod Rep*, 28, 1054-1086.

- DANINO, O., GOTTLIEB, H. E., GROSSMAN, S. & BERGMAN, M. 2009. Antioxidant activity of 1,3-dicaffeoylquinic acid isolated from *Inula viscosa*. *Food Res Int*, 42, 1273-1280.
- DE FALCO, B., INCERTI, G., PEPE, R., AMATO, M. & LANZOTTI, V. 2016. Metabolomic fingerprinting of Romaneschi globe artichokes by NMR spectroscopy and multivariate data analysis: Metabolomics of artichokes by NMR and chemometrics. *Phytochem Anal*, 27, 304-314.
- DEBBAB, A., ALY, A.H., LIN, W. H. & PROKSCH, P. 2010. Bioactive compounds from marine bacteria and fungi. *Microb Biotechnol*, 3, 544-563.
- DEMAIN, A.L. & FANG, A. 2000. The natural functions of secondary metabolites. *Adv Biochem Eng Biotechnol*, 69, 1-39.
- DI FERDINANDO, M., BRUNETTI, C., AGATI, G. & TATTINI, M. 2014. Multiple functions of polyphenols in plants inhabiting unfavorable Mediterranean areas. *Environ Exp Bot*, 103, 107-116.
- DIAS, D. A., URBAN, S. & ROESSNER, U. 2012. A historical overview of natural products in drug discovery. *Metabolites*, 2, 303-336.
- DING, Z., XU, X., LI, T., WANG, J., SUN, J. & TANG, L. J. 2021. ZR-75-1 breast cancer models to study the utility of 18 F-FES by PET imaging. *Transl Cancer Res*, 10, 1430-1438.
- DO, C.-T., POLLET, B., THÉVENIN, J., SIBOUT, R., DENOUE, D., BARRIÈRE, Y., LAPIERRE, C. & JOUANIN, L. 2007. Both caffeoyl Coenzyme A 3-O-methyltransferase 1 and caffeic acid O-methyltransferase 1 are involved in redundant functions for lignin, flavonoids and sinapoyl malate biosynthesis in *Arabidopsis*. *Planta*, 226, 1117-1129.
- DONA, A.C., KYRIAKIDES, M., SCOTT, F., SHEPHARD, E. A., VARSHAVI, D., VESELKOV, K. & EVERETT, J. R. 2016. A guide to the identification of metabolites in NMR-based metabolomics/metabonomics experiments. *Comput Struct Biotech*, 14, 135-153.
- DRAPER, J., LLOYD, A.J., GOODACRE, R. & BECKMANN, M. 2013. Flow infusion electrospray ionisation mass spectrometry for high throughput, non-targeted metabolite fingerprinting: a review. *Metabolomics*, 9, 4-29.
- DUKE, S. O. & DAYAN, F. E. 2011. Modes of action of microbially-produced phytotoxins. *Toxins*, 3, 1038-1064.
- DUNN, W. B., BAILEY, N. J. & JOHNSON, H. E. 2005. Measuring the metabolome: current analytical technologies. *Analyst*, 130, 606-625.
- DWIVEDI, P., WU, P., KLOPSCH, S. J., PUZON, G. J., XUN, L. & HILL, H. H. 2008. Metabolic profiling by ion mobility mass spectrometry (IMMS). *Metabolomics*, 4, 63-80.
- EBADA, S. S., EDRADA, R. A., LIN, W. & PROKSCH, P. 2008. Methods for isolation, purification and structural elucidation of bioactive secondary metabolites from marine invertebrates. *Nat Protoc*, 3, 1820-1831.
- EBEL, R. 2010. Terpenes from marine-derived fungi. *Mar Drugs*, 8, 2340-2368.

- EFFERTH, T., FU, Y.-J., ZU, Y.-G., SCHWARZ, G., KONKIMALLA, V. S. B. & WINK, M. 2007. Molecular target-guided tumor therapy with natural products derived from traditional Chinese medicine. *Curr Med Chem*, 14, 2024-2032.
- EL-BEIH, A.A., KATO, H., TSUKAMOTO, S. & OHTA, T. 2007. CYP3A4 inhibitors isolated from a marine derived fungus *Penicillium* species. *J Nat Med*, 61, 175-177.
- FARIED, A., KURNIA, D., FARIED, L., USMAN, N., MIYAZAKI, T., KATO, H. & KUWANO, H. 2007. Anticancer effects of gallic acid isolated from Indonesian herbal medicine, *Phaleria macrocarpa* (Scheff.) Boerl, on human cancer cell lines. *Int J Oncol*, 30, 605-613.
- FORINO, M., TENORE, G. C., TARTAGLIONE, L., CARMELA, D. A., NOVELLINO, E. & CIMINIELLO, P. 2015. (1S,3R,4S,5R)5-O-Caffeoylquinic acid: Isolation, stereo-structure characterization and biological activity. *Food Chem*, 178, 306-310.
- FRISVAD, J. C. & SAMSON, R. A. 2004. *Emericella venezuelensis*, a new species with stellate ascospores producing sterigmatocystin and aflatoxin B1. *Syst Appl Microbiol*, 27, 672-680.
- GAJEWSKI, J., PAVLOVIC, R., FISCHER, M., BOLES, E. & GRININGER, M. 2017. Engineering fungal de novo fatty acid synthesis for short chain fatty acid production. *Nat Comm*, 8, 1-8.
- GALLAND, S., MORA, N., ABERT-VIAN, M., RAKOTOMANOMANA, N. & DANGLES, O. 2007. Chemical synthesis of hydroxycinnamic acid glucosides and evaluation of their ability to stabilize natural colors via anthocyanin copigmentation. *J Agric Food Chem*, 55, 7573-7579.
- GALLOP, M. A., BARRETT, R. W., DOWER, W. J., FODOR, S. P. & GORDON, E. M. 1994. Applications of combinatorial technologies to drug discovery. 1. Background and peptide combinatorial libraries. *J Med Chem*, 37, 1233-1251.
- GAMBOA-ANGULO, M. M., ALEJOS-GONZÁLEZ, F. & PEÑA-RODRÍGUEZ, L. M. 1997. Homozinnol, a new phytotoxic metabolite from *Alternaria solani*. *J Agric Food Chem*, 45, 282-285.
- GARDES, M. & BRUNS, T. D. 1993. ITS primers with enhanced specificity for basidiomycetes - application to the identification of mycorrhizae and rusts. *Mol Ecol*, 2, 113-118.
- GELADI, P. 2003. Chemometrics in spectroscopy. Part 1. Classical chemometrics. *Spectrochim Acta B*, 58B, 767-782.
- GERIS DOS SANTOS, R. M., RODRIGUES-FO, E., CALDAS ROCHA, W. & SIMAS TEIXEIRA, M. F. 2003. Endophytic fungi from *Melia azedarach*. *World J Microbiol Biotech*, 19, 767-770.
- GERIS, R. & SIMPSON, T. J. 2009. Meroterpenoids produced by fungi. *Nat Prod Rep*, 26, 1063-1094.
- GHFAR, A.A., EL-METWALLY, M. M., SHAABAN, M., GABR, S. A., GABR, N. S., DIAB, M. S. M., AQEL, A., HABILA, M. A., AL-QAHTANI, W. H., ALFAIFI, M. Y., ELBEHAIRI, S. E. I. & ALJUMAH, B. A. 2021. Production of terretinin N and butyrolactone I by thermophilic *Aspergillus terreus* TM8 promoted

- apoptosis and cell death in human prostate and ovarian cancer cells. *Molecules*, 26.
- GILLESPIE, D. E., BRADY, S. F., BETTERMANN, A.D., CIANCIOTTO, N. P., LILES, M. R., RONDON, M. R., CLARDY, J., GOODMAN, R. M. & HANDELSMAN, J. 2002. Isolation of antibiotics turbomycin A and B from a metagenomic library of soil microbial DNA. *Appl Environ Microbiol*, 68, 4301-6.
- GIORDANO, L., GONTHIER, P., VARESE, G., MISERERE, L. & NICOLOTTI, G. 2009. Mycobiota inhabiting sapwood of healthy and declining Scots pine (*Pinus sylvestris* L.) trees in the Alps. *Fungal Divers*, 38, 69-83.
- GONZALEZ-DOMINGUEZ, R., SAYAGO, A. & FERNANDEZ-RECAMALES, A. 2017. Direct infusion mass spectrometry for metabolomic phenotyping of diseases. *Bioanalysis*, 9, 131-148.
- GONZALEZ, B., FRANÇOIS, J. & RENAUD, M. 1997. A rapid and reliable method for metabolite extraction in yeast using boiling buffered ethanol. *Yeast*, 13, 1347-1355.
- GRAYER, R. J. & KOKUBUN, T. 2001. Plant-fungal interactions: The search for phytoalexins and other antifungal compounds from higher plants. *Phytochemistry*, 56, 253-263.
- GRIFFITHS, W. J., KOAL, T., WANG, Y., KOHL, M., ENOT, D. P. & DEIGNER, H.-P. 2010. Targeted metabolomics for biomarker discovery. *Angew Chem Int Ed Engl*, 49, 5426-5445.
- GUNATILAKA, A.A.L. 2006. Natural products from plant-associated microorganisms: Distribution, structural diversity, bioactivity, and implications of their occurrence. *J Nat Prod*, 69, 509-526.
- HAN, D. Y., LEE, H. R., KIM, B. G. & AHN, J.-H. 2016. Biosynthesis of ferulic acid 4-O-glucoside and feruloyl glucoside using *Escherichia coli* harboring regioselective glucosyltransferases. *Appl Biol Chem*, 59, 481-484.
- HANSON, J. R. 2003. Natural products: the secondary metabolites. In: ABEL, E. W. (ed.). Royal Society of Chemistry.
- HAO, D., CHEN, S., XIAO, P. & PENG, Y. 2010. Authentication of medicinal plants by DNA-based markers and genomics. *Chin Herb Med*, 2, 250-261.
- HARDOIM, P. R. & VAN ELSAS, J. D. 2013. Properties of bacterial endophytes leading to maximized host fitness. In: DE BRUIJN, F. J. (ed.) *Molecular Microbial Ecology of the Rhizosphere*. Wiley-Blackwell.
- HARVEY, A.L. 2008. Natural products in drug discovery. *Drug Discov Today*, 13, 894-901.
- HARVEY, A.L., EDRADA-EBEL, R. & QUINN, R. J. 2015. The re-emergence of natural products for drug discovery in the genomics era. *Nat Rev Drug Discov*, 14, 111-129.
- HASHIDOKO, Y., NISHIZUKA, H., TANAKA, M., MURATA, K., MURAI, Y. & HASHIMOTO, M. 2019. Isolation and characterization of 1-palmitoyl-2-linoleoyl-sn-glycerol as a hormogonium-inducing factor (HIF) from the coralloid roots of *Cycas revoluta* (Cycadaceae). *Sci Rep*, 9, 4751.

- HATAMZADEH, S., RAHNAMA, K., NASROLLAHNEJAD, S., FOTOUHIFAR, K. B., HEMMATI, K., WHITE, J. F. & TALIEI, F. 2020. Isolation and identification of L-asparaginase-producing endophytic fungi from the Asteraceae family plant species of Iran. *PeerJ*, 8, e8309.
- HAUKAAS, T., EUCEDA, L., GISKEØDEGÅRD, G. & BATHEN, T. 2017. Metabolic portraits of breast cancer by HR MAS NMR spectroscopy of intact tissue samples. *Metabolites*, 7, 18.
- HAYES, M. A., WRIGLEY, S. K., CHETLAND, I., REYNOLDS, E. E., AINSWORTH, A.M., RENNO, D. V., LATIF, M. A., CHENG, X.-M., HUPE, D. J. & CHARLTON, P. 1996. Novel drimane sesquiterpene esters from *Aspergillus ustus* var. *pseudodeflectus* with endothelin receptor binding activity. *J Antibiot*, 49, 505-512.
- HE, J., XU, Q., WANG, M., LI, C., QIAN, X., SHI, Z., LIU, L. Z. & JIANG, B. H. 2012. Oral administration of apigenin inhibits metastasis through AKT/P70S6K1/MMP-9 pathway in orthotopic ovarian tumor model. *Int J Mol Sci*, 13, 7271-7282.
- HENTSCHEL, U., SCHMID, M., WAGNER, M., FIESELER, L., GERNERT, C. & HACKER, J. 2001. Isolation and phylogenetic analysis of bacteria with antimicrobial activities from the Mediterranean sponges *Aplysina aerophoba* and *Aplysina cavernicola*. *FEMS Microbiol Ecol*, 35, 305-312.
- HONG, S., JOO, T. & JHOO, J.-W. 2015. Antioxidant and anti-inflammatory activities of 3, 5-dicaffeoylquinic acid isolated from *Ligularia fischeri* leaves. *Food Sci Biotech*, 24, 257-263.
- HORAI, H., ARITA, M., KANAYA, S., NIHEI, Y., IKEDA, T., SUWA, K., OJIMA, Y., TANAKA, K., TANAKA, S. & AOSHIMA, K. 2010. MassBank: a public repository for sharing mass spectral data for life sciences. *J Mass Spec*, 45, 703-714.
- HORMAN, I., BADOUD, R. & AMMANN, W. 1984. Food-related applications of one- and two-dimensional high-resolution proton-NMR: structure and conformation of cynarin. *J Agric Food Chem*, 32, 538-540.
- HORTON, T. R. & BRUNS, T. D. 2001. The molecular revolution in ectomycorrhizal ecology: peeking into the black-box. *Mol Ecol*, 10, 1855-1871.
- HOSTETLER, G. L., RALSTON, R. A. & SCHWARTZ, S. J. 2017. Flavones: Food sources, bioavailability, metabolism, and bioactivity. *Adv Nutr*, 8, 423-435.
- HUANG, Y., HOEFGEN, S. & VALIANTE, V. 2021. Biosynthesis of fungal drimane-type sesquiterpene esters. *Angew Chem Int Ed Engl*, 60, 23763-23770.
- HUGHES, J. P., REES, S., KALINDJIAN, S. B. & PHILPOTT, K. L. 2011. Principles of early drug discovery. *Brit J Pharmacol*, 162, 1239-1249.
- HUMMEL, J., SELBIG, J., WALTHER, D. & KOPKA, J. 2007. The Golm Metabolome Database: a database for GC-MS based metabolite profiling. *Metabolomics*. Springer.
- ICHIHARA, A., TAZAKI, H. & SAKAMURA, S. 1983. Solanapyrones A, B and C, phytotoxic metabolites from the fungus *Alternaria solani*. *Tetrahedron Lett*, 24, 5373-5376.

- INFORMA 2021. Dictionary of Natural Products. Boca Raton FL 33487 USA: CRC Press.
- INOUE, M., SUZUKI, R., KOIDE, T., SAKAGUCHI, N., OGIHARA, Y. & YABU, Y. 1994. Antioxidant, gallic acid, induces apoptosis in HL-60RG cells. *Biochem Biophys Res Comm*, 204, 898-904.
- ISAAC, O. 1979. [Pharmacological investigations with compounds of chamomile i. on the pharmacology of (-)-alpha-bisabolol and bisabolol oxides (review) (author's transl)]. *Planta Med*, 35, 118-124.
- JOHNSON, C. H., IVANISEVIC, J. & SIUZDAK, G. 2016. Metabolomics: beyond biomarkers and towards mechanisms. *Nat Rev Mol Cell Biol*, 17, 451-459.
- JOSEPH, B. & PRIYA, R. M. 2011. Bioactive compounds from endophytes and their potential. *Am J Biochem Mol Biol*, 1, 291-309.
- JURJEVIC, Z. & PETERSON, S. W. 2016. *Aspergillus asper* sp. nov. and *Aspergillus collinsii* sp. nov., from *Aspergillus* section *Usti*. *Int J Syst Evol Microbiol*, 66, 2566-2572.
- KALAITZIS, J. A. 2013. Discovery, biosynthesis, and rational engineering of novel enterocin and wailupemycin polyketide analogues. *Methods Mol Biol*, 1055, 171-189.
- KATAJAMAA, M. & ORESIC, M. 2005. Processing methods for differential analysis of LC/MS profile data. *BMC Bioinform*, 6.
- KAUFMANN, A., BUTCHER, P., MADEN, K., WALKER, S. & WIDMER, M. 2011. Semi-targeted residue screening in complex matrices with liquid chromatography coupled to high resolution mass spectrometry: current possibilities and limitations. *Analyst*, 136, 1898-1909.
- KAUL, S., GUPTA, S., AHMED, M. & DHAR, M. K. 2012. Endophytic fungi from medicinal plants: a treasure hunt for bioactive metabolites. *Phytochem Rev*, 11, 487-505.
- KELLER, N. P., TURNER, G. & BENNETT, J. W. 2005. Fungal secondary metabolism—from biochemistry to genomics. *Nat Rev Microbiol*, 3, 937-947.
- KHAN, T., ALI, M., KHAN, A., NISAR, P., JAN, S. A., AFRIDI, S. & SHINWARI, Z. K. 2019. Anticancer plants: A review of the active phytochemicals, applications in animal models, and regulatory aspects. *Biomolecules*, 10, 47.
- KIKUZAKI, H., HISAMOTO, M., HIROSE, K., AKIYAMA, K. & TANIGUCHI, H. 2002. Antioxidant properties of ferulic acid and its related compounds. *J Agric Food Chem*, 50, 2161-8.
- KIM, B. G. 2006. Synthesis of ermanin, 5,7-dihydroxy-3,4'-dimethoxyflavone from kaempferol, 3,5,7,4'-tetrahydroxyflavone with two *O*-methyltransferases expressed in *E. coli*. *Bull Korean Chem Soc*, 27, 357-358.
- KIND, T., WOHLGEMUTH, G., LEE, D. Y., LU, Y., PALAZOGLU, M., SHAHBAZ, S. & FIEHN, O. 2009. FiehnLib: mass spectral and retention index libraries for metabolomics based on quadrupole and time-of-flight gas chromatography/mass spectrometry. *Anal Chem*, 81, 10038-10048.

- KJER, J., DEBBAB, A., ALY, A.H. & PROKSCH, P. 2010. Methods for isolation of marine-derived endophytic fungi and their bioactive secondary products. *Nat Protoc*, 5, 479-490.
- KLOEPFER, J. W. & RYU, C.-M. 2006. Bacterial endophytes as elicitors of induced systemic resistance. In: SCHULZ, B. J. E., BOYLE, C. J. C. & SIEBER, T. N. (eds.) *Microbial Root Endophytes*. Berlin, Heidelberg: Springer Berlin Heidelberg.
- KOPUSTINSKIENE, D. M., JAKSTAS, V., SAVICKAS, A. & BERNATONIENE, J. 2020. Flavonoids as anticancer agents. *Nutrients*, 12, 457.
- KRUG, D. & MÜLLER, R. 2014. Secondary metabolomics: the impact of mass spectrometry-based approaches on the discovery and characterization of microbial natural products. *Nat Prod Rep*, 31, 768-783.
- KURKIN, V. A., LAMRINI, M. & KLOCHKOV, S. G. 2008. Lavandoside from *Lavandula spica* flowers. *Chem Nat Compd*, 44, 169-170.
- KUSARI, S., SINGH, S. & JAYABASKARAN, C. 2014. Biotechnological potential of plant-associated endophytic fungi: hope versus hype. *Trends Biotechnol*, 32, 297-303.
- KUSARI, S. & SPITELLER, M. 2011. Are we ready for industrial production of bioactive plant secondary metabolites utilizing endophytes? *Nat Prod Rep*, 28, 1203-1207.
- LAATSCH, H. 2011. *AntiBase 2014: the natural compound identifier*, Wiley-Vch Weinheim, Germany.
- LANDIS-PIWOWAR, K. R., MILACIC, V. & DOU, Q. P. 2008. Relationship between the methylation status of dietary flavonoids and their growth-inhibitory and apoptosis-inducing activities in human cancer cells. *J Cell Biochem*, 105, 514-523.
- LANKADURAI, B. P., NAGATO, E. G. & SIMPSON, M. J. 2013. Environmental metabolomics: an emerging approach to study organism responses to environmental stressors. *Environ Rev*, 21, 180-205.
- LI, K., CHEN, S., PANG, X., CAI, J., ZHANG, X., LIU, Y., ZHU, Y. & ZHOU, X. 2022. Natural products from mangrove sediments-derived microbes: Structural diversity, bioactivities, biosynthesis, and total synthesis. *Eur J Med Chem*, 230, 114117.
- LIN, L., YU, Q., YAN, X., HANG, W., ZHENG, J., XING, J. & HUANG, B. 2010. Direct infusion mass spectrometry or liquid chromatography mass spectrometry for human metabolomics? A serum metabolomic study of kidney cancer. *Analyst*, 135, 2970-2978.
- LINDON, J. C., NICHOLSON, J. K. & WILSON, I. D. 2000. Directly coupled HPLC–NMR and HPLC–NMR–MS in pharmaceutical research and development. *J Chromatogr B: Biomed Sci Appl*, 748, 233-258.
- LIU, H., EDRADA-EBEL, R., EBEL, R., WANG, Y., SCHULZ, B., DRAEGER, S., MULLER, W. E., WRAY, V., LIN, W. & PROKSCH, P. 2009. Drimane sesquiterpenoids from the fungus *Aspergillus ustus* isolated from the marine sponge *Suberites domuncula*. *J Nat Prod*, 72, 1585-8.

- LIU, L. F., DESAI, S. D., LI, T. K., MAO, Y., SUN, M. & SIM, S. P. 2000. Mechanism of action of camptothecin. *Ann New York Acad Sci*, 922, 1-10.
- LIU, R., LI, X. & LAM, K. S. 2017. Combinatorial chemistry in drug discovery. *Curr Opin Chem Biol*, 38, 117-126.
- LIU, X.-H., MIAO, F.-P., QIAO, M.-F., CICHEWICZ, R. H. & JI, N.-Y. 2013. Terretinin, ophiobolin, and drimane terpenes with absolute configurations from an algicolous *Aspergillus ustus*. *RSC Adv*, 3, 588-595.
- LOMMEN, A. 2009. MetAlign: interface-driven, versatile metabolomics tool for hyphenated full-scan mass spectrometry data preprocessing. *Anal Chem*, 81, 3079-3086.
- LOPES, A.S., CRUZ, E. C., SUSSULINI, A. & KLASSEN, A. 2017. Metabolomic strategies involving mass spectrometry combined with liquid and gas chromatography. *Adv Exp Med Biol*, 965, 77-98.
- LOPEZ-GRESA, M. P., CABEDO, N., GONZALEZ-MAS, M. C., CIAVATTA, M. L., AVILA, C. & PRIMO, J. 2009. Terretonins E and F, inhibitors of the mitochondrial respiratory chain from the marine-derived fungus *Aspergillus insuetus*. *J Nat Prod*, 72, 1348-1351.
- LOU, J., FU, L., PENG, Y. & ZHOU, L. 2013. Metabolites from *Alternaria* fungi and their bioactivities. *Molecules*, 18, 5891-5935.
- LU, Z., WANG, Y., MIAO, C., LIU, P., HONG, K. & ZHU, W. 2009. Sesquiterpenoids and benzofuranoids from the marine-derived fungus *Aspergillus ustus* 094102. *J Nat Prod*, 72, 1761-1767.
- LUDWIG-MULLER, J. 2015. Plants and endophytes: equal partners in secondary metabolite production? *Biotechnol Lett*, 37, 1325-1334.
- LUGTENBERG, B. J. J., CHIN-A-WOENG, T. F. C. & BLOEMBERG, G. V. 2002. Microbe-plant interactions: principles and mechanisms. *Antonie van Leeuwenhoek*, 81, 373-383.
- MACINTYRE, L., ZHANG, T., VIEGELMANN, C., JUAREZ MARTINEZ, I., CHENG, C., DOWDELLS, C., ABDELMOHSEN, U. R., GERNERT, C., HENTSCHEL, U. & EDRADA-EBEL, R. 2014. Metabolomic tools for secondary metabolite discovery from marine microbial symbionts. *Mar Drugs*, 12, 3416-3448.
- MADJI HOUNOUM, B., BLASCO, H., EMOND, P. & MAVEL, S. 2016. Liquid chromatography–high-resolution mass spectrometry-based cell metabolomics: Experimental design, recommendations, and applications. *Trends Anal Chem*, 75, 118-128.
- MADUNIC, J., MADUNIC, I. V., GAJSKI, G., POPIC, J. & GARAJ-VRHOVAC, V. 2018. Apigenin: A dietary flavonoid with diverse anticancer properties. *Cancer Lett*, 413, 11-22.
- MAFUVADZE, B., LIANG, Y., BESCH-WILLIFORD, C., ZHANG, X. & HYDER, S. M. 2012. Apigenin induces apoptosis and blocks growth of medroxyprogesterone acetate-dependent BT-474 xenograft tumors. *Horm Cancer*, 3, 160-171.
- MANDAL, S., MOUDGIL, M. N. & MANDAL, S. K. 2009. Rational drug design. *Eur J Pharmacol*, 625, 90-100.

- MANI, V. M., SOUNDARI, A.P., KARTHIYAINI, D. & PREETH, K. 2015. Bioprospecting endophytic fungi and their metabolites from medicinal tree *Aegle marmelos* in Western Ghats, India. *Mycobiology*, 43, 303-310.
- MARSHALL, A.G. & HENDRICKSON, C. L. 2008. High-resolution mass spectrometers. *Ann Rev Anal Chem*, 1, 579-599.
- MATOUQ, M., EL-HASAN, T., AL-BILBISI, H., ABDELHADI, M., HINDIYEH, M., ESLAMIAN, S. & DUHEISAT, S. 2013. The climate change implication on Jordan: A case study using GIS and artificial neural networks for weather forecasting. *J Taibah Univ Sci*, 7, 44-55.
- MATSUDA, Y. & ABE, I. 2016. Biosynthesis of fungal meroterpenoids. *Nat Prod Rep*, 33, 26-53.
- MATSUDA, Y., MITSUHASHI, T., QUAN, Z. & ABE, I. 2015. Molecular basis for stellatic acid biosynthesis: A genome mining approach for discovery of sesterterpene synthases. *Org Lett*, 17, 4644-4647.
- MAZLAN, N. W., CLEMENTS, C. & EDRADA-EBEL, R. 2020A. Targeted isolation of anti-trypanosomal naphthofuran-quinone compounds from the mangrove plant *Avicennia lanata*. *Mar Drugs*, 18, 661.
- MAZLAN, N. W., TATE, R., YUSOFF, Y. M., CLEMENTS, C. & EDRADA-EBEL, R. 2020b. Metabolomics-guided isolation of anti-trypanosomal compounds from endophytic fungi of the mangrove plant *Avicennia lanata*. *Curr Med Chem*, 27, 1815-1835.
- MCKAY, D. L. & BLUMBERG, J. B. 2006. A Review of the bioactivity and potential health benefits of chamomile tea (*Matricaria recutita* L.). *Phytother Res*, 20, 519-530.
- MCMURRAY, J., SEIDELIN, P. & STRUTHERS, A. 1989. Evidence for a proximal and distal nephron action of atrial natriuretic factor in man. *Nephron*, 51, 39-43.
- MOHARRAM, F. A., EL DIB, R. A.E. M., MARZOUK, M. S., EL-SHENAWY, S. M. & IBRAHIM, H. A. 2017. New apigenin glycoside, polyphenolic constituents, anti-inflammatory and hepatoprotective activities of *Gaillardia grandiflora* and *Gaillardia pulchella* aerial parts. *Pharmacog Mag*, 13, S244-S249.
- MOHS, R. C. & GREIG, N. H. 2017. Drug discovery and development: Role of basic biological research. *Alzheimers Dementia (N. Y.)*, 3, 651-657.
- MORENO-ESCOBAR, J., PUC-CARRILLO, A., CACERES-FARFAN, M., PENA-RODRIGUEZ, L. M. & GAMBOA-ANGULO, M. M. 2005. Two new zinniol-related phytotoxins from *Alternaria solani*. *Nat Prod Res*, 19, 603-607.
- MORISON, J. & LAWLOR, D. 1999. Interactions between increasing CO₂ concentration and temperature on plant growth. *Plant Cell Environ*, 22, 659-682.
- MORLOCK, G. E., RISTIVOJEVIC, P. & CHERNETSOVA, E. S. 2014. Combined multivariate data analysis of high-performance thin-layer chromatography fingerprints and direct analysis in real time mass spectra for profiling of natural products like propolis. *J Chromatogr A*, 1328, 104-112.
- MOUSAVI, B., MT, H., SEYEDMOUSAVI, S., HEDAYATI, M. & ILKIT, M. 2016. *Aspergillus* species in indoor environments and their possible occupational and public health hazards. *Curr Med Mycol*, 2, 36-42.

- MUCCIARELLI, M., SCANNERINI, S., BERTEA, C. & MAFFEI, M. 2003. In vitro and in vivo peppermint (*Mentha piperita*) growth promotion by nonmycorrhizal fungal colonization. *New Phytol*, 158, 579-591.
- NADUMANE, V. K., VENKATACHALAM, P. & GAJARAJ, B. 2016. Chapter 19 - Aspergillus applications in cancer research. In: GUPTA, V. K. (ed.) *New and Future Developments in Microbial Biotechnology and Bioengineering*. Amsterdam: Elsevier.
- NAH, J.-H., KIM, H.-J., LEE, H.-N., LEE, M.-J., CHOI, S.-S. & KIM, E.-S. 2013. Identification and biotechnological application of novel regulatory genes involved in *Streptomyces* polyketide overproduction through reverse engineering strategy. *BioMed Res Int*, 2013, 549737.
- NEJADGHOLI, I. & BOLIC, M. 2015. A comparative study of PCA, SIMCA and Cole model for classification of bioimpedance spectroscopy measurements. *Comp Biol Med*, 63, 42-51.
- NEJUMAL, K. K., DINEEP, D., MOHAN, M., KRISHNAN, K. P., ARAVIND, U. K. & ARAVINDAKUMAR, C. T. 2017. Presence of bisphenol S and surfactants in the sediments of Kongsfjorden: a negative impact of human activities in Arctic? *Environ Monitor Assess*, 190, 22.
- NISA, H., KAMILI, A.N., NAWCHOO, I. A., SHAFI, S., SHAMEEM, N. & BANDH, S. A. 2015. Fungal endophytes as prolific source of phytochemicals and other bioactive natural products: A review. *Microb Pathog*, 82, 50-59.
- NOGUÉS, I., LLUSIÀ, J., OGAYA, R., MUNNÉ-BOSCH, S., SARDANS, J., PEÑUELAS, J. & LORETO, F. 2014. Physiological and antioxidant responses of *Quercus ilex* to drought in two different seasons. *Plant Biosyst*, 148, 268-278.
- OGAWA, A., MURAKAMI, C., KAMISUKI, S., KURIYAMA, I., YOSHIDA, H., SUGAWARA, F. & MIZUSHINA, Y. 2004. RES-1149-1 and-2, novel non-peptidic endothelin type B receptor antagonists produced by *Aspergillus* sp. III. Biochemical properties of RES-1149-1,-2 and structure-activity relationships. *Bioorg Med Chem Lett*, 14, 3539.
- OGAWA, T., ANDO, K., ANAKA, T. T., UOSAKI, Y. & MATSUDA, Y. 1996. RES-1149-1 and -2, Novel non-peptidic endothelin type B receptor antagonists produced by *Aspergillus* sp. *J Antibiot*, 49, 1-5.
- OKAMURA, N., HARAGUCHI, H., HASHIMOTO, K. & YAGI, A. 1993A. Altersolanol-related antimicrobial compounds from a strain of *Alternaria solani*. *Phytochemistry*, 34, 1005-1009.
- OKAMURA, N., YAGI, A., HARAGUCHI, H. & HASHIMOTO, K. 1993b. Simultaneous high-performance liquid chromatographic determination of altersolanol A, B, C, D, E and F. *J Chromatogr A*, 630, 418-422.
- OLA, A.R. B., THOMY, D., LAI, D., BROETZ-OESTERHELT, H. & PROKSCH, P. 2013. Inducing secondary metabolite production by the endophytic fungus *Fusarium tricinctum* through Coculture with *Bacillus subtilis*. *J Nat Prod*, 76, 2094-2099.
- OLEINIKOVA, G. K., DENISENKO, V. A., BERDYSHEV, D. V., PUSHILIN, M. A., KIRICHUK, N. N., MENZOROVA, N. I., KUZMICH, A.S., YURCHENKO, E.

- A., ZHURAVLEVA, O. I. & AFIYATULLOV, S. S. 2016. Two new sesterterpenoids, terretonins H and I, from the marine-derived fungus *Aspergillus ustus*. *Phytochem Lett*, 17, 135-139.
- OLENNIKOV, D. N. & KASHCHENKO, N. I. 2016. New acylated apigenin glycosides from edge flowers of *Matricaria chamomilla*. *Chem Nat Compd*, 52, 996-999.
- OLIVER, S. G., WINSON, M. K., KELL, D. B. & BAGANZ, F. 1998. Systematic functional analysis of the yeast genome. *Trends Biotechnol*, 16, 373-378.
- ORMEÑO, E., BALDY, V., BALLINI, C. & FERNANDEZ, C. 2008. Production and diversity of volatile terpenes from plants on calcareous and siliceous soils: effect of soil nutrients. *J Chem Ecol*, 34, 1219-1229.
- OWEN, N. L. & HUNDLEY, N. 2004. Endophytes: The chemical synthesizers inside plants. *Sci Prog*, 87, 79-99.
- PATEL, S., SUBRAMANIAN, R. & JHA, Y. 2011. A simple and rapid method for isolation of alternaric acid from *Alternaria solani*. *Curr Trends Biotechnol Pharm*, 5, 1098-1103.
- PATTI, G., YANES, O. & SIUZDAK, G. 2012. Innovation: Metabolomics: the apogee of the omics trilogy. *Nat Rev Mol Cell Biol*, 13, 263-269.
- PEARSON, W. A. & SPESSARD, G. O. 1975. α [alpha]- and β [bet] aD-glucose pentaacetate. An experiment in structure assignment using NMR. *J Chem Educ*, 52, 814.
- PEAY, K. G., KENNEDY, P. G. & BRUNS, T. D. 2008. Fungal community ecology: A hybrid beast with a molecular master. *BioSci*, 58, 799-810.
- PENCE, H. E. & WILLIAMS, A. 2010. ChemSpider: An online chemical information resource. *J Chem Educ*, 87, 1123-1124.
- PEREIRA, F. & AIRES-DE-SOUSA, J. 2018. Computational methodologies in the exploration of marine natural product leads. *Mar Drugs*, 16, 236.
- PETIT, C., FRÉVILLE, H., MIGNOT, A., COLAS, B., RIBA, M., IMBERT, E., HURTREZ-BOUSSÉS, S., VIREVAIRE, M. & OLIVIERI, I. 2001. Gene flow and local adaptation in two endemic plant species. *Biol Conserv*, 100, 21-34.
- PIRZAD, A., ALYARI, H., SHAKIBA, M., ZEHTAB-SALMASI, S. & MOHAMMADI, A. 2006. Essential oil content and composition of German chamomile (*Matricaria chamomilla* L.) at different irrigation regimes. *J Agron*, 5, 451-455.
- PLUSKAL, T., CASTILLO, S., VILLAR-BRIONES, A. & OREŠIČ, M. 2010. MZmine 2: modular framework for processing, visualizing, and analyzing mass spectrometry-based molecular profile data. *BMC Bioinform*, 11, 1-11.
- POHO, P., LIPPONEN, K., BESPALOV, M. M., SIKANEN, T., KOTIAHO, T. & KOSTIAINEN, R. 2019. Comparison of liquid chromatography-mass spectrometry and direct infusion microchip electrospray ionization mass spectrometry in global metabolomics of cell samples. *Eur J Pharm Sci*, 138, 104991.
- QURESHI, I. H., HUSAIN, S. A., NOORANI, R., MURTAZA, N., IITAKA, Y., IWASAKI, S. & OKUDA, S. 1980. Stellatic acid: a new class of sesterterpenoid; X-ray crystal structure. *Tetrahedron Lett*, 21, 1961-1962.

- RAJALAHTI, T. & KVALHEIM, O. M. 2011. Multivariate data analysis in pharmaceuticals: a tutorial review. *Int J Pharmaceut*, 417, 280-290.
- RAMAKRISHNA, A. & RAVISHANKAR, G. 2011. Influence of abiotic stress signals on secondary metabolites in plants. *Plant Signal Behav*, 6, 1720–1731.
- RAMIREZ, T., DANESHIAN, M., KAMP, H., BOIS, F. Y., CLENCH, M. R., COEN, M., DONLEY, B., FISCHER, S. M., EKMAN, D. R. & FABIAN, E. 2013. Metabolomics in toxicology and preclinical research. *Altex*, 30, 209.
- REDDY, A.R., CHAITANYA, K. V. & VIVEKANANDAN, M. 2004. Drought-induced responses of photosynthesis and antioxidant metabolism in higher plants. *J Plant Physiol*, 161, 1189-1202.
- REICHLING, J., BEIDERBECK, R. & BECKER, H. 1979. Vergleichende Untersuchungen über sekundäre Inhaltsstoffe bei Pflanzentumoren, Blüte, Kraut und Wurzel von *Matricaria chamomilla* L. *Planta Med*, 36, 322-332.
- REINHOLD-HUREK, B. & HUREK, T. 2011. Living inside plants: bacterial endophytes. *Curr Opin Plant Biol*, 14, 435-443.
- RINEHART, K. & LITHGOW-BERELLONI, A. 1991. *Novel antiviral and cytotoxic agent*. PCT Int. Pat. Appl. WO 91.04985.
- RIVAS-UBACH, A., GARGALLO-GARRIGA, A., SARDANS, J., ORAVEC, M., MATEU-CASTELL, L., PÉREZ-TRUJILLO, M., PARELLA, T., OGAYA, R., URBAN, O. & PEÑUELAS, J. 2014. Drought enhances folivory by shifting foliar metabolomes in *Quercus ilex* trees. *New Phytol*, 202, 874-885.
- ROBINETTE, S. L., BRÜSCHWEILER, R., SCHROEDER, F. C. & EDISON, A.S. 2012. NMR in metabolomics and natural products research: two sides of the same coin. *Acc Chem Res*, 45, 288-297.
- ROBOTTI, E. & MARENGO, E. 2016. Chemometric multivariate tools for candidate biomarker identification: LDA, PLS-DA, SIMCA, Ranking-PCA. *Methods Mol Biol*, 1384, 237-267.
- RODRIGUES DE CARVALHO, C., VIEIRA, M. D. L. A., CANTRELL, C. L., WEDGE, D. E., ALVES, T. M. A., ZANI, C. L., PIMENTA, R. S., SALES JUNIOR, P. A., MURTA, S. M. F., ROMANHA, A.J., ROSA, C. A. & ROSA, L. H. 2016. Biological activities of ophiobolin K and 6-epi-ophiobolin K produced by the endophytic fungus *Aspergillus calidoustus*. *Nat Prod Res*, 30, 478-481.
- RODRIGUEZ, R. & REDMAN, R. 2008. More than 400 million years of evolution and some plants still can't make it on their own: plant stress tolerance via fungal symbiosis. *J Exp Bot*, 59, 1109-14.
- ROHLOFF, J. & BONES, A.M. 2005. Volatile profiling of *Arabidopsis thaliana* – Putative olfactory compounds in plant communication. *Phytochemistry*, 66, 1941-1955.
- SADRAEI, H., ASGHARI, G., KHANABADI, M. & MINAIYAN, M. 2017. Anti-inflammatory effect of apigenin and hydroalcoholic extract of *Dracocephalum kotschyi* on acetic acid-induced colitis in rats. *Res Pharm Sci*, 12, 322-329.
- SAK, K. 2014. Cytotoxicity of dietary flavonoids on different human cancer types. *Pharmacog Rev*, 8, 122-146.

- SALEHI, B., VENDITTI, A., SHARIFI-RAD, M., KRĘGIEL, D., SHARIFI-RAD, J., DURAZZO, A., LUCARINI, M., SANTINI, A., SOUTO, E. B., NOVELLINO, E., ANTOLAK, H., AZZINI, E., SETZER, W. N. & MARTINS, N. 2019. The therapeutic potential of apigenin. *Int J Mol Sci*, 20, 1305.
- SALIM, A.A., CHIN, Y.-W. & KINGHORN, A.D. 2008. Drug Discovery from Plants. In: RAMAWAT, K. G. & MERILLON, J. M. (eds.) *Bioactive Molecules and Medicinal Plants*. Berlin, Heidelberg: Springer Berlin Heidelberg.
- SAMAGA, P. V. & RAI, V. R. 2016. Diversity and bioactive potential of endophytic fungi from *Nothapodytes foetida*, *Hypericum mysorense* and *Hypericum japonicum* collected from Western Ghats of India. *Ann Microbiol*, 66, 229-244.
- SAMPAIO, B. L., EDRADA-EBEL, R. & DA COSTA, F. B. 2016. Effect of the environment on the secondary metabolic profile of *Tithonia diversifolia*: a model for environmental metabolomics of plants. *Sci Rep*, 6, 29265.
- SARKER, S. D. & NAHAR, L. 2012. An introduction to natural products isolation. *Methods Mol Biol*, 864, 1-25.
- SCALBERT, A., BRENNAN, L., FIEHN, O., HANKEMEIER, T., KRISTAL, B. S., VAN OMMEN, B., PUJOS-GUILLOT, E., VERHEIJ, E., WISHART, D. & WOPEREIS, S. 2009. Mass-spectrometry-based metabolomics: limitations and recommendations for future progress with particular focus on nutrition research. *Metabolomics*, 5, 435-458.
- SCHERLACH, K. & HERTWECK, C. 2009. Triggering cryptic natural product biosynthesis in microorganisms. *Org Biomol Chem*, 7, 1753-1760.
- SCHILCHER, H. 1987. *Die Kamille: handbuch für ärzte, apotheker und andere Naturwissenschaftler*, Wissenschaftliche Verlagsgesellschaft Stuttgart.
- SCHULZ, B., BOYLE, C., DRAEGER, S., ROEMMERT, A.-K. & KROHN, K. 2002. Endophytic fungi: a source of novel biologically active secondary metabolites. *Mycol Res*, 106, 996-1004.
- SEO, H.-S., KU, J. M., CHOI, H.-S., WOO, J.-K., JANG, B.-H., SHIN, Y. C. & KO, S.-G. 2014. Induction of caspase-dependent apoptosis by apigenin by inhibiting STAT3 signaling in HER2-overexpressing MDA-MB-453 breast cancer cells. *Anticancer Res*, 34, 2869-2882.
- SEO, H. S., JO, J. K., KU, J. M., CHOI, H. S., CHOI, Y. K., WOO, J. K., KIM, H. I., KANG, S. Y., LEE, K. M., NAM, K. W., PARK, N., JANG, B. H., SHIN, Y. C. & KO, S. G. 2015A. Induction of caspase-dependent extrinsic apoptosis by apigenin through inhibition of signal transducer and activator of transcription 3 (STAT3) signalling in HER2-overexpressing BT-474 breast cancer cells. *Biosci Rep*, 35, e00276.
- SEO, H. S., KU, J. M., CHOI, H. S., WOO, J. K., JANG, B. H., GO, H., SHIN, Y. C. & KO, S. G. 2015b. Apigenin induces caspase-dependent apoptosis by inhibiting signal transducer and activator of transcription 3 signaling in HER2-overexpressing SKBR3 breast cancer cells. *Mol Med Rep*, 12, 2977-2984.
- SEYEDMOUSAVI, S., GUILLOT, J., ARNÉ, P., DE HOOOG, G. S., MOUTON, J. W., MELCHERS, W. J. & VERWEIJ, P. E. 2015. *Aspergillus* and aspergilloses in

- wild and domestic animals: a global health concern with parallels to human disease. *Med Mycol*, 53, 765-797.
- SHAH, A., HASSAN, Q. P., MUSHTAQ, S., SHAH, A.M., HUSSAIN, A., SHAH, A., HASSAN, Q. P., SHAH, A.M. & HUSSAIN, A. 2017. Chemoprofile and functional diversity of fungal and bacterial endophytes and role of ecofactors - A review. *J Basic Microbiol*, 57, 814-826.
- SHANG, R.-Y., CUI, J., LI, J.-X., MIAO, X.-X., ZHANG, L., XIE, D.-D., ZHANG, L., LIN, H.-W. & JIAO, W.-H. 2022. Nigerin and ochracenes J–L, new sesquiterpenoids from the marine sponge symbiotic fungus *Aspergillus niger*. *Tetrahedron*, 104.
- SHANKAR, E., GOEL, A., GUPTA, K. & GUPTA, S. 2017. Plant flavone apigenin: An emerging anticancer agent. *Curr Pharmacol Rep*, 3, 423-446.
- SHEHAB, N. G., MAHDY, A., KHAN, S. & NOUREDDIN, S. 2011. Chemical constituents and biological activities of *Fagonia indica* Burm F. *Res J Med Plant*, 5, 531-546.
- SHERAMETI, I., SHAHOLLARI, B., VENUS, Y., ALTSCHMIED, L., VARMA, A. & OELMUELLER, R. 2005. The endophytic fungus *Piriformospora indica* stimulates the expression of nitrate reductase and the starch-degrading enzyme glucan-water dikinase in tobacco and Arabidopsis roots through a Homeodomaintranscription factor that binds to a conserved motif in their promoters. *J Biol Chem*, 280, 26241-26247.
- SHIONO, Y., HIRAMATSU, F., MURAYAMA, T., KOSEKI, T., FUNAKOSHI, T., UEDA, K. & YASUDA, H. 2007. Two drimane-type sesquiterpenes, strobilactones A and B, from the liquid culture of the edible mushroom *Strobilurus ohshimae*. *Z Naturforsch B*, 62, 1585-1589.
- SIEBER, T. N. 2007. Endophytic fungi in forest trees: are they mutualists? *Fungal Biol Rev*, 21, 75-89.
- SIMON, H.-U., HAJ-YEHIA, A. & LEVI-SCHAFFER, F. 2000. Role of reactive oxygen species (ROS) in apoptosis induction. *Apoptosis*, 5, 415-418.
- SINGH, O., KHANAM, Z., MISRA, N. & SRIVASTAVA, M. K. 2011. Chamomile (*Matricaria chamomilla* L.): An overview. *Pharmacog Rev*, 5, 82-95.
- SINGH, S. B., SMITH, J. L., SABNIS, G. S., DOMBROWSKI, A.W., SCHAEFFER, J. M., GOETZ, M. A. & BILLS, G. F. 1991. Structure and conformation of ophiobolin K and 6- epiophiobolin K from *Aspergillus ustus* as a nematocidal agent. *Tetrahedron*, 47, 6931-6938.
- SINHA, S., AMIN, H., NAYAK, D., BHATNAGAR, M., KACKER, P., CHAKRABORTY, S., KITCHLU, S., VISHWAKARMA, R., GOSWAMI, A. & GHOSAL, S. 2015. Assessment of microtubule depolymerization property of flavonoids isolated from *Tanacetum gracile* in breast cancer cells by biochemical and molecular docking approach. *Chem-Biol Interact*, 239, 1-11.
- SMITH, C. A., O'MAILLE, G., WANT, E. J., QIN, C., TRAUGER, S. A., BRANDON, T. R., CUSTODIO, D. E., ABAGYAN, R. & SIUZDAK, G. 2005. METLIN: a metabolite mass spectral database. *Ther Drug Monit*, 27, 747-751.

- SOHI, K. K., MITTAL, N., HUNDAL, M. K. & KHANDUJA, K. L. 2003. Gallic acid, an antioxidant, exhibits antiapoptotic potential in normal human lymphocytes: A Bcl-2 independent mechanism. *J Nutr Sci Vitaminol*, 49, 221-227.
- SOHRETOGLU, D., BARUT, B., SARI, S., OZEL, A. & ARROO, R. 2020. In vitro and in silico assessment of DNA interaction, topoisomerase I and II inhibition properties of chrysofenetin. *Int J Biol Macromol*, 163, 1053-1059.
- SPICER, R., SALEK, R. M., MORENO, P., CAÑUETO, D. & STEINBECK, C. 2017. Navigating freely-available software tools for metabolomics analysis. *Metabolomics*, 13, 1-16.
- SRIVASTAVA, J. K. & GUPTA, S. 2015. Chapter 18 - Chamomile: A herbal agent for treatment of diseases of the elderly. In: WATSON, R. R. (ed.) *Foods and Dietary Supplements in the Prevention and Treatment of Disease in Older Adults*. San Diego: Academic Press.
- SRIVASTAVA, J. K., SHANKAR, E. & GUPTA, S. 2010. Chamomile: A herbal medicine of the past with bright future. *Mol Med Rep*, 3, 895-901.
- STEVENS, D. C., CONWAY, K. R., PEARCE, N., VILLEGAS-PENARANDA, L. R., GARZA, A.G. & BODDY, C. N. 2013. Alternative sigma factor over-expression enables heterologous expression of a type II polyketide biosynthetic pathway in *Escherichia coli*. *PLOS ONE*, 8, e64858.
- STIERLE, A., STROBEL, G. & STIERLE, D. 1993. Taxol and taxane production by *Taxomyces andreanae*, an endophytic fungus of Pacific yew. *Science*, 260, 214-216.
- STOESSL, A., UNWIN, C. H. & STOTHERS, J. B. 1979. Metabolites of part V. Biosynthesis of altersolanol A and incorporation of altersolanol A-13C_x into altersolanol B and macrosporin. *Tetrahedron Lett*, 20, 2481-2484.
- STRANGE, R. N. 2007. Phytotoxins produced by microbial plant pathogens. *Nat Prod Rep*, 24, 127-144.
- STROBEL, G. & DAISY, B. 2003. Bioprospecting for microbial endophytes and their natural products. *Microbiol Mol Biol Rev*, 67, 491-502.
- STROBEL, G. A. 2003. Endophytes as sources of bioactive products. *Microbes Infect*, 5, 535-544.
- SUDHA, V., GOVINDARAJ, R., BASKAR, K., AL-DHABI, N. A. & DURAIPANDIYAN, V. 2016. Biological properties of endophytic fungi. *Braz Arch Biol Technol*, 59, e16150436/1-e16150436/7.
- SUEMITSU, R., HORIUCHI, K., KUBOTA, M. & OKAMATSU, T. 1990. Production of alterporriols, altersolanols and macrosporin by *Alternaria porri* and *A. solani*. *Phytochemistry*, 29, 1509-1511.
- SUN, H., ZHANG, A. & WANG, X. 2012. Potential role of metabolomic approaches for Chinese medicine syndromes and herbal medicine. *Phytother Res*, 26, 1466-1471.
- SUNG, B., CHUNG, H. Y. & KIM, N. D. 2016. Role of apigenin in cancer prevention via the induction of apoptosis and autophagy. *J Cancer Prev*, 21, 216-226.

- TAKAYA, Y., KONDO, Y., FURUKAWA, T. & NIWA, M. 2003. Antioxidant constituents of radish sprout (Kaiware-daikon), *Raphanus sativus* L. *J Agric Food Chem*, 51, 8061-8066.
- TALHOUK, R., KARAM, C., FOSTOK, S., EL-JOUNI, W. & BARBOUR, E. 2007. Anti-inflammatory bioactivities in plant extracts. *J Med Food*, 10, 1-10.
- TAWFIKE, A.F., TATE, R., ABBOTT, G., YOUNG, L., VIEGELMANN, C., SCHUMACHER, M., DIEDERICH, M. & EDRADA-EBEL, R. 2017. Metabolomic tools to assess the chemistry and bioactivity of endophytic *Aspergillus* strain. *Chem Biodivers*, 14.
- TAWFIKE, A.F., VIEGELMANN, C. & EDRADA-EBEL, R. 2013. Metabolomics and dereplication strategies in natural products. *Methods Mol Biol*, 1055, 227-244.
- TAYLOR, T. N. & TAYLOR, E. L. 2000. The Rhynie chert ecosystem: a model for understanding fungal interactions. In: BACON, C. W. & WHITE JR., J. F. (eds.) *Microbial Endophytes*. New York: Marcel Dekker, Inc.
- THEANTANA, T., HYDE, K. D. & LUMYONG, S. 2009. Asparaginase production by endophytic fungi from Thai medicinal plants: cytotoxicity properties. *Int J Integrat Biol*, 7, 1-8.
- THOMMA, B. P. 2003. *Alternaria* spp.: from general saprophyte to specific parasite. *Mol Plant Pathol*, 4, 225-236.
- TOLONEN, A., JOUTSAMO, T., MATTLA, S., KAMARAINEN, T. & JALONEN, J. 2002. Identification of isomeric dicaffeoylquinic acids from *Eleutherococcus senticosus* using HPLC-ESI/TOF/MS and 1H-NMR methods. *Phytochem Anal*, 13, 316-328.
- TOYA, Y. & SHIMIZU, H. 2013. Flux analysis and metabolomics for systematic metabolic engineering of microorganisms. *Biotechnol Adv*, 31, 818-826.
- TSUGAWA, H., CAJKA, T., KIND, T., MA, Y., HIGGINS, B., IKEDA, K., KANAZAWA, M., VANDERGHEYNST, J., FIEHN, O. & ARITA, M. 2015. MS-DIAL: data-independent MS/MS deconvolution for comprehensive metabolome analysis. *Nat Methods*, 12, 523-526.
- TUNGMUNNITHUM, D., THONGBOONYOU, A., PHOLBOON, A. & YANGSABAI, A. 2018. Flavonoids and other phenolic compounds from medicinal plants for pharmaceutical and medical aspects: An overview. *Medicines (Basel)*, 5, 93.
- UOSAKI, Y., YOSHIDA, M., OGAWA, T. & SAITOH, Y. J. T. 1996. RES-1149-1 and-2, novel non-peptidic endothelin type B receptor antagonists produced by *Aspergillus* sp. II. Structure determination and derivatization. *J Antibiot*, 49, 6-12.
- URDIALES, J., MORATA, P., DE CASTRO, I. N. & SÁNCHEZ-JIMÉNEZ, F. 1996. Antiproliferative effect of dehydrodidemnin B (DDB), a depsipeptide isolated from Mediterranean tunicates. *Cancer Lett*, 102, 31-37.
- VAN AGTMAEL, M. A., EGGELTE, T. A. & VAN BOXTEL, C. J. 1999. Artemisinin drugs in the treatment of malaria: from medicinal herb to registered medication. *Trends Pharmacol Sci*, 20, 199-205.

- VERMA, V. C., KHARWAR, R. N. & STROBEL, G. A. 2009. Chemical and functional diversity of natural products from plant associated endophytic fungi. *Nat Prod Commun*, 4, 1511-1532.
- VIANT, M. R., ROSENBLUM, E. S. & TJEERDEMA, R. S. 2003. NMR-based metabolomics: a powerful approach for characterizing the effects of environmental stressors on organism health. *Environ Sci Technol*, 37, 4982-4989.
- VICTOR, M., DAVID, J., SAKUKUMA, M., FRANÇA, E. & NUNES, A. 2017. A simple and efficient process for the extraction of naringin from grapefruit peel waste. *Green Process Synth*, 7, 524-529.
- VILLAS-BÔAS, S. G., MAS, S., ÅKESSON, M., SMEDSGAARD, J. & NIELSEN, J. 2005. Mass spectrometry in metabolome analysis. *Mass Spectrom Rev*, 24, 613-646.
- VONTHRON-SÉNÉCHEAU, C., WENIGER, B., OUATTARA, M., BI, F. T., KAMENAN, A., LOBSTEIN, A., BRUN, R. & ANTON, R. 2003. In vitro antiplasmodial activity and cytotoxicity of ethnobotanically selected Ivorian plants. *J Ethnopharmacol*, 87, 221-225.
- WALL, P. E. 2005. *Thin-layer chromatography: a modern practical approach*, Royal Society of Chemistry.
- WAN, C., LI, S., LIU, L., CHEN, C. & FAN, S. 2017. Caffeoylquinic acids from the aerial parts of *Chrysanthemum coronarium* L. *Plants*, 6, 10.
- WANG, Q. X., YANG, J. L., QI, Q. Y., BAO, L., YANG, X. L., LIU, M. M., HUANG, P., ZHANG, L. X., CHEN, J. L., CAI, L. & LIU, H. W. 2013. 3-Anhydro-6-hydroxy-ophiobolin A, a new sesterterpene inhibiting the growth of methicillin-resistant *Staphylococcus aureus* and inducing the cell death by apoptosis on K562, from the phytopathogenic fungus *Bipolaris oryzae*. *Bioorg Med Chem Lett*, 23, 3547-50.
- WANI, Z. A., ASHRAF, N., MOHIUDDIN, T. & RIYAZ-UL-HASSAN, S. 2015. Plant-endophyte symbiosis, an ecological perspective. *Appl Microbiol Biotechnol*, 99, 2955-2965.
- WECKWERTH, W. 2003. Metabolomics in systems biology. *Ann Rev Plant Biol*, 54, 669-689.
- WENYU, D., QIAN, Y., HUI-MIN, X. & LIAO-BIN, D. 2022. Drimane-type sesquiterpenoids from fungi. *Chin J Nat Med*, 20, 1-13.
- WIKLUND, S. 2008. *Multivariate Data Analysis for Omics*, Umeå, Sweden, MKS Umetrics Ltd.
- WILSON, D. 1995. Endophyte: The evolution of a term, and clarification of its use and definition. *Oikos*, 73.
- WISHART, D. S. 2008. Metabolomics: applications to food science and nutrition research. *Trends Food Sci Technol*, 19, 482-493.
- WISHART, D. S. 2016. Emerging applications of metabolomics in drug discovery and precision medicine. *Nat Rev Drug Discov*, 15, 473-484.
- WISHART, D. S., KNOX, C., GUO, A. C., EISNER, R., YOUNG, N., GAUTAM, B., HAU, D. D., PSYCHOGIOS, N., DONG, E., BOUATRA, S., MANDAL, R., SINELNIKOV, I., XIA, J., JIA, L., CRUZ, J. A., LIM, E., SOBSEY, C. A.,

- SHRIVASTAVA, S., HUANG, P., LIU, P., FANG, L., PENG, J., FRADETTE, R., CHENG, D., TZUR, D., CLEMENTS, M., LEWIS, A., DE SOUZA, A., ZUNIGA, A., DAWE, M., XIONG, Y., CLIVE, D., GREINER, R., NAZYROVA, A., SHAYKHUTDINOV, R., LI, L., VOGEL, H. J. & FORSYTHE, I. 2009. HMDB: a knowledgebase for the human metabolome. *Nucleic Acids Res*, 37, D603-10.
- WISHART, D. S., TZUR, D., KNOX, C., EISNER, R., GUO, A.C., YOUNG, N., CHENG, D., JEWELL, K., ARNDT, D. & SAWHNEY, S. 2007. HMDB: the human metabolome database. *Nucleic Acids Res*, 35, D521-D526.
- WOLD, S., ESBENSEN, K. & GELADI, P. 1987. Principal component analysis. *Chemom Intell Lab Syst*, 2, 37-52.
- WU, C., KIM, H. K., VAN WEZEL, G. P. & CHOI, Y. H. 2015. Metabolomics in the natural products field – a gateway to novel antibiotics. *Drug Discov Today Technol*.
- XIAN, F., HENDRICKSON, C. L. & MARSHALL, A.G. 2012. High resolution mass spectrometry. *Anal Chem*, 84, 708-19.
- YAGI, A., OKAMURA, N., HARAGUCHI, H., ABOT, T. & HASHIMOTO, K. 1993. Antimicrobial tetrahydroanthraquinones from a strain of *Alternaria solani*. *Phytochemistry*, 33, 87-91.
- YAN, J., PANG, J., LIANG, J., YU, W., LIAO, X., AOBULIKASIMU, A., YI, X., YIN, Y., DENG, Z. & HONG, K. 2022. The biosynthesis and transport of ophiobolins in *Aspergillus ustus* 094102. *Int J Mol Sci*, 23, 1903.
- YANG, T., LU, Z., MENG, L., WEI, S., HONG, K., ZHU, W. & HUANG, C. 2012. The novel agent ophiobolin O induces apoptosis and cell cycle arrest of MCF-7 cells through activation of MAPK signaling pathways. *Bioorg Med Chem Lett*, 22, 579-585.
- YU, H., ZHANG, L., LI, L., ZHENG, C., GUO, L., LI, W., SUN, P. & QIN, L. 2010. Recent developments and future prospects of antimicrobial metabolites produced by endophytes. *Microbiol Res*, 165, 437-449.
- YUAN, Z.-L., DAI, C.-C. & CHEN, L.-Q. 2007. Regulation and accumulation of secondary metabolites in plant-fungus symbiotic system. *Afr J Biotechnol*, 6, 1266-1271.
- YULIANA, N. D., KHATIB, A., CHOI, Y. H. & VERPOORTE, R. 2011. Metabolomics for bioactivity assessment of natural products. *Phytother Res*, 25, 157-69.
- YUN, J., LV, Y., YAO, Q., WANG, L., LI, Y. & YI, J. 2012. Wortmannin inhibits proliferation and induces apoptosis of MCF-7 breast cancer cells. *Eur J Gynaec Oncol*, 33, 367-369.
- ZANATTA, A.C., VILEGAS, W. & EDRADA-EBEL, R. 2021. UHPLC-(ESI)-HRMS and NMR-based metabolomics approach to access the seasonality of *Byrsonima intermedia* and *Serjania marginata* from Brazilian Cerrado flora diversity. *Front Chem*, 9, 710025.
- ZHANG, D., FUKUZAWA, S., SATAKE, M., LI, X., KURANAGA, T., NIITSU, A., YOSHIZAWA, K. & TACHIBANA, K. 2012. Ophiobolin O and 6-Epi-

- Ophiobolin O, Two New Cytotoxic Sesterterpenes from the Marine Derived Fungus *Aspergillus* Sp. *Natural Product Communications*, 7, 1934578X1200701102.
- ZHANG, P., LI, X. & WANG, B.-G. 2016. Secondary metabolites from the marine algal-derived endophytic fungi: chemical diversity and biological activity. *Planta Med*, 82, 832-842.
- ZHANG, Z., HE, X., ZHANG, G., CHE, Q., ZHU, T., GU, Q. & LI, D. 2017. Inducing secondary metabolite production by combined culture of *Talaromyces aculeatus* and *Penicillium variable*. *J Nat Prod*, 80, 3167-3171.
- ZHENG, C. J., SHAO, C. L., GUO, Z. Y., CHEN, J. F., DENG, D. S., YANG, K. L., CHEN, Y. Y., FU, X. M., SHE, Z. G., LIN, Y. C. & WANG, C. Y. 2012. Bioactive hydroanthraquinones and anthraquinone dimers from a soft coral-derived *Alternaria* sp. fungus. *J Nat Prod*, 75, 189-97.
- ZHOU, Y., ZHENG, J., LI, Y., XU, D. P., LI, S., CHEN, Y. M. & LI, H. B. 2016. Natural Polyphenols for Prevention and Treatment of Cancer. *Nutrients*, 8.
- ZWENGER, S. & BASU, C. J. B. 2008. Plant terpenoids: applications and future potentials. *Biotechnol Mol Biol Rev*, 3, 1.

10. Appendix

Appendix 1 : nucleotide sequence of *Aspergillus ustus*

>1-ITS1

```
cTGCcncGGGcaGGCCTAACCTCCcaCCCGTGAATACCTGACCAACGTTGCTTCGGCGG
TGCGCCCCCGGGGTAGCCGCCGAGACCACATTGAACCTCTTGTCTTTAGTGTTGT
CTGAGCTTGATAGCAAACCTATTAAACTTTCAACAATGGATCTCTTGGTTCCGGCATC
GATGAAGAACGCAGCGAACTGCGATAAGTAATGTGAATTGCAGAATTCAGTGAATCATC
GAGTCTTTGAACGCACATTGCGCCCCCTGGCATTCCGGGGGGGCATGCCTGTCCGAGCGT
CATTGCTGCCCTTCAAGCCCGGCTTGTGTGTTGGGTCGTCGTCCTCCCTGGGGGACGGG
CCCGAAAGGCAGCGGCGGCACCGCGTCCGGTCTCGAGCGTATGGGGCTTTGTCACCCG
CTCGATTAGGGCCGGCCGGGCGCCAGCCGGCGTCTCCAACCTTCTATTTTACCAGGTTG
ACCTCGGATCAGGTAGGGATACCCGCTGAACTTAAGCATATCAATAAnngga
```

>1- ITS1-EDIT

```
GCCTAACCTCCCACCCGTGAATACCTGACCAACGTTGCTTCGGCGGTGCG
CCCCCGGGGGTAGCCGCCGAGACCACATTGAACCTCTTGTCTTTAGT
GTTGTCTGAGCTTGATAGCAAACCTATTAAACTTTCAACAATGGATCTC
TTGGTTCCGGCATCGATGAAGAACGCAGCGAACTGCGATAAGTAATGTGA
ATTGCAGAATTCAGTGAATCATCGAGTCTTTGAACGCACATTGCGCCCCC
TGGCATTCCGGGGGGCATGCCTGTCCGAGCGTCATTGCTGCCCTTCAAGC
CCGGCTTGTGTGTTGGGTCGTCGTCCTCCCTGGGGGACGGGCCCAGAAAG
CAGCGGCGGCACCGCGTCCGGTCTCGAGCGTATGGGGCTTTGTCACCCG
CTCGATTAGGGCCGGCCGGGCGCCAGCCGGCGTCTCCAACCTTCTATTTT
ACCAGGTTGACCTCGGATCAGGTAGGGATACCCGCTGAACTTAAGCATAT
CAA
```

>1-ITS4

```
gatCcGAGGTCACCTGGTAAAATAGAAGGtTGGAGACGCCGGCTGGCGCCCCGGCCGGCC
CTAATCGAGCGGGTGACAAAGCCCCATACGCTCGAGGACCGGACGCGGTGCCGCCGCTG
CCTTTCGGGCCCGTCCCCAGGGGGGACGACGCCAACACACAAGCCGGGCTTGAAGG
GCAGCAATGACGCTCGGACAGGCATGCCCCCCGGAATGCCAGGGGGCGCAATGTGCGTT
CAAAGACTCGATGATTCACTGAATTCTGCAATTCACATTACTTATCGCAGTTCGCTGCG
TTCTTCATCGATGCCGGAACCAAGAGATCCATTGTTGAAAGTTTTAATAGGTTTGCTAT
CAAGCTCAGACAACACTAAAGACAAGAGGTTCAATGTGGTCTCCGGCGGCTACCCCGG
GGGGGCGCACCCCGAAGCAACGTTGGTCAGGTATTCACGGGTGGGAGGTTAGGCCTGC
CCGGGGGCAGACCTGCACTCGGTAATGATCCTTCCGCAGGTTnAcCCTACGGAAg
```

```

>1- ITS4-EDIT
TGGAGACGCCGGCTGGCGCCCCGGCCGCCCTAATCGAGCGGGTGACAAAG
CCCCATACGCTCGAGGACCGGACGCGGTGCCCGCGCTGCCTTTCGGGCC
GTCCCCCAGGGGGACGACGACCCAACACACAAGCCGGGCTTGAAGGGCA
GCAATGACGCTCGGACAGGCATGCCCCCGGAATGCCAGGGGGCGCAATG
TGC GTTCAAAGACTCGATGATTCACTGAATTCTGCAATTCACATTACTTA
TCGCAGTTCGCTGCGTTCTTCATCGATGCCGGAACCAAGAGATCCATTGT
TGAAAGTTTTAATAGGTTTGCTATCAAGCTCAGACAACACTAAAGACAAG
AGGTTCAATGTGGTCTCCGGCGGCTACCCCCGGGGGGGCGCACCGCCGAA
GCAACGTTGGTCAGGTATTCACGGGTGGGAGGTTAGGCCTGCCCGGGGGC
AGACCTGCACTCGGTAATGATCCTTCCGCAGG

```

BLAST result of *A. ustus* showing 100% similarity

Download GenBankGraphics Next Previous Descriptions

A. ustus strain ATCC 58983 18S ribosomal RNA gene, partial sequence; internal transcribed spacer 1, 5.8S ribosomal RNA gene, and internal transcribed spacer 2, complete sequence; and 28S ribosomal RNA gene, partial sequence

Sequence ID: AY373874.1 Length: 594 Number of Matches: 1

Range 1: 57 to 559 GenBankGraphics Next Match Previous Match

Alignment statistics for match #1

Score	Expect	Identities	Gaps	Strand
929 bits(503)	0.0	503/503(100%)	0/503(0%)	Plus/Plus
Query 1				
GCCTAACCTCCCACCCGTGAATACCTGACCAACGTTGCTTCGGCGGTGCGCCCCCGGG				60
Sbjct 57				
GCCTAACCTCCCACCCGTGAATACCTGACCAACGTTGCTTCGGCGGTGCGCCCCCGGG				116
Query 61				
GGTAGCCGCCGGAGACCACATTGAACCTCTTGTCTTTAGTGTTGTCTGAGCTTGATAGCA				120
Sbjct 117				
GGTAGCCGCCGGAGACCACATTGAACCTCTTGTCTTTAGTGTTGTCTGAGCTTGATAGCA				176
Query 121				
AACCTATTAACCTTTCAACAATGGATCTCTTGGTTCCGGCATCGATGAAGAACGCAGCG				180

```

|||||
Sbjct 177
AACCTATTAACCTTTCAACAATGGATCTCTTGGTTCCGGCATCGATGAAGAACGCAGCG 236

Query 181
AACTGCGATAAGTAATGTGAATTGCAGAATTCAGTGAATCATCGAGTCTTTGAACGCACA 240

|||||
Sbjct 237
AACTGCGATAAGTAATGTGAATTGCAGAATTCAGTGAATCATCGAGTCTTTGAACGCACA 296

Query 241
TTGCGCCCCCTGGCATTCCGGGGGGCATGCCTGTCCGAGCGTCATTGCTGCCCTTCAAGC 300

|||||
Sbjct 297
TTGCGCCCCCTGGCATTCCGGGGGGCATGCCTGTCCGAGCGTCATTGCTGCCCTTCAAGC 356

Query 301
CCGGCTTGTGTGTTGGGTCGTCGTCCCCCCTGGGGGACGGGCCCCGAAAGGCAGCGGCGGC 360

|||||
Sbjct 357
CCGGCTTGTGTGTTGGGTCGTCGTCCCCCCTGGGGGACGGGCCCCGAAAGGCAGCGGCGGC 416

Query 361
ACCGCGTCCGGTCCTCGAGCGTATGGGGCTTTGTCACCCGCTCGATTAGGGCCGGCCGGG 420

|||||
Sbjct 417
ACCGCGTCCGGTCCTCGAGCGTATGGGGCTTTGTCACCCGCTCGATTAGGGCCGGCCGGG 476

Query 421
CGCCAGCCGGCGTCTCCAACCTTCTATTTTACCAGGTTGACCTCGGATCAGGTAGGGATA 480

|||||
Sbjct 477
CGCCAGCCGGCGTCTCCAACCTTCTATTTTACCAGGTTGACCTCGGATCAGGTAGGGATA 536

Query 481 CCCGCTGAACTTAAGCATATCAA 503
          |||||
Sbjct 537 CCCGCTGAACTTAAGCATATCAA 559

```

Appendix 2 : nucleotide sequence of *A. solani*

>1-ITS1

GGGCTGGCaCCTCCCGGGGTGGCCaGCCTTGCTGAATTATTCCACCCGTGTCTTTTGGC
TACTTCTTGTTTCCTTGGTGGGCTCGCCCACCACAAGGACCAACCATAAACCTTTTGG
CAATGGCAATCAGCGTCAGTAACAATGTAATAATTTACAACCTTCAACAACGGATCTCT
TGGTTCTGGCATCGATGAAGAACGCAGCGAAATGCGATAAGTAGTGTGAATTGCAGAAT
TCAGTGAATCATCGAATCTTTGAACGCACATTGCGCCCTTTGGTATTCCAAAGGGCATG
CCTGTTTCGAGCGTCATTTGTACCCTCAAGCTTTGCTTGGTGTGGGGCGTCTTTTTGTCT
CCCCTTGCGGGAGACTCGCCTTAAAGTCATTGGCAGCCGGCCTACTGGTTTCGGAGCGC
AGCACAAGTCGCGCTCTTCCAGCCCCAAGGTCTAGCATCCACCAAGCCTTTTTTTTC
AACTTTTGACCTCGGATCAGGTAGGGATACCCGCTGAACTTAAGCATATCAATAancGG
AGGAa

>1- ITS1-EDIT

GGGCTGGATGATGCGGGCTGGCACCTCCCGGGGTGGCCAGCCTTGCTGAATTATTCCAC
CCGTGTCTTTTGGTACTTCTTGTTTCCTTGGTGGGCTCGCCCACCACAAGGACCAACC
CATAAACCTTTTTGCAATGGCAATCAGCGTCAGTAACAATGTAATAATTTACAACCTTC
AACCAACGGATCTCTTGGTTCTGGCATCGATGAAGAACGCAGCGAAATGCGATAAGTAGT
GTGAATTGCAGAATTCAGTGAATCATCGAATCTTTGAACGCACATTGCGCCCTTTGGTA
TTCCAAAGGGCATGCCTGTTTCGAGCGTCATTTGTACCCTCAAGCTTTGCTTGGTGTGG
GCGTCTTTTTGTCTCCCCTTGCGGGAGACTCGCCTTAAAGTCATTGGCAGCCGGCCTAC
TGGTTTCGGAGCGCAGCACAAGTCGCGCTCTCTTCCAGCCCCAAGGTCTAGCATCCACC
AAGCCTTTTTTTTTCAACTTTTGACCTCGGATCAGGTAGGGATACCCGCTGAACTTAAGC
ATATCAATAAGCGGAGGAA

>1-ITS4

GTTGAAAAAAAGGcTTGGTGGATGCTAGACCTTGGGGCTGGAAGAGAGCGCGACTTGT
GCTGCGCTCCGAAACCAGTAGGCCGGCTGCCAATGACTTTAAGGCGAGTCTCCCGCAAG
GGGAGACAAAAAGACGCCCAACACCAAGCAAAGCTTGAGGGTACAAATGACGCTCGAAC
AGGCATGCCCTTTGGAATACCAAAGGGCGCAATGTGCGTTCAAAGATTTCGATGATTCAC
TGAATTCTGCAATTCACACTACTTATCGCATTTCGCTGCGTTCTTCATCGATGCCAGAA
CCAAGAGATCCGTTGTTGAAAGTTGTAAATTATTACATTGTTACTGACGCTGATTGCCA
TTGCAAAAAGGTTTATGGGTTGGTCCTTGTGGTGGGCGAGCCCACCAAGGAAACAAGAA
GTACGCAAAAAGACACGGGTGGAATAATTAGCAAGGCTGGCCACCCGGGAGGTGCCAG
CCCGCCTTCATATTTGTGTAATGATCCCTCCGCAgGTTACcTACGGAa

```
>1- ITS4-EDIT
GTTGAAAAAAAAGGcTTGGTGGATGCTAGACCTTGGGGCTGGAAGAGAGCGCGACTTGT
GCTGCGCTCCGAAACCAGTAGGCCGGCTGCCAATGACTTTAAGGCGAGTCTCCCGCAAG
GGGAGACAAAAAGACGCCCAACACCAAGCAAAGCTTGAGGGTACAAATGACGCTCGAAC
AGGCATGCCCTTTGGAATACCAAAGGGCGCAATGTGCGTTCAAAGATTCGATGATTCAC
TGAATTCTGCAATTCACACTACTTATCGCATTTCGCTGCGTTCTTCATCGATGCCAGAA
CCAAGAGATCCGTTGTTGAAAGTTGTAAATTATTACATTGTTACTGACGCTGATTGCCA
TTGCAAAAAGGTTTATGGGTTGGTCCTTGTGGTGGGCGAGCCCACCAAGGAAACAAGAA
GTACGCAAAAAGACACGGGTGGAATAATTCAGCAAGGCTGGCCACCCCGGGAGGTGCCAG
CCCGCCTTCATATTTGTGTAATGATCCCTCCGCAGGTTACACtACGGAA
```

BLAST result of *A. solani* showing 100% similarity

A. solani isolate AS-14 internal transcribed spacer 1, partial sequence; 5.8S ribosomal RNA gene and internal transcribed spacer 2, complete sequence; and large subunit ribosomal RNA gene, partial sequence

Sequence ID: KY462708.1 Length: 539 Number of Matches: 1

Range 1: 2 to 539 GenBank Graphics Next Match Previous Match

Alignment statistics for match #1

Score	Expect	Identities	Gaps	Strand
994 bits(538)	0.0	538/538(100%)	0/538(0%)	Plus/Plus

```
Query 13
GCGGGCTGGCACCTCCCGGGGTGGCCAGCCTTGCTGAATTATTCCACCCGTGTCTTTTGC 72
|||||
Sbjct 2
GCGGGCTGGCACCTCCCGGGGTGGCCAGCCTTGCTGAATTATTCCACCCGTGTCTTTTGC 61

Query 73
GTACTTCTTGTTTCCTTGGTGGGCTCGCCCACCACAAGGACCAACCCATAAACCTTTTTG 132
|||||
Sbjct 62
GTACTTCTTGTTTCCTTGGTGGGCTCGCCCACCACAAGGACCAACCCATAAACCTTTTTG 121

Query 133
CAATGGCAATCAGCGTCAGTAACAATGTAATAATTTACAACCTTCAACAACGGATCTCTT 192
|||||
```

Sbjct 122
CAATGGCAATCAGCGTCAGTAACAATGTAATAATTTACAACCTTTCAACAACGGATCTCTT 181

Query 193
GGTTCTGGCATCGATGAAGAACGCAGCGAAATGCGATAAGTAGTGTGAATTGCAGAATTC 252

|||||
Sbjct 182
GGTTCTGGCATCGATGAAGAACGCAGCGAAATGCGATAAGTAGTGTGAATTGCAGAATTC 241

Query 253
AGTGAATCATCGAATCTTTGAACGCACATTGCGCCCTTTGGTATTCCAAAGGGCATGCCT 312

|||||
Sbjct 242
AGTGAATCATCGAATCTTTGAACGCACATTGCGCCCTTTGGTATTCCAAAGGGCATGCCT 301

Query 313
GTTTCGAGCGTCATTTGTACCCTCAAGCTTTGCTTGGTGTGGGCGTCTTTTTGTCTCCCC 372

|||||
Sbjct 302
GTTTCGAGCGTCATTTGTACCCTCAAGCTTTGCTTGGTGTGGGCGTCTTTTTGTCTCCCC 361

Query 373
TTGCGGGAGACTCGCCTTAAAGTCATTGGCAGCCGGCCTACTGGTTTCGGAGCGCAGCAC 432

|||||
Sbjct 362
TTGCGGGAGACTCGCCTTAAAGTCATTGGCAGCCGGCCTACTGGTTTCGGAGCGCAGCAC 421

Query 433
AAGTCGCGCTCTCTTCCAGCCCCAAGGTCTAGCATCCACCAAGCCTtttttttCAACTTT 492

|||||
Sbjct 422
AAGTCGCGCTCTCTTCCAGCCCCAAGGTCTAGCATCCACCAAGCCTTTTTTTTCAACTTT 481

Query 493 TGACCTCGGATCAGGTAGGGATACCCGCTGAACTTAAGCATATCAATAAGCGGAGGAA
550

|||||
Sbjct 482 TGACCTCGGATCAGGTAGGGATACCCGCTGAACTTAAGCATATCAATAAGCGGAGGAA
539

Appendix 3: dilution curves of *Aspergillus ustus* against ZR-75 and HS-27 cells

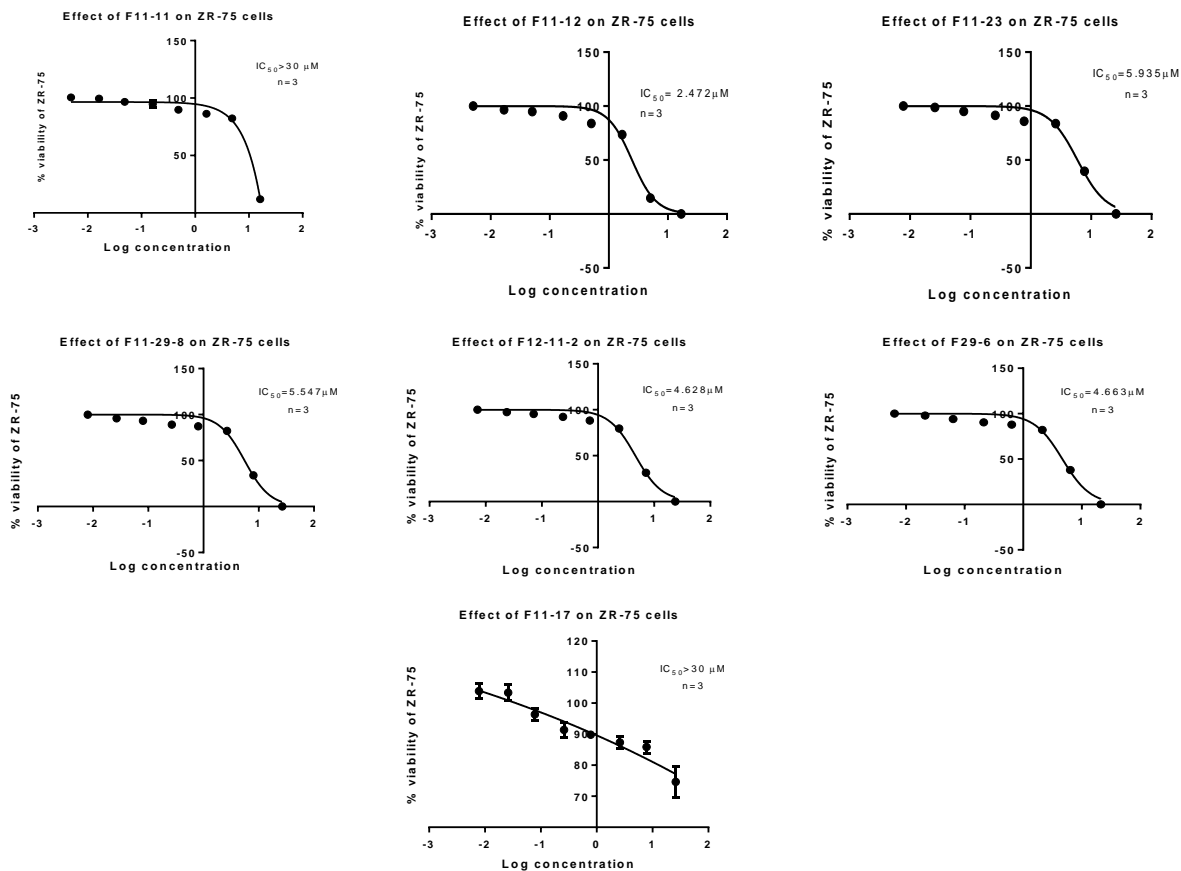


Figure 1: Dilution curves for the compounds isolated from *A. ustus* when tested against breast cancer (ZR-75) cell line to determine their IC_{50} values in μM .

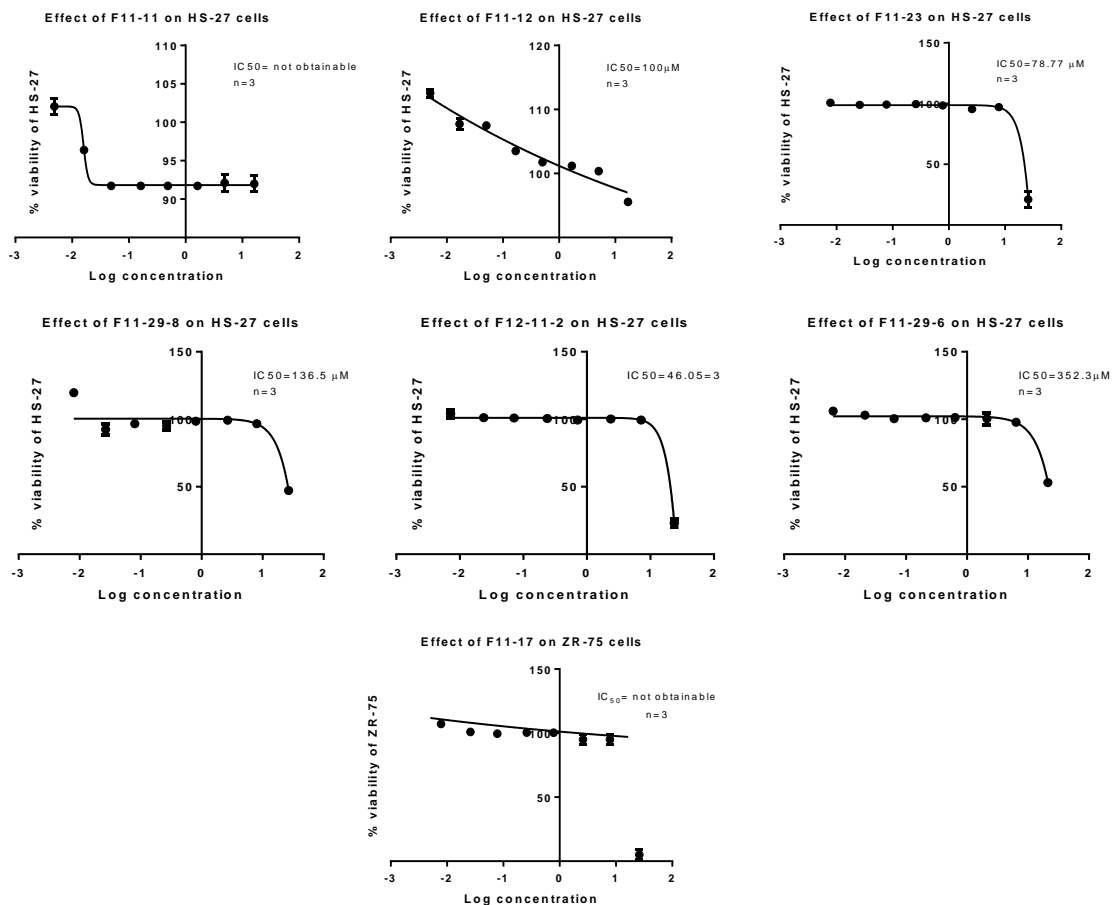


Figure 2: Dilution curves for the compounds isolated from *A. ustus* when tested against normal fibroblast Foreskin (HS-27) cell line to determine their IC₅₀ values in μM